DOTTORATO DI RICERCA IN
" SCIENZE DELL'INGEGNERIA "

CICLO XXXV

COORDINATORE Prof. Ing. Stefano Trillo

LOCAL SITE SEISMIC RESPONSE IN AN INTER-ANDEAN VALLEY: GEOTECHNICAL CHARACTERIZATION AND SEISMIC AMPLIFICATION ZONATION OF THE SOUTHERN QUITO AREA

Settore Scientifico Disciplinare ICAR/07

Dottorando
Dott. Jorge David Albuja Sánchez

Jorge Albuja
____
(firma)

Tutore
Prof. Ing. Vincenzo Fioravante

____
(firma)

Anni 2019/2022

ACKNOWLEDGEMENTS

Funding for this research was provided as part of the development of the Local seismic response of Quito project, which is financed by the Municipality of the Metropolitan District of Quito, Escuela Politécnica Nacional, and the Pontificia Universidad Católica del Ecuador, the latter who provided support to the author to follow a *Dottorato di Ricerca in Scienze dell'Ingegnería* (Ph.D. Course in Engineering Science) at Università degli Studi di Ferrara.

The author thanks the collaboration and assistance of Istituto Sperimentale Modelli Geotecnici ISMGEO S.r.l., who supported the author to perform a research period in Seriate (Bergamo), Italy, to carry out the execution and interpretation of advanced geotechnical tests, including the resonant column, needed for the culmination of the present thesis. The review, comments, and suggestions to improve this work made by Prof. Daniela Giretti (Dipartimento di Ingegneria e Scienze Applicate, Università degli Studi di Bergamo), Ing. Francesca Bozzoni (Dip. Scenari di Rischio, EUCENTRE) and Prof. Giuseppe Lanzo (Dip. Ingegneria Strutturale e Geotecnica, Sapienza Università di Roma) are sincerely appreciated. The support from the Soil Mechanics and Geotechnics laboratory of the Pontifical Catholic University of Ecuador is also estimated, entity that allowed me to use their equipment to perform the field and laboratory tests required, especially the assistance and brace from Mariela Anaguano.

The honest advice and thorough supervision from Prof. Vincenzo Fioravante during the development of this dissertation are sincerely acknowledged. This endeavor would not have been possible without his guidance, support, and encouragement.

Finally, I must express my very profound gratitude and love to my parents, María and Jorge, and to my sister, Ana Mercedes, who provided me with unfailing support and continuous encouragement not only through the process of the program and the development of the dissertation but throughout my entire life. Words cannot express my gratitude to my girlfriend Andrea Fernanda, for sharing her love, patience, and time, especially in difficult moments. This accomplishment would not have been possible without them. We made it together. Thank you so much for everything.

ABSTRACT

Over the last century, earthquakes have claimed the lives of thousands of people and caused considerable damage to existing buildings in several places in South America. According to Chunga et al (2018), in Ecuador, there are records since 1906 showing significant events with magnitudes between Mw 7.1 and Mw 8.8. However, the population has not been aware of the potential effects of an earthquake of these magnitudes, causing considerable seismic vulnerability due to unstudied and low-cost informal constructions. For this reason, the necessity to analyze the local seismic response of the South Quito area arises, evaluating the seismic amplification considering the lithostratigraphic and geomorphological characteristics of the inter-Andean area. To achieve this, 20 boreholes of 30 m depth distributed in this area were complemented with a campaign of 1332 field tests and 2774 laboratory tests. The information obtained from the campaign was used to form 9 zones consisting of one or a group of boreholes according to their geographic location, physical and mechanical characteristics, generating a soil column for each zone. Three types of analysis were carried out to define the soil dynamic parameters: with theoretical values, with parameters derived from dry and remolded samples, performing a total of 46 resonant column tests. The results showed that, for the 9 defined zones in southern Quito, the amplification factors ranged between 3.07 and 7.74, which helps us to evaluate the vulnerability of this area of the city, by zoning and risk mapping. Nevertheless, the need for further investigation of the subsoil is emphasized, in addition to the analysis of amplification factors based on the earthquakes in this sector.

INDEX

LIST OF FIGURES

LIST OF TABLES

LIST OF SYMBOLS

Roman (Uppercase)

A	amplitude
C_c	compressibility coefficient
E_{50}	elasticity modulus at 50% of failure, kg/cm^2.
F	damping force
F_r	normalized friction ratio
Fs	factor of safety against to liquefaction
H	total height of considered soil
H_i	thickness of the discretized soil layers
IP	plasticity index, percentage.
LL	liquid limit
LP	plastic limit, percentage.
N	number of blows of SPT Test
N_1, $N_{1(60)}$	corrected number of blows (granular soils)
PI	plastic index

Q_t	normalized cone resistance
S_a	pseudo-spectrum acceleration
S_d	pseudo-spectrum displacement
S_v	pseudo-spectrum velocity
V_{si}	i-stratum shear wave velocity
V_s	shear wave velocity unto interest-site
V_s	shear wave velocity, m/s.
V_p	compression wave velocity, m/s.
$\%G$	gravel percentage.
$\%S$	sand percentage.

Roman (Lowercase)

a	area ratio of the cone
a_{max}	peak horizontal acceleration at ground surface
c	damping coefficient
c	cohesion of soil, kg/cm^2.
e_0	initial void ratio
g	acceleration of gravity
h_i	i-stratum height.
n	number of considered stratums of soils.
p_a	atmospheric pressure = 1 bar ≈ 100kPa
q_c	CPT tip resistance
q_t	corrected cone resistance
r_d	depth stress reduction factor
t	time
$w, \%w$	moisture content
w_L	liquid limit
w_n	natural moisture content
$\ddot{x}_g$	external acceleration
z	displacement

Greek (Uppercase)

Greek (Lowercase)

ζ	fraction of critical damping or damping ratio.

σ_c	confinement stress, kg/cm^2.
σ_{vo}, σ_v	overburden pressure (total)
σ'_v	overburden pressure (effective)
ϕ	friction angle, °.
ω	angular velocity, rad per unit of time
ω_d	damped natural frequency
ω_n	undamped natural circular frequency

CHAPTER 1

Introduction

1.1. Background

Over the past century, earthquakes have caused significant damage and tens of thousands of casualties along South America (Petersen et al. 2018), with significant events of moments magnitude between Mw 7.1 and Mw 8.8 occurring in Ecuador, having records from these events since 1906 (Chunga et al. 2018). However, Ecuadorians were unaware for decades of the potential effects of an earthquake of this magnitude, building at a low cost without taking into consideration seismic properties, resulting in a considerable seismic vulnerability (Villalobos et al. 2018).

On April 16, 2016, a powerful earthquake with a moment magnitude of Mw 7.8 shook the northern coastal provinces of Ecuador, with its epicenter located near the city of Pedernales (Lopez J., Vera-Grunauer X., Rollins K. 2018; Mera et al. 2017). A lot of structural and nonstructural damage was caused, with more than 30.000 buildings affected, more than 7.000 were totally or partially destroyed, and the associated damages were estimated in around 3.34 billion US Dollars (Mera et al. 2017). Thus, generating both human and economic calamities. The collapse of the buildings and infrastructure caused 663 deceases, nine missing people, 6274 injured, and 28,775 displaced (Goretti, Molina Hutt, and Hedelund 2017).

Most of the damage suffered by the buildings was caused by the influence of the site's amplification of the soil, liquefaction phenomena, wrong structural typologies, and inadequate construction practices predominant in Ecuador (Mera et al. 2017). An adequate understanding of these causes could prevent similar losses to happen again and allow civil society and governmental authorities to prepare more resiliently for future events. For this reason, a study to obtain adequate soil parameters, both through laboratory and field tests, could provide the knowledge to develop a more robust approach with safer and more cost-effective viable designs, highly beneficial in a developing country like Ecuador, especially considering future investment in much-needed infrastructure of various kinds.

This research will focus on Quito, the capital city of Ecuador (Fig. 1a), which is situated in a narrow Inter-Andean depression at 2200-3000 meters above the sea level, in a zone of high seismic and volcanic activities, and that has been damaged historically by earthquakes (Alfonso Naya et al. 2012a; Alvarado et al. 2014; Escuela Politecnica Nacional et al. 1994; Pacheco et al. 2022; Watson et al. 2022) The population of Quito is nearly 3 million inhabitants, the city is built over a hanging wall of an active reverse fault system, named the Quito Fault System (QFS), which accommodates an estimate of 4.3-5.3 mm per year, limits the extension of Quito to the east, and allows a seismic events of magnitude 6-5-7.0 to be possible (Alvarado et al. 2014; Laurendeau et al. 2017).

The possibility of seismic events due to the several faults and volcanoes around Quito, the presence of soft compressible soils (Albuja-Sánchez 2021; Peñafiel 2008), the lack of adequate studies, the abundance of inadequate construction methods, and the possibility of seismic amplification, especially in the South of Quito (Alfonso Naya et al. 2012a) could be devastating, making the seismic hazard assessment an important issue for the city (Alfonso Naya et al. 2012a; Alvarado et al. 2014; Escuela Politecnica Nacional et al. 1994; A Laurendeau et al. 2017; Mariniere et al. 2020; Pacheco et al. 2022; Watson et al. 2022).

To evaluate the seismic response of the south of Quito, several field geotechnical testing of Cone Penetration tests (CPT), Seismic Dilatometer tests (SDMT) and Standard Penetration tests (SPT), laboratory tests to determine the mechanical and dynamical properties of the soils, and the use of geophysical data will be combined for interpretation. This methodology for site has been previously performed in potentially seismic areas, using the CPT (Giretti and Fioravante 2017) and both CPT and SDMT combined with advanced laboratory tests (Castelli and Lentini 2017; Cavallaro, Capilleri, and Grasso 2018) performed in Italy, obtaining methods to evaluate dynamic properties of soil for seismic evaluation and design. A similar development is what this research project aims to achieve for the case of Quito, Ecuador. The results from this research will be used as part of the development of the Local seismic response of Quito, which is financed by the *Municipality of Quito*, *Escuela Politécnica Nacional* and the *Pontificia Universidad Católica del Ecuador*, and could be used for future studies.

1.2. Objective

The main objective of this thesis is to analyze the local-site seismic response in the Southern Quito area, located in an Inter-Andean valley in the north of Ecuador, South America, evaluating possible seismic amplification phenomena, considering its lithostratigraphic and geomorphological specific characteristics obtained from the geology, geophysics, and geotechnics. To achieve this objective, the following secondary objectives will be carried out:

- Compilation of the available literature that identify the geological and structural settings, as well as the geophysical and geotechnical data.
- Geotechnical study to determine the static and dynamic response parameters, with field and laboratory tests.
- Evaluation of the input seismic motion for the amplification effect analysis at the surface.
- Proposal of a synthetic map of the analyzed area with the obtained results. The obtained results will be expressed in terms of amplification ratio function.

1.3. Thesis structure

For a better understanding and organization, the thesis structure will be divided in the chapters reviewed in this dissertation; also, a synthesis of the chapter.

Chapter 2 – Tectonic and Geological setting

A geological, geoformological and geographical analysis of the Interandean Depression in the Andes Mountain range (2400–3000 m in elevation), where Quito is located, was reviewed. Three N–S trending geological and geomorphic zones were distinguished: (1) the coastal plain to the west (Costa), (2) the central Andean mountainous area and (3) the eastern lowlands (Oriente) which are part of the upper Amazon basin. The Andean range, 150 km wide on average, includes three geological and geomorphic zones: the Western Cordillera, the Interandean Valley, and the Eastern Cordillera (Cordillera Real). The Interandean Valley is a geomorphic depression not wider than 30 km that is very well developed between the two cordilleras and filled with Quaternary volcanoclastic and pyroclastic deposits (Beauval et al. 2013). This region has over 18 volcanic centers, which can be seen. Its morphology is marked by volcanic fillings and their interaction with Quaternary to recent Holocene glaciers or alluvial deposits. (Alvarado et al. 2014).

Quito has approximately 127.7 square kilometers, where 53.7 kilometers make up the southern valley and is known as "Turubamba". A summary of the geological formation in this area was presented. The subsoil has a very strong presence of lake deposits and anthropic fillings, which explain the lack of acceptable mechanical properties in upper layers (Albuja-Sánchez 2021; Avilés 2013; Santander 2013; Celi and Moyano 2017). Five zones are known, with the worst being a lithologically deposited in fluvio-lacustrine environments and belong to silt-sandy sequences, filled areas, swampy areas with abundant content of organic matter and peat, have low resistance to penetration, have problems of low bearing capacity, high humidity, low to medium plasticity, and surface water tables (Avilés 2013). (See figure 14).

Ecuador is situated in a complicated geodynamic setting involving a continental tectonic block and a microplate, in front of an active subduction zone. Some of the greatest earthquakes occurred due to subduction of the Nazca plate. However, lower magnitude but shallower and more destructive earthquakes have originated in crustal faults near populated areas, in this case caused by the Quito Fault System – QFS (Alvarado et al. 2014).

Several seismic hazard measurements have been performed in Quito; however, they were performed mostly using correlations of the dynamic properties based on the Unified Soil Classification System (USCS), and limited laboratory available information. In the case of southern Quito, only one point has been considered for the entire area. Being highly heterogeneous, and being the area that according to the literature is more prone to suffering devastating effects from an earthquake, there is a need to broadly deepen the study in this area, with a greater number of perforations, field and laboratory tests, geotechnical interpretation, and obtaining the shear modulus of the soil G, shear wave velocity Vs, the damping ratios and the reduction modulus G/Gmax versus shear strain, which is proposed in this research.

Chapter 3 – Experimental set-up

Considering the heterogeneity, as well as the existence of soft soils, 20 points were planned, each one with an SPT, CPT, DMT, and SDMT test, as well as obtaining samples up to 30 meters deep. For each test meter, it was complemented with a set of complete geotechnical tests to characterize the strata, including granulometry, hydrometry, liquid and plastic limit, water content, natural density, one-dimensional consolidation, unconfined compression, and consolidated undrained triaxials. A total of 2774 physical and mechanical tests were performed in the recovered altered and unaltered samples, combined with the 1332 field tests.

All the information was processed and analyzed, and it was defined that there are 9 zones with similar geotechnical characteristics (see section 5.2.1). In addition to the determined areas, 6 cross-sectional profiles and 4 longitudinal profiles were evaluated. With the geotechnical profiles, as well as the compiled graphs of each zone, 25 strata with similar properties were determined, in order to carry out the resonant column tests.

Chapter 4 – Dynamic properties of soil

Due to the complex nature, geometry, distribution, and propagation of seismic waves in the ground, it is necessary to define their behavior under dynamic loads by means of dynamic parameters. Nowadays, there are different field and laboratory techniques to evaluate these parameters, each one with its own advantages and limitations. For this reason, it is important to define the deformation levels to which the analysis will be exposed. In the present case study, the effect of wave propagation in the soil was analyzed for low levels of deformation. For this purpose, it was necessary to define the theoretical context to be applied as: Linear Equivalent Analysis, factors influencing the dynamic behavior (Confinement pressure, duration of confinement application, degree of OCR, number of loading cycles), as well as the results obtained by equations or regressions based on literature, for example: Rollins et al. (1998), Darendeli (2001), Zhang et al. (2005), among others.

Furthermore, the equipment used in the resonant column test, TSH-100 developed by GCTS Testing Systems, is described. This system allows us to simulate a fixed-free system that allows us to apply a torque on the upper part of the specimen. Three types of analysis were performed: theoretical, dry specimens, remolded specimens. However, for the analysis on dry and remolded samples it was planned to perform 25 resonant columns, however, due to the absence of material, 23 were performed for each analysis, thus generating a total of 46 resonant columns, from which we obtained the degradation curves of shear modulus and damping, generating a total of 92 curves. These curves were obtained using the TSH-100 resonant column testing equipment, which is performed through an interative process with the objective of obtaining a set of data that helps to elaborate shear modulus and damping degradation curves by means of parametric regressions using MATLAB.

Chapter 5 – Local seismic response

The local seismic response is described as the set of changes in amplitude, duration and frequency of a seismic motion related to bedrock. This represents a key parameter for seismic hazard assessment and risk mitigation, since subsurface conditions can greatly influence the level of amplification of ground motion amplification at the surface level due to the action of an earthquake. The deep structure of the Quito basin has not yet been studied, so its shape, extension and the impact of seismic waves are unknown. Therefore, the need to study local conditions arises. In conjunction with the field and laboratory tests established in Chapter 3 and the information provided by (Pacheco et al. 2022), to define the depth of bedrock, 9 zones have been defined, which are represented by a soil column representing a well or a group of wells grouped based on their geographic location and physical and mechanical properties.

Section 5.3. defines the earthquakes or input movements that will act on the bedrock, taking into consideration that the Quito fault corresponds to a 60 km long reverse blind fault system, with magnitudes from 5.7 to 6.6, thus obtaining 7 input movements. In addition, the types of analysis and models used to determine the soil response analysis are mentioned, such as: Linear, Linear Equivalent and Non-linear analysis. Finally, the results obtained from the theoretical analysis and the analysis with dry and remolded samples for each zone are presented.

Finally in Chapter 7, the conclusions of the thesis will be presented.

CHAPTER 2

Tectonic and Seismo-Tectonic Framework

2.1. Geological overview

2.1.1. Geography and geomorphology

Quito, the capital city of Ecuador, is the most populated metropolitan district in the country, with 2,781,641 inhabitants projected for 2020 (INEC 2022), located inland in a narrow valley (~5 to 8 km wide and 40 km long), called Interandean Depression in the Andes mountain range (2400–3000 m in elevation), surrounded by active and potentially active volcanoes (up to 5897 meters in elevation at the Cotopaxi Volcano) located on the western and eastern (also known as *"Cordillera Real"*) mountain ranges parallel to each other (Courboulex et al. 2022; Aurore Laurendeau et al. 2017) (Figs. 1 and 2).

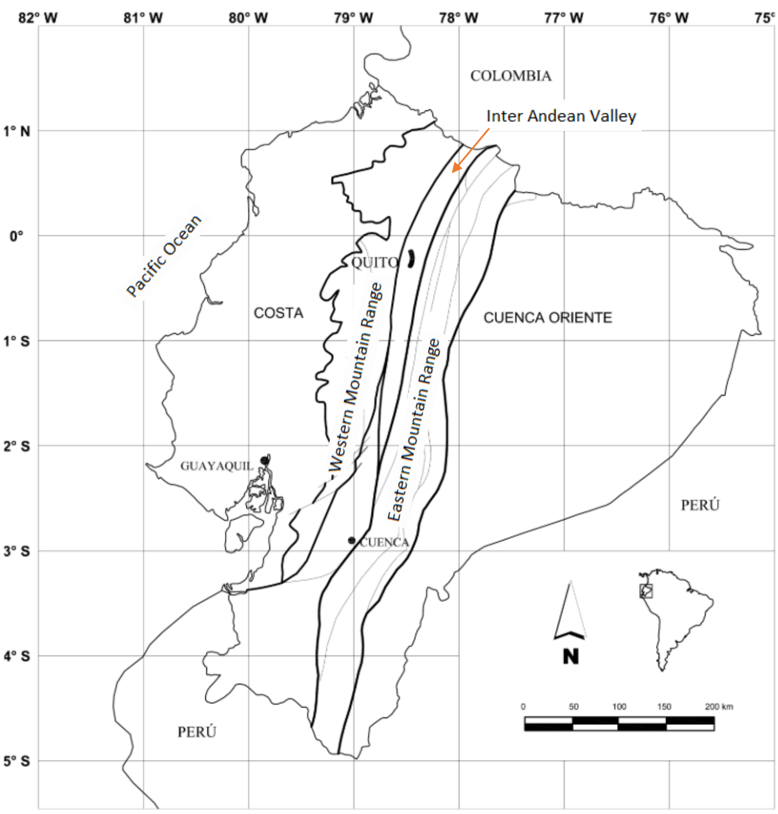

Figure 1. Location of Quito in the Inter Andean Valley, between the Eastern and Western Mountain range, modified from (Peñafiel 2008)

Based on Beauval et al. 2013, in Ecuador, three N–S trending geological and geomorphic zones can be distinguished: (1) the coastal plain to the west (Costa), (2) the central Andean mountainous area and (3) the eastern lowlands (Oriente) which are part of the upper Amazon basin and can be seen in Figure 1 and 2. The Andean range, 150 km wide on average, includes the three geological and geomorphic zones mentioned: the Western Cordillera, the Interandean Valley, and the Eastern Cordillera (Cordillera Real). The high Interandean Valley is a geomorphic depression not wider than 30 km that is very well developed between the two cordilleras and filled with Quaternary volcanoclastic and pyroclastic deposits north of latitude 1.7◦ S. South of 1.7◦ S, spacious intramountainous basins show sedimentary fillings lacking the fresh volcanic deposits of the Interandean Valley due to the absence of Quaternary volcanic activity. Almost half of the Ecuadorian population resides in the Andean mountainous area. (Beauval et al. 2013)

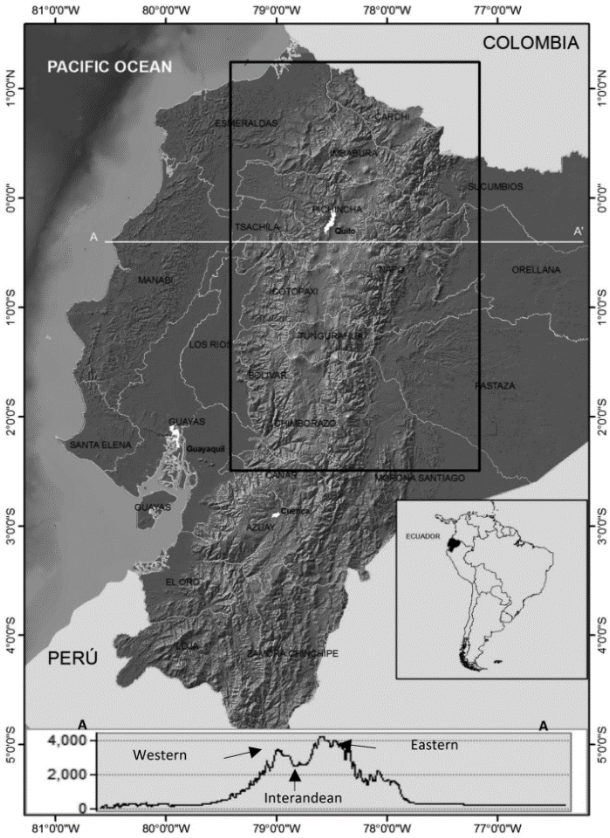

Figure 2. Location of Quito in the Inter Andean Valley. A-A' is topographic profile showing the Interandean Valley and both bordering mountain ranges: the Western and Eastern Cordilleras. Obtained from (Beauval et al. 2013)

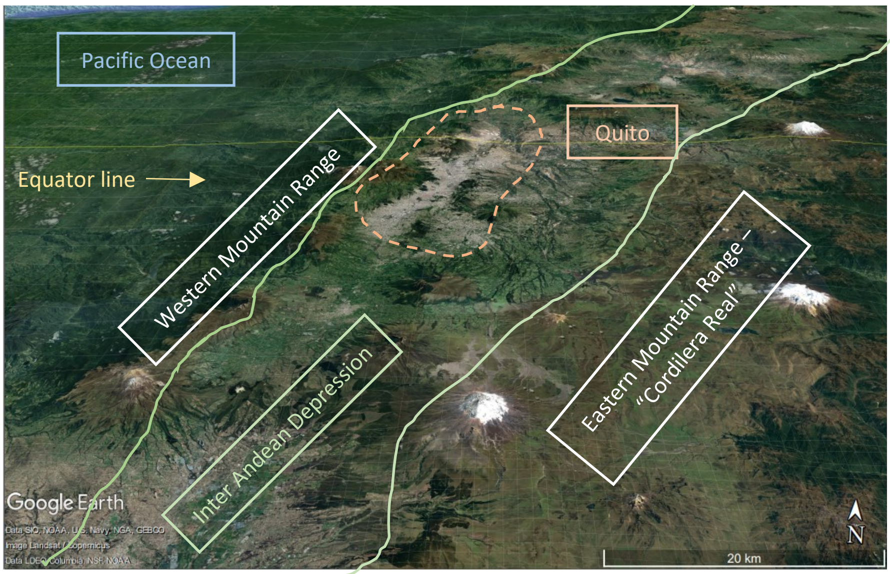

Figure 3. Satellite image of Quito in the Inter Andean depression, adapted from Google Earth Pro

As mentioned before, the city of Quito is in a topographic depression, forming a basin that bears the same name, in an N-S direction. This basin was formed by the activity of the Quito reverse fault system, which has generated a series of elongated hills on the edges of the city (Villagómez 2003). This basin is approximately 30 km long and up to 5 km wide, which is divided into 3 sub-basins, the first one called the central-north sub-basin, the second one called the south sub-basin, divided by the *"Machángara"* River, and by the dome *"El Panecillo"* [(Albuja-Sánchez 2021; Alvarado 1996; Peñafiel 2008; Villagómez 2003).

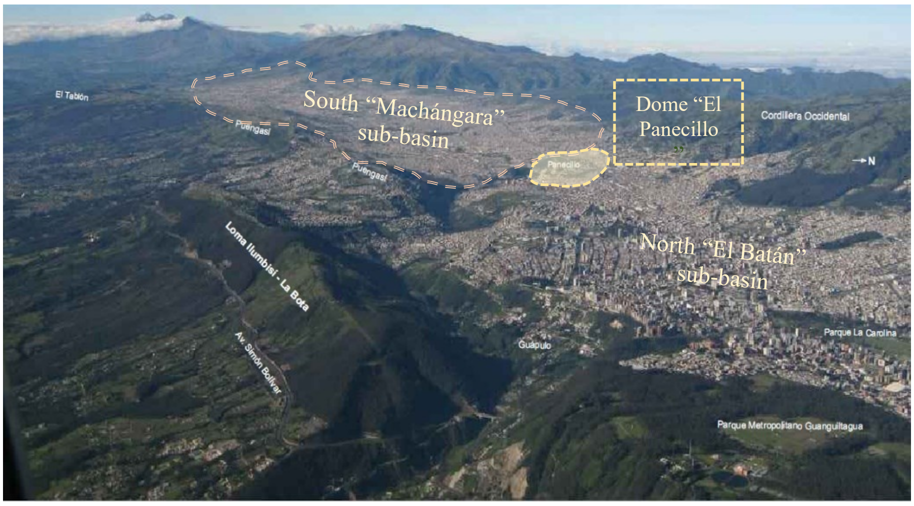

Figure 4. Aerial image of Quito in the Inter Andean depression, adapted from (Trujillo Tamayo 2015)

A third sub-basin north from Quito is mentioned by Alvarado 2013, “The San Antonio sub-basin”. The division of the first two sub-basins is transferred to the sectors that are given to the city, being the south everything that is south of the Dome “*El Panecillo*”, and the north the opposite. A 3d section obtained with *Infraworks* allows us to see this division more clearly, as well as part of the inter-Andean depression mentioned in this introduction in Figure 5. An aerial view obtained from (Trujillo Tamayo 2015) can be seen in Figure 4.

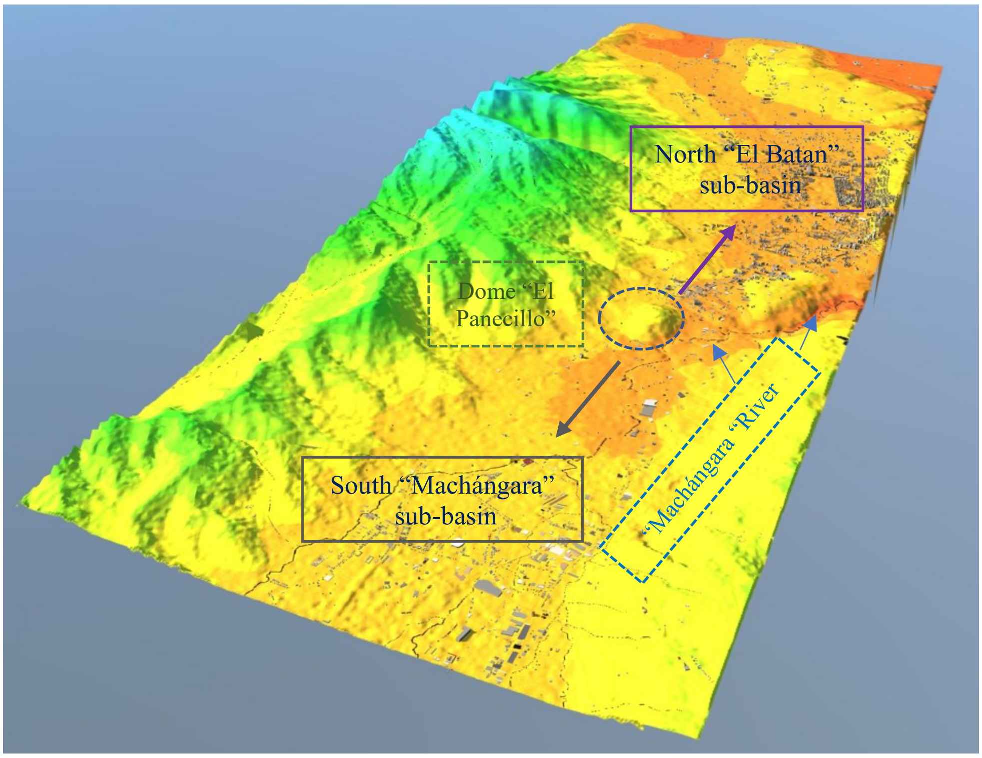

Figure 5. Satellite image of Quito in the Inter Andean depression, adapted from *Infraworks*, 2022.

Due to the increasing urban and industrial development, Quito grows towards the North, the valleys, or towards the South, being in this last sector where there are the greatest number of construction problems, mainly settlements due to highly compressible soft and organic soils (Albuja-Sánchez 2021; Santander 2013). The southern sub-basin is made up of a system of streams that drain towards the “Machángara” River to the north, and to the “Saguanchi” ravine to the south, with a variable height between 3080 and 2800 meters over the sea level, which can be seen in Figure 6. Quito has an approximate of 127.7 square kilometers, where 53.7 kilometers make up the southern valley of Quito, and which is known as

"Turubamba". In this region it is thought that previously existed a lagoon, which during its partial drainage to the “Machángara” River, left a high-water level, with traces of organic material, forming a swampy terrain, called "Turubamba" by the locals, which translates into "Plain of mud" or "Land of Swamps". (Albuja-Sánchez 2021; Avilés 2013; Santander 2013).

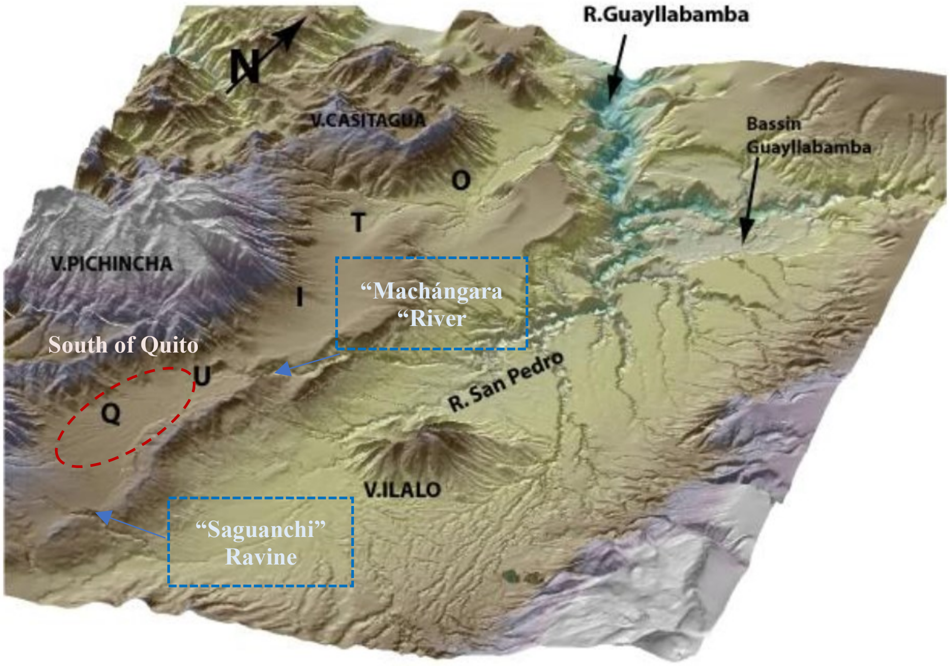

Figure 6. 3D view towards the NE of the Quito area, with a complete view of the Inter Andean depression and some of its surrounding volcanoes, from (Alvarado 2013). The red dashed line shows the place of analysis in the present work

The two cordilleras are crowned by several volcanic peaks. This region has over 18 volcanic centers, which can be seen in Figure 7. Its morphology is marked by volcanic fillings and their interaction with Quaternary to recent Holocene glaciers or deposits. The last building to erupt was the Guagua Pichincha volcano, between 1999 and 2001, and is considered the only seismically active volcano in this region (Alvarado et al. 2014), with its eruptive products mainly directed towards the west, its crater being open towards this direction. Apart from this eruption, the volcano Cotopaxi is considered the most active. (Alvarado 2013).

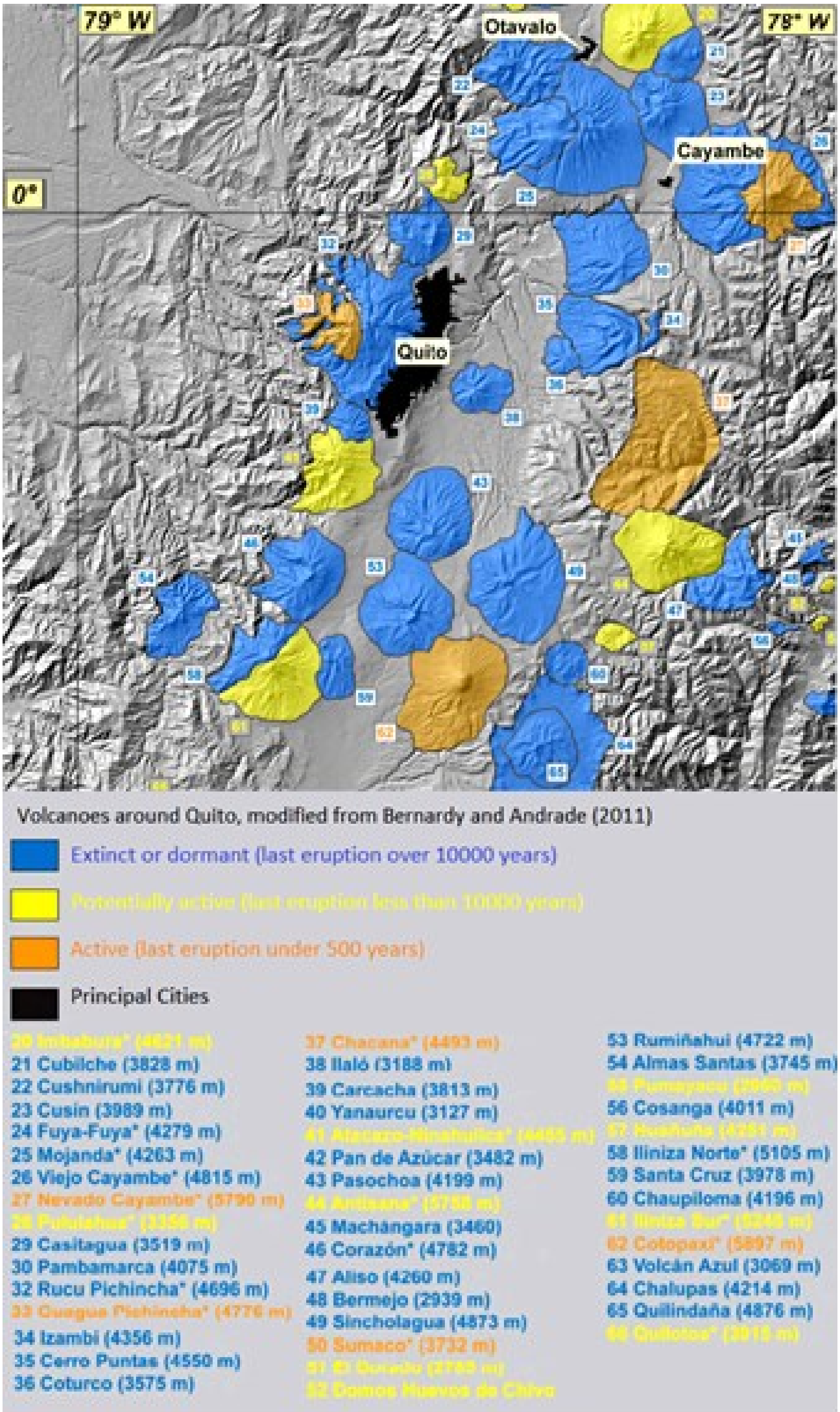

Figure 7. Location of volcanoes around Quito,
obtained and adapted from (Bernard and Andrade 2011)

The altitude of the Inter-Andean Depression varies between 3000 msnm (south) and 2400 msnm (center). In this depression in the topographical sense of the term, there are also volcanic centers: southeast the Rumiñahui, Pasochoa, Sincholagua and Cotopaxi volcanoes. These buildings participated in the morphological evolution of the bottom of the basin to form a platform, which shows on average an altitude of ~3800 msnm and that stands out from the morphology general. To the northwest, the Quito region is also uplifted, with an altitude of ~2800 msnm, and is also marked by an average increase of 400% in slopes, as can be seen in Figure 8 (Alvarado 2013).

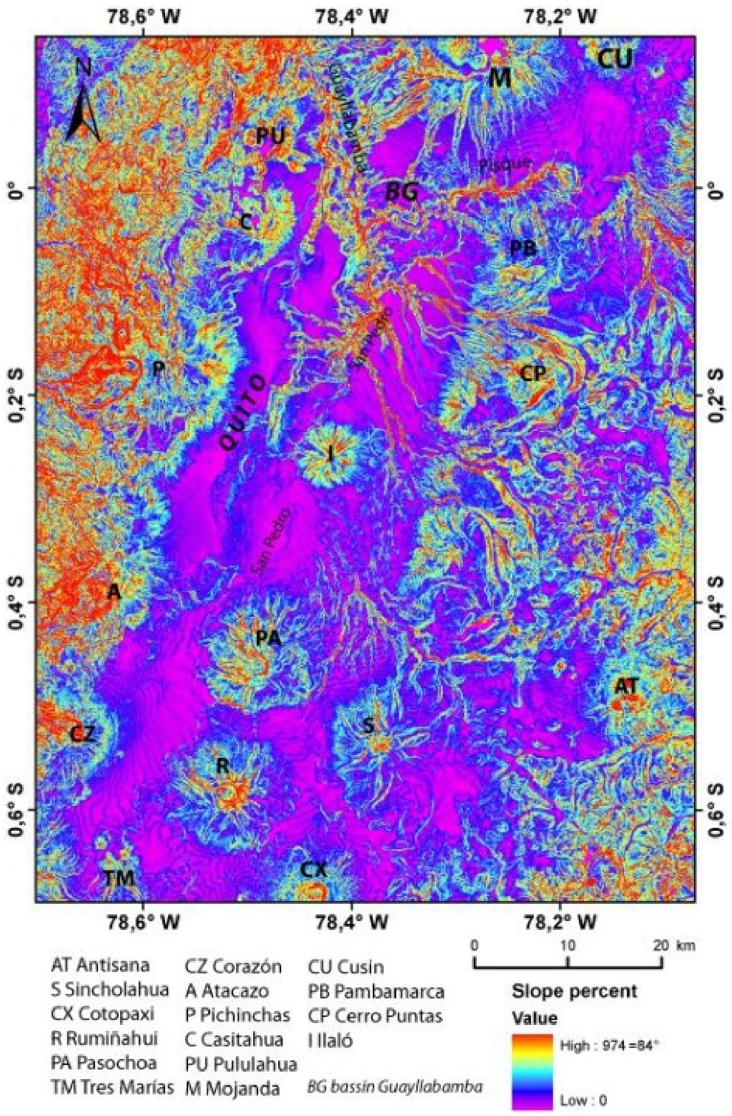

Figure 8. Slope distribution, described by slope percent.
Calculations performed on the with ArcMap software, from (Alvarado 2013)

2.1.2. Geology and stratigraphy

Ecuador has three predominant structural domains: the coastal region (fore-arc); the Andean region (volcanic arc) and the Oriente Basin (foreland), as seen in Figure 9 (Tamay et al. 2021). Based on (Jaillard 2022), the forearc zone comprises basins resting on the oceanic basement (Aizprua et al. 2020) and constitutes the coastal zone. The arc zone includes the Western Cordillera made of an uplifted part of the accreted oceanic terranes, the Inter-Andean Valley infilled by the products of the Tertiary-Recent volcanic arc (Hungerbühler et al. 2002; Lavenu et al. 1992) and the Eastern Cordillera mainly composed of metamorphic rocks (Pratt, Duque, and Ponce 2005). The subandean zone is made of mainly Meso-Cenozoic, folded sedimentary and volcaniclastic rocks, and the Oriente Basin infilled by Mesozoic-Quaternary deposits (Jaillard 2022; Jaillard et al. 1997). A detail of the mentioned zones and its predominant geology can be seen in Figure 9.

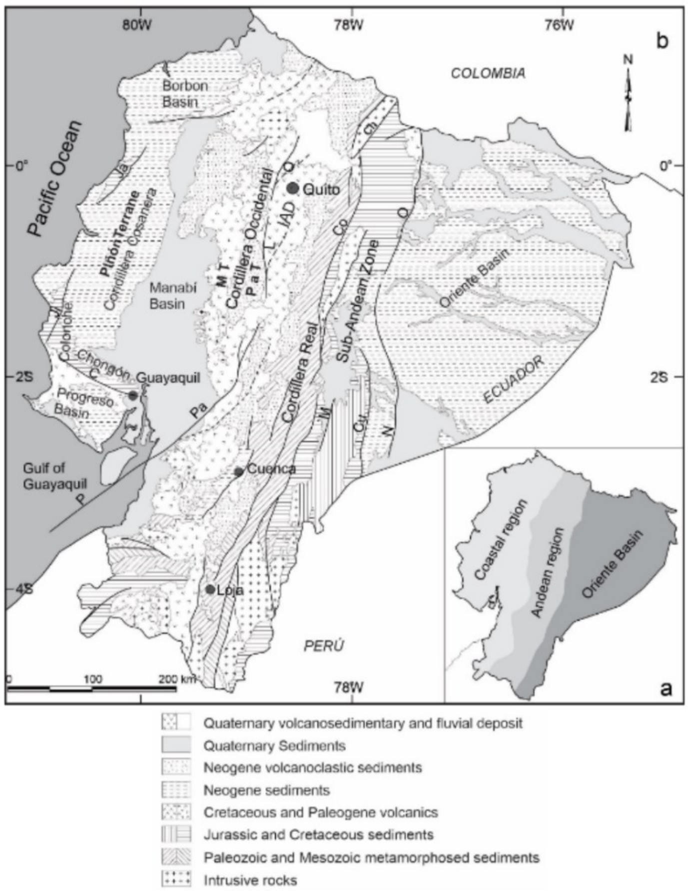

Figure 9. Location of the three structural domains in Ecuador (Villagómez 2003)

Villagómez, in 2003, studied the Plio-quaternary geological evolution of the Inter-Andean central valley in Ecuador, with bibliographic and cartographic compilation of the study area, interpretation of aerial photos and satellite images, recognition of structures, as well as a facies analysis of the defined stratigraphic units. These research lead to the determination of the morphological changes produced in the Plio-Quaternary, based on sedimentological, tectonic and morphotectonic analysis. It is concluded that the opening of the Central Inter Andean Valley, probably occurred towards the Late Pliocene in response to major dextral displacements mainly along its western edge. The sedimentary fill has been divided into two large sequences, an upper sequence with a thickness of 345 meters and a lower one of approximately 410 meters, separated by a major nonconformity of about 100 meters in thickness. The lower sequence consists of lavas, tuffs, lahars, alluvial, fluvial, deltaic, and lacustrine sediments. The upper sequence consists of primary volcanic deposits, lahars, hyperconcentrated flows, and fluvial deposits, corresponding to the Fms. Guayllabamba, Chiche, Machángara, Mojanda and Cangahua. The lower sequence was deposited in a mild ~E-W extensional regime, from the Late Pliocene to Early Pleistocene, and the upper sequence was deposited from the Middle Pleistocene to the Holocene in a ~E-W compressional regime. This compression that began in the Middle Pleistocene and continues to the present day produced a set of three ridges that have been called: Loma Calderón-Catequilla (CCR), Loma Batán-La Bota (BBR), Loma Ilumbisí-Puengasí (IPR) that can be seen in Figure 10. In the Loma Batán-La Bota ridge, located in the southwest, and of greatest interest for this study, Villagómez estimates that the Cangahua formation has an approximate thickness of 45 meters, followed by the Machangara formation with 139 meters, and the Chiche formation with 116 meters thickness.

These mounds divided the large basin into three sub-basins which subsequently evolved individually. These hills have played a fundamental role in the evolution of the sub-basins and are morphological expressions of the Reverse Fault System of Quito, which would essentially include the Catequilla Fault, the Quito Fault, and the Botadero Fault. The hills are elongated chains of N-S direction, whose formation was not contemporary but rather grew progressively from the north as evidenced by morphological, tectonic, and stratigraphic evidence.

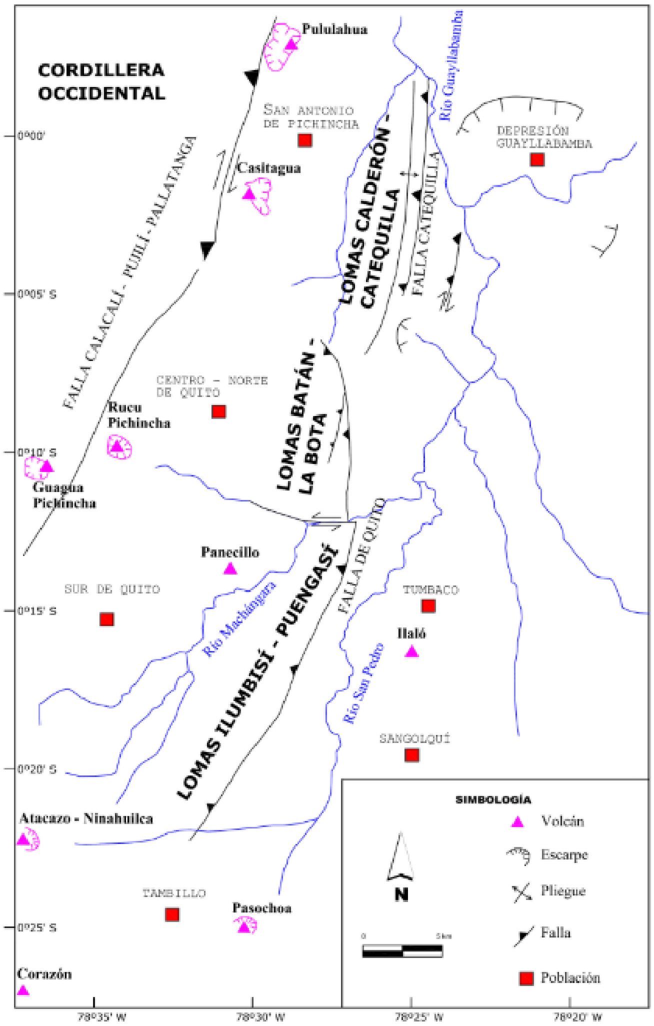

Figure 10. Location of the three ridges in Quito (Villagómez 2003)

Peñafiel, in 2008, made a thesis called "Geology and analysis of underground water resource of the sub-basin of the south of Quito", deepening the conclusions obtained by (Villagómez 2003), finding that in the sub - basin of the south of Quito, three informal lithologic units have been identified: *Basamento, Volcanosedimentaria Guamaní* and *Fluvio – Lacustre El Pintado* units. They are correlated with the *Machángara* formation. The *Basamento* unit underlies the *Volcanosedimentaria Guamaní* unit in erosive discordance. Both *Fluvio – Lacustre El Pintado* and *Volcanosedimentaria Guamaní* units are in transicional contact. The *Cangahua* formation overlies these units, and it is in erosive discordance with the *Volcanosedimentaria Guamaní* unit.

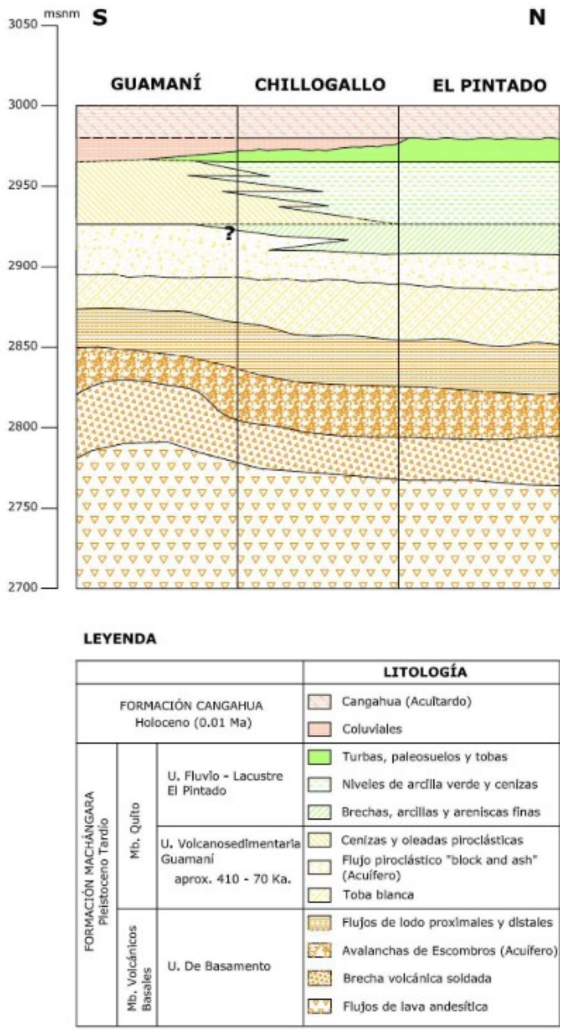

Figure 11. Simplified units in the south of Quito, from (Peñafiel 2008)

The *Basamento* Unit is formed by lava flows of andesitic composition, debris avalanches and mudflows. This unit is part of the Basal Volcanic member of the *Machángara* formation, of Pleistocene age. The *Volcanosedimentaria Guamaní* Unit overlies unconformity erosive to the Basement Unit and is formed by primary deposits that include pyroclastic flows, tuffs, pumice falls and ash. This unit is part of the Quito member of the *Machángara* formation, and its minimum age would be 410 Ka. The El Pintado Fluvio-Lacustrine Unit was deposited mainly in the north of the sub-basin and is in transitional contact with the *Volcanosedimentaria Guamaní* Unit. It is made up of volcanic breccias, fine sandstone, green clay, and peat. It is part of the Quito member of the *Machángara* formation.

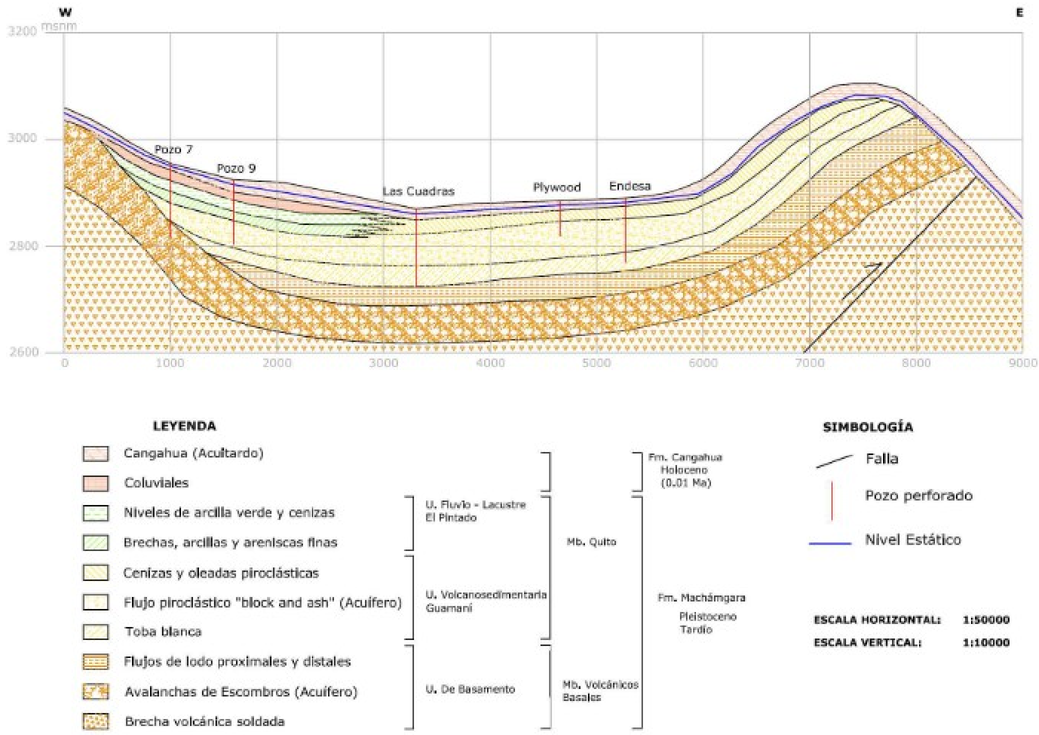

Figure 12. Simplified schematic of the Quito basin showing a transversal profile, modified from (Peñafiel 2008)

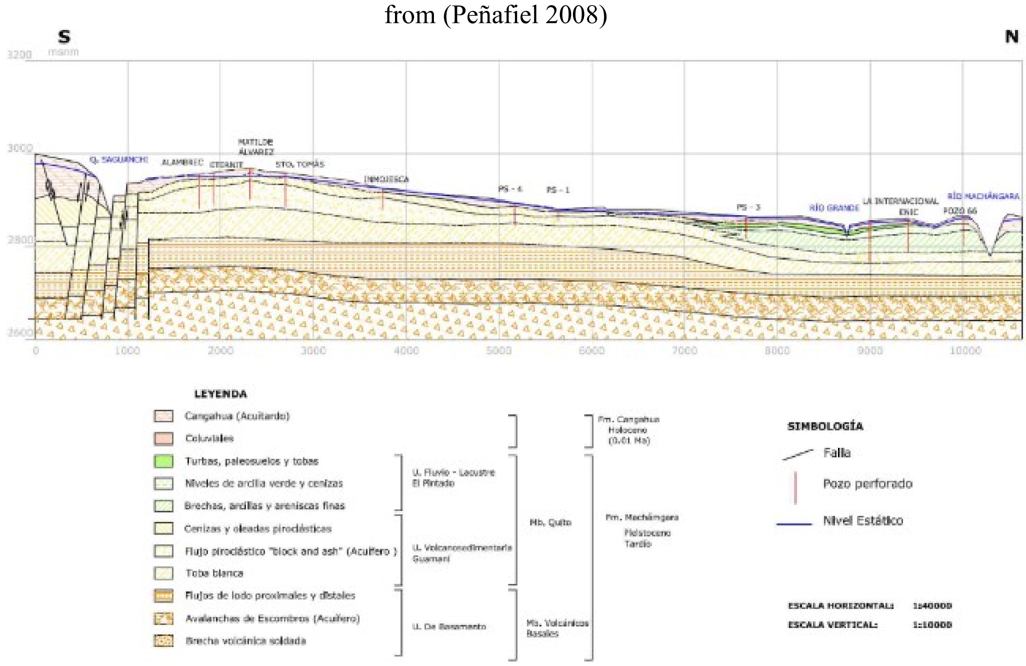

Figure 13. Simplified schematic of the Quito basin showing a longitudinal profile, modified from (Peñafiel 2008)

It was also found that the Quito reverse fault system presents an evident reverse component, but the existence of a dextral transcurrent movement component is also suggested, which segments the main antiform in the Loma Ilumbisí - Puengasí in the Guápulo sector and would give rise to the development of an extensive zone (pull - apart) along the southern end of the fault, in the sector of the Saguanchi creek. (Peñafiel 2008).

Avilés, in 2013 performed the geological-geotechnical characterization of the south of the city of Quito, by carrying out the lithology distribution, distribution of the phreatic levels, origin and geological characteristics of the materials, observations, field measurements and the help of geographic information systems, which allowed to zone and classify the south of the city of Quito, through techniques of superimposition of previously elaborated thematic maps, plus the information of boreholes from previous studies. The map was generated up to 10 meters depth, obtaining the following result:

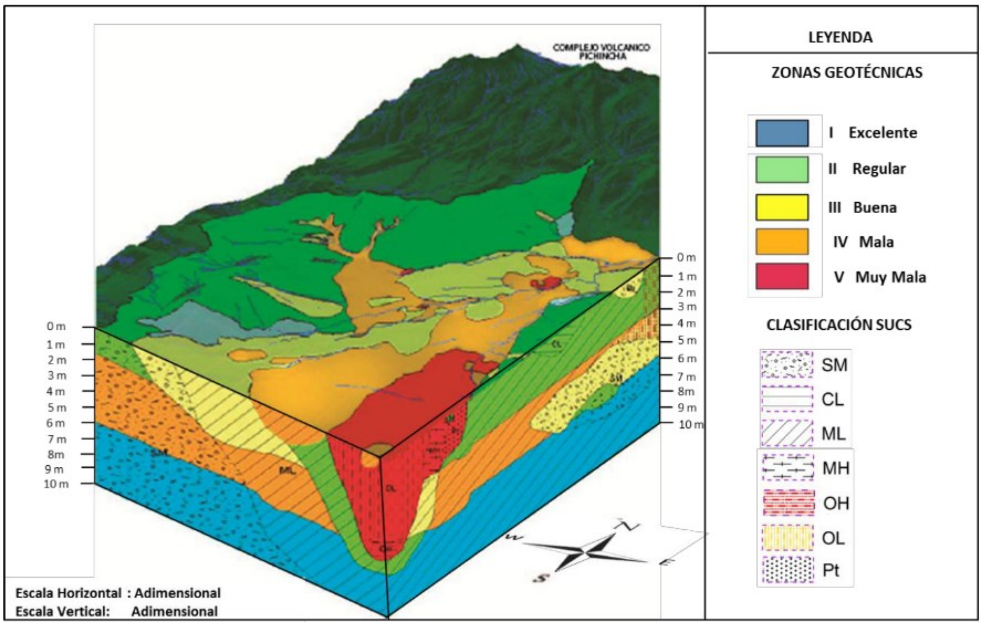

Figure 14. Conceptual Model of Geotechnical Zoning of the South of the City of Quito. Prepared by Lucia Avilés (Avilés 2013)

The generated map mentions five zones, from I to V, going from best to worst with respect to its geomechanical capabilities and support capacity. Zone I and II presents excellent soil conditions for construction, lithologically it corresponds to cangahuas, colluvial, alluvial, and areas where basement units' outcrop such as: Atacazo Volcanic Unit, Pichincha Volcanic Unit, and Undifferentiated Volcanic units. Low to no plasticity, low moisture content with no ground water level detected. Zone III presents soils deposited in fluvio-lacustrine environments (silt and clay), of heterogeneous composition, cangahuas and fillers of anthropic origin, which are considered materials of regular competence as support for foundations, low to medium humidity and plasticity, and surface water tables. Zone IV are lithologically deposited in fluvio-lacustrine environments and belong to silt-sandy sequences and in fill areas, usually presenting problems of low bearing capacity, medium to high humidity, low to medium plasticity, surface water table levels. Zone V, are lithologically deposited in fluvio-lacustrine environments and belong to silt-sandy sequences, filled areas, swampy areas with abundant content of organic matter and peat, have low resistance to penetration, have problems of low bearing capacity, high humidity, low to medium plasticity, surface water tables. (Avilés 2013)

The stratum conformation in the south of Quito has a very strong presence of lake deposits and anthropic fillings, which explain the lack of acceptable mechanical properties in upper layers. Recent urban settling has brought many soil-related problems, due to this ground being formerly occupied for agronomic purposes and for being used without the proper ground research. Moreover, Quito presents an important seismic risk, extremely threatening since most of Southern Quito constructions have a poor quality in design. (Celi and Moyano 2017).

2.1.3. Structural setting

The location and displacement record of fault sources constitute basic insights for seismic hazard assessment (SHA), helping to conduct more appropriate evaluations for a specific structure or region (Costa et al. 2020). Along the western margin of Ecuador, the oceanic Nazca plate is subducting obliquely the continental North Andean block and the South America plate for the past 5 Ma, along a trend of N83°E (Alvarado et al. 2014; Kendrick et al. 2003), at a convergence rate of 58 ± 2 mm/a (Trenkamp et al. 2002). The inherited geological and structural patterns and discontinuities of the Andes orogen, as well as the present plate tectonic setting, cause a wide variety of neotectonic environments in terms of both structural styles and strain rate, under different morphoclimatic conditions (Costa et al. 2020). Many of South America's capital cities are established nearby crustal fault sources, whose seismogenic capability is known or suspected, such as Quito (Alvarado et al. 2014; Beauval et al. 2013; Costa et al. 2020; Aurore Laurendeau et al. 2017; Mariniere et al. 2020). The the distribution of major hazardous faults with a dominance of strike-slip motion in South America can be seen in Figure 15, obtained from (Costa et al. 2020)

Figure 15. Types of hazardous faults in South America, obtained from (Costa et al. 2020)

Ecuador is situated in a complicated geodynamic setting involving a continental tectonic block and a microplate, in front of an active subduction zone. (Alvarado et al. 2014). Because of the oblique subduction, the entire northwest Andean area has broken away from stable South America and is moving northeastward as the North Andes Block (White, Trenkamp, and Kellogg 2003), which can be seen in figure 16, obtained from (Pousse-Beltran et al. 2017). All three typical types of plate boundaries (convergent, divergent, transform) can be found in this region, including other features such as multiple triple junctions, hotspots, and subduction (EEFIT 2018).

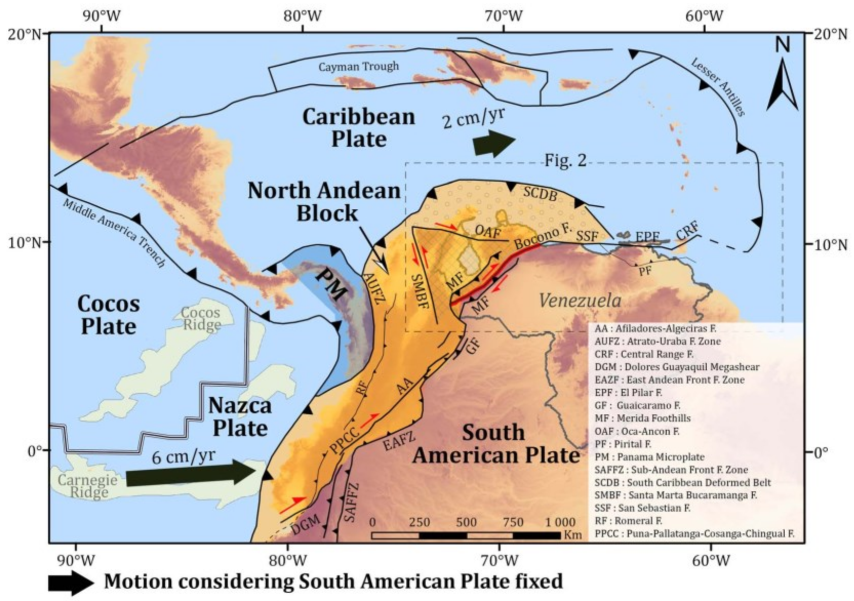

Figure 16. The North Andean Block (in yellow) composed of minor blocks accommodates part of the relative displacement between the South American, Nazca, and Caribbean plates, obtained form (Pousse-Beltran et al. 2017)

Due to the presence of the North Andean Block, the northern Andes (Ecuador, Colombia, and Venezuela) have shown a different geodynamics evolution compared to the southern Andes. The Northern Andes are formed by a succession of accumulations of oceanic terrain, initiated in the late Cretaceous (Hughes and Pilatasig 2002) until the Paleocene. These accumulations that didn't present subduction are the current substratum of the Interandean depression and the Western Cordillera (Alvarado 2013).

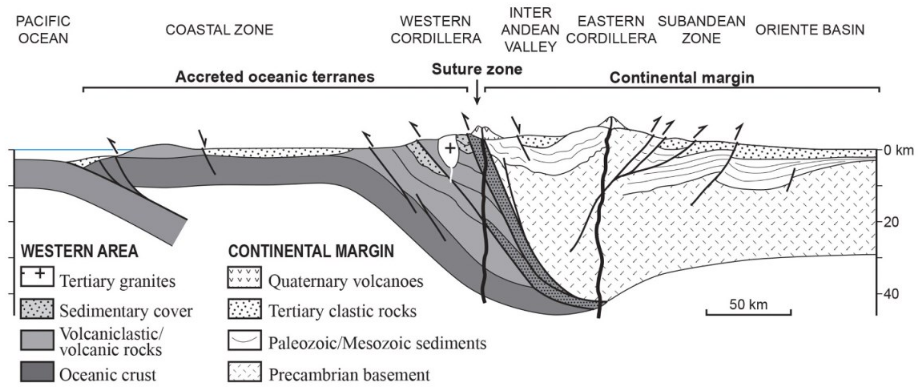

Figure 17. Schematic cross section of the Ecuadorian Andes (Jaillard 2022; Mégard 1989)

Based on (Mégard 1987; Mégard 1989), the build-up of the Ecuadorian Andes can be seen as resulting from the interaction of a western wedge made of accumulated terranes, followed by a subsequent, eastern, East-verging wedge made of continental basement and sedimentary cover and represented by the Eastern Cordillera and the Subandean zone, as seen in figure 16. To confirm this model, (Bonnardot 2003) performed a 2D numerical modelling of the accretion of a low-density oceanic terrane divided by oblique, pre-existing faults**,** reproducing consistently the proposed scenario as seen in figure 18 (Jaillard 2022)**.**

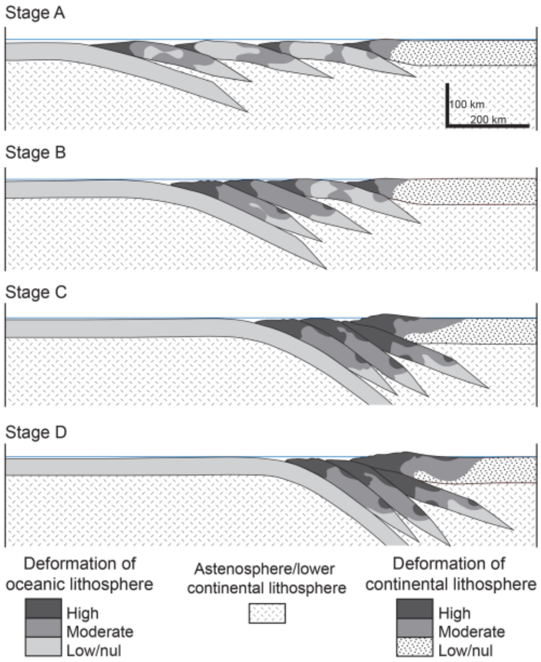

Figure 18. 2D numerical modelling of the accretion of a low-density oceanic terrane divided by oblique, pre-existing faults, from (Bonnardot 2003; Jaillard 2022)

In 2013, Alvarado established and defined the characteristics of the main active systems of Ecuador, proposing a model of the evolution of a large continental fault system: Chingual-Cosanga-Pallatanga-Puná (CCPP), which continues towards Colombia, and represents the limit between the North Andean Block and the South American plate, and suggesting the existence of a micro block called Quito-Latacunga, in response to the evolution of the deformation towards the east, as seen in figure 19. (Alvarado 2013).

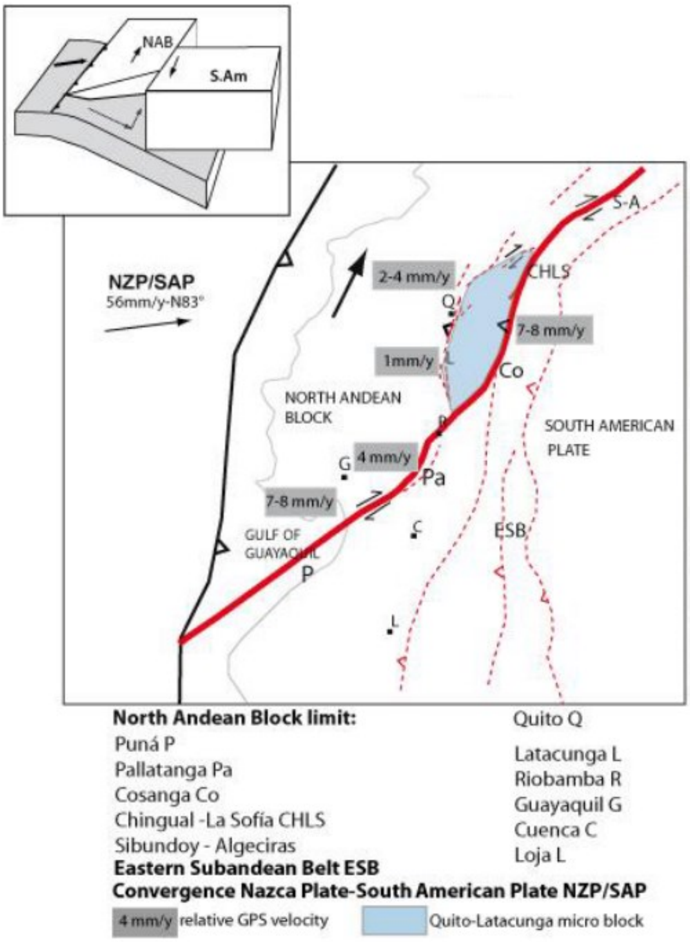

Figure 19. Geodynamic model of Ecuador, from (Alvarado 2013)

From a geomorphic study and satellite mapping in Quito, made by (Alvarado et al. 2014), widely distributed faults and folds are actively deforming the Plio-Quaternary volcanic deposits in the secondary Machángara or Guayllabamba as can be seen in figure 20. The orientation and throw of these faults follow the major fault trends of N-S to NE-SW, ~45° west dipping blind thrust with an overall length of 60km, and it is probable that the active fault map based upon field observations shows only an under representative subset of what may exist. (Alvarado et al. 2014)

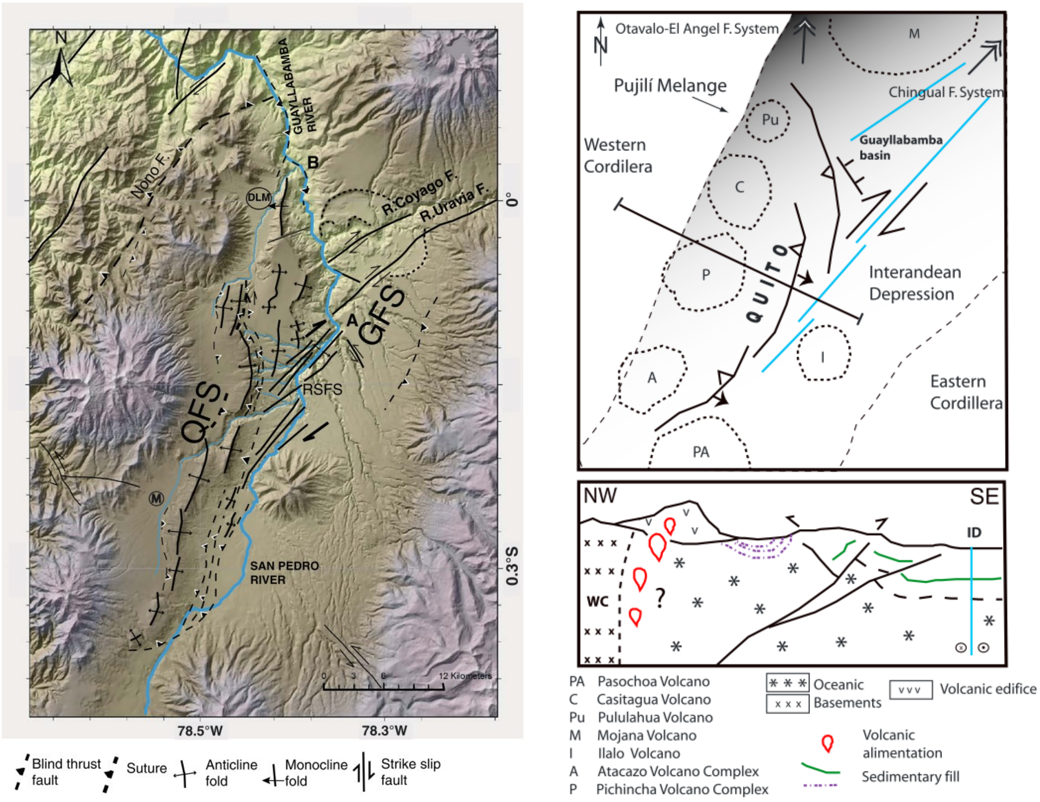

Figure 20. Geodynamic model of Quito, from (Alvarado et al. 2014)

2.1.4. Seismic Response

Some of the greatest earthquakes in the 20th century and the present in South America occur in Ecuador and Colombia due to subduction of the Nazca plate (White et al. 2003). Since 1906, five earthquakes with magnitude larger than 7.7 have occurred in the shallow portion of the subduction zone, in 1906, 1942, 1958, 1979, and 2016 (Alvarado et al. 2018; Yoshimoto et al. 2017), as can be seen in figure 21. However, lower magnitude but shallower and more destructive earthquakes have originated in crustal faults near populated areas (Alvarado et al. 2018) . At least 13 destructive earthquakes of this type have occurred in the last five centuries (Alvarado et al. 2018; Beauval et al. 2010; Courboulex et al. 2022). The known historical earthquakes that have damaged Quito were located on the faults of the Cordillera, such as the Guaylabamba 1587, Riobamba 1797, Quito 1859, and Ibarra 1868 earthquakes (Alvarado et al. 2014; Beauval et al. 2010; del Pino and Yepes 1990). Quito is built on the hanging wall over an active reverse fault that generates moderate size earthquakes (Alvarado et al. 2014; Vaca et al. 2019) and is partially creeping (Courboulex et al. 2022; Mariniere et al. 2020). as mentioned in the previous chapter.

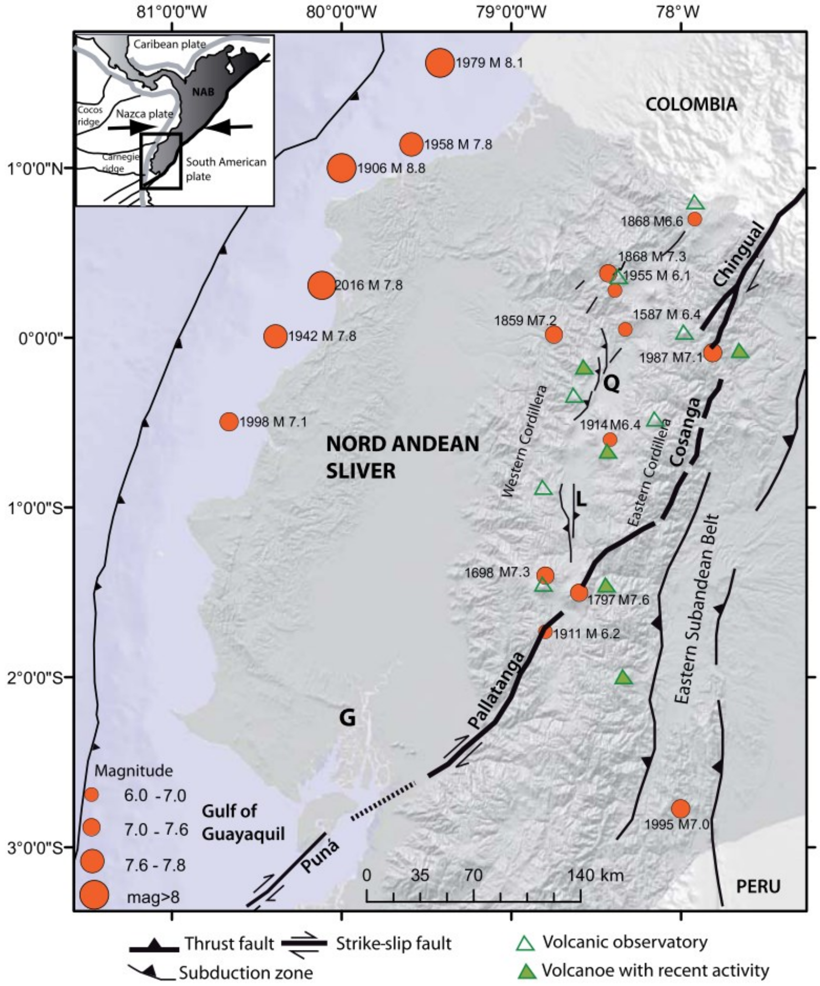

Figure 21. Geodynamic model of Quito, from (Alvarado et al. 2014)

A first compilation of the seismicity of Quito was performed by (del Pino and Yepes 1990), concluding that in the last 456 years, in the Medvedev-Sponheuer-Karnik (MSK) Scale, three grade 9, two grade 8 and four grade 7 earthquakes affected the city, representing a return period of 50 years for strong earthquakes, noting that possibly only 2 of them were caused by the Quito Fault System (QFS), and the others from faults north or south from Quito (del Pino and Yepes 1990).

The zoning of the city of Quito began with the engineers Acosta and Armendariz, who elaborated in 1979 a "Contribution to the Zoning of the City of Quito", based on criteria of admissible capacity of the soil at different depths, they determined statistically 26 zones within the city. In 1987, the engineers Lecaro, Leon and Moyano determined 23 zones of different characteristics in Quito based on criteria of geology, urban plans, dynamic parameters of the soil, presence of streams and drainage. In addition, by using 619 SPT studies, they established equations for each zone at each depth to determine in an indirect way the shear wave velocity and the shear modulus as a function of the number of SPT blows. Furthermore, in 1992, Eng. Aguinaga, through an "Estimation of the vibration period as a function of local soil conditions", tried to apply experimental field methods such as micro-vibrations and Cross-Hole to evaluate the dynamic properties of the soil, however, the number of tests was insufficient. (Valverde et al. 2001). Finally, the first dynamic response of Quito´s soils was performed by J. Torres, evaluating a deposit in central north Quito using the software SHAKE, followed by Aguinaga, 1992 performing cross hole tests and micro vibrations and the city of Quito, which between 1992 and 1994 created a project called "Quito - Ecuador Seismic Risk Management Project" to evaluate the seismic hazard in Quito dividing the city into 20 different seismic response microzones, where the eastern flanks of the Pichincha (F), lake deposits (L) and volcanic ashes with cangahua formations (Q) were identified. The flanks of Pichincha are formed by alluvial deposits, mainly cangahua and volcanic ash, where zones F4 and F6 are the most representative. The lacustrine deposits (L) are found mainly in the superficial strata of the central depression of the city. For example, zone L2 is a formation of zone F1 covered by zone L1 in the most superficial layers. And finally, at the eastern part of the city there are morphologically elevated zones, which are entirely formed by cangahua (Q), where zone Q3 corresponds to a cangahua formation with soft soil deposits on the surface and zone Q4 is a zone related to more recent deposits of cangahua covered by volcanic sands.

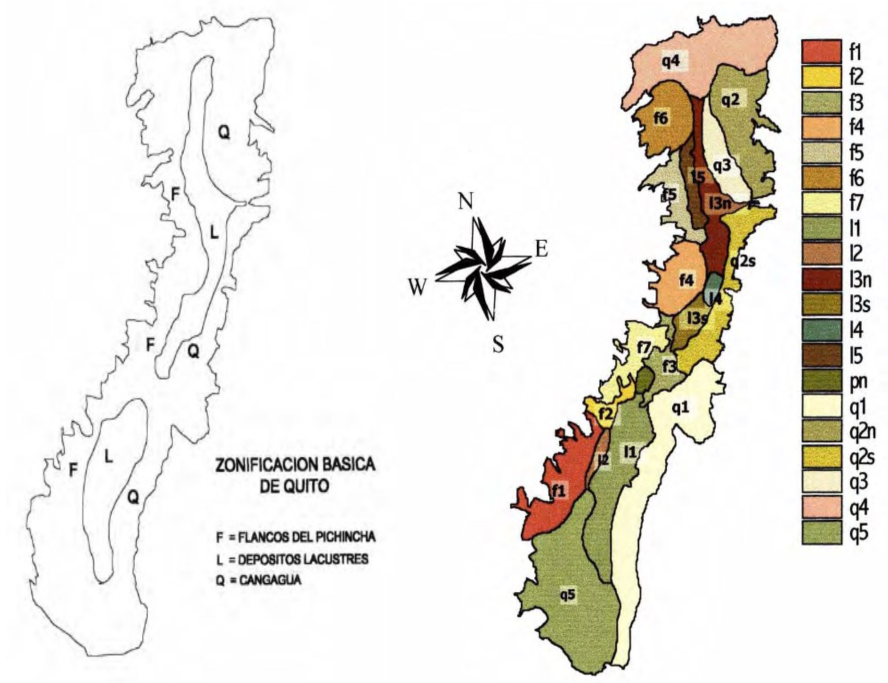

Figure 22. Zonification of the City of Quito in 1994. (Valverde et al. 2001).

In 2001, based on the 1992-1994 seismic hazard project, (Valverde et al. 2001) performed the first micro seismic zonation of Quito. This micro seismic zonation used studies from previous years, over 2000 boreholes, topography, geotechnics and surface geology, to establish a representative soil column up to a depth of 20 m. This column was used to evaluate the dynamic response in the different zones of the city by mostly using correlations of the dynamic properties based on the Unified Soil Classification System (USCS), adding the field seismic registers and laboratory available information, mentioning that an ideal model would be possible with the use of properties obtained in laboratory (the shear modulus of the soil G, shear wave velocity Vs, the damping ratios and the reduction modulus G/Gmax versus shear strain) validated in field, using all the dynamic parameters (acceleration, period, frequency content, duration) of a group of real seismic signals recorded in the city. However, the modeling proposed in the study gives a global and approximate idea of the potential seismic hazard zones in the city of Quito. First a basic zonation of the city in North, central and south is performed, and later, the column response with the experimental curves defined for each soil classification were obtained from the technical literature summarized in the SHAKEDIT program. The average curves of each material are indicated and the experimental curve of the

Cangahua obtained from a cyclic triaxial test obtained from a laboratory in Peru was also included. (Valverde et al. 2001).

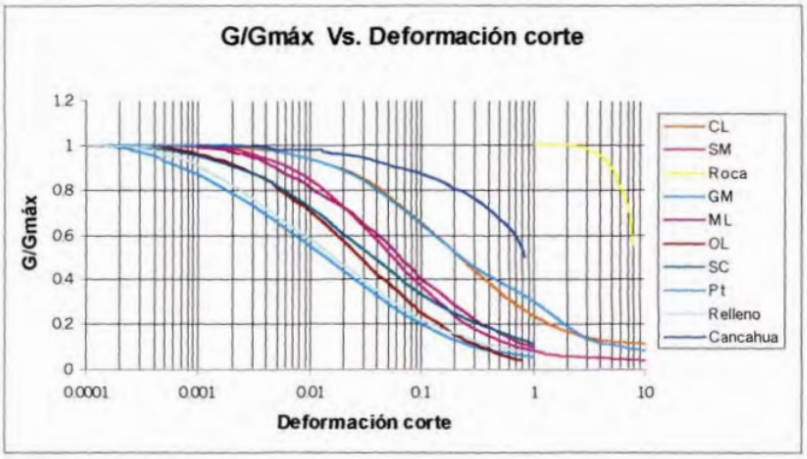

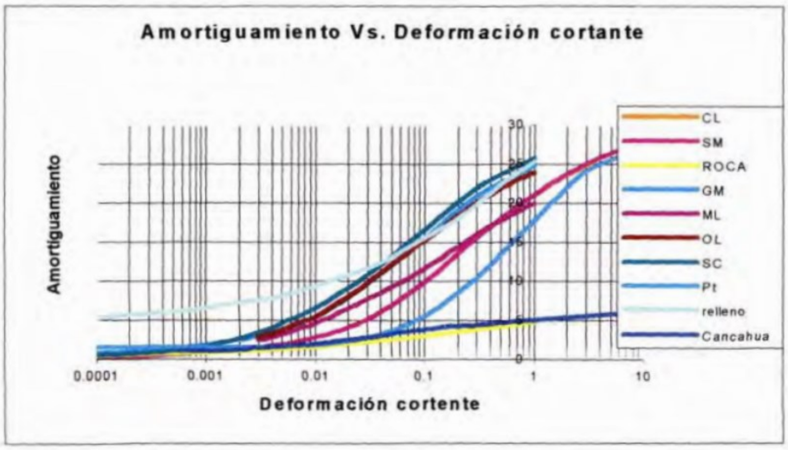

SUCS	Módulo G/Gmáx Vs. Deformación	Amortiguamiento Vs. Deformación
CL	Modulus for clay (Seed & Sun 1989)	Damping for clay (Idriss 1990)
SM	Modulus for sand (Seed & Idriss 1970)	Damping for sand (Idriss 1990)
GM	G/Gmáx Gravel Average (Seed et al. 1986)	Damping Gravel Average (Seed et al. 1986)
ML	G/Gmáx Soil PI=15 OCR=1-15	Damping Soil PI=15 OCR=1-8
OL	G/Gmáx Soil PI=0 OCR=1-15	Damping Soil PI=0 OCR=1-8
SC	G/Gmáx Sand S2 (Sand CP=1-3 KSC) 1988	Damping for sand average(Seed &Idriss 1970)
Pt	G/Gmáx of Young Bay Mud (Sun, EERC-88/15)	Damping for Bay Mud
Cancahua	G/Gmáx Cancahua CISMID Proyecto Quito	Damping Cancahua CISMID Proyecto Quito
Roca	Atenuation of rock average	Damping in rock

Figure 23. The damping ratios and the reduction modulus G/Gmax versus shear strain obtained from literature, in spanish, from (Valverde et al. 2001)

With the mentioned data, the transfer functions, and the response spectral curves where generated. The response spectral curves for every zone in Quito is generated based on resonant column tests, however a detailed conclusion of the south of Quito or its possible dynamic amplification is not mentioned.

Nevertheless, this study determined four types of soil profiles. Soil profile S1 corresponds to soils that have a shear velocity greater than 750 m/s and a vibration period of less than 0.2 s, for example: healthy or partially altered rock, dense or dry sandy, silty or clayey gravels, dense sands and hard cohesive soils. Soil profile S2 corresponds to soils with intermediate characteristics between soils S1 and S3, for example, not very consolidated thin cangahuas, lacustrine deposits and laharitic deposits overlying strong strata of tuff and cangahuas. The S3 profile corresponds to those soft soils or deep strata with a fundamental period greater than 0.6 s, including strong layers of poorly consolidated sands and gravels, organic silt deposits with a high-water table and fill zones located in old river beds. Finally, profile S4 corresponds to special soils such as: peat, mud, uncontrolled fills, high plasticity clays and silts, clay deposits greater than 30 m and soils with high liquefaction potential, collapsible and sensitive.

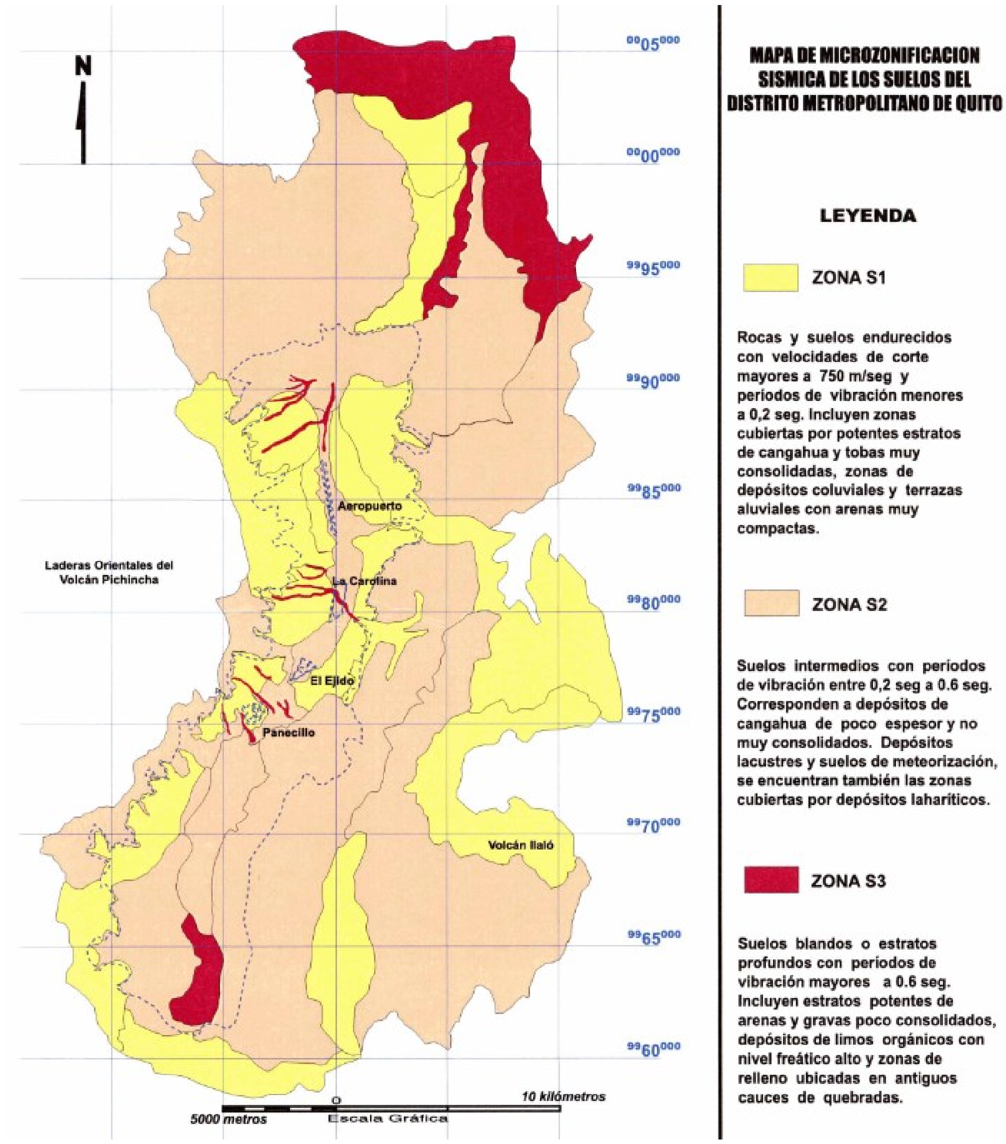

Figure 24. Zonification of the City of Quito in 2001. (Valverde et al. 2001)

In 2012, ERN compiled the 1994 and 2001 studies and developed a method to calculate the hazard based on the classical seismology theory, elaborating a simplified hazard model considering the seismic tectonic characteristics and the seismicity of the Ecuadorian territory, in addition to including field research and the performance of laboratory tests, with the objective of improving knowledge on the behavior of the soil against cyclic loads, particularly dynamic loads similar to those generated by earthquakes. Based on this objective, the result of this study was the characterization, from the dynamic behavior point of view, of the superficial deposits of clays, silts, sands and their combinations, present in the upper layers of the stratigraphy. This study was carried out by the execution of 14 boreholes that contributed to characterize some new areas of the city or those for which there was insufficient information, and for the performance of in-situ geotechnical and geophysical tests, to obtain direct information of the physical, mechanical and dynamic characteristics of the subsoil and to obtain undisturbed samples for the performance of 293 laboratory tests, of which 15 corresponded to tests to evaluate the dynamic behavior of the soil, such as: the cyclic triaxial test, the resonant column test and the shear wave velocity test (Bender Element). Based on the results of the tests performed, this study adopted a different methodology that consisted of building a 3D model of the geology of the study area, assigning zones of influence for each of the soundings for which wave velocity profiles were available and characterizing the main geological formations with an expected dynamic behavior based on the results obtained from the dynamic laboratory tests, and the final product was the presentation of seismic microzonation maps for the city in terms of Fa, Fd and Fs, for a return period of 475 years. (ERN 2012).

In 2013 and 2017, (Aguiar 2013, 2017) performed an study with additional information based on the Metro of Quito and the Evaluation of Natural Risks (Evaluación de Riesgos Naturales of Colombia, ERN in Spanish), performed between 2011 and 2012, with the objective to find the response spectral curves for the horizontal component of the ground, in each one of the five zones of Quito defined, which are: South, Central South; Center; North and North Center.

On the other hand, the generation of the response spectral curves for the vertical component of soil movement and spectral relationships V/H was also considered for each area of Quito (Aguiar 2013). The response spectral curves are presented, however no mention to the possible dynamic amplification is mentioned.

Combined with the information from (Valverde et al. 2001), additional and an in-depth analysis will be performed in the discussions chapter in this thesis.

In 2017, (Aurore Laurendeau et al. 2017) found that the southern part of the Quito basin presents a strong site amplification at low frequencies (peak around 0.35 Hz with an amplitude larger than 3) that is not present in the northern part. The recordings of the 16 April 2016 Mw 7.8 Pedernales earthquake that occurred on the subduction interface 150 km away from Quito confirm this low-frequency amplification in the southern part of the city, by observing larger amplitudes and longer durations of the signals. To deepen these findings, an experimental set up of field and laboratory tests are presented in Chapter 3.

In 2019, the first phase of the study of the most recent microzonation of the city of Quito was executed, which included the study of 2500 Ha corresponding to Zone 2 in the south of the city, which is delimited from Av. Ajaví in Solanda, to the New Terminal of the Ecovía in San Juan de Turubamba. The preparation of this report required 21 boreholes with a depth limit of 30 m, from which a detailed lithological description was made with the objective to identify and interpret the different types of lithological materials and to limit them. A total of 2774 physical and mechanical tests were carried out during this study, combined with 1332 field tests, from which 4 longitudinal and 6 transverse profiles were obtained from density, N60 and S-wave velocity, and from which it was determined that in all the boreholes, the first 15 m correspond to ML sandy silts and SM silty sands. Meanwhile, below 15 m to 30 m there are alluvial deposits composed of pure sands or gravels with low percentages of silt and clay less than 5% or between 5 -12%. Furthermore, the geophysical tests determined that the shear wave velocity up to 30 m depth is less than 360 m/s, considering that the lowest values are found in the eastern part, at the foot of the hill that borders the Puengasí basin and that the highest values are found in the central part of the Machángara sub-basin. (Gobierno Autónomo Descentralizado del Distrito Metropolitano de Quito, Escuela Politécnica Nacional, and Pontificia Universidad Católica del Ecuador 2019). The information gathered in this study was used to develop this research.

In 2022, the most recent study, developed by the Global Earthquake Model (GEM), proposed an intensity amplification model for the city of Quito, estimating that the seismic hazard corresponds to an average peak acceleration (PGA) of 0.52

g in rock, with an exceedance probability of 10% in 50 years. Additionally, it determined that the Quito soil response is amplified in all zones, except MSQ11, until reaching an amplification factor of 5 in 2 s, in zone MSQ3. The study also determined the highest amplifications, greater than 3, are found in zones MSQ1, MSQ3, MSQ6 and MSQ11. While, in the southern part, in stations MSQ8, MSQ10 and MSQ1, the maximum amplification is reached at 2.0 s, indicating a longer resonance period in the southern part of the city. The location of the zones can be found in figure 25. (Global Earthquake Model (GEM) Foundation 2022).

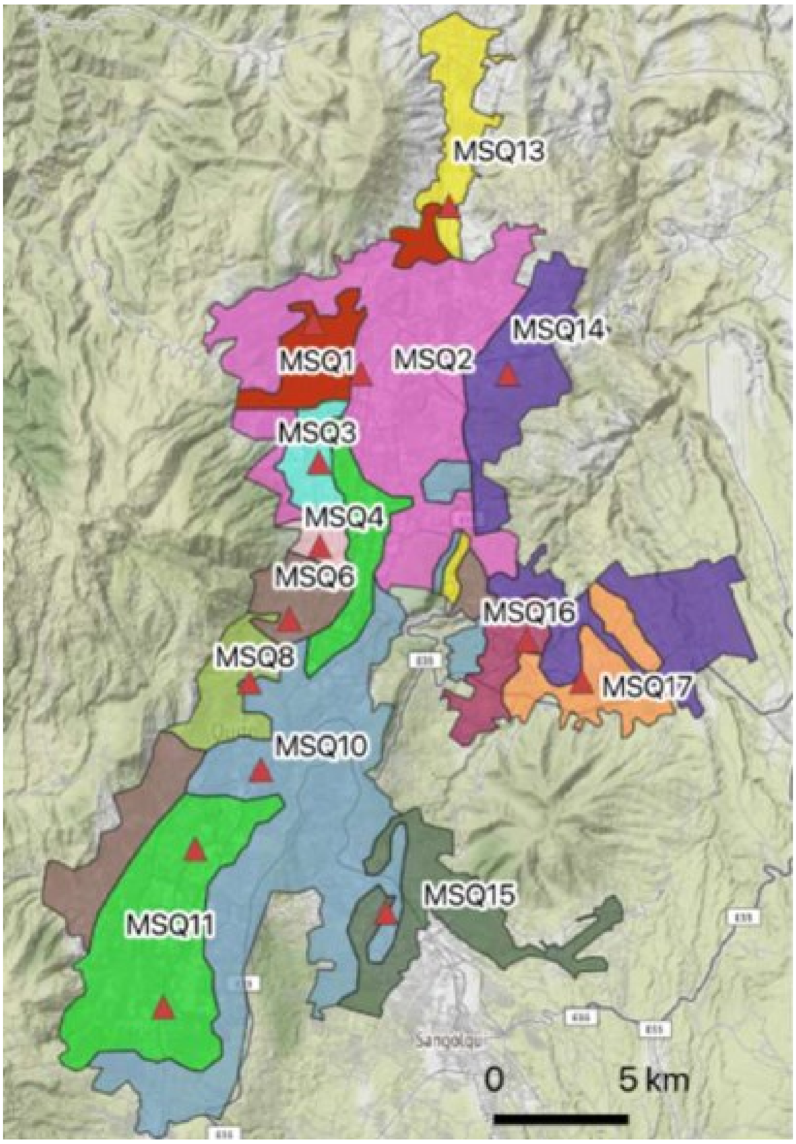

Figure 25. Location of seismic zones. (Global Earthquake Model (GEM) Foundation 2022)

Local site conditions are known to often play a significant role in determining the characteristics of earthquake ground motion at soil tests. Uzielli et al. (2022), mentioned that early studies investigated qualitatively the influence of topography and surface irregularities on surficial ground motion. These studies pointed out the significant influence of topography and basin geometry on the ground motion, where alluvial valleys and sedimentary basins are generally exposed to surface motion amplification and highlighting a relation between peak amplitude and maximum sediment thickness. Furthermore, some investigations performed in recent decades have pointed four main aspects that shape strong ground motions: the first is the amplification of displacement, the second is the resonance of the flat layers developed mechanically at specific frequencies, the third is the non-linear stress-strain behavior of soils, as soil is a inhomogeneous and anisotropic material and the last is the effects due to the wave propagation variation in soil half-space, which may change if it has multilayered site conditions with stratigraphic heterogeneities (Ozaslan et al., 2022). Therefore, considering these aspects, the determination of the local site conditions becomes difficult and the need to determine how it can affect structures due to the presence of other buildings will have a significant impact on the site effect increment (Jiang et al., 2020). To solve this necessity the researchers have been developed numerical approaches which use parametric analyses or theoretical models for different basin geometries, soil properties and incident waves, using a variety of techniques, from which the more complex is the 3D analysis.

The “easiest” numerical modelling is 1D, so it is considered inadequate to assess the ground surface motion of sediment-filled basins and cannot correctly account for resonant frequencies, that is why the use of 2D, or 3D numerical methods is required to estimates satisfactory seismic response (Uzielli et al., 2022). For example, Bustos et al. (2023) studied the seismic response of the Santiago Basin, Chile; using a 2D simulation which can show the effects obtaining from this analysis, are more evident in softer sediments and even more pronounced as the depths of the deposits increase, and the 2D simulation have considerably longer durations than those obtained in 1D simulations. Panzera et al. (2022) reconstructed a 3D model to determine the local amplification of the upper Rhone valley in Switzerland, where mentioned the importance to have a detailed knowledge of the geometry, thickness and velocity of the main sedimentary layers from the valley and validated the final 3D velocity model using the 1D velocity profiles, providing interesting insights about 2D and 1D site effects in realistic geological configurations. McGann et al. (2021), developed a 2D finite element model for the Thordon basin which shown that the simple 2D model could capture the basin reverberations and basin edge effects. Rodriguez-Plata et al. (2021), analyzed the seismic response of the Norcia basin in Central Italy using both 1D and 2D ground response numerical models, where the results showed the 2D amplification (on Fourier spectra) at the fundamental mode was higher in 30%-50% than the 1D response. Consequently, the 1D amplification is indeed inadequate to consider the complex wave propagation phenomena, it may provide unsafe estimates, as they cannot take into account the buried morphological irregularities and lateral confinement of sedimentary basins, because they may be responsible for the generation of the edge-indiced surface waves which may further increase the amplitude and duration of ground motion. The performance of 2D and 3D seismic wave propagation analyses for site-effects would be the natural way to account the complex site effects, however, is an approach expensive and computationally difficult to develop, for this reason is not routinely done in engineering practice (Rodriguez-Plata et al., 2021). For these reasons, the results presented in this thesis are a first approximation of the potential dynamic amplification factors of the ground, which were obtained from a 1D analysis. The information collected is presented as geotechnical profiles in both directions and will serve as a base for 2D modeling to take into account the effects of topography and the irregular arrangement of the highly heterogeneous sediments presented in this thesis.

CHAPTER 3

Experimental set-up

The Southern Quito soils have considerable weak geomechanics properties, being easily deformable (Albuja-Sánchez 2021; Peñafiel 2008; Santander 2013), and vulnerable to seismic activity (Aurore Laurendeau et al. 2017). In most cases they are conformed by mainly organic soils and peats, whose properties cannot be easily determined. For this reason, a characterization is highly required, and can only be obtained by a series of tests and correlations.

The present work aims to a general characterization of southern Quito soils, through the static penetration cone test (CPT), Marchetti´s seismic dilatometer (SDMT) and the standard penetration test (SPT) in complementarity and correlation with usually performed and advanced laboratory tests, to determine their dynamic properties and evaluate their response.

This can be achieved (i) performing in-situ tests in 20 points from 10 to 30 meters deep for each site (CPT, SDMT, SPT), plus two additional boreholes up to 30 meters depth to obtain additional representative of the soils implementing the Unified Soil Classification System (USCS) for each bore hole executed; (ii) granulometry, specific gravity, organic content, Ph, chloride and sulphate content, and natural density of representative samples; (iii) obtainment of wave velocities Vs30 for each point through the interpretation of the SDMT and complementary geophysical tests; (iv) determination of mechanical properties of soils utilizing one-dimensional consolidation, direct shear, triaxial and resonant column tests; (v) establishment of correlations between the different physical-mechanical properties obtained in the laboratory with in situ test results; (vi) and determination of the dynamic response of Quito south sector.

The experimental set up allow the compilation of important mechanic and seismic soil properties with field and laboratory data that can give a more direct approach to soil parameters. A combination of SPT, CPT, DMT or SDMT, and laboratory tests can provide a precise approach to soil characterization, if implemented with the correlations and considerations mentioned above. Being meaningful to research of particularly complex stratigraphic profiles and/or important seismic risk zones such as the ones present in the southern Quito sector.

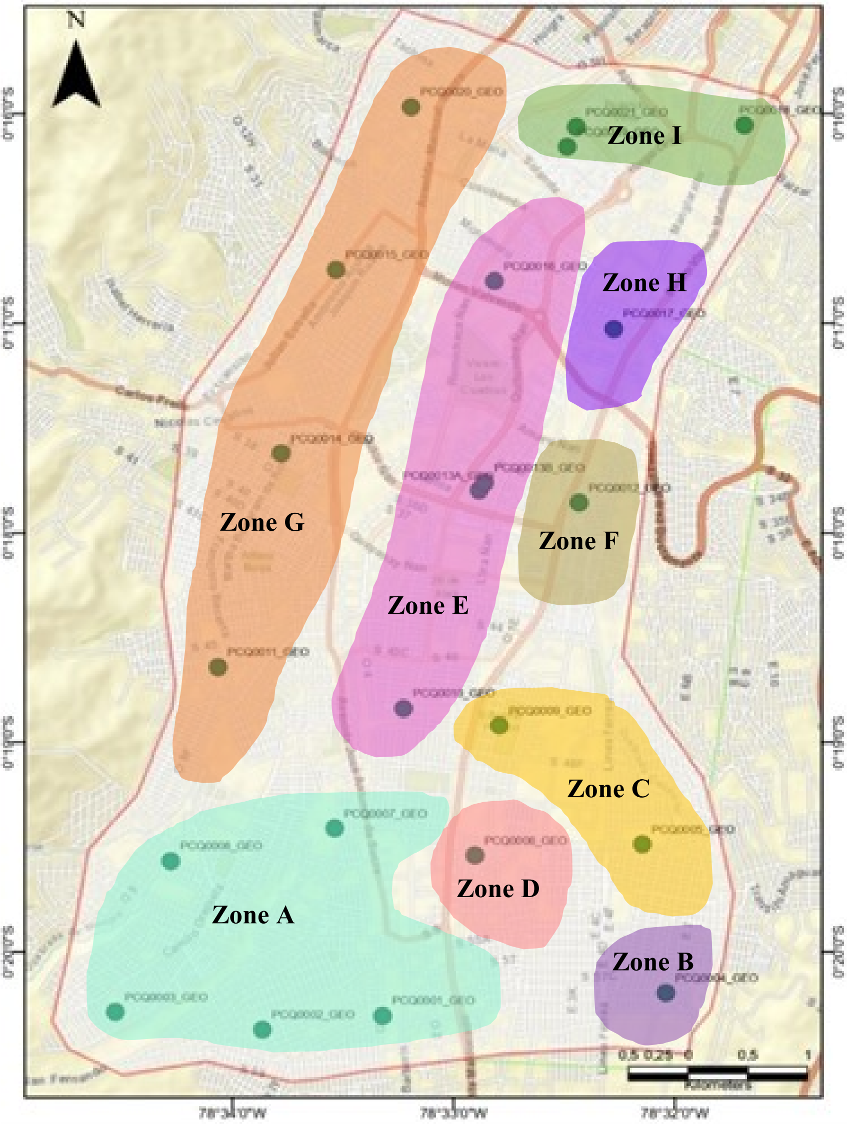

Figure 26. Location of the 20 points where field tests were performed.

The following is a scheme of the location of the field tests corresponding to each borehole, which were located at 1.5 m radius from the central point.

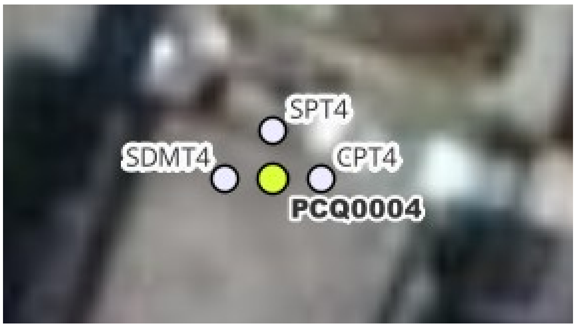

Figure 27. Schematic diagram of the location of the field tests performed by each borehole.

Based on the profiles obtained during the first two years, which can be seen in section 3.3., the information from the field trials was analyzed to group the 20 points of boreholes and field tests into 9 zones based on geographic location and similar physical and mechanical properties. For each of the zones, a summary of the field results was analyzed and presented, as shown in figures 28 and 29. Additional laboratory data was analyzed in the thesis, which included the processing sieving tests, Atterberg limits, natural density, Unified Soil Classification System (USCS), one-dimensional consolidation, and triaxial tests.

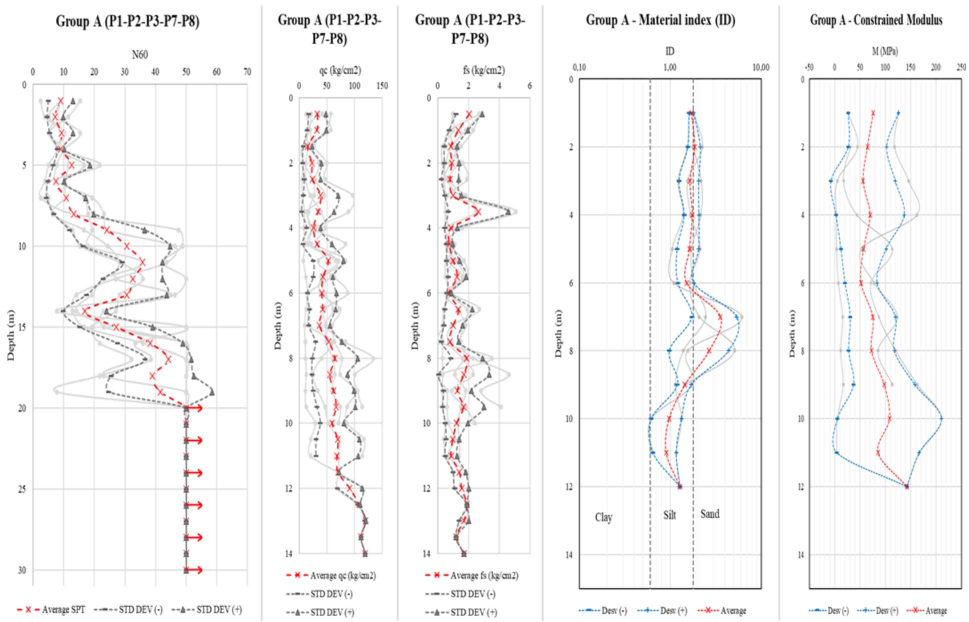

Figure 28. Geotechnical profile Boreholes of Zone A

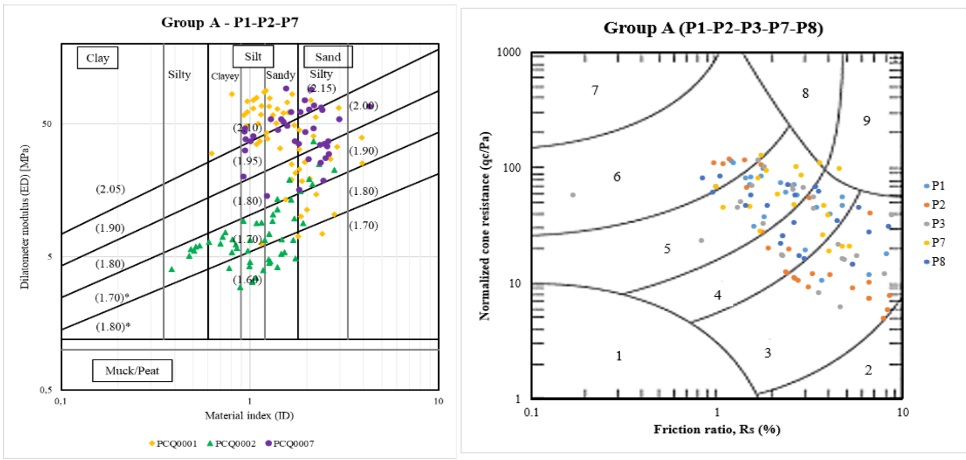

(a) (b)

Figure 29. (a) CPT results from Zone A (b) DMT results from Zone A

Based on all the data processed, a proposed soil columns are presented for each zone, as shown in section 5.2.1. To define the structure and geometry of the subsurface physical model, the research reported by Pacheco et al. 2022, was considered. Based on this research, the basin depth is estimated to be over 800 meters in the south of Quito, so this was used in the columns from the 9 zones detected.

3.1. Field tests

Before describing the field tests that were developed, it is important to mention that PUCE only financed the geotechnical tests. However, shear wave velocities in soils were determined using the Seismic Dilatometer Test (SDMT) and a data set obtained from the Seismic Refraction Test that were provided by the Escuela Politécnica Nacional (EPN).

3.1.1. Standard Penetration Test (SPT)

The standard penetration test (SPT) is still the most used in-situ tests for obtaining the required geotechnical parameters for foundation analysis and design all over the world (Arifuzzaman and Anisuzzaman 2022), been used and studied for over 100 years (Rogers 2006; Skempton 1987). In Ecuador, despite the recent developments and use of the Cone Penetration Test CPT, Piezocone (CPTu), and the Seismic Marchetti Dilatometer (SDMT), it still is the most used test over the country, sometimes used even without the adequate knowledge of its application, as it's a more affordable alternative and possess an extensive experience database (Ahmed, Agaiby, and Abdel-Rahman 2013).

This test is a dynamic intermittent test carried out on a borehole at typically 1.0 m intervals of depth. A standard 50 mm outside diameter split-spoon penetrometer is driven into the soil with repeated blows of a 63.5 kg weight falling through a 760 mm fixed height, also enabling the extraction of disturbed soil samples for identification and classification purposes (Burland et al. 2012). The resistance of the soil to penetration of the sampler is evaluated through the number of blows (N) required to achieve a penetration of 300 mm, having an initial seating drive of 150 mm. This value must be subjected to the application of corrections to obtain a corrected N value for standard hammer energy and overburden pressure (ASTM D1586-11 2011a; Skempton 1987).

(a) (b)

Figure 30. a) Acker Ace b) Longyear

For the tests, two equipment were used. The first, a Boart Longyear Delta Base 520 rig that has a tower that reaches 7 meters in height and works by means of a diesel engine with a capacity of 4 liters which drives the hydraulic circuit; this hydraulic system feeds all the operation, configuration and drilling functions using varied rotary methods, as well as an automatic system for the SPT. The equipment's drilling capacity is up to 200 meters deep in alluvial materials; and in soils it is possible to reach depths of up to 400 meters; a picture can be seen in figure 30. The second equipment was an Acker Ace which is operated through a 28 HP motor that allows the advance of a well to a desired depth, by means of a rotating probe, to which the sampler tubes and drill pipes that have couplings attach. Can reach depths in current conditions of 50-100 meters. Both can be seen in figure 31.

Figure 31. a. Left-Boart Longyear Delta Base 520 b. Right-Acker Ace

The test in both equipment presents several possible variables that has to do with some factors such as the weight of the hammer, the verticality of the system, equipment conditions, the operator capacity, the type of hammer that generates the impact which produces a necessity to normalize the N values measured by any method to a standard rod energy, which is suggested to be 60% (Skempton 1987). For this reason, as part of a thesis in the Pontificia Universidad Católica del Ecuador, D. Ocaña in 2019 performed a dynamic penetration energy calibration method according to ASTM D4633 – 16 with an SPT Analyzer (Ocaña 2019) allowing the corrected N value obtained from the SPT to be used as a means through which the mechanical behavior can be homogenized in all the investigated points, generating through correlations, values of shear wave velocity "S", and thus find similarity between the different layers. The results from the energy measurements on both equipment's can be seen in Table 1.

Table 1. Energy measurement from each drill rig, adapted from (Ocaña 2019)

Drill Rig	*Hammer Type*	*Energy %*
Acker Ace	Safety	77
Boart Longyear DB520	Automatic	85

The summary of the results obtained for the 21 test sites is shown in figure 32. An average standard deviation of 7, with a minimum value of 3 and a maximum value of 33 for each meter in depth indicates a wide dispersion in the data obtained, which will be verified with the geotechnical profiles.

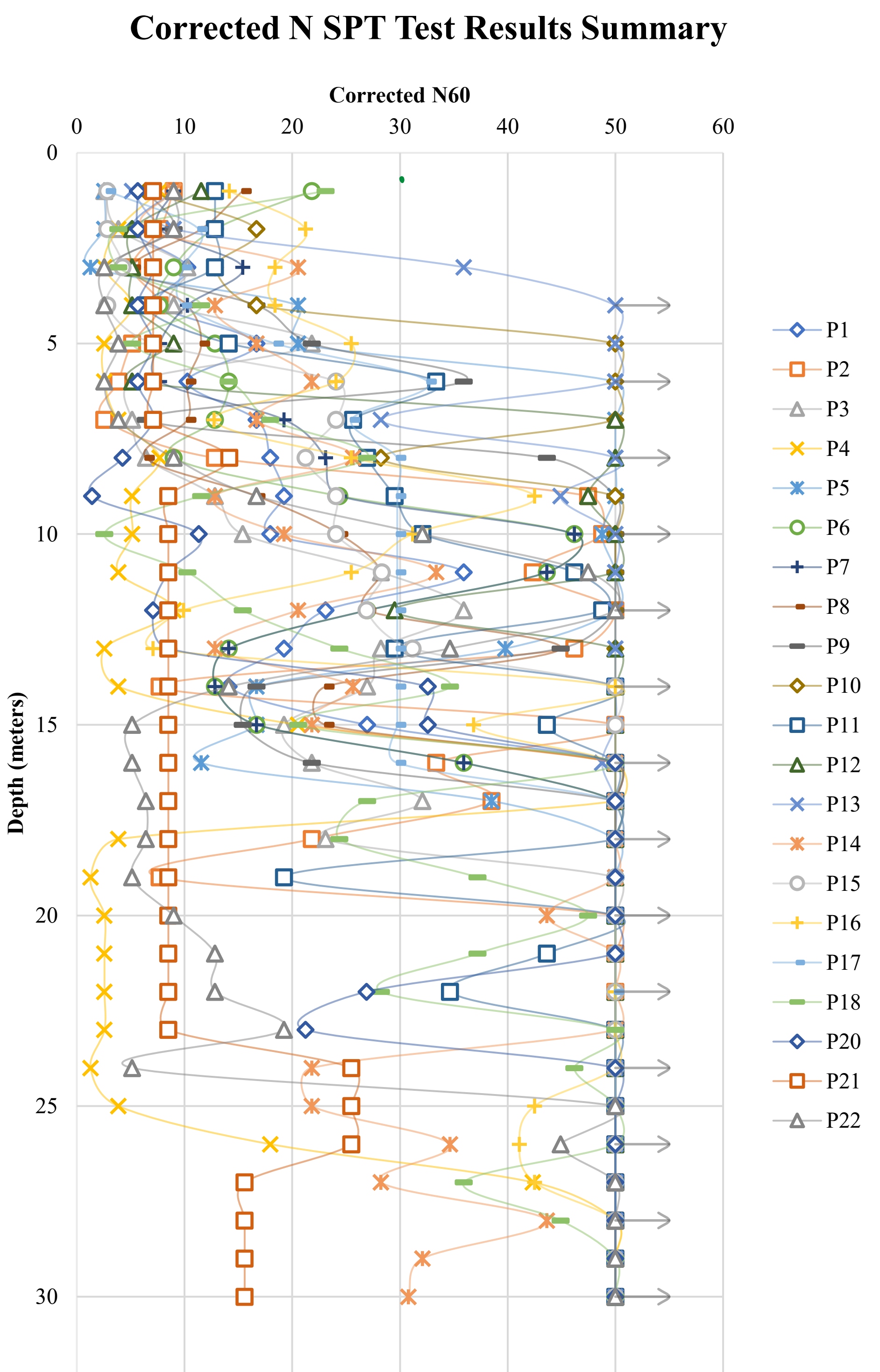

Figure 32. Corrected N SPT Test Results Summary

3.1.2. Cone Penetration Test (CPT)

The static cone penetration test (CPT) has been used widely all over the world in all type of soils since 1932, showing great repeatability and adaptability to updates such as the electrical cone penetration test with the possibility to measure pore water pressures, known as the piezocone (CPTu), or the seismic piezometer to measure shear waves (SCPT) (Lunne, Robertson, and Powell 1997; S. Gundersen et al. 2019).

The results can generate detailed ground profiles, its classification, and can be used to accurately calculate a wide range of parameters in short periods of time. The standard diameter of a 60° cone is 35.7 mm, and the area of the friction sleeve is 150 cm2. Results from both CPT and CPTU deliver a vast range of ground parameters, most through correlations. (Burland et al., 2012b).

The summary of the results from the penetration resistance (qc), friction resistance (fs) and friction relation (fs/qc x100) obtained for the 21 test sites is shown in figure 34, 35 and 36. An average standard deviation of 33 was find for each test in depth, with a minimum value of 7 and a maximum value of 61 for each meter in depth, which indicates a wide dispersion in the data obtained expected from the SPT, again verifying the need of the geotechnical profiles. An additional calculation was performed to obtain the type of soil from the Nomogram proposed by (Lunne et al. 1997; Robertson 2009, 2016; Robertson et al. 1986). The Nomogram, shown in figure 37, indicates a presence of 4% Organic Soils, 27% Clays, 44% Silts to Clays and 24% Sands to Silts, indicating a clear higher number of fine soils over all the site tests.

Figure 33. CPT Test being performed in the South of Quito

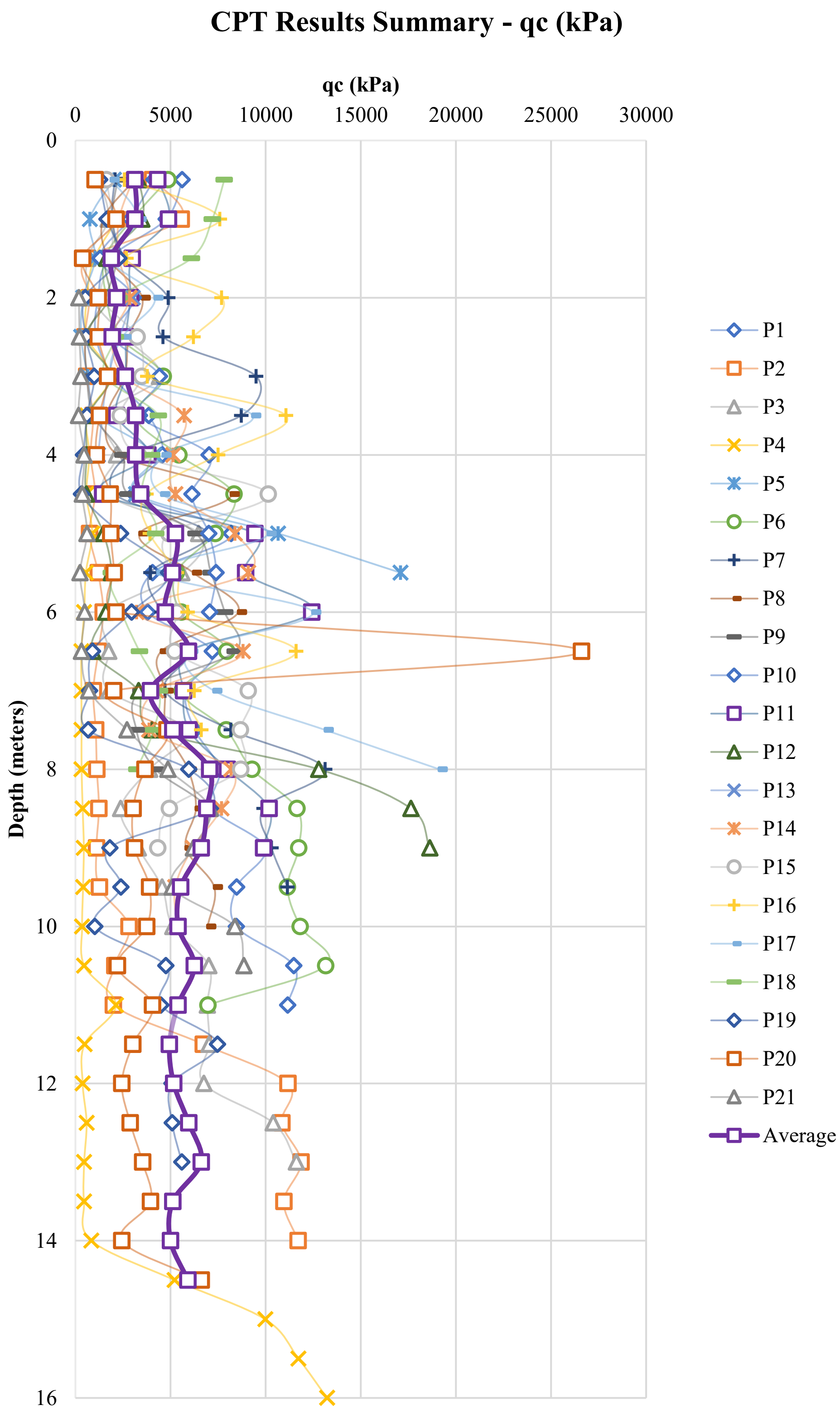

Figure 34. Penetration Resistance qc from CPT Test Results Summary

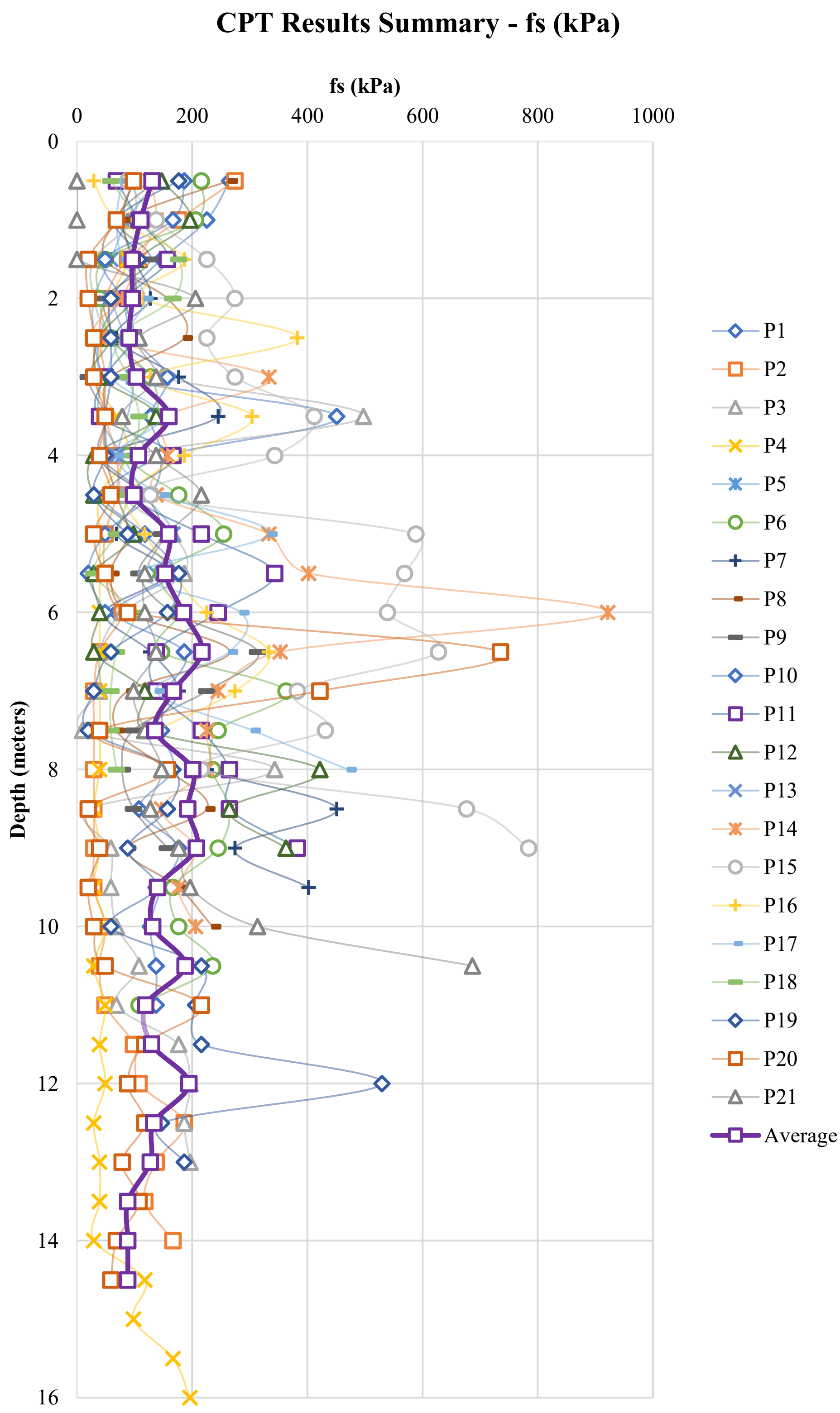

Figure 35. Penetration Resistance fs from CPT Test Results Summary

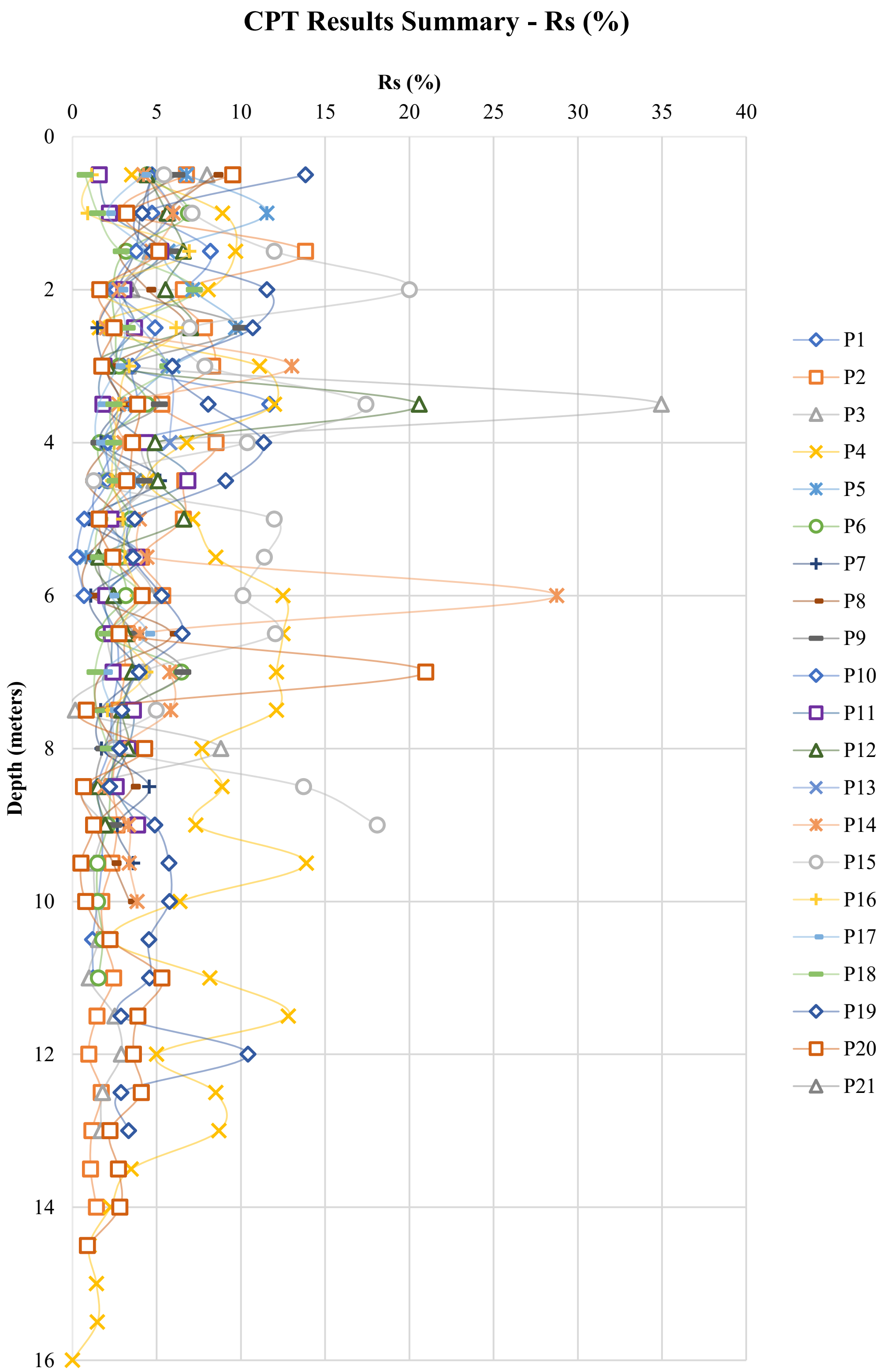

Figure 36. Penetration Resistance Rs from CPT Test Results Summary

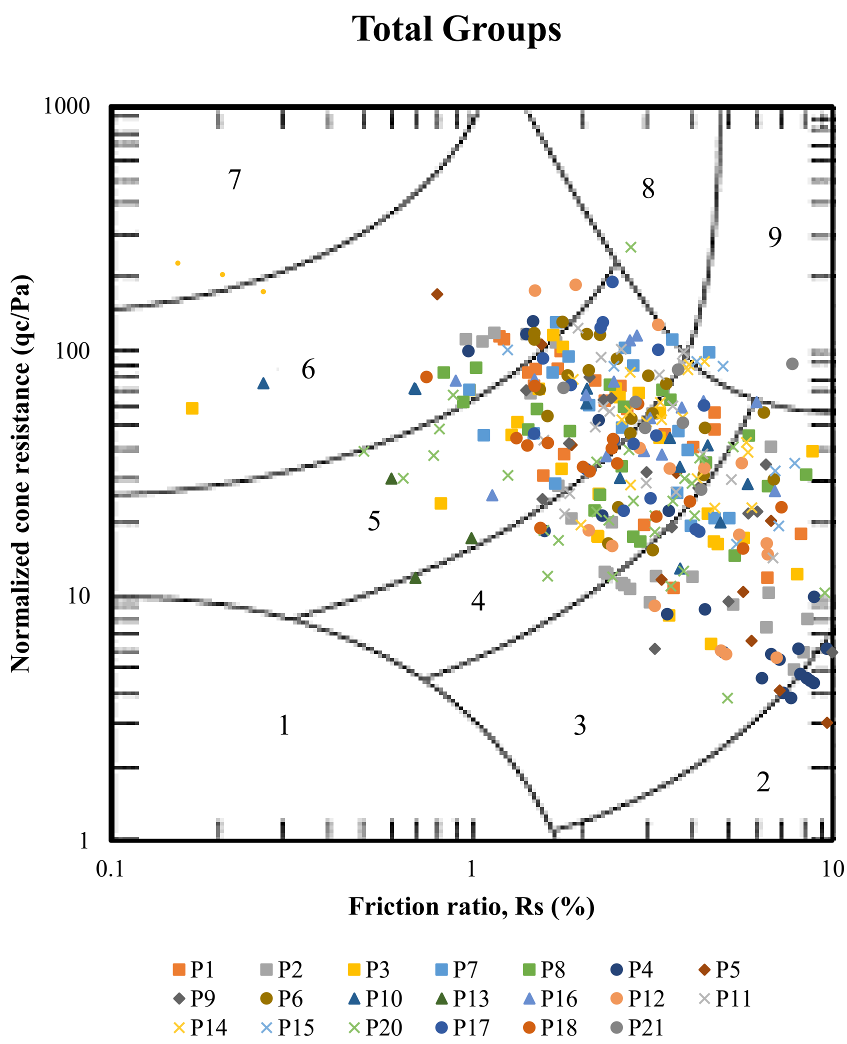

Figure 37. Penetration Resistance Rs from CPT Test Results Summary

3.1.3. Seismic Marchetti Dilatometer Test (SDMT)

The DMT is a static in situ test that consist in the vertical increment of penetration, accompanied by the expansion of a flat, circular, metallic membrane into the surrounding soil. The standard equipment includes a 96 mm wide blade with a thickness of 15 mm that contains a 60 mm diameter steel membrane. The blade is connected through rods to a control unit that possess a pressure readout system, with which the test parameters can be measured. (ASTM D6635-15 2008; Marchetti 1980; Marchetti and Crapps 1981) “At regular intervals, generally of 0.2 m, penetration is halted, and the test is performed by inflating the membrane by gas pressure” (Burland et al. 2012b; Marchetti 1980).

This test is mostly suitable for sands, silts, and clays, where particle size is not as large as the membrane diameter; nevertheless, is not appropriate for gravels. The test can be applied to settlements of shallow foundations in clays and sands, axial capacity of piles, lateral behaviour of piles, compaction control, liquefaction of sands, and detection of slip surface (Burland et al. 2012b). SDMT is the implementation of the normal DMT test with the addition of seismic sensors to measure shear waves velocity Vs. The estimation of Vs is produced through two sensors 50 cm apart of each other. When a surface wave is generated, it arrives first in the top sensor, after a delay, it is registered by the lower sensor. Wave velocity is obtained with the relation of the difference of distances measured from the source and the two receptors and the delay between the first and second sensor. (Marchetti et al., 2013).

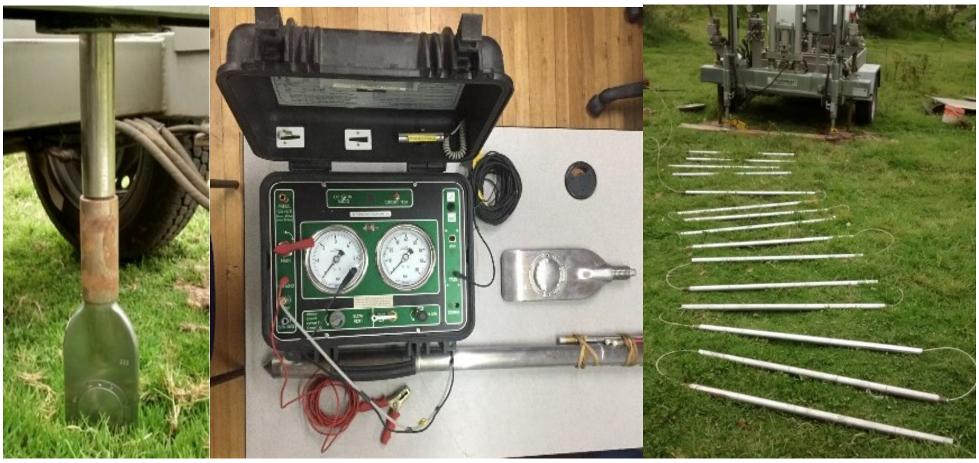

Figure 38. DMT being calibrated and performed in Quito

The nomogram in Figure 39 relates the dilatometer modulus (ED) and the material index (ID), a total of 270 points were plotted, where it is found that the predominant material is silt with 50.4%, followed by sand with 36.7%. In addition, clays are found in 5.9% and muck/peat from borehole 4 representing 7.0%.

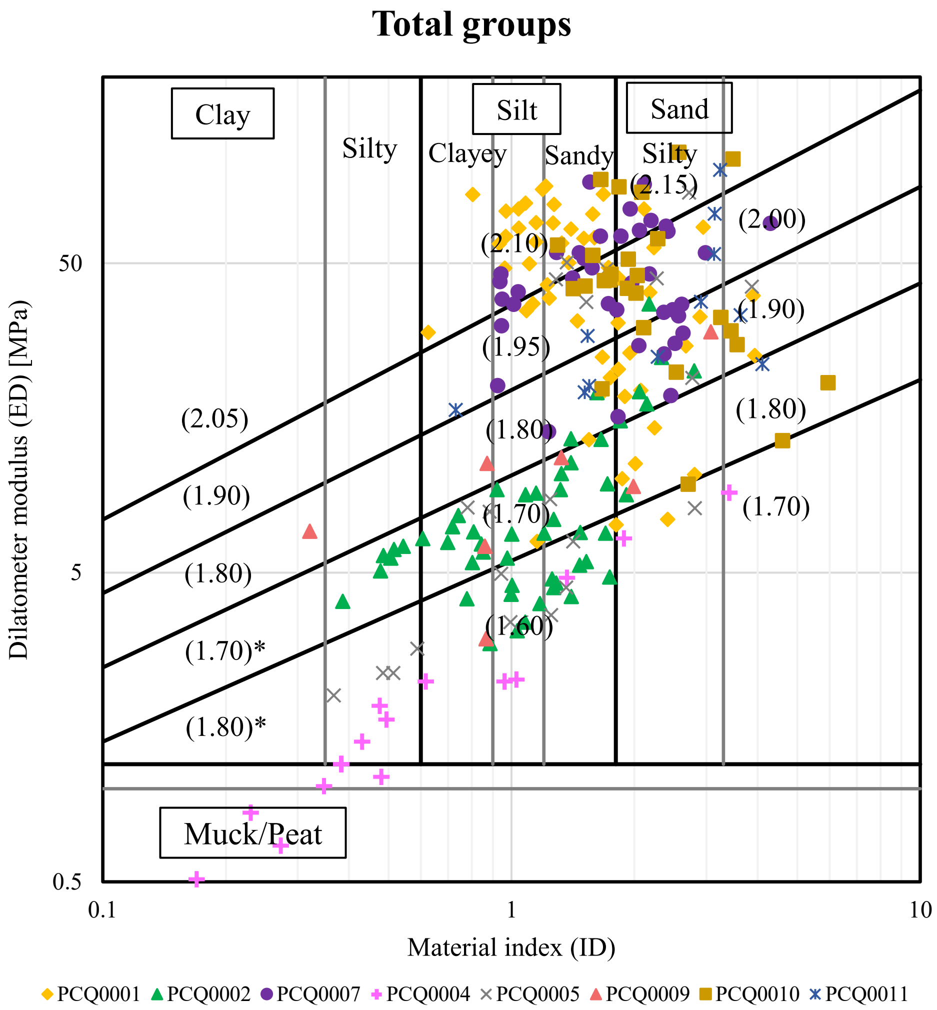

Figure 39. DMT results.

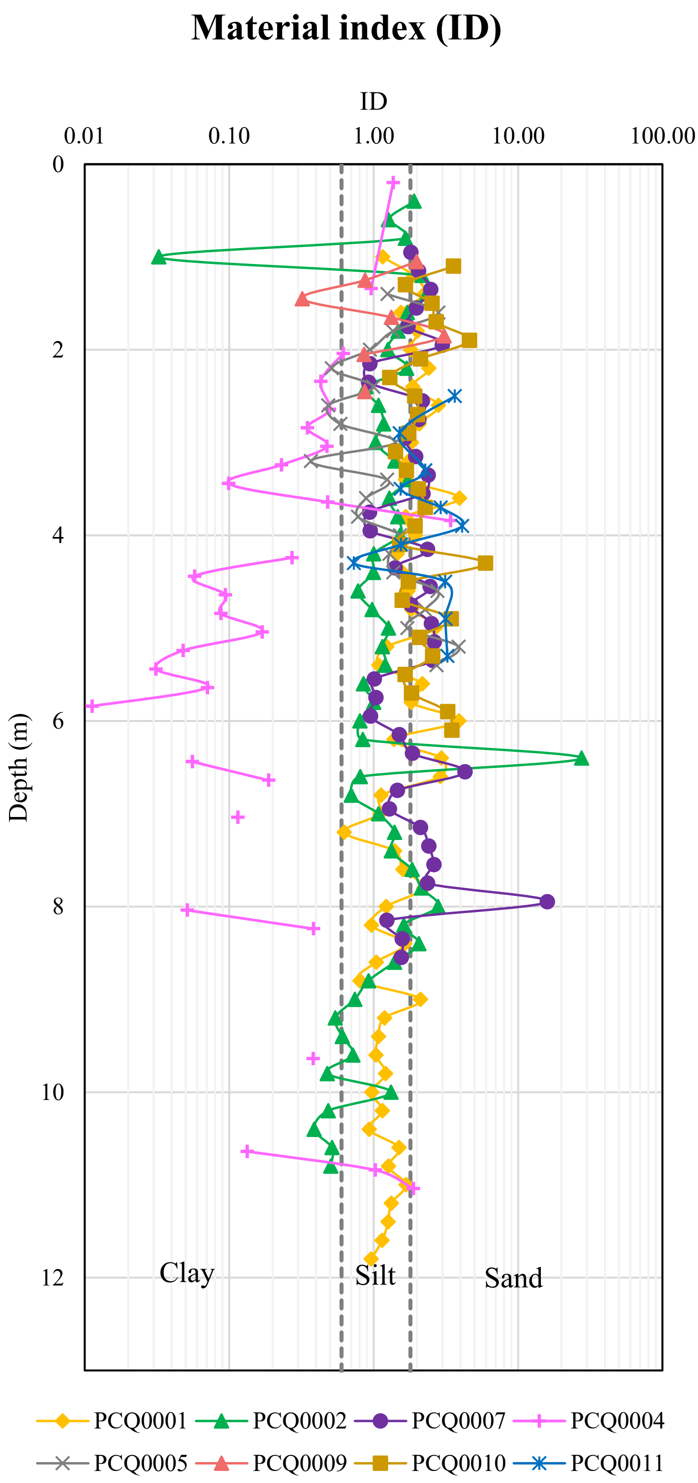

Figure 40. Material index (I_D) results.

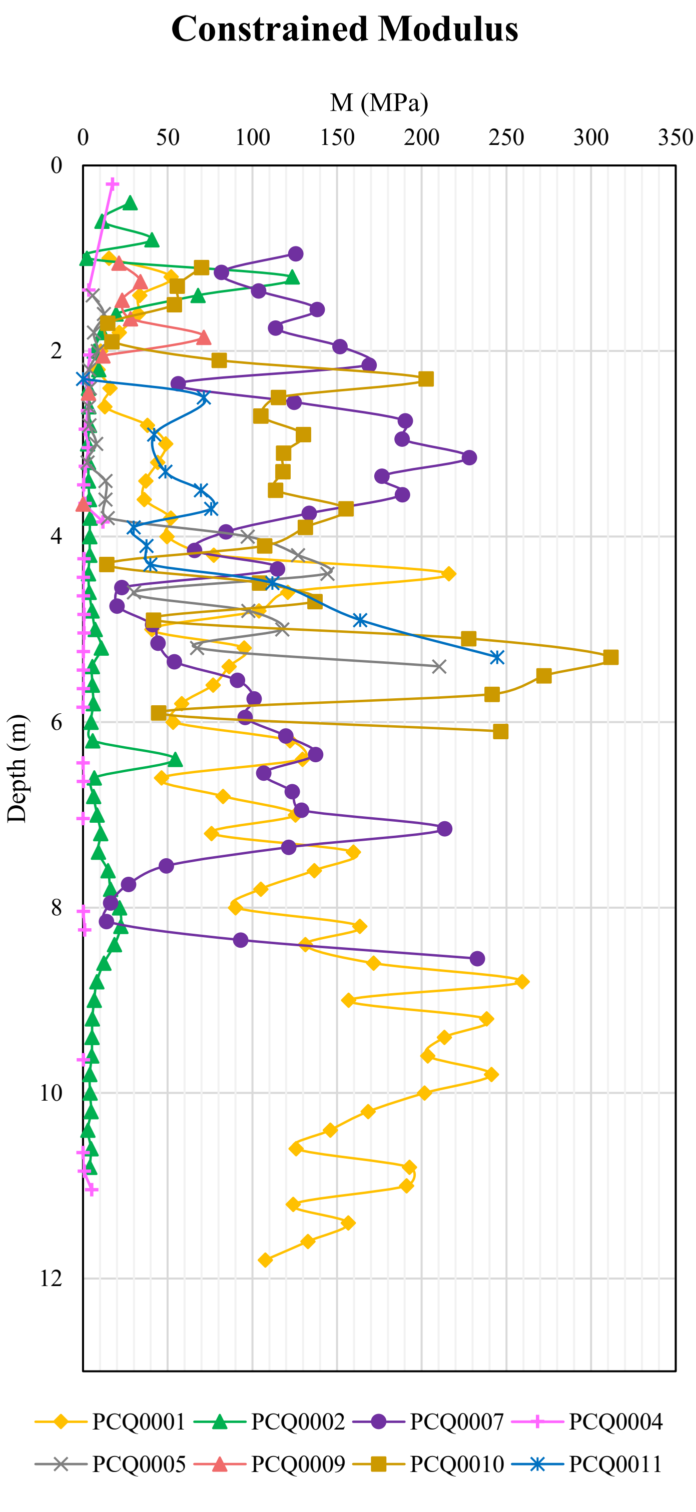

Figure 41. Constrained Modulus (M) results.

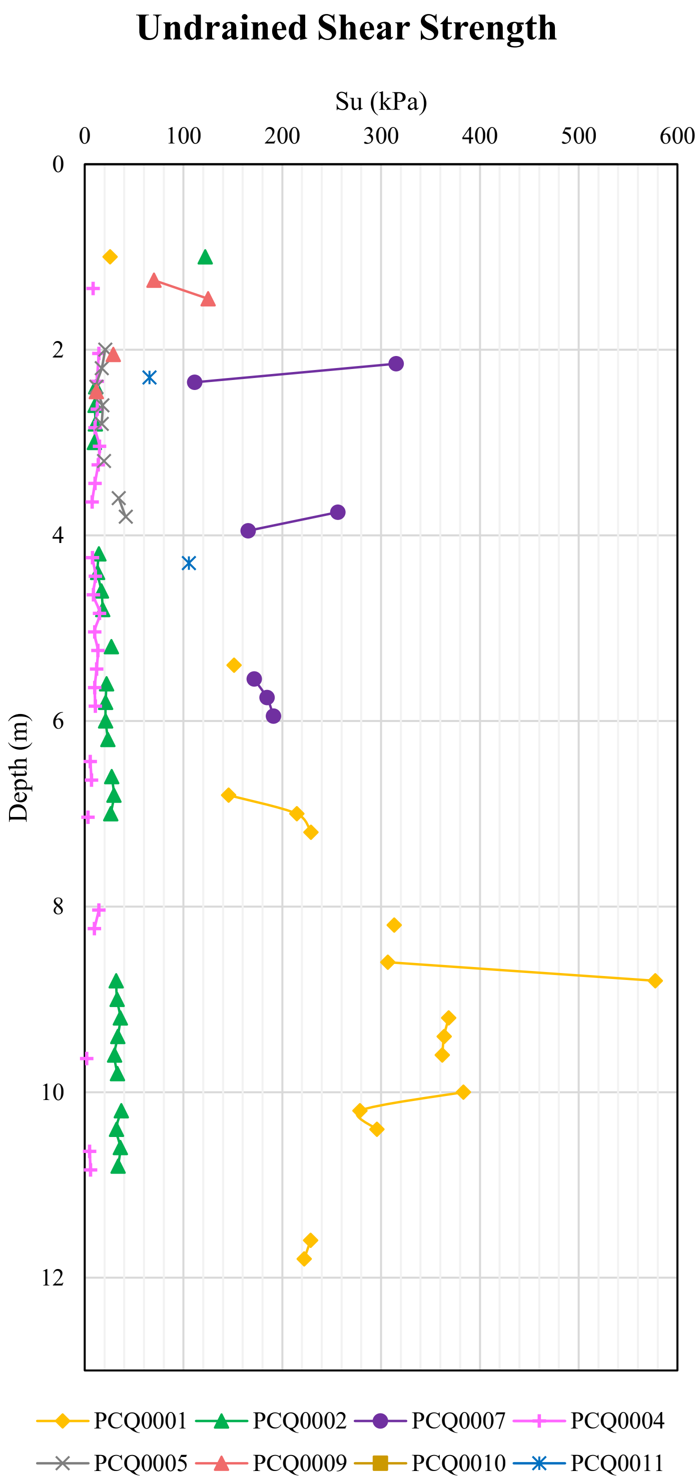

Figure 42. Undrained Shear Strength (Su) results.

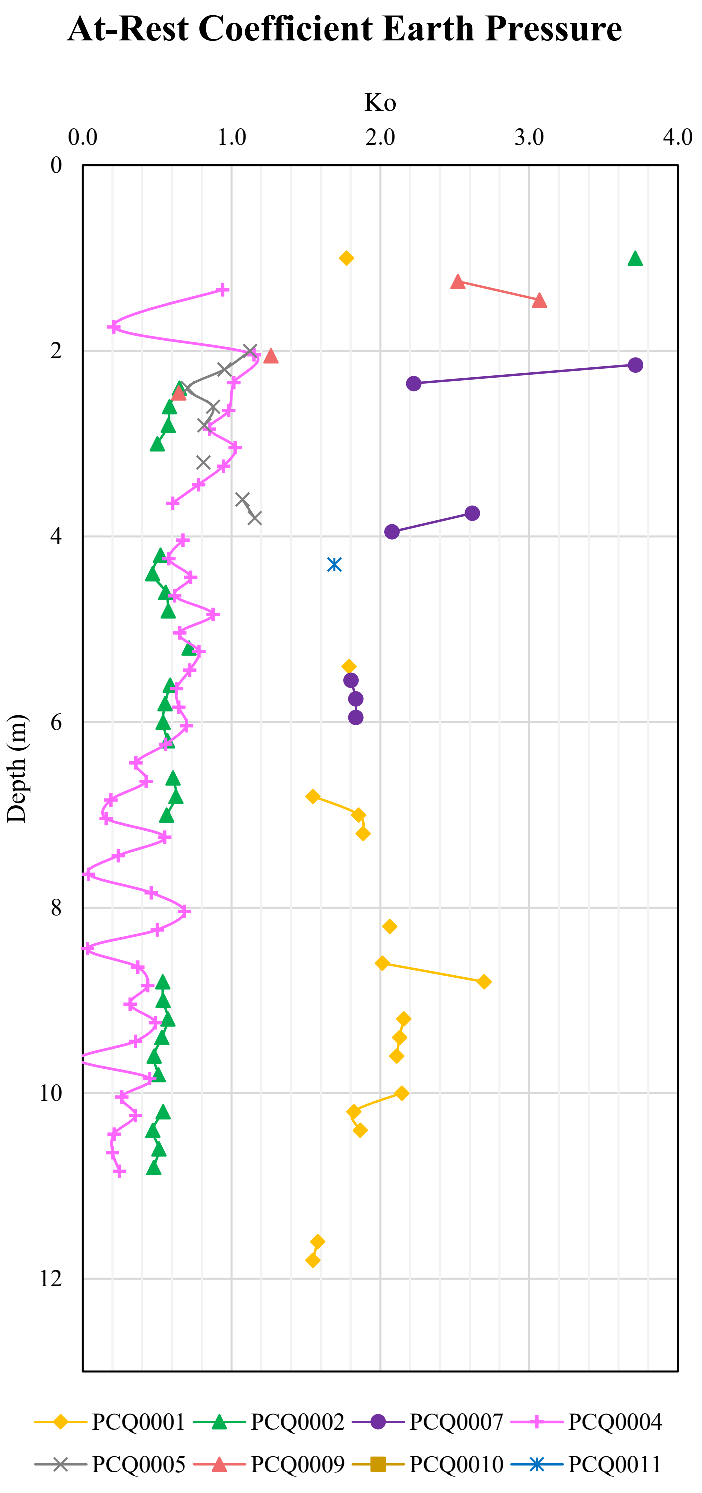

Figure 43. Undrained Shear Strength (Su) results.

3.2. Summary of tests and sampling

All in-situ tests were performed during 2019. In addition, in the 21 sites additional to the maximum depths of SPT, CPT and SDMT achieved, 2 additional boreholes were performed to obtain altered and unaltered samples. The altered samples were obtained through continues drilling with a dual wall core barrel, and the unaltered samples with Shelby tubes following (D1587 2008).

Table 2. Summary of field tests and samples obtained.

Borehole	**DRILLING**				
	Continuos Altered Sampling	**SPT**	**CPT**	**SDMT**	**Unaltered Samples**
		Test (m)	**Test (m)**	**Test (m)**	
PCQ0001	30	30	10,6	23	35
PC00002	30	30	14,2	30,4	33
PCQ0003	30	30	13,4	24,4	39
PCQ0004	30	30	52,4	21,1	46
PCQ0005	30	30	5,6	10,2	31
PCQ0006	30	30	11,4	15	39
PCQ0007	30	30	10,2	29,4	22
PCQ0008	30	30	10,2	18,4	30
PCQ0009	30	30	10	10,7	16
PCQ0010	30	30	6,4	11,2	20
PCQ0011	30	30	9,2	9,6	15
PCQ0012	30	30	9,2	14,54	22
PCQ0013	30	30	2	10,4	18
PCQ0014	30	30	11	26,4	16
PCQ0015	30	30	9	22,5	11
PCQ0016	30	30	7,65	58,4	11
PCQ0017	30	30	8	53	12
PCQ0018	30	30	8	32,9	49
PCQ0019	30	30	13	-	15
PCQ0020	30	30	17	16,4	8
PCQ0021	30	31	10,6	13,8	17
Sum	**630**	**631**	**249,05**	**451,74**	**505**

Figure 44. Example of the continuous sampling in Borehole 14, applied to the 21 sites.

Figure 45. Example of the continuous sampling from a. Longyear DB520 b. Acker Ace

Figure 46. Example of the Shelby Sampling

With the altered samples, soil classification was performed following (ASTM 2488-09a 2009; ASTM D2487-17 2017), and with the unaltered Shelby Samples, geomechanical tests were performed. A summary of the tests performed can be seen in Table 2, and the detail of each test with the results obtained is presented in the following sub chapters.

3.2.1. Specific Gravity

Twenty-four specific gravity tests were carried out in 2022, with materials belonging to the boreholes corresponding to each of the zones established based on Figure 26 at different depths. The results were as follows:

- Over the first 20 meters the Gs values range between 2.4 and 2.8, except for a point in zone B, which at 9.50 meters presents a Gs value of 2.17.
- The last 6 meters have Gs values between 2.6 and 2.8.

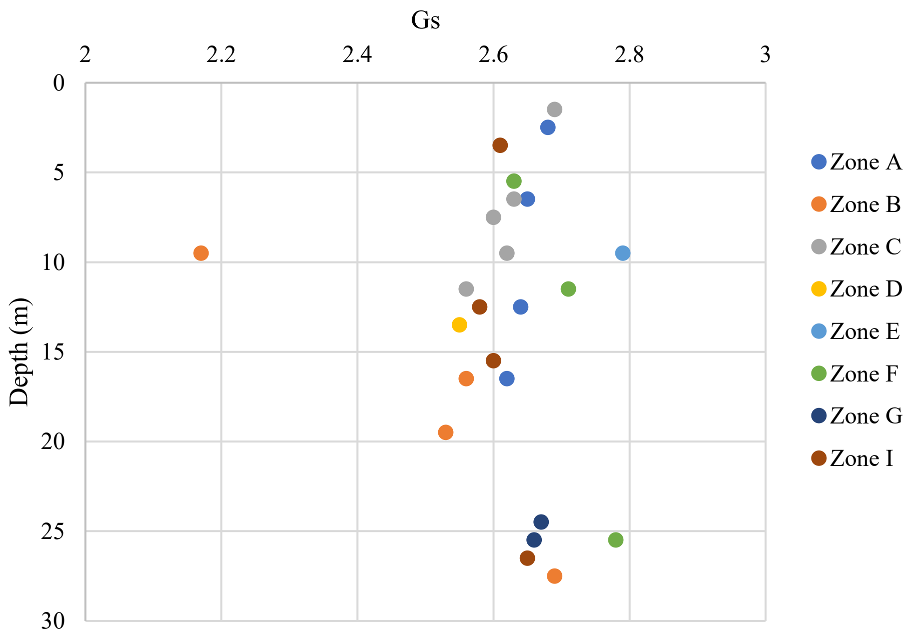

Figure 47. Gs results.

3.2.2. Unified Soil Classification System (USCS)

USCS is a test aimed to classify mineral and organo-mineral soils for engineering purposes, based on a series of laboratory parameters such as moisture content (ASTM D2216-10 2010), particle-size distribution, liquid limit, plastic limit, and plasticity index (ASTM D4318, ASTM D 4318-10, and D4318-05 2005). From these results a material description and symbology are obtained. (ASTM D2487-17, 2017).

Table 3. Summary of USCS tests

Borehole Point	USCS laboratory tests		
	Water content	Plasticity	Sieving
1	30	30	30
2	31	31	31
3	34	34	34
4	43	43	43
5	31	31	31
6	34	34	34
7	31	31	31
8	22	22	22
9	35	35	35
10	31	31	31
11	23	23	23
12	36	36	36
13	46	46	46
14	39	39	39
15	33	33	33
16	34	34	34
17	35	35	35
18	34	34	34
19	30	30	30
20	23	23	23
21	28	28	28

3.2.2.1. Water Content

On average, the water content of the soil is 38% in all the depth of the 21 boreholes, with an average per meter in depth minimum value of 21%, and a maximum average per meter depth of 62%. The average standard deviation per meter is 7, with max and min values of 47 and 7, which reduces to 3 when the borehole 4 (which has an average water content of 164, with values up to 319% at 13m depth) is not considered in the average.

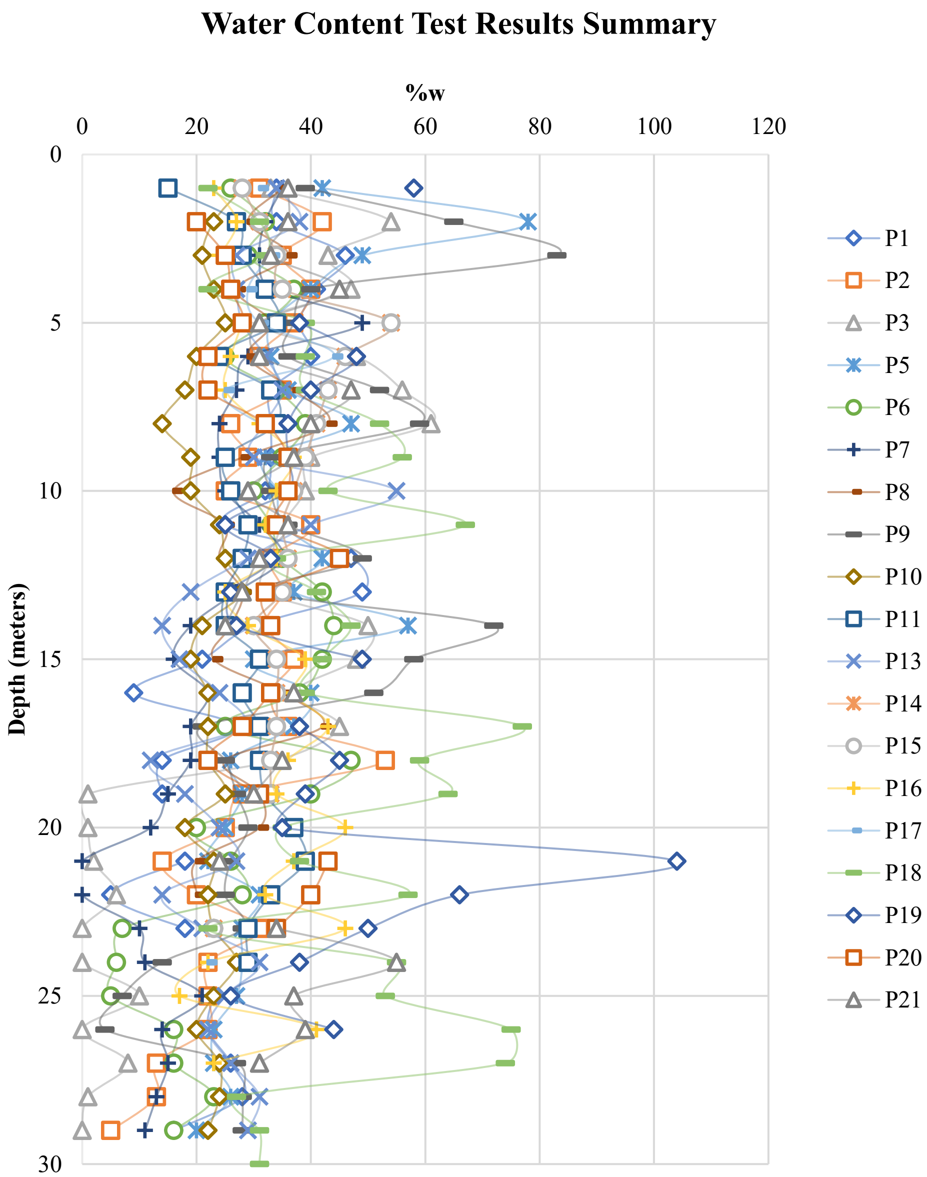

Figure 48. Water Content Test Results Summary

3.2.2.2. Liquid Limit

The Liquid Limit (LL) tests showed two different behaviors, the first between 0 to 15 meters, with an average LL of 43 and a standard deviation of 9, while from 16 to 30 meters the LL reduces on average to 15, with a standard deviation of 6, mostly due to the presence of non-plastic soils. In between the data, several layers of erratic non-plastic soils appear, indicating the possibility of drainage stratums. Point 4 goes off the charts with an average LL of 148, with an average of 213 the first 15 meters, indicating the possibility of high plasticity organic soils, founded in previous research (Albuja-Sánchez 2021).

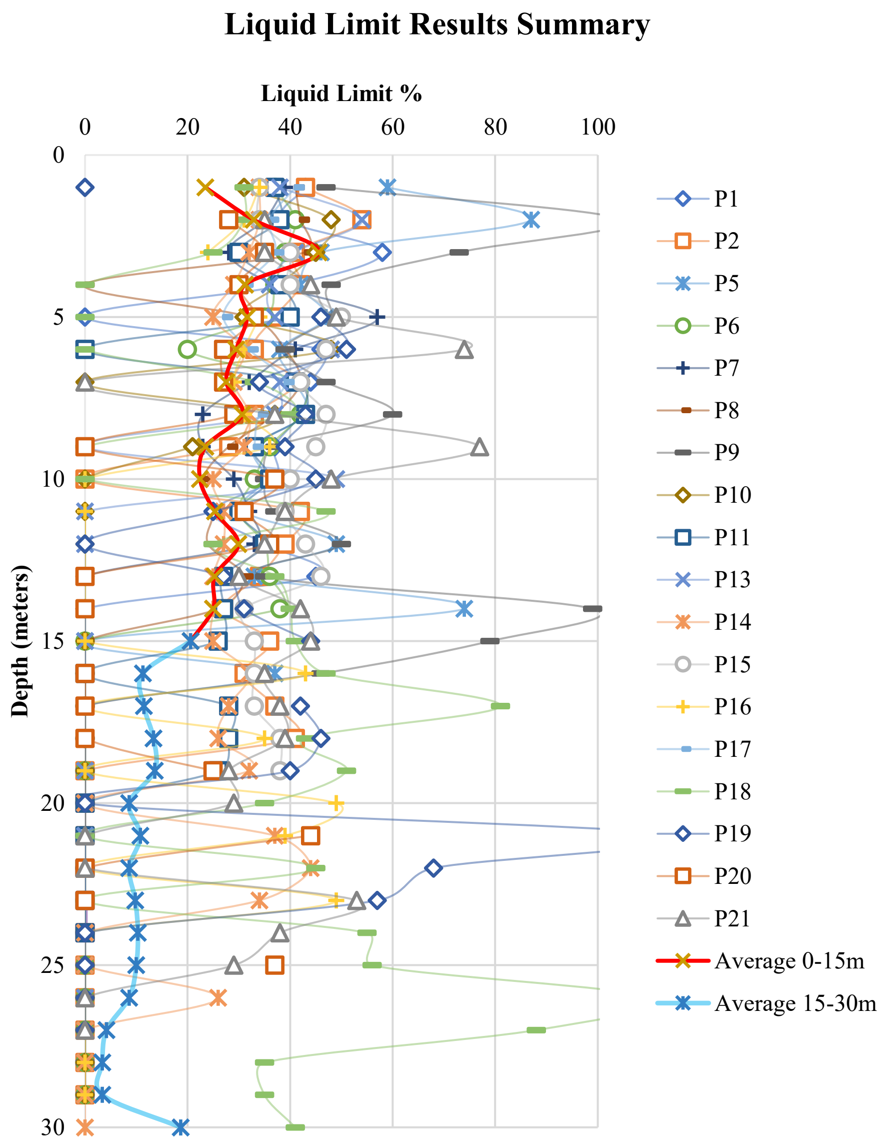

Figure 49. Liquid Limit Test Results Summary

3.2.2.3. Plastic Limit

Plastic Limit (PL) tests showed a similar behavior, the first between 0 to 15 meters, with an average PL of 31 and a standard deviation of 6, while from 16 to 30 meters the LL reduces on average to 11, with an standard deviation of 4, Point 4 data shows an average PL of 98 in all the depth, while the first 15 meters average is 141.

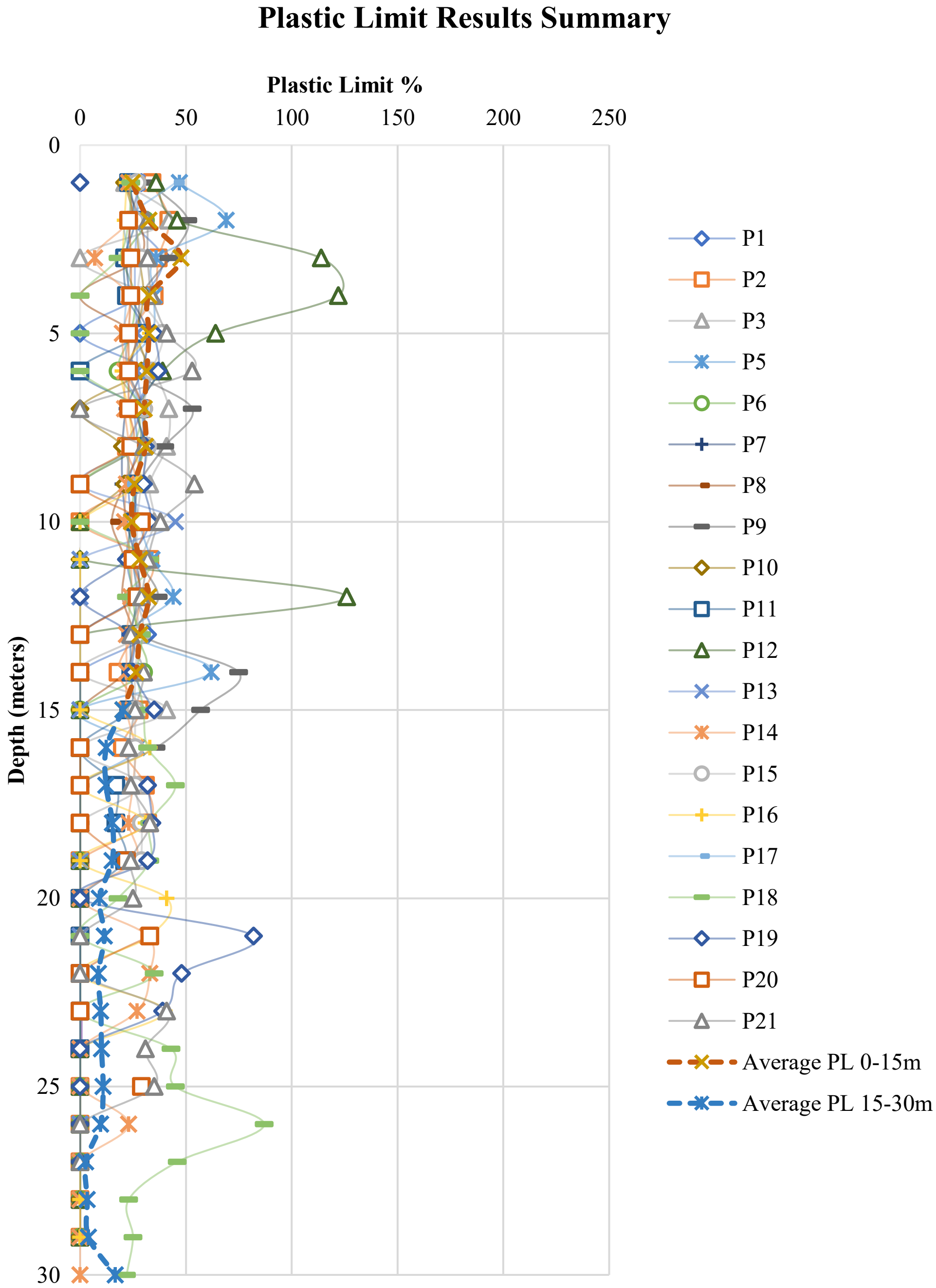

Figure 50. Water Content Test Results Summary

3.2.2.4. Plastic Index

The average Plastic Index the first 15 meters is 12, with a standard deviation of 3. The last 15 meters is 4, with a standard deviation of 2. Point 4 PI average the first 15 meters is 71, and the last 15 meters is 28.

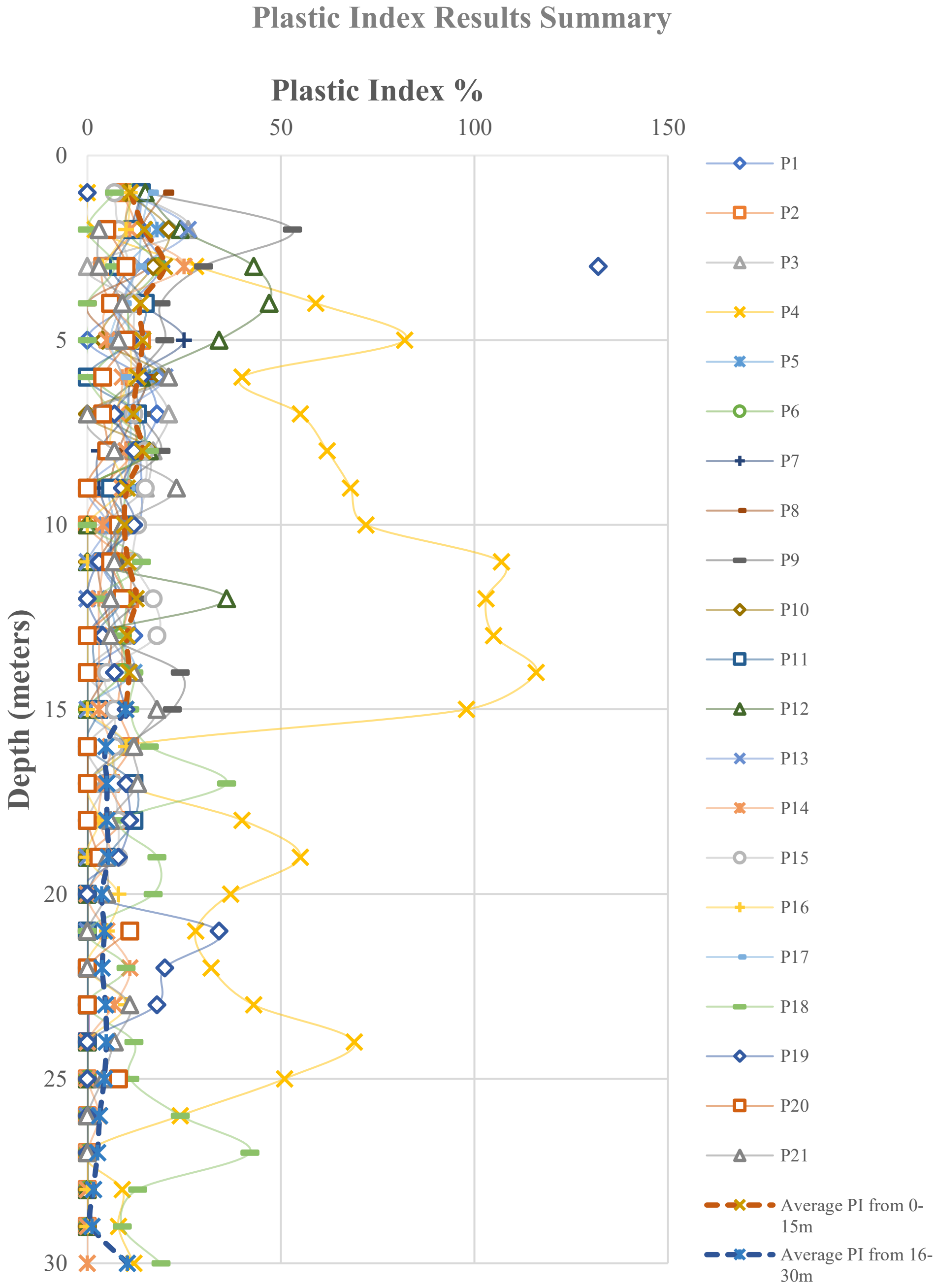

Figure 51. Plastic Index Results Summary

3.2.2.5. Plasticity Chart

The results from LL and PI were plotted in the plasticity chart of the USCS which can be seen in figure 52. From the results, near the 60% of soil has plasticity, and from that percentage of fine soil, nearly 82% is Silty Sand ML, 9% is Silty Clay CL, and 9% is High Plasticity Silt or High Plasticity organic soil (some points are off the presented chart) which corresponds to sites P4 and P12.

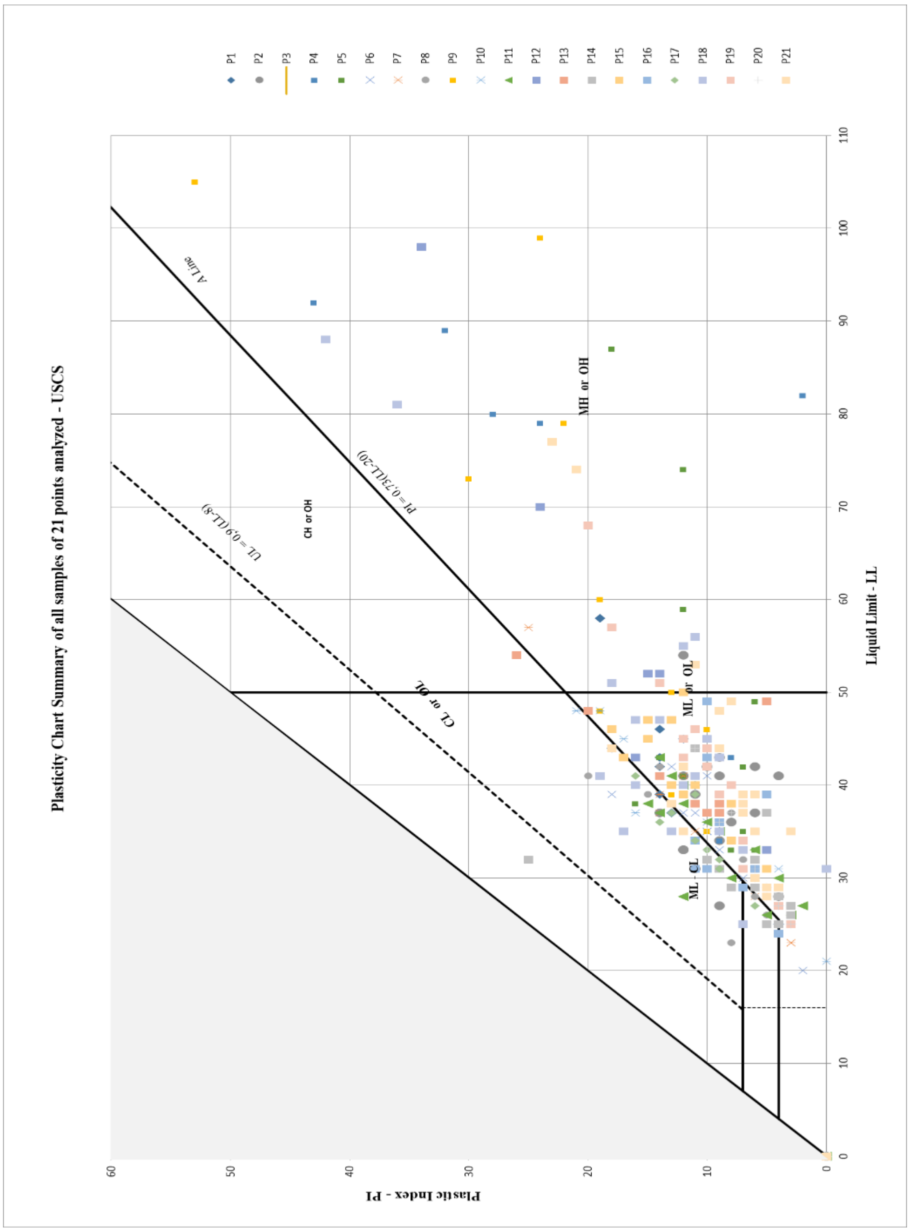

Figure 52. Plastic Chart Results Summary

3.2.2.6. Material Passing Sieve N°200 Results

A compilation of the percentage of soil passing the N° 200 Sieve (0.075mm) is plotted in Figure 53. On average, the percentage reduces from 61 to 23 in the 30 meters depth profile, matching the plastic behavior indicated previously. The average of the first 15 meters in 58%, and the last 15 meters is 30%, both with an standard deviation of 6.8.

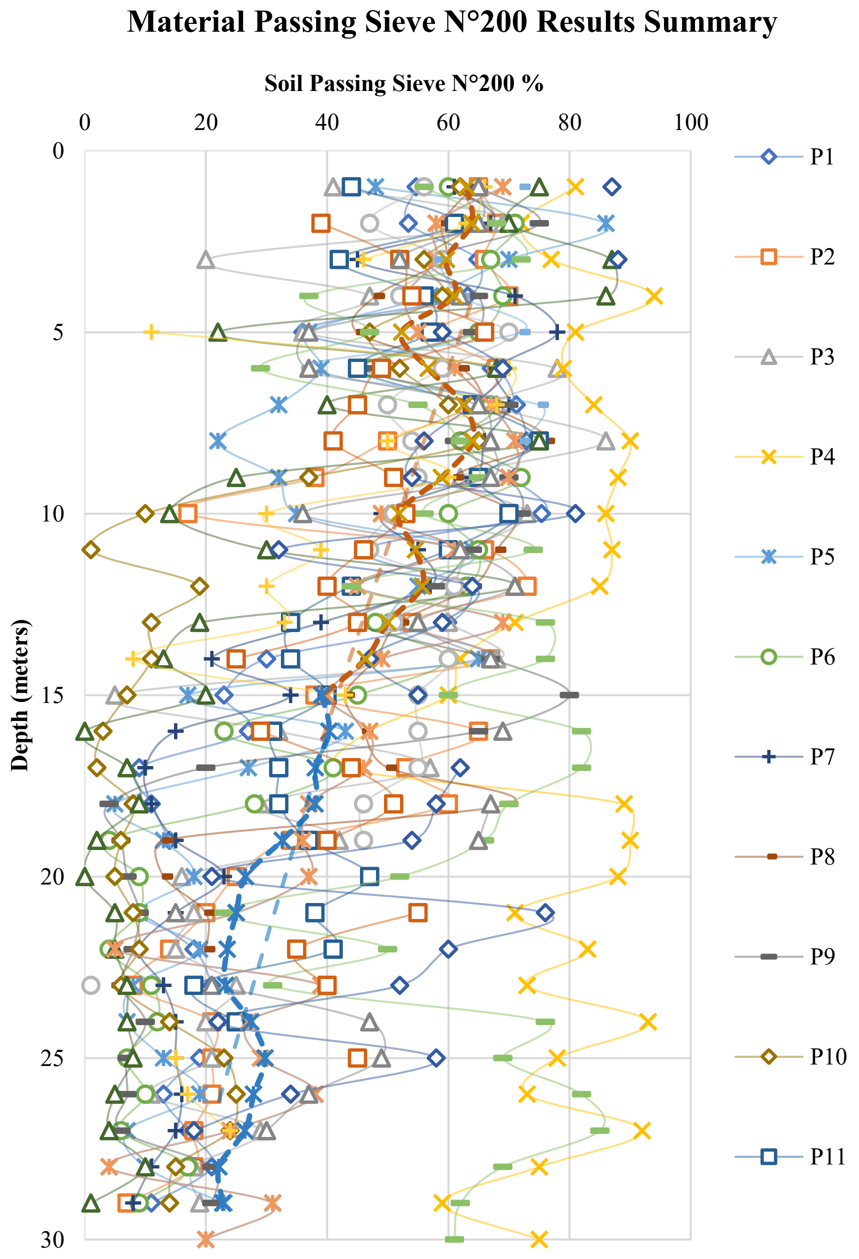

Figure 53. Soil Passing Sieve N°200 Results Summary

3.2.2.7. **Sieving and Hydrometry**

A compilation of the sieving tests is presented in the figure 54.

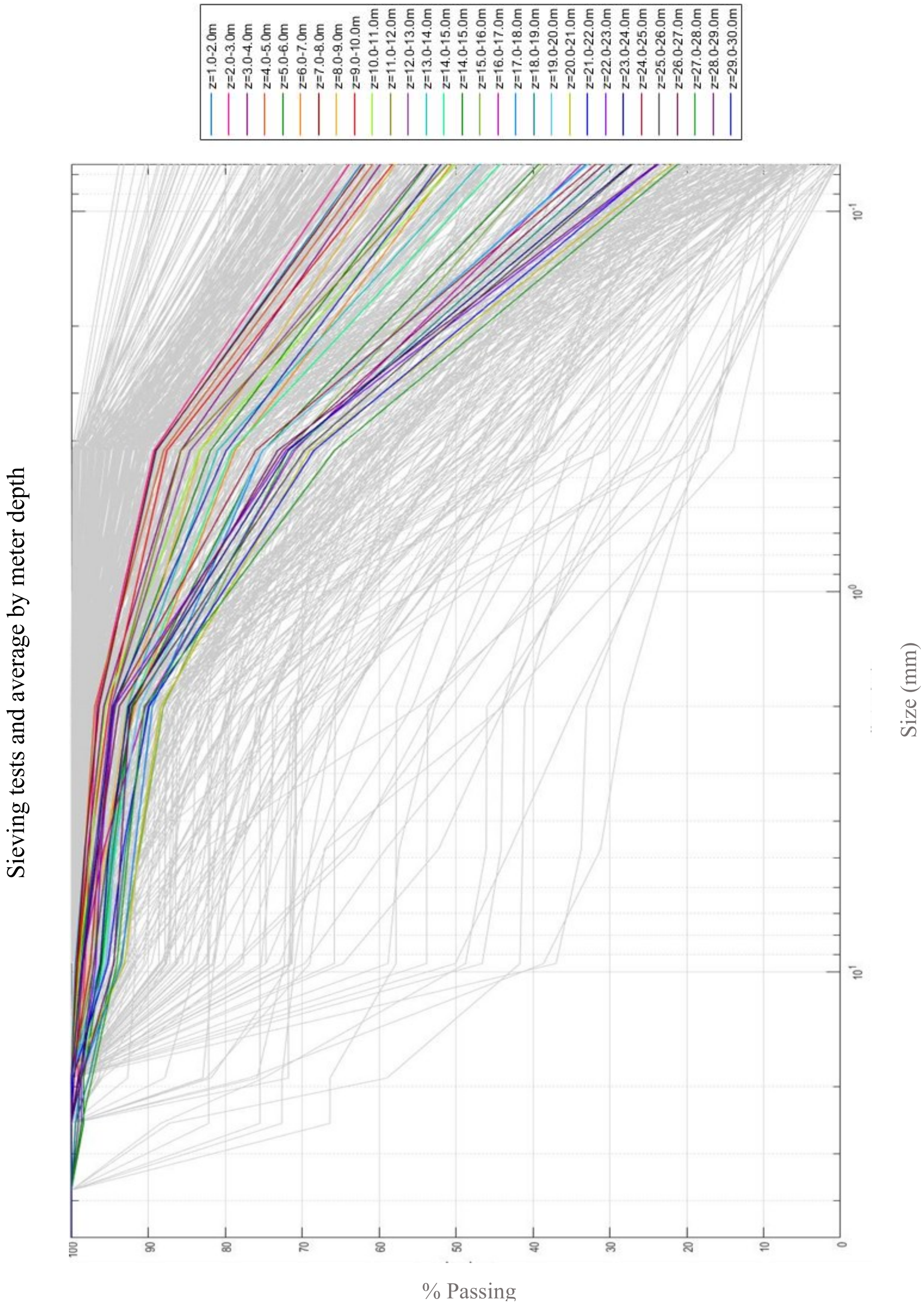

Figure 54. Soil Passing Sieve N°200 Results Summary

Considering most of the soils had percentages passing sieve N200, 100 hydrometer tests were performed.

The results can be seen in figure 55.

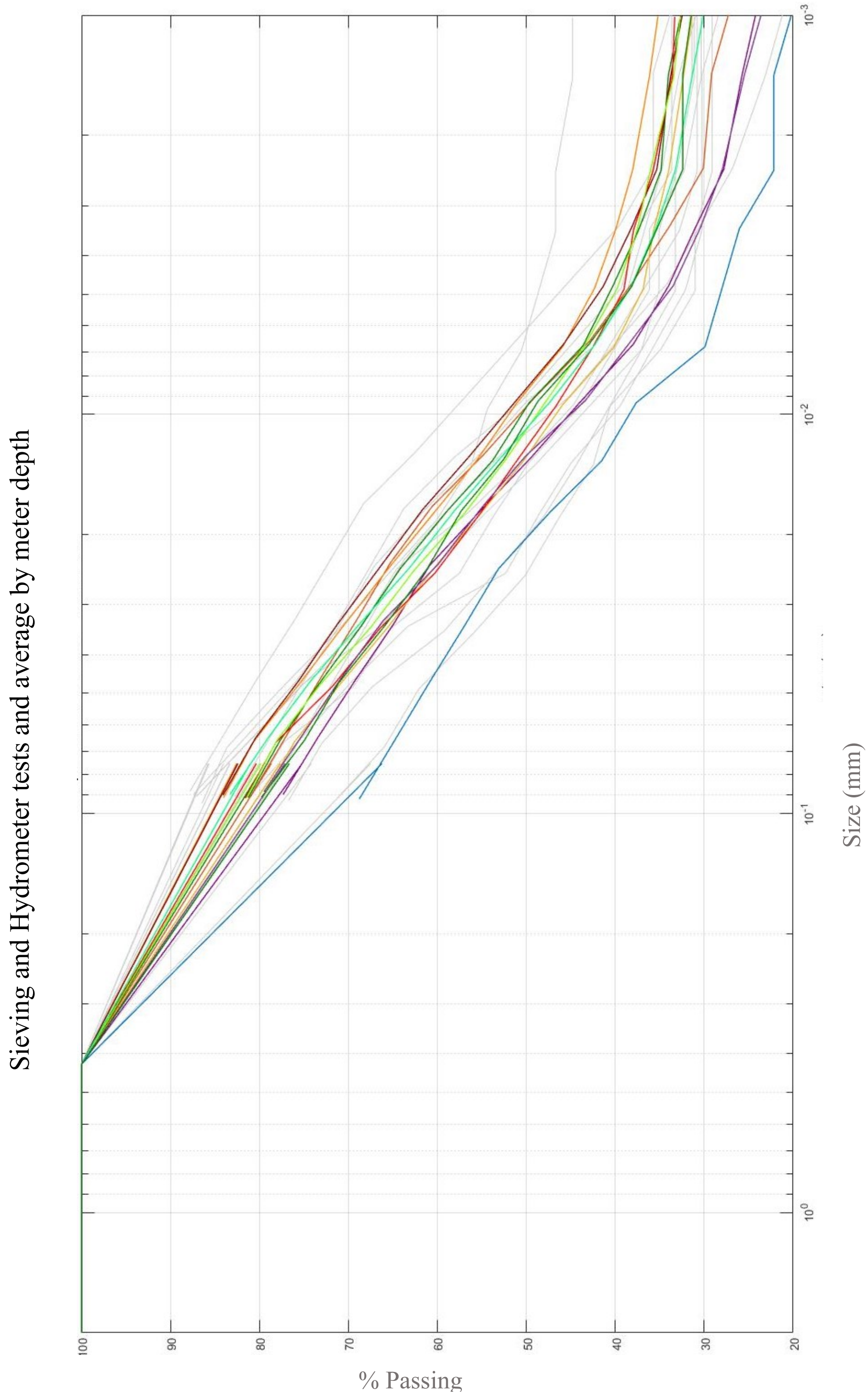

Figure 55. Sieving and Hydrometer tests and average by meter depth Summary

3.2.3. Total and Dry Unit Weight

The total unit weight was calculated based on (ASTM D7263 2021) from intact specimens obtained from thin-walled sampling tubes, performing in total 397 tests. On average on all sites, total unit weight didn't vary considerably in depth, with an average of 16,48 kN/m^3, with a standard deviation of 0.68. The summary of the total unit weight results is shown in Figure 56.

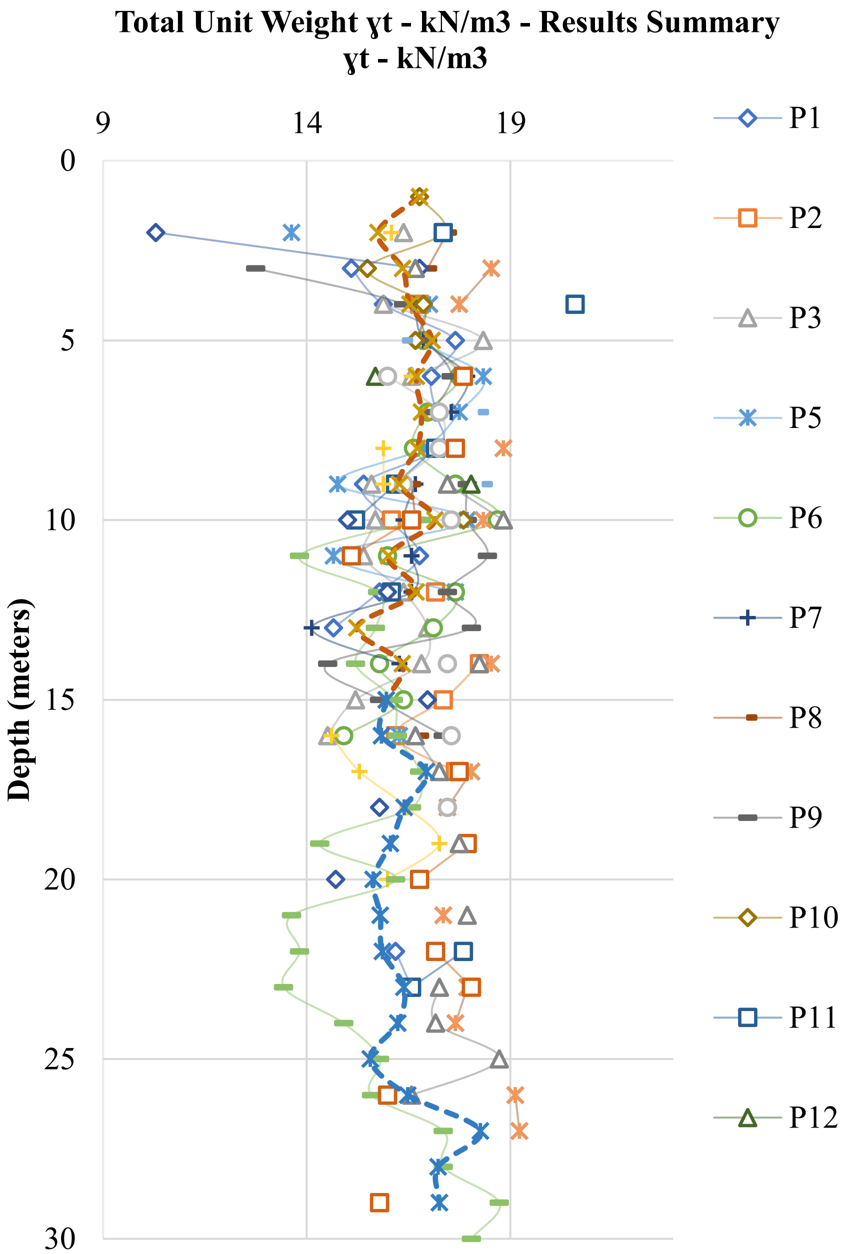

Figure 56. Total Unit Weight Results Summary

With the water content of each sample, the dry unit weight was calculated and plotted in Figure 57. The overall average is 11.92 kN/m3 with a standard deviation of 1.07. In borehole 4 and 19, several soils have dry density below 9.8 kN/m3, which indicates the possible presence of organic soils.

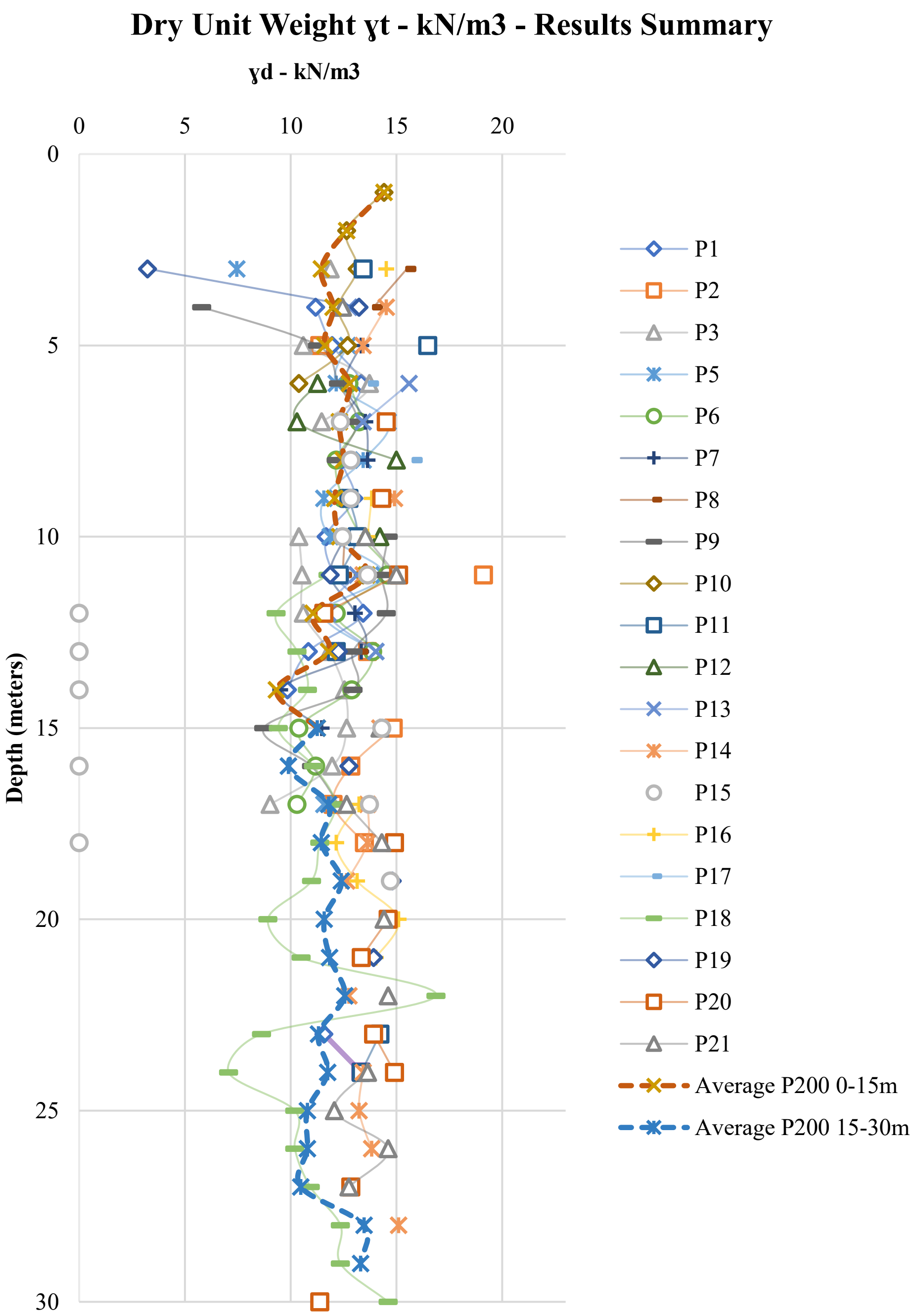

Figure 57. Dry Unit Weight Results Summary

3.2.4. Oedometer and Triaxial tests

3.2.4.1. Consolidaded Undrained Triaxial Test

3.2.3.1.1 Results of PCQ3-TCU-2.00-2.50

Table 4. Results of triaxial test in PCQ3 with depth 2.00-2.50m

	Total Stress	Effective Stress
C (kPa)	23,76	23,60
φ (°)	20,46	21,89
ρ_{bulk} (g/cm^3)	1,553	

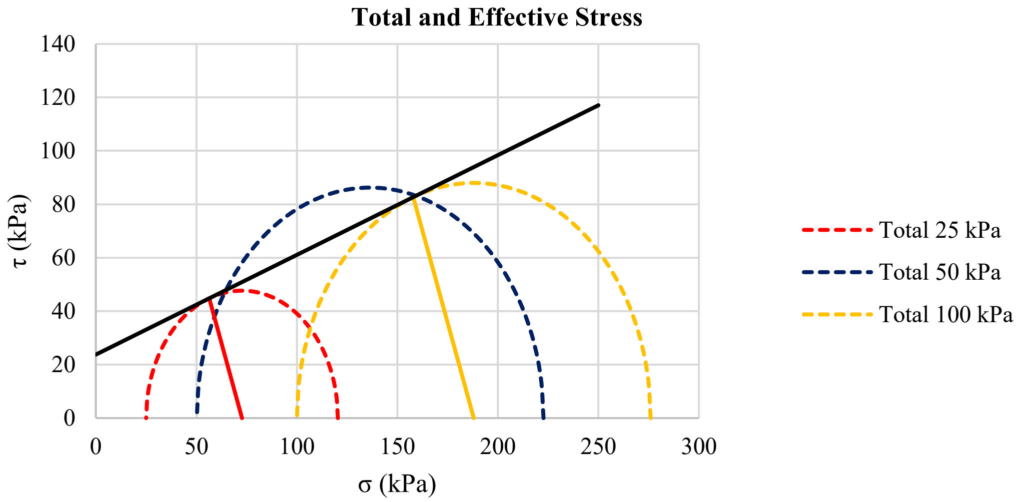

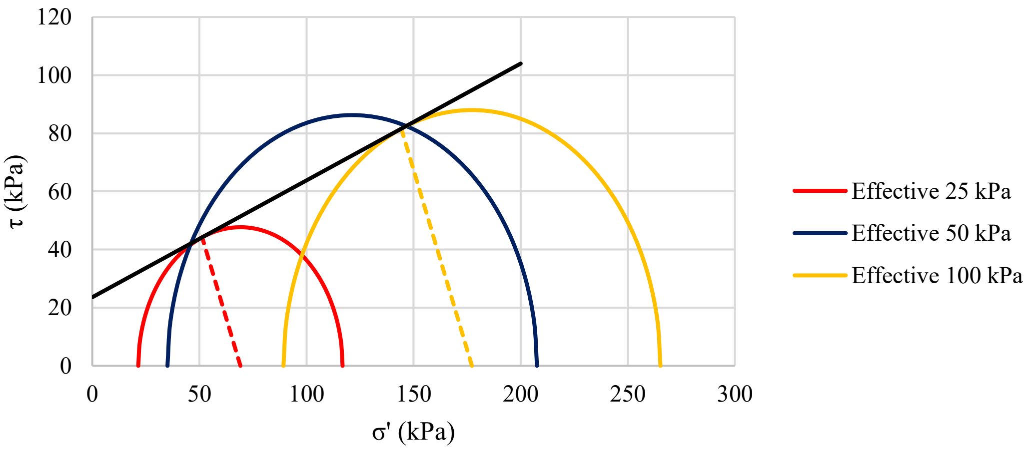

Figure 58. Grafics of total and effective stress of PCQ3

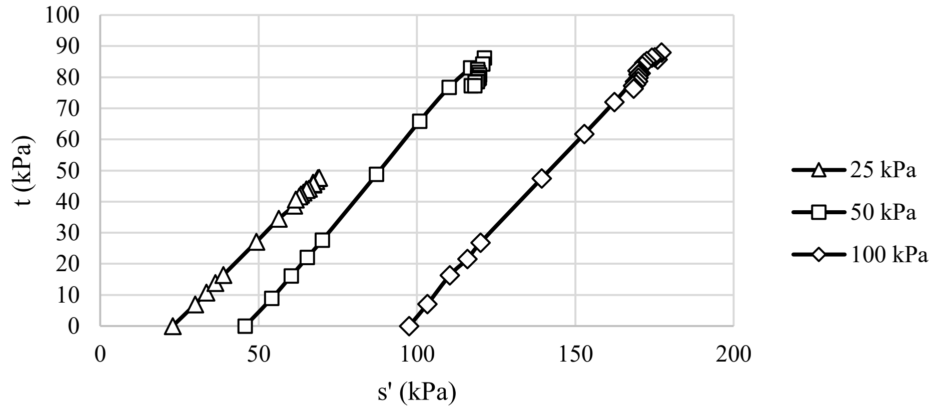

Figure 59. Grafic of t vs. s'. PCQ3

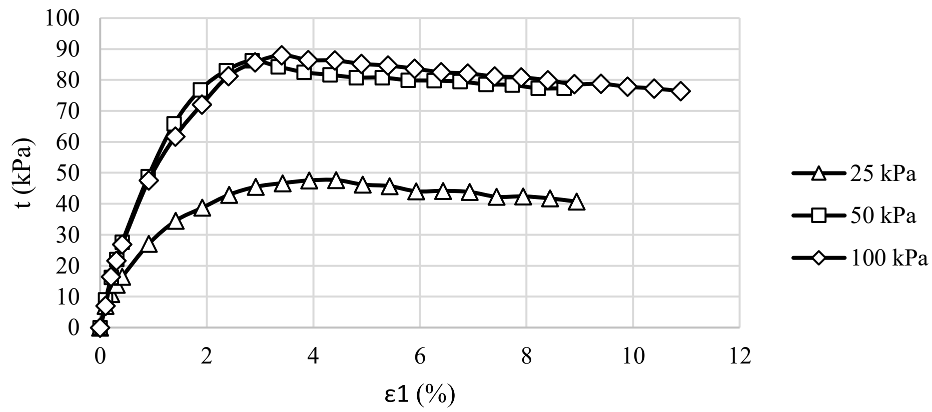

Figure 60. Grafic of t vs. ε_1. PCQ3

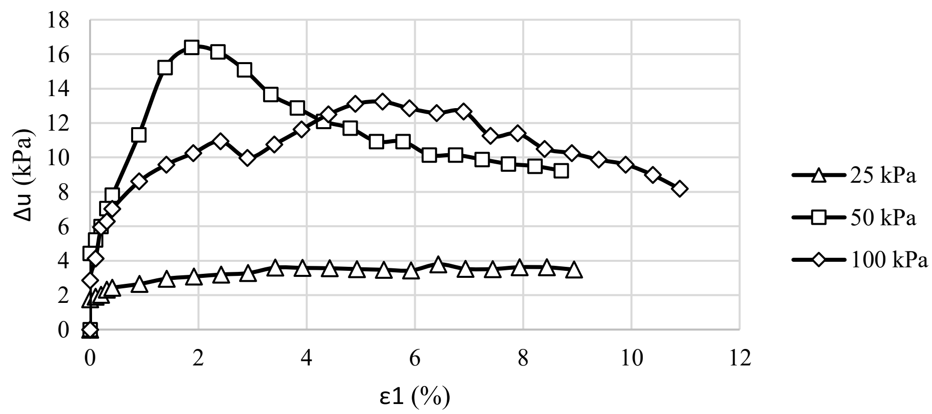

Figure 61. Grafic of Δu vs. ε_1. PCQ3

3.2.3.1.2. Results of PCQ6-TCU-2.00-2.50

Table 5. Results of triaxial test in PCQ6 with depth 2.00-2.50m

	Total Stress	Effective Stress
C (kPa)	10,93	13,76
ϕ (°)	36,51	36,58
ρ_{bulk} (g/cm^3)	1,794	

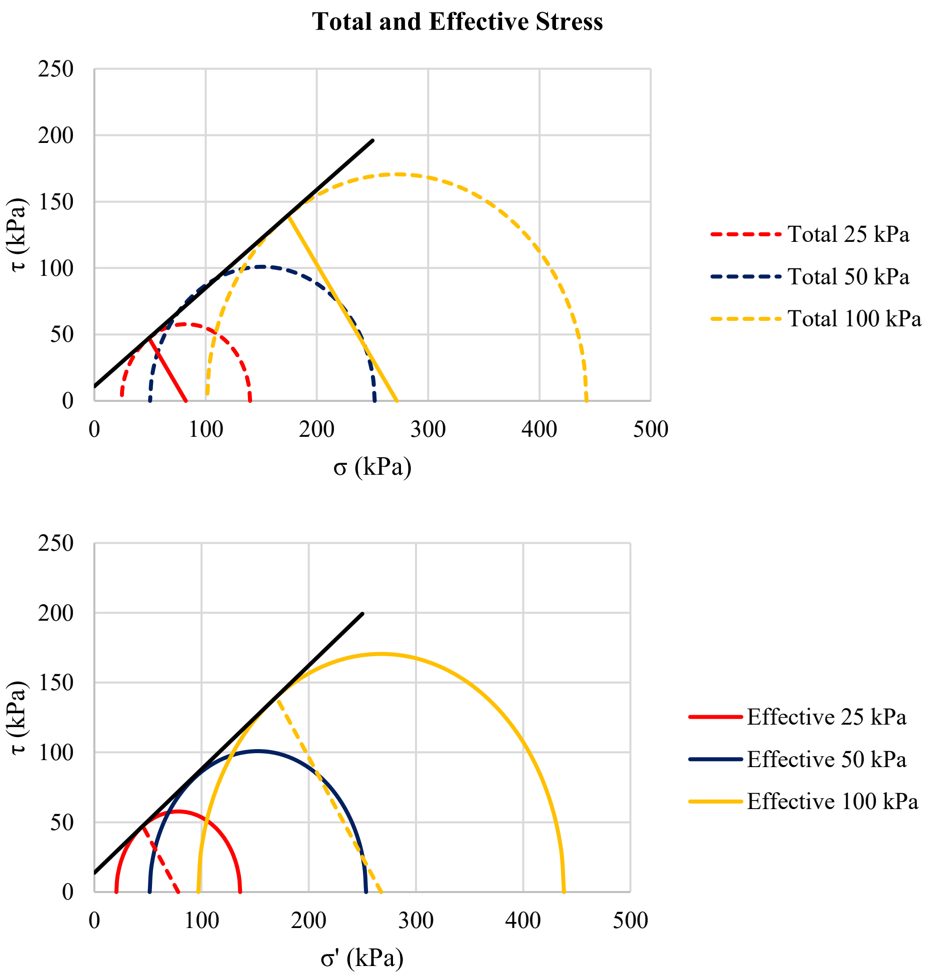

Figure 62. Grafics of total and effective stress of PCQ6

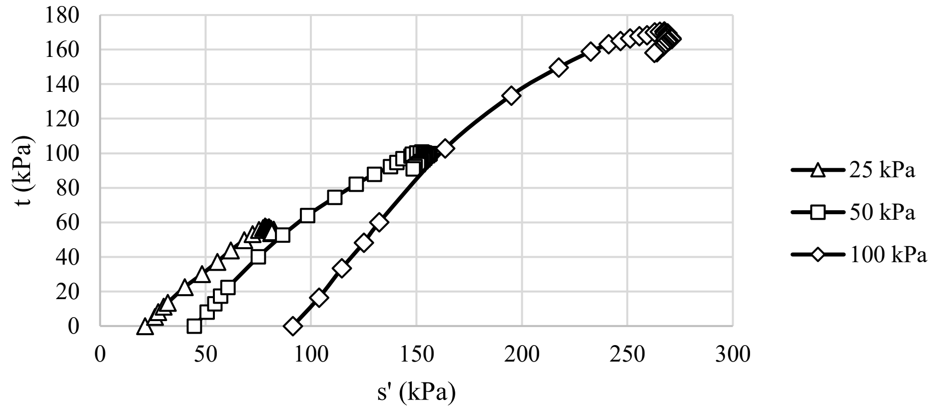

Figure 63: Grafic of t vs. s’. PCQ6

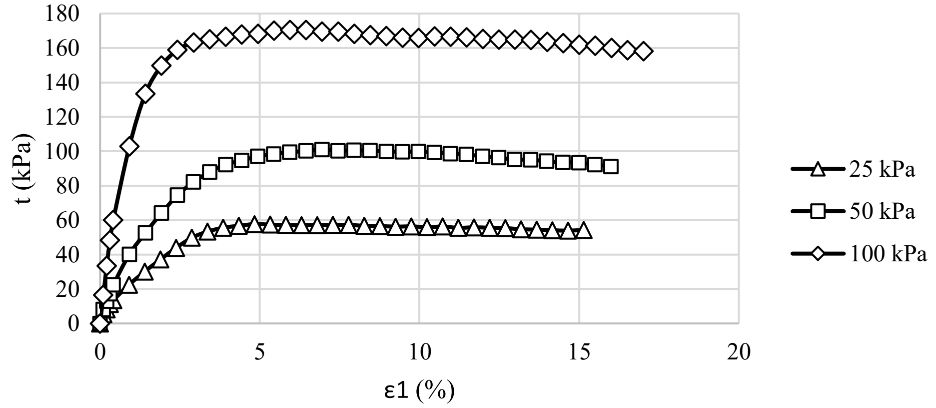

Figure 64. Grafic of t vs. ε_1. PCQ6

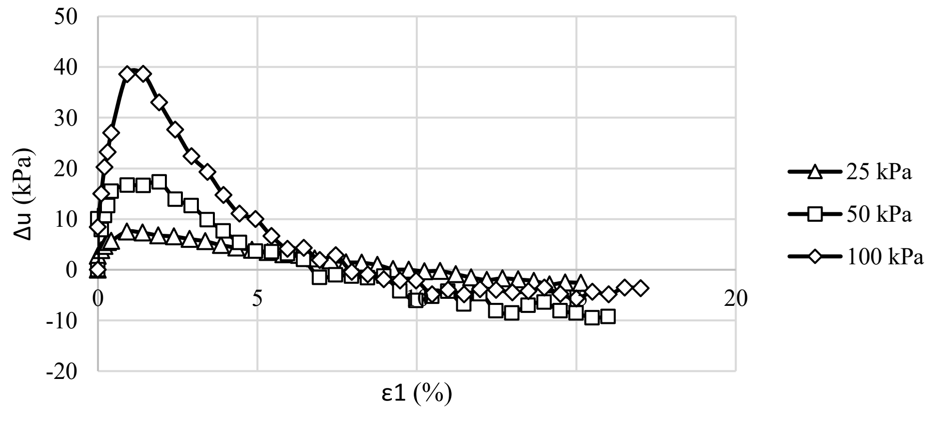

Figure 65. Grafic of Δu vs. ε_1. PCQ6

3.2.3.1.2 Results of PCQ8-TCU-3.00-3.50m

Table 6. Results of triaxial test in PCQ8 with depth 3.00-3.50m

	Total Stress	Effective Stress
C (kPa)	43,60	20,68
ϕ (°)	19,24	29,22
ρ_{bulk} (g/cm^3)	1,812	

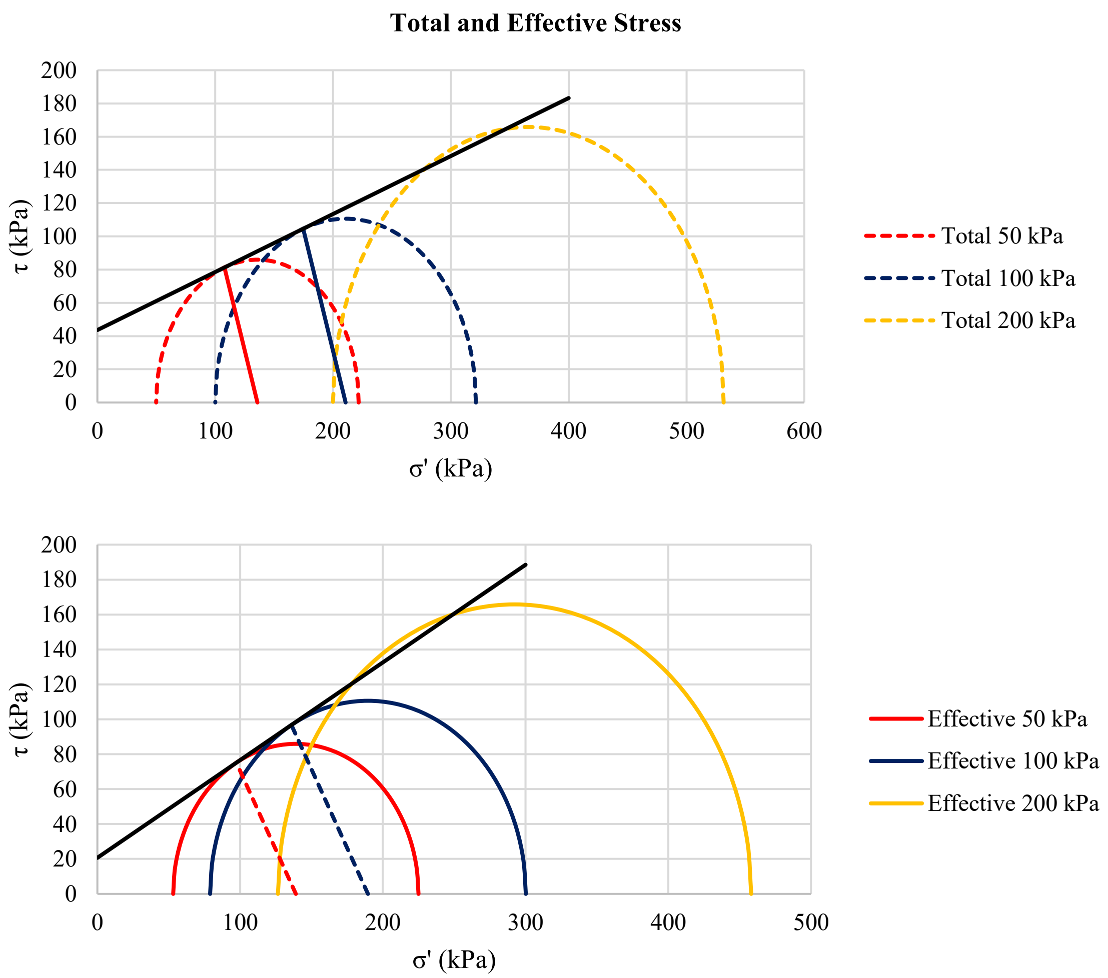

Figure 66. Grafics of total and effective stress of PCQ8

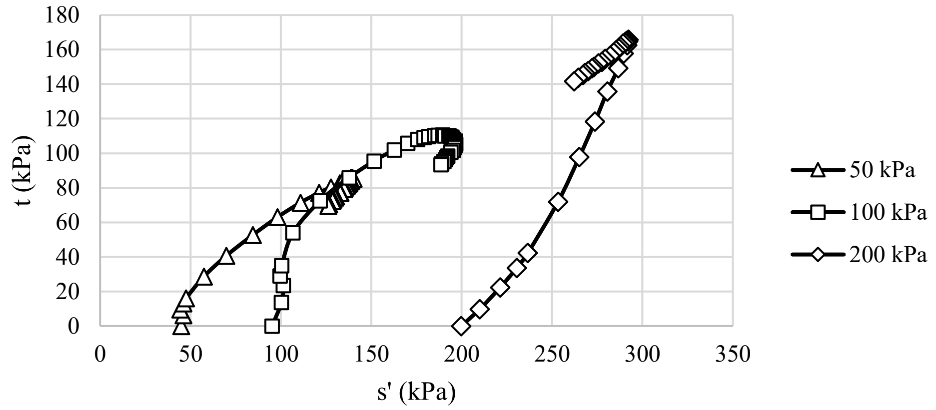

Figure 67: Grafic of t vs. s'. PCQ8

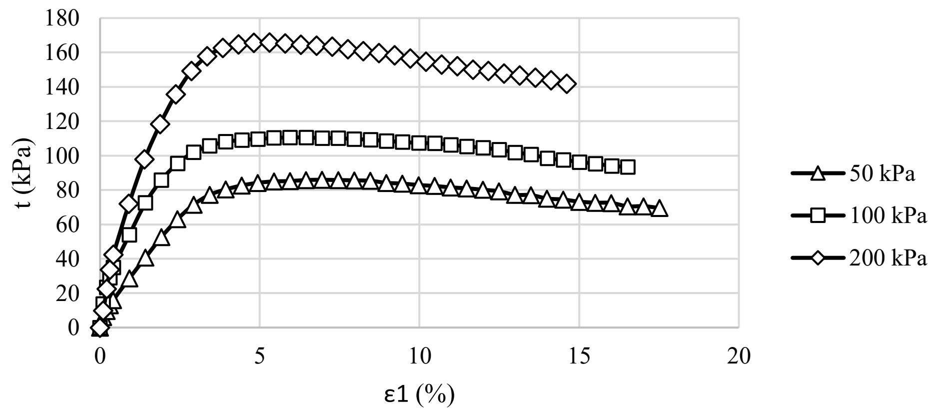

Figure 68. Grafic of t vs. ε_1. PCQ8

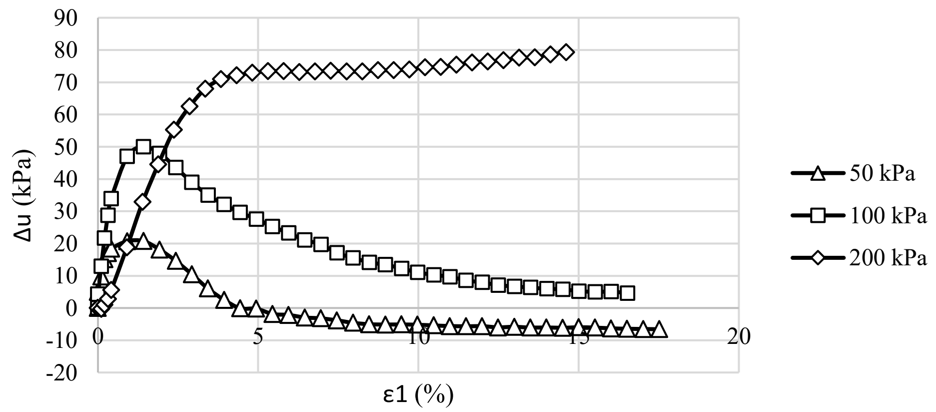

Figure 69. Grafic of Δu vs. ε_1. PCQ8

3.2.3.1.3 Results of PCQ14-TCU-12.10-12.60m

Table 7. Results of triaxial test in PCQ14 with depth 12.10-12.60m

	Total Stress	Effective Stress
C (kPa)	322,96	187,46
φ (°)	11,75	27,40
ρ_{bulk} (g/cm³)	1,814	

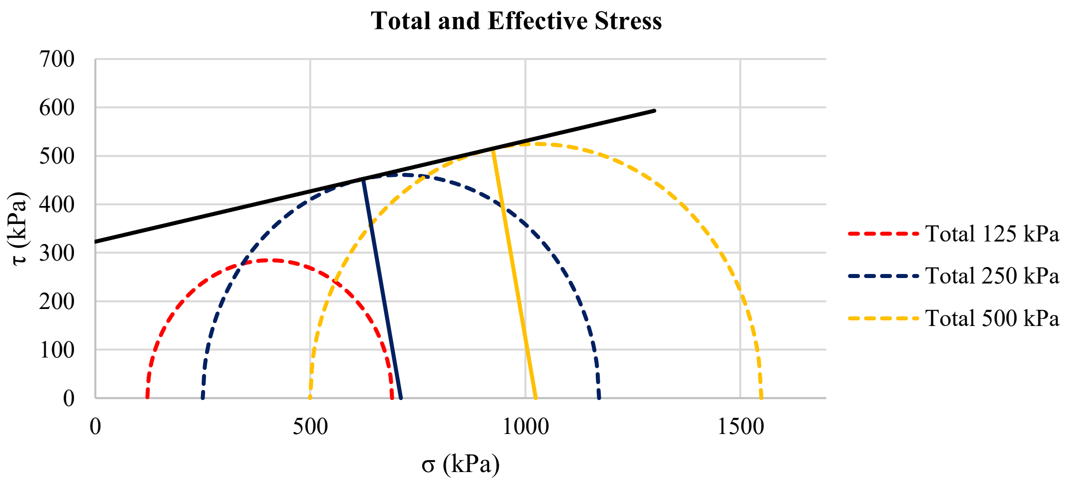

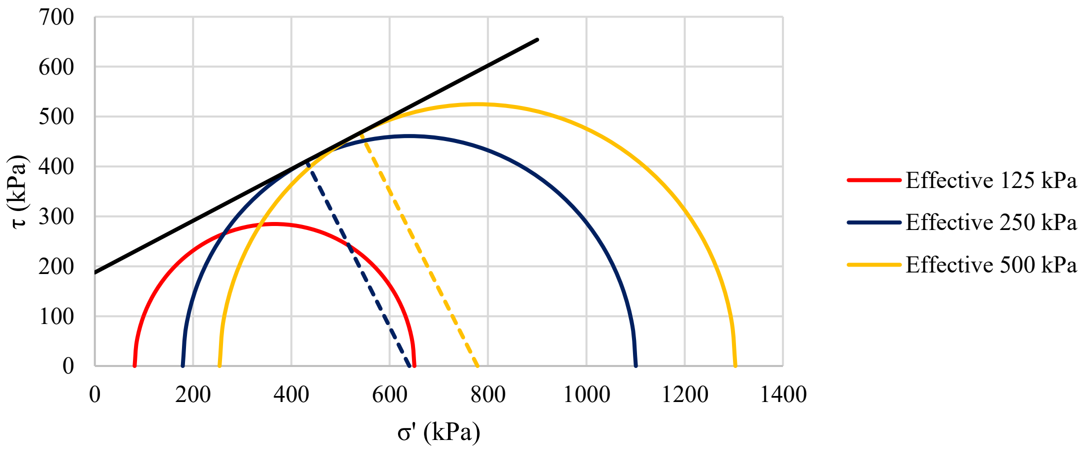

Figure 70. Grafics of total and effective stress of PCQ14

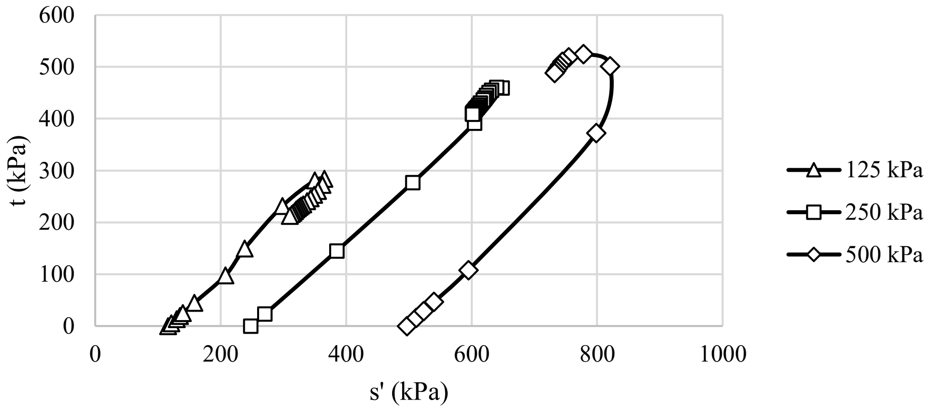

Figure 71 Grafic of t vs. s’. PCQ14

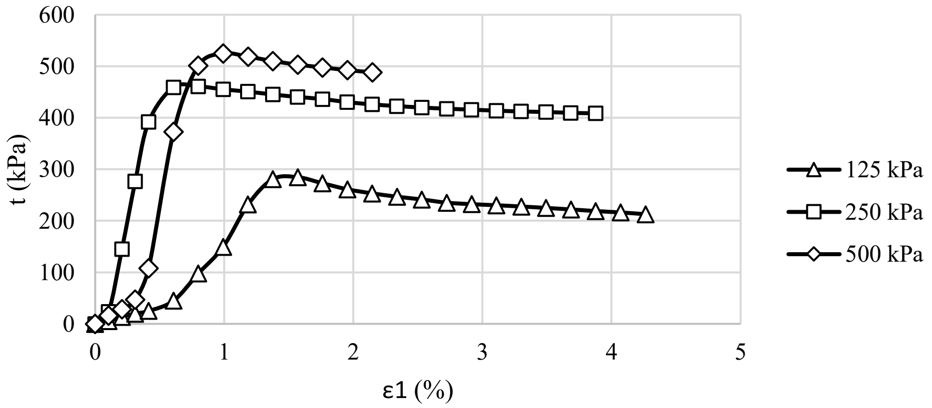

Figure 72. Grafic of t vs. ε_1. PCQ14

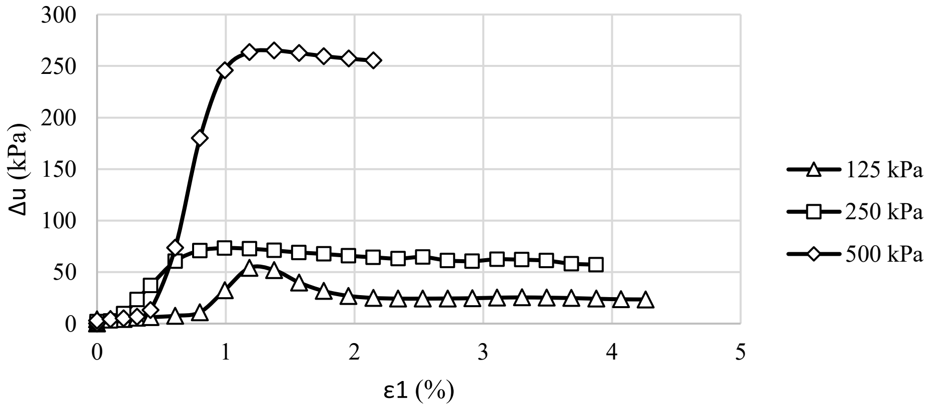

Figure 73. Grafic of Δu vs. ε_1. PCQ14

3.2.4.2. Oedometer tests

Table 8. Consolidation test results

Worehole	Depth (m)		Cc and Cs		Average coefficient	Preconsolidation Stress (Kpa)
PCQ1-2.00-2.50m	2	2,5	Cc	0,114	0,114	210
			Cs	0,027	0,027	
PCQ1-4.00-4.50m	4	4,5	Cc	0,091	0,091	205
			Cs	0,018	0,018	
PCQ3-1.00-1.50m	1	1,5	Cc	0,195	0,195	205
			Cs	0,017	0,017	
PCQ3-7.00-7.50m	7	7,5	Cc	0,413	0,413	205
			Cs	0,033	0,033	
PCQ4-1.00-1.50m	1	1,5	Cc1	0,092	0,154	105
			Cs1	0,146		
			Cc2	0,216	0,092	
			Cs2	0,039		
PCQ4-3.00-3.50m	3	3,5	Cc1	1,903	1,892	105
			Cs1	2,382		
			Cc2	1,881	1,244	
			Cs2	0,106		
PCQ4-6.00-6.50m	6	6,5	Cc1	6,328	5,255	550
			Cs1	4,916		
			Cc2	4,182	2,555	
			Cs2	0,194		
PCQ4-8.00-8.50m	8	8,5	Cc1	1,037	1,118	105
			Cs1	1,286		
			Cc2	1,198	0,682	
			Cs2	0,078		
PCQ6-3.00-3.50m	3	3,5	Cc1	0,079	0,095	201
			Cs1	0,069		
			Cc2	0,110	0,041	
			Cs2	0,014		
PCQ6-5.00-5.50m	5	5,5	Cc1	0,051	0,066	210
			Cs1	0,058		
			Cc2	0,081	0,036	
			Cs2	0,013		
PCQ8-2.00-2.50m	2	2,5	Cc	0,225	0,225	53
			Cs	0,017	0,017	
PCQ8-5.00-5.50m	5	5,5	Cc	0,053	0,053	103
			Cs	0,013	0,013	
PCQ9-3.50-4.00m	3,5	4	Cc1	0,303	0,335	105
			Cs1	0,356		
			Cc2	0,368	0,188	
			Cs2	0,021		

PCQ9-14.50-15.00m	14,5	15	Cc1	0,087	0,172	150
			Cs1	0,172		
			Cc2	0,256	0,104	
			Cs2	0,037		
PCQ10-1.50-2.00m	1,5	2	Cc1	0,077	0,125	200
			Cs1	0,066		
			Cc2	0,173	0,042	
			Cs2	0,018		
PCQ10-2.00-2.50m	2	2,5	Cc	0,080	0,080	210
			Cs	0,020	0,020	
PCQ10-4.00-4.50m	4	4,5	Cc1	0,050	0,155	450
			Cs1	0,083		
			Cc2	0,260	0,053	
			Cs2	0,023		
PCQ11-3.00-3.50m	3	3,5	Cc	0,131	0,131	55
			Cs	0,013	0,013	
PCQ11-4.00-4.50m	4	4,5	Cc	0,093	0,093	105
			Cs	0,016	0,016	
PCQ12-2.00-2.50m	2	2,5	Cc1	0,473	0,495	100
			Cs1	0,462		
			Cc2	0,516	0,247	
			Cs2	0,032		
PCQ12-3.00-3.50m	3	3,5	Cc1	0,473	0,624	120
			Cs1	0,666		
			Cc2	0,774	0,357	
			Cs2	0,048		
PCQ12-5.00-5.50m	5	5,5	Cc1	0,461	0,493	110
			Cs1	0,520		
			Cc2	0,525	0,275	
			Cs2	0,030		
PCQ12-5.50-6.00m	5,5	6	Cc1	0,210	0,263	110
			Cs1	0,244		
			Cc2	0,315	0,135	
			Cs2	0,026		
PCQ14-3.45-4.10m	3,45	4,1	Cc1	0,013	0,115	205
			Cs1	0,082		
			Cc2	0,217	0,048	
			Cs2	0,014		
PCQ14-8.20-8.60m	8,2	8,6	Cc1	0,087	0,249	410
			Cs1	0,139		
			Cc2	0,411	0,085	
			Cs2	0,030		
PCQ14-12.10-12.60m	12,1	12,6	Cc1	0,089	0,250	350
			Cs1	0,137		

			Cc2	0,411	0,084	
			Cs2	0,030		
PCQ21-3.50-3.95m	3,5	3,95	Cc1	0,081	0,096	80
			Cs1	0,093		
			Cc2	0,111	0,053	
			Cs2	0,013		

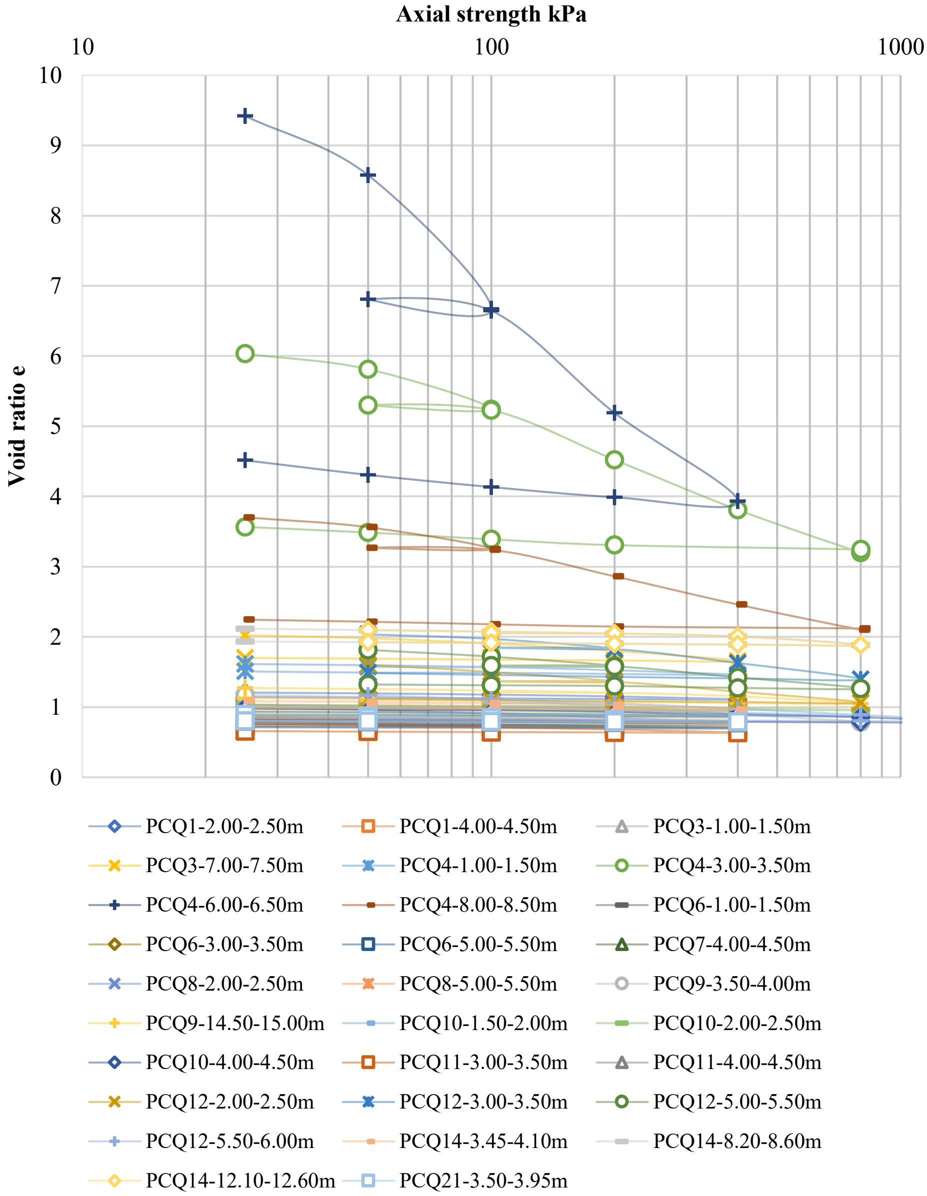

Figure 74. Consolidation results

3.2.5. Summary of all tests performed

To perform a geotechnical characterization, and due to the high heterogeneity of soil, a total of 2774 physical and mechanical tests were performed during 2019, using recovered altered and unaltered samples, the details can be seen in Table 9. Combined with the 1332 tests performed with SPT, CPT and SDMT, geotechnical profiles were performed, detailed in sub section 3.3.

Table 9. Summary of laboratory tests

Borehole Number	Soil Mechanics Laboratory Tests									
	Siev.	Hydr.	Plast.	%w	Density kN/m3	Organic Content	Consol.	Unconf. Compr.	Triaxial CU	Sum
PCQ0001	30	2	30	30	13	10	2	-	-	117
PC00002	31	4	31	31	21	9	5	-	-	132
PCQ0003	34	3	34	34	23	17	1	-	1	147
PCQ0004	43	4	43	43	38	1	4	14	-	190
PCQ0005	31	2	31	31	24	9	2	-	-	130
PCQ0006	34	3	34	34	22	12	3	-	1	143
PCQ0007	31	-	31	31	16	15	-	-	-	124
PCQ0008	22	3	22	22	9	3	1	-	1	83
PCQ0009	35	12	35	35	20	2	2	3	-	144
PCQ0010	31	7	31	31	11	2	7	-	-	120
PCQ0011	23	3	23	23	18	8	1	-	-	99
PCQ0012	36	7	36	36	9	1	1	1	-	127
PCQ0013	46	5	46	46	11	-	-	-	-	154
PCQ0014	39	9	39	39	23	-	3	2	3	157
PCQ0015	33	3	33	33	14	-	-	-	-	116
PCQ0016	34	6	34	34	16	-	-	14	-	138
PCQ0017	35	6	35	35	12	-	-	9	-	132
PCQ0018	34	4	34	34	44	11	1	-	-	162
PCQ0019	30	10	30	30	10	-	-	-	-	110
PCQ0020	23	3	23	23	19	-	-	6	-	97
PCQ0021	28	4	28	28	24	-	24	16	-	152
Sum	683	100	683	683	397	100	57	65	6	**2774**

3.3. Geotechnical Profiles

From all the field and laboratory processed data, profiles were created and homogenized in transverse and longitudinal directions. As a result, 6 cross-sectional profiles and 4 longitudinal profiles were obtained, as seen in Figure 75.

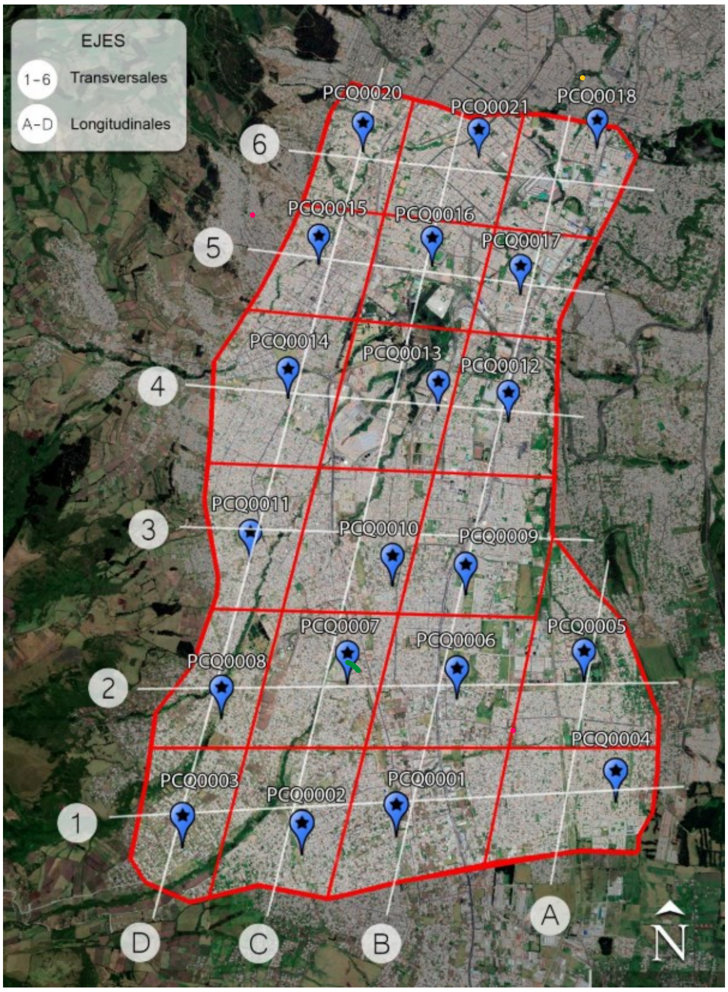

Figure 75. Transverse and longitudinal profiles.

A total of 10 geotechnical profiles were generated based on the field and laboratory processed data. The elevation and distance between the evaluated points can be seen in the profiles, and an analysis of the columns to be evaluated with the dynamic parameters will be discussed on the following chapters. Overall, from all the profiles, a low plasticity silt ML, with intermediate layers of Sandy silt SM, and clays of low plasticity CL, transitions to a Silty Sand SM with layers of Poorly graded Gravel in the last 15 meters. Some boreholes, like Point No. 4, differs from the others drastically, presenting organic soils in the first 15 meters, followed by soft low plasticity silts. With all these variables, the profiles were attempted, first being presented to the Municipality of Quito in the final Report of the "Tripartite Technical Cooperation Agreement between the Decentralized Autonomous Government of the Metropolitan District of Quito, the National Polytechnic School, and the Pontifical Catholic University of Ecuador, in matters of Education" (“Convenio Tripartito de Cooperación Técnica entre el Gobierno Autónomo Descentralizado del Distrito Metropolitano de Quito, la Escuela Politécnica Nacional, y la Pontificia Universidad Católica del Ecuador, en materia de Educación”), which funded the project, with the aid of Prof. Guillermo Realpe, Eng. Doménica Ocaña and Eng. Melissa Tapia from the *Pontificia Universidad Católica del Ecuador*, being modified later with additional interpretation for the present work.

To develop the cross-sectional and longitudinal profiles, no algorithms were used to define the subsurface model. These were developed by hand based on the similarity of physical and mechanical parameters and borehole locations. Therefore, other engineers supported the development of the profiles presented in this thesis.

❖ Cross-sectional profiles

Profile axis 1: PCQ0003 – PCQ0001 – PCQ0002 – PCQ0004
Profile axis 2: PCQ0008 – PCQ0007 – PCQ0006 – PCQ0005
Profile axis 3: PCQ0011 – PCQ0010 – PCQ0009
Profile axis 4: PCQ0014 – PCQ0013 – PCQ0012
Profile axis 5: PCQ0015 – PCQ0016 – PCQ0017
Profile axis 6: PCQ0020 – PCQ0021 – PCQ0018

❖ Longitudinal profiles:

Profile axis A: PCQ0004 – PCQ0005
Profile axis B: PCQ0001 – PCQ0006 – PCQ0009 – PCQ0012 – PCQ0017 – PCQ0018
Profile axis C: PCQ0002 – PCQ0007 – PCQ0010 – PCQ0013 – PCQ0016 – PCQ0021
Profile axis D: PCQ0003 – PCQ0008 – PCQ0011 – PCQ0014 – PCQ0015 – PCQ0020

3.3.1. Profile axis 1: PCQ0003 – PCQ0001 – PCQ0002 – PCQ0004

The following information is detailed for boreholes 1, 2 and 3:

In the first 5 meters a light brown low plasticity silt (ML) with an N60 between 6 - 8, with a liquid limit (LL) of 45 and a plasticity index (PI) between 12 - 14 with a Vs between 160 - 170 m/s is encountered.

Between the 5th and 6th meter, a gray silty sand (SM) with an N60 between 6-8 is found. While from meter 6 to meter 11 on average in boreholes 2 and 3 there is a column of low plasticity silts (ML) with an N60 between 30-47 and a Vs between 250 - 288 m/s; while in borehole 1 there is a sequence of low plasticity silts and clays up to meter 12, with an N60 of 23 and a Vs equal to 221 m/s. Between the 11th and 12th meter on average there is a gray silty sand stratum with an N60 between 30 - 47, after this stratum there is a low plasticity silt stratum (ML) with an N60 between 35-42, to finally find up to the 30th meter a group of silty sands, well graded and poorly graded sands (SM, SW, SP) of gray color with N60 greater than 50 and a Vs of 360 m/s.

The information for borehole 4 is detailed below:

The first 14 meters are described as a black high plasticity organic stratum (OH) with an LL = 213, N60 = 4 and a Vs = 100 m/s. From meter 14 to meter 17 there is the presence of a dark brown silty sand (SM) with an LL =37, N60 = 51 and a Vs = 300 m/s. Between the 17th and 25th meters, a black silt of high plasticity (MH) is found, which has an LL = 123, N60 = 4 and a Vs of 100 m/s. At the end of meter 30 there is a low plasticity silt (ML) with LL = 40, N60 greater than 50 and Vs = 329 m/s.

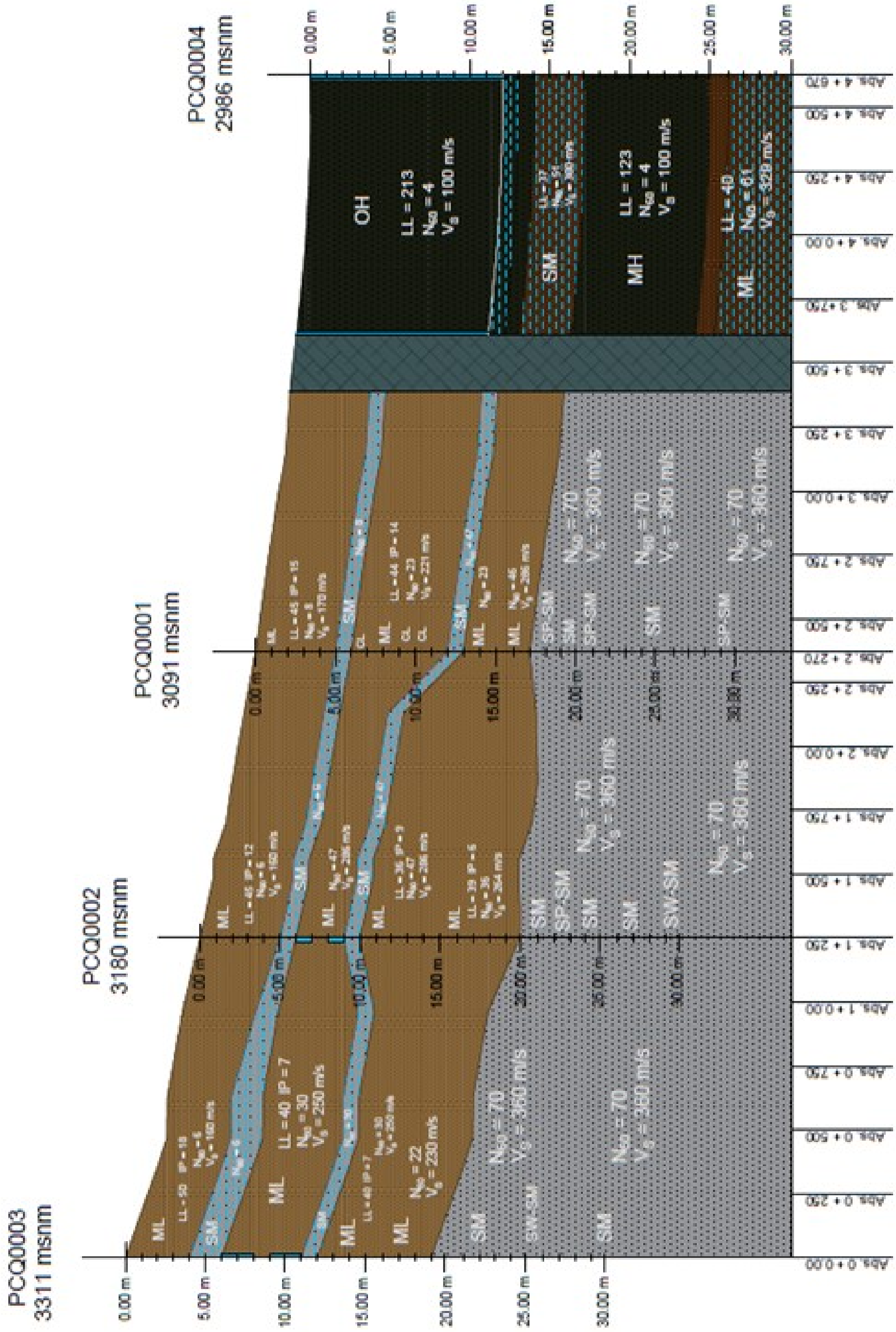

Figure 76. Geotechnical Profile axis 1: PCQ0003 – PCQ0001 – PCQ0002 – PCQ0004

3.3.2. Profile axis 2: PCQ0008 – PCQ0007 – PCQ0006 – PCQ0005

The following information is detailed for boreholes 6, 7 and 8:

In the first 7 meters on average there are silts and clays of low plasticity (ML-CL) of light brown color, where in boreholes 7 and 8 N60 is between 8 - 10 and Vs between 200 - 210 m/s. While in borehole 6 the N60 is between 14 - 22 and the Vs = 264 m/s. A gray-brown silty sand (SM) with an N60 between 6 - 9 is encountered between meter 7 and 8. From meter 8 to 12.50 on average, a light brown low plasticity silt (ML) is found, with an N60 between 28 - 45 and a Vs between 280 - 325 m/s. Subsequent to meter 12.50, up to meter 15.50, a gray-brown silty sand layer (SM) is encountered, with an N60 between 15 - 23 and a Vs between 237 - 270 m/s. Finally, boreholes 6 and 7 up to meter 30, have a silty sand layer, a well graded sand and a poorly graded sand (SM, SW, SP) of gray color, with an N60 greater than 50 and a Vs = 360 m/s, and borehole 8 has a cemented silty sand layer (SM) of gray color, with an N60 greater than 50 and a Vs = 360 m/s.

The information for borehole 5 is detailed below:

The first three meters have a set of high and low plasticity silts (ML/MH) of light brown color, with an N60 = 2 and a Vs = 124 m/s. From meter 3 to meter 6 there are low plasticity silts (ML) of light brown color, with an N60 = 21 and a Vs = 243 m/s. From meter 6 to meter 8, a gray-brown silty sand (SM) with N60 greater than 50 and Vs = 350 m/s is present. While until meter 14 a low plasticity silt (ML) of light brown color with a N60 = 49 and a Vs = 300 m/s is found. Between the 14th and 16th meter there is a gray-brown silty sand (SM) with a N60 = 17 and a Vs = 230 m/s, and finally up to the 30th meter there is an alluvial rock of gray color with a Vs = 360 m/s.

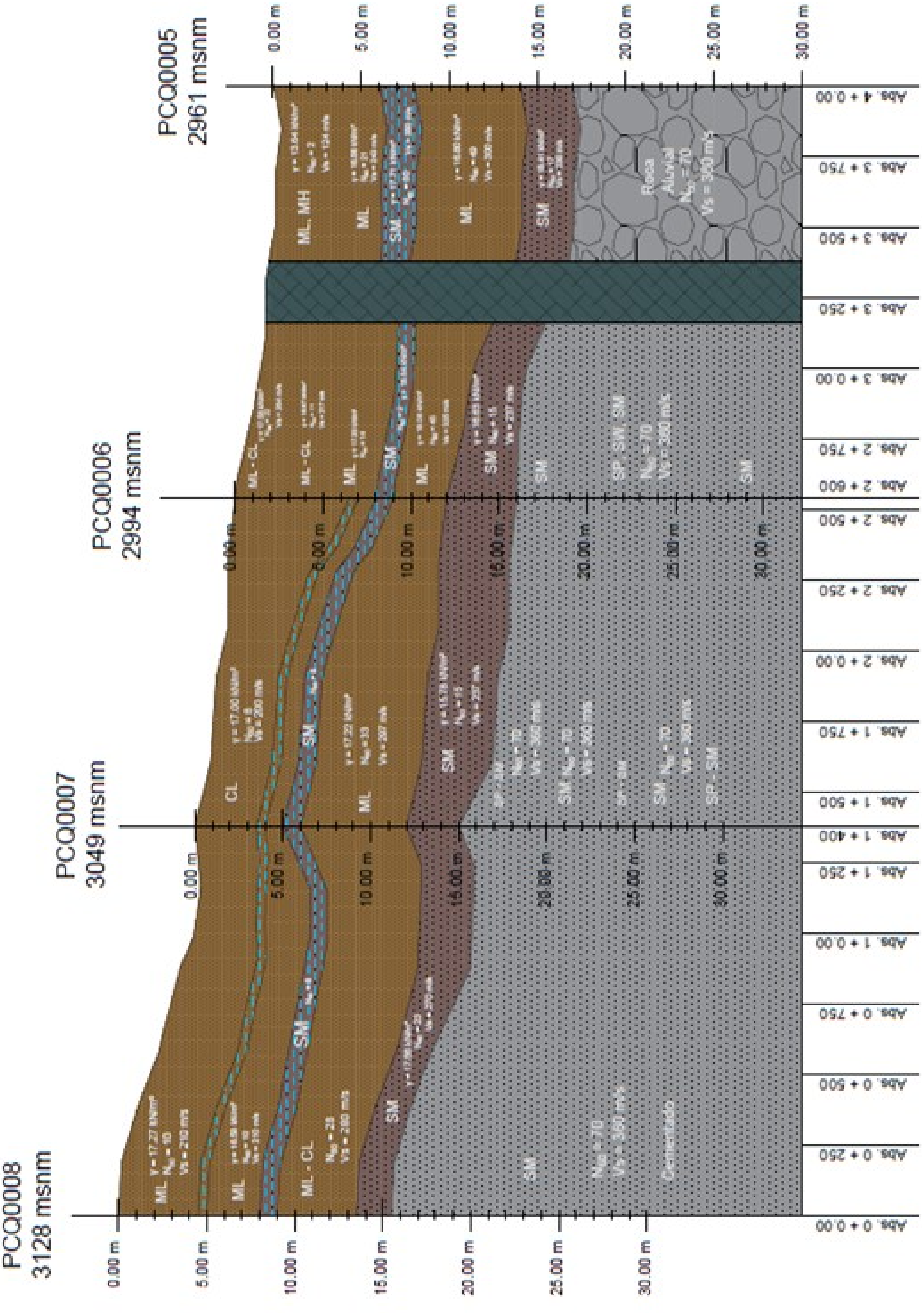

Figure 77. Geotechnical Profile axis 2: PCQ0008 – PCQ0007 – PCQ0006 – PCQ0005

3.3.3. Profile axis 3: PCQ0011 – PCQ0010 – PCQ0009

The following information is detailed for boreholes 10 and 11:

The first three meters present silts and clays of low plasticity (CL/ML) of light brown color, with an N60 between 13 - 16 and a Vs between 227 - 240 m/s. From meter 3 to 4 in well 10, a silt of low plasticity (ML) is found, while in borehole 11 a silty sand (SM) is found, however, the N60 and the Vs of both strata have the same range as the first three meters. From meters 4 to 6, in borehole 10 a light brown silty sand (SM) with N60 = 56 and Vs = 345 m/s is found, followed by a 50 cm layer of a low plasticity silt (ML), whereas in borehole 11 a light brown low plasticity clay (CL) with N60 = 13 and Vs = 227 m/s is observed. From meter 7 to meter 11 on average, a greenish brown low plasticity silt (ML) with N60 = 35 and Vs = 300 m/s is observed in borehole 11, and in borehole 10 a low plasticity clay (CL) with N60 greater than 50 and Vs = 360 m/s is found. After this depth, the materials of both boreholes are different, since in borehole 11, from meter 11 on average up to meter 30, there is a silty sand column (SM) with a 30 < N60 < 50 and a Vs between 289 - 360 m/s. In borehole 10, from meter 11 to 10 there is a silty sand stratum (SM) with an N60 greater than 50 and a Vs = 360 m/s, followed by a 12 meter stratum of poorly graded gravel, well graded sand, silty sand and poorly graded sand (GP/SW/SM/SP), with an N60 = 70 and a Vs = 360 m/s, finally, up to meter 30 there is a silty sand (SM) with N60 greater than 50 and a Vs = 360 m/s.

The information for borehole 9 is detailed below:

The first three meters have a high plasticity silt (MH) of dark brown color, with a N60 = 6 and a Vs = 180 m/s. From meter 3 to 6 there is a set of low plasticity silts (ML) and silty sands (SM), with an N60 = 25 and a Vs = 274 m/s, followed by a meter of clayey sand (SC) with the same N60 and Vs values of the previous stratum. Next, from meter 7 to 8 is a high plasticity silt (MH) with an N60 = 6. From meter 10 to 12 is a low plasticity silt (ML) with an N60 = 81 and a Vs = 380 m/s. Followed by one meter of silty sand (SM) and 4 meters of low plasticity silt (ML) with an N60 between 17 - 22 and a Vs = 245 m/s. From meter 17 to 23 there is a silty sand and poorly graded sand (SM/SP) with N60 greater than 50 and a Vs = 360 m/s, and finally a 7 m layer of silty sand (SM) with the same properties as the previous layer.

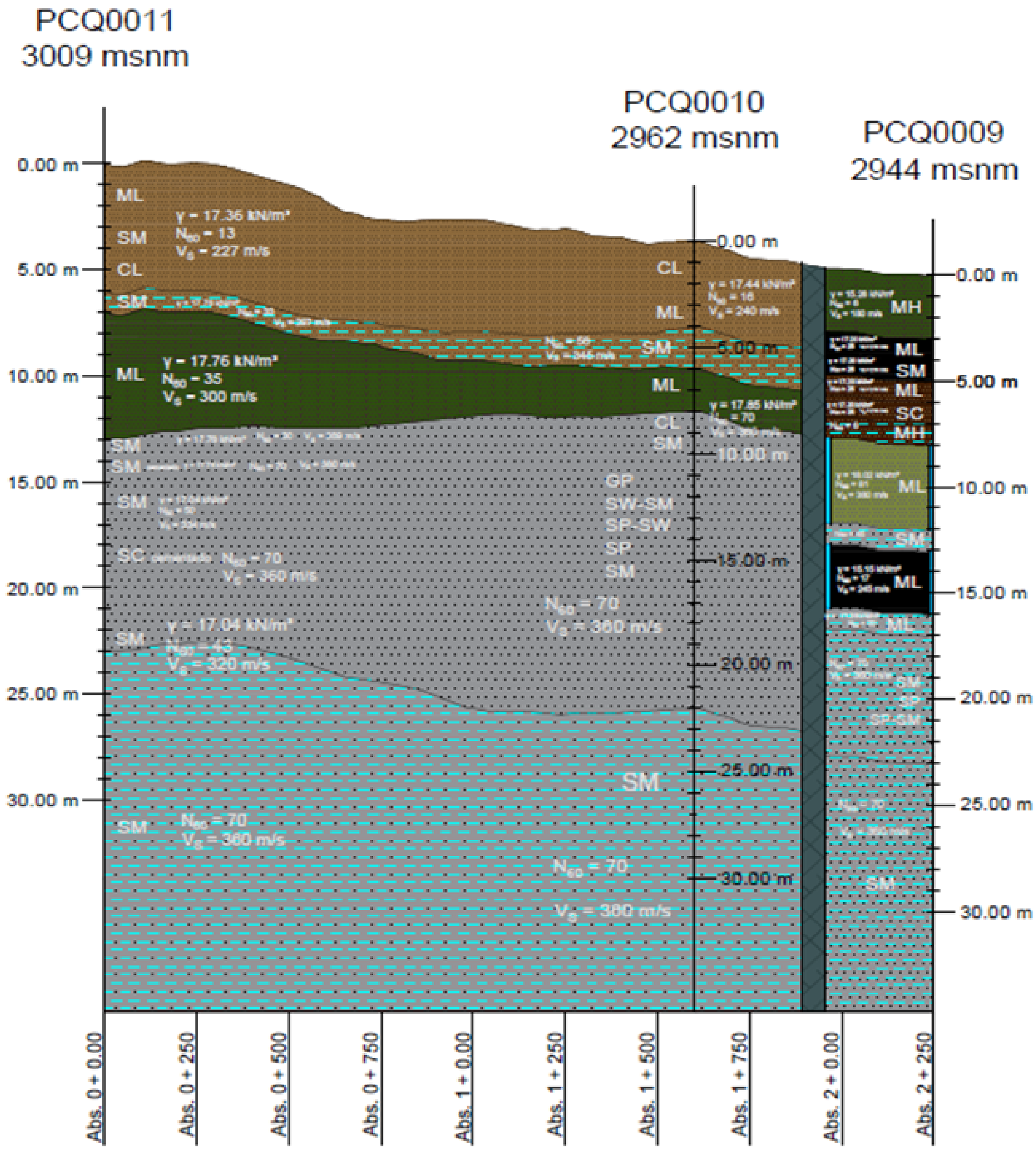

Figure 78. Geotechnical Profile axis 3: PCQ0011 – PCQ0010 – PCQ0009

3.3.4. Profile axis 4: PCQ0014 – PCQ0013 – PCQ0012

Due to the heterogeneity of the strata, they will be described separately.

The information for borehole 12 is detailed below:

The first 4 meters present silts and clays of low plasticity of light brown color (ML/CL), with a N60 = 4 and a Vs = 162 m/s. From meter 4 to 7, a layer of light brown silty sand (SM) is observed, with N60 = 4 and Vs = 162 m/s. While up to meter 9 there are silts and low plasticity clays of light brown color (ML/CL), with a N60 = 16 and a Vs = 241 m/s. From meter 9 to meter 12 a low plasticity silt (ML) is found, with an N60 =7 and a Vs = 190 m/s. From meter 12 to the 19, a series of low and high plasticity silts (ML/MH) is found, with an N60 range between 21 - 25 and a Vs between 260 - 274 m/s. Followed by a 3-meter stratum of low plasticity silts and clays (ML/CL) and poorly graded sands (SP) with N60 = 42 and Vs = 318 m/s. Followed by two meters of silty sand with 28 < N60 <50 and Vs between 350 - 383 m/s. Finally, from meter 24 to 30 there is a set of high and low plasticity silts (MH/ML) and low plasticity clays (CL), with a 40 < N60 < 50 and a Vs between 313 - 372 m/s.

The information for borehole 13 is detailed below:

The first two meters have a low plasticity silt (ML), with an N60 = 8 and a Vs = 198 m/s. In meters 2 to 7 there are high and low plasticity silts (MH/ML) with N60 = 2 and Vs = 133 m/s. While the following two meters have low plasticity silts (ML) and silty sands (SM) with an N60 = 8 and a Vs = 196 m/s. From meter 9 to 13, low plasticity silts (ML) are observed with a N60 = 36 and a Vs = 304 m/s, next are two meters of low plasticity silts (ML) with a N60 = 21 and a Vs = 260 m/s. Between the 15th and 20th meter there are low plasticity silts (ML) with an N60 = 5 and a Vs = 173 m/s. Followed by 4 meters of high and low plasticity silts (MH/ML), with an N60 = 15 and a Vs = 237 m/s. A silty sand stratum is encountered between meter 24 and 25 with an N60 = 5 and a Vs = 173 m/s, followed by 3 meters of low plasticity silts (ML) and silty sands (SM) with an N60 = 5 and a Vs = 343 m/s. Finally, low plasticity silts (ML) with organic matter are found up to meter 30.

The information for borehole 14 is detailed below:

The first 13.50 m have a fill with N60 between 6 - 7 and a Vs between 182 - 190 m/s. From 13.50 m to 21 m, there are low plasticity silts (ML) and silty sands (SM) with an N60 of 38 and a Vs = 309 m/s, followed by 4 meters of low plasticity silts (ML) with an N60 = 30 and a Vs range between 257 - 343 m/s. A silty sand (SM) with pumice particles is present from meter 25 to 28 with N60 = 55 and Vs = 279 m/s, followed by 50 cm of low plasticity silt (ML) with N60 greater than 50 and Vs = 360 m/s. Finally, from meter 28.50 to meter 30 there is an alluvial with N60 greater than 50 and Vs = 360 m/s.

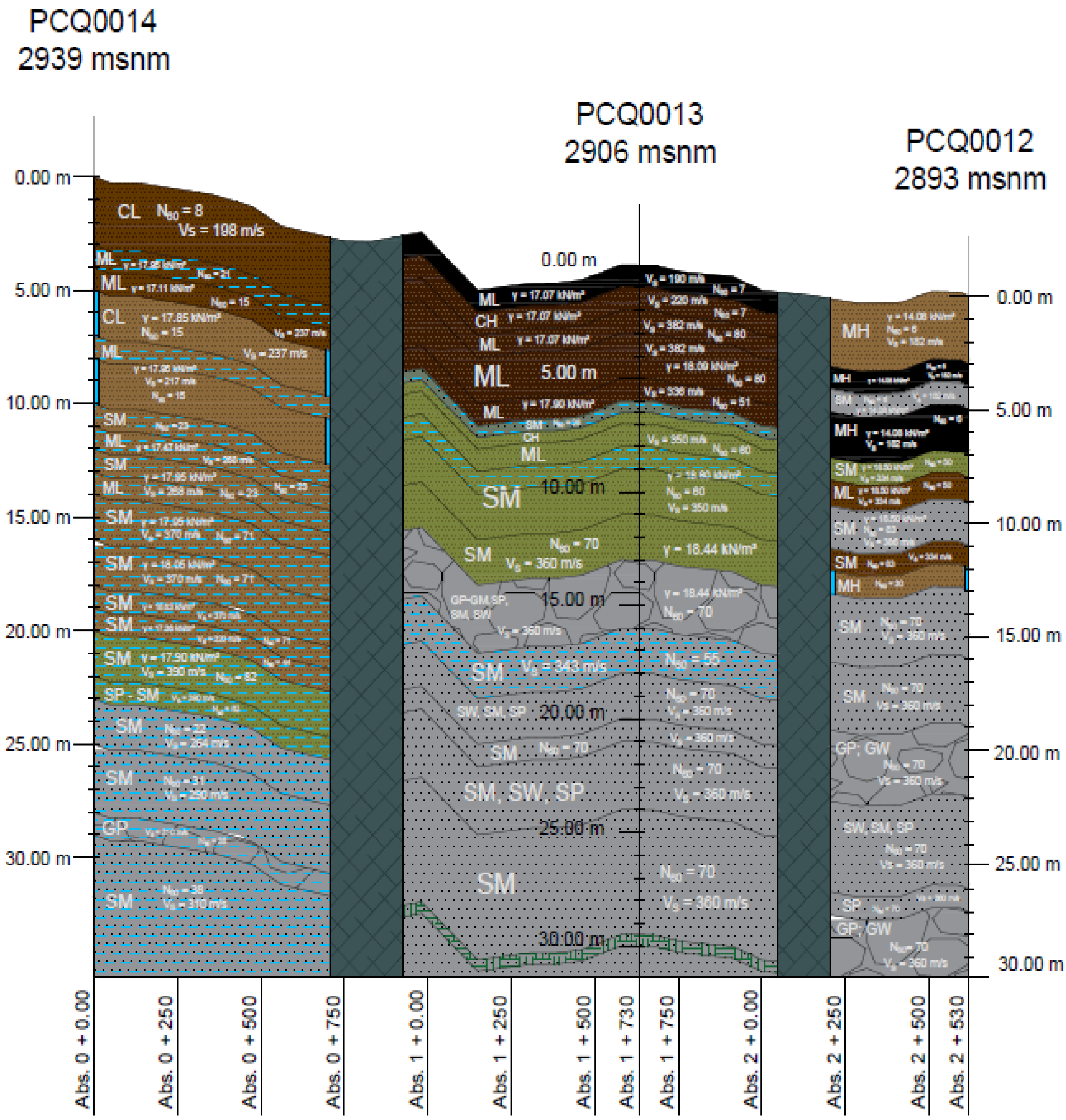

Figure 79. Geotechnical Profile axis 4: PCQ0014 – PCQ0013 – PCQ0012

3.3.5. Profile axis 5: PCQ0015 – PCQ0016 – PCQ0017

Due to the heterogeneity of the strata, they will be described separately.

The information for borehole 15 is detailed below:

The first 3 meters have light brown low plasticity clays (LC) with an N60 = 8 and a Vs = 198 m/s, followed by a meter of low plasticity silts (ML) with an N60 = 21. From meter 4 to 10 there are low plasticity silts and clays (ML/CL), with an N60 = 15 and a Vs between 217 - 237 m/s. The next 4 meters has a set of low plasticity silts (ML) and silty sands (SM) with an N60 = 23 and a Vs = 268 m/s. Between meters 14 and 19 is a silty sand (SM) stratum with an N60 greater than 50 and a Vs = 370 m/s, followed by a silty sand (SM) meter with an N60 = 44 and Vs = 322 m/s. From meter 20 to 23 there is a set of silty sands and poorly graded sands (SM-SP), with N60 greater than 50 and a Vs = 390 m/s, the next 5 meters have a silty sand (SM) with an N60 ranging between 22 - 31 and a Vs between 264 - 290 m/s. Finally, up to 30 meters there is a poorly graded gravel (GP) and silty sand (SM) with a N60 = 38 and a Vs = 310 m/s.

The information for borehole 16 is detailed below:

The first two meters present silts and clays of low plasticity (ML/CL) with an N60 = 7 and with a Vs between 190 - 220 m/s. From meter 2 to 6 there are low plasticity silts (ML) with an N60 greater than 50 and a Vs between 336 - 382 m/s, followed by a meter of silty sands (SM) and high plasticity clays (CH). A silty sand (SM) stratum with an N60 greater than 50 and a Vs between 350 - 360 m/s is found between meter 7 and 13. The next 3 meters constitute a stratum of silty sand, well graded sand, poorly graded sand, poorly graded gravel and silty gravel (GP-GM/SP/SM/SW) with an N60 greater than 50 and a Vs = 360 m/s, followed by two meters of silty sand (SM) with an N60 = 55 and a Vs = 343 m/s. At the 18th to 30th meter, silty sands, well graded sands, poorly graded sands (SM/SW/SP) with N60 greater than 50 and Vs = 360 m/s are present.

The information for borehole 17 is detailed below:

The first 7 meters are composed of a high plasticity silt (MH) with an N60 = 6 and a Vs = 182 m/s, followed by a 2-meter-thick stratum composed of a low plasticity silt (ML) and a silty sand (SM) with an N60 = 50 and a Vs = 334 m/s. From meters 9 to 12 a silty sand layer (SM) with a N60 = 83 and a Vs between 334 - 386 m/s is present, followed by a one-meter layer of a high plasticity silt (MH) with a N60 = 30. From meter 13 to 19 there is a silty sand (SM) with a N60 greater than 50 and a Vs = 360 m/s, followed by a 3-meter-thick layer of poorly graded gravel and well graded gravel (GP/GW) with a N60 greater than 50 and a Vs = 360 m/s. From meters 22 to 27 there is silty sand, poorly graded sand, well graded sand (SM/SP/SW) with N60 greater than 50 and Vs = 360 m/s. Finally, the last 3 meters are composed of a poorly graded gravel and a well graded gravel (GP/GW) with N60 greater than 50 and Vs = 360 m/s.

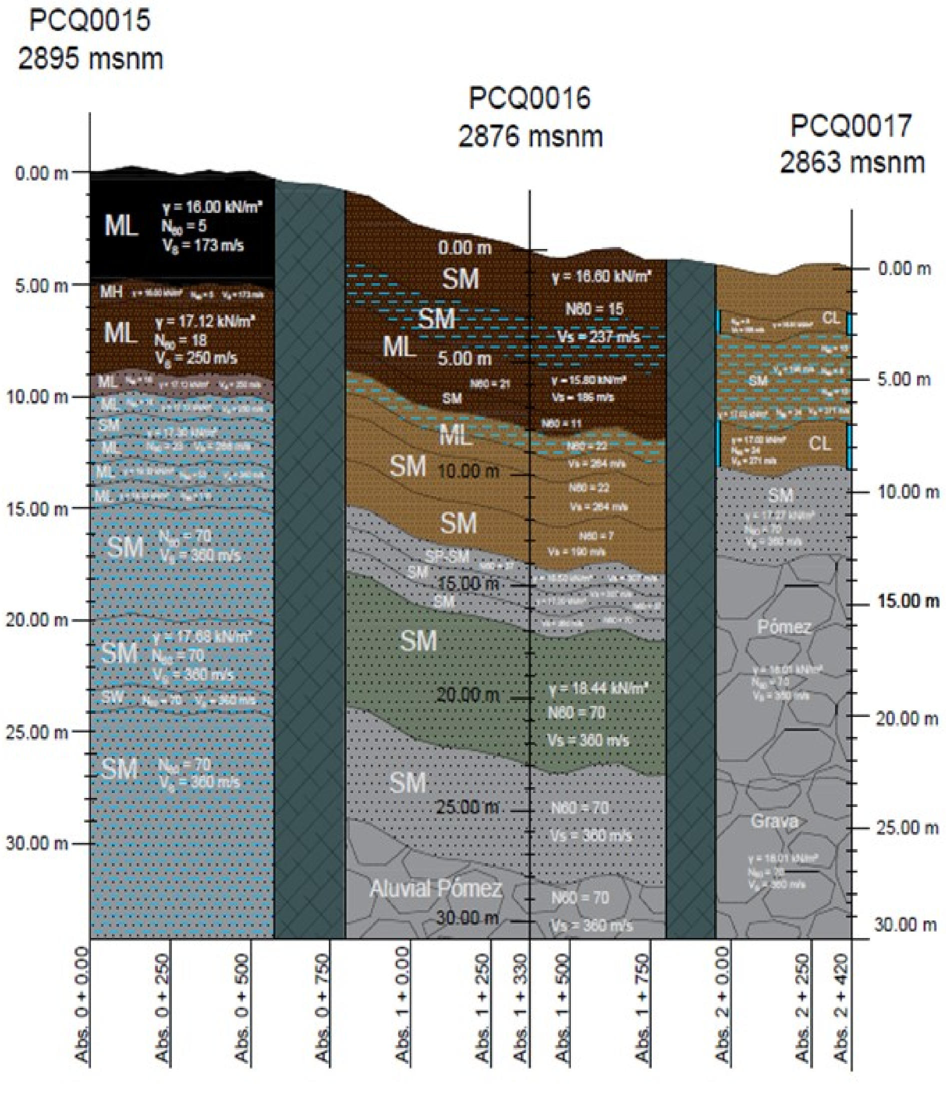

Figure 80. Geotechnical Profile axis 5: PCQ0015 – PCQ0016 – PCQ0017

3.3.6. Profile axis 6: PCQ0020 – PCQ0021 – PCQ0018

Due to the heterogeneity of the strata, they will be described separately.

The information for borehole 18 is detailed below:

The first 6 meters are composed of low plasticity clays (CL) and silty sands (SM) with an N60 between 8 - 15 and a Vs = 198 m/s. The same material is found between meter 6 and 9 as in the first meters, however, N60 = 24 and Vs = 271 m/s. From meters 9 to 13 there is a silty sand with N60 greater than 50 0 and a Vs = 360 m/s, while from meter 13 to 23 there is a pumice stratum with N60 greater than 50 and Vs = 360 m/s. In the last 7 meters there is a gray gravel with the same characteristics of the previous stratum.

The information for borehole 20 is detailed below:

The first 6 meters have high and low plasticity silts (MH/ML) with N60 = 5 and Vs = 173 m/s. From meters 6 to 11 there are low plasticity silts (ML) with N60 = 18 and a Vs = 250 m/s, followed by 2 meters of a silty sand (SM) with N60 = 23 and a Vs = 268 m/s. From meter 13 to 15 meters there is a low plasticity silt (ML) with N60 = 53 and Vs = 340 m/s. Finally, from meter 15 to 30 there is a set of silty sands (SM) and well graded sands (SW) with an N60 greater than 50 and a Vs = 360 m/s.

The information for borehole 21 is detailed below:

The first 5 meters have a silty sand (SM) with an N60 = 15 and a Vs = 237 m/s, followed by a 2-meter layer of a low plasticity silt (ML) with an N60 = 21 and a Vs = 186 m/s. From meters 7 to 8 a silty sand (SM) with a N60 = 11 is observed, while from meter 8 to 12 a low plasticity silt (ML) with a N60 = 22 and a Vs = 264 m/s is present. The next 2 meters have a silty sand with an N60 = 7 and a Vs = 190 m/s, followed by 2 meters of silty sand and poorly graded sand (SP-SM) with an N60 = 37 and a Vs = 307 m/s. From meter 16 to 28, a silty sand (SM) with an N60 greater than 50 and a Vs = 360 m/s is observed, followed by the last two meters of a pumice alluvial material with an N60 greater than 50 and a Vs = 360 m/s.

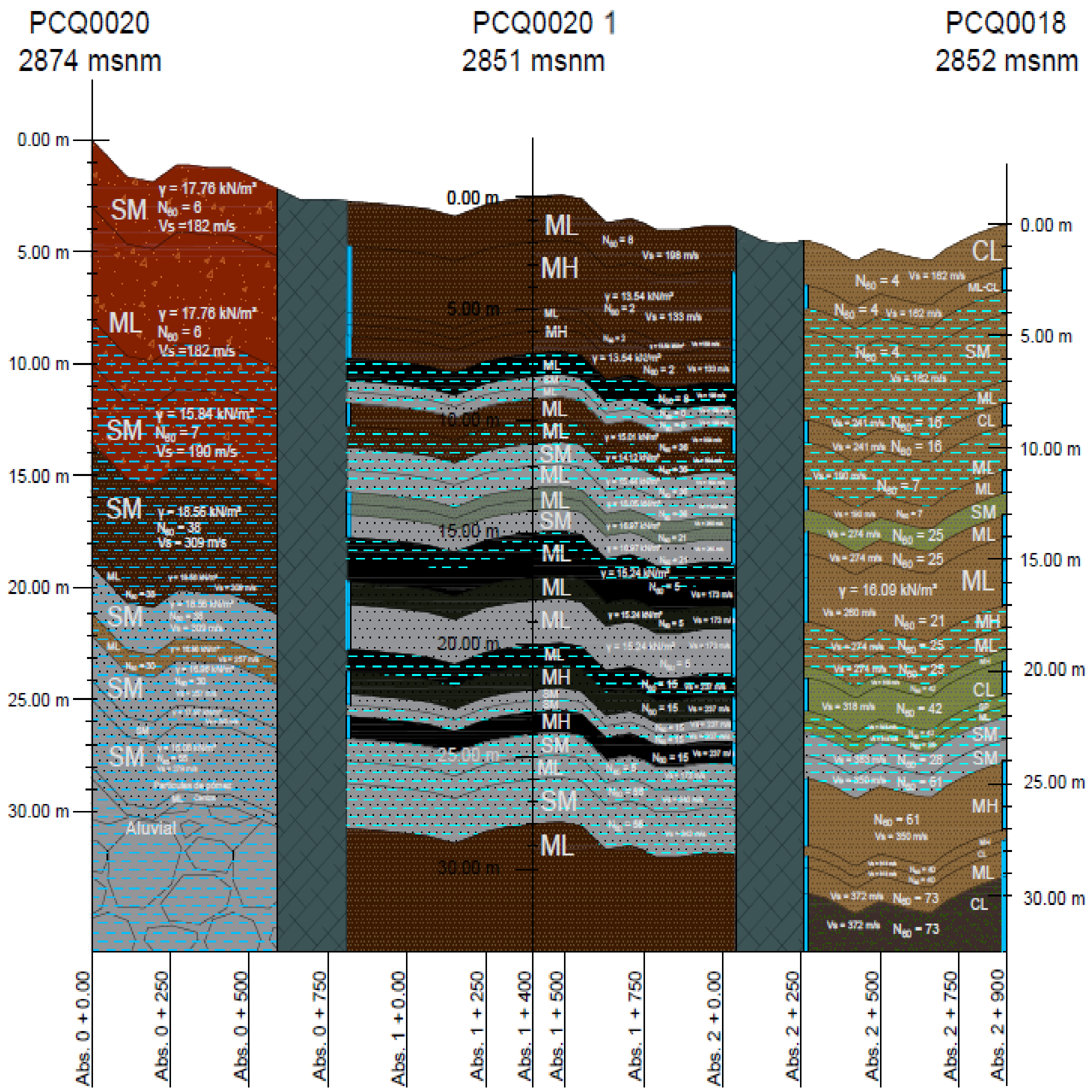

Figure 81. Geotechnical Profile axis 6: PCQ0020 – PCQ0021 – PCQ0018

3.3.7. Profile axis A: PCQ0004 – PCQ0005

In this profile it can be identified that the wells are different, since well 4 has organic material (OH) in the first 14 meters approximately, followed by a set of high and low plasticity silts (MH/ML) up to 30m, while well 5 presents a series of high and low plasticity silts (MH/ML), and silty sands (SM) up to 17 meters approximately and from this to 30 m there is a competent stratum of an alluvial-rock material.

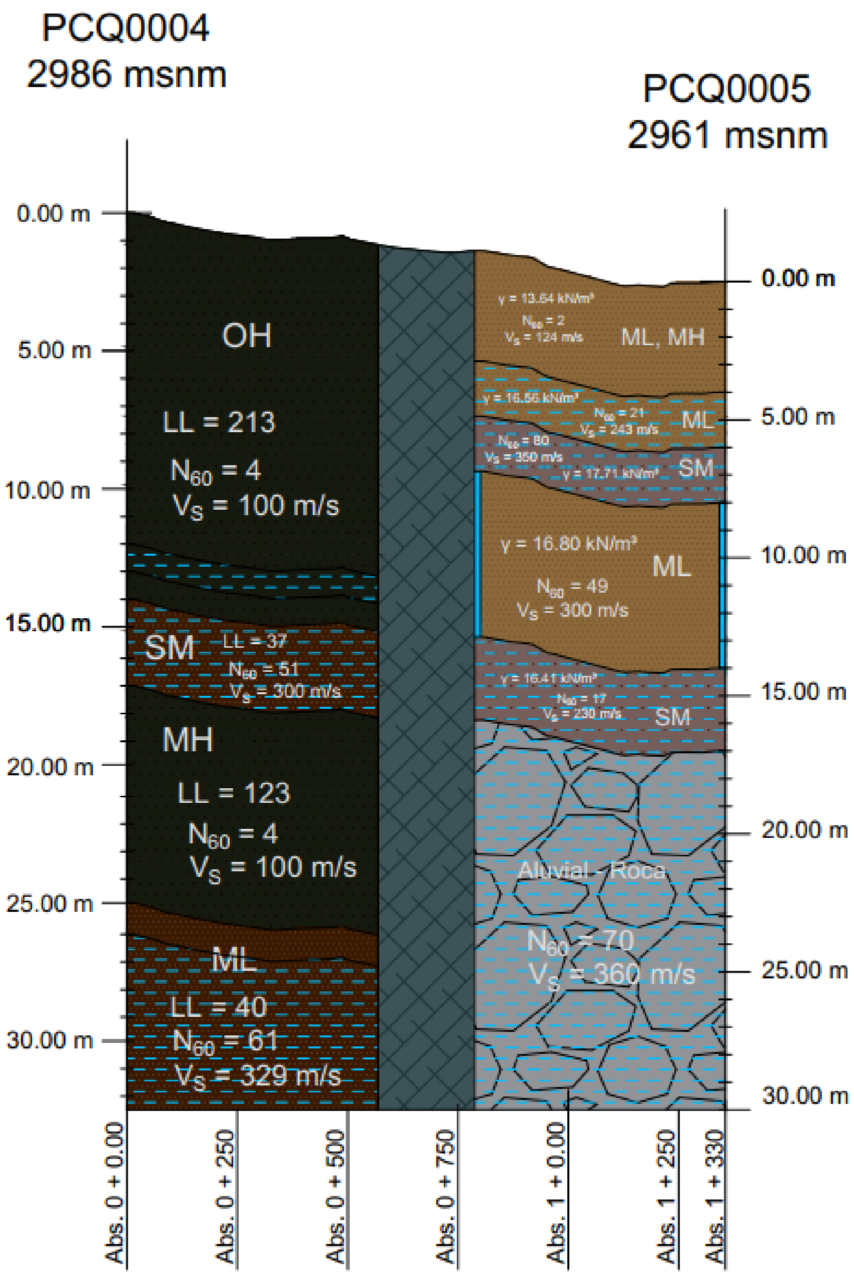

Figure 82. Geotechnical Profile axis A: PCQ0004 – PCQ0005

3.3.8. Profile axis B: PCQ0001 – PCQ0006 – PCQ0009 – PCQ0012 – PCQ0017 – PCQ0018

In the profile we can observe the similarity of materials between wells 1, 6 and 17. However, the characteristics of each of these are different, for example, the N60 and Vs, where it is identified that boreholes 1 and 6 present superficial layers with a greater consistency with respect to the other boreholes, which also present the same competent stratum from 16-17 meters up to 30m.

Borehole 17, in contrast to boreholes 1 and 6, shows pumice and gravels from 20 m to 30 m depth.

In addition, it is evident that boreholes 9, 12 and 18 are completely different, since they have different types of materials along the 30m depth. Borehole 9 to meter 18 has a series of low and high plasticity silts (ML/MH), silty and clayey sands (SM/SC) with N60 between 6 and 81. From 18 meters onwards, a competent stratum of silty sands (SM), poorly graded sands (SP), poorly graded gravels and silty gravels (GP-GM) is observed.

Borehole 12 up to 13 meters has a set of high and low plasticity silts (MH/ML) and silty sands (SM), with the particularity that up to meter 7 the stratum has a low consistency, while from meter 13 to 30 a competent stratum of silty sands (SM), poorly graded sands (SP), silty gravels (GM) and poorly graded gravels (GP) is observed.

Borehole 18 along the 30 m depth has a set of low and high plasticity silts (ML/MH), silty sands (SM) and low plasticity clays (CL), where the first 11 meters have a low consistency, which increases with depth.

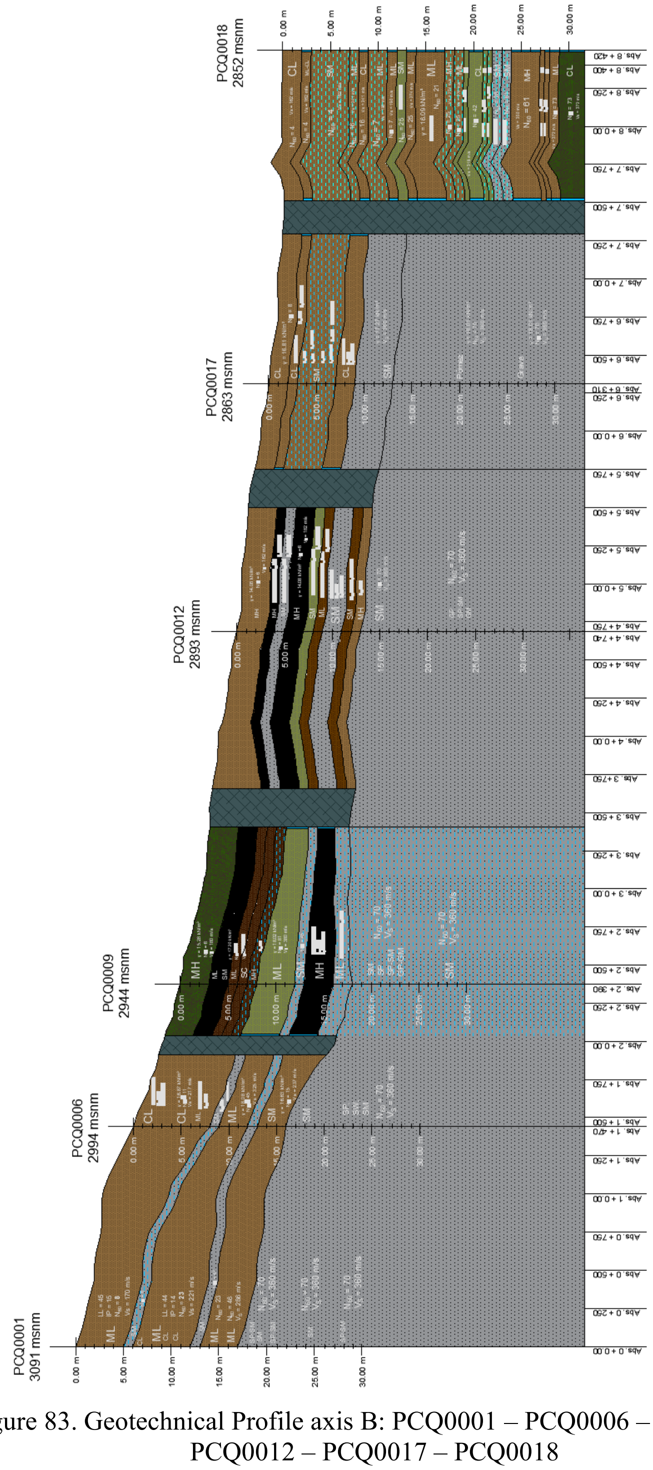

Figure 83. Geotechnical Profile axis B: PCQ0001 – PCQ0006 – PCQ0009 – PCQ0012 – PCQ0017 – PCQ0018

3.3.9. Profile axis C: PCQ0002 – PCQ0007 – PCQ0010 – PCQ0013 – PCQ0016 – PCQ0021

It can be observed in the profile that boreholes 2, 7 and 10 have similar characteristics on average up to 12 m, since the following materials are observed: low plasticity silts (ML) and silty sands (SM), intercalated among them. It is also observed that up to 30 m depth they present the same competent stratum composed of silty sands (SM), well graded sands (SW) and poorly graded sands (SP), with the particularity that in well 2 this begins at 20 m, while in wells 7 and 10 it begins at 10 meters.

Borehole 13 presents the same competent stratum as the previously mentioned boreholes from meter 11, however, the surface strata of this one are composed of low plasticity silts (ML), high plasticity clays (CH) and silty sands (SM), which have a low consistency in the first 3 meters.

Borehole 16 up to 28 m has silty sands (SM) as the predominant material, which at surface level have low consistency, which increases with depth, while in the last 2 m there is a competent stratum composed of an alluvial-pumice material.

Borehole 21 along the 30 m depth has a set of low and high plasticity silts (ML/MH) and silty sands (SM) where the first 9 meters have a low consistency, which increases with depth.

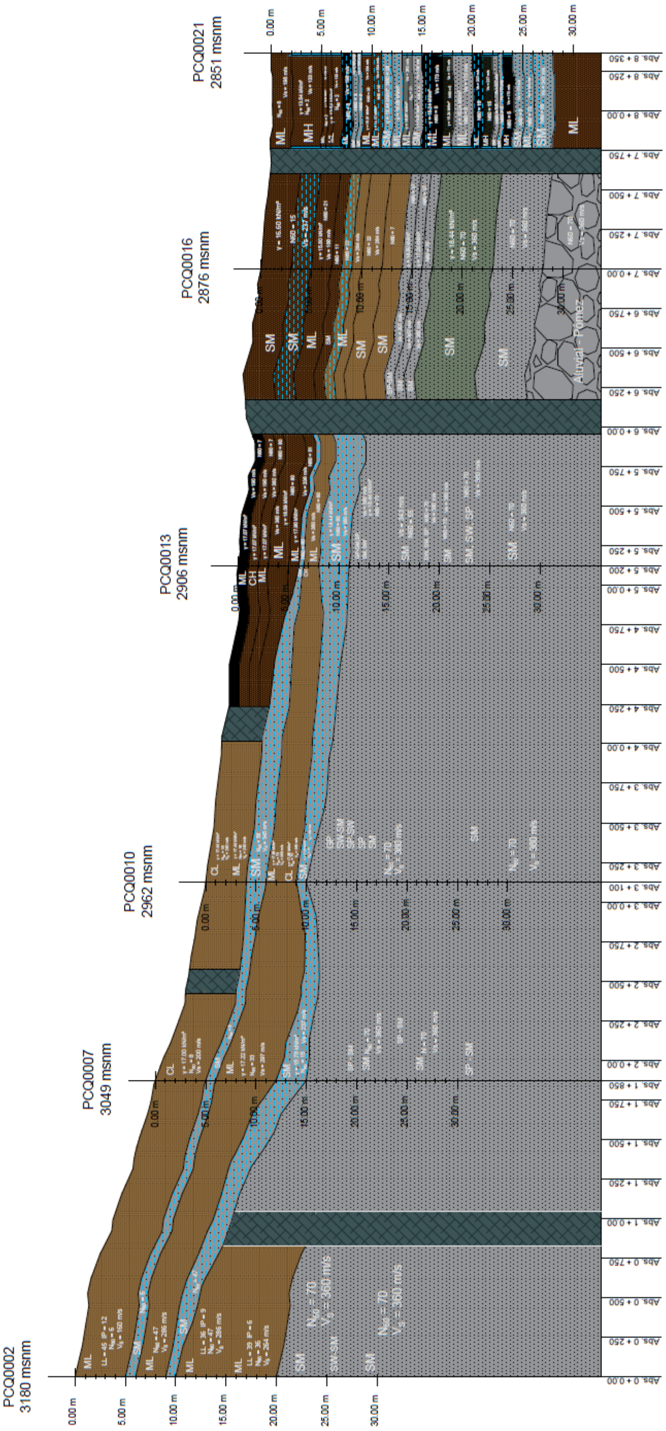

Figure 84. Geotechnical Profile axis C: PCQ0002 – PCQ0007 – PCQ0010 – PCQ0013 – PCQ0016 – PCQ0021

3.3.10. Profile axis D: PCQ0003 – PCQ0008 – PCQ0011 – PCQ0014 – PCQ0015 – PCQ0020

In the profile it can be observed that boreholes 3, 8, 11 and 14 have similar materials, which are low plasticity silts (ML), low plasticity clays (CL) and silty sands (SM), however their characteristics are different. Furthermore, it is evident that the wells present a similar competent stratum composed of silty sands (SM), however the depth where this stratum begins is different, for example, in well 3 the competent stratum begins at 19 m, while in borehole 14 it starts at 14 m.

Boreholes 15 and 20 are different, so they have independent characteristics. Borehole 15 in the first 10 meters presents a layer of low to medium consistency composed of low and high plasticity silts (ML/MH), after 10 m to 15 m there is a layer of low plasticity silts (ML) of medium to high consistency, finally to 30 m there is a competent layer composed of silty sands (SM).

Borehole 20 has a layer composed of low plasticity silts (LMA) and silty sands up to 27 m, but the first 13.50 m have low consistency, after that its consistency increases with depth until reaching 27 m. The last 3 meters present a competent stratum composed of an alluvial.

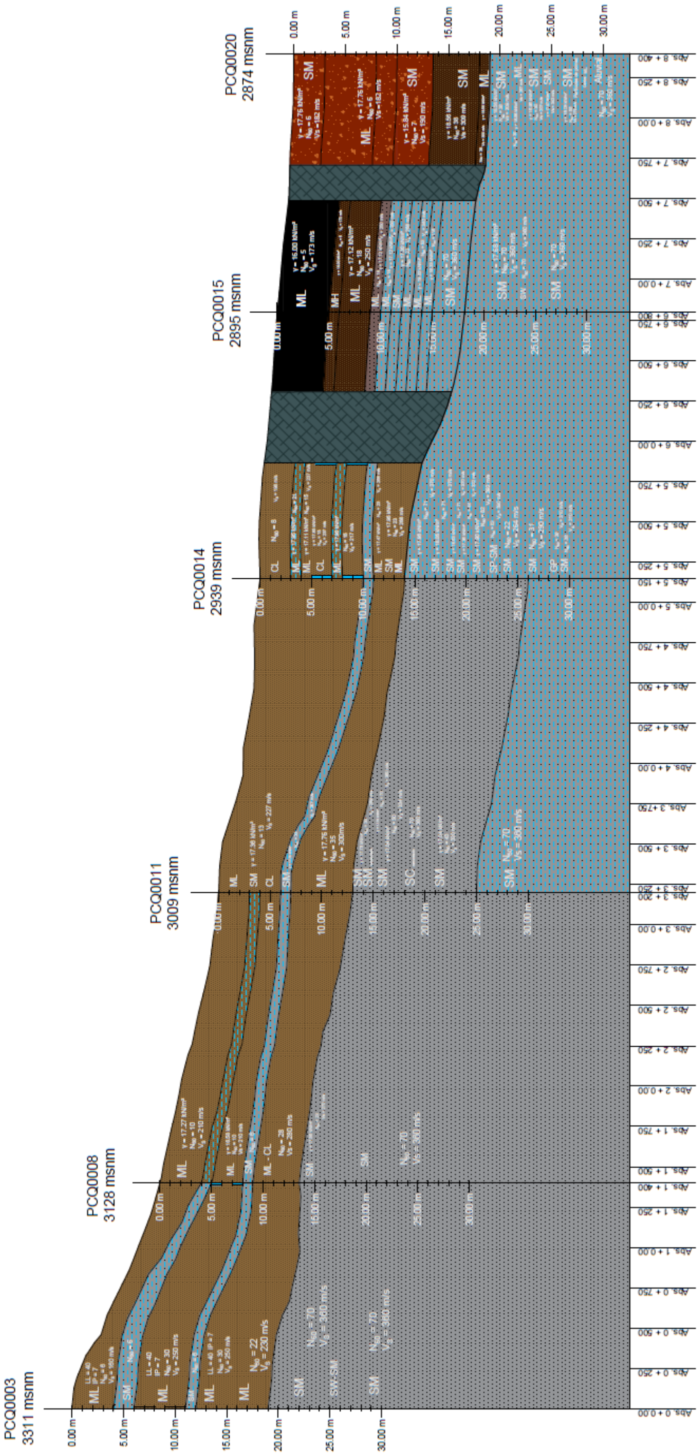

Figure 85. Geotechnical Profile axis D: PCQ0003 – PCQ0008 – PCQ0011 – PCQ0014 – PCQ0015 – PCQ0020

CHAPTER 4

Dynamic properties of soils

The complex nature, geometry and distribution of the generation and propagation mechanisms of the seismic waves in the soil, plus the equally complex response of the ground to the resulting dynamic stresses, can affect the conceptual and applicative treatment of the seismic response of the soil. To achieve the engineering objective, its necessary to perform a series of simplifications and reduction of the mentioned problems, both in the actions and response of the soil (Lanzo and Silvestri 1999). The behavior of soils subjected to dynamic loading is governed by the dynamic soil properties, and to evaluate this response different field and laboratory techniques are available, each with different advantages and limitations with respect to different problems. For example, for problems dominated by wave propagation effects, only low levels of strain are induced in the soil, while in the case of issues related with the stability of soil masses, large strains are induced in the soil. The selection of the proper techniques for characterizing the soil behavior as a function of strain level requires careful consideration and understanding of what is being trying to be solved. (Carrer 2013; Kramer 1996)

4.1. Nonlinear and dissipative behavior of soils

The nonlinear stress-strain behavior of soils can be represented more accurately by cyclic nonlinear models that follow the actual stress-strain path during cyclic loading. Such models can represent the shear strength of the soil, and with an appropriate pore pressure generation model, changes in effective stress during undrained cyclic loading (Kramer 1996). Three wide classes of soils models can be used to represent the stress-strain behavior of cyclically loaded soils: equivalent linear models, cyclically nonlinear models, and advanced constitutive models. Equivalent linear models are the simplest and most used but have limited ability to represent many aspects of soil behavior under cyclically loaded conditions.

At the other hand, advanced constitutive models can represent many details, but they are complex and difficult to calibrate, so impractical for many common problems (Carrer 2013; Kramer 1996). A detailed mathematical description of these models can be found in (Chen and Mizuno 1990; Kramer 1996; Potts and Zdravković 1999). The conceptual criteria for the mentioned models can be seen in Figure 86. Considering that the model to be used in the numerical simulations here discussed is the Equivalent Linear Model, in the next section is a description of it and its properties:

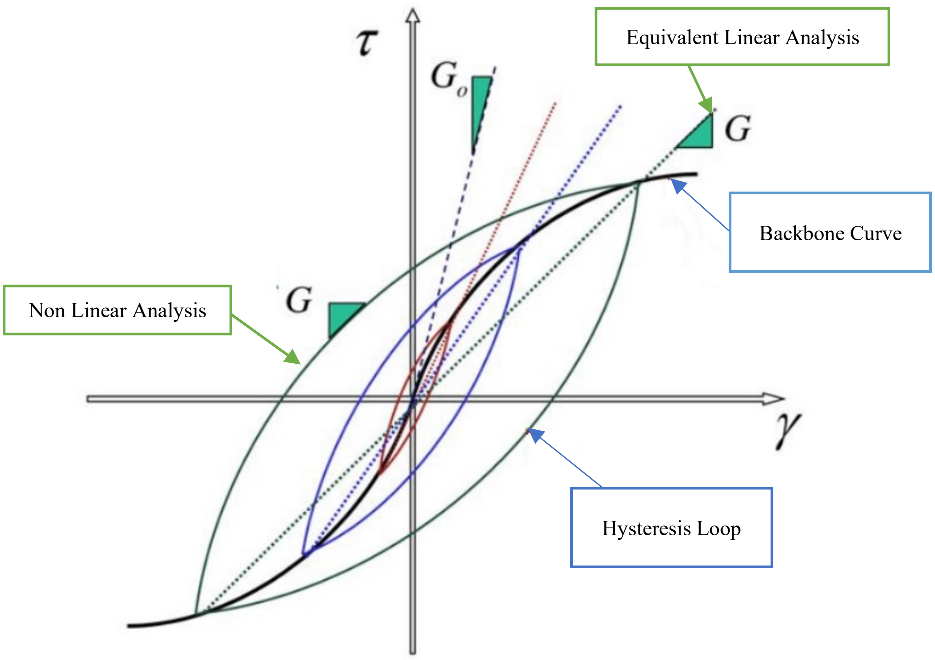

Figure 86. Cyclic nonlinear models, modified from (Carrer 2013; Kramer 1996)

4.1.1. Equivalent Linear Model

The equivalent linear approach is most used in practice in geotechnical engineering. It assumes that a multi-layered soil subjected to a symmetric cyclic shear loading exhibits a hysteresis loop as seen in Figure 87, which relates the shear stresses τ to the cyclic distortion γ (de Martin 2010).

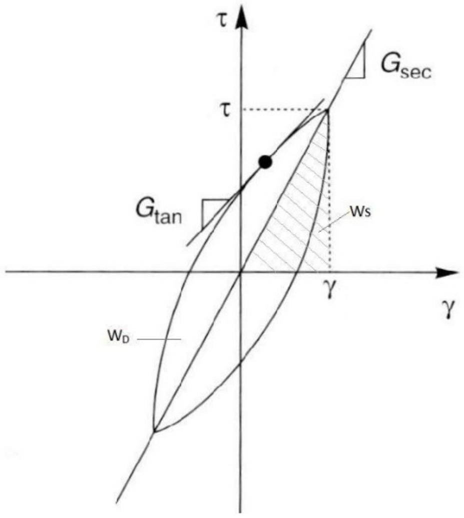

Figure 87. Definition of parameters of an equivalent linear model (Carrer 2013; Kramer 1996)

This hysteresis loop can be described in two ways: (i) by the actual path of the loop itself, and (ii) by parameters that describe its general shape. Two important characteristics of the shape of hysteresis loop are its inclination and its breadth. The inclination of the loop depends on the stiffness of the soil and can be described at any point during the loading process by the tangent shear modulus, Gtan which varies throughout a cycle of loading, but its average value over the entire loop can be approximate by the secant shear modulus Gsec (Carrer 2013; Kramer 1996).

$$G_{sec} = \frac{\tau}{\gamma}$$

Equation 1. Equation for Gsec. (Carrer 2013; Kramer 1996).

where τ and γ are the shear stress and shear strain amplitudes, respectively. Hence, G_{sec} describes the general inclination of the hysteresis loop. The behavior of the soil can´t be described based only on the shear modulus G, and an additional parameter must be found that describes the dissipative behavior of the soil (Crespellani and Facciorusso 2014). The breadth of the hysteresis loop is related to the area, it is a measure of energy dissipation and can be described by the damping ratio D:

$$D = \frac{W_D}{4\pi * W_S} = \frac{1}{2\pi}\frac{A_{loop}}{G_{sec} * \gamma^2}$$

Equation 2. Equation for the damping ratio D.

where WD is the dissipated energy, WS the maximum strain energy stored in the system, and Aloop the area of the hysteresis loop (Carrer 2013; Kramer 1996).

The parameters G_{sec} and D are often referred to as equivalent linear material parameters. Once these parameters are obtained, the equivalent linear procedure then consists in providing G - γ and D - γ curves, expressing the evolution of both parameters with respect to the cyclic distortion. These curves can be constructed by laboratory tests, as can be seen in (Seed et al. 1986; Seed and Idriss 1970) and then used for numerical computations (de Martin 2010).

It is important to mention that the assumption in the model allows a very efficient class of computational models to be used for ground response analyses, and it is commonly employed for that reason (Carrer 2013; Kramer 1996; de Martin 2010). However, this model is only an approximation of the real nonlinear behavior due to the assumption of linearity embedded in its use and cannot be applied to problems involving permanent deformation or failure. This imply that the strain will always return to zero after cyclic loading, and since a linear material has no limiting strength, failure cannot occur (Kramer 1996).

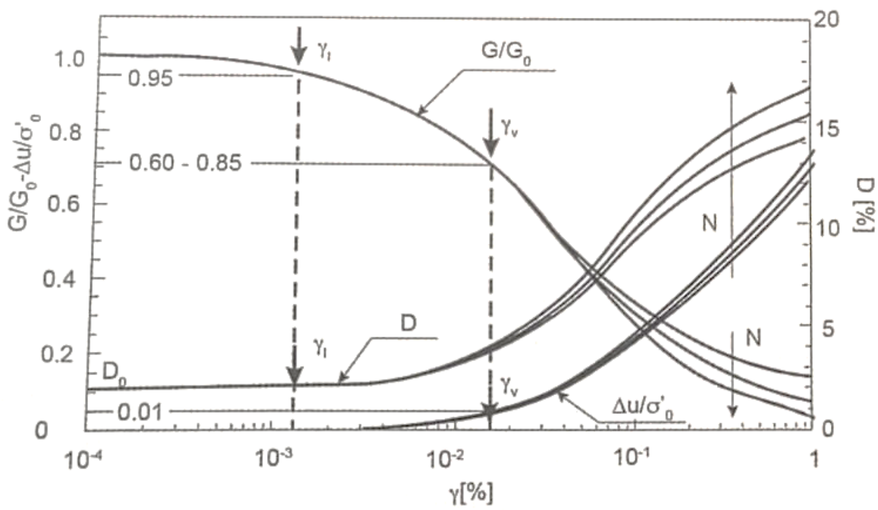

Figure 88. Behavior of soil under change of ɣ and increase in cycles N, adapted from (Crespellani and Facciorusso 2014)

The shear modulus G and the damping ratio D change with the level of the shear tangential deformation ɣ. It is possible to follow the evolution of the stiffness and of the damping ratio as the amplitude of the shear deformation and the number of cycles increase. It can be noted that when the volumetric threshold is exceeded in undrained conditions, an increase in interstitial pressure takes place which increases with the number of cycles in Figure 88. (Crespellani and Facciorusso 2014)

4.1.2. Shear Modulus G_0

A vast amount of experimental data has been accumulating in the geotechnical literature, relative to both on-site and laboratory tests for the values of Go in the different materials and on the factors that influence it (Huang et al. 2021; Naik, Patra, and Malik 2022; Pua et al. 2021; Shinde and Kumar 2022). The initial stiffness is in fact a fundamental parameter, relevant not only for the prediction of seismic behavior, but also in soil-structure interaction problems. The determination of Go has historically been one of the first objectives of the dynamics of soils and the techniques of measurement of Go are still the subject of great scientific attention as the determination of Go requires an instrumentation capable of appreciating extremely low deformation levels (less than 10 ^ -5%) (Crespellani and Facciorusso 2014).

Based on (Kramer 1996), laboratory tests have shown that soil stiffness is influenced by cyclic strain amplitude, void ratio, mean principal effective stress, plasticity index, over consolidation ratio, and number of loading cycles. The secant shear modulus of an element of soil varies with cyclic shear strain amplitude.

- At low strain amplitudes, the secant shear modulus is high, but it decreases as the strain amplitude increases. The locus of points corresponding to the tips of hysteresis loops of various cyclic strain amplitudes is called a backbone (or skeleton) *curve*; its slope at the origin (zero cyclic strain amplitude) represents the largest value of the shear modulus, G_o.
- At greater cyclic strain amplitudes, the *modulus ratio* Gsec/Gmax drops to values of less than 1.

Characterization of the stiffness of an element of soil therefore requires consideration of both Gmax and the way the modulus ratio G/Gmax varies with cyclic strain amplitude and other parameters. The variation of the modulus ratio with shear strain is described graphically by a *modulus reduction curve*. The modulus reduction curve presents the same information as the backbone curve; either one can be determined from the other (Kramer 1996) and can be seen in Figure 89.

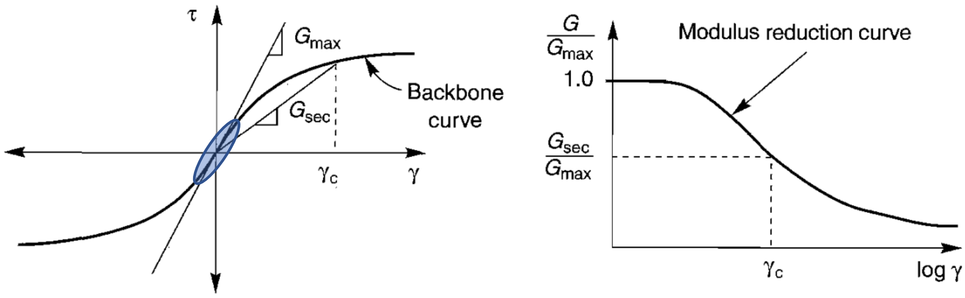

Figure 89. Behavior of soil under change of ɣ and increase in cycles N, modified from (Kramer 1996)

Seismic geophysical tests induce shear strains lower than about 3 x 10-4%, so the measured shear wave velocities can be used to compute Gmax by the equation:

$$G_{max} = \rho * V_s^2$$

Equation 3. Equation to compute Gmax.

The use of measured shear wave velocities is generally the most reliable means of evaluating the in-situ value of Gmax for a particular soil deposit, and the seismic geophysical tests are commonly used for that purpose (Kramer 1996). However, when dealing with sites where highly anisotropic stress conditions exists, such as the South of Quito, care must be taken in the interpretation of shear wave velocity as wave velocities might vary with the direction of wave propagation and particle movement (Escribanoa and Nashb 2015; Hao and Lok 2008; Kramer 1996; Stokoe, Lee, and Knox 1985).

4.1.3. Initial Damping Ratio Do

The influence of constitutive factors and state variables on low strain damping (D) is, both quantitatively and qualitatively, less documented in the literature than for stiffness. This is because the measurement of D is more affected by experimental uncertainties than that of G_0, or V_s. For a given terrain, the damping decreases with the increase in the effective stress state, but the trends and typical values of D, vary from material to material, not always allowing for a clear assessment of the effects of constituent factors (Lanzo and Silvestri 1999). The ranges of variation researched by several authors (Dobry and Vucetic 1987; Huang et al. 2021; Stokoe et al. 1985), and has been compiled by (Vinale, Mancuso, and Silvestri 1996) that can be seen in Figure 90.

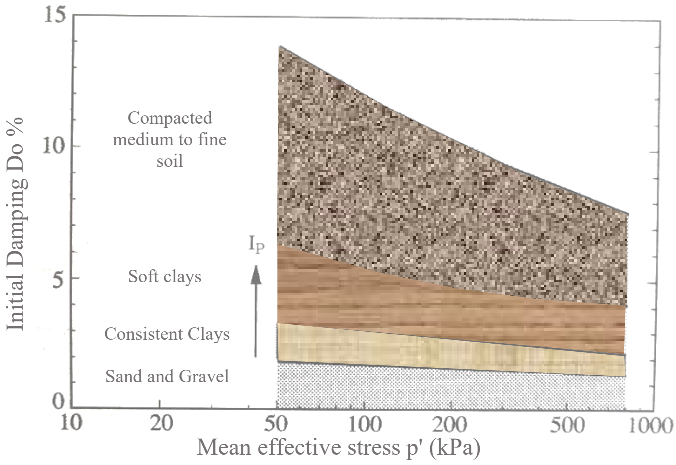

Figure 90. Dependence of the initial damping factor Do on the type of soil and the mean effective stress p’, modified from (Vinale et al. 1996)

Analyzing to a higher extent, Figure 90 indicate that for granular soils (sands, gravels, rockfill), the range of variation of D_0, with the state and the stress history is narrow, and the values close to zero; for natural fine-grained soils, the typical values and the decrease gradient of D_0, with the effective tension increase, passing from firm to soft clays; moreover, with the same state and stress history, the characteristic values of D_0 increase with the index of plasticity; finally, the values of D_0 for compacted soils with medium to fine grain are greater than those typical of natural clays, due to the lack of diagenesis process in the formation of the soil, and the consequent lower stability and continuity of the microstructure (Lanzo and Silvestri 1999; Vinale et al. 1996).

4.1.4. Shear Modulus and Damping Ratio in the nonlinear field

It is possible to experimentally observe how the decay curves depend on the state parameters and physical properties of the soil, as well as on the cyclic load. In particular, the greatest influence is given by the variations in the plasticity index and by the effective confinement pressure. The loading frequency, the number of cycles and the degree of over-consolidation are less influential on the performance of these curves.

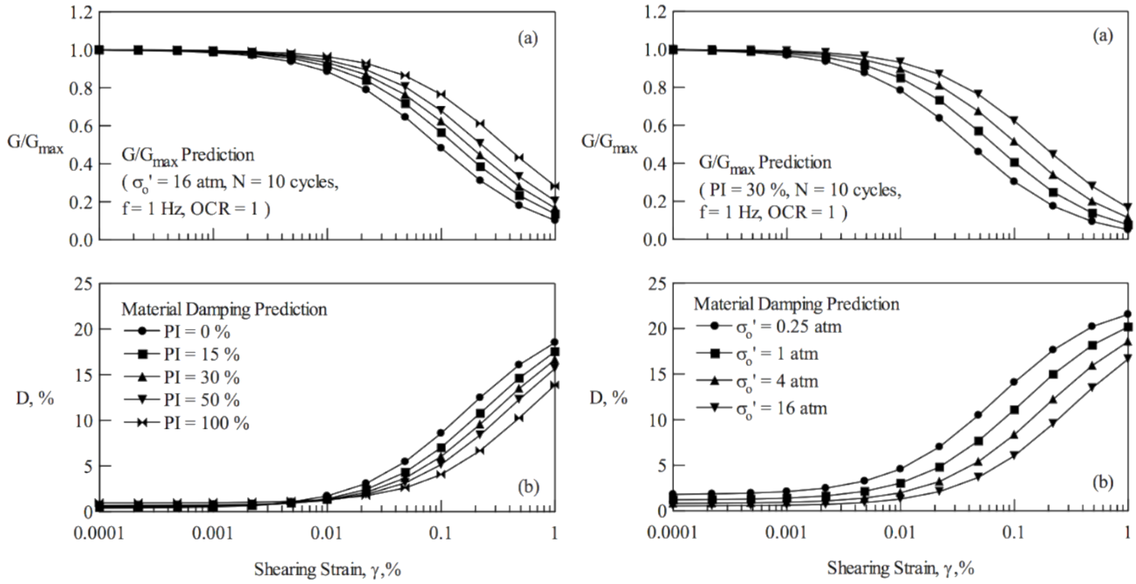

Figure 91. Dependence of the initial damping factor Do on the type of soil and the mean effective stress p', modified from (Darendeli 2001)

For clayey materials, an important role is assumed by the plasticity index, while for sandy materials, the main role is assumed by the confinement tension, since, by increasing confinement, the grains have less possibility to move, and the material will be more rigid. In this way, the linearity threshold will move towards higher deformation levels, and this will lead to less energy dissipation, since the frictional forces will be less significant. This does not happen in clays because the prevailing mechanism in the variation of the modulus and dissipation is linked to interparticle chemical bonds, therefore the confinement tension plays a secondary role for this type of material, as can be seen in Figure 91. In addition to these main factors, the curves are affected, albeit to a lesser extent, by the degree of over-consolidation, the load frequency, and the number of cycles.

The granular materials (gravels and sands) therefore tend to dissipate little energy at small deformations as there are small displacements and, consequently, no significant frictional forces are developed, contrary to what happens in clays where there is a greater dissipation at low levels. deformative. As the deformation increases, the granular materials first pass in non-linear conditions because the relative displacement between the particles becomes important and therefore more energy is dissipated than clays. It should be emphasized that high plasticity clays dissipate little energy and remain in a linear condition up to high deformations; this is a fundamental fact because in the presence of a strong earthquake, for these soils, the wave component is attenuated little, and the effects are more marked (Cuffaro 2020; Darendeli 2001)

4.2. Influence factors over the mechanical behavior of soil

Based on a literature review (Chetry 2018; Cuffaro 2020; Darendeli 2001; Hardin and Drnevich 1972b, 1972a; Park et al. 2004a; Vinale et al. 1996; Vucetic 1992), the dynamic characteristics of a terrain are influenced to a greater or lesser extent by certain parameters, which can be divided into two main groups: (1) Load condition parameters and (2) Parameters related to the type of material. The parameters that define the load conditions, are for example, the deformation level, the extent of the confinement pressure and its duration (long-term effect), number of cycles, frequency of loading, and degree of over-consolidation, as detailed in the following paragraphs:

a. Influence of confinement pressure

The influence of confining pressure for deep soil deposits is very important but has been generally neglected in most response analysis studies (Park et al. 2004a). The trend of the shear modulus G, of the damping ratio D and of the void index is shown in Figure 92 as the effective confinement pressure increases in a range from 0.1 to 10 atm, up to the development of the consolidation of the sample considered. It is possible to note how the three graphs show a bilinear trend due to the initial state of over-consolidation of the analyzed soil, and the subsequent normal consolidation with the development of greater sensitivity to the variation of the three parameters considered. (Chetry 2018)

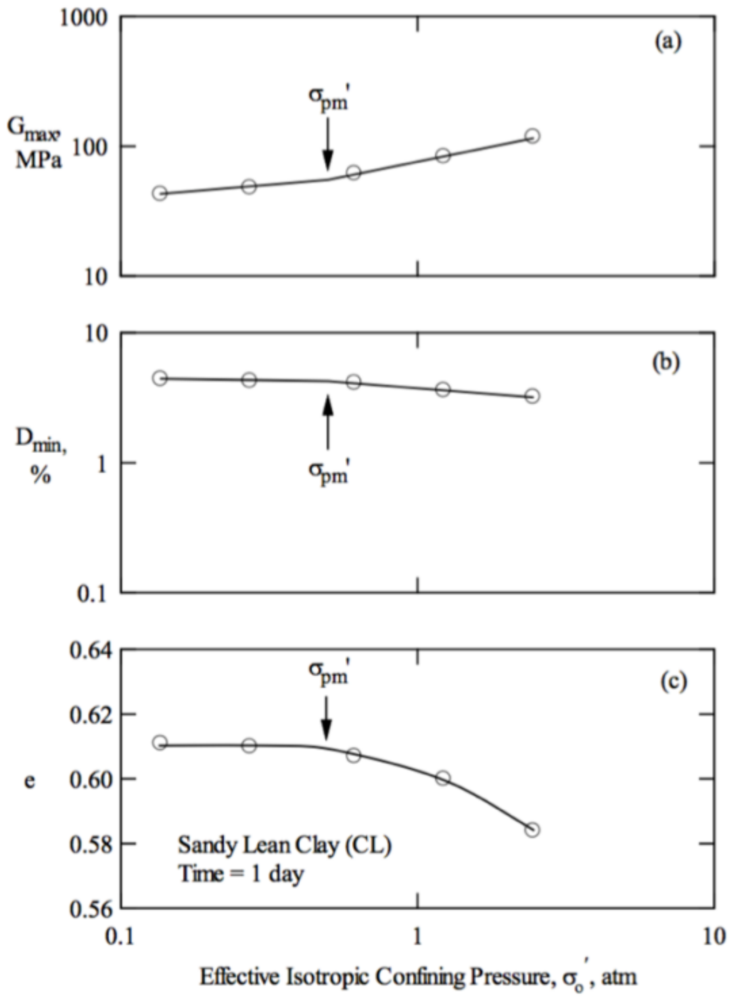

Figure 92. Trend of the shear modulus and of the damping ratio at low deformation, and of the void index at variation in the effective confinement pressure (Darendeli 2001)

Darendeli in 2001 developed the trend of decay curve of the shear modulus and of the damping ratio curve as a function of the deformation level for two values of confinement pressure greater than the pre-consolidation stress of the sample, seen in Figure 93. As the confinement pressure increases, an increase of the linearity limit of both the shear modulus and the ratio of damping is present. Consequently, with the same deformation level, as the effective confinement pressure increases, there is a higher shear modulus and a lower ratio of damping (Carrer 2013; Chetry 2018; Darendeli 2001; Park et al. 2004a).

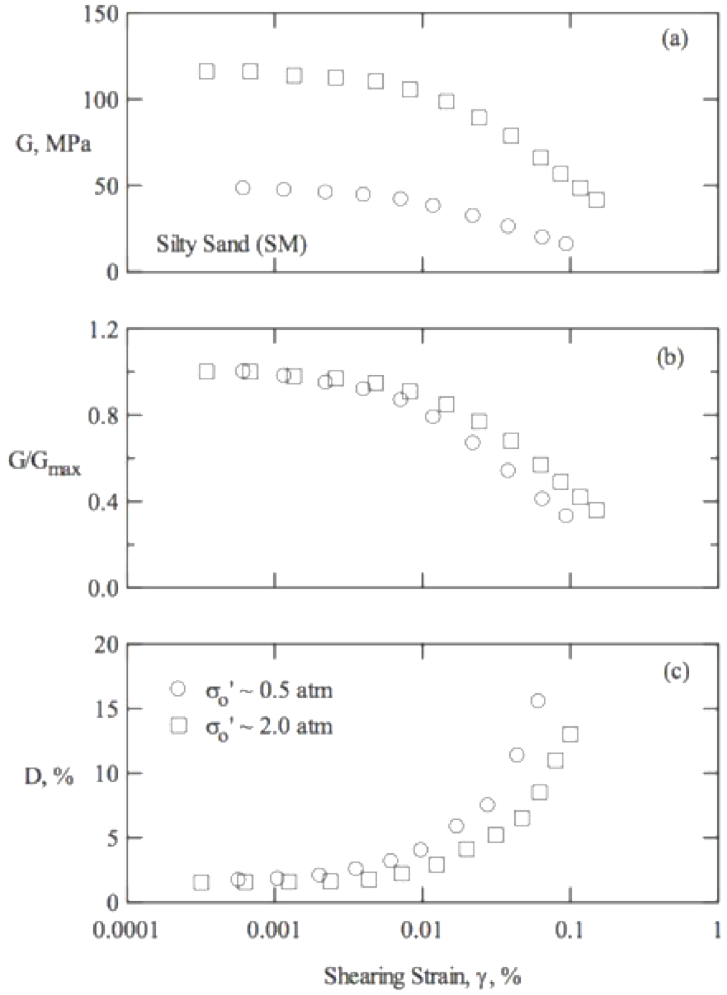

Figure 93. Trend of the shear modulus G, of the normalized shear modulus with respect to the maximum value and of the ratio of damping as a function of the deformation level for two different values of the confinement stress. Results obtained by resonant column tests from (Darendeli 2001)

b. Influence of the duration of application of the confinement pressure

Figure 94 show the trend of the shear modulus, of as a function of different pressure values of isotropic confinement and the relative duration of application. The value of the shear modulus at small deformations increases as the damping ratio and void ratio index decrease. Conversely, the damping ratio at small deformations and the void index reduces as both the confinement pressure and its duration of application increases. (Chetry 2018; Darendeli 2001) Overall, the shear modulus decreases, and damping ratio decreases with increasing void ratio in undisturbed cohesive soils. (Carrer 2013).

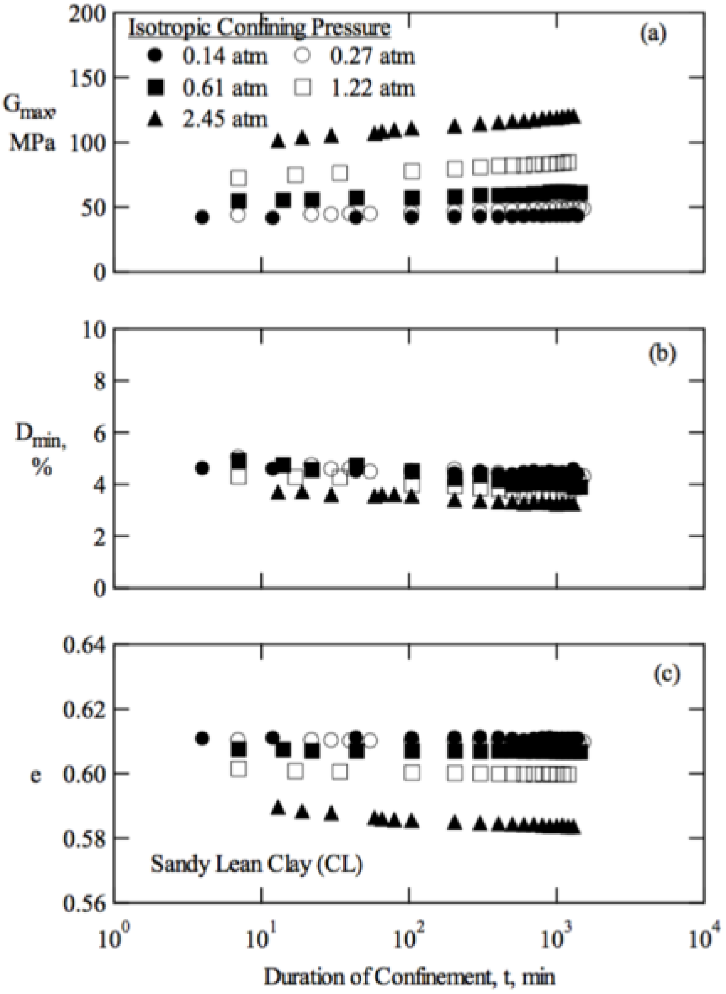

Figure 94. Trend of the shear modulus and of the damping ratio at low deformations, and of the void index at variation in the confinement pressure and its duration of application (Darendeli 2001)

c. Influence of the degree of over-consolidation

Over-consolidation has a more significant influence on the dynamic properties of soils with a certain level of plasticity. In experiments performed by (Darendeli 2001), a consolidation of a sample at 0.34 atm was subsequently tested with confinement pressures varying between 0.09 and 1.36 atm, to then be discharged again at 0.34 atm. The trends obtained from resonant column tests performed on the sample with OCR equal to 1 and on the sample with OCR equal to 4 are shown in Figure 95. From the results, the degree of over-consolidation does not present a significant influence in the variation of dynamic properties. In fact, the graphs of the normalized shear modulus and the damping ratio show, respectively, a slight increase and a slight reduction in the case related to the degree of major over-consolidation. (Chetry 2018; Darendeli 2001)

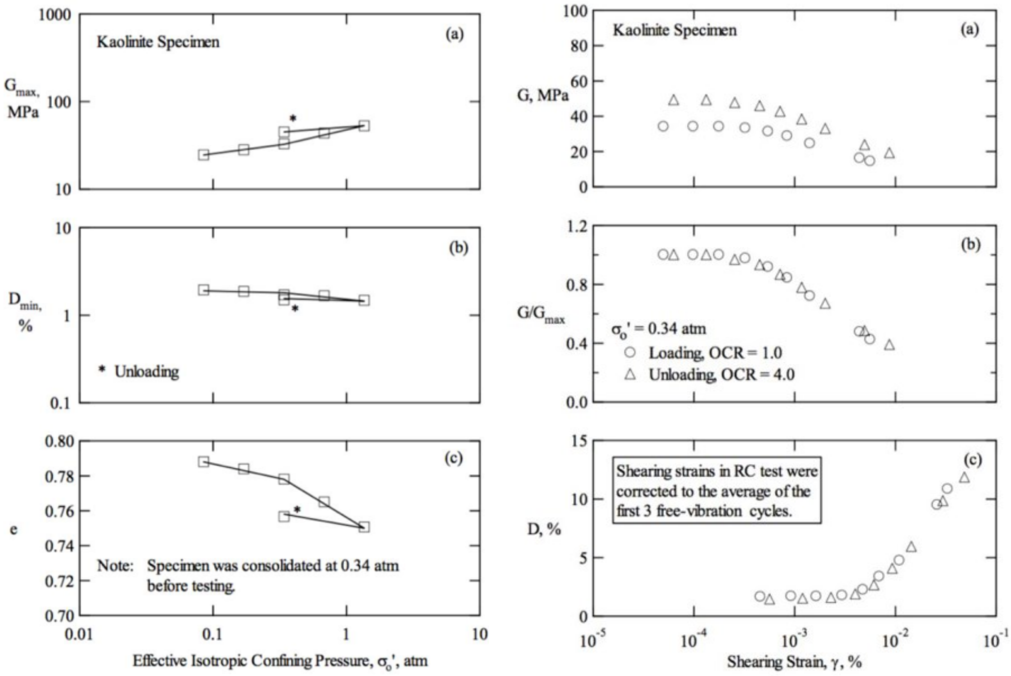

Figure 95. Trend of the shear modulus and of the damping ratio at low deformations, and of the void index at variation in the confinement pressure and its duration of application (Darendeli 2001)

d. Influence of the number of load cycles

The effect of the number of cycles was evaluated using the resonant column and cyclic torsional shear by (Darendeli 2001). Comparisons were made between the shear modulus trends (dimensional and normalized) and the damping ratio in relation to the first and tenth cycle of the cyclic torsional shear test and resonant column test results (N approximate1000 cycles). From the results, the value of the shear modulus at small deformations measured with the resonant column test is greater than the corresponding evaluated with the torsional shear test. However, this effect is mainly related to different load frequency. Once the elastic threshold is exceeded, there is a similar reduction in shear modulus in the three load cycle configurations considered (Chetry 2018; Cuffaro 2020; Darendeli 2001; Stokoe et al. 1999)

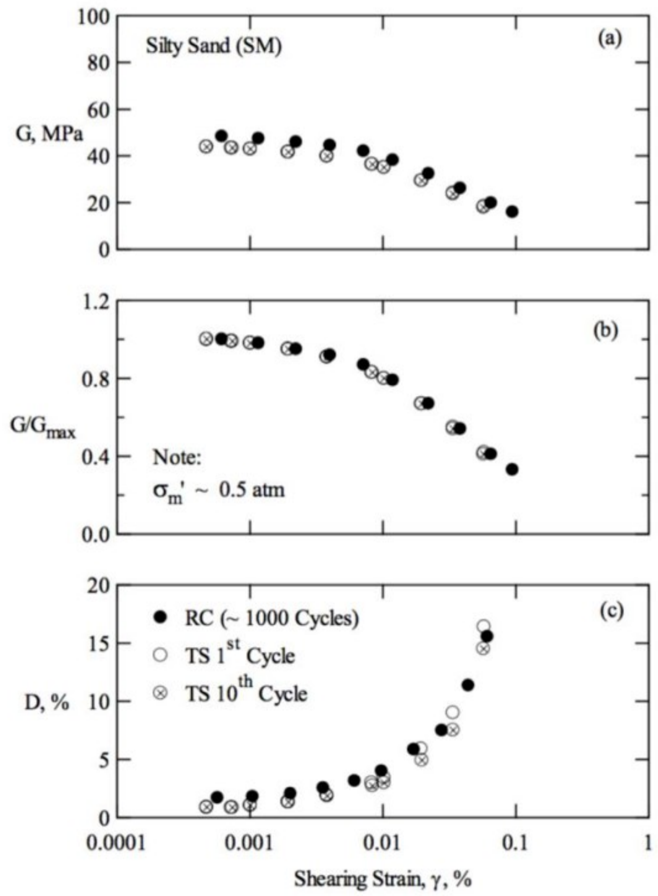

Figure 96. Trend of the shear modulus and of the damping ratio at low deformations, and of the void index at variation in the confinement pressure and its duration of application (Darendeli 2001)

e. Influence of frequency

The variation consists of an increment of G of about 10% for each order of magnitude of increment of the load frequency. Conversely, the damping ratio at small deformations is more sensitive to this variation. In fact, for frequencies greater than 10 Hz a 100% increase occurs after a logarithmic load cycle. Therefore, this (Park et al. 2004a; Vucetic 1992) same, or during the resonant column tests (Chetry 2018). The shear modulus decreases for fine cohesive soils and increases marginally for cohesionless soils with the number of cycles of loading. The damping ratio decreases with the logarithm of the number of cycles of loading in both cohesive and cohesionless soils, up to about 50.000 cycles (Carrer 2013).

A wider range of all the environmental and loading factors that influence the shear modulus degradation and damping ratio was summarized by (Hardin and Drnevich 1972a, 1972b; Park et al. 2004a; Vucetic 1992), and can be seen in Table 10.

Table 10. Summary of the different environmental and loading conditions influencing shear modulus degradation and damping ratio in normally and moderately consolidated soils, from (Park et al. 2004a; Vucetic 1992)

Factors	G/G_{max}	*Damping ratio*
Effective confining pressure, σ'_m	Increases with σ'_m; effect decreases with increasing PI	Decreases with σ'_m; effect decreases with increasing PI
Void ratio, e	Increases with e	Decreases with e
Geologic age, t_g	May increase with t_g	Decreases with t_g
Cementation, c	May increase with c	May decrease with c
Overconsolidation ratio, OCR	Not affected	Not affected
Plasticity index, PI	Increases with PI	Decreases with PI
Cyclic strain, γ_c	Decreases with γ_c	Increases with γ_c
Strain rate, $\dot{\gamma}$	G increases with $\dot{\gamma}$, but G/G_{max} probably not affected if G and G_{max} are measured at same $\dot{\gamma}$.	Stays constant or may increase with $\dot{\gamma}$
Number of loading cycles, N	Decreases after N cycles of large γ_c (G_{max} measured before N cycles) for clays; for sands, can increase (under drained conditions) or decrease under undrained conditions	Not significant for moderate γ_c and N

4.3. Experimental characterization techniques

4.3.1. Resonant Column at Pontificia Universidad Católica del Ecuador parts and description

The equipment used in this research corresponds to a TSH-100, a *fixed-free* Resonant Column manufactured by GCTS Testing Systems (Geotechnical Consulting and Testing Services – GCTS), shown in Figure 97, which is described below:

Figure 97. GCTS TSH-100 Resonant Column

1. Pressure panel
2. Soil triaxial cell
3. Load frame

Equipment components:

1) *Total TSH-100 equipment*

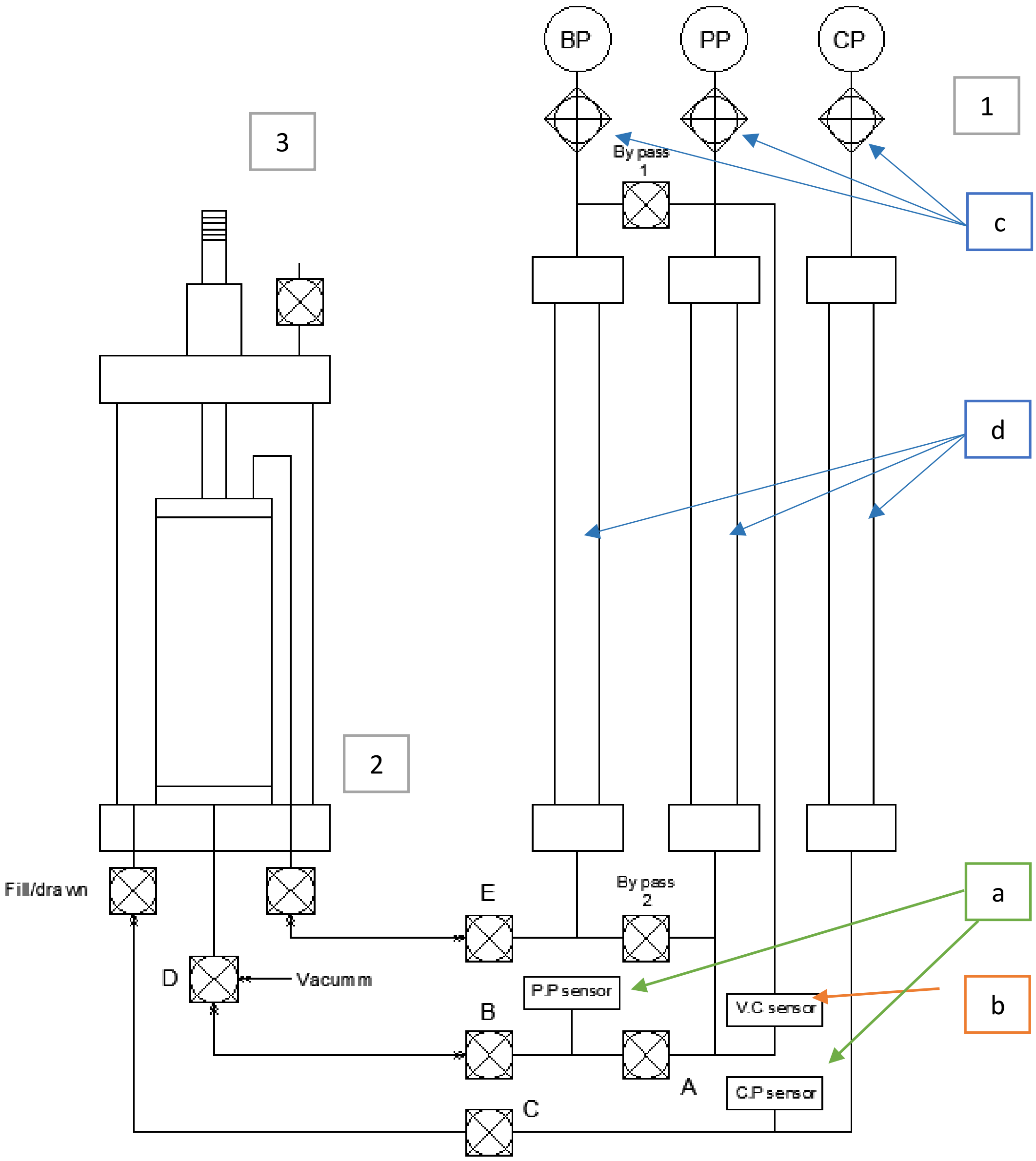

Figure 98. GCTS TSH-100 Resonant Column - Front scheme of the pressure panel

1. Pressure panel
2. Soil triaxial cell
3. Load frame

2) *Pressure panel (PCP – 200)*

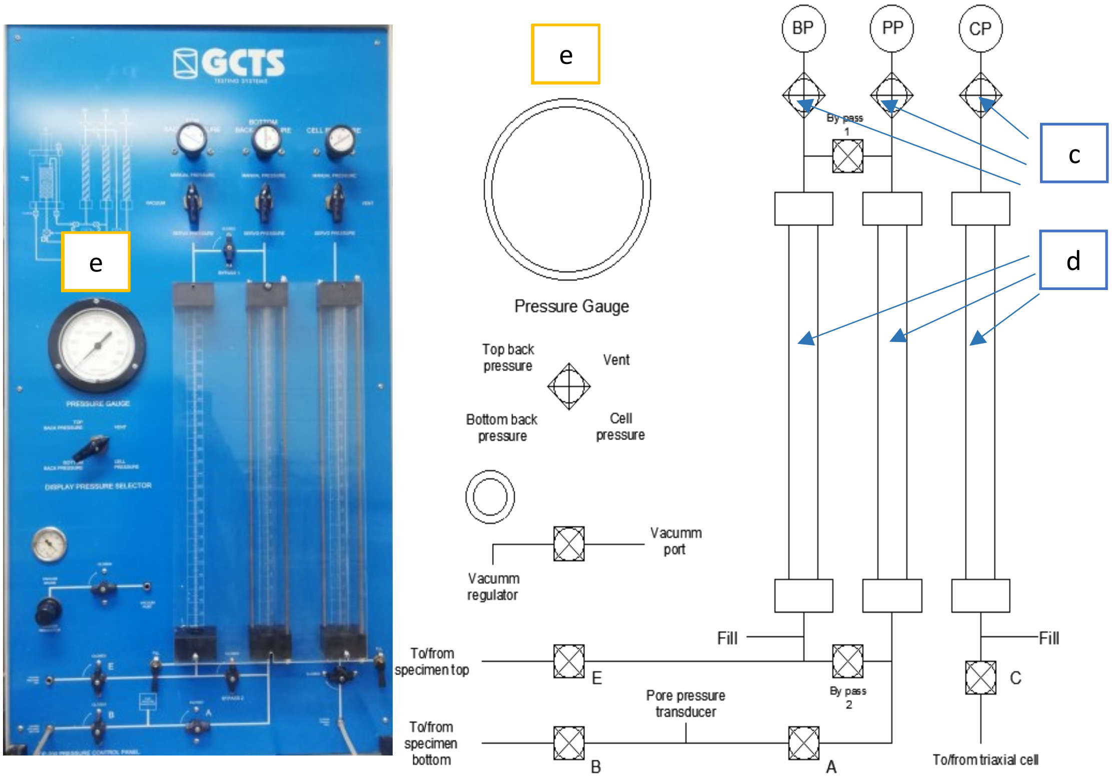

Figure 99. GCTS TSH-100 Resonant Column - Pressure panel. PCP-200.

Table 11. Pressure Panel PCP-200 Specifications (GCTS Testing Systems 2007)

Pressure panel (PCP-200)		
General specifications		
Maximum pressure		*1 000 kPa*
Volume capacity		150 cc capacity with 0.01 cc resolution
Components		*Specifications*
a	Pressure transducers	***Linearity:*** 0.25% ***Pressure range***: 1 000 kPa.
b	Volume change differential pressure transducer	***Linearity:*** 0.25% ***Pressure range***: 500 mm-H_2O.
c	Regulators for manual pressure	***Three regulators for manual control:*** cell, top, and bottom back pressures.
d	Graded water level sight tubes	They are for manual readings with 1 mm of accuracy.
e	Single pressure gauge	Measures pressure differences with a resolution of 2.5 kPa (0.5 psi).
-	Volume change device	The volume change meter is monitored using a volume change differential pressure transducer (b) with a water column in the range of 500 mm.

3) *Soil Triaxial Cell (TRX-100)*

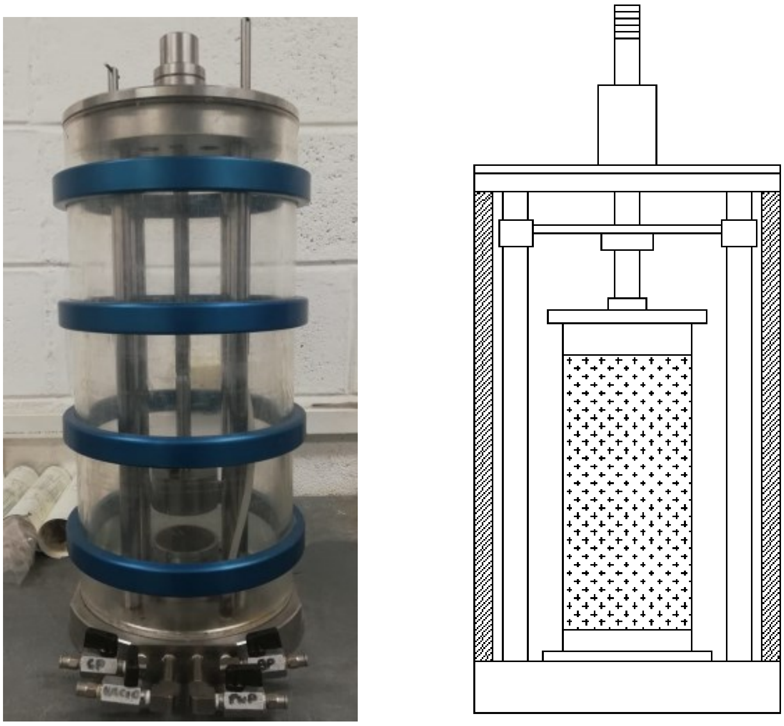

Figure 100. GCTS Soil triaxial cell. TSH-100.

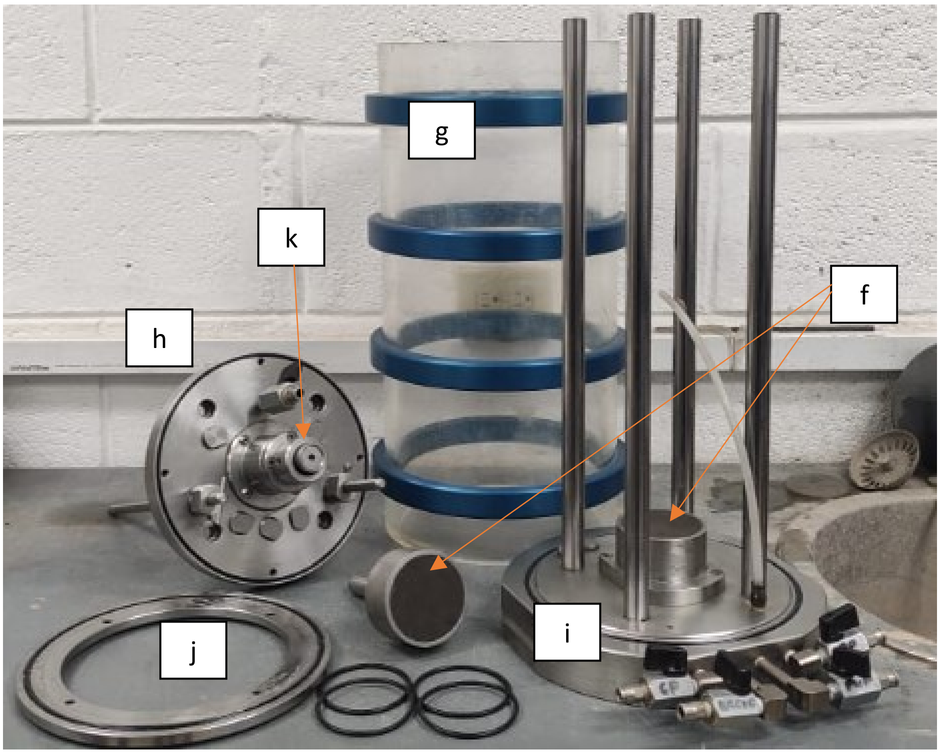

Figure 101. GCTS Soil triaxial cell. TSH-100 *components*

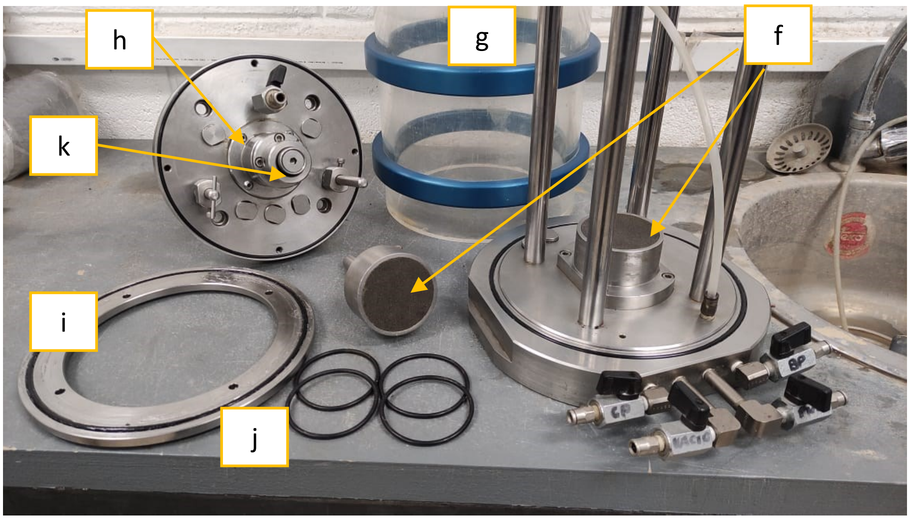

Figure 102. GCTS Soil triaxial cell. TSH-100 *components*

Table 12. Triaxial Cell TSH-100 Specifications (GCTS Testing Systems 2007)

Soil triaxial cell (TSH-100)		
General specifications		
Maximum confining pressure		1 000 kPa (150 psi)
Drainage lines		Top and bottom
Components		***Specifications***
f	Specimen heads	***Specimen diameter:*** 70 mm. ***Material:*** They are made of metal with porous stones attached.
g	Transparent cell wall	***External diameter:*** 228 mm. ***Internal diameter:*** 200 mm. ***Thickness:*** approximately 13 mm. ***Material:*** It is made of an acrylic tube reinforced with metal rings.
h	Cell top lid	***External diameter:*** 200 mm. ***Material:*** It is made of metal. It has four holes for internal columns.
i	Cell base	***Material:*** It is made of metal. It has 4 internal columns. It has 4 ports on the base.
j	Retention ring	***External diameter:*** 228 mm. ***Internal diameter:*** 165 mm. It has an o'ring to hermetically seal the cell.
k	Loading piston	***Diameter:*** 15.9 mm (5/8”).
-	Specimen	***Diameter:*** 70 mm. ***Height:*** 2 to 2.5 times the diameter.

4) *Load frame (FRM-10P)*

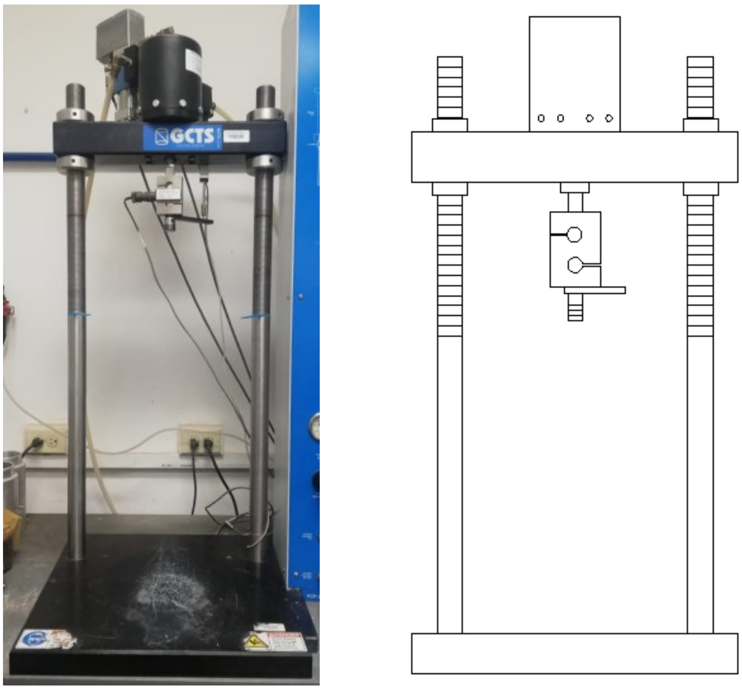

Figure 103. GCTS Load frame. FRM-10P.

Table 13. Triaxial Cell TSH-100 Specifications (GCTS Testing Systems 2007)

Soil triaxial cell (TSH-100)	
General specifications	
Standard capacity	10 kN
Stroke	50 mm (2 inch)
Actuator load capacity	+/- 10kN
Frequency response	8mm peak to peak am
Maximum vertical daylight opening	940 mm
Horizontal daylight opening	340 mm

Source: *GCTS Catalog* (p.47). GCTS Testing Systems, 2009.

5) *Additional elements*

Table 14. Additional Elements Specifications (GCTS Testing Systems 2007; Muñoz 2017)

Additional elements	
Component	*Specifications*
Servo electric motor actuator	***Torque loads:*** 2.33N-m (peak) and 0.78 N-m (continuous). ***Rotation:*** +/- 25 degrees of stroke ***Frequency:*** up to 250 Hz.

Motor controller	Uses a +/- 10 volt command input and includes TTL enabled input to disable the power stage and perform vibration free testing with minimal EMF. 110 V.
Fiber optic strain sensor with dual output	***Low strain range:*** +/- 0.1 mm ***High strain range:*** +/- 6.0 mm ***Flat frequency response:*** 0-15 kHz
Strain sensor	***Deformation:*** ± 6 mm ***Linearity:*** 0.25%.
Acquisition controller and digital servo system	***Resolution:*** 16 bits ***Max. Inputs:*** 8 universal ***Max. Outputs:*** 4 ***Microprocessor:*** 850 MHz ***Voltage:*** 90-260VAC - 50 - 60 Hz ***Max. Power:*** 0.4 KW
Calibration specimen	Aluminum construction. Includes added removable dough.

4.3.2. Resonant Column at Pontificia Universidad Católica del Ecuador operation and use

The theorical background is based on CATS Resonant Column & Torsional Shear Test Mode (GCTS Testing Systems 2007), it is detailed below:

- The GCTS Resonant Column apparatus applies a harmonic torsional excitation on the top of the specimen by an electromagnetic loading system or motor.
- A torsional harmonic load with a constant amplitude is applied over a range of frequencies and the response curve is measured.
- The shear wave is obtained by measuring the first-mode resonant frequency.
- The shear modulus is calculated from this shear wave velocity and the soil density.
- Material damping can be obtained from either the free-vibration decay after the forced vibration is moved (The free vibration decay method) or from the width of the frequency response curve assuming viscous damping (Half-power bandwidth method).

This method is based on the one-dimensional wave equation derived from the theory of linear-elastic vibration as the solution for non-linear vibration, which is extremely complex. Due to this, is one of the factors that limit the resonant column test to medium and low strain amplitudes even it can measure larger strains. The

GTCS Resonant Column device is fixed-free system where the soil column is fixed at the base and free to rotate at the top, as shown in figure 104.

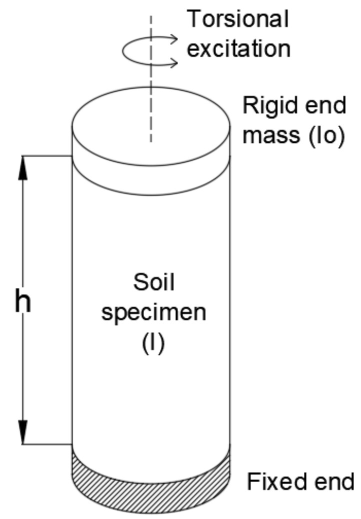

Figure 104. Idealized fixed-free resonant column specimen.

First, the soil specimen is consolidated and then an external cyclic torsional load is applied on the top of the specimen. The loading frequency is gradually changed until the maximum response is found (strain amplitude). The fundamental frequency of the soil specimen and the driving device is the lowest frequency at which the strain amplitude is maximized, that is why the fundamental frequency is a function of the soil stiffness, specimen geometry and the characteristics of the resonant column device.

4.3.2.1. Shear modulus

The governing equation of motion for the fixed-free resonant column test as idealized in figure 104 for torsional vibration with a Kelvin-Voigt soil model is derived as follows:

First, a torque T is applied to an elastic soil cylinder an incremental angle of twist, dθ, along an incremental length of the specimen, dz, generates a torque, T, equal to:

$$T = G\,J\,\frac{d\theta}{dz}$$

Equation 4. Equation to calculate the Torque.

Where:

T: torque.

G: shear modulus of the soil.

J: polar moment of inertia of the cross-sectional area.

From the diagram shown un figure 105, the torque on the two faces of the soil element are T y T+$\frac{\partial T}{\partial z} dz$. Using the torque T from equation 4 we obtain:

$$\frac{\partial T}{\partial z} dz = G\,J\,\frac{\partial^2 \theta}{\partial z^2} dz$$

Equation 5. Equation result from the combination of the diagram on figure 105 and the equation 4.

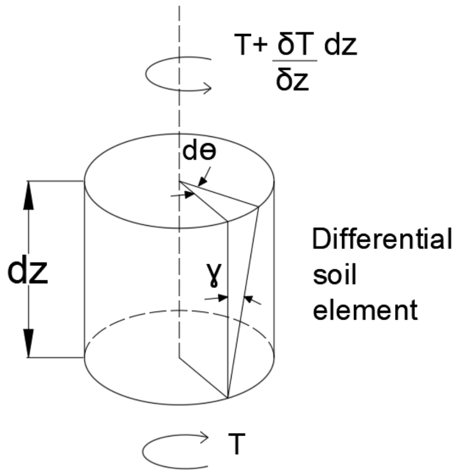

Figure 105. Differential soil element.

Applying Newton's second law to the motion of the soil column and equating this net torque to the product of the mass polar moment of inertia and the angular acceleration:

$$\frac{\partial T}{\partial z} dz = I\,\frac{\partial^2 \theta}{\partial t^2} = \rho\,J\,dz\,\frac{\partial^2 \theta}{\partial t^2}$$

Equation 6. Equation result of the application of Newton's second law to the motion of soil column.

Where:

I: mass moment of inertia = ρ J dz.

ρ: soil mass density.

Substituting $\frac{\partial T}{\partial z}$ from equation 4 and using the relationship between the shear wave velocity, Vs, shear modulus, and mass density ($G = \rho V_s^2$) we obtain the wave equation in torsion for an elastic rod:

$$\frac{\partial^2 \theta}{\partial z^2} = \frac{1}{V_s^2} \frac{\partial^2 \theta}{\partial t^2}$$

Equation 7. Wave equation in torsion for an elastic rod.

The general solution to equation 7 is found using separation of variables as:

$$\theta(z,t) = \left[Asin\left(\frac{\omega}{Vs}z\right) + \ Bcos\left(\frac{\omega}{Vs}z\right)\right] \cdot \ e^{-i\omega t}$$

Equation 8. Solution of equation 7.

Where:

ω: the angular frequency.

A y B = constants that depend on the boundary conditions of the soil column.

The boundary conditions in the GCTS Resonant Column system are:

1. The angular displacement at the bottom (fixed end) is zero.
2. The torque at the top of soil specimen (free end) is equal to the inertia torque of the drive system but opposite.

From the first boundary condition we find the B = 0 by substituting θ = 0 at z = 0. The second derivative of the general solution with respect to time is:

$$\frac{\partial^2 \theta}{\partial t^2} = \frac{\partial^2 \left[Asin\left(\frac{\omega\ z}{V_s}\right) e^{i\omega t}\right]}{\partial t^2} = -\omega^2 A\ \ sin\ sin\ \left(\frac{\omega\ z}{V_s}\right)\ e^{i\omega t}$$

Equation 9. Second derivative of the general solution with respect to time.

From the second boundary condition, the torque at the free end of the soil specimen is:

$$T_{z=h} = \ -I_o\ \frac{\partial^2 \theta}{\partial t^2}$$

Equation 10. Equaton for the torque at the free end of soil specimen.

Where:

I_o: mass moment of inertial of drive system.

h: height of soil specimen.

Substituting $\frac{\partial^2\theta}{\partial t^2}$ from the equation 9 into equation 10:

$$T_{z=h} = I_o\omega^2 A \sin \sin\left(\frac{\omega h}{V_s}\right) e^{i\omega t}$$

Equation 11. $\frac{\partial^2\theta}{\partial t^2}$ from equation 9 into equation 10.

Combining equations 4 and 11 we obtain:

$$G\,J\,\frac{d\theta}{dz} = I_o\omega^2 A \sin \sin\left(\frac{\omega h}{V_s}\right) e^{-i\omega t} \; @\; z = h$$

Equation 12. Combination of equations 4 and 11.

Finding the derivative of θ with respect to z for z = h in equation 8 results in:

$$\left(\frac{\partial\theta}{\partial z}\right)_{z=h} = \frac{A\omega}{V_s} \cos \cos\left(\frac{\omega h}{V_s}\right) e^{-i\omega t}$$

Equation 13. Derivative of θ with respect to z for z = h.

Substituting equation 13 into equation 12:

$$G\,J\,\frac{\omega}{V_s} \cos \cos\left(\frac{\omega z}{V_s}\right) = I_o\omega^2 \sin \sin\left(\frac{\omega h}{V_s}\right)$$

Equation 14. Substitution of equation 13 into equation 12.

Using again the relationship $G = \rho\, V_s^2$ in equation 14 it becomes:

$$\rho V_s J\omega \;\cos \cos\left(\frac{\omega z}{V_s}\right) = I_o\omega^2 \sin \sin\left(\frac{\omega h}{V_s}\right) \quad (12)$$

Equation 15. Equation 14 with the relationship $G = \rho\, V_s^2$

Equation 15 is further reduced using the relationship I = ρ J h to:

$$\frac{I}{h} V_s\,\omega\;\cos \cos\left(\frac{\omega z}{V_s}\right) = I_o\omega^2 \sin \sin\left(\frac{\omega h}{V_s}\right)$$

Equation 16. Equation 15 reduced using the relationship I.

Rearranging the terms in equation 16 results in the following expression:

$$\frac{I}{I_o} = \frac{\omega\, h}{V_s} tan \left(\frac{\omega h}{V_s}\right)$$

Equation 17. Equation 16 once the terms have been rearranged.

Where:

I: mass moment of inertia of the soil column.

I_0: mass moment of inertia of the drive system including the top cap.

Once the shear wave velocity, Vs, is determined, the shear modulus, G, is calculated as follows:

$$G = \rho V_s^2$$

Equation 18. Equation to obtain the shear modulus G.

Equations 17 and 18 are used by the GCTS software to reduce the data from the resonant column tests.

4.3.2.2. Shear strain

The shear strain in a solid cylindrical resonant column specimen loaded in torsion varies from zero at the center line of the specimen (or a minimum value at the inner surface of a hollow specimen) to a maximum value at its outer edge as shown un figure 106. The shear strain, γ, is calculated as follows:

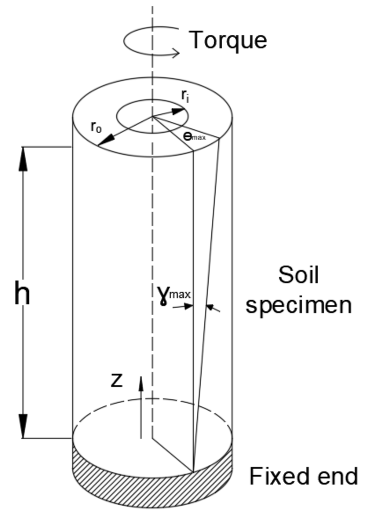

Figure 106. Shear strain in soil specimen

$$\Upsilon(r) = \frac{r\, \theta_{max}}{h}$$

Equation 19. Equation to obtain the shear strain γ.

Where:
r: radial distance from the soil column axis.
θ_{max}: máximum angle of twist.
h: specimen height.

Because the shear strain is not constant throughout the radial distance, an equivalent shear strain, γ is required to represent the average shear strain. This variation of the shear strain makes it desirable to test hollow specimens instead of solid ones minimizing the variation of shear strain amplitude across the specimen.

Regardless of the type of specimen, solid or hollow, a single or unique value of shear strain amplitude associated with the measured shear modulus, G, is required. Conventionally, r_{eq} is assumed as 2/3 de r_o for solid specimens with radius r_o and (r_i + r_o)/2 for hollow specimens with an inside radius r_i and an outside radius r_o. Chen and Stokoe found that value of r_{eq} varied from 0.82 r_o for a peak shear strain below 0.001% to 0.79 r_o for peak shear strain of 0.1% for solid specimens.

In the GCTS Resonant Column device, the angle of twist at the top of the specimen, θ_{max}, can be measured with either an accelerometer or proximitors mounted atop of the specimen at radius r_{sensor}. If an accelerometer is used to measure the shear strain, the acceleration value is double integrated with respect to time to determine the torsional displacement, x, of the sensor support plate at the accelerometer location. The calculation of the torsional displacement, x, from the acceleration, $\ddot{x}$, is:

$$x = -\frac{\ddot{x}}{\omega^2} = -\frac{\ddot{x}}{4\pi^2 f^2}$$

Equation 20. Equation to calculate the torsional displacement from the acceleration.

Where:
ω: circular frequency.

f: is the linear frequency.

Assuming small angles, the angle of twist of the top plate is calculated by dividing the sensor displacement output by the radius to the position of the sensor, r_{sensor}.

$$\theta_{max} = \frac{x}{r_{sensor}}$$

Equation 21. Equation to obtain the angle of twist of the top plate.

$$\Upsilon(r) = \frac{r_{eq}\,\theta_{max}}{h}$$

Equation 22. Equation to obtain $\Upsilon(r)$

4.3.2.3. Viscous Damping

It is not easy to define true material damping but is common practice to express the damping of real materials in terms of its equivalent viscous damping ratio. The free vibration response for a system with a single degree of freedom with viscous damping can be expressed as:

$$0 = m\ddot{x} + c\dot{x} + kx$$

Equation 23. Equation for a system with a single degree of freedom with viscous damping.

Where:
$\ddot{x}$: acceleration.
$\dot{x}$: velocity.
x: displacement.
m: mass.
c: viscous damping coefficient.
k: spring constant.

Considering the following relationships:

$$D = \frac{c}{c_c}$$

Equation 24. Equation to calculate the viscous damping ratio.

$$c_c = 2\sqrt{km}$$

Equation 25. Equation to calculate the critical damping coefficient.

$$\omega_n^2 = \frac{k}{m}$$

Equation 26. Equation to calculate the natural frequency (undamped).

Where:

D: viscous damping ratio.

c_c: critical damping coefficient.

ω_n: natural frequency (undamped).

From the above relationships and dividing the equation 23 by the mass, m, we obtain:

$$0 = \ddot{x} + 2D\omega_n\dot{x} + \omega_n^2 x$$

Equation 27. Equation to calculate the viscous damping ratio.

There are three general solutions for equation 27 that depend on whether the single degree of freedom system is underdamped, critically damped or overdamped. Free vibration of soil specimens in the resonant column test normally exhibits an undedamped behavior and the general solution to this case is:

$$x(t) = Ce^{-\omega_n Dt} sin\,(\omega_d t + \varphi)\, sin\left(\frac{\omega_n h}{V_s}\right)$$

Equation 28. Equation for undamped behavior and general solution for Free vibration of soil specimens in the resonant column test.

Where:

C: constant.

ω_d: damped resonant frequency.

$$\omega_d = \omega_n\sqrt{1 - D^2} \quad (24)$$

Equation 29. Equation to calculate the damped resonant frequency.

The ratio of any two peaks depicted in figure 107 is given as:

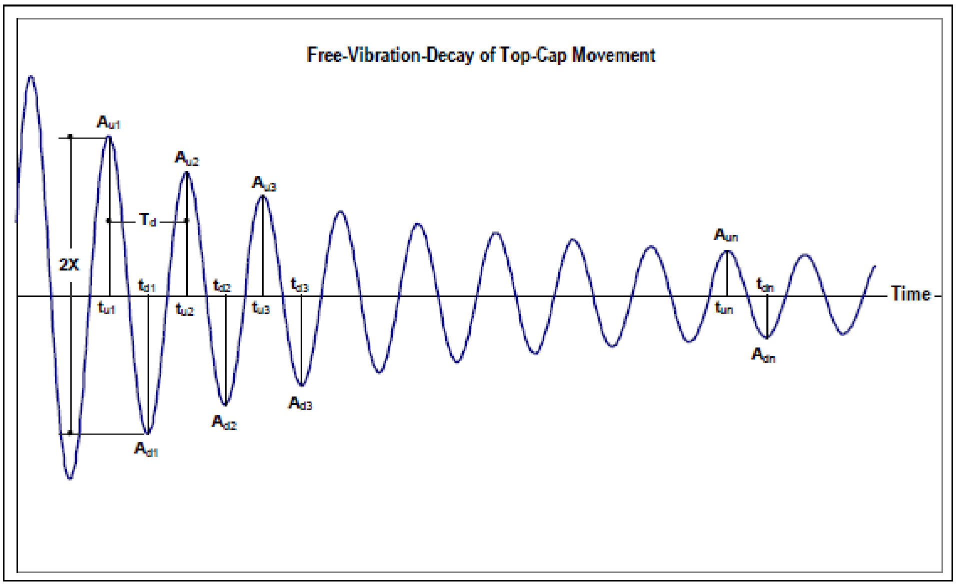

Figure 107. Free-vibration decay (GCTS Testing Systems 2007)

$$\frac{x_n}{x_{n+1}} = e^{-\omega_n D(t_n + t_{n+1})} = e^{\frac{2\pi D}{\sqrt{1-D^2}}} \quad (25)$$

Equation 30. Equation to obtain the ratio of any two peaks.

Where:

$t_{n+1} = t_n + 2\pi/\omega_d$. The logarithmic decrement, δ, is found by taking the natural logarithm of equation 29.

$$\delta = ln\frac{x_n}{x_{n+1}} = \frac{2\pi D}{\sqrt{1-D^2}}$$

Equation 31. Equation for the logarithmic decrement, δ.

The damping ratio is calculated as:

$$D = \sqrt{\frac{\delta^2}{4\pi^2 + \delta^2}}$$

Equation 32. Equation to calculate the damping ratio from the logarithmic decrement.

The GCTS Resonant Column software records the free vibration data for all the cycles with a shear strain amplitude of at least 15% of the maximum shear strain obtained during the forced vibration test. This program calculates the natural logarithm of the normalized decay amplitude for each cycle and determines the logarithmic decrement using a linear least-square curve fitting.

4.3.2.4. Half-Power Bandwidth

A second method to measure material damping in the resonant column test is the half-power bandwidth method. From the forced-vibration test, the logarithmic decrement is calculated by measuring the width of the frequency response curve near resonance.

$$\delta = \frac{\pi(f_2^2 - f_1^2)}{2f_r^2}\sqrt{\frac{x^2}{{x_{max}}^2 - x^2}}\frac{\sqrt{1-D^2}}{1-D^2}$$

Equation 33. Equation to define the logarithmic decrement by Half-Power Bandwith Method.

Where:

f_1: frequency below the resonance where the strain amplitude is A.

f_2: frequency above the resonance where the strain amplitude is A.

f_r: resonant frequency.

D: material damping.

When the damping is small and the amplitude A is $\frac{A_{max}}{\sqrt{2}}$, equation 33 can be simplified as:

$$\delta \cong \frac{\pi(f_2 - f_1)}{f_r}$$

Equation 34. Simplification of equation 33.

Then the damping ratio can be expressed as:

$$D \cong \frac{f_2 - f_1}{f_r}$$

Equation 35. Equation to calculate the damping ratio by Half-Power Bandwith Method.

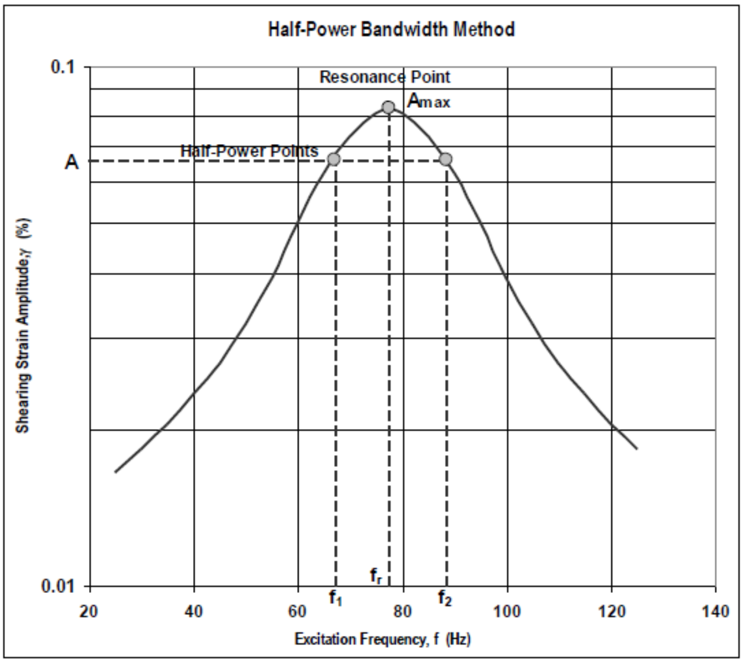

Figure 108. Material damping from Half-Power Bandwidth Method (GCTS Testing Systems 2007)

4.3.2.5. Calibration of the drive system

The calibration of the GCTS Resonant Column system is performed using a metallic specimen instead of a real soil specimen. The metallic specimen is assumed to have a cero, or close to zero, damping and a constant torsional stiffness, k. Then, from the Newton's second law, the mass moment of inertia is related to the natural or resonant frequency, ω, as follows:

$$I = \frac{K}{\omega^2}$$

Equation 36. Equation to calculate the inertia using the natural or resonant frequency, ω.

Even though the torsional stiffness, k, of the calibration specimen can be found by applying a constant torque and measuring the angular rotation, this is not normally done. Without knowing the torsional stiffness, k, the mass moment of inertia, I, in equation 36 cannot be solved.

The recommended procedure to find the mass moment of inertia of the drive system, I_0, is to perform two resonant column tests with the metal calibration specimen, one by itself and the other with an added mass. Perform a frequency sweep with constant force amplitude to find the resonant frequency for each configuration. The force amplitude is selected to excite the calibration specimen within the limits of the installed sensors (proximeters or accelerometer) but still provide a large enough signal to measure the response accurately. Then solution to equation 36 for the first calibration run without the added mass becomes:

$$I_o + I_{cal} = \frac{K}{{\omega_1}^2}$$

Equation 37. Solution of equation 36 for the first calibration run without added mass.

Where:

I_0: mass moment of inertia of the drive system and any other fixture that will be used during actual soil testing.

I_{cal}: mass moment of inertia of the calibration specimen.

ω_1: resonant frequency of calibration specimen without the added mass.

The second equation for the second calibration run attaching the added mass is:

$$I_o + I_{cal} + I_{masa} = \frac{K}{{\omega_2}^2}$$

Equation 38. Equation for second calibration run attaching the added mass.

Where:

I_{mass}: mass moment of inertia of the added mass.

ω_2: resonant frequency of calibration specimen with added mass.

Now, to find the mass moment of inertia of the driving system that will be used to solve equation 17 and find Vs, we combine the equations 37 and 38 to get:

$$I_o = \frac{(I_{cal} + I_{masa}){\omega_2}^2 - I_{cal}{\omega_1}^2}{{\omega_1}^2 - {\omega_2}^2}$$

Equation 39. Equation to calculate moment of inertia of the driving system.

Keep in mind that for the GCTS Resonant Column system, the specimen top cap is not used during the calibration procedure. Therefore, its mass moment of inertia has to be added to the result of equation 39 to calculate the actual I_0 value that is entered into the GCTS software.

4.3.2.6. Calibration of the resonant column system GCTS

To calibrate the GCTS resonant column system it is first necessary to calculate the moment of inertia of the calibration sample, I_{cal}, and the moment of inertia of the calibration sample plus additional mass, I_{mass}. These values are calculated from the geometry and the respective mass of each part.

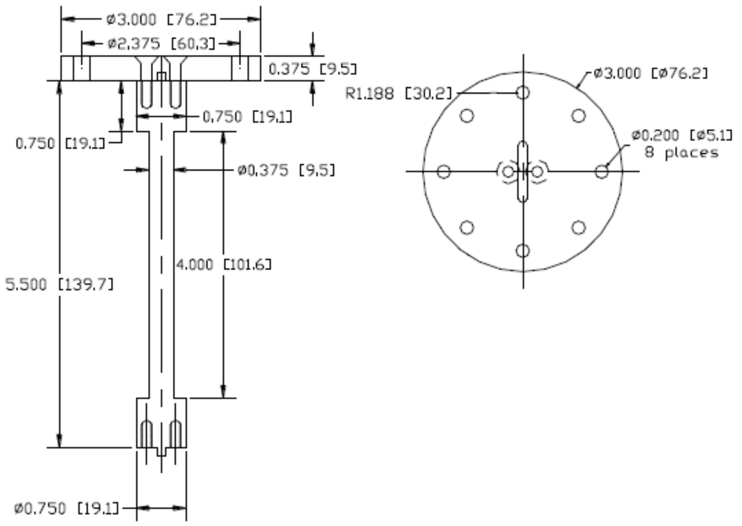

Figure 109. Calibration specimen geometry (GCTS Testing Systems 2007)

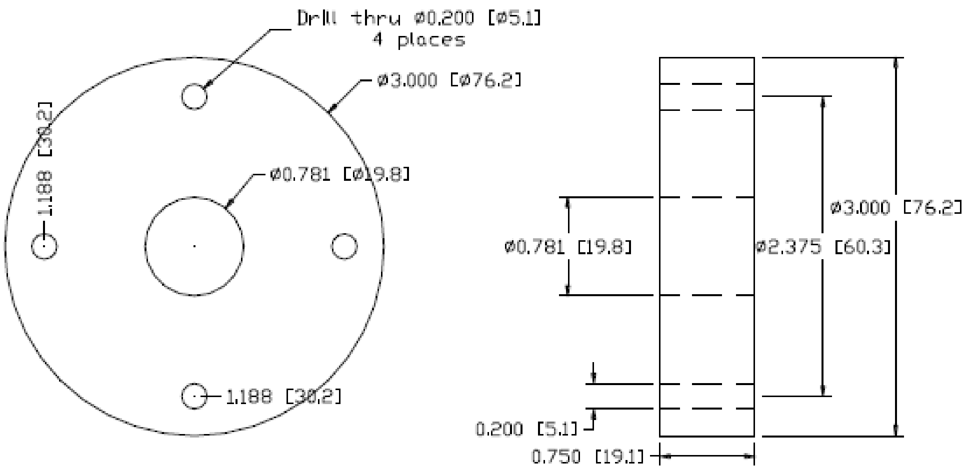

Figure 110. Added mass geometry (GCTS Testing Systems 2007)

First, the moment of inertia of calibration specimen is calculated. The calibration specimen is made of 6061-T6 aluminium with a mass density of 2.7

g/cm^3. This calculation is done in three parts using the principle of superposition. Then I_{cal} is calculated as:

$$I_{cal} = I_{cal-plate} + I_{cal-rod-end} + I_{cal-rod} - I_{cal-holes}$$

Equation 40. Equation to calculate the moment of inertia of calibration specimen.

$$I_{cal-plate} = \frac{1}{2}mR^2 = \frac{1}{2}\times\ 0{,}117\ kg\ \times\ (38{,}1mm)^2 = 84{,}9\ kg \cdot mm^2$$

$$I_{cal-rod-end} = \frac{1}{2}mR^2 = \frac{1}{2}\times\ 0{,}015\ kg\ \times\ (9{,}5mm)^2 = 0{,}7\ \ kg \cdot mm^2$$

$$I_{cal-rod} = \frac{1}{2}mR^2 = \frac{1}{2}\times\ 0{,}019kg\ \times\ (4{,}7mm)^2 = 0{,}20\ \ kg \cdot mm^2$$

$$I_{cal-holes} = 8\lfloor I_{hole} +\ md^2$$

$$I_{cal-holes} = 8\left[\frac{1}{2}\times\ 0{,}001kg\ \times\ (2{,}5mm)^2 + 0{,}001kg\ \times (30{,}2mm)^2\right] = 3{,}8\ kg \cdot mm^2$$

Then:

$$I_{cal} = 84{,}9 + 0{,}7 + 02 - 3{,}8 = 82{,}0\ kg \cdot mm^2$$

Note that the threaded holes used to attach the top plate to the bar of the calibration specimen are included in the calculation. The voids will be filled with the screws and even though they have a larger density than the aluminum, the error is negligible.

The added mass is made of 303 stainless steel with a mass density of 7.7 g/cm^3. Then the moment of inertia of the added mass is calculated as:

$$I_{mass} = I_{mass-base} - I_{mass-holes}$$

Equation 41. Equation to calculate the moment of inertia of the added mass.

$$I_{mass-base} = \frac{1}{2}m\left[R_i^2 + R_o^2\right] = \frac{1}{2} \times 0{,}624kg \times \lfloor (9{,}9)^2 + (38{,}1)^2 \rfloor =$$
$$483.\,kg.\,mm^2$$

$$I_{mass-holes} = 4\lfloor I_{holes+} md^2 \rfloor$$

$$I_{mass-holes} = 4\left[\frac{1}{2} \times\ 0{,}003kg\ x\ (2{,}5mm)^2 + 0{,}003\ kg\ \times\right.$$
$$\left.(30{,}2mm)^2\right] = 11{,}0\ kg.mm^2$$

Then:

$$I_{mass} = 483{,}5 - 11{,}0 = 472{,}5\ kg.mm^2$$

By performing resonant column tests on the calibration specimen, first without the added mass and then with added mass we obtain the following resonant frequencies:

$$w_{\text{no addedmass}} = w_1 = 74{,}5Hz$$

$$w_{with\ addedmass} = w_2 = 61{,}0Hz$$

Then from equation 39 we obtain:

$$I_0 = \frac{(82{,}2 + 472{,}5)x(61{,}0)^2 - (82{,}0)x(74{,}5)^2}{(74{,}5)^2 - (61{,}0)^2} = 879.1\ kg \cdot mm^2$$

Because the top specimen cap was not used during this calibration procedure, the mass moment of inertia of the top cap needs to be added to the above value.

For the equipment in which research was performed the upper head has this inertia:

$$I_{top\ cap} = 206.7\ kg \cdot mm^2$$

4.4. Results obtained from literature

The variation of the damping ratio D with the amplitude of the deformation of shear is affected by the same factors that affect Do and is generally derived from resonant column and cyclic torsional shear tests. The correlation between G and D is negative, as the decay of G corresponds to an increase in D (Crespellani and Facciorusso 2014). Since the first correlations obtained from (Hardin and Drnevich 1972a, 1972b; Seed and Idriss 1970), several authors have proposed several more complex expressions that will be reviewed and summarized, to obtain shear modulus and damping ratio curves that can be used to evaluate the local seismic response, and later be compared with the curves obtained in laboratory.

4.4.1. Equations proposed by Rollins et al. (1998) for sands

According to (Rollins et al. 1998), the equation of the curve that best fits within the data range for gravelly sands defined by (Seed and Idriss 1970) is:

$$\frac{G}{G_{max}} = \frac{1}{[1 + 20\gamma * (1 + 10^{-10*\gamma})]}$$

Equation 42. Equation to calculate G/Gmax. (Rollins et al. 1998).

Where:
γ: shear strain [%]

The best-fit damping equation within the data range for gravels and sands established by (Seed et al. 1986) is:

$$D = 0.8 + 18 * (1 + 0.15\gamma^{-0.9})^{-0.75}$$

Equation 43. Equation to calculate damping D. (Seed et al. 1986).

Where:
γ: shear strain [%]
D: damping ratio [%]
The results for gravely sands can be seen in Figure 111:

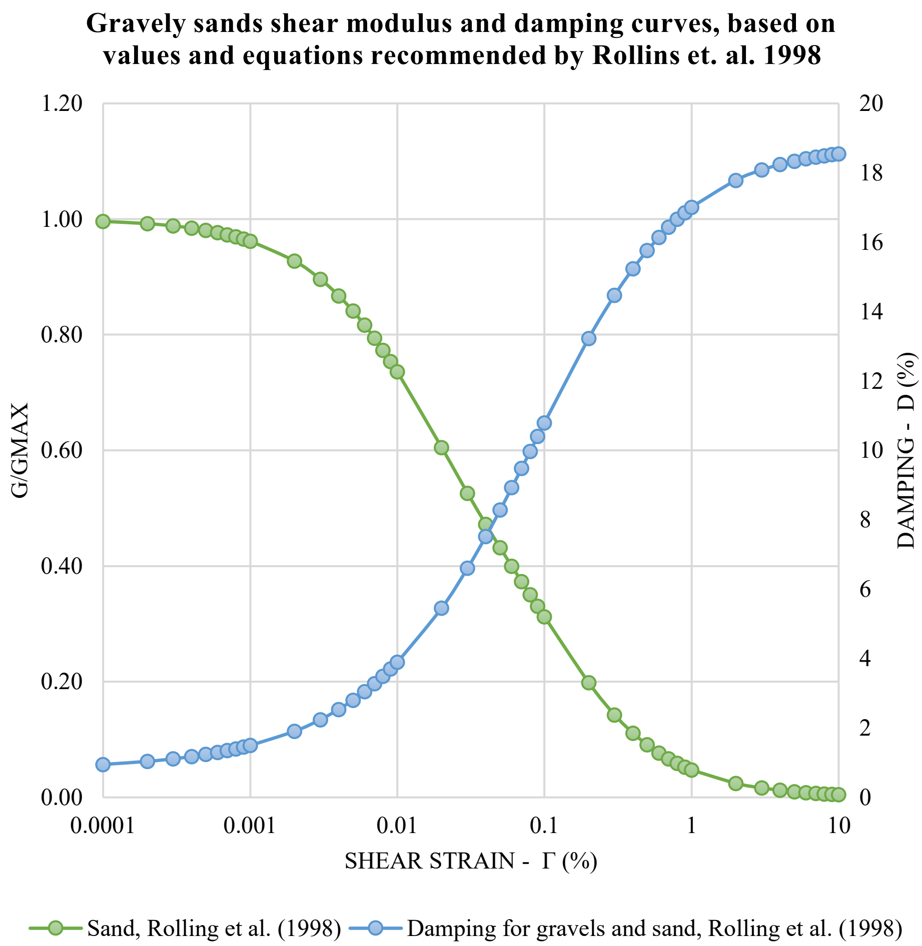

Figure 111. Gravely sands shear modulus and damping curves, based on values and equations recommended by Rollins et. al. 1998

4.4.2. Regression model proposed by Darendeli, 2001

Due to the necessity of developing an empirical framework that can be used to generate normalized modulus reduction and material damping curves, (Darendeli 2001) performed a regression analysis based on 110 resonant column tests and 20 torsional shear tests from 20 different locations. Samples were drawn from 4 regions: Northern California, Southern California, South Carolina, and Taiwan. Darendeli observed that there were no significant differences between geographic regions and soil types in the study. An eighteen-parameter model that relates reference strain, curvature coefficient, small-strain material damping ratio and scaling coefficient to soil type and loading conditions, and that characterizes the covariance structure of the predicted normalized modulus reduction and material damping curves is presented:

Model Parameters*	"Clean" Sands		Sands with High Fines Content		Silts		Clays	
	Mean	Variance	Mean	Variance	Mean	Variance	Mean	Variance
ϕ_1	4.74E-02	9.62E-06	3.34E-02	2.06E-06	4.16E-02	5.18E-06	2.58E-02	5.68E-06
ϕ_2	-2.34E-03	1.63E-07	-5.79E-05	8.09E-09	6.89E-04	7.74E-09	1.95E-03	1.84E-08
ϕ_3	2.50E-01	1.00E-02	2.49E-01	9.94E-03	3.21E-01	7.56E-03	9.92E-02	1.64E-03
ϕ_4	2.34E-01	1.08E-03	4.82E-01	7.46E-04	2.80E-01	8.63E-04	2.26E-01	3.48E-04
ϕ_5	8.95E-01	4.30E-04	8.45E-01	1.49E-04	1.00E+00	4.10E-04	9.75E-01	1.60E-04
ϕ_6	6.88E-01	7.82E-03	8.89E-01	5.86E-03	7.12E-01	3.55E-03	9.58E-01	2.93E-03
ϕ_7	1.22E-02	2.43E-05	2.02E-02	1.91E-05	3.03E-03	2.65E-06	5.65E-03	2.79E-06
ϕ_8	-1.00E-01	2.50E-03	-1.00E-01	2.50E-03	-1.00E-01	2.50E-03	-1.00E-01	2.50E-03
ϕ_9	-1.27E-01	4.00E-03	-3.72E-01	1.83E-03	-1.89E-01	1.95E-03	-1.96E-01	5.21E-04
ϕ_{10}	2.88E-01	3.14E-03	2.33E-01	1.35E-03	2.34E-01	2.60E-03	3.68E-01	1.19E-03
ϕ_{11}	7.67E-01	1.59E-03	7.76E-01	7.71E-04	5.92E-01	8.09E-04	4.66E-01	2.69E-04
ϕ_{12}	-2.83E-02	2.79E-05	-2.94E-02	1.70E-05	-7.67E-04	1.61E-05	2.23E-02	7.13E-06
ϕ_{13}	-4.14E+00	4.17E-02	-3.98E+00	1.82E-02	-5.02E+00	8.98E+00	-5.65E+00	3.37E-02
ϕ_{14}	3.61E+00	5.97E-02	4.32E+00	3.30E-02	3.93E+00	2.47E-02	4.00E+00	1.21E-02
ϕ_{15}	-5.15E+00	8.80E+00	-5.34E+00	8.55E+00	-5.20E+00	8.76E+00	-5.00E+00	9.00E+00
ϕ_{16}	-2.32E-01	7.56E-03	-2.66E-01	3.40E-03	-6.42E-01	4.78E-03	-7.25E-01	1.92E-03
ϕ_{17}	5.15E+00	6.91E-02	4.92E+00	3.74E-02	4.06E+00	8.96E+00	7.67E+00	3.51E-01
ϕ_{18}	3.12E+00	2.88E-02	2.68E+00	1.38E-02	1.94E+00	1.98E-02	2.16E+00	8.08E-03

$$\frac{G}{G_{max}} = \frac{1}{1 + \left(\frac{\gamma}{\gamma_r}\right)^{\alpha}}$$

Equation 44. Equation to calculate G/Gmax. (Darendeli 2001)

$$\gamma_r = \left(\emptyset_1 + \emptyset_2 * PI * OCR^{\emptyset_3}\right) * \sigma'_m{}^{\emptyset_5}$$

Equation 45. Equation to calculate the reference strain. (Darendeli 2001)

$$\alpha = \emptyset_5$$

Equation 46. Equation to obtain the curve parameter. (Darendeli 2001)

$$D_{Adjusted} = b * \frac{G}{G_{max}}^{0,1} * D_{Masing} + D_{min}$$

$$b = \emptyset_{11} + \emptyset_{12} * \ln{(N)}$$

Equation 47. Equation to calculate the damping. (Darendeli 2001)

Where:

σ'_m: mean effective confining stress [atm]

α: curvature parameter.

PI: plasticity index [%]

γ: shear strain [%]

γ_r: reference strain

The results for 1atm of confining pressure for different plasticity values can be seen in Figure 112:

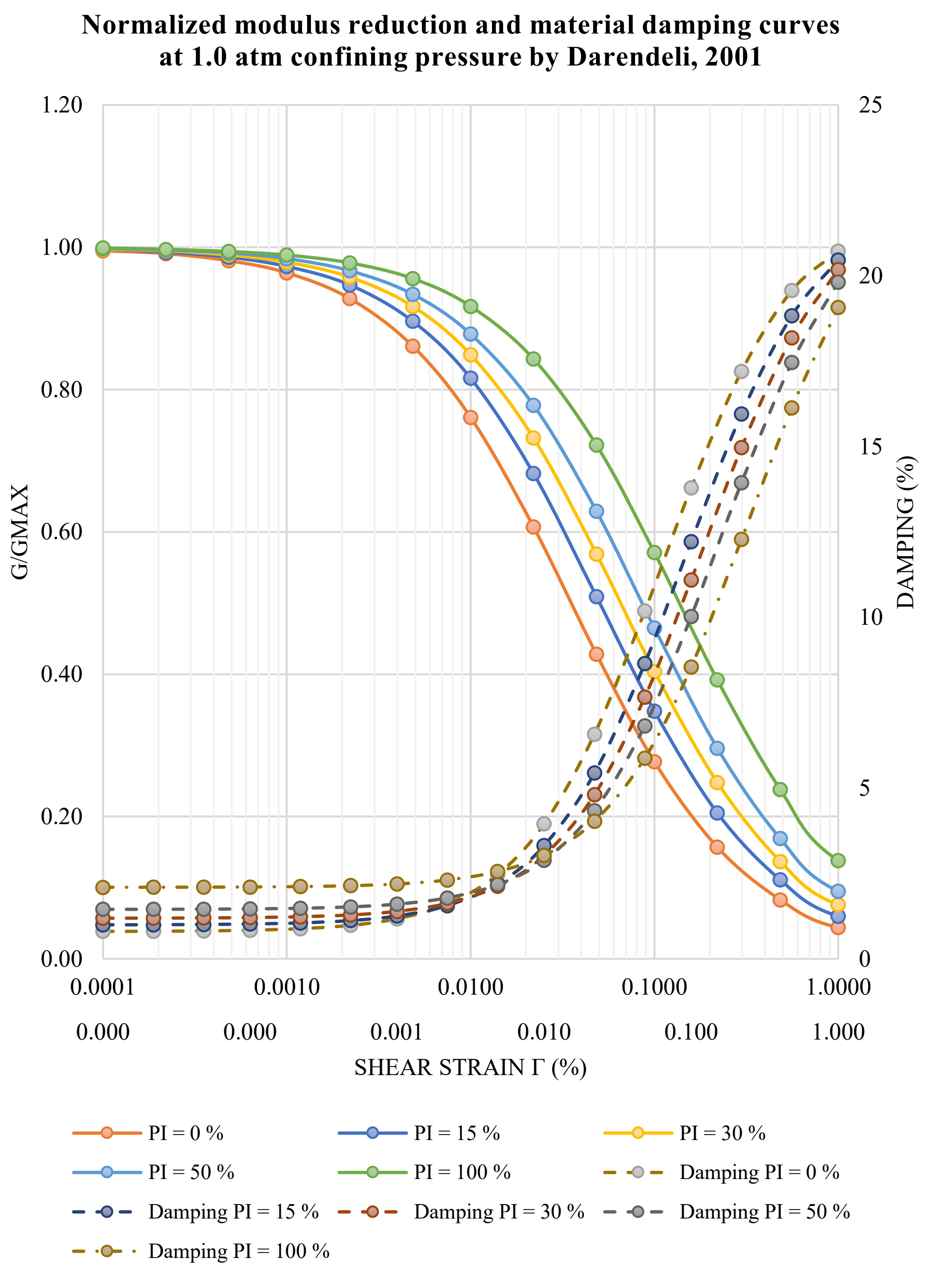

Figure 112. Normalized at 1.0 atm confining pressure, based on values and equations recommended by (Darendeli 2001)

4.4.3. Equations proposed by Zhang et. al., 2005

These authors elaborated their equations based on a modified hyperbolic model and on a statistical analysis resulting from resonant column tests and torsional shear of 122 samples obtained in South Carolina, North Carolina, and Alabama; using as variables the amplitude of the shearing strain, the confining stress, and the plasticity index (PI).

For the G/Gmax ratio, the following equation suggested by Stokoe et al. (1999).

$$\frac{\boldsymbol{G}}{\boldsymbol{G_{max}}} = \frac{\mathbf{1}}{\mathbf{1} + \left(\frac{\boldsymbol{\gamma}}{\boldsymbol{\gamma_r}}\right)^{\boldsymbol{\alpha}}}$$

$$\boldsymbol{\alpha} = \boldsymbol{A} * \boldsymbol{PI} + \boldsymbol{B}$$

Equation 48. Equation to calculate G/Gmax suggested by Stokoe et al. (1999).

Because the values of $\boldsymbol{\gamma_r}$ can vary significantly with respect to $\boldsymbol{\sigma'_m}$, the following equation from Stokoe et al. 1995 is used:

$$\gamma_r = \gamma_{r1} * \left(\frac{\sigma'_m}{Pa}\right)^k$$

Equation 49. Equation to calculate reference strain suggested by Stokoe et al. (1995).

$$\gamma_{r1} = C * PI + D$$

Equation 50. Equation to calculate reference strain at a mean effective confining stress of 100 kPa, suggested by Stokoe et al. (1995).

$$k = E * e^{(F*PI)}$$

Equation 51. Equation to calculate the exponent k suggested by Stokoe et al. (1995).

$$\sigma'_m = \frac{\sigma'_v * (1 + 2 * K'_o)}{3}$$

Equation 52. Equation to calculate the main effective confining stress, suggested by Stokoe et al. (1995).

	Quaternary Soil	***Tertiary and older soil***	***Residual/saprolite soil***
A	0.0021	0.0009	0.0043
B	0.834	1.026	0.794
C	0.0011	0.0004	0.0009
D	0.0749	0.0311	0.0385
E	0.316	0.316	0.420
F	-0.0142	-0.0110	-0.0456

Where:

α: curvature parameter.

PI: plasticity index, [%]

γ: shear strain [%]

γ_{r1}: reference strain at a mean effective confining stress of 100 kPa.

Pa: reference stress of 100 kPa.

σ'_m: mean effective confining stress

σ'_v: vertical effective stress

K'_o: coefficient of effective earth stress at rest.

The general damping equation adopted for the study is:

$$D = f\left(\frac{G}{G_{max}}\right) + D_{min}$$

$$D = 10.6 * \left(\frac{G}{G_{max}}\right)^2 - 31.6 * \left(\frac{G}{G_{max}}\right) + 21.0 + D_{min}$$

Equation 53. Equation to calculate the damping, D. (Zhang et. al., 2005)

$$D_{min} = D_{min1} * \left(\frac{\sigma'_m}{Pa}\right)^{\frac{-k}{2}}$$

$$D_{min1} = a * PI + b$$

Where:

σ'_m: mean effective confining stress

Pa: reference stress of 100 kPa.

k: the same exponent used previously.

a,b: fitting parameters equal to about 0.008 and 0.82 respectively.

The results for 1atm of confining pressure for different plasticity values can be seen in Figure 113:

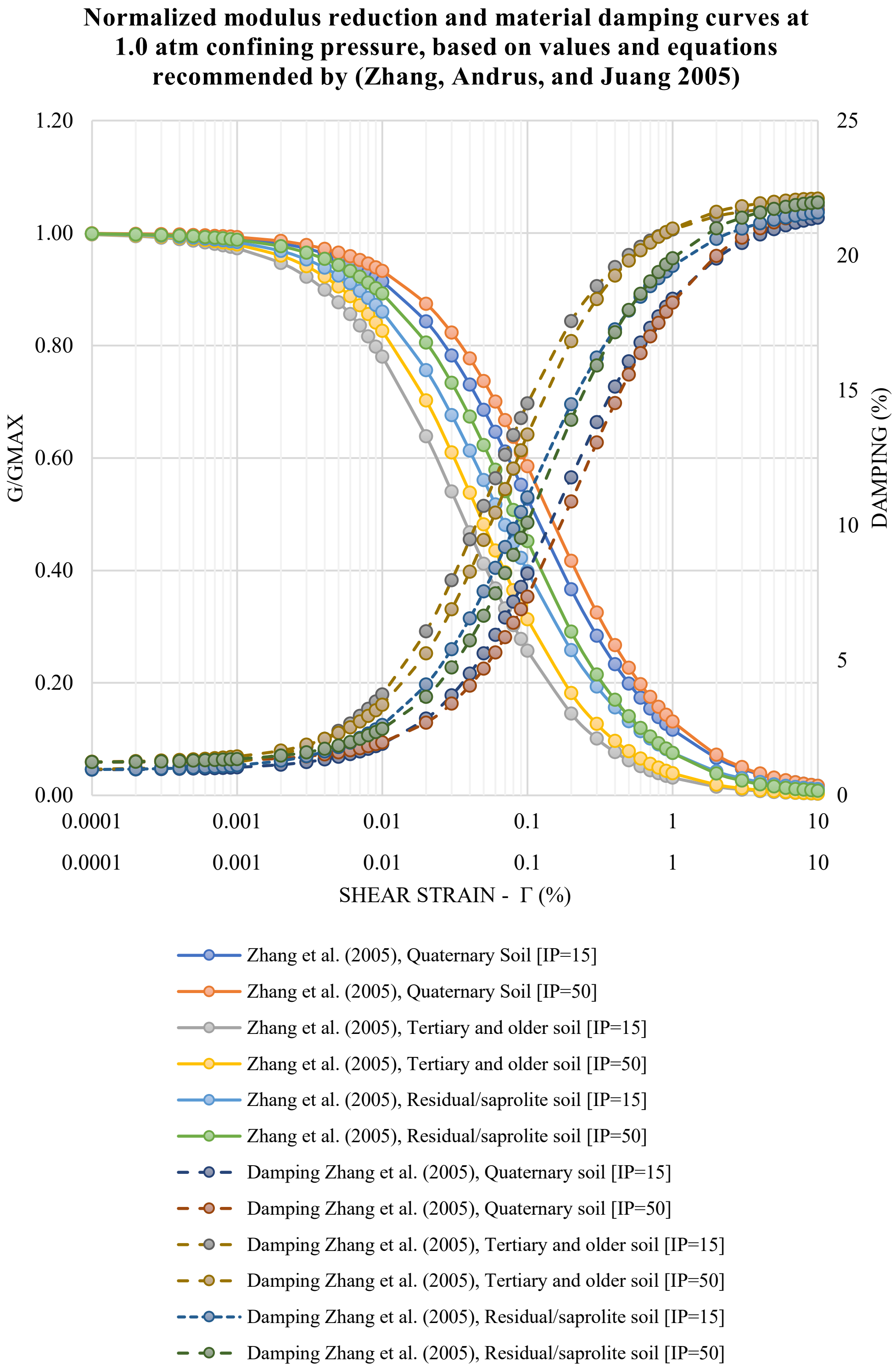

Figure 113. Normalized modulus reduction and material damping curves at 1.0 atm confining pressure, based on values and equations recommended by (Zhang, Andrus, and Juang 2005)

4.4.4. Equations from Senetakis, Anastasiadis & Pitilakis, 2013

(Senetakis, Anastasiadis, and Pitilakis 2013) presents a laboratory investigation of the strain dependent dynamic properties of volcanic granular soils composed of a rhyolitic crushed rock along with additional experiments on quartz sand.

$$\frac{G}{G_o} = \frac{1}{1 + \left(\frac{\gamma}{\gamma_{ref}}\right)}$$

Equation 54. Equation to calculate the G/Go. (Senetakis et al. 2013)

Where:

γ: shear strain [%]

γ_{ref}: reference strain

For quartz sands:

$$\gamma_{ref} = 0.159 * e^{-0.419 * C_u} * \left(\frac{\sigma'_m}{Pa}\right)^{0.42}$$

Equation 55. Equation to calculate the reference strain for quartz sands. (Senetakis et al. 2013)

For volcanic sands:

$$\gamma_{ref} = 0.100 * \left(\frac{\sigma'_m}{Pa}\right)^{0.08}$$

Equation 56. Equation to calculate the reference strain for volcanic sands. (Senetakis et al. 2013)

Where:

C_u: coefficient of uniformity

σ'_m: mean effective confining pressure, [kPa]

Pa: atmospheric pressure, [kPa]

To obtain the damping ratio this study used the following equation:

$$D - D_o = 7.22 * \left(\frac{G}{G_o}\right)^2 - 25.25 * \left(\frac{G}{G_o}\right) + 17.96$$

$$D = 7.22 * \left(\frac{G}{G_o}\right)^2 - 25.25 * \left(\frac{G}{G_o}\right) + 17.96 + D_o$$

Equation 57. Equation to calculate the damping. (Senetakis et al. 2013)

Where:

D: damping ratio [%]

D_o: small-strain damping ratio [%].

Where the expressions for the small strain damping ratio, Do, for the sands of this study have been presented by (Senetakis, Anastasiadis, and Pitilakis 2012)

For quartz sands:

$$D_o = 0.62 * \left(\frac{\sigma'_m}{Pa}\right)^{-0.11}$$

Equation 58. Equation to calculate the small-strain damping ratio for quartz sands. (Senetakis et al. 2012)

For volcanic sands:

$$D_o = 0.52 * \left(\frac{\sigma'_m}{Pa}\right)^{-0.13}$$

Equation 59. Equation to calculate the small.damping ratio for volcanic sands. (Senetakis et al. 2012)

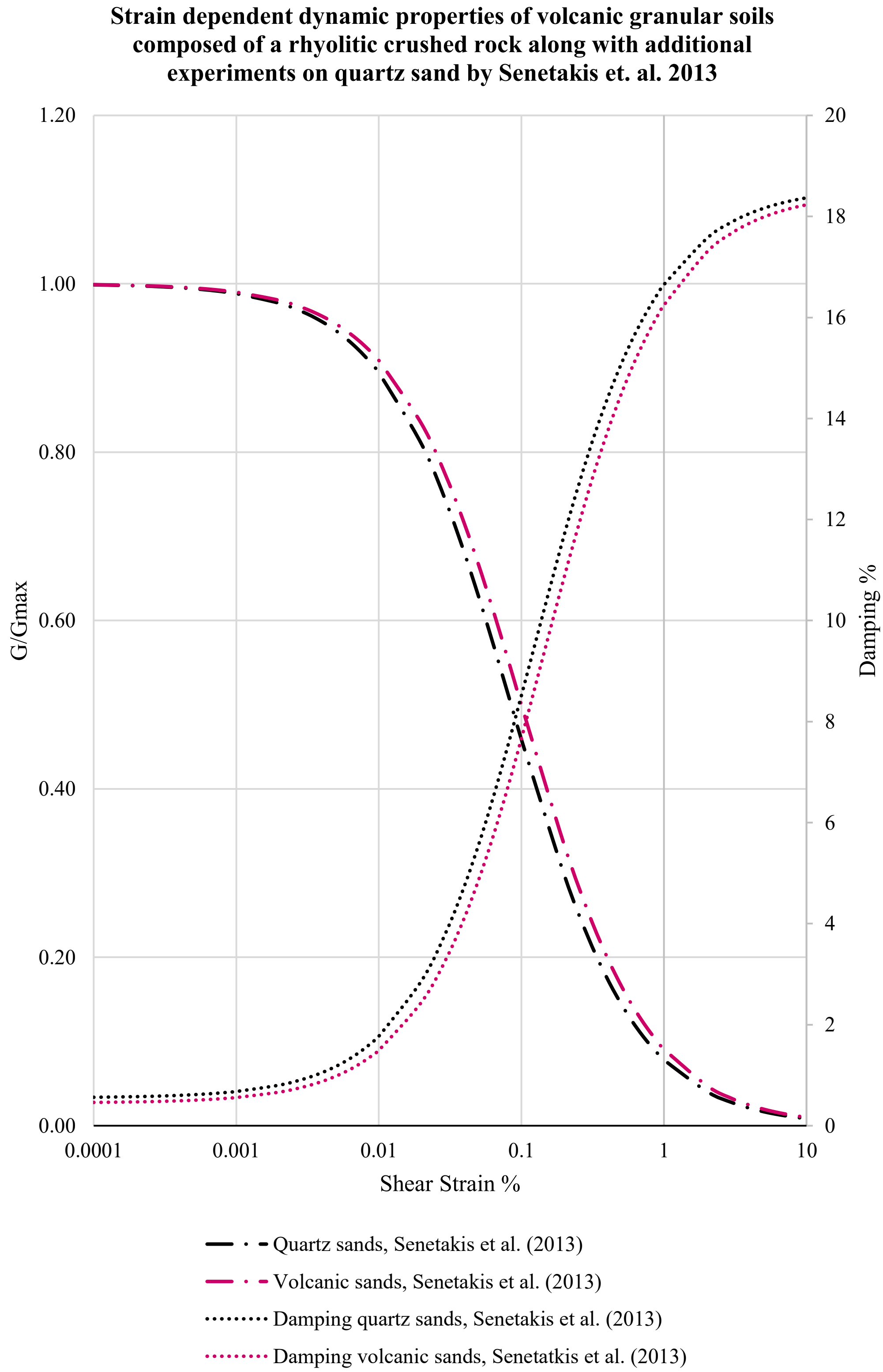

Figure 114. Graph of strain dependent dynamic properties of volcanic granular soils composed of a rhyolitic crushed rock along with additional experiments on quartz sand by Senetakis et. al. 2013

4.4.5. Equations proposed by Rollins, Singh & Roy, 2020.

Based on lab tests on gravels from 18 investigations, simplified equations to define G=Gmax and the damping ratio as a function of shear strain, γ,have been developed by (Rollins, Singh, and Roy 2020). The G=Gmax versus γ equations rely on two parameters that can be defined in terms of confining pressure and uniformity coefficient. Increasing confining pressure leads to a more linear curve, while increasing the uniformity coefficient leads to a more nonlinear curve shape. G=Gmax versus γ curves for gravels tend to plot somewhat below curves for sands under similar conditions. (Rollins et al. 2020)

For gravels:

$$\frac{G}{G_{max}} = \frac{1}{\left\{1 + \left[\frac{\gamma}{\gamma_{ref}}\right]^{0.84}\right\}}$$

Equation 60. Equation to calculate G/Gmax. (Rollins et al. 2020)

$$\gamma_{ref} = 0.0046 * C_u{}^{-0.197} * \sigma'_o{}^{0.52}$$

Equation 61. Equation to calculate the reference strain. (Rollins et al. 2020)

$$D = 26.05 * \left(\frac{\gamma}{1+\gamma}\right)^{0.375} * C_u^{0.08} * \sigma'_o{}^{-0.07}$$

Equation 62. Equation to calculate the damping, D. (Rollins et al. 2020)

Where:

γ: shear strain [%]

γ_{ref}: reference strain

C_u: coefficient of uniformity

σ'_o: confining pressure, [kPa]

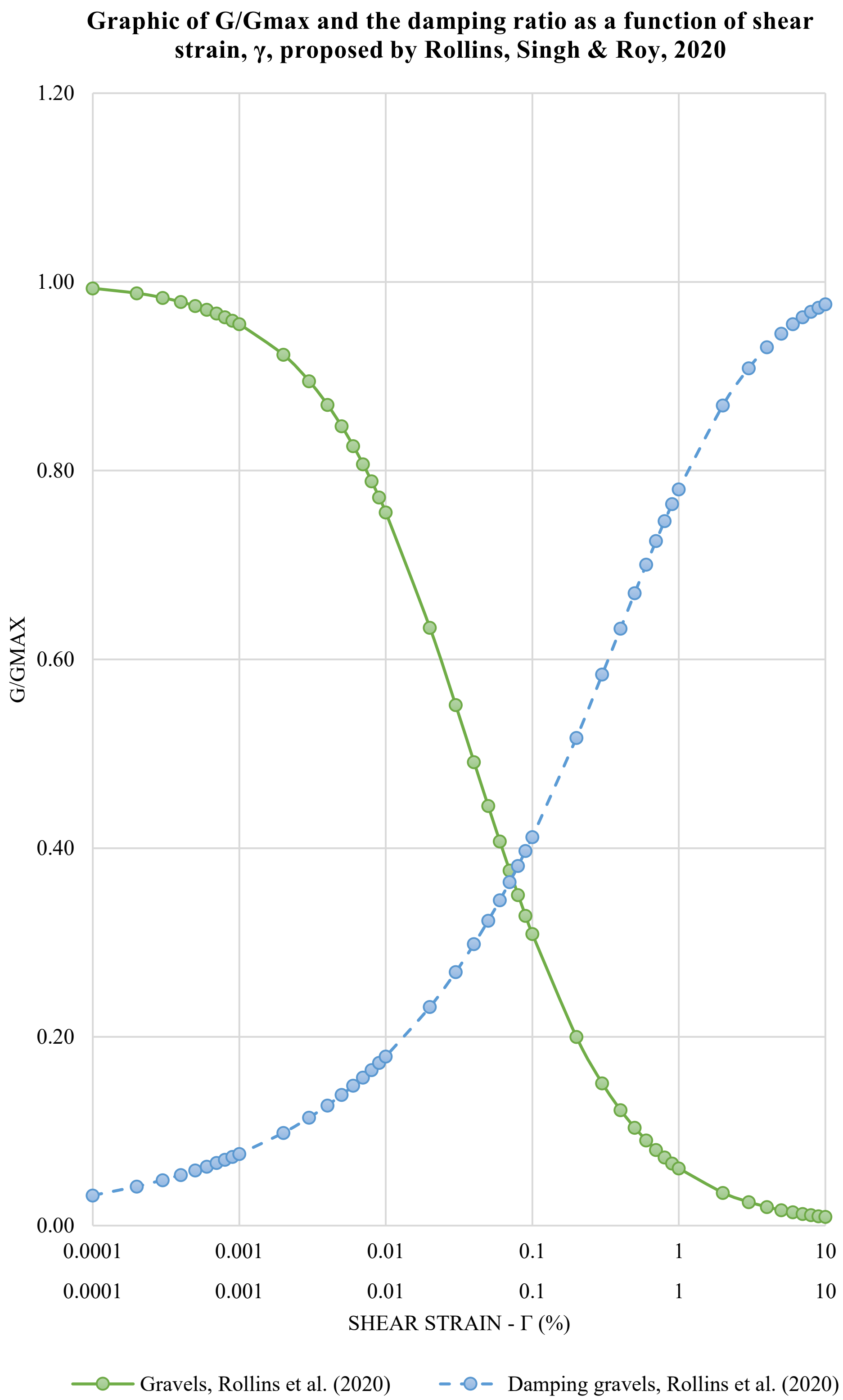

Figure 115. Graphic of G/Gmax and the damping ratio as a function of shear strain, γ, proposed by Rollins, Singh & Roy, 2020

4.4.6. Summary of modulus reduction and material damping curves

A summary of all the proposed equations for the G/Gmax and the damping ratio as a function of shear strain is presented in figure 116.

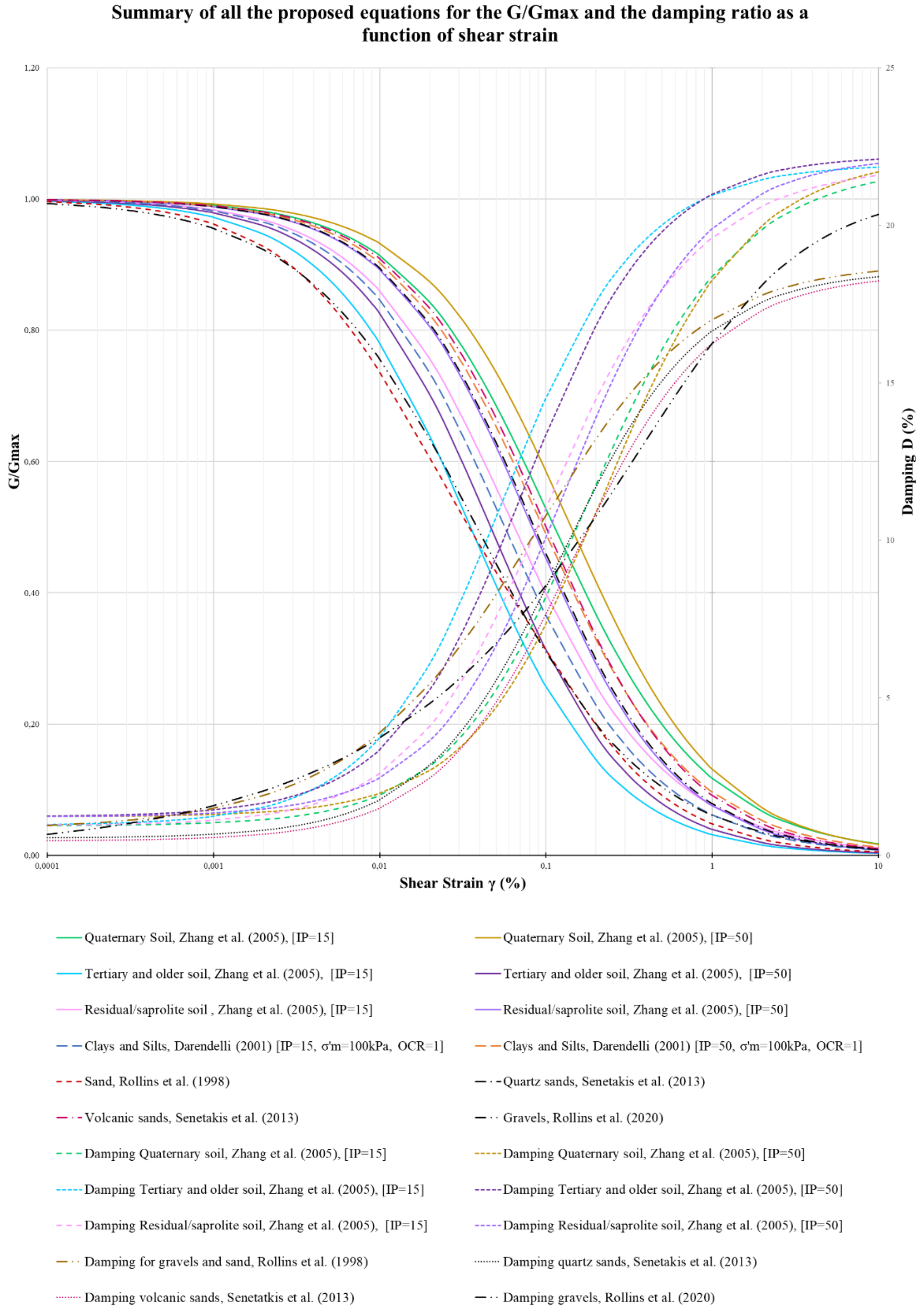

Figure 116. Summary of all the proposed theoretical equations for the G/Gmax and the damping ratio as a function of shear strain

Based on the empirical families of curves, the proposed theoretical equations for the G/Gmax and the damping ratio as a function of shear strain, and based on the review presented by (Guerreiro, Kontoe, and Taborda 2012), overall the Ishibashi & Zhang (1993) curves may require the adoption of additional restrictions in order not to violate two physical principles (i.e. G/Gmax>1 and ξ<0%), recommending the use of Darendeli (2001) curves as a better alternative as them capture all major effects across the entire strain range (Guerreiro et al. 2012). Additionally, the Darendeli (2001) curves consider a range from clean sands to clays, present in the current study, with broad intervals of plasticity, confining pressure, OR, and sampling depth, plus the possibility to use them in the Deepsoil software. For these reasons, the Darendeli (2001) curves were used for the theoretical analysis of amplification.

4.5. Results obtained from the Resonant Column tests

These tests were performed during 2022, using different types of samples. Dry and remolded samples were used in this research.

4.5.1. Test specimens:

For the test, different test specimens were selected, which represent the distinct stratums that make up the soil profiles of each of the 9 proposed zones. Most of the unaltered specimens presented a dry condition. However, it was necessary to remold some of them in order to obtain complete information for the execution of the resonant column test. These had the following approximate dimensions: 60 mm in diameter and 120 mm in height. The unaltered specimens in dry condition and the remolded specimens are presented below:

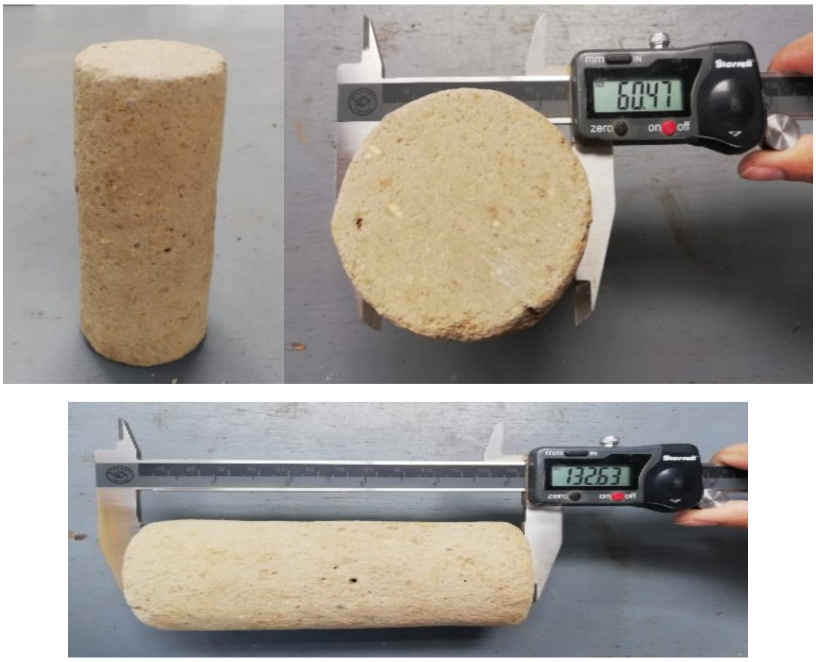

Figure 117. Unaltered sample

Figure 118. Remolded sample

4.5.2. Test procedure

- **Equipment assembly**

1. Locate the sample between the top and bottom platens, while properly covered with a membrane and O'rings.

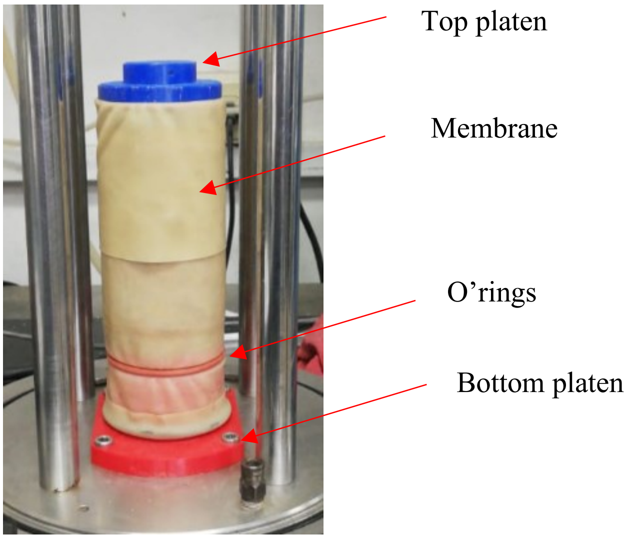

Figure 119. Initial specimen assembly.

2. Place the accelerometer between the two columns in a horizontal position adjusting it to the top platten, verifying an appropriate connection between these two elements.

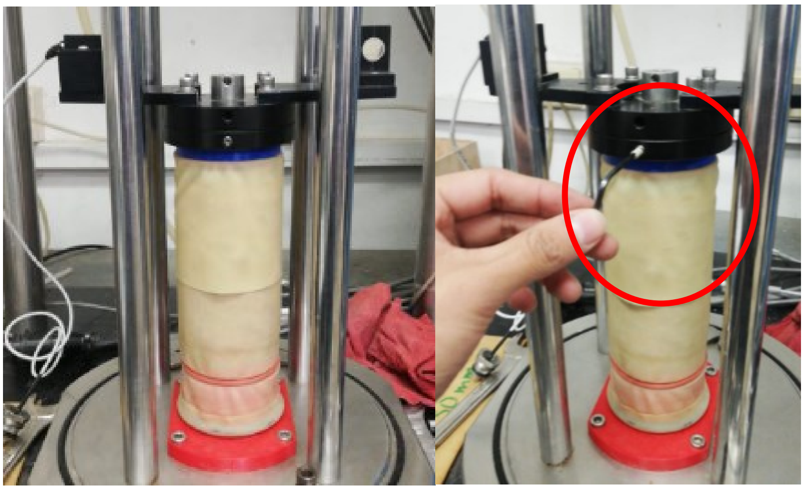

Figure 120. Place and adjust accelerometer.

3. Place the torsional motor in a diagonal position between both columns.

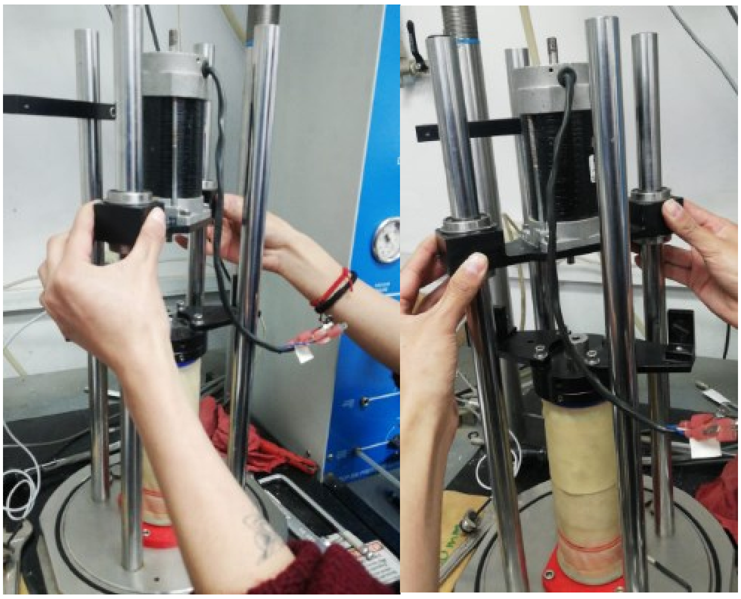

Figure 121. Place the torsional motor.

4. Fit and adjust the motor axle with the top section of the accelerometer.

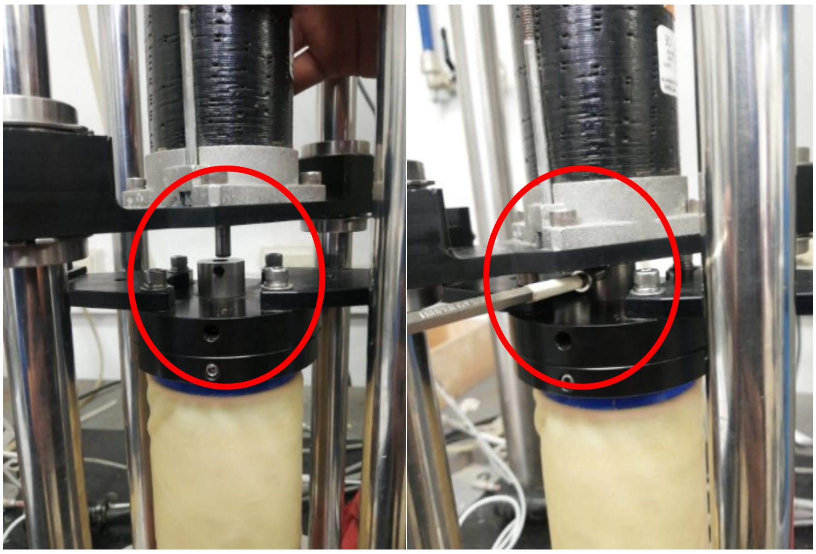

Figure 122. Fit and adjust the motor axle with the accelerometer.

5. For protection, place a safety piece on the left side of the equipment, aligned with the bottom section of the accelerometer.

Figure 123. Place piece in the left side.

6. Place the top cover of the chamber, tighten the column screws and connect all the necessary cables.

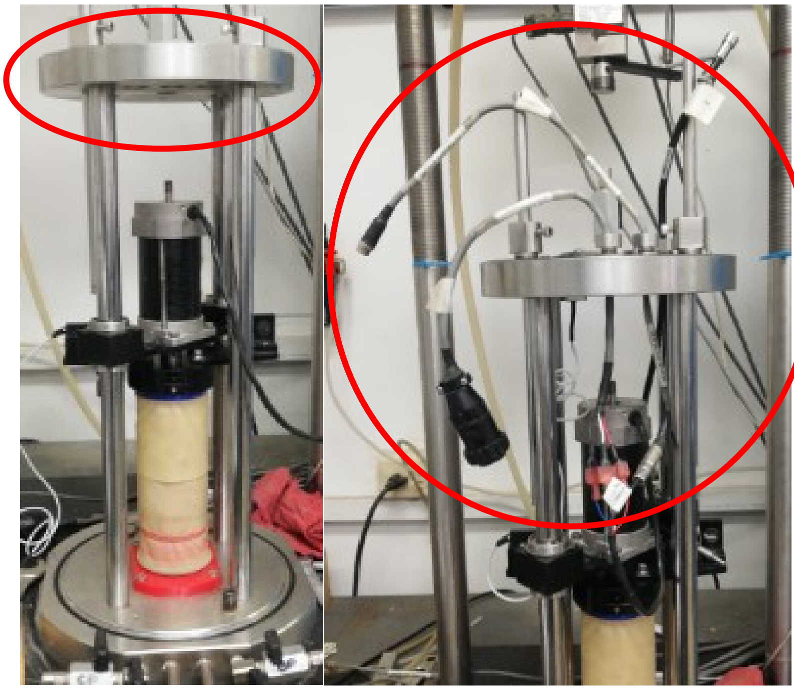

Figure 124. Place the top cover and cables.

6.1. CBL-RC-MOT-FT cables must be connected in the following order: black-blue, white-white, red-red.

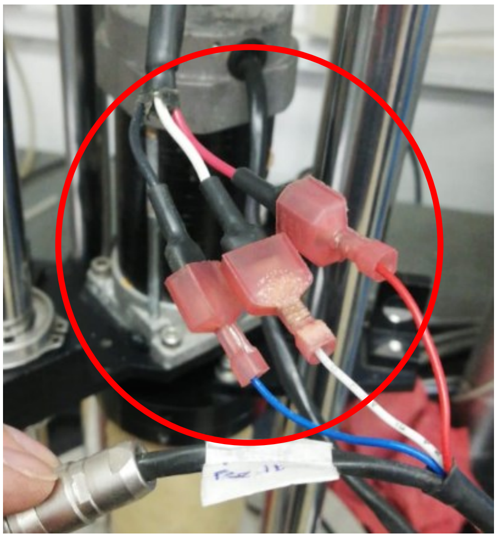

Figure 125. Connection the cable CBL-RC-MOT-FT.

a) CBL-RC-FB-FT. S/N: C3235, cable corresponds Motor Feedback.

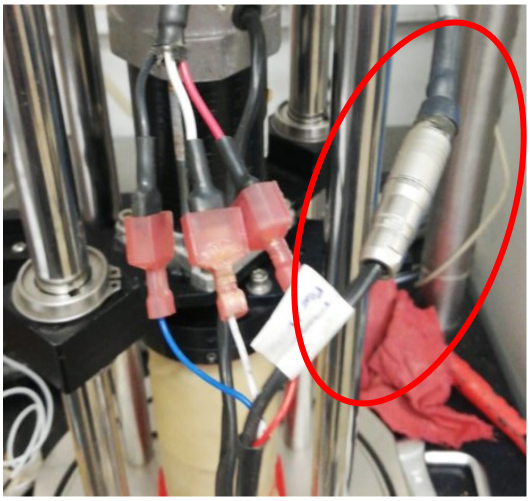

Figure 126. Connection the cable CBL-RC-FB-FT. S/N: C3235.

b) The white cable, assigned to the accelerometer, is in the bottom section of the chamber top cover.

c) TD125/2859, laser cable. For appropriate installation of this cable, the next steps must be followed:

7. Locate the cable support in the inside section of the chamber.

Figure 127. Support the cable

8. Place the cable tip, adjusting it in the intermediate section.

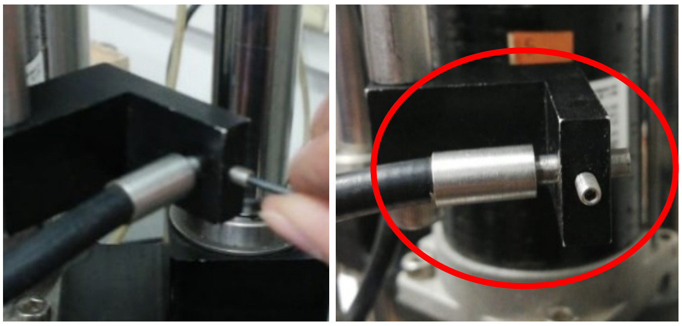

Figure 128. Place and adjusting the laser.

9. Verify that the support section is aligned with the top section of the mirror.

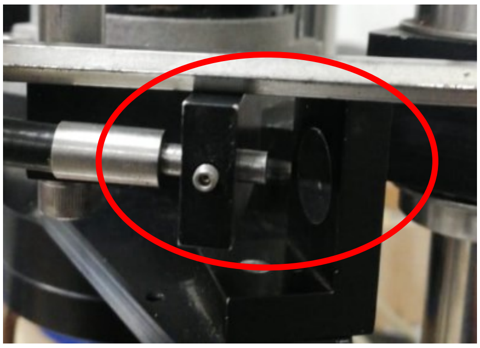

Figure 129. Verify that the level of the laser and mirror are equal.

10. Mount the chamber’s external coverage.

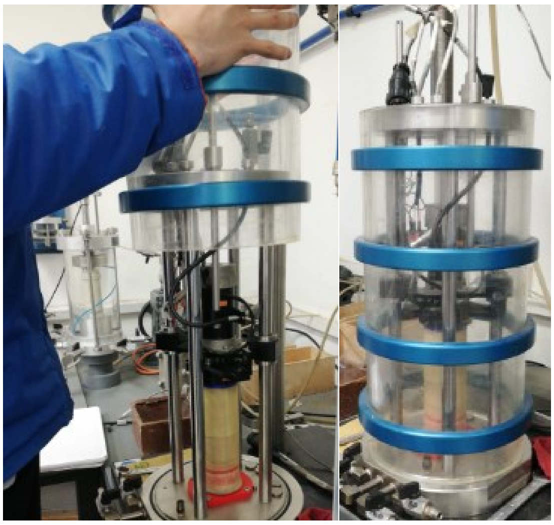

Figure 130. Mount the chamber’s external coverage.

11. Mount the top ring, tighten the screws, and connect the upper cables.

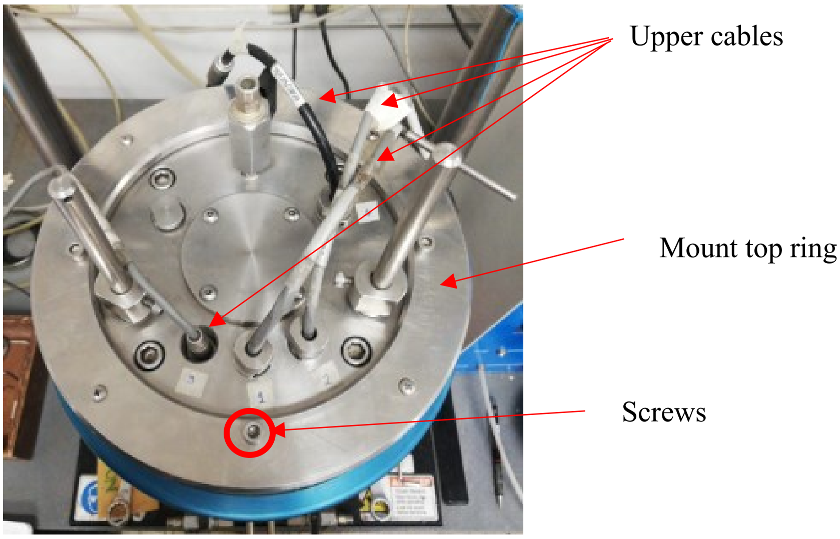

Figure 131. Top view of the armed chamber.

12. Connect a hose to the upper cover to achieve chamber confinement.

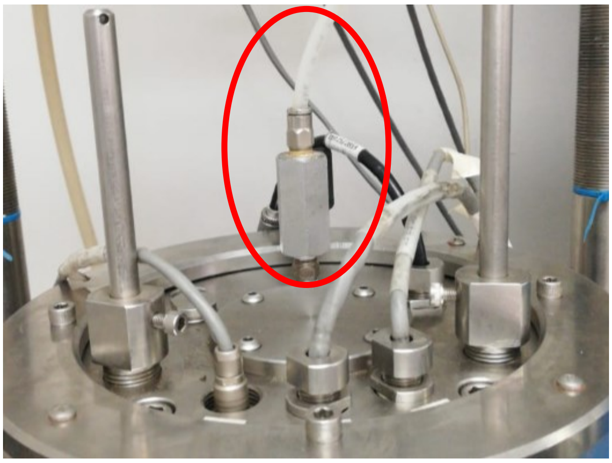

Figure 132. Connect to the confinement of the chamber.

4.5.3. Test description

For the elaboration of the tests, the implementation of GCTS Standard software is required. In this program, data corresponding to probe properties need to be entered, such as: diameter, height, and mass. Next, an iterative process is used until a frequency range in which the resonance frequency can be located for any Torque (T) is found.

The iterative process starts with the user definition of a random range and establishing a low Toque value (T). It is relevant to mention that the software only allows working on frequency ranges lower than 101 and in the test only 10 cycles were used. Additionally, it is possible to select the main entry angular displacement through the laser usage (Proximitor) and the acceleration through the accelerometer; this investigation mainly used the accelerometer.

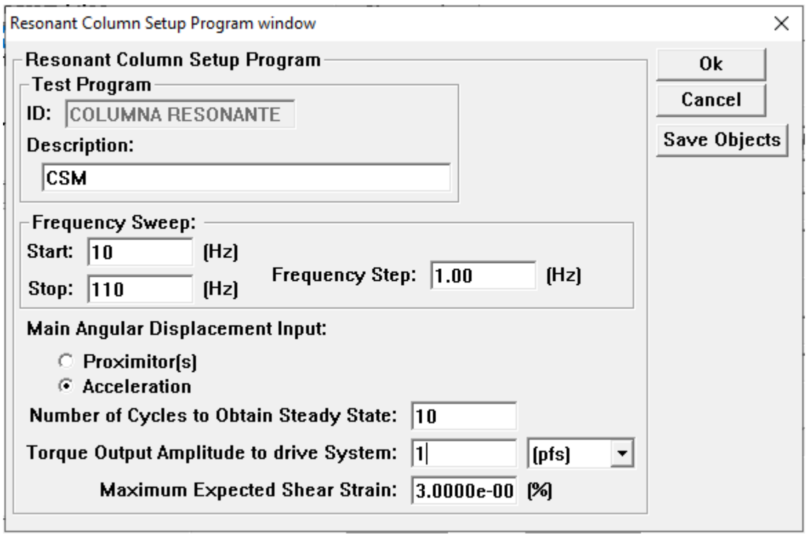

Figure 133. Resonant Column Setup Window.

Previous to the test beginning the OK button, is selected once the mentioned parameters are set. subsequently all the configuration is set, the RUN button should be selected.

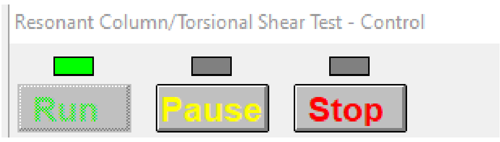

Figure 134. Resonant Column Test Control.

Once the test starts a window as represented below appears, in which during the execution of this, the increase of the shear deformation with respect to the frequency will start to be visualized, and at the same time, the torque with respect to the shear deformation will be visualized.

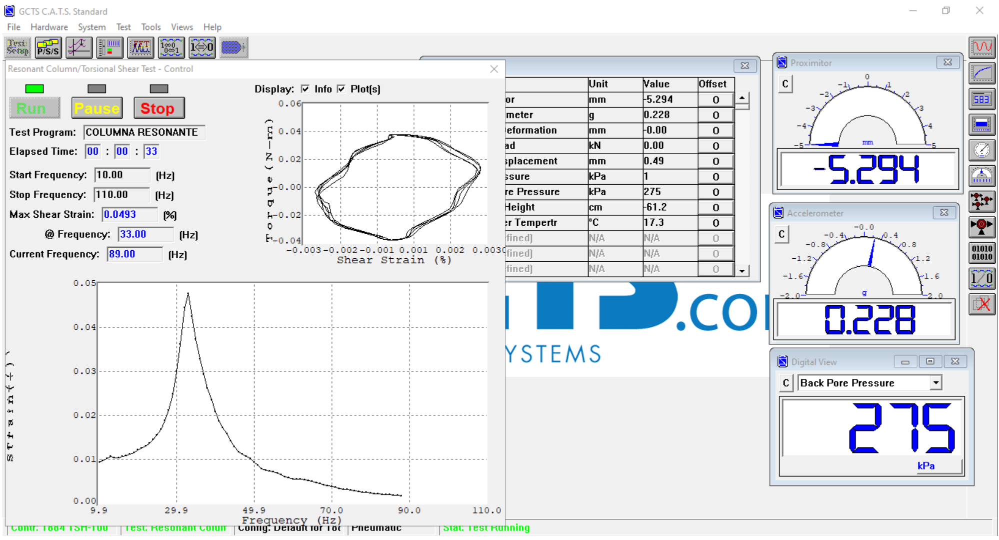

Figure 135. Resonant Column Test Execution.

This process must be made by means of a controlled torque increment in which the maximum resonance frequency value is present, all of this aimed to achieve favorable results.

4.5.4. *Test Results*

Once the test is completed, the following results are obtained:

a) Maximum share deformation (%)

b) Resonance frequency (Hz)

c) Damping Ratio (%)

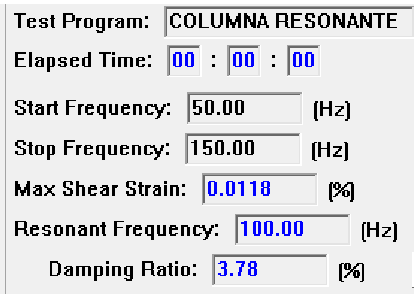
Test Program: COLUMNA RESONANTE
Elapsed Time: 00 : 00 : 00
Start Frequency: 50.00 [Hz]
Stop Frequency: 150.00 [Hz]
Max Shear Strain: 0.0118 [%]
Resonant Frequency: 100.00 [Hz]
Damping Ratio: 3.78 [%]

Figure 136. Preliminary results of resonant column test.

However, a data depuration of the program selected data related to the damping ratio calculation is in order, given the possibility of the next scenario:

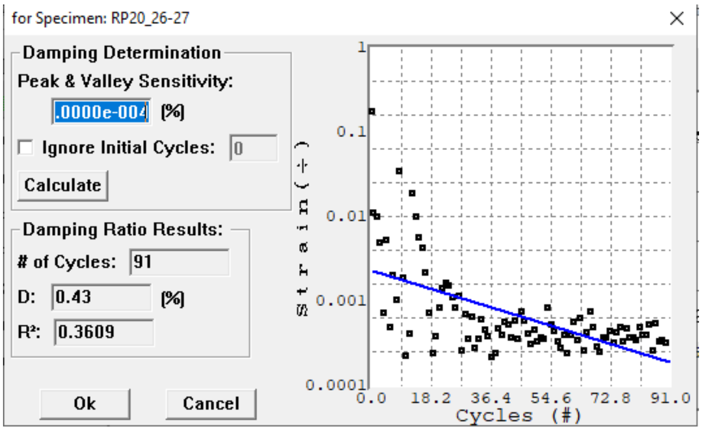

Figure 137. Preliminary results of damping ratio based on the program.

Due this situation, depuration is necessary to obtain a defined number of cycles similar to the one defined previous to the test initialization, for this investigation this value must be equal to 10.

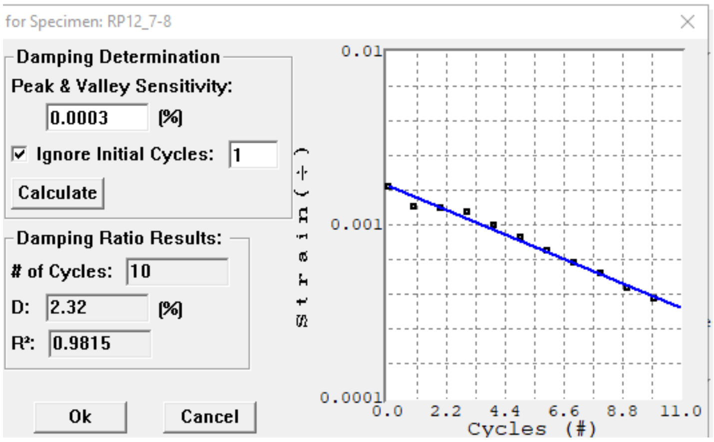

Figure 138. Results refined to obtain damping ratio.

With this refinement data, a linear trajectory of negative slope can be established, demonstrating favorable damping results.

This way, for each iteration, results will be obtained similar to the following:

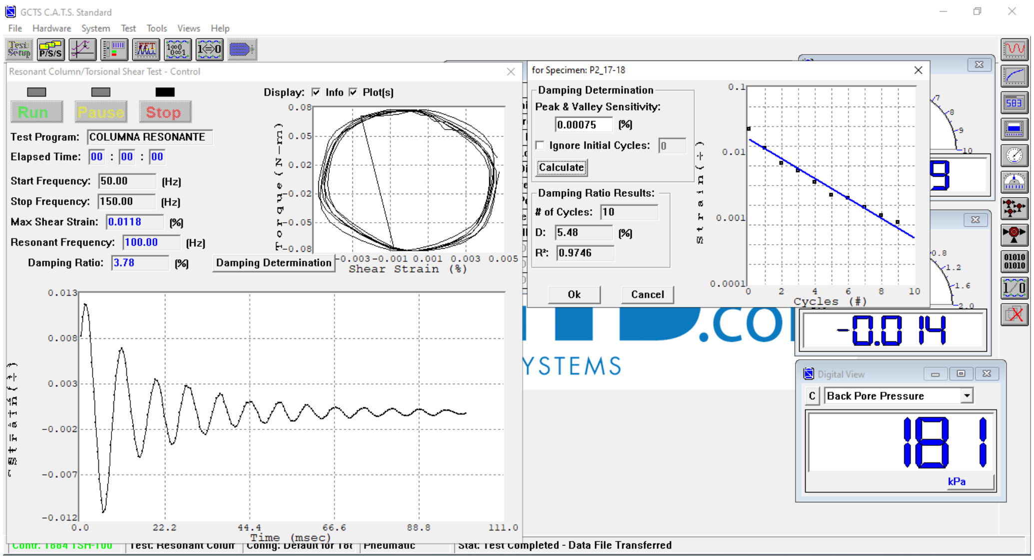

Figure 139. Final results of resonant column test.

To elaborate the degradation curves of the shear modulus and damping, is necessary to compile the data provided by the program for different torque values, which are: maximum shear deformation, resonance frequency and damping ratio. In this way, a data trajectory will be obtained that will allow us to establish an expression that will define the trend of these data.

MATLAB software was used to define the expression, using the "Fit" command, which based on statistical parametric regression models from a previously defined expression and the data set. In this way, the coefficients of the expression adjusted to achieve the lowest possible error.

The following expressions were used:

$$\frac{G}{Go} = a * \exp(b * x) + c * \exp\,(d * x)$$

Equation 63. Parametric equation used to obtain G/Go using MATLAB.

$$D = \frac{e}{(1 + \exp(f * x) + g)}$$

Equation 64. Parametric equation used to obtain the damping, D, using MATLAB.

With help of the before expressions based on the data set, the following graphs were obtained:

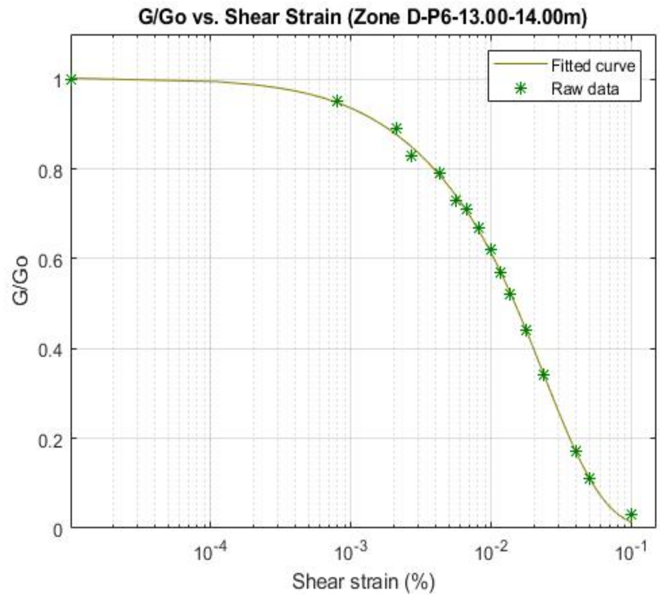

Figure 140. Shear modulus degradation.

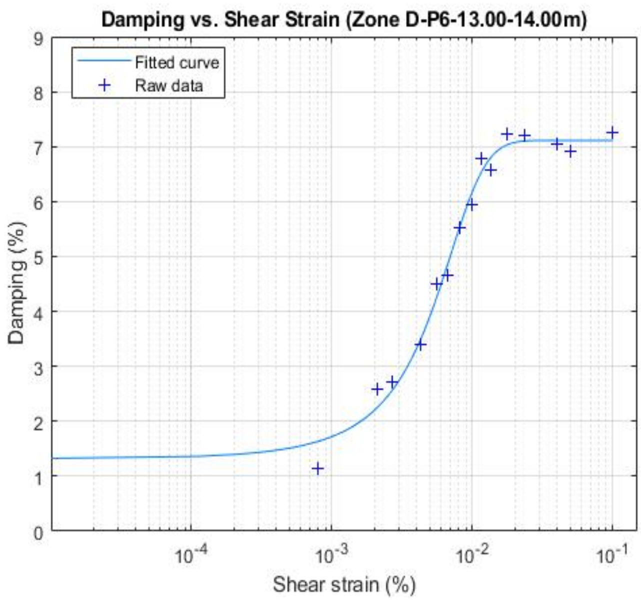

Figure 141. Damping (%)

The following is a compilation of the curves developed.

4.5.5. *Results for dry samples*

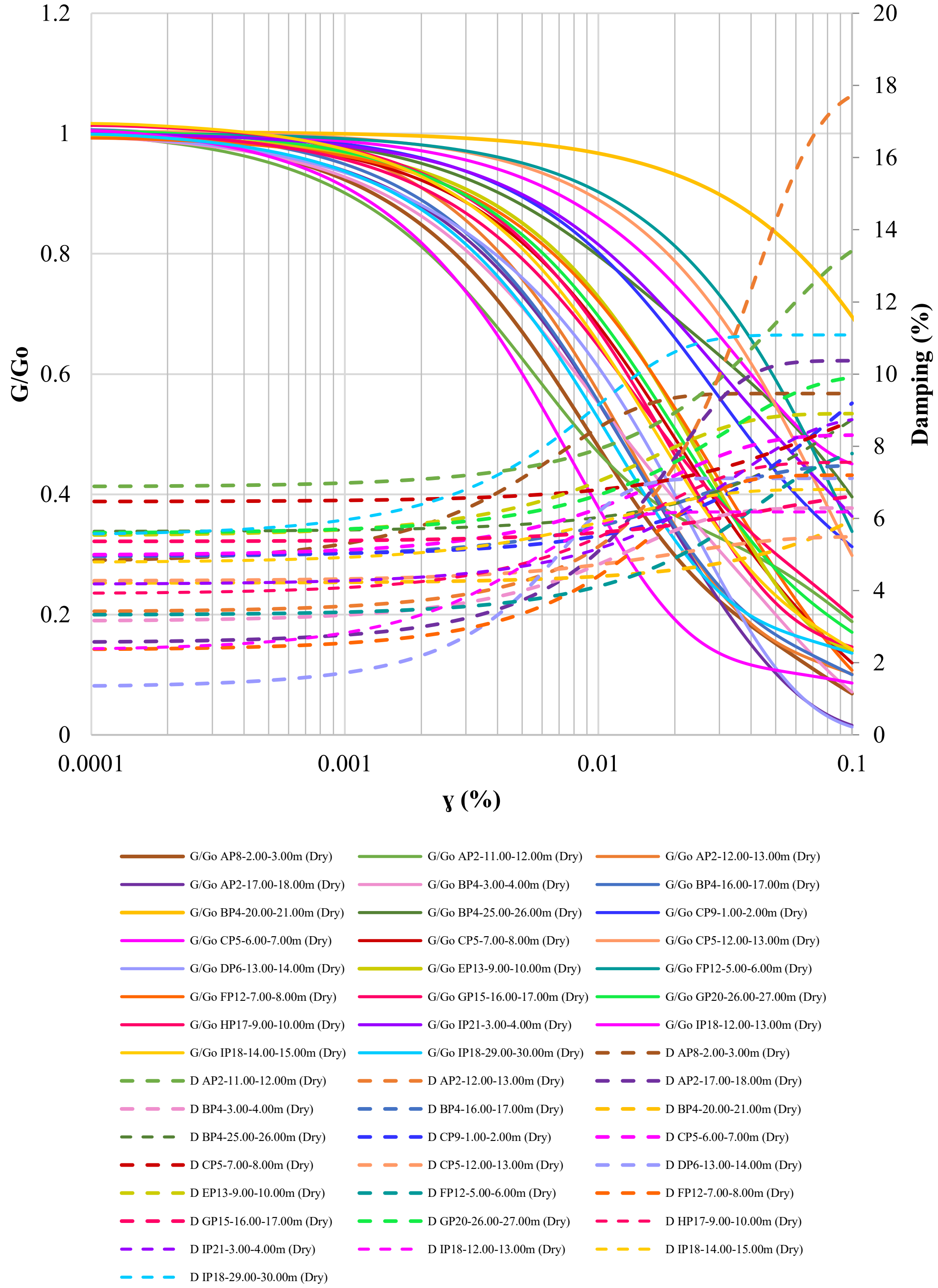

Figure 142. Compilation of the curves developed with dry samples.

Zone A

The curves corresponding to each of the strata in zone A are shown. Where the following is observed:

- The shear modulus degradation curves present similar trajectories, except for the curve of the second layer, which changes its trajectory starting at a shear strain of 0.008%, for this reason it presents the highest G/Go value for a strain of 0.1%, which is approximately 0.19.

- The shear modulus degradation curves of the first, third and fourth layers present G/Go values between 0.016 and 0.10.

- The damping curves of the first, third and fourth layers present similar trajectories. However, the damping values are different for a deformation of 0.0001%, which are 4.84, 3.43 and 2.58 respectively. While the curve of the second layer has the highest damping value for this level of shear strain, which is 6.89.

- For a shear strain level of 0.1%, the curves corresponding to the first and fourth stratum have similar damping values, which are 9.46 and 10.37. The second stratum has a value of 13.37, while the third stratum has the highest value, which is 17.68.

Note: The information of the shear modulus degradation and damping curve of the fourth layer was placed in the fifth layer, due to absence of material.

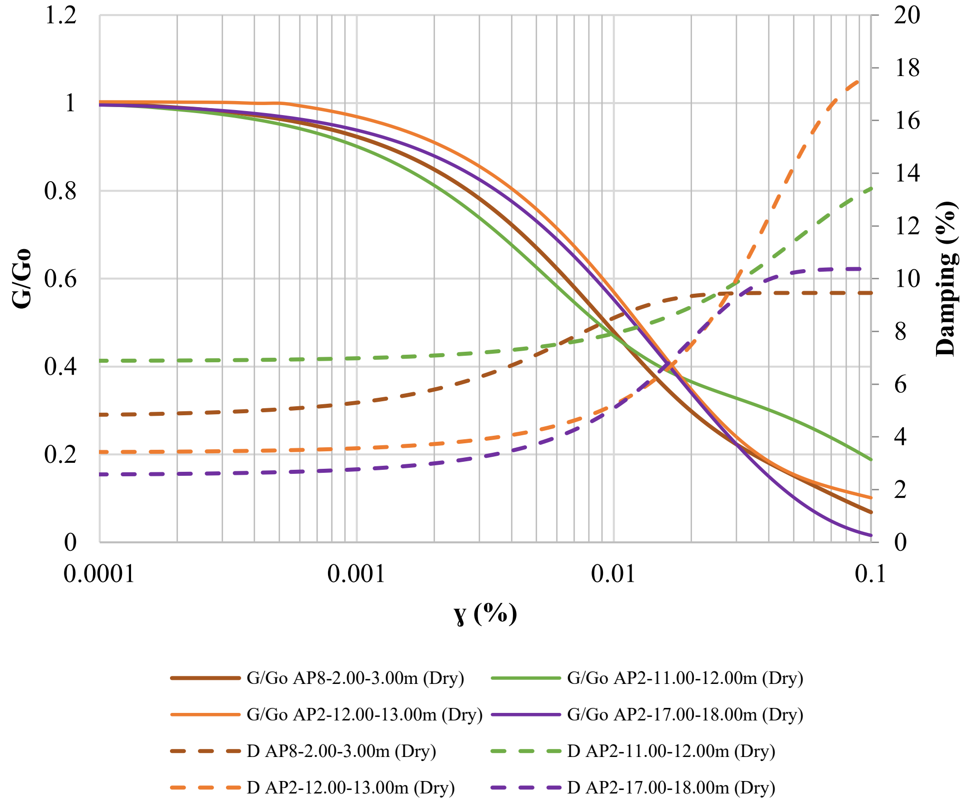

Figure 143. G/Go and Damping curves for Zone A (Dry samples)

Zone B

The curves corresponding to each of the strata in zone B are shown. Where the following is observed:

- The shear modulus degradation curves of the third and fourth layers are similar and present the highest G/Go values for a shear strain of 0.1%, with respect to the remaining layers, which are 0.69 and 0.40, respectively. While the first and second, for the same level of deformation present the lowest values, which are 0.07 and 0.1, they also present two intersections between these curves, which are at a shear strain level of approximately 0.01% and 0.07%.

- The damping curves of the first and second layers present similar trajectories. For a shear strain of 0.0001%, the first stratum has the lowest value with respect to the other results, which is 3.17 and the second stratum has a value of 4.95. Meanwhile, for a shear strain of 0.1%, values of 6.27 and 7.46 are presented for the first and second stratum, respectively.

- The third and fourth layers have similar damping curve trajectories. The curve corresponding to the fourth layer has the maximum values for strains of 0.0001% and 0.1%, which are 5.64 and 8.71, respectively. While, the third layer presents a damping of 4.21 for a shear strain of 0.0001% and 5.94 for a shear strain of 0.1%.

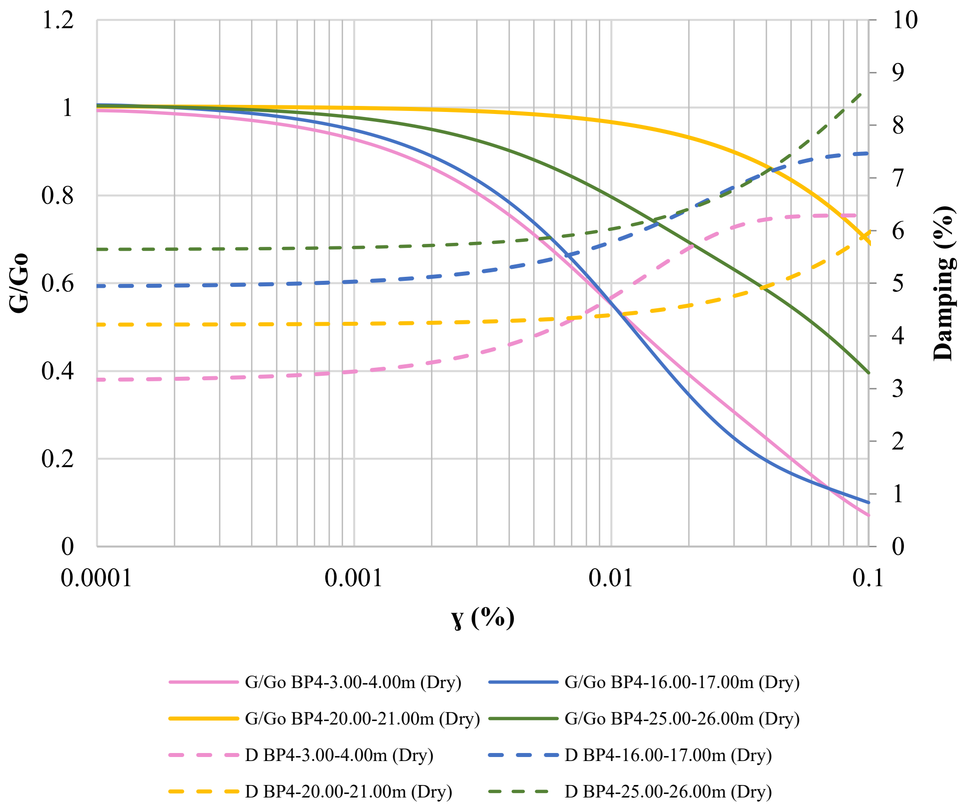

Figure 144. G/Go and Damping curves for Zone B (Dry samples)

Zone C

The curves corresponding to each of the strata in zone C are shown. Where the following is observed:

- The trajectories of the shear modulus degradation curves are similar, except for the one corresponding to the fourth layer, which intersects the curve of the first layer at a shear strain of approximately 0.09% and intersects the curve of the second layer at a shear strain of approximately 0.048%. In addition, it is observed that for a shear strain of 0.1%, the maximum value of G/Go is 0.45 corresponding to the second layer and the minimum value is 0.12 corresponding to the third layer.

- The damping curves of the second, fourth and fifth layers have similar trajectories, however they have different damping values. For a shear strain of 0.0001%, the following values are obtained: 4.99, 4.27 and 5.61 for the second, fourth and fifth layers, respectively. While for a shear shear of 0.1% the following is observed: the fifth layer has the maximum value, which is 9.90, the minimum value is 5.49 corresponding to the fourth layer, while the second layer presents a value of 8.31.

- The trajectories of the damping curves of the first and third layers are similar, however, the curve of the first layer coincides with the curve of the second layer at a shear strain of 0.0001%, while for the same value of shear strain the curve of the third layer has a value of 6.47. For a shear strain of 0.1%, values of 9.11 and 8.69 are presented for the first and third stratum, respectively.

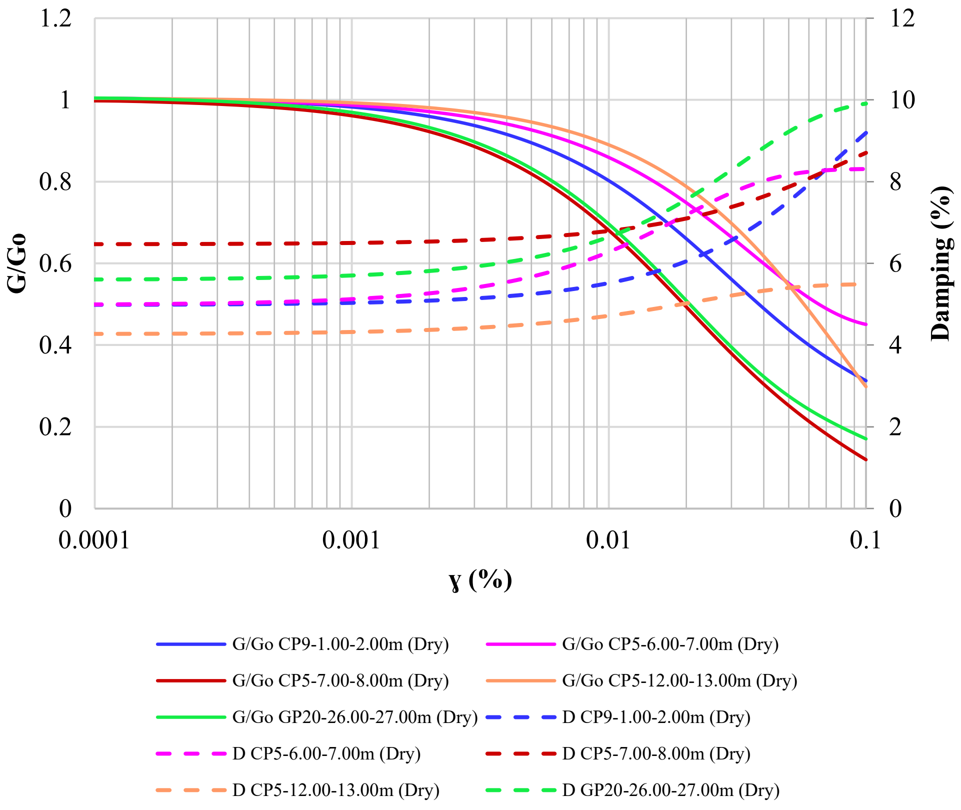

Figure 145. G/Go and Damping curves for Zone C (Dry samples)

Zone D

The curves corresponding to each of the strata in zone D are shown. Where the following is observed:

- The shear modulus degradation curves have similar trajectories except the second layer, which changes trajectory at a shear strain of 0.008%. In addition, it intersects the three remaining curves, the curve of the first layer at a shear strain of 0.012%, the curve of the third layer at a shear strain of 0.019% and the curve of the fourth layer at a shear strain of 0.023%. Moreover, it presents the maximum value of G/Go for a shear strain of 0.1%, which is 0.19.

- The shear modulus degradation curve of the fourth layer intersects the curves of the first and third layers at a shear strain of approximately 0.038%. It also has the minimum value of G/Go for a shear strain of 0.1%, with a value of 0.014.

- The damping curves of the first and fourth layers have similar and parallel trajectories to each other, where the minimum damping value for a deformation of 0.0001% corresponds to the curve of the fourth layer with a value of 1.36, while the first layer has a damping of 4.84. For a shear strain of 0.1%, damping values of 9.46 and 7.11 were obtained for the first and fourth strata, respectively.

- The third and second stratum have independent damping paths, however, the curve of the third stratum presents the maximum damping value for a shear strain of 0.1%, which is 17.68. While the curve of the second stratum has the maximum value for a deformation of 0.0001%, which is 6.89.

Note: The information of the shear modulus degradation and damping curve of the fourth layer was placed in the fifth layer, due to absence of material.

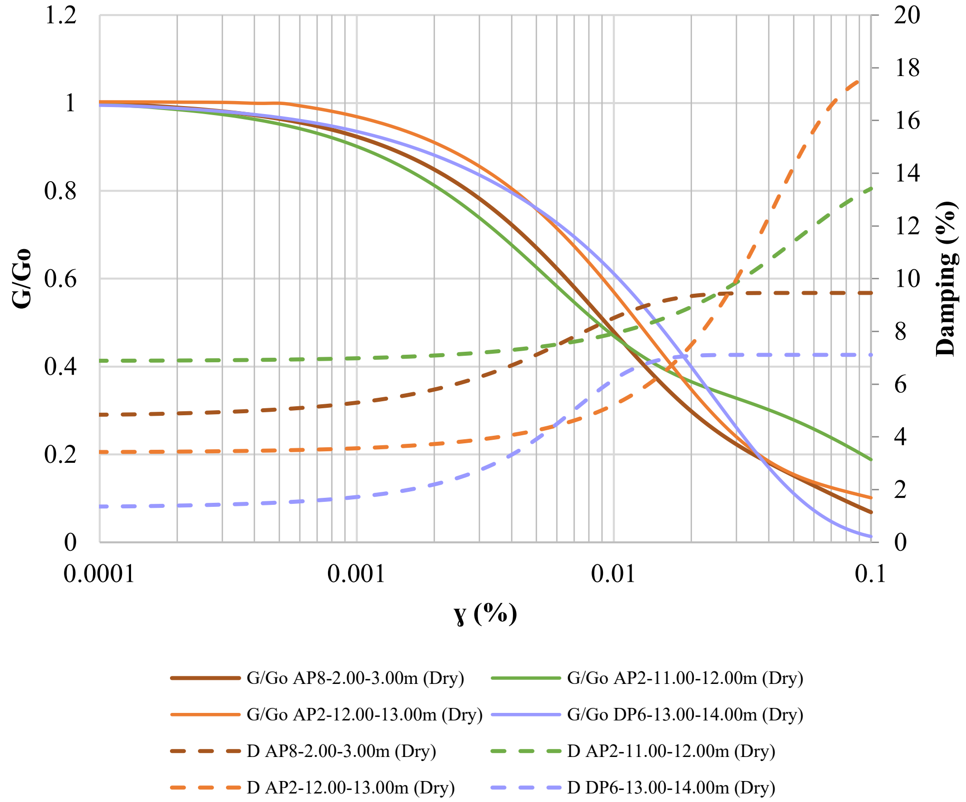

Figure 146. G/Go and Damping curves for Zone D (Dry samples)

Zone E

The curves corresponding to each of the strata in zone E are shown. Where the following is observed:

- The shear modulus degradation curves present similar trajectories, where the minimum value of G/Go for a shear strain of 0.1% is 0.017 corresponding to the fourth stratum, while the maximum value belongs to the second stratum and has a value of 0.19. In addition, it is observed that the curves of the third and fifth stratum have a G/Go value of 0.15 approximately.

- The damping curves corresponding to the first, third, fourth and sixth layers have a damping value between 4.84 and 5.61 for a shear strain of 0.0001%. While for this value of shear strain, the maximum value is presented in the second stratum with a value of 6.89 and the minimum value belongs to the fourth stratum, which is 2.58.

- For a shear strain of 0.1%, the minimum value is 6.61 corresponding to the fifth stratum, while the maximum value is 13.39 corresponding to the second stratum.

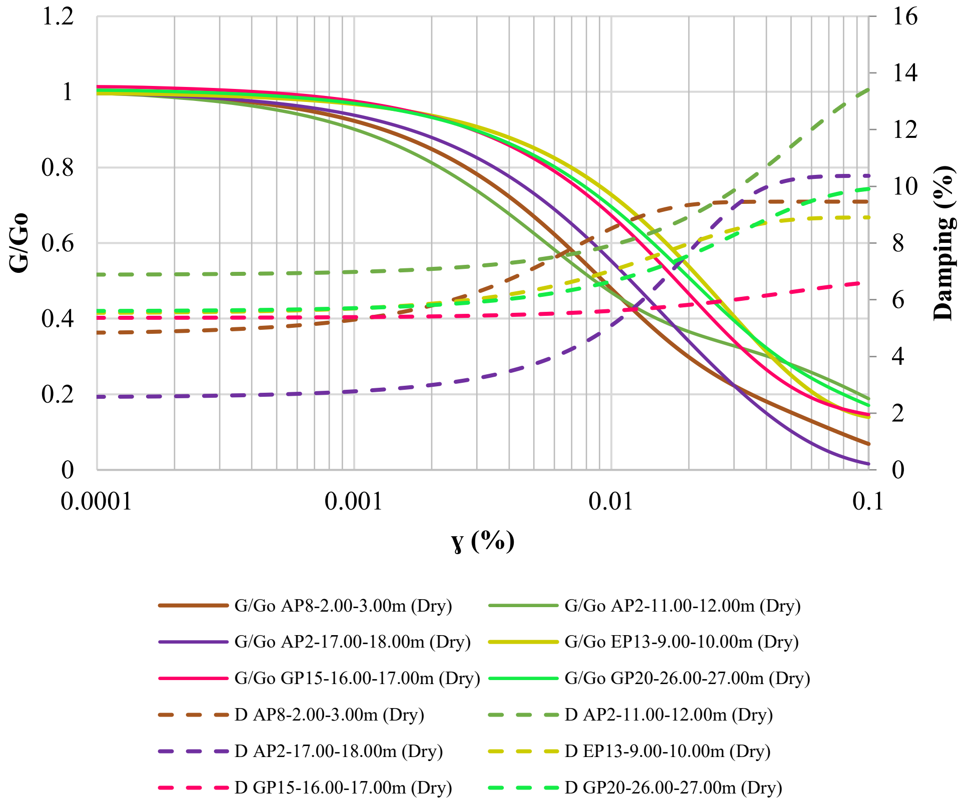

Figure 147. G/Go and Damping curves for Zone E (Dry samples)

Zone F

The curves corresponding to each of the strata in zone F are shown. Where the following is observed:

- The shear modulus degradation curves present similar trajectories, however, the curve corresponding to the second layer intersects the third at a shear strain of 0.04%. In addition, the maximum value of G/Go for a shear strain of 0.1% is 0.34 and the minimum value is 0.11.

- The damping curves have similar trajectories, however, they present different damping values for a shear strain of 0.0001%, which are 3.33, 2.37 and

3.93 corresponding to the first, second and third layers, respectively. While for a shear strain of 0.1%, the maximum value is 7.79 corresponding to the first layer and the minimum value is 7.20 corresponding to the second layer.

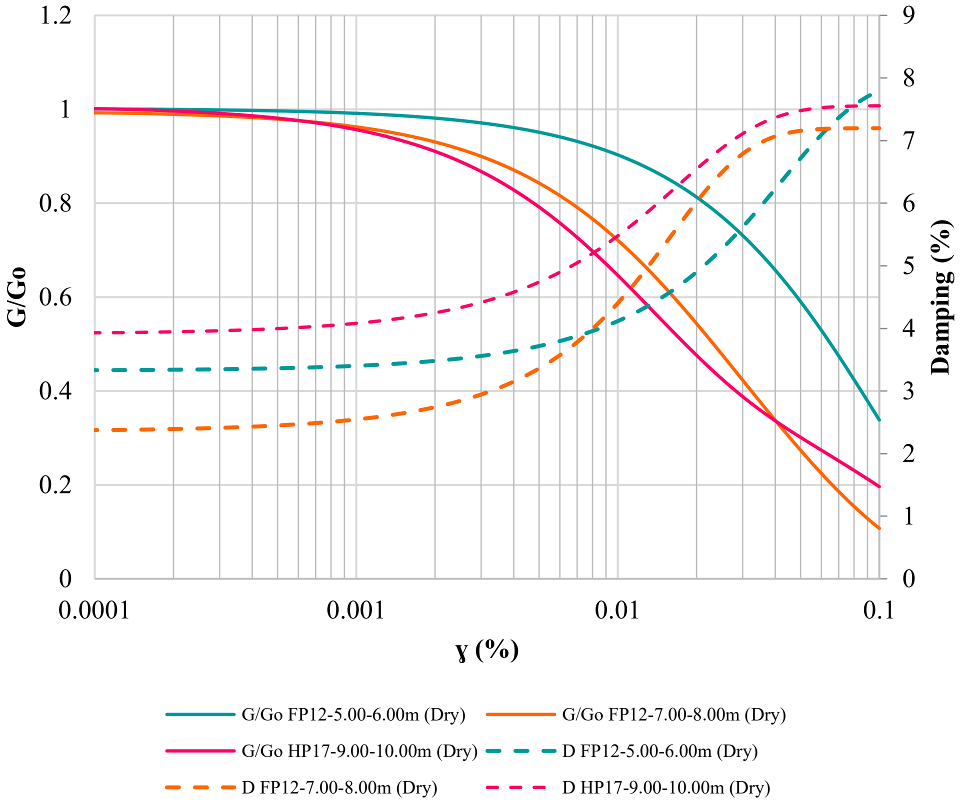

Figure 148. G/Go and Damping curves for Zone F (Dry samples)

Zone G

The curves corresponding to each of the strata in zone G are shown. Where the following is observed:

- The shear modulus degradation curves present similar trajectories, except for the curve of the second layer which intersects each of the remaining curves. In addition, the curve of this stratum presents the maximum value of G/Go for a shear strain of 0.1%, which is 0.17.

- The degradation curve of the first and third stratum have a common point at a shear strain of approximately 0.046%. While the minimum value of G/Go is 0.069 corresponding to the curve of the first layer.

- The damping curves present similar trajectories, however, for a shear strain of 0.0001%, the curves of the first, fourth and fifth stratum present damping values between 4.84 and 5.61. While the maximum value for this shear strain is 6.89 corresponding to the second layer, and the minimum is 3.43 corresponding to the third layer.

- For a shear strain of 0.1%, the maximum damping value is 17.71 and the minimum is 6.61.

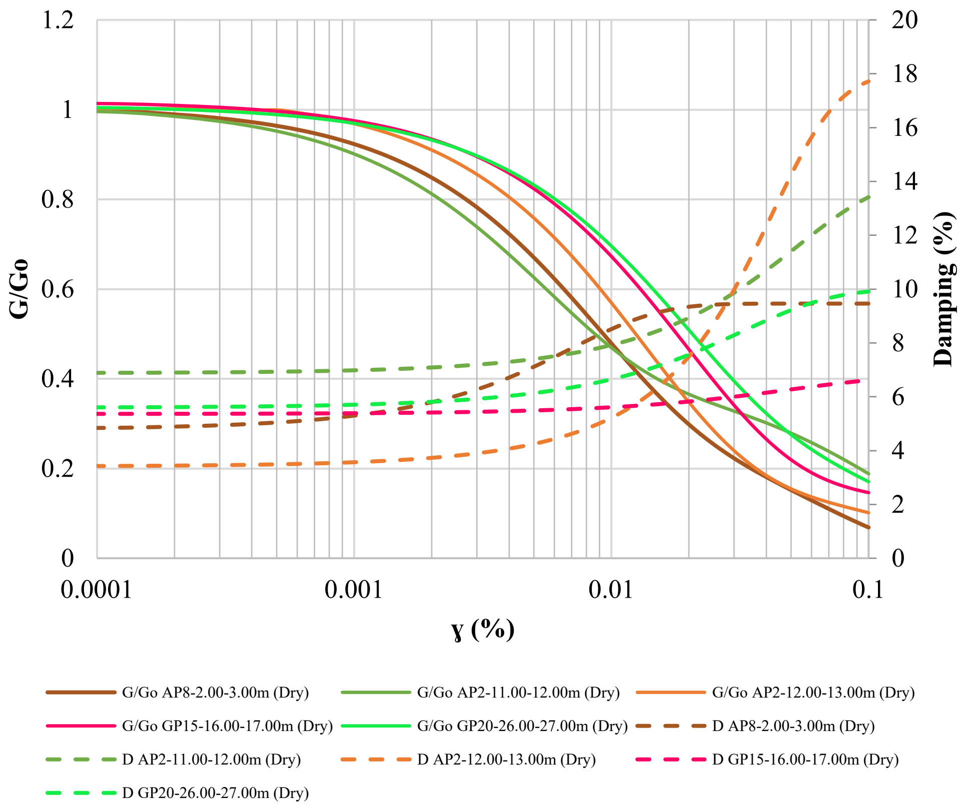

Figure 149. G/Go and Damping curves for Zone G (Dry samples)

Zone H

The curves corresponding to each of the strata in zone H are shown. Where the following is observed:

- The shear modulus degradation curves present similar trajectories; however, the curve of the second layer intersects the curve of the third layer at a shear strain of 0.04%. In addition, for a shear strain of 0.1% there is a maximum value of G/Go of approximately 0.20 and a minimum of 0.069.

- The damping curves present similar and parallel curves in which, for a shear strain of 0.0001%, the maximum damping value is 4.84, while the minimum is 2.37. While for a shear strain of 0.1% the maximum value is 9.46 and the minimum is 7.20.

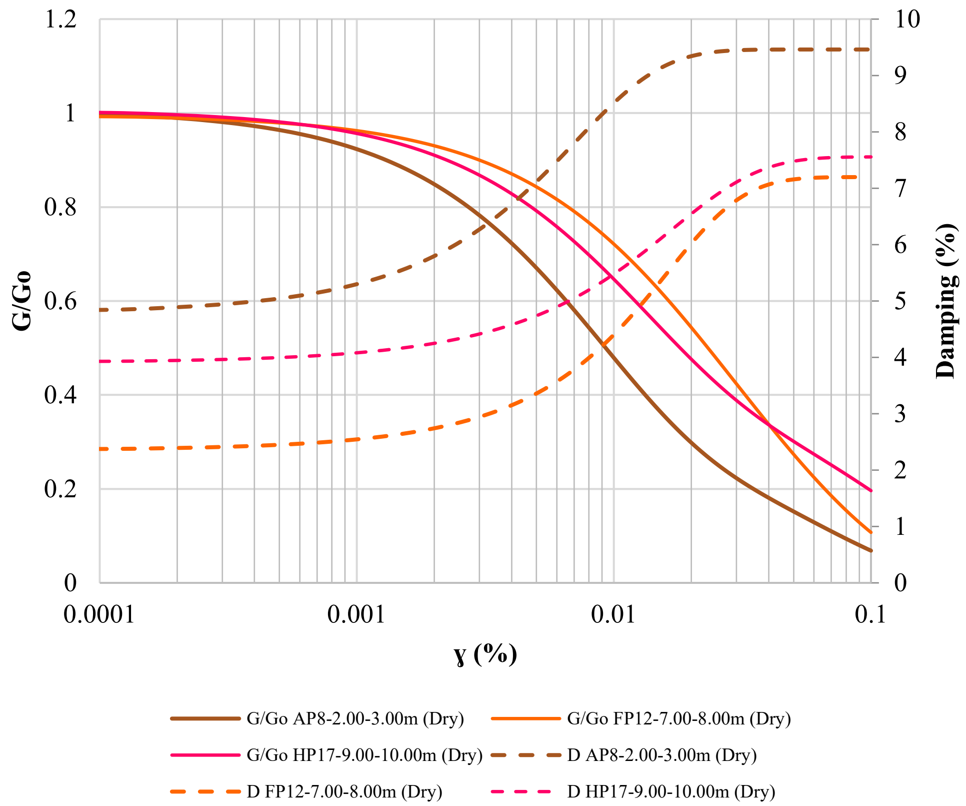

Figure 150. G/Go and Damping curves for Zone H (Dry samples)

Zone I

The curves corresponding to each of the strata in zone I are shown. Where the following is observed:

- The shear modulus degradation curves have similar trajectories; however, the curve corresponding to the second layer intersects all the curves except that of the first layer. In addition, for a shear strain of 0.1%, there is a maximum value of G/Go of 0.36 corresponding to the first layer and a minimum value of 0.086 corresponding to the third layer.

- The damping curves show similar trajectories; however, for a shear strain of 0.0001%, there is a maximum damping value of 6.89 and a minimum of 2.39, corresponding to the second and third stratum, respectively. Meanwhile, for a shear strain of 0.1%, a maximum damping value of 13.39 and a minimum of 6.18 are presented.

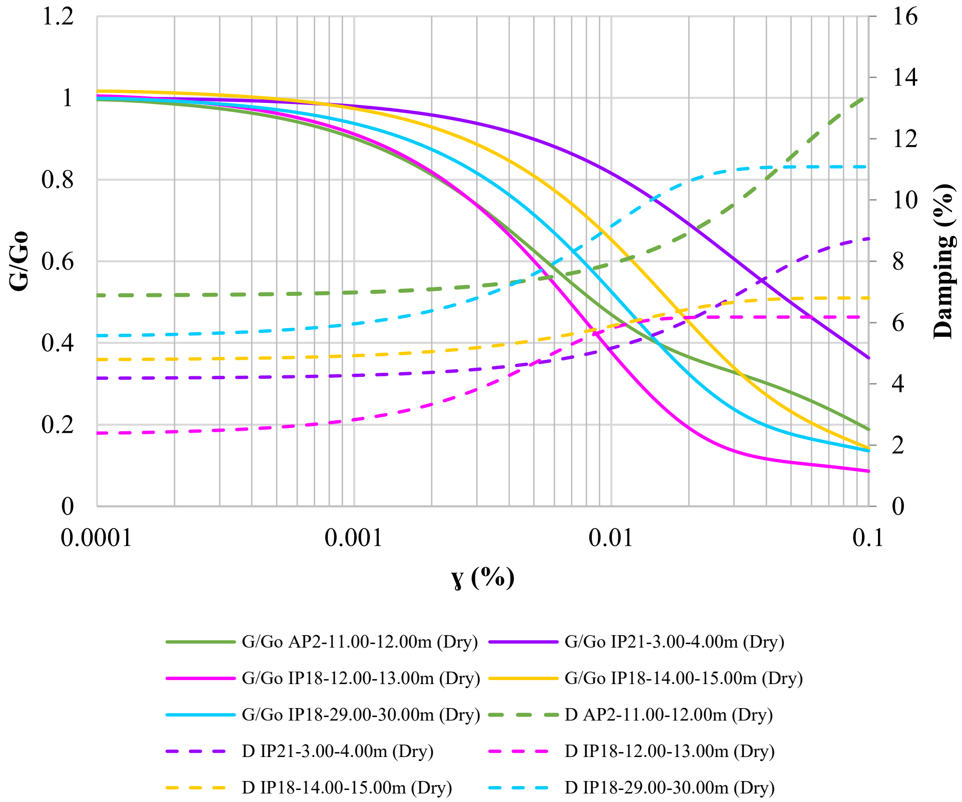

Figure 151. G/Go and Damping curves for Zone I (Dry samples)

4.5.6. *Results for remolded samples*

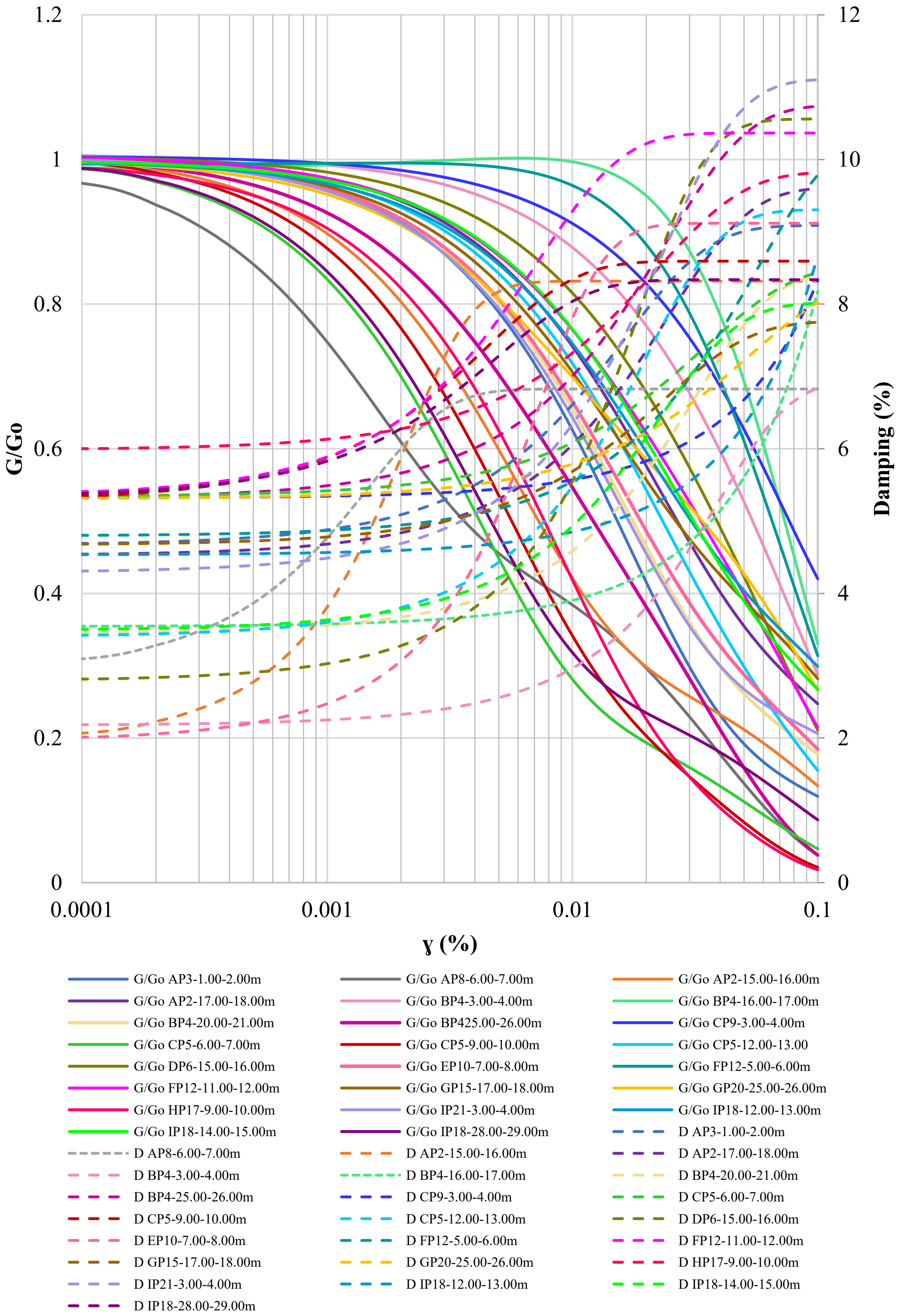

Figure 152. Compilation of the curves developed with remolded samples.

Zone A

The curves corresponding to each of the strata in zone A are shown. Where the following is observed:

- The trajectories of the degradation curves of the shear modulus and damping of the first and fourth layers are similar. However, for a shear strain of 0.1%, the values of G/Go are approximately 0.12 and 0.25, respectively. While, for the damping curve, it is found that for a shear strain of 0.00001%, the damping values are quite close, while for a shear strain of 0.1%, the difference is 0.51.

- The damping curves of the second and third layers show similar trajectories. However, for a shear strain of 0.00001% a difference of 1.02 is evident, while for a shear strain of 0.1% the difference is 1.49.

- The shear modulus degradation curves of the second and third layers have independent paths. However, the curve belongs to the third layer intersects the shear modulus degradation curve of the first layer at an approximate value of shear strain of 0.04% and has a tangent point with the curve of the second layer at a shear strain of 0.018%.

Note: The information of the shear modulus degradation and damping curve of the fourth layer was placed in the fifth layer, due to absence of material.

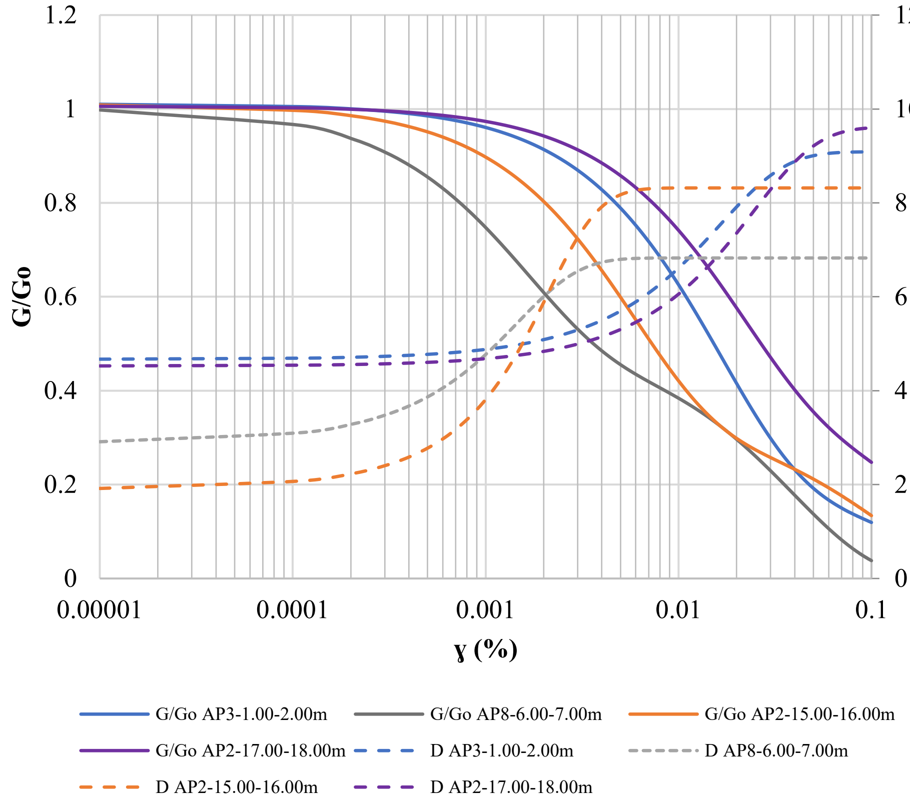

Figure 153. G/Go and Damping curves for Zone A (Remolded samples)

Zone B

The curves corresponding to each of the strata in zone B are shown. Where the following is observed:

- The damping curves of the first, third and fourth layers have similar and parallel trajectories to each other, with an average difference of 1.58 for a shear deformation of 0.0001% and an average difference of 1.96 for a shear strain of 0.1%. While the damping curve corresponding to the second layer has an independent trajectory with respect to the other layers.

- The trajectories of the shear modulus degradation curves of the first and second layers are similar. However, for a shear strain of 0.1% there is a difference of 0.04. While for the third and fourth layers similar trajectories are evident from 0.0001% to 0.02%, from this point the trajectories change, generating a difference of 0.14 for a shear strain of 0.1%.

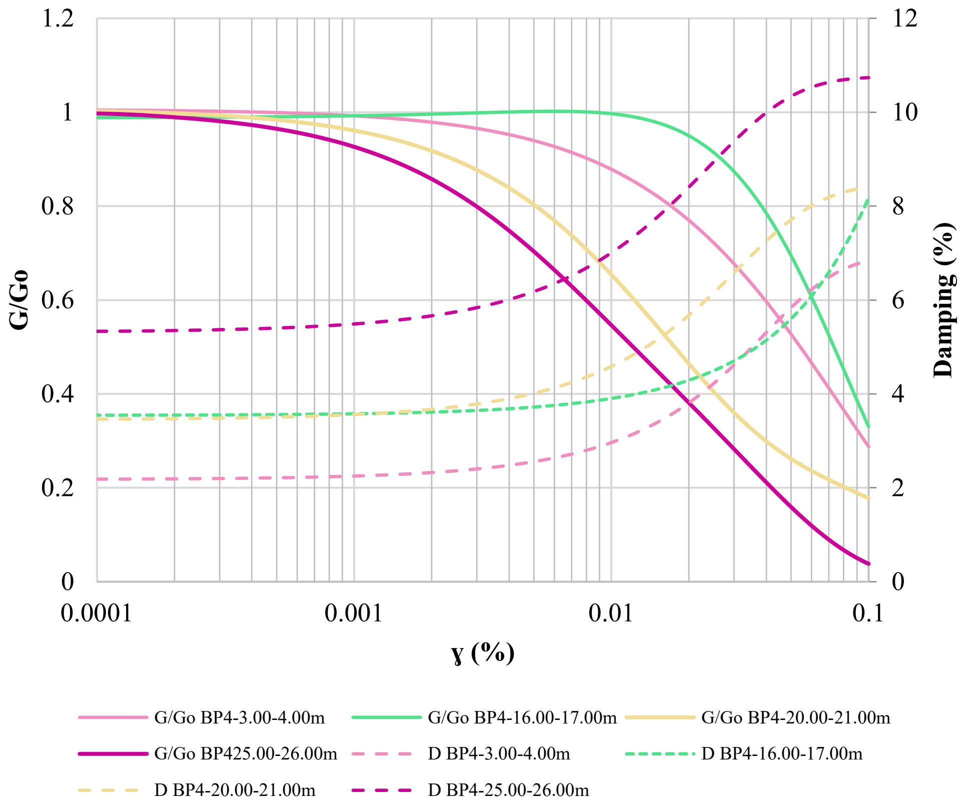

Figure 154. G/Go and Damping curves for Zone B (Remolded samples)

Zone C

The curves corresponding to each of the strata in zone C are shown. Where the following is observed:

- The shear modulus degradation curves of the second and third strata are similar, however, they intersect around a shear strain of 0.024%. While for a shear strain of 0.1% there is a difference of 0.026 for G/Go.

- The shear modulus degradation curves of the first and fourth layers present similar trajectories, however, for a shear strain of 0.1% they present a difference of 0.26. The curve of the fifth layer presents an independent trajectory that intersects the curve of the fourth layer at a shear strain value of 0.013 approximately.

- The damping curves of all the strata, except the fourth stratum, for a shear strain of 0.0001% present a damping value of approximately 5.31. Meanwhile, for a shear strain of 0.1% the damping values range between 7.98 to 8.59.

- The trajectories of the damping curves of the second and fifth layers are similar, while the third and first layer damping curves have independent trajectories.

- The damping curve corresponding to the fourth stratum has the lowest damping value in relation to the other curves with a value of 3.42 for a shear strain of 0.0001%, while the damping curve for the third and first stratum has independent trajectories.

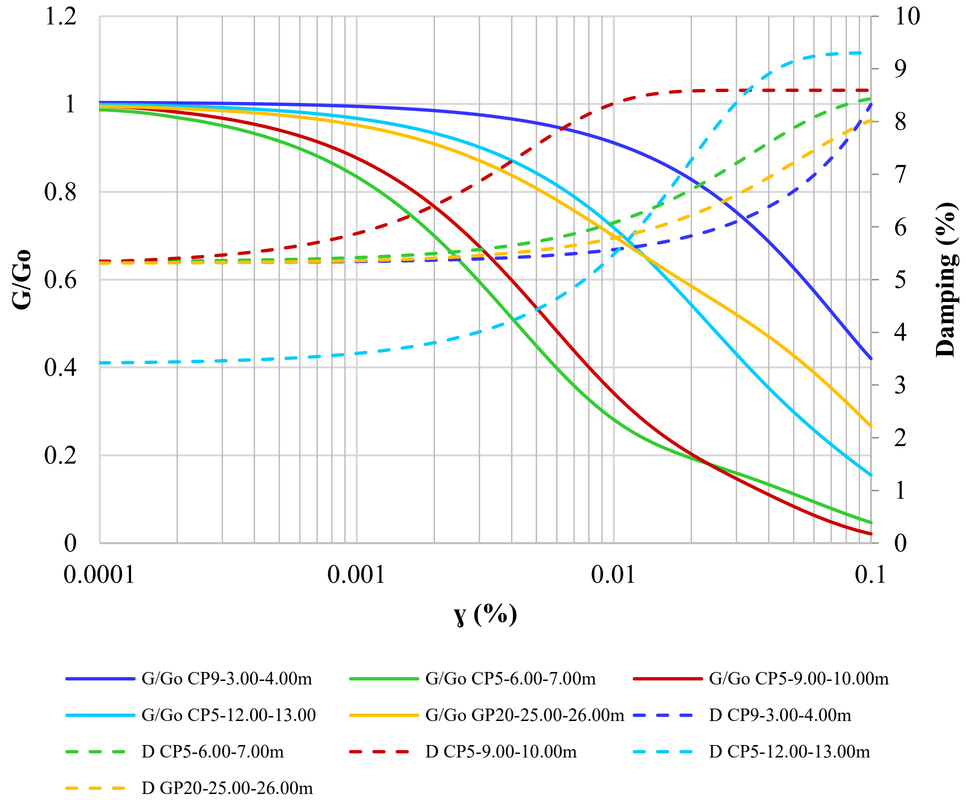

Figure 155. G/Go and Damping curves for Zone C (Remolded samples)

Zone D

The curves corresponding to each of the strata in zone D are shown. Where the following is observed:

- The shear modulus degradation curves of the first, third and fourth layers have similar trajectories; however, the curve corresponding to the third layer intersects the curves of the first and second layers in shear strain values of approximately 0.04% and 0.019%, respectively.

- The shear modulus degradation curves for a shear strain of 0.1% present different values, with the highest difference between the curves corresponding to the second and fourth stratum, with a value of 0.182. While the lowest difference is between the curves of the first and third stratum, with a value of 0.02.

- The damping curves of the second and fourth strata have close values for a shear strain of 0.00001%, presenting the smallest difference for this strain value, which is 0.12. However, for a strain of 0.1%, the highest difference is presented, with a value of 3.63.

- The damping curves of the first and third layers show the greatest difference for a shear strain of 0.00001%, with a value of 2.77. While, for a shear strain of 0.1%, the smallest difference is found with a value of 0.77.

Note: The information of the shear modulus degradation and damping curve of the fourth layer was placed in the fifth layer, due to absence of material.

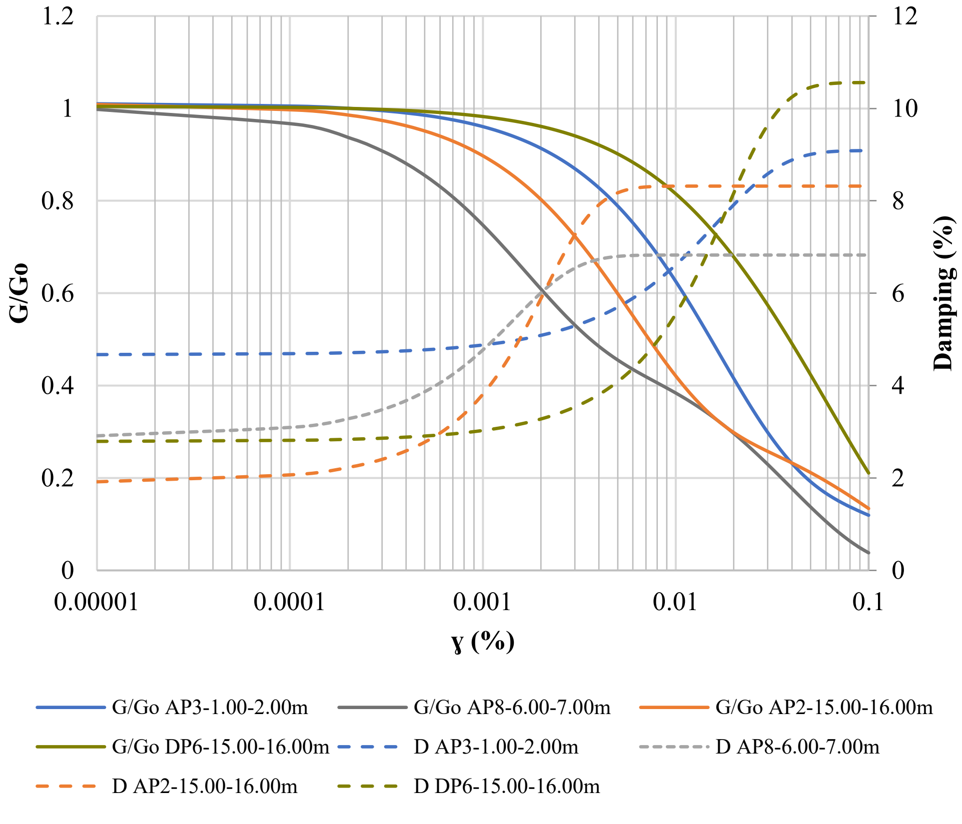

Figure 156. G/Go and Damping curves for Zone D (Remolded samples)

Zone E

The curves corresponding to each of the strata in zone E are shown. Where the following is observed:

- The shear modulus degradation curves of all the strata, except the second stratum, have similar trajectories where it is observed that the curves corresponding to the fifth and sixth stratum intersect in two values of shear strain, which are: 0.012% and 0.08%. While the curves corresponding to the fourth and fifth layers intersect at a shear strain value of 0.028%.

- For a shear strain of 0.00001% in the damping curves the following is observed: the first and fifth layers have the same value which is 4.67, while the curve of the fourth layer has a value very close to the previous one of 4.52, the curves of the second, third and sixth layers have independent damping values for this level of deformation, which are 3.11, 1.97 and 5.32, respectively.

- For a shear strain of 0.1% in the damping curves, the following is observed: the first and fifth stratum have a difference of 1.37, the curve of the fourth stratum has a value of 9.60. However, the second, third and sixth stratum curves have values of 6.83, 9.12 and 8.01, respectively. Furthermore, it is evident that for this level of deformation the first and third stratum have the same value.

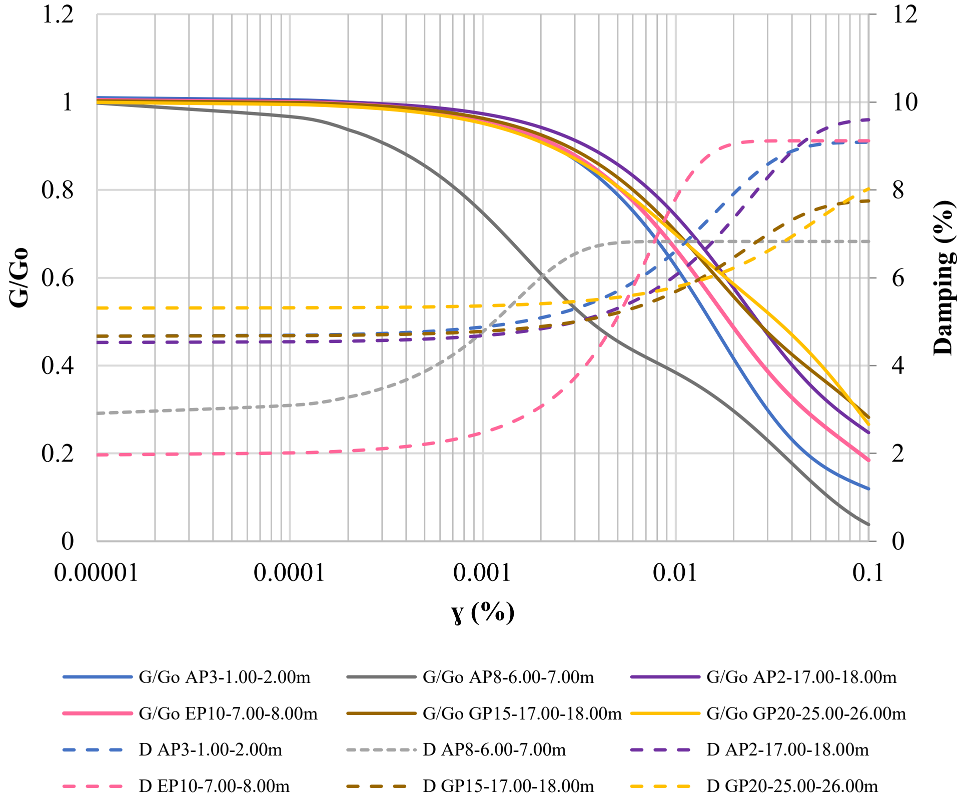

Figure 157. G/Go and Damping curves for Zone E (Remolded samples)

Zone F

The curves corresponding to each of the strata in zone F are shown. Where the following is observed:

- The shear modulus degradation curves have similar trajectories, however, it is observed that for a shear strain of 0.1% the G/Go values for the first, second and third layers are 0.32, 0.22 and 0.018 respectively. It is evident that the difference between the first and second layers is 0.10, while the difference between the second and third layers is 0.202, which is double the above mentioned pair.

- For a shear strain of 0.0001% in the damping curves, the following is observed: for the first, second and third layers, the following values were obtained: 4.80, 5.41 and 6.00 respectively. While for a shear deformation of 0.1% it is observed that stratum one and three have the same value of 9.82, while stratum two has a value of 10.37.

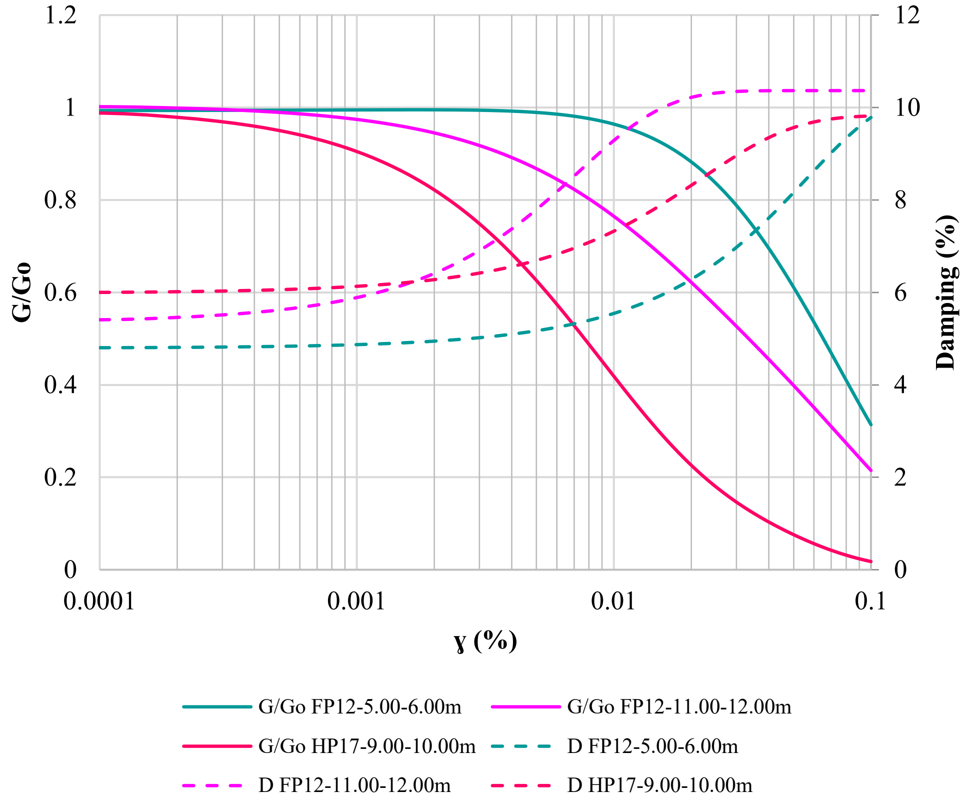

Figure 158. G/Go and Damping curves for Zone F (Remolded samples)

Zone G

The curves corresponding to each of the strata in zone G are shown. Where the following is observed:

- With respect to the shear modulus degradation curves, it is observed that the curve of the third stratum intersects the curve of the first and second stratum at shear strain values of 0.039% and 0.019%, respectively. Meanwhile, in the fourth and fifth stratum, these curves intersect at two shear deformation values of 0.012% and 0.08%.

- For a shear strain of 0.00001%, we observe the same value of damping in the first and fourth stratum, which is 4.67. While, for the second, third and fifth layers the values are 2.91, 2.08 and 5.31 respectively.

- For a shear deformation of 0.1%, it is observed that the damping values range between 6.83 and 9.09.

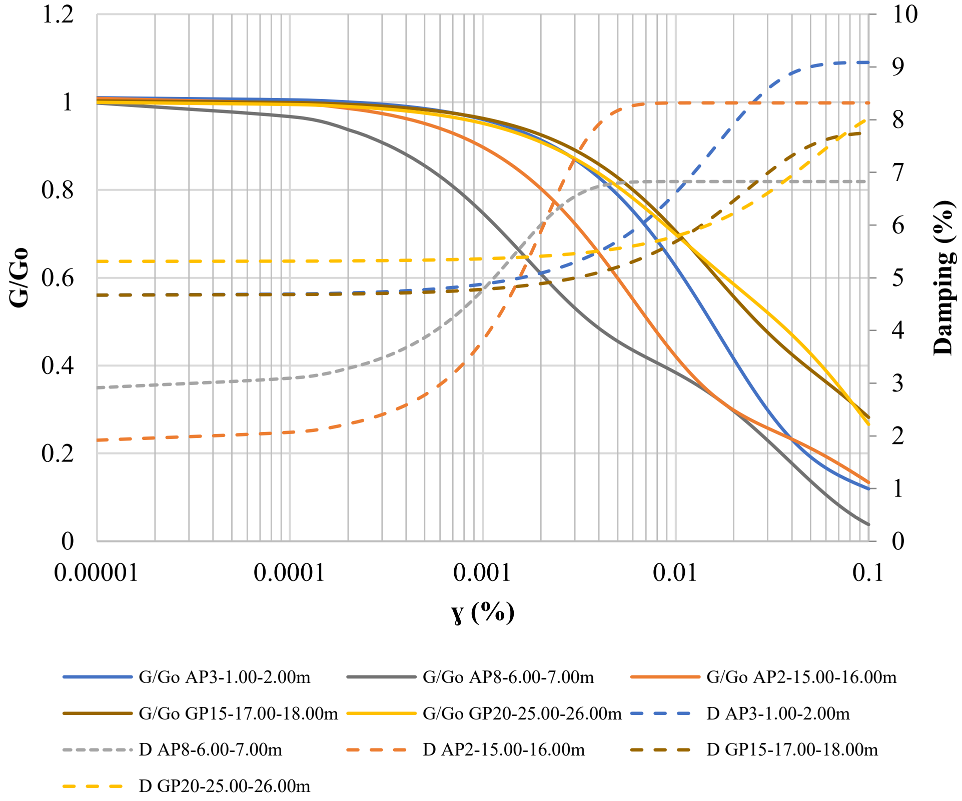

Figure 159. G/Go and Damping curves for Zone G (Remolded samples)

Zone H

The curves corresponding to each of the strata in zone H are shown. Where the following is observed:

- The shear modulus degradation curves have similar trajectories, however, they have different G/Go values for a shear strain of 0.1%. The first layer has a value of 0.12, the second one of 0.21 and the third one of 0.018.

- The damping curves have similar trajectories, however, they have different values for a shear strain of 0.0001%, which are 4.69, 5.41 and 6.00, for the first, second and third layers, respectively. While, for a shear strain of 0.1% the values range between 9.09 and 10.37.

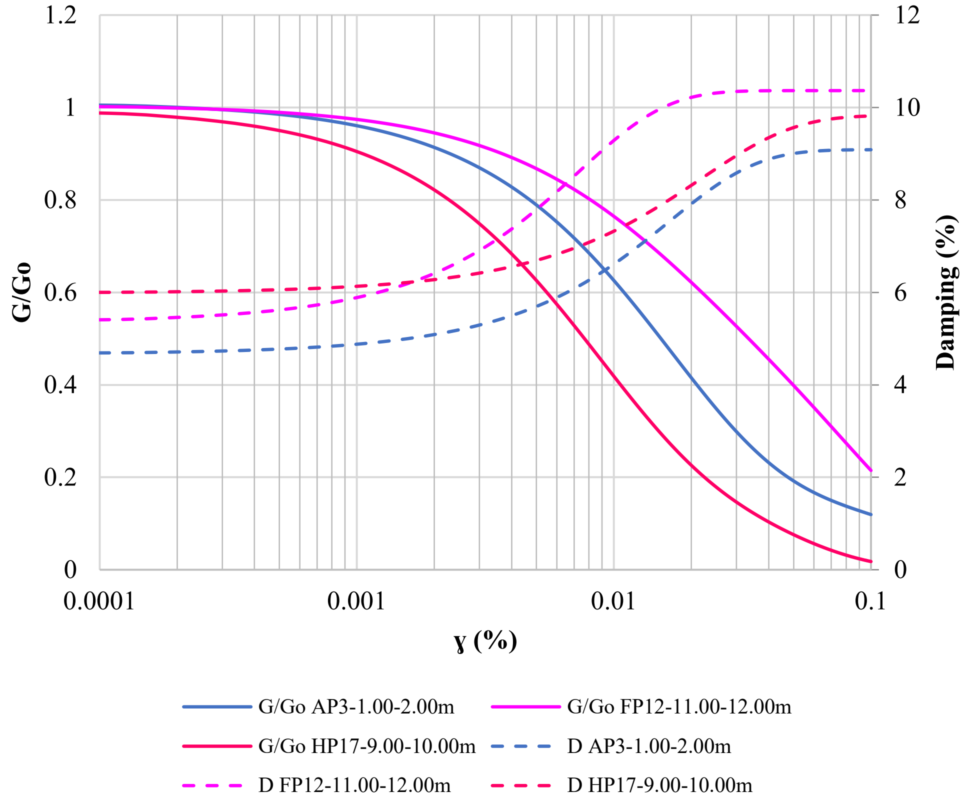

Figure 160. G/Go and Damping curves for Zone H (Remolded samples)

Zone I

The curves corresponding to each of the strata in zone I are shown. Where the following is observed:

- The degradation curves of the third and fourth strata have quite similar trajectories, which have a point of intersection, which has a shear strain of 0.036%. Furthermore, the trajectories of the curves of the first and fifth stratum are similar, however, the one of the fifth stratum intersects the curve of the second stratum at two points, which have the following shear strain values: 0.039% and 0.006 %.

- The damping values for a shear strain of 0.00001% are very close for the first and third layers, with a value of 4.31 and 4.53 respectively. While, for the second, fourth and fifth layers the values are: 3.11, 3.50 and 5.33 respectively.

- For the third, fourth and fifth layers, the damping values for a shear strain of 0.1% range between 8.01 and 8.60. Meanwhile, the first layer has a damping of 11.10 and the second layer has a damping of 6.83.

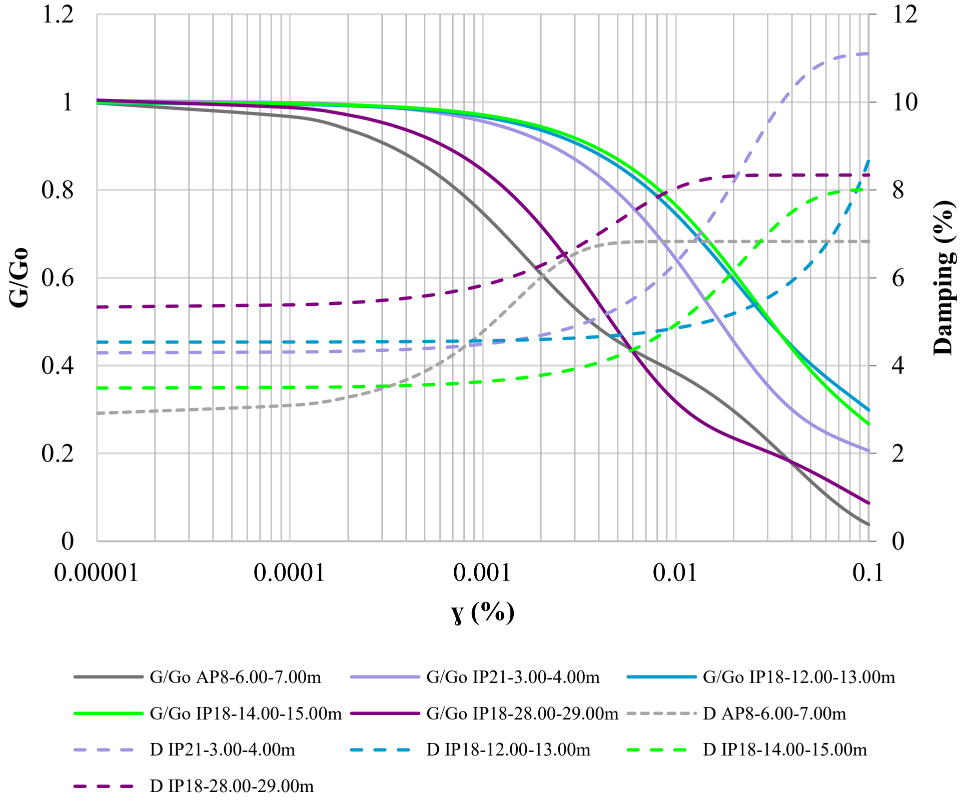

Figure 161. G/Go and Damping curves for Zone I (Remolded samples)

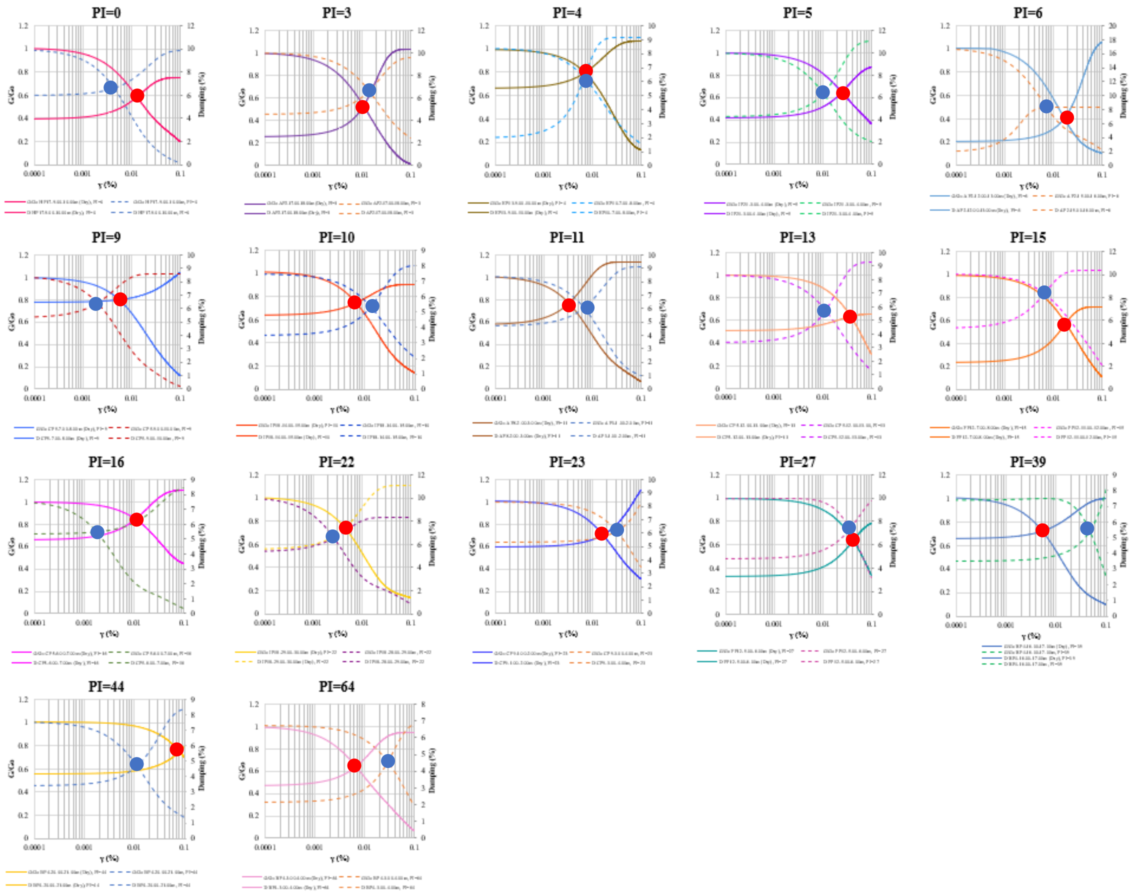

Figure 162. Intersection points of G/Go and damping curves of dry and remolded samples.

Figure 162 shows the points of intersection between shear modulus degradation (G/Go) and damping (D) for each value of the plasticity index for the dry (red) and remolded (blue) samples. As a result, in 11 of the 17 plots the red points, corresponding to the dry samples, are on the right and the blue points, corresponding to the remolded samples are on the left, representing 64.71%. Meanwhile, 35.29% corresponds to 6 of the 17 graphs that do not have the same previous behavior for both types of samples.

Prior to the analysis of the trajectory behavior for each of the shear modulus and damping degradation curves, it is important to mention that the curves with a continuous line correspond to dry samples and the curves with a dashed line correspond to remolded samples.

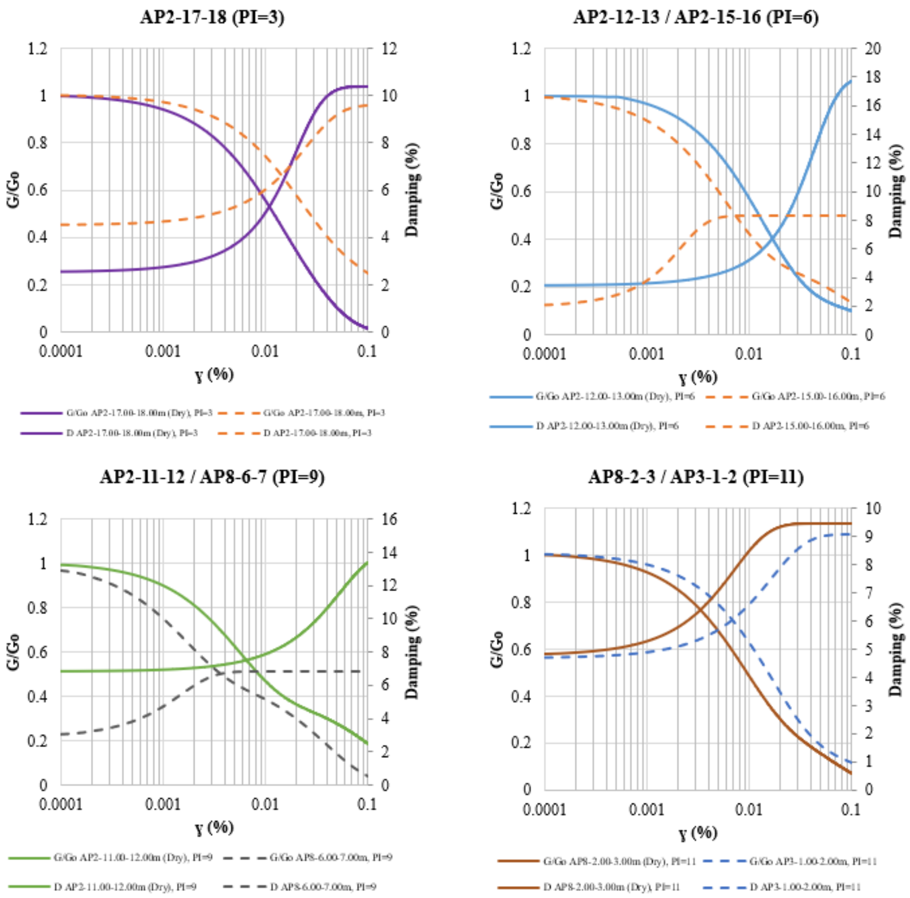

Figure 163. Shear modulus degradation and damping curves for zone A.

The shear modulus degradation curves (G/Go) and damping (D) corresponding to Zone A showed the following:

- In the second, third and fourth plots of dry samples show that as the plasticity index increases the damping decreases, in agreement with Darendelli (2001), as for a shear strain of 0.1% the damping decreases from 18 to 10. Meanwhile, the damping curves of remolded samples have the same behavior in the first, second and third plots.

- The shear modulus degradation values for a shear strain of 0.1% range from 0.0 to 0.2.

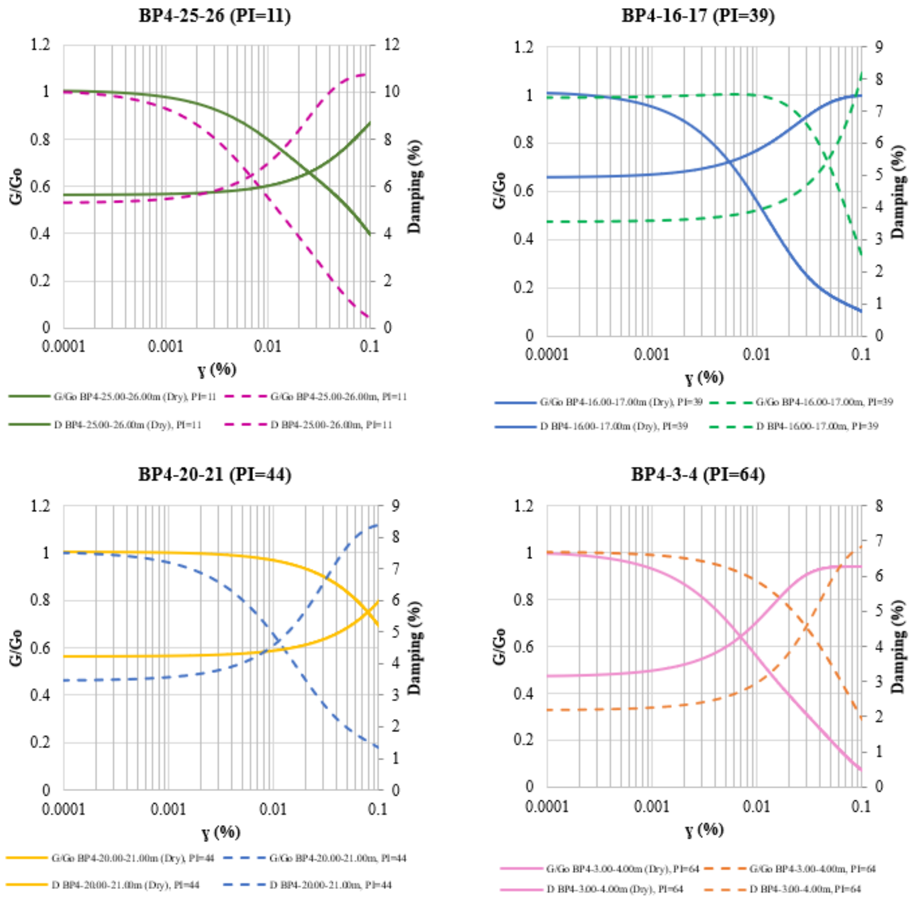

Figure 164. Shear modulus degradation and damping curves for Zone B.

Zone B has the highest plasticity index values of all the zones because this zone has a water table 1 m deep and high plasticity organic soils (OH) are found in the first 14 m, see section 3.3.1. The trajectory of the G/Go and D curves of the dry and remolded samples are in agreement with Darendelli (2001), who proposed that as the plasticity index increases, the damping decreases.

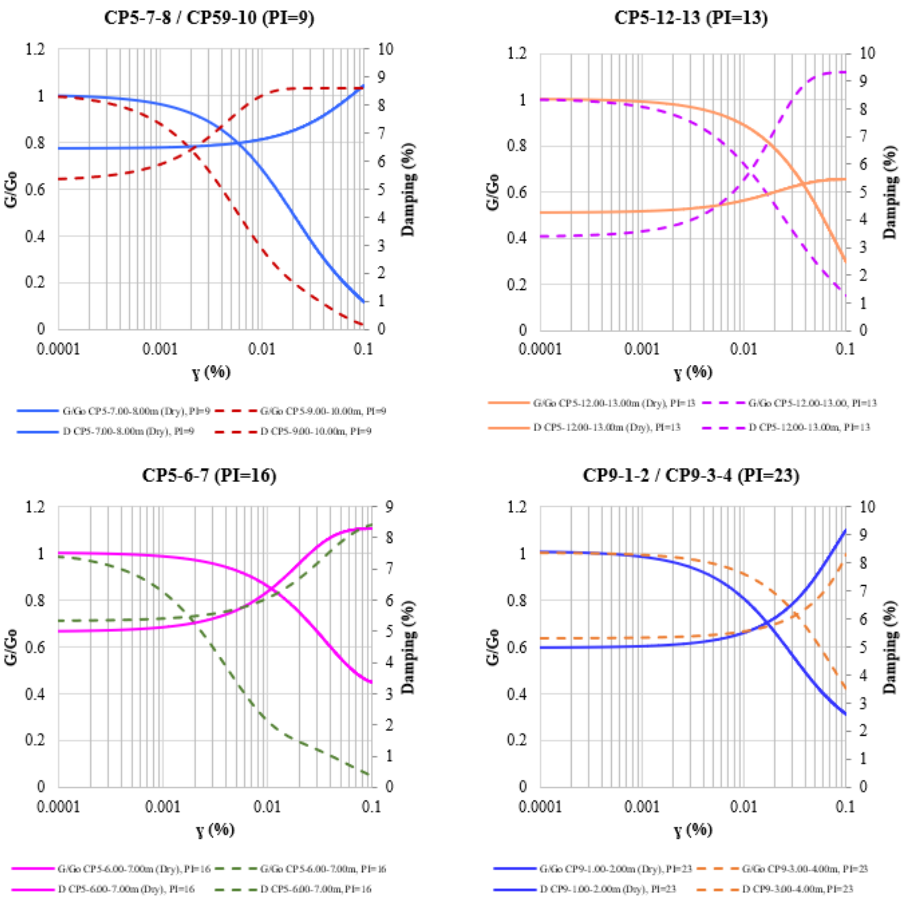

Figure 165. Shear modulus degradation and damping curves for Zone C.

The damping curves of the dry samples for a plasticity index of 9 and 13, for a shear strain of 0.1% decrease from 8.59 to 5.50. However, for a plasticity index of 16 and 23, for the same shear strain, the damping increases from 8.43 to 9.14. Otherwise, the damping curves of the remolded samples have a behavior in agreement with Darendelli (2001), with the exception of the second plot, which for a plasticity index of 13, the damping increases compared to the first plot with a plasticity index of 9.

The shear modulus degradation curves of the dry samples, for a shear strain of 0.1%, show a decrease of the damping values in the first and second plots and, for the same shear strain, the third and fourth plots show an increase. While, for the remolded samples, in the first, second and fourth graphs the G/Go increases as the plasticity index increases, but the third plot does not have the same behavior.

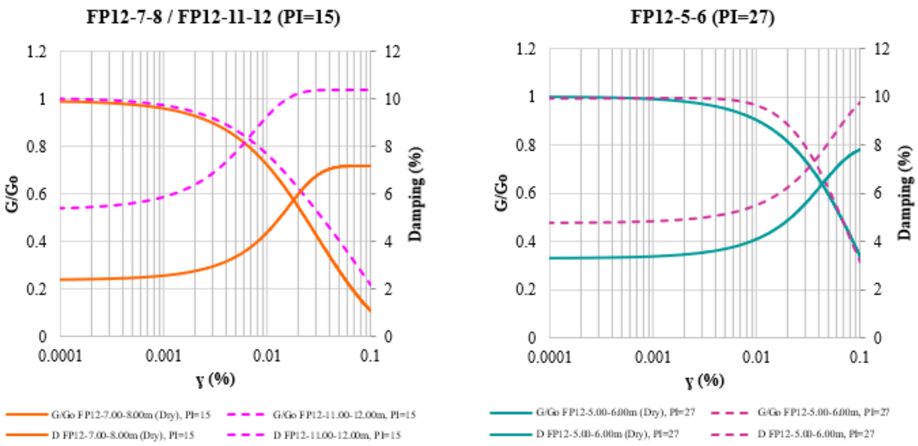

Figure 166. Shear modulus degradation and damping curves for Zone F.

The behavior of the damping curve for dry samples with a plasticity index of 15, for a shear strain of 0.1%, the damping value is 7.20 becoming asymptotic, while for a plasticity index of 27, for the same shear strain, the damping is 7.77 with a tendency to increase. Also, the G/Go curves for both types of curves agree with Darendelli (2001), where the G/Go increases with the plasticity index.

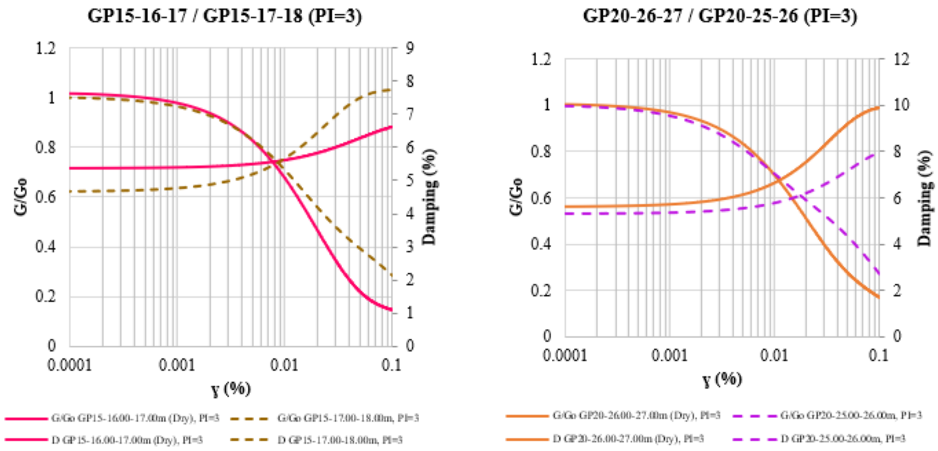

Figure 167. Shear modulus degradation and damping curves for Zone G.

In Zone G the specimens have the same plasticity index, however the first plot shows a dry specimen obtained from meter 16 to 17, which has a damping value of 6.61 for a shear strain of 0.1%, while the remolded specimen obtained from the next meter, for the same shear strain, has a damping value of 7.75, and the intersection points are too close. The remolded sample obtained from 25 to 26 m, in the second plot, shows a damping value of 8.02 for a shear strain of 0.1%.

Meanwhile, the dry sample obtained from the next meter has a damping value of 9.91. Finally, the shear modulus degradation curves of the dry and remolded samples present similar trajectories in both plots.

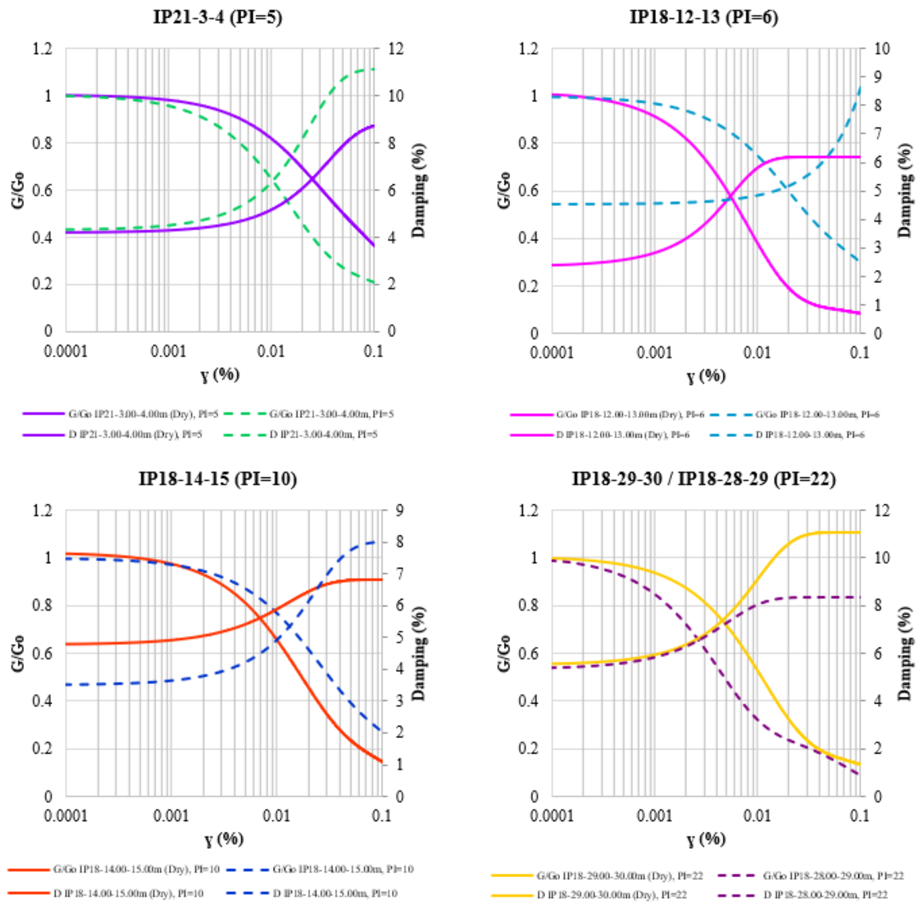

Figure 168. Shear modulus degradation and damping curves for Zone I.

Figure 168 shows that the damping curves for dry samples, in the first and second plots, show a behavior in accordance with Derendelli (2001); however, for the third and fourth plots, a different behavior is evidenced, where the damping increases with the plasticity index. The damping curves of the remolded samples show a behavior in accordance with Darendelli (2001) in the second, third and fourth plots. Regarding the shear modulus degradation curves in dry samples, for a shear strain of 0.1% the G/Go increases as the plasticity index increases in the second, third and fourth graphs. Although the degradation curves of shear modulus in remolded samples in the first and second show a behavior according to Darendelli, however the third and fourth for the same shear strain show a reduction of G/Go.

CHAPTER 5

Local seismic response

The local seismic response, from a physical point of view, can be described as the set of changes in amplitude, duration, and frequency that a seismic motion, related to a basic rock formation, undergoes by crossing the overlying soil layers up to the surface (Lanzo and Silvestri 1999). Also, the local seismic response estimation is a key parameter for seismic hazard assessment and risk mitigation, since local lithostratigraphic conditions can strongly influence the level of ground motion amplification during an earthquake (Bonnefoy-Claudet et al. 2006; Borcherdt 1970; van Ginkel et al. 2022). In the response analysis, near-surface low-velocity sediments overlying stiffer bedrock modify earthquake ground motions in terms of amplitude and frequency content, as for instance observed in L'Aquila, Italy in 2009, or Mexico City in 1985 (van Ginkel et al. 2022). The site amplification is known as the amplitude peak of the spectrum ratio between the ground surface and the base layer, and it is influenced by several factors such as the shear wave velocity of the surface sediment and the base layer, the density of the sediment layer, and the internal damping of each sediment layer (Marjiyono, Setiadi, and Setiawan 2021).

In Quito, the basin deep structure, shape and extension remains unknown, and the potential impact of seismic waves has yet to be evaluated. Also, the seismic velocities of the infilling material, which is mainly composed of volcanic ashes and magmatic intrusions, along with most of its mechanical properties also are unknown. Several observations from previous studies indicate that this basin should greatly amplify seismic waves. (Alfonso Naya et al. 2012a; Guéguen et al. 2000; Aurore Laurendeau et al. 2017). The local lithographic conditions to perform this analysis will be the ones described in Chapter 3, and the bedrock depth will be considered based on the recent research performed by (Pacheco et al. 2022) profiling the Quito basin using seismic ambient noise.

5.1. Local seismic response set-up

To evaluate the local site response, three main approaches exist: (1) the seismic attenuation approach, (2) the code-factor approach, and (3) the site response analysis approach. The first uses seismic attenuation relationships or ground motion prediction equations with soil properties. The code-factor approach, computes response spectra at bedrock and modifies them by generic soil amplification factors. The third approach, used in this study, evaluates a site-specific response analysis by a multi-disciplinary method involving geology, geophysics, geotechnics, and computational science (Carrer 2013; Kramer 1996)

An indispensable condition for the interpretation of the local effects produced by an earthquake on a site is to have a database, both seismic and geotechnical, recorded in sufficient quantity and quality to be able to reconstruct the local amplification phenomenon with a degree of reliability proportional to the complexity of the problem. The fundamental information for the analysis of the local seismic amplification consists of characteristics of the seismic input to the substrate, geometric stratigraphic reconstruction of the subsoil, and physical-mechanical properties of the soils (Lanzo and Silvestri 1999). To achieve this, the following procedure is presented, based on (Carrer 2013):

1. Definition of structure and geometry of the subsurface physical model.
2. Evaluation and definition of the seismic input acting at the bedrock-soil interface.
3. Application of the calculation code for numerical simulations.

For this purpose, a set of input data is required:

a) Depth of the seismic bedrock (based on the research with seismic ambient noise performed by (Pacheco et al. 2022))
b) Number and thickness of deposits overlying the bedrock; material and seismic properties of bedrock and deposits (unit weight, shear-wave velocity, dynamic properties, etc., based on Chapter 3 and 4 of this thesis)
c) Depth of the aquifer.
d) Ground motion time histories.

All these parameters influence at different levels numerical models and results. In particular, the depth of bedrock-deposits interface and the seismic velocity structure play the main role (Barani, de Ferrari, and Ferretti 2013).

5.2. Definition of structure and geometry of the subsurface physical model.

To define the soil profile and the boundary between the soil profile and the underlying rock layer, the data detailed in Chapter 3 for the soil geomechanical properties, the dynamical properties in Chapter 4 for, and the research of (Pacheco et al. 2022) to determine the rock layer will be taken into consideration.

(Pacheco et al. 2022), deployed 20 broad and medium frequency band seismic stations in Quito's urban area between May 2016 and July 2018 that continuously recorded ambient seismic noise. First, they computed horizontal-to-vertical spectral ratios to determine the resonant frequency distribution in the entire basin. Then, they correlated seismic stations operating simultaneously to retrieve interstation's surface wave Green's functions in the frequency range of 0.1–2 Hz. Finally, they computed Love wave phase-velocity dispersion curves and invert them in conjunction with the HVSR curves to obtain shear-wave velocity profiles throughout the city. The inversions highlight a clear difference in the basin's structure between its north and south of the city.

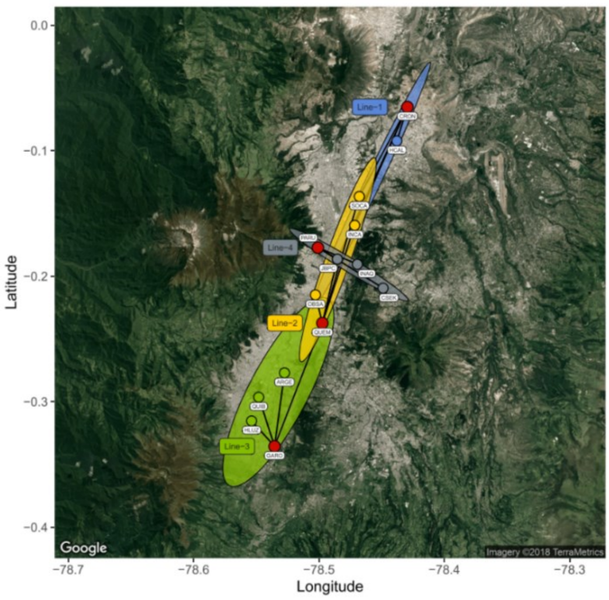

Figure 169. Seismic stations and lines throughout the city of Quito, from (Pacheco et al. 2022)

In the Vs computed models by (Pacheco et al. 2022), the difference in the half-space depth is significant. On CRON station and the nearby stations, this limit is around 200 m deep. However, the half-space depth on ARGE QUIB and HLUZ, located in the south of Quito, is greater than 700 m, as seen in Figure 170. It is also important to note that the Vs of the half-space in the south stations is higher (around 2500 ms−1) than the observed in the north and center stations (around 1700 ms−1) (Pacheco et al. 2022).

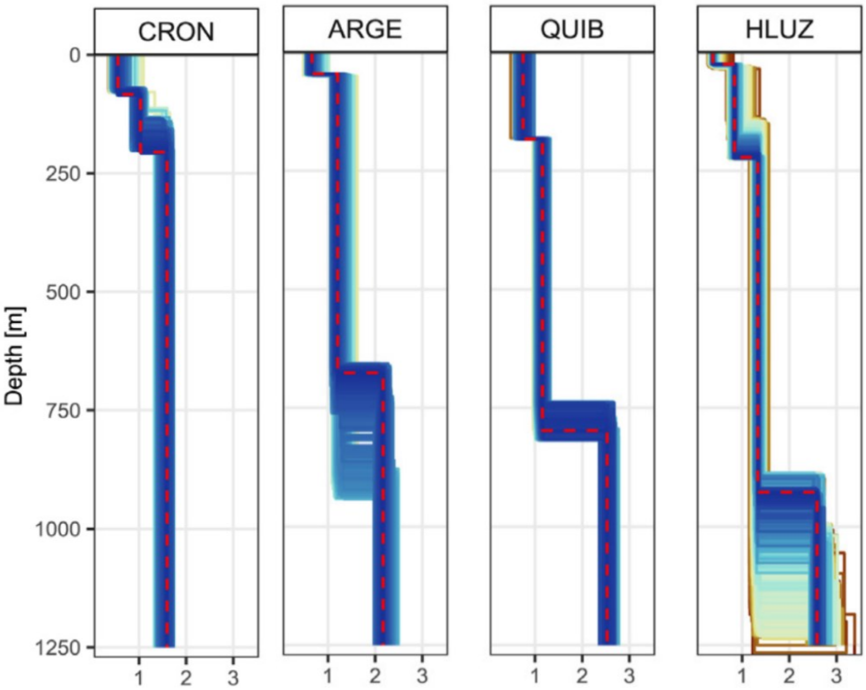

Figure 170. Interpretation of stations ARGE, QUIB and HLUZ from (Pacheco et al. 2022)

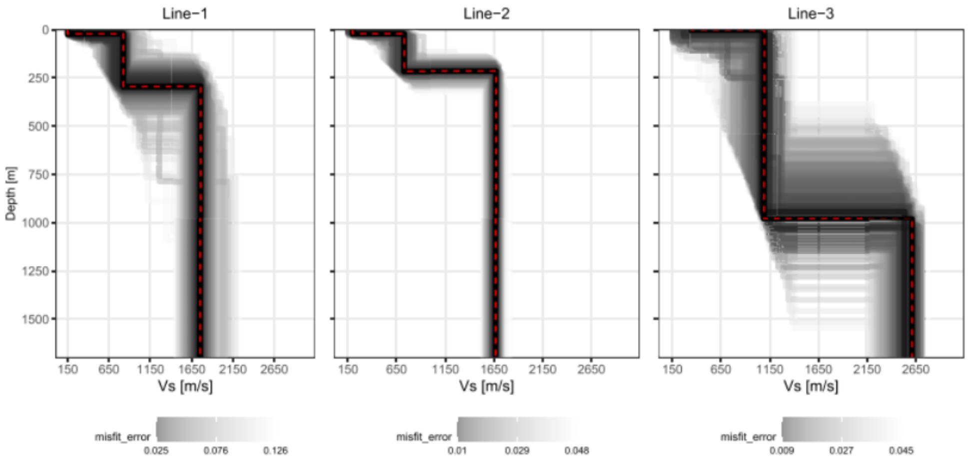

Figure 171. Differences in the Basin Depth from North of Quito (Line 1 and 2) and South (Line 3) from (Pacheco et al. 2022)

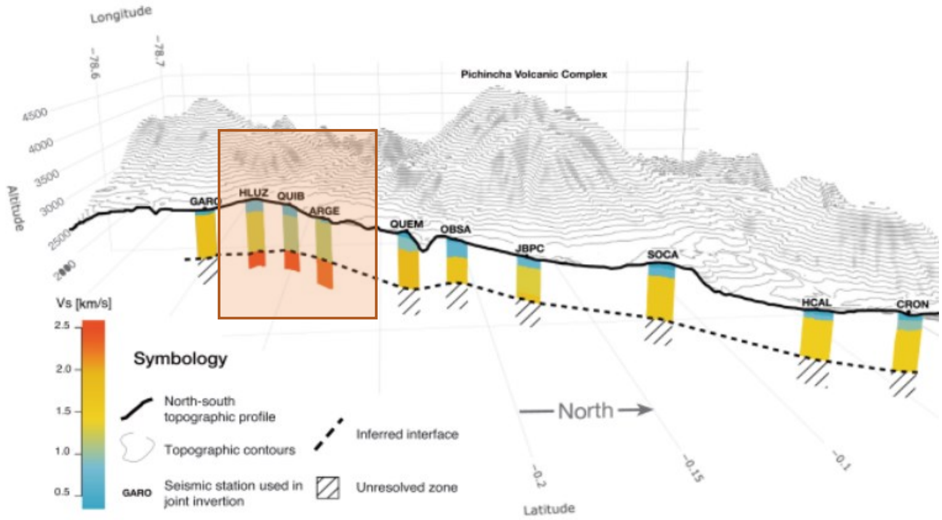

Figure 172. Cross-sectional and Longitudinal Geotechnical profiles

The geotechnical model below 30 m has no calibration because the research considered the model established by Pacheco et al. (2022) because there are no boreholes for this depth, on average 800 m.

With the basin depth reported by (Pacheco et al. 2022), plus the geotechnical data obtained for the surficial layers obtained from laboratory and field tests in Chapter 3, different columns to calculate the seismic response in linear equivalent and nonlinear analysis will be performed. The six transversal profiles 1 to 6 will be considered. In each profile, an analysis based on similitude of properties in the profile's boreholes, and a column of soil to be used in the local site response will be generated.

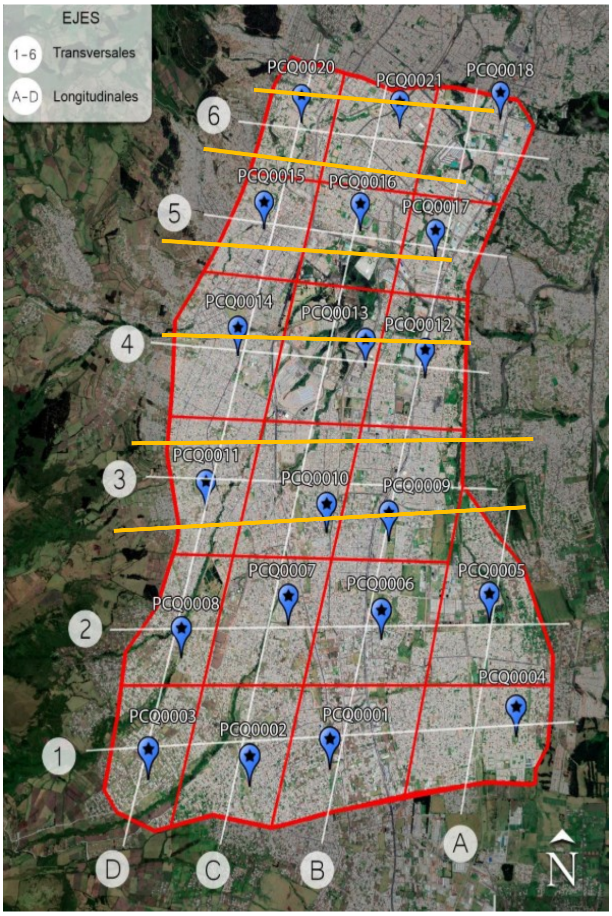

Figure 173. Cross-sectional and Longitudinal Geotechnical profiles

1. *Profile axis 1:* PCQ0003 – PCQ0001 – PCQ0002 – PCQ0004
2. *Profile axis 2:* PCQ0008 – PCQ0007 – PCQ0006 – PCQ0005
3. *Profile axis 3:* PCQ0011 – PCQ0010 – PCQ0009
4. *Profile axis 4:* PCQ0014 – PCQ0013 – PCQ0012
5. *Profile axis 5:* PCQ0015 – PCQ0016 – PCQ0017
6. *Profile axis 6:* PCQ0020 – PCQ0021 – PCQ0018

The depth of the basin in the south of Quito, based on the research performed by (Pacheco et al. 2022), is variable. For this reason, the profiles nearer the stations analyzed by (Pacheco et al. 2022) were given the depth on each station:

- Profile axis 1 and 2: Station HLUZ
- Profile axis 3 and 4: Station QUIB
- Profile axis 5 and 6: Station ARGE

5.2.1. Soil columns

5.2.1.1. Zone A - PCQ0001-PCQ0002-PCQ0003-PCQ0007- PCQ0008

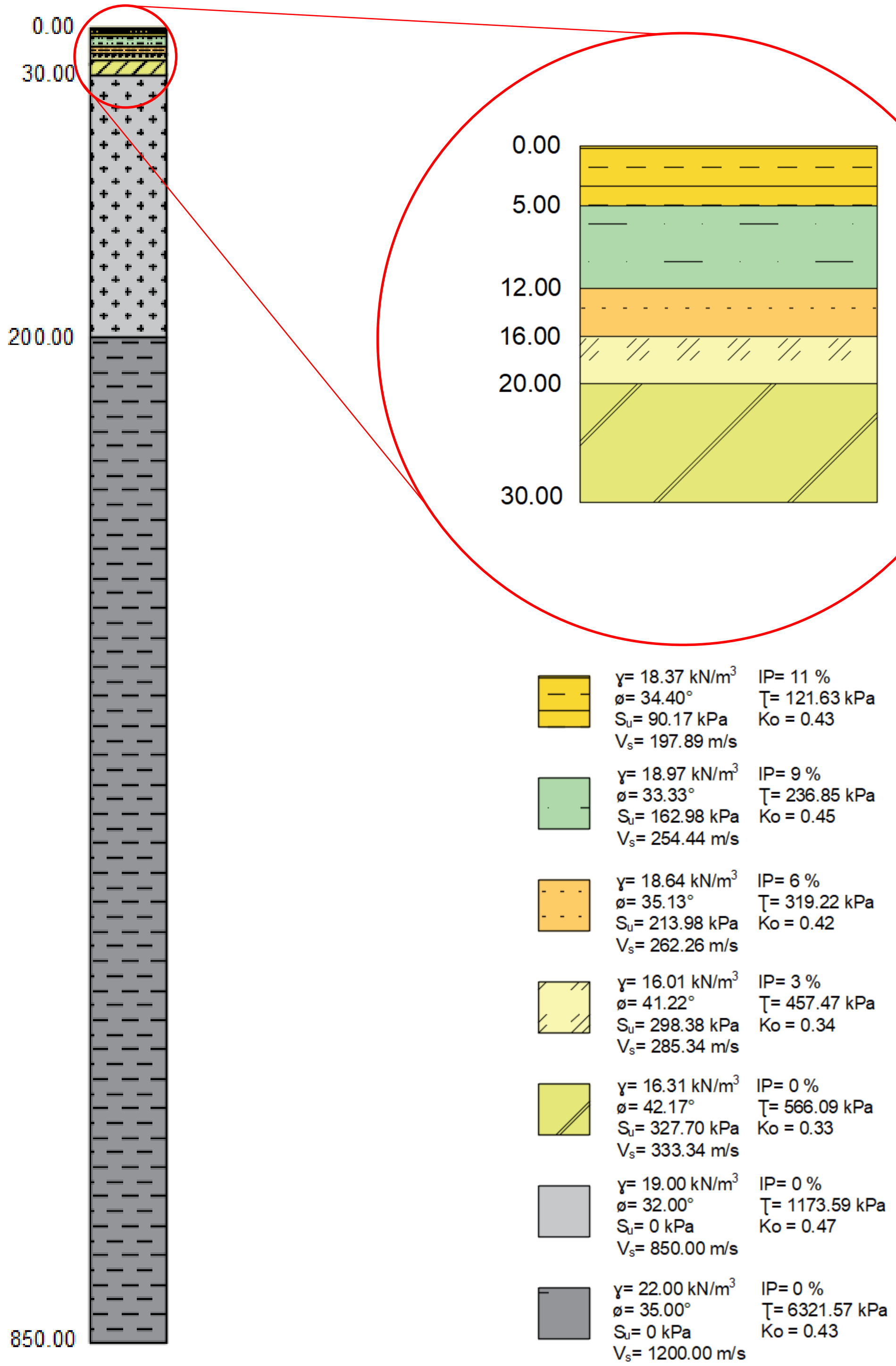

Figure 174. Soil column of Zone A

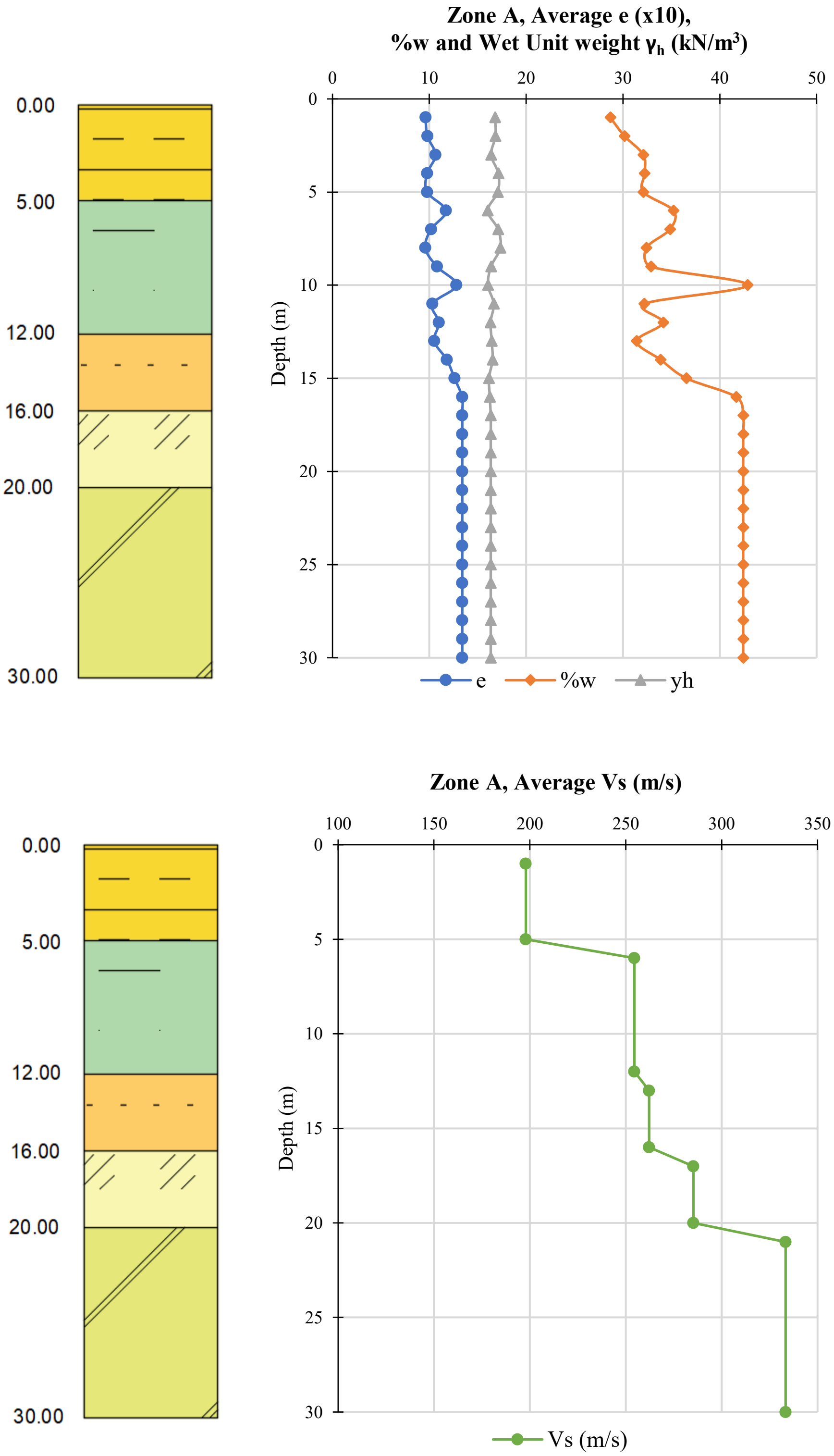

Figure 175. Cross-sectional and Longitudinal Geotechnical profiles

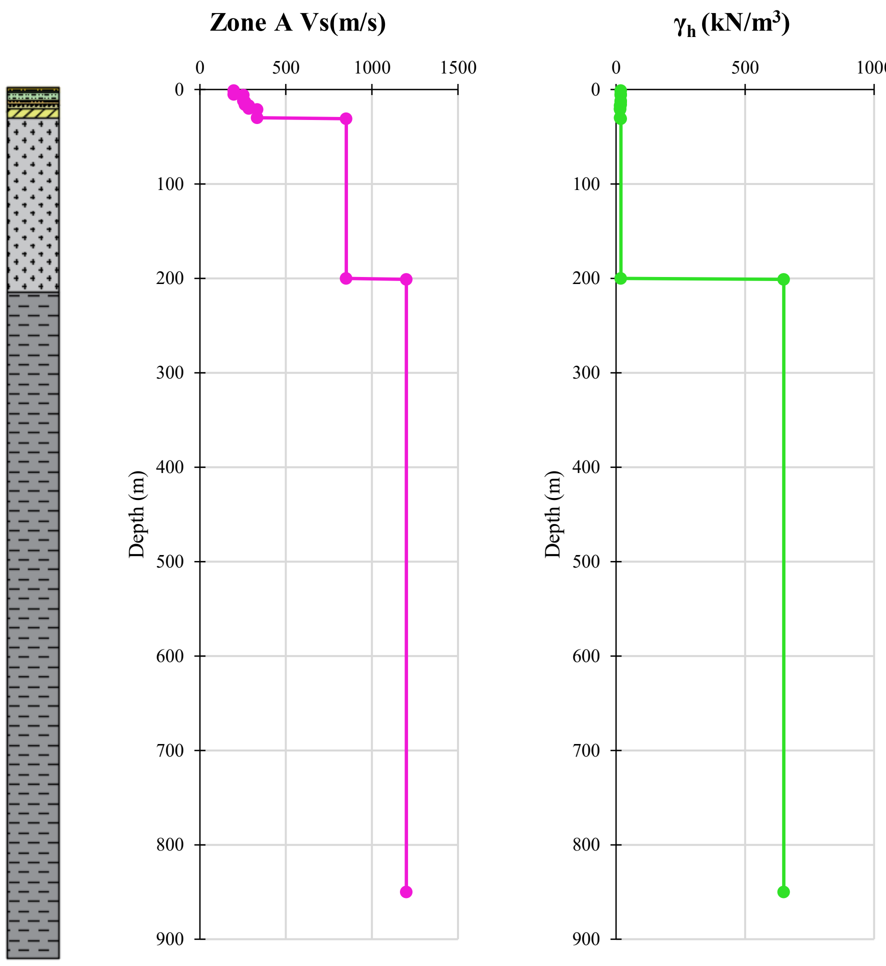

Figure 176. Cross-sectional and Longitudinal Geotechnical profiles

Table 15. Summary of Zone A

Zone A									
Depth (m)	Width (m)	γ (kN/m^3)	φ (°)	Su (kPa)	Vs (m/s)	$\sigma_{m\ prom}$ (kPa)	τ (kPa)	Ko	PI (%)
1.00 5.00	5.00	18.37	34.40	90.17	197.89	45.94	121.63	0.43	11
6.00 12.00	7.00	18.97	33.33	162.98	254.44	112.32	236.85	0.45	9
13.00 16.00	4.00	18.64	35.13	213.98	262.26	149.60	319.22	0.42	6
17.00 20.00	4.00	16.01	41.22	298.38	285.34	181.61	457.47	0.34	3
21.00 30.00	10.00	16.31	42.17	327.70	333.34	263.14	566.09	0.33	0
31.00 200.00	170.00	19.00	32.00	0.00	850.00	1878.14	1173.59	0.47	0
201.00 850.00	650.00	22.00	35.00	0.00	1200.00	9028.14	6321.57	0.43	0

Table 16. Summary of the dynamic parameters of dry samples from Zone A

Zone A (Dry)						
Stratum	**Depth (m)**	**γ (kg/m^3)**	**Vs (m/s)**	**Go (kPa)**	**Damping (%)**	
					Min	**Max**
1	0,00 - 5,00	1847,23	49,91	4601,97	4,84	9,46
2	5,00 - 12,00	1540,88	24,45	921,20	6,56	13,92
3	12,00 - 16,00	1460,94	25,48	948,56	1,74	16,85
4	16,00 - 20,00	1519,83	65,96	6612,07	2,58	10,37
5	20,00 - 30,00	1519,83	65,96	6612,07	2,58	10,37

Table 17. Summary of the dynamic parameters of remolded samples from Zone A

Zone A (Remolded)						
Stratum	**Depth (m)**	**γ (kg/m^3)**	**Vs (m/s)**	**Go (kPa)**	**Damping (%)**	
					Min	**Max**
1	0,00 - 5,00	1916,60	55,14	5806,38	4,69	9,09
2	5,00 - 12,00	1912,63	67,42	8694,29	3,09	6,83
3	12,00 - 16,00	1826,38	43,32	3427,31	2,06	8,32
4	16,00 - 20,00	1488,51	25,27	950,43	4,54	9,60
5	20,00 - 30,00	1488,51	25,27	950,43	4,54	9,60

5.2.1.2.Zone B- PCQ0005-PCQ0006-PCQ0007-PCQ0008

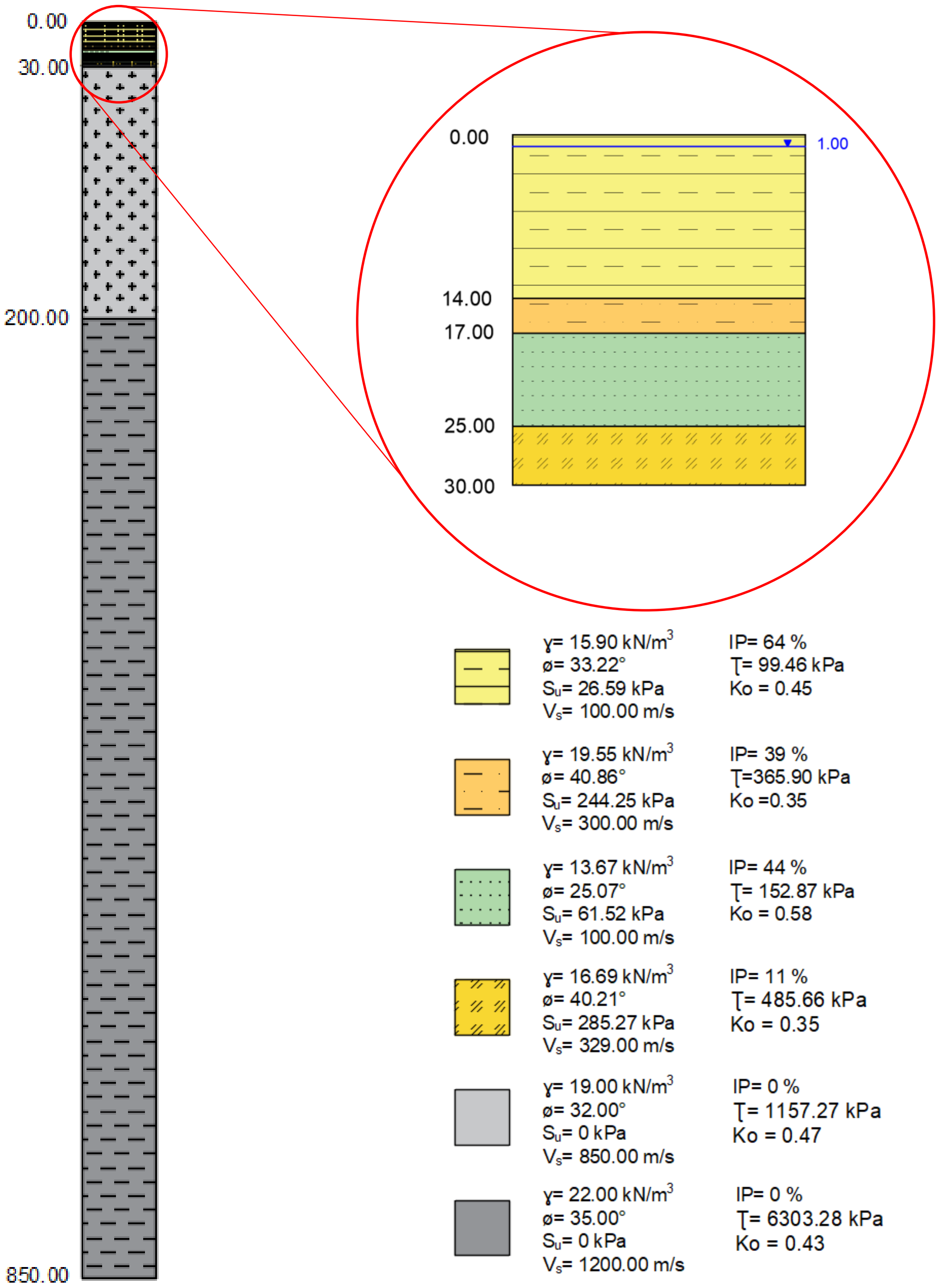

Figure 177. Soil Column of Zone B

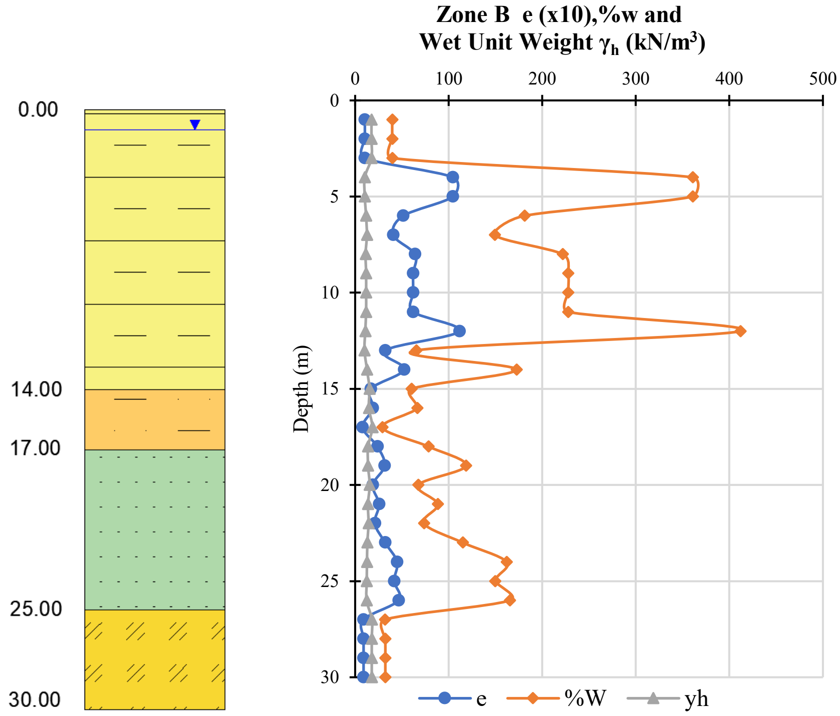

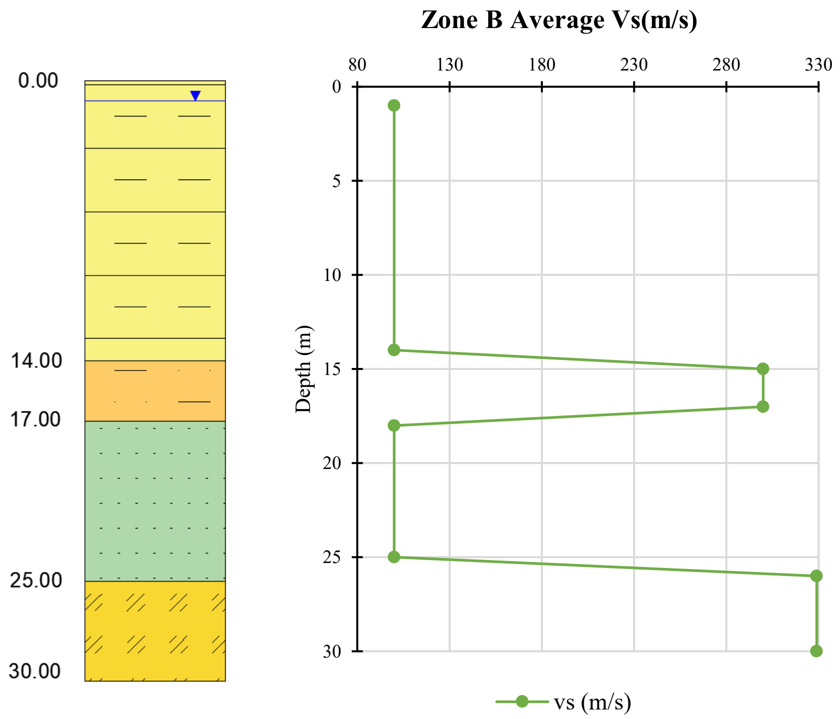

Figure 178. Cross-sectional and Longitudinal Geotechnical profiles

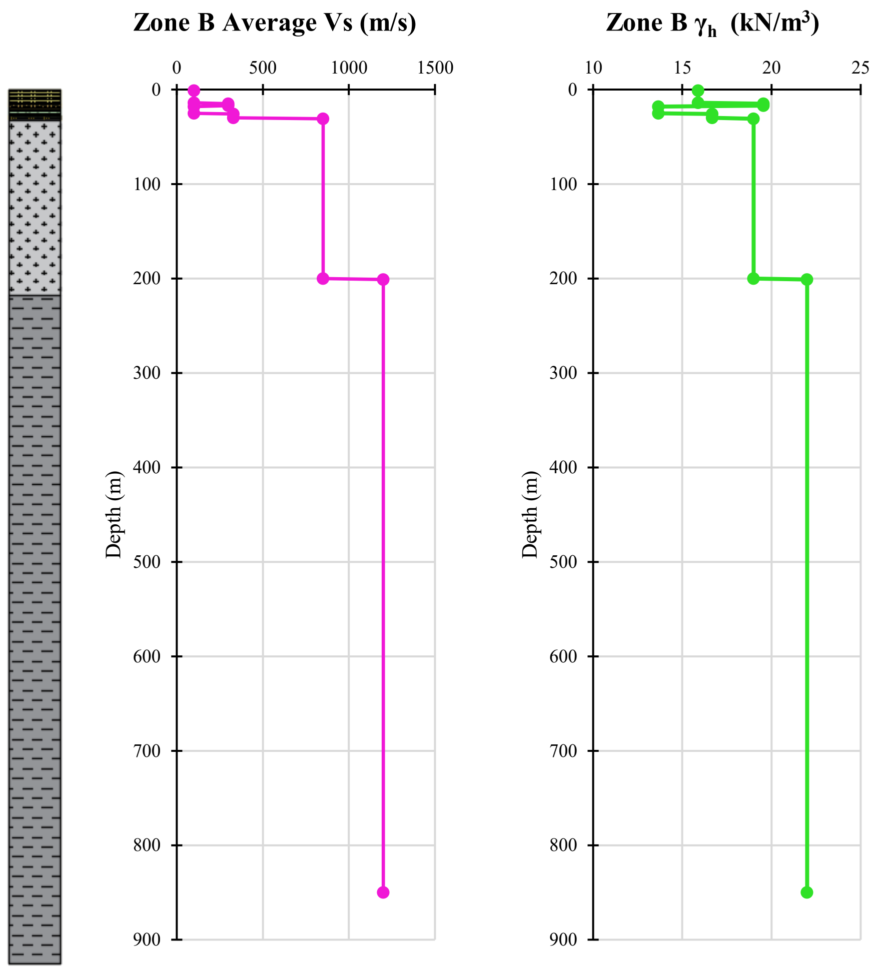

Figure 179. Cross-sectional and Longitudinal Geotechnical profiles

Table 18. Summary of Zone B

Zone B									
Depth (m)	Width (m)	γ (kN/m^3)	φ (°)	Su (kPa)	Vs (m/s)	$\sigma_{m\ prom}$ (kPa)	τ (kPa)	Ko	PI (%)
1.00 14.00	14.00	15.90	33.22	26.59	100.00	111.29	99.46	0.45	64
15.00 17.00	3.00	19.55	40.86	244.25	300.00	140.61	365.90	0.35	39
18.00 25.00	8.00	13.67	25.07	61.52	100.00	195.29	152.87	0.58	44
26.00 30.00	5.00	16.69	40.21	285.27	329.00	237.02	485.66	0.35	11
31.00 200.00	170.00	19.00	32.00	0.00	850.00	1852.02	1157.27	0.47	0
201.00 850.00	650.00	22.00	35.00	0.00	1200.00	9002.02	6303.28	0.43	0

Table 19. Summary of the dynamic parameters of dry samples from Zone B

Zone B (Dry)						
Stratum	Depth (m)	γ (kg/m^3)	Vs (m/s)	Go (kPa)	Damping (%)	
					Min	Max
1	0,00 - 14,00	1325,54	41,87	2323,72	3,17	6,29
2	14,00 - 17,00	1246,09	35,84	1600,94	4,94	7,46
3	17,00 - 25,00	1497,49	14,53	316,21	4,95	7,47
4	25,00 - 30,00	1641,64	13,86	315,48	5,69	8,22

Table 20. Summary of the dynamic parameters of remolded samples from Zone B

Zone B (Remolded)						
Stratum	Depth (m)	γ (kg/m^3)	Vs (m/s)	Go (kPa)	Damping (%)	
					Min	Max
1	0,00 - 14,00	1323,45	37,93	2310,60	2,18	6,83
2	14,00 - 17,00	1621,52	33,70	2272,75	3,55	8,18
3	17,00 - 25,00	1683,84	52,06	3906,27	3,46	8,40
4	25,00 - 30,00	1796,08	67,29	7825,27	5,33	10,73

5.2.1.3.Zone C – PCQ0005-PCQ0009

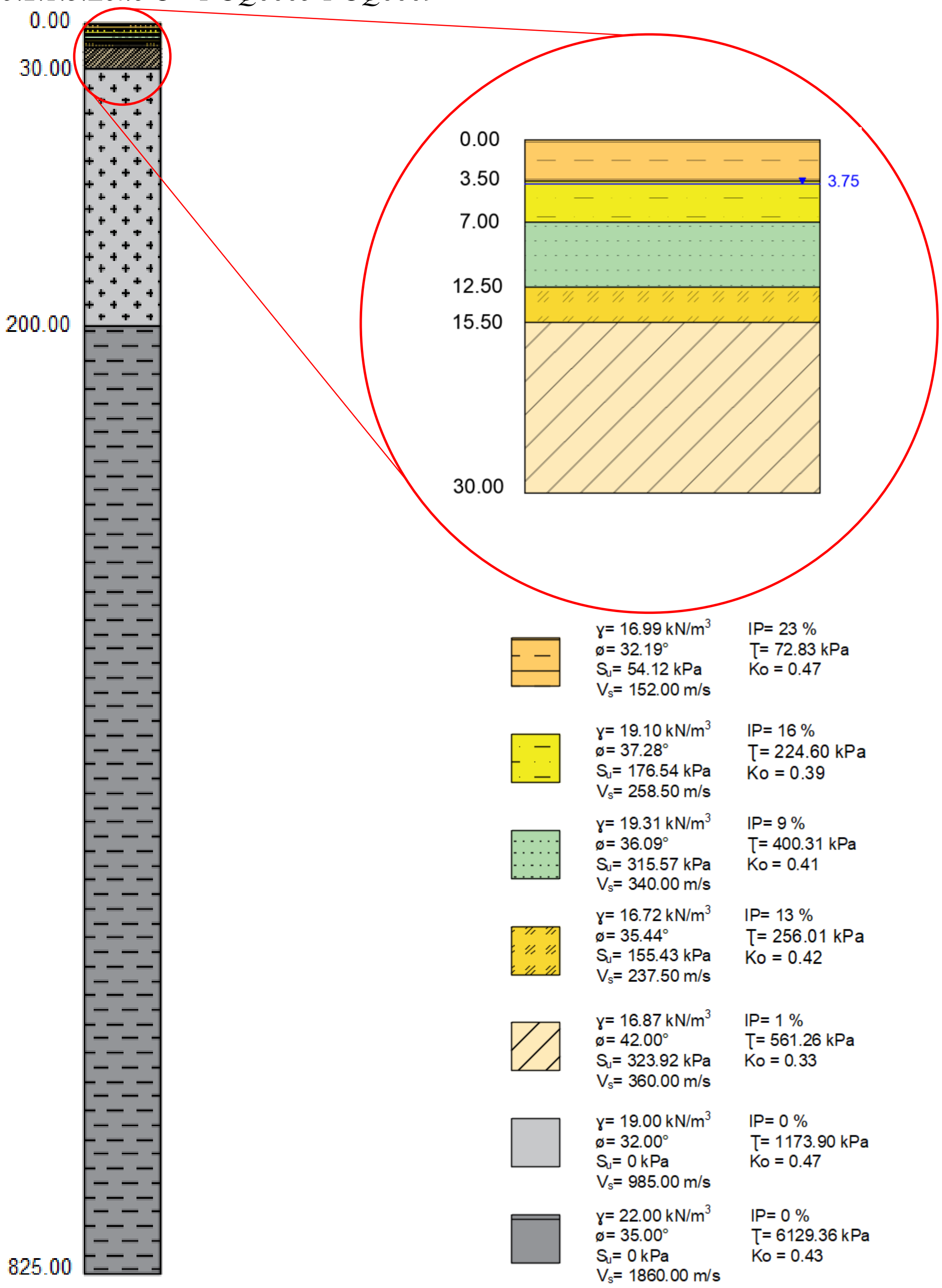

Figure 180. Soil Column of Zone C

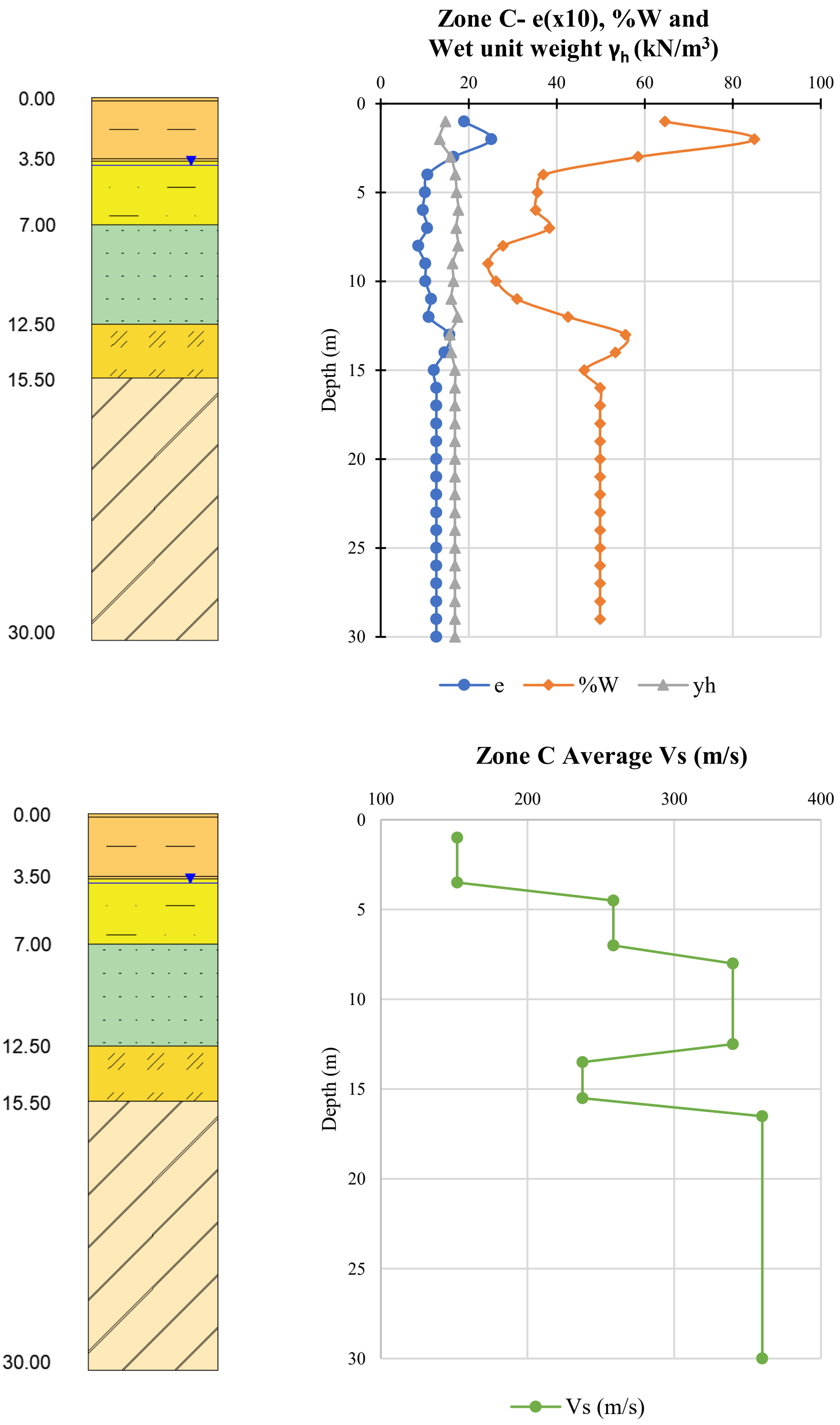

Figure 181. Cross-sectional and Longitudinal Geotechnical profiles

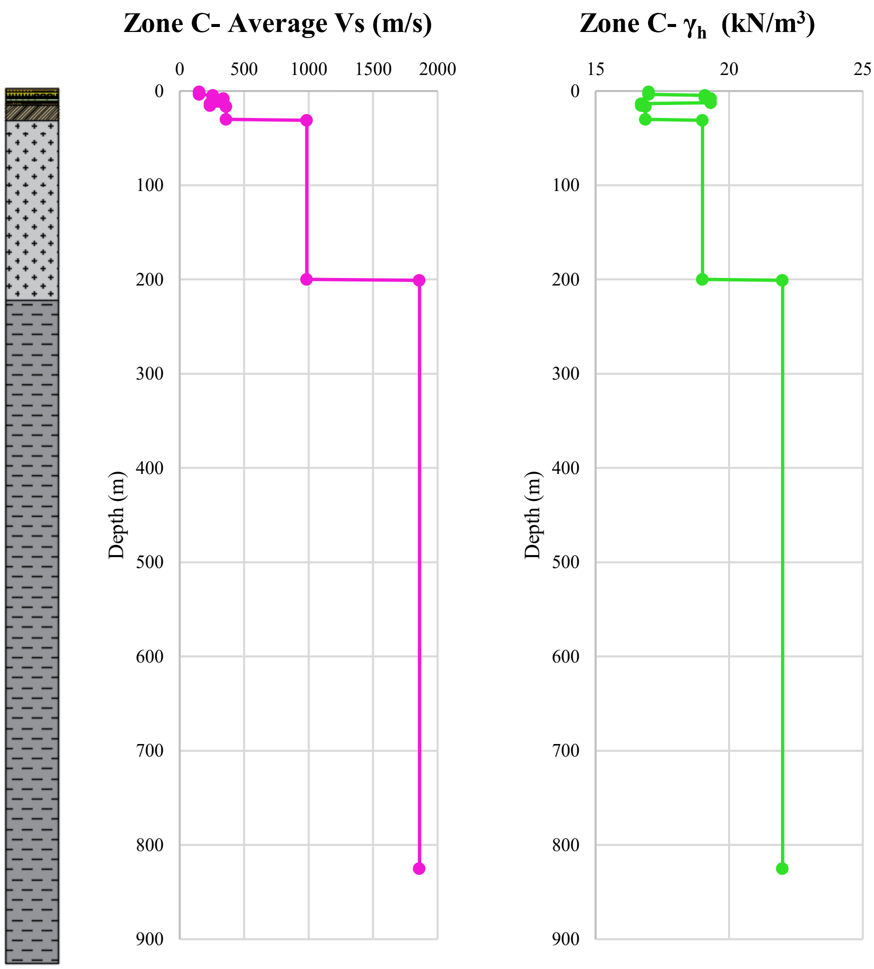

Figure 182. Column 3 Shear wave Vs and Wet Unit Weight

Table 21. Summary of Zone C

Zone C									
Depth (m)	Width (m)	γ (kN/m^3)	φ (°)	Su (kPa)	Vs (m/s)	$\sigma_{m\ prom}$ (kPa)	τ (kPa)	Ko	PI (%)
1.00 3.50	3.50	16.99	32.19	54.12	152.00	29.73	72.83	0.47	23
4.50 7.00	3.50	19.10	37.28	176.54	258.50	63.15	224.60	0.39	16
8.00 12.50	5.50	19.31	36.09	315.57	340.00	116.25	400.31	0.41	9
13.50 15.50	3.00	16.72	35.44	155.43	237.50	141.33	256.01	0.42	13
16.50 30.00	14.50	16.87	42.00	323.92	360.00	263.63	561.26	0.33	1
31.00 200.00	170.00	19.00	32.00	0.00	985.00	1878.63	1173.90	0.47	0
201.00 825.00	625.00	22.00	35.00	0.00	1860.00	8753.63	6129.36	0.43	0

Table 22. Summary of the dynamic parameters of dry samples from Zone C

Zone C (Dry)						
Stratum	Depth (m)	γ (kg/m^3)	Vs (m/s)	Go (kPa)	Damping (%)	
					Min	Max
1	0,00 - 3,50	1738,26	23,56	964,85	4,52	7,72
2	3,50 - 7,00	1594,09	19,06	579,25	5,00	8,31
3	7,00 - 12,50	1462,80	28,09	1154,08	6,47	8,71
4	12,50 - 15,50	1346,15	23,02	713,34	4,28	5,49
5	15,50 - 30,00	1725,15	28,88	1438,89	5,60	9,91

Table 23. Summary of the dynamic parameters of remolded samples from Zone C

Zone C (Remolded)						
Stratum	Depth (m)	γ (kg/m^3)	Vs (m/s)	Go (kPa)	Damping (%)	
					Min	Max
1	0,00 - 3,50	1760,77	28,76	1456,75	5,32	8,33
2	3,50 - 7,00	1923,21	62,06	7407,77	5,35	8,44
3	7,00 - 12,50	1872,14	82,81	12837,08	5,35	8,60
4	12,50 - 15,50	1763,73	50,27	4378,13	3,42	9,30
5	15,50 - 30,00	1614,32	34,78	2151,11	5,31	8,02

5.2.1.4.Zone D- PCQ0006

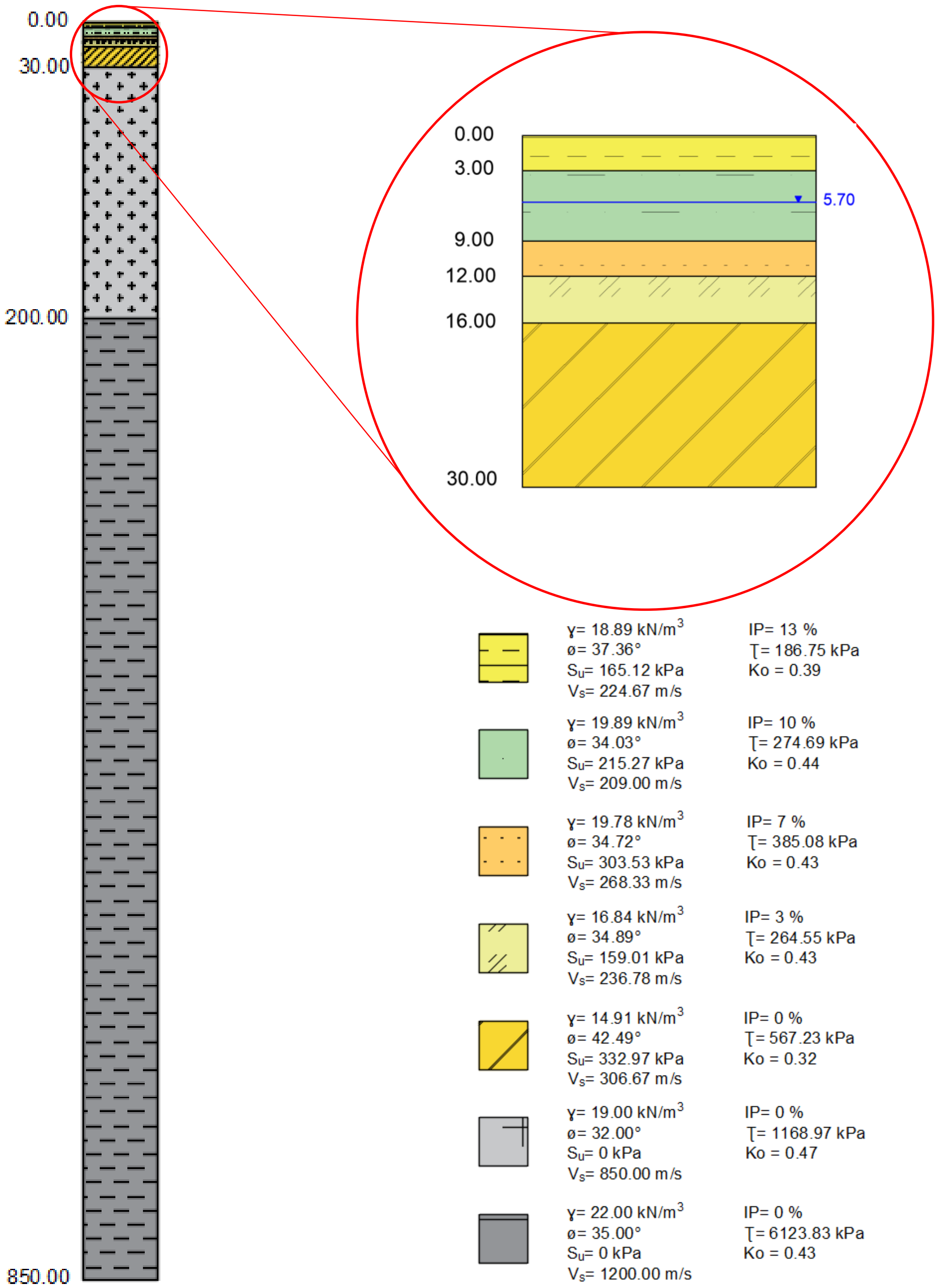

Figure 183. Soil Column of Zone D

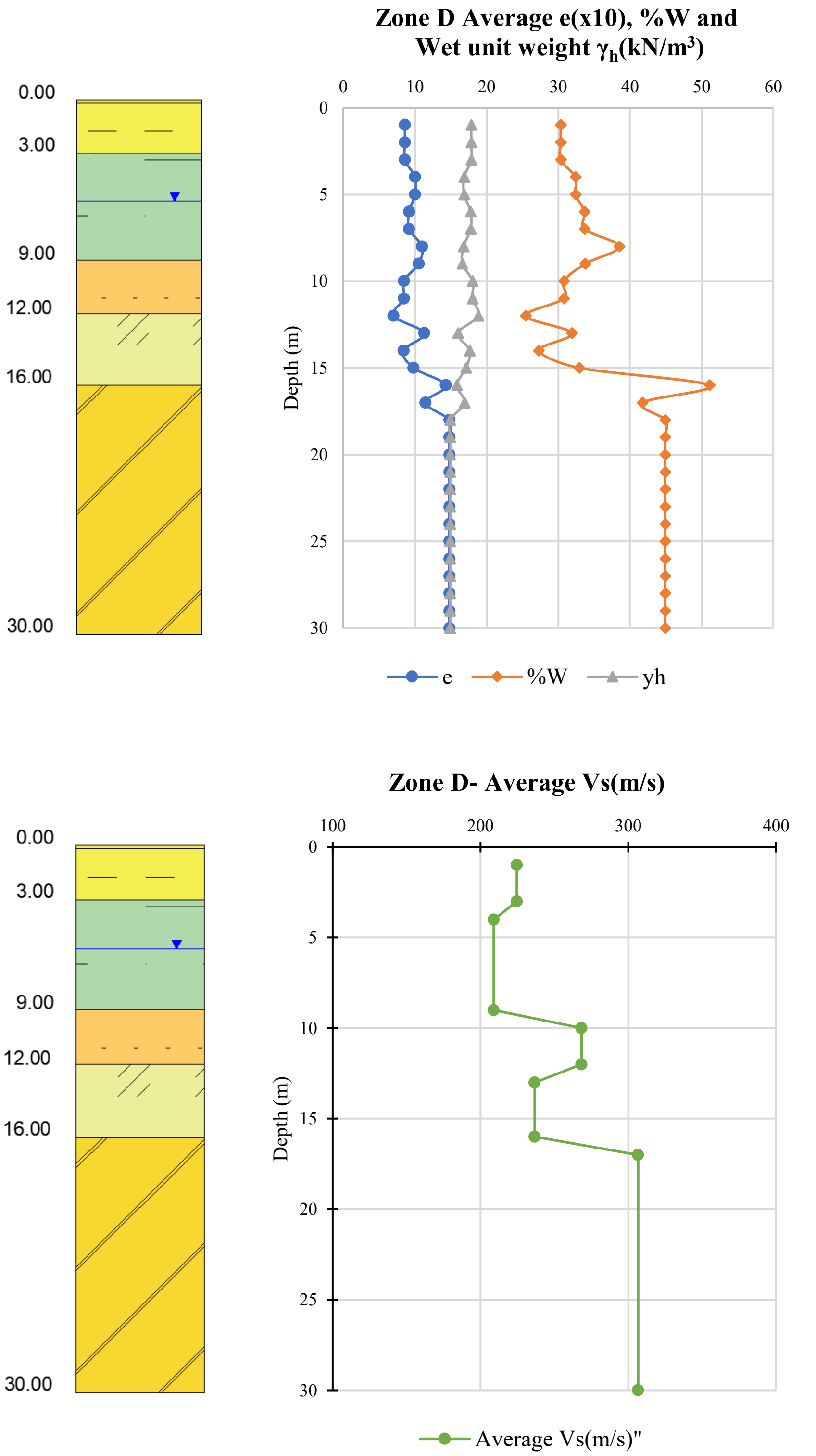

Figure 184. Cross-sectional and Longitudinal Geotechnical profiles

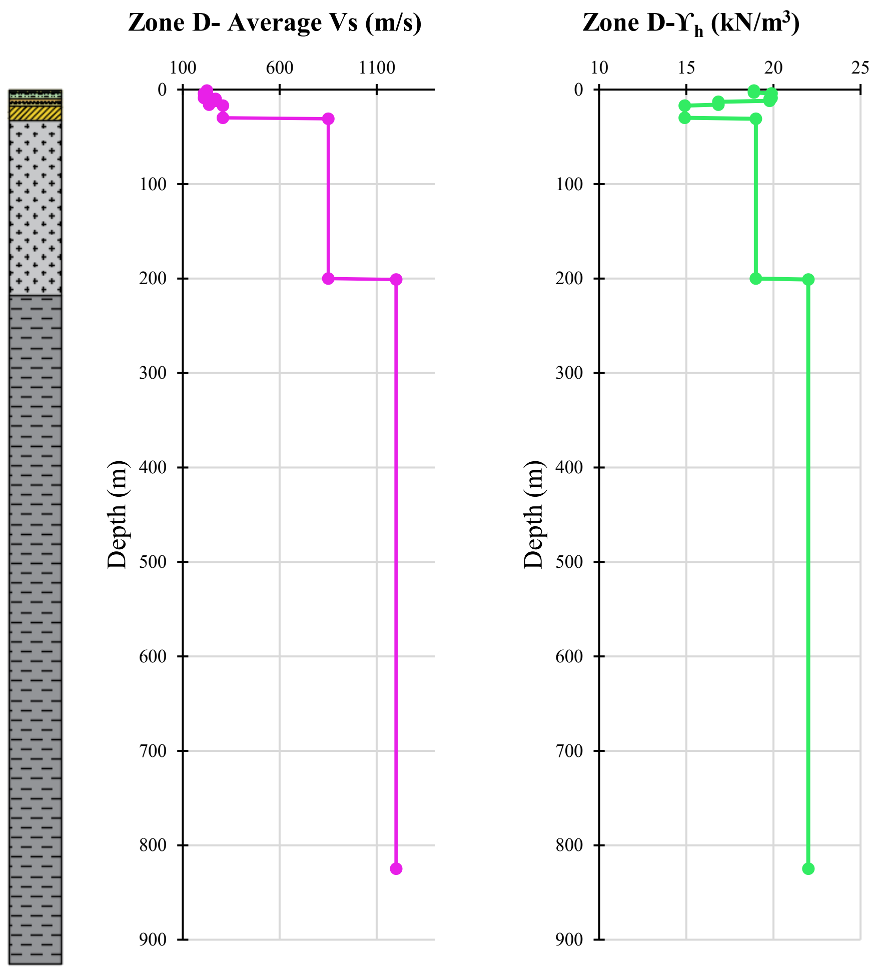

Figure 185. Cross-sectional and Longitudinal Geotechnical profiles

Table 24. Summary of Zone D

Zone D									
Depth (m)	Width (m)	γ (kN/m^3)	φ (°)	Su (kPa)	Vs (m/s)	$\sigma_{m\ prom}$ (kPa)	τ (kPa)	Ko	PI (%)
1.00 3.00	3.00	18.89	37.36	165.12	224.67	28.33	186.75	0.39	13
4.00 9.00	6.00	19.89	34.03	215.27	209.00	88.01	274.69	0.44	10
10.00 12.00	3.00	19.78	34.72	303.53	268.33	117.69	385.08	0.43	7
13.00 16.00	4.00	16.84	34.89	159.01	236.78	151.37	264.55	0.43	3
17.00 30.00	14.00	14.91	42.49	332.97	306.67	255.74	567.23	0.32	0
31.00 200.00	170.00	19.00	32.00	0.00	850.00	1870.74	1168.97	0.47	0
201.00 825.00	625.00	22.00	35.00	0.00	1200.00	8745.74	6123.83	0.43	0

Table 25. Summary of the dynamic parameters of dry samples from Zone D

Zone D (Dry)						
Stratum	**Depth (m)**	**γ (kg/m³)**	**Vs (m/s)**	**Go (kPa)**	**Damping (%)**	
					Min	**Max**
1	0,00 - 3,00	1847,23	49,91	4601,97	4,84	9,46
2	3,00 - 9,00	1540,88	24,45	921,20	6,56	13,92
3	9,00 - 12,00	1460,94	25,48	948,56	1,74	16,85
4	12,00 - 16,00	1716,60	44,80	3445,05	1,36	7,11
5	16,00 - 30,00	1716,60	44,80	3445,05	1,36	7,11

Table 26. Summary of the dynamic parameters of remolded samples from Zone D

Zone D (Remolded)						
Stratum	**Depth (m)**	**γ (kg/m³)**	**Vs (m/s)**	**Go (kPa)**	**Damping (%)**	
					Min	**Max**
1	0,00 - 3,00	1916,60	55,14	5806,38	4,69	9,09
2	3,00 - 9,00	1912,63	67,42	8694,29	3,09	6,83
3	9,00 - 12,00	1826,38	43,32	3427,31	2,06	8,32
4	12,00 - 16,00	1771,40	42,85	3251,82	2,81	10,56
5	16,00 - 30,00	1771,40	42,85	3251,82	2,81	10,56

5.2.1.5.Zone E- PCQ010-PCQ013-PCQ016

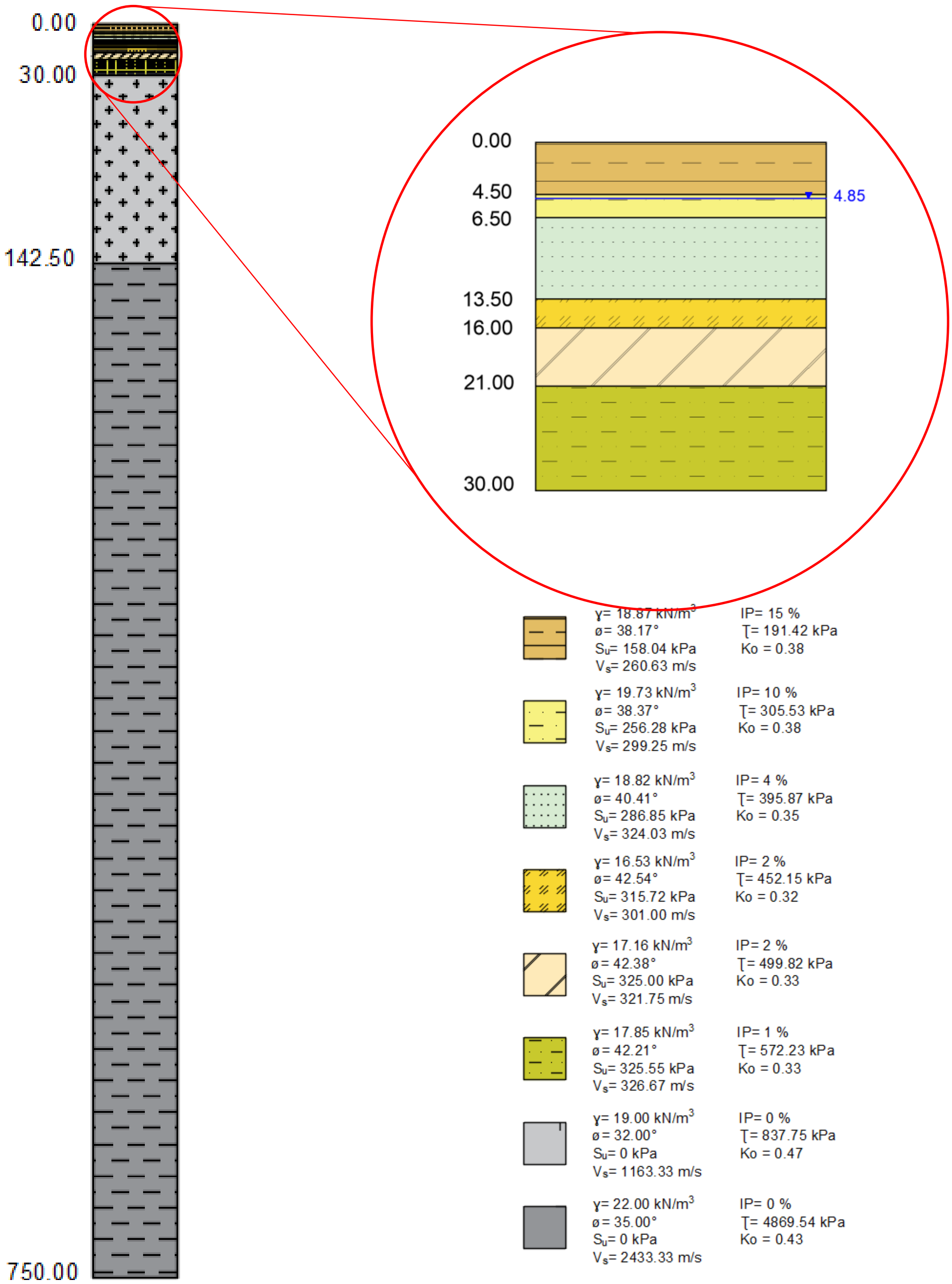

Figure 186. Soil Column of Zone E

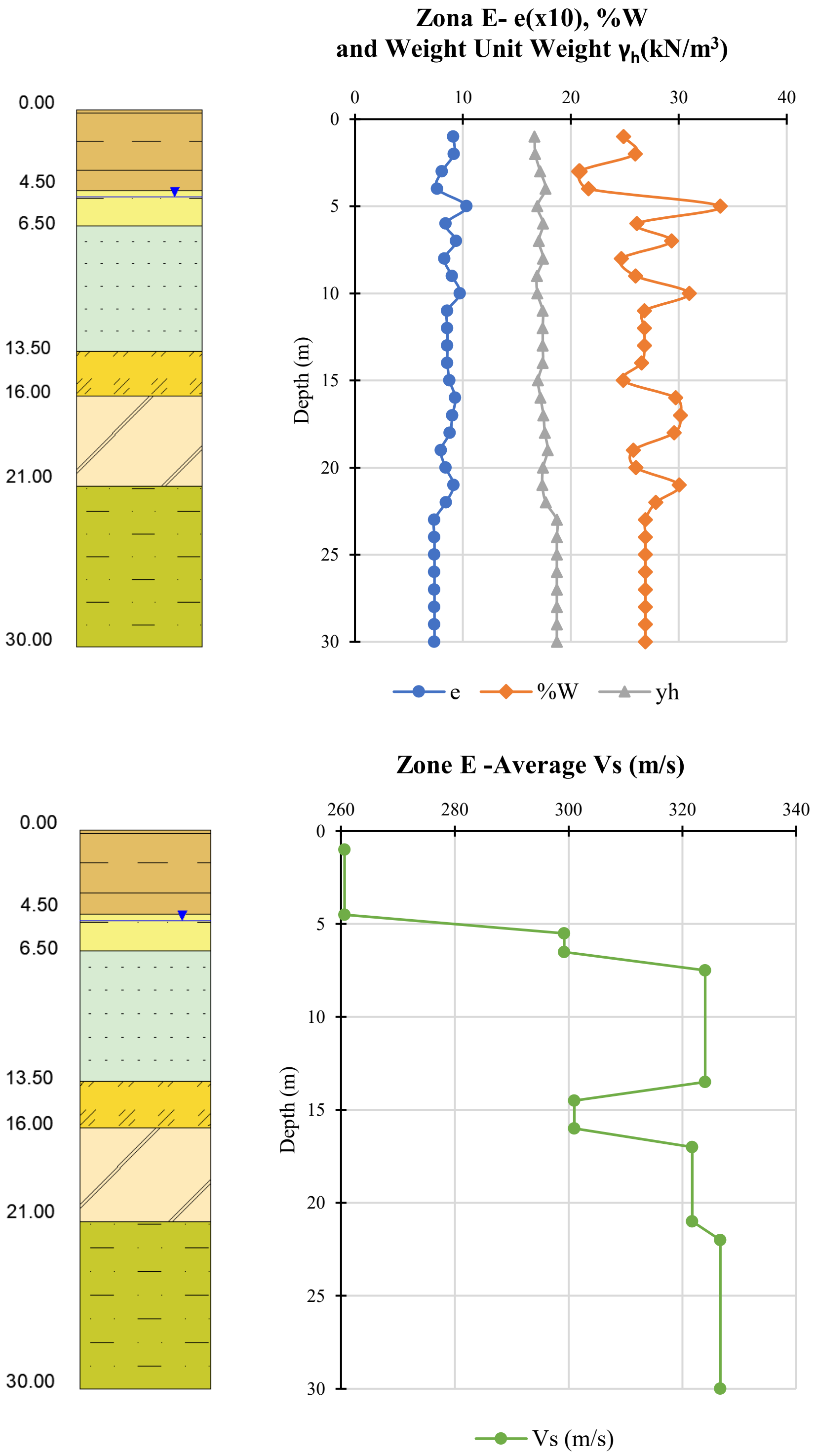

Figure 187. Cross-sectional and Longitudinal Geotechnical profiles

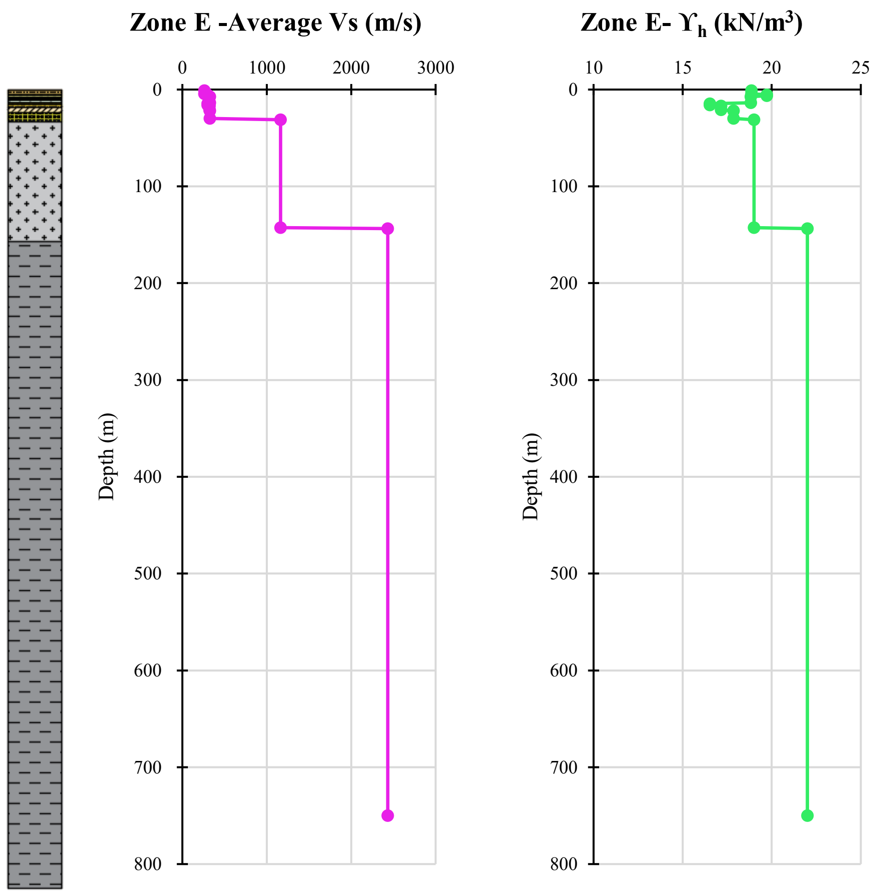

Figure 188. Cross-sectional and Longitudinal Geotechnical profiles

Table 27. Summary of Zone E

Zone E									
Depth (m)	Width (m)	γ (kN/m^3)	φ (°)	Su (kPa)	Vs (m/s)	$\sigma_{m\ prom}$ (kPa)	τ (kPa)	Ko	PI (%)
1.00 4.50	4.50	18.87	38.17	158.04	260.63	42.46	191.42	0.38	15
5.50 6.50	2.00	19.73	38.37	256.28	299.25	62.19	305.53	0.38	10
7.50 13.50	7.00	18.82	40.41	286.85	324.03	128.05	395.87	0.35	4
14.50 16.00	2.50	16.53	42.54	315.72	301.00	148.70	452.15	0.32	2
17.00 21.00	5.00	17.16	42.38	325.00	321.75	191.60	499.82	0.33	2
22.00 30.00	9.00	17.85	42.21	325.55	326.67	271.92	572.23	0.33	1
31.00 142.50	112.50	19.00	32.00	0.00	1163.33	1340.67	837.75	0.47	0
143.50 750.00	607.50	22.00	35.00	0.00	2433.33	6954.42	4869.54	0.43	0

Table 28. Summary of the dynamic parameters of dry samples from Zone E

Zone E (Dry)						
Stratum	**Depth (m)**	**γ (kg/m³)**	**Vs (m/s)**	**Go (kPa)**	**Damping (%)**	
					Min	**Max**
1	0,00 - 4,50	1847,23	49,91	4601,97	4,84	9,46
2	4,50 - 6,50	1540,88	24,45	921,20	6,56	13,92
3	6,50 - 13,50	1651,66	28,71	1361,37	5,54	8,90
4	13,50 - 16,00	1519,83	65,96	6612,07	2,58	10,37
5	16,00 - 21,00	1660,63	31,31	1628,37	5,36	6,61
6	21,00 - 30,00	1725,15	28,88	1438,89	5,60	9,91

Table 29. Summary of the dynamic parameters of remolded samples from Zone E

Zone E (Remolded)						
Stratum	**Depth (m)**	**γ (kg/m³)**	**Vs (m/s)**	**Go (kPa)**	**Damping (%)**	
					Min	**Max**
1	0,00 - 4,50	1916,60	55,14	5806,38	4,69	9,09
2	4,50 - 6,50	1912,63	67,42	8694,29	3,09	6,83
3	6,50 - 13,50	1843,01	45,01	3734,26	2,01	9,12
4	13,50 - 16,00	1488,51	25,27	950,43	4,54	9,60
5	16,00 - 21,00	1906,68	30,84	1751,10	4,68	7,75
6	21,00 - 30,00	1614,32	34,78	2151,11	5,31	8,02

5.2.1.6.Zone F-PCQ0012

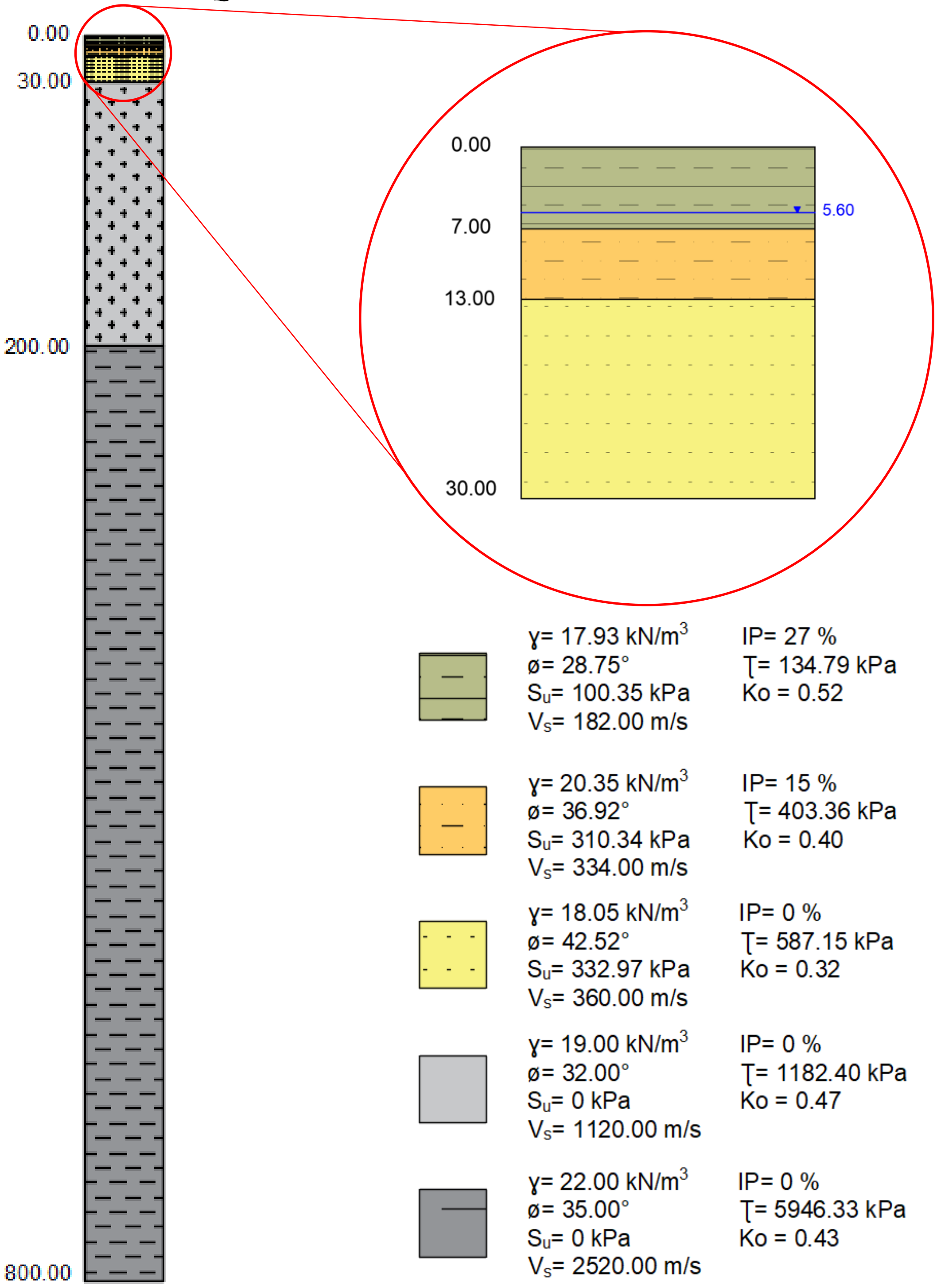

Figure 189. Soil Column of Zone F

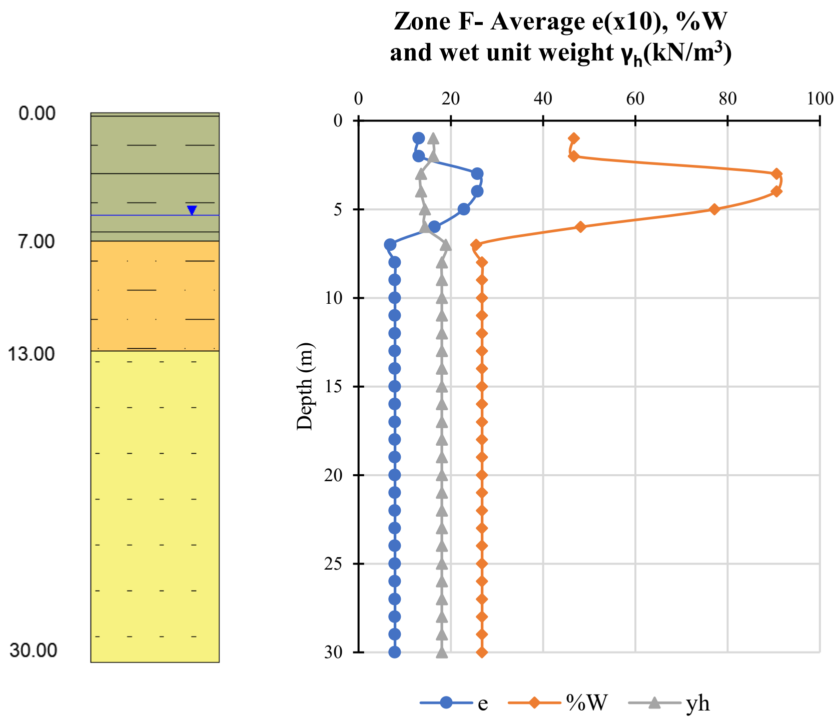

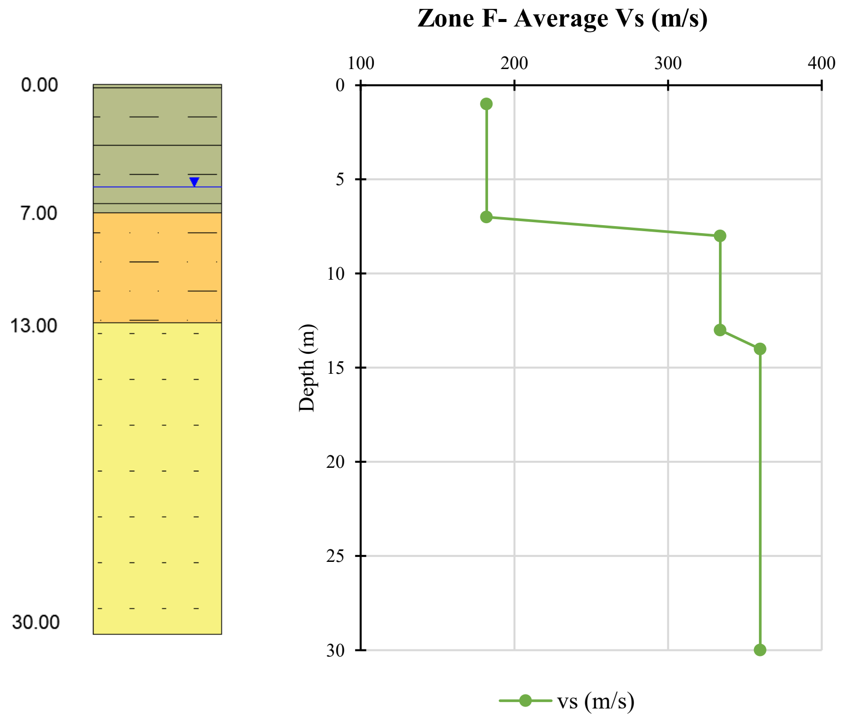

Figure 190. Cross-sectional and Longitudinal Geotechnical profiles

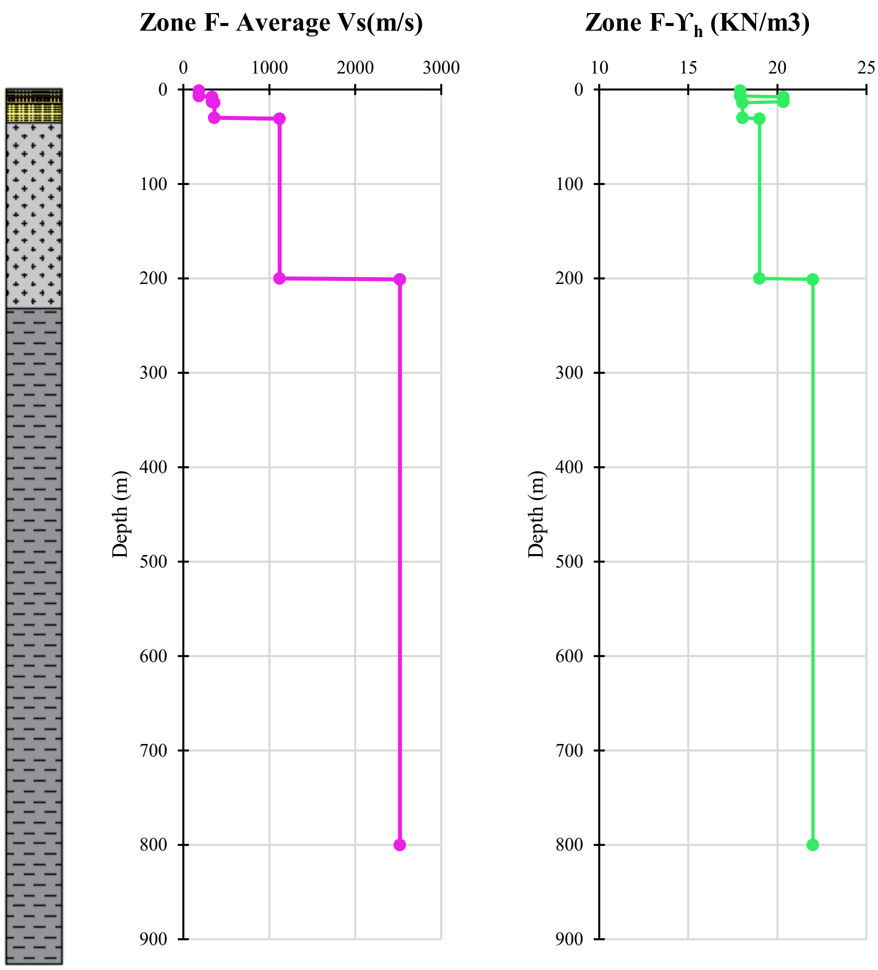

Figure 191. Cross-sectional and Longitudinal Geotechnical profiles

Table 30. Summary of Zone F

Zone F									
Depth (m)	Width (m)	γ (kN/m^3)	φ (°)	Su (kPa)	Vs (m/s)	$\sigma_{m\ prom}$ (kPa)	τ (kPa)	Ko	PI (%)
1.00 7.00	7.00	17.93	28.75	100.35	182.00	62.76	134.79	0.52	27
8.00 13.00	6.00	20.35	36.92	310.34	334.00	123.81	403.36	0.40	15
14.00 30.00	17.00	18.05	42.52	332.97	360.00	277.23	587.15	0.32	0
31.00 200.00	170.00	19.00	32.00	0.00	1120.00	1892.23	1182.40	0.47	0
201.00 800.00	600.00	22.00	35.00	0.00	2520.00	8492.23	5946.33	0.43	0

Table 31. Summary of the dynamic parameters of dry samples from Zone F

Zone F (Dry)						
Stratum	**Depth (m)**	**γ (kg/m³)**	**Vs (m/s)**	**Go (kPa)**	**Damping (%)**	
					Min	**Max**
1	0,00 - 7,00	1818,96	24,76	1114,92	3,33	7,80
2	7,00 - 13,00	2015,19	45,54	4179,40	2,54	7,52
3	13,00 - 30,00	1594,60	18,44	542,17	3,93	7,56

Table 32. Summary of the dynamic parameters of remolded samples from Zone F

Zone F (Remolded)						
Stratum	**Depth (m)**	**γ (kg/m³)**	**Vs (m/s)**	**Go (kPa)**	**Damping (%)**	
					Min	**Max**
1	0,00 - 7,00	1766,53	34,80	2177,64	4,80	9,78
2	7,00 - 13,00	1833,67	44,29	3596,30	5,78	11,85
3	13,00 - 30,00	1831,67	58,17	6228,16	6,00	9,82

5.2.1.7.Zone G – PCQ012

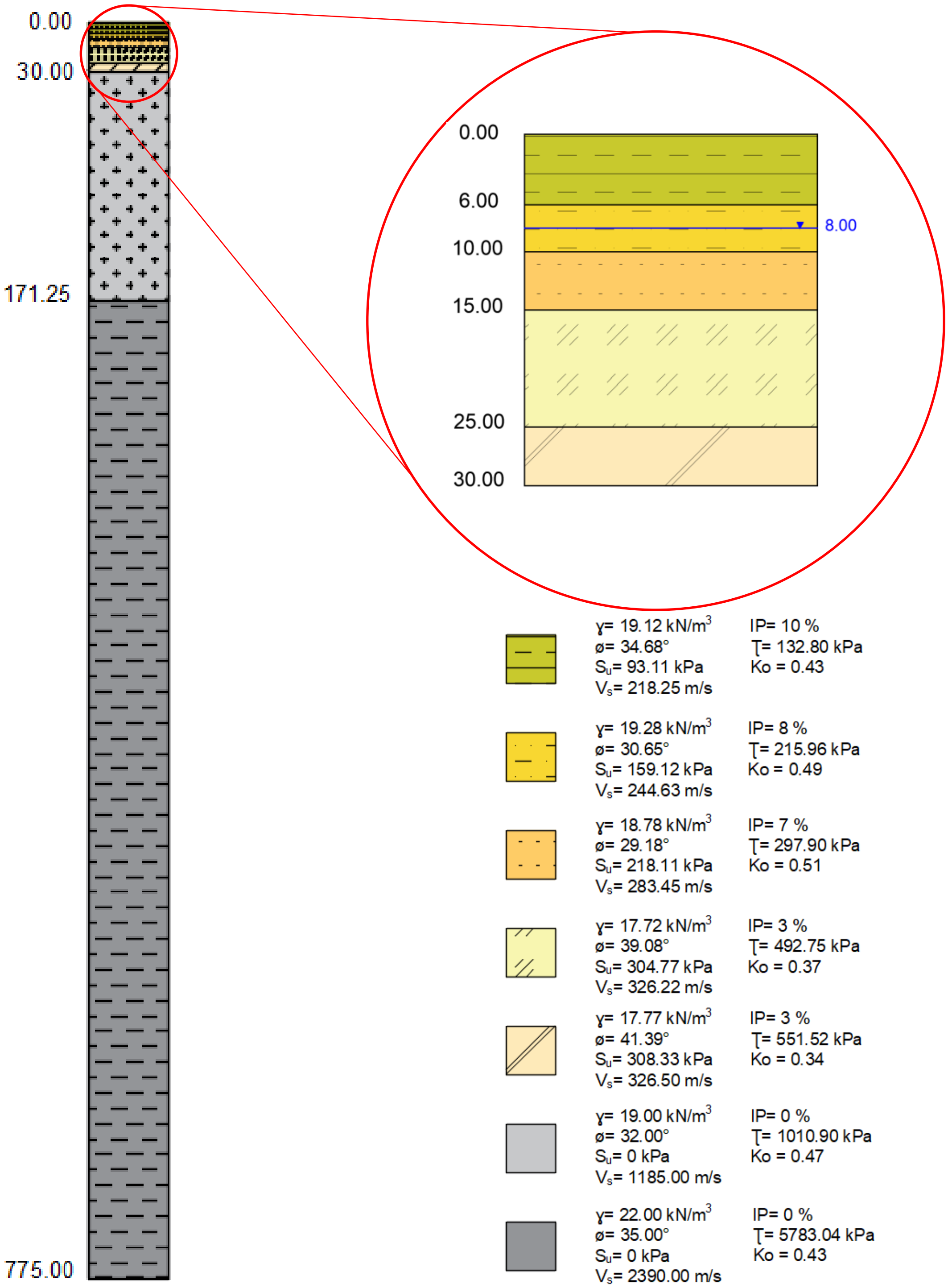

Figure 192. Soil Column of Zone G

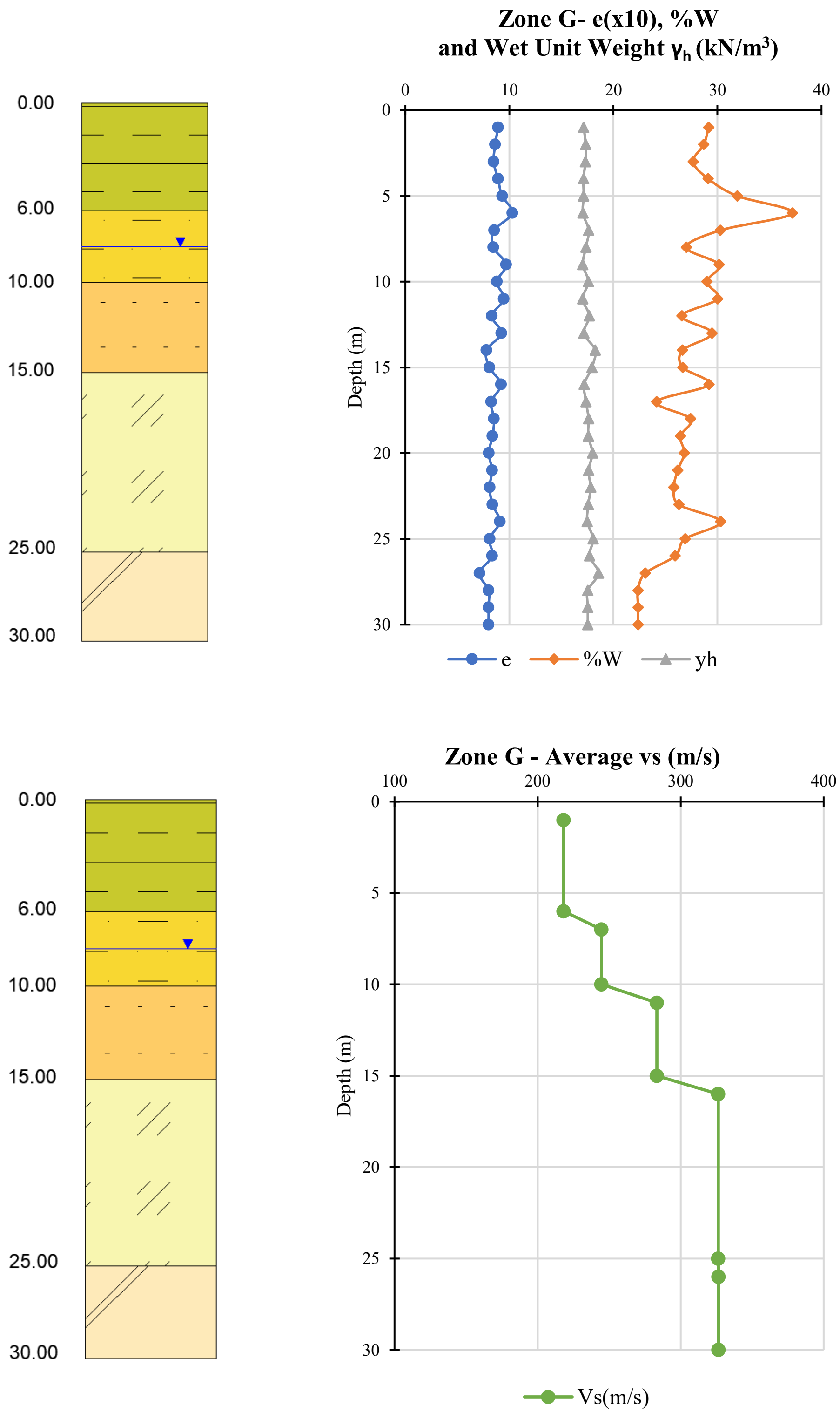

Figure 193. Cross-sectional and Longitudinal Geotechnical profiles

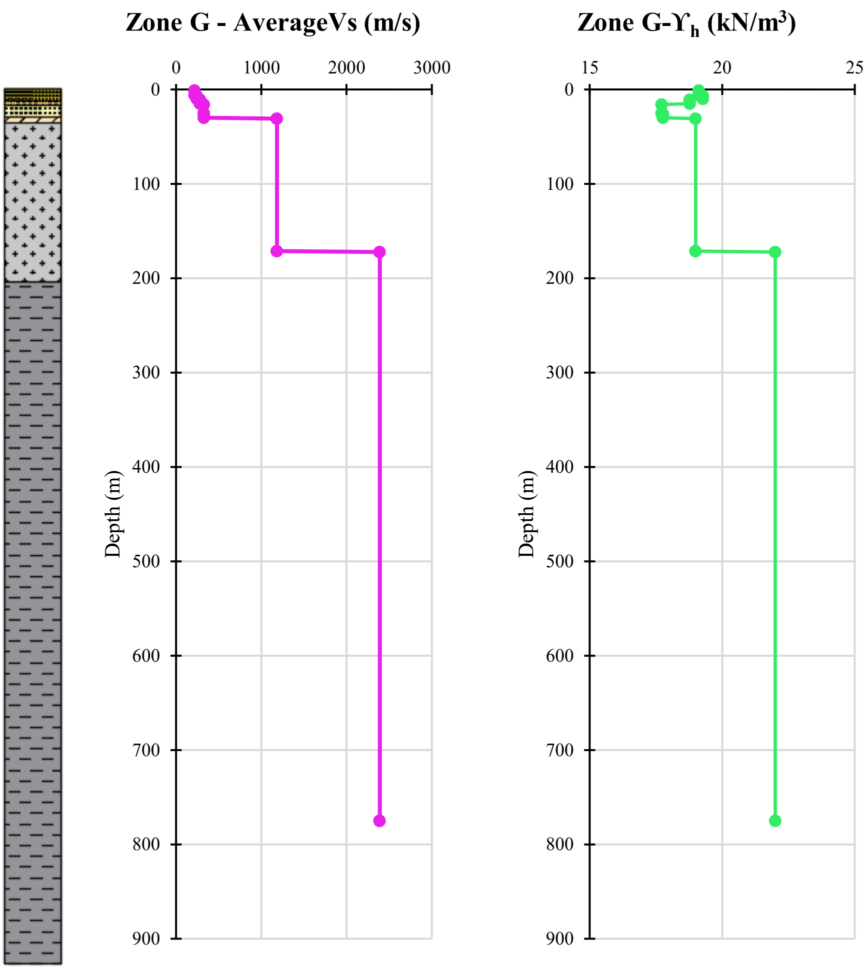

Figure 194. Cross-sectional and Longitudinal Geotechnical profiles

Table 33. Summary of Zone G

Zone G									
Depth (m)	Width (m)	γ (kN/m³)	φ (°)	Su (kPa)	Vs (m/s)	$\sigma_{m\ prom}$ (kPa)	τ (kPa)	Ko	PI (%)
1.00 6.00	6.00	19.12	34.68	93.11	218.25	57.36	132.80	0.43	10
7.00 10.00	4.00	19.28	30.65	159.12	244.63	95.92	215.96	0.49	8
11.00 15.00	5.00	18.78	29.18	218.11	283.45	142.87	297.90	0.51	7
16.00 25.00	10.00	17.72	39.08	304.77	326.22	231.49	492.75	0.37	3
26.00 30.00	5.00	17.77	41.39	308.33	326.50	275.91	551.52	0.34	3
31.00 171.25	141.25	19.00	32.00	0.00	1185.00	1617.78	1010.90	0.47	0
172.25 775.00	603.75	22.00	35.00	0.00	2390.00	8259.03	5783.04	0.43	0

Table 34. Summary of the dynamic parameters of dry samples from Zone G

Zone G (Dry)						
Stratum	**Depth (m)**	**γ (kg/m^3)**	**Vs (m/s)**	**Go (kPa)**	**Damping (%)**	
					Min	**Max**
1	0,00 - 6,00	1847,23	49,91	4601,97	4,84	9,46
2	6,00 - 10,00	1540,88	24,45	921,20	6,56	13,92
3	10,00 - 15,00	1460,94	25,48	948,56	1,74	16,85
4	15,00 - 25,00	1660,63	31,31	1628,37	5,36	6,61
5	25,00 - 30,00	1725,15	28,88	1438,89	5,60	9,91

Table 35. Summary of the dynamic parameters of remolded samples from Zone G

Zone G (Remolded)						
Stratum	**Depth (m)**	**γ (kg/m^3)**	**Vs (m/s)**	**Go (kPa)**	**Damping (%)**	
					Min	**Max**
1	0,00 - 6,00	1916,60	55,14	5806,38	4,69	9,09
2	6,00 - 10,00	1912,63	67,42	8694,29	3,09	6,83
3	10,00 - 15,00	1826,38	43,32	3427,31	2,06	8,32
4	15,00 - 25,00	1906,68	30,84	1751,10	4,68	7,75
5	25,00 - 30,00	1614,32	34,78	2151,11	5,31	8,02

5.2.1.8.Zone H-PCQ0017

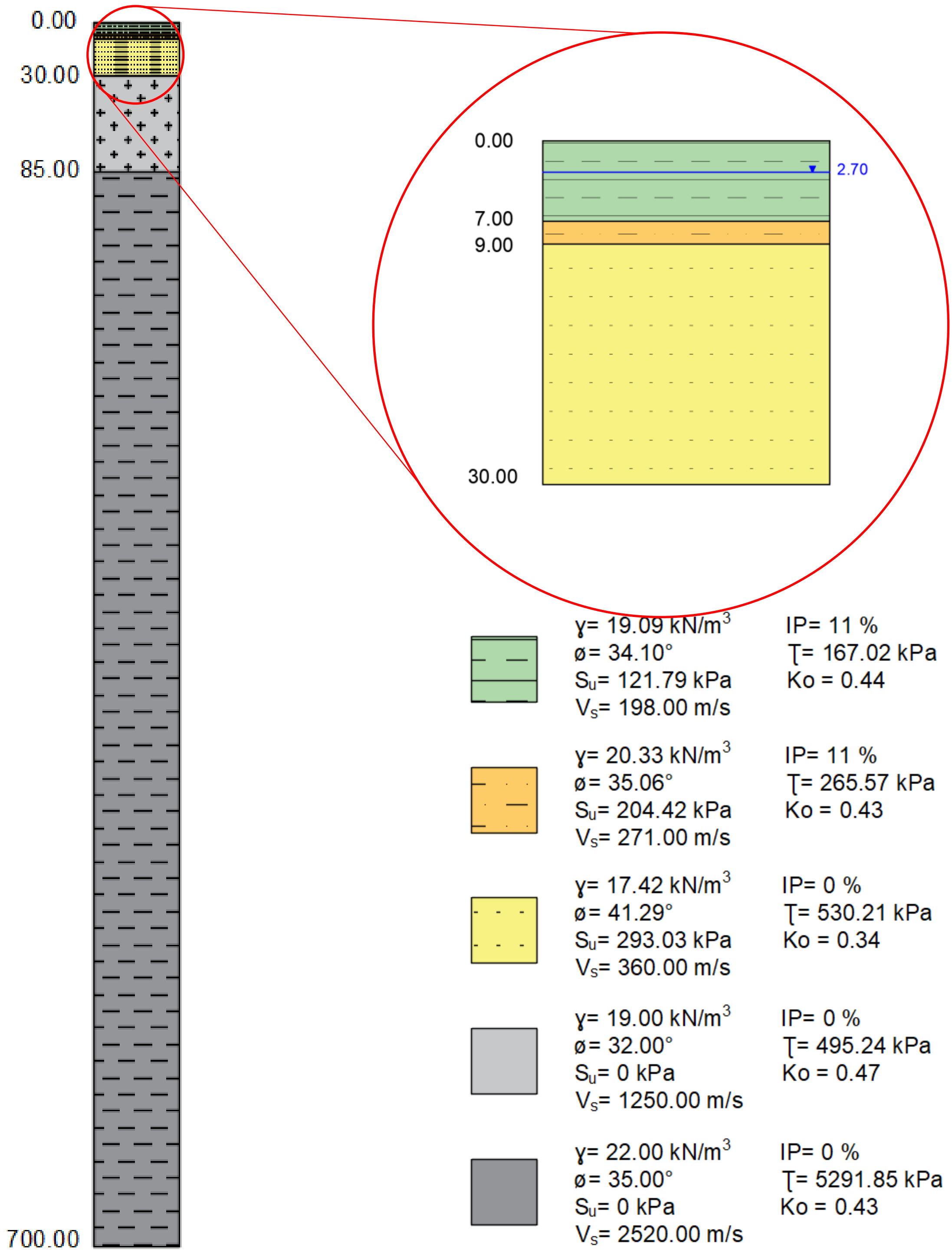

Figure 195. Soil Column of Zone H

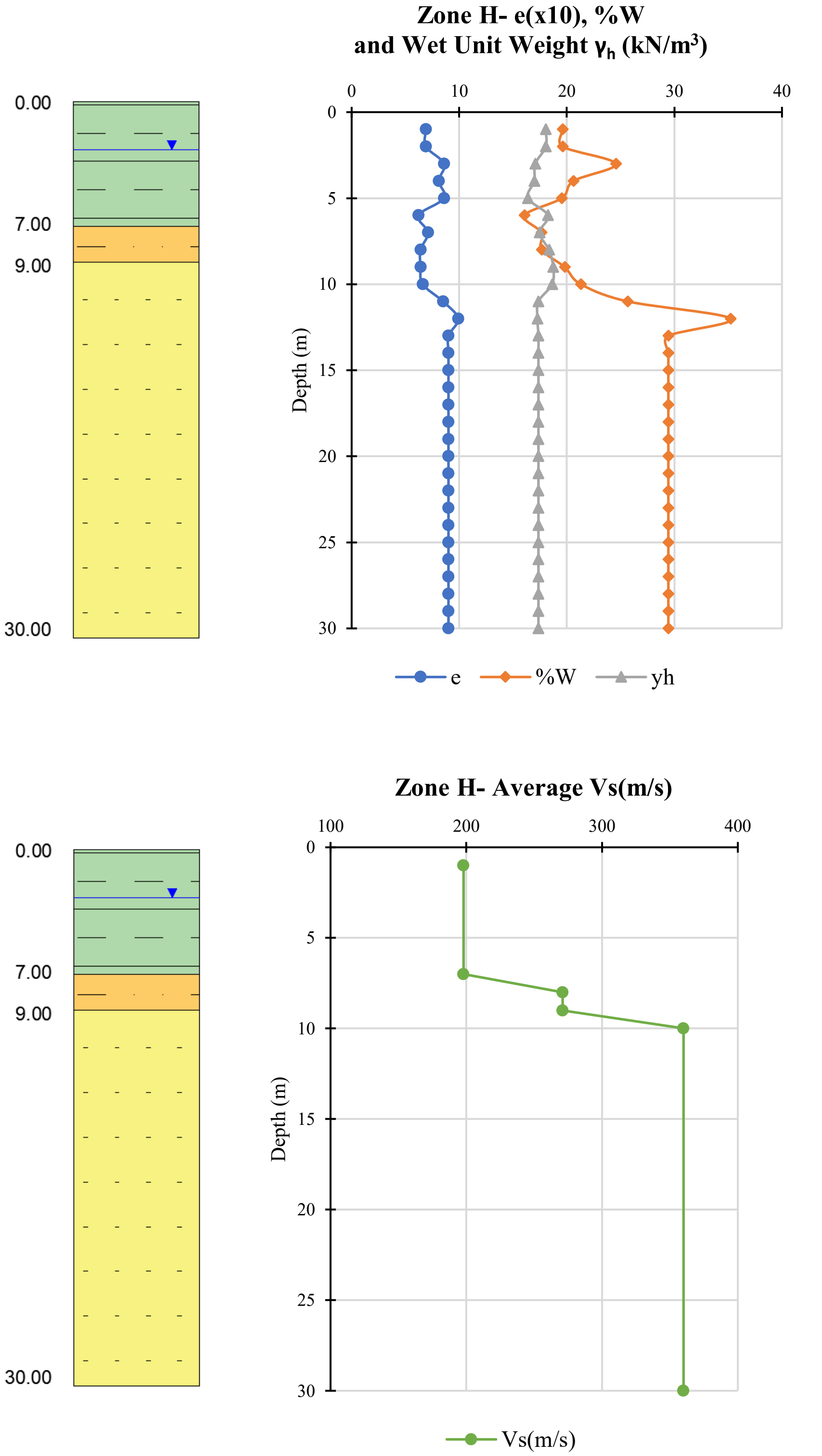

Figure 196. Cross-sectional and Longitudinal Geotechnical profiles

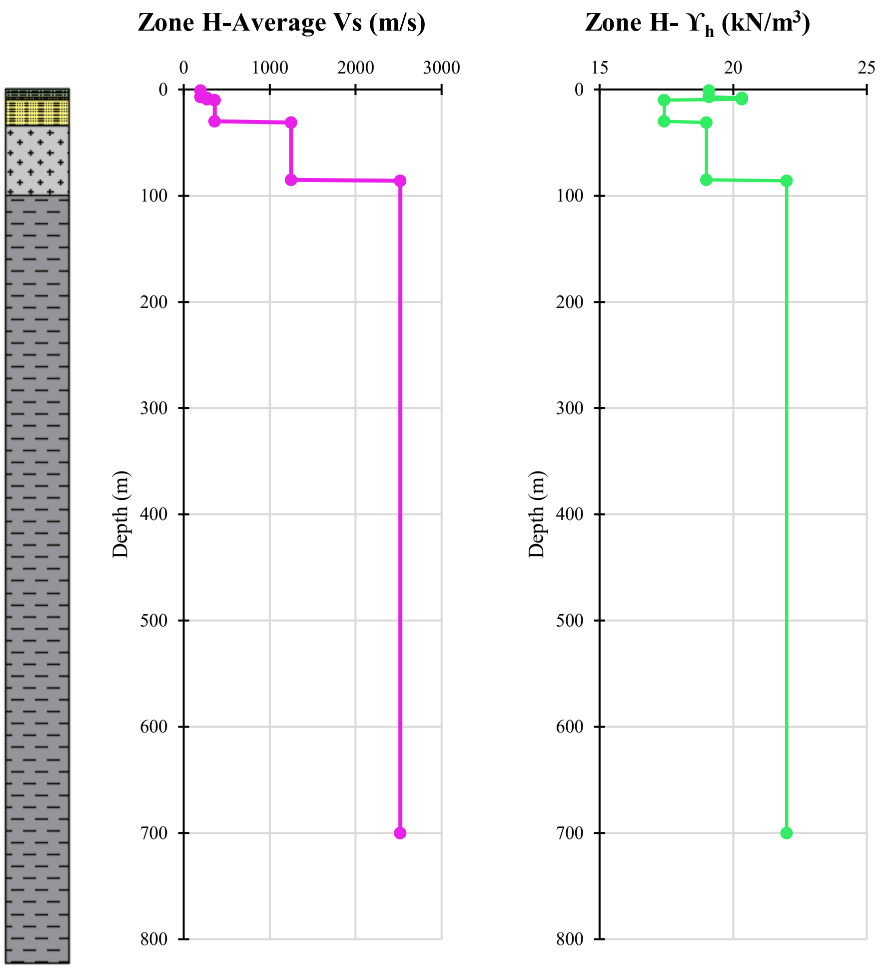

Figure 197. Cross-sectional and Longitudinal Geotechnical profiles

Table 36. Summary of Zone H

Zone H									
Depth (m)	Width (m)	γ (kN/m^3)	φ (°)	Su (kPa)	Vs (m/s)	$\sigma_{m\ prom}$ (kPa)	τ (kPa)	Ko	PI (%)
1.00 7.00	7.00	19.09	34.10	121.79	198.00	66.80	167.02	0.44	11
8.00 9.00	2.00	20.33	35.06	204.42	271.00	87.14	265.57	0.43	11
10.00 30.00	21.00	17.42	41.29	293.03	360.00	270.05	530.21	0.34	0
31.00 85.00	55.00	19.00	32.00	0.00	1250.00	792.55	495.24	0.47	0
86.00 700.00	615.00	22.00	35.00	0.00	2520.00	7557.55	5291.85	0.43	0

Table 37. Summary of the dynamic parameters of dry samples from Zone H

Zone H (Dry)						
Stratum	Depth (m)	γ (kg/m^3)	Vs (m/s)	Go (kPa)	Damping (%)	
					Min	Max
1	0,00 - 7,00	1847,23	49,91	4601,97	4,84	9,46
2	7,00 - 9,00	2015,19	45,54	4179,40	2,54	7,52
3	9,00 - 30,00	1594,60	18,44	542,17	3,93	7,56

Table 38. Summary of the dynamic parameters of remolded samples from Zone H

Zone H (Remolded)						
Stratum	Depth (m)	γ (kg/m^3)	Vs (m/s)	Go (kPa)	Damping (%)	
					Min	Max
1	0,00 - 7,00	1916,60	55,14	5806,38	4,69	9,09
2	7,00 - 9,00	1833,67	44,29	3596,30	5,78	11,85
3	9,00 - 30,00	1831,67	58,17	6228,16	6,00	9,82

5.2.1.9.Zone I- PCQ0018, PCQ0021

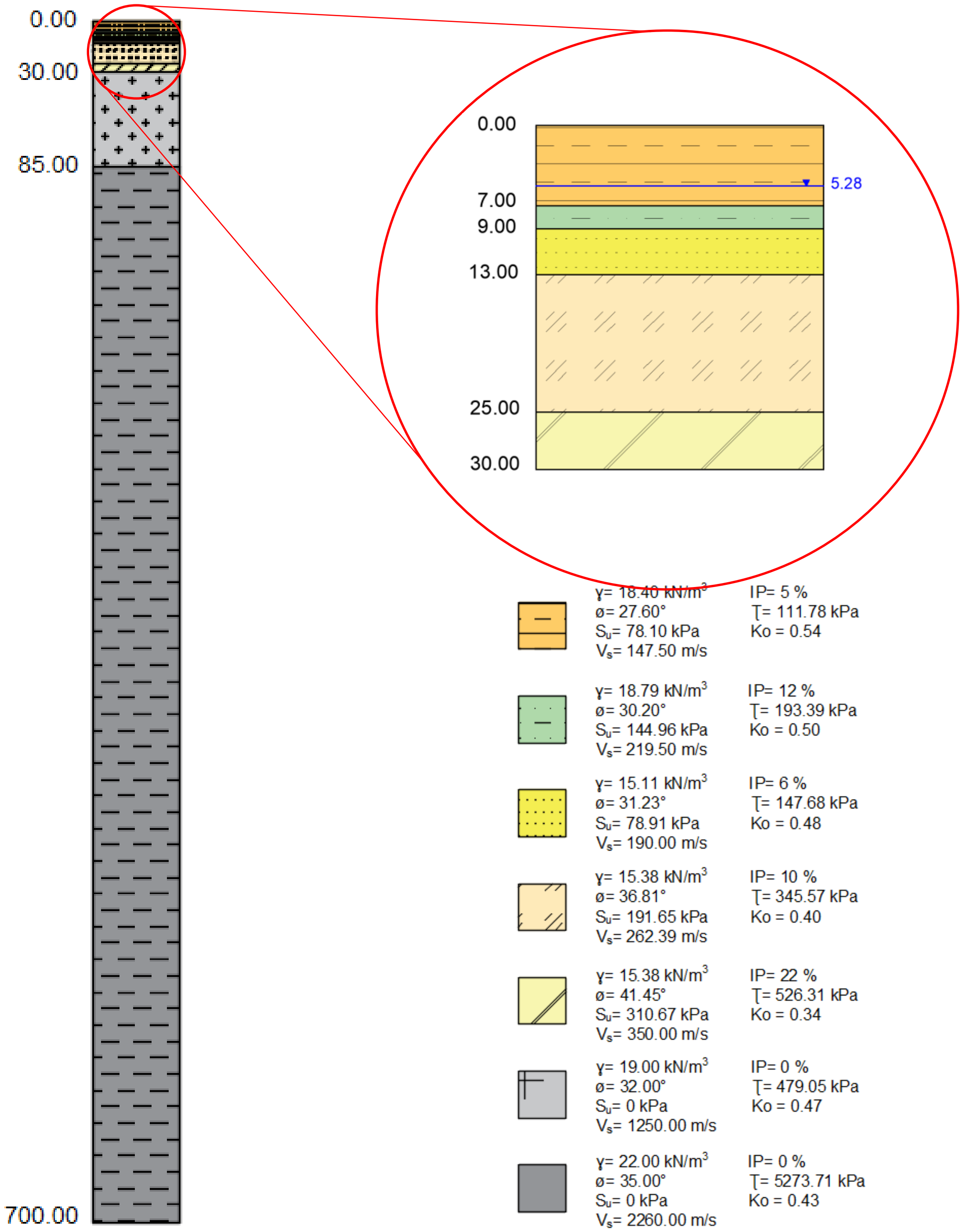

Figure 198. Soil Column of Zone I

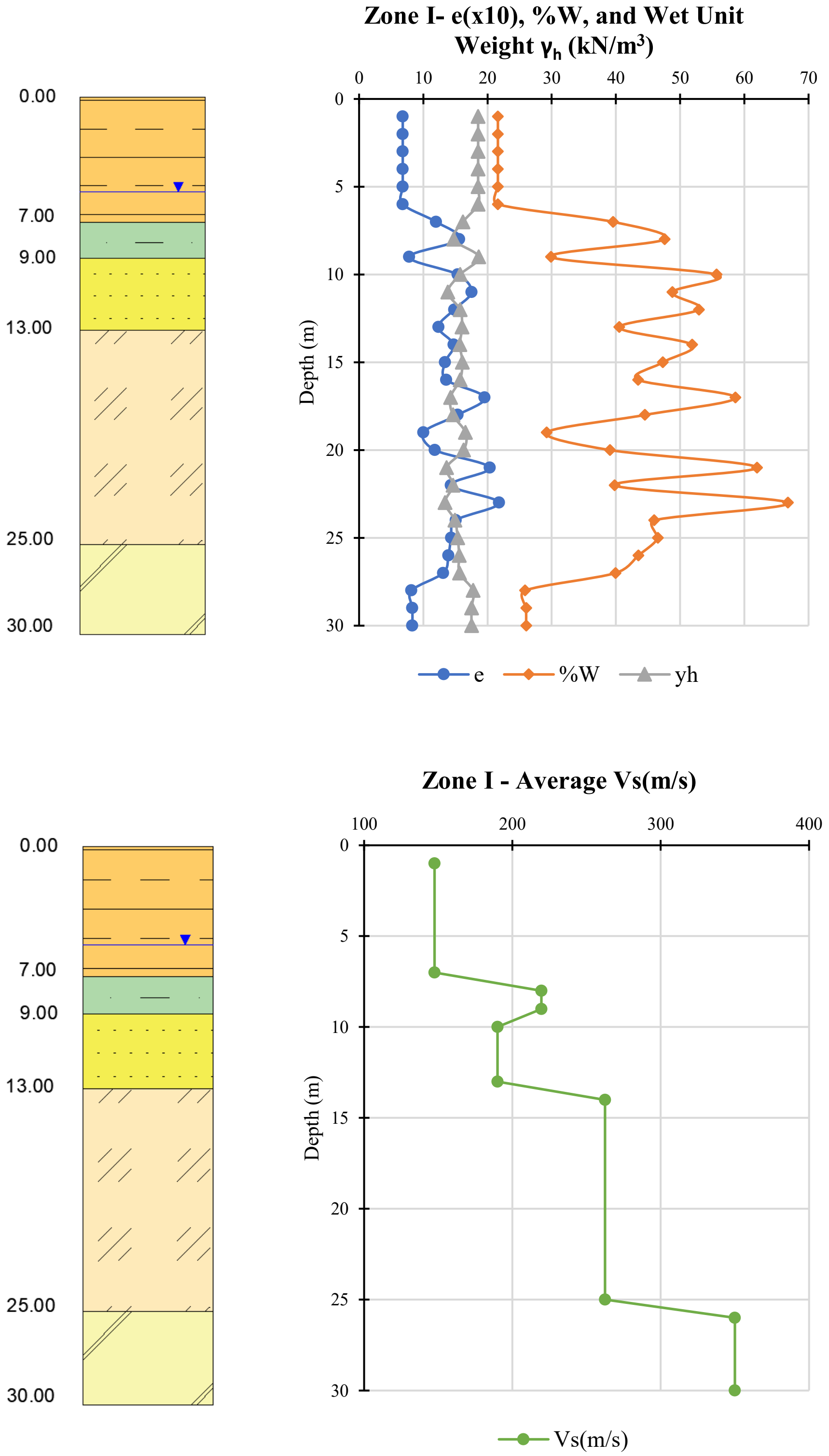

Figure 199. Cross-sectional and Longitudinal Geotechnical profiles

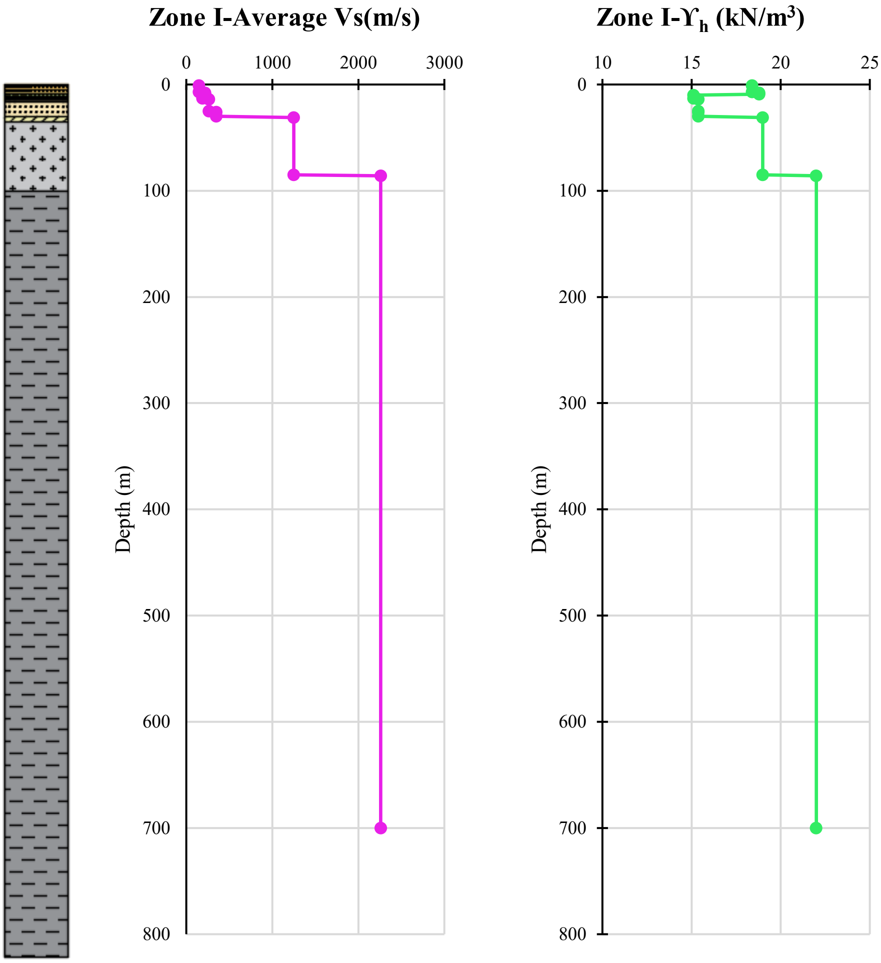

Figure 200. Cross-sectional and Longitudinal Geotechnical profiles

Table 39. Summary of Zone I

Zone I									
Depth (m)	Width (m)	γ (kN/m³)	φ (°)	Su (kPa)	Vs (m/s)	$\sigma_{m\ prom}$ (kPa)	τ (kPa)	Ko	PI (%)
1.00	7.00	18.40	27.60	78.10	147.50	64.42	111.78	0.54	5
7.00									
8.00	2.00	18.79	30.20	144.96	219.50	83.21	193.39	0.50	12
9.00									
10.00	4.00	15.11	31.23	78.91	190.00	113.43	147.68	0.48	6
13.00									
14.00	12.00	15.38	36.81	191.65	262.39	205.69	345.57	0.40	10
25.00									
26.00	5.00	15.38	41.45	310.67	350.00	244.14	526.31	0.34	22
30.00									
31.00	55.00	19.00	32.00	0.00	1250.00	766.64	479.05	0.47	0
85.00									
86.00	615.00	22.00	35.00	0.00	2260.00	7531.64	5273.71	0.43	0
700.00									

Table 40. Summary of the dynamic parameters of dry samples from Zone I

Zone I (Dry)						
Stratum	Depth (m)	γ (kg/m^3)	Vs (m/s)	Go (kPa)	Damping (%)	
					Min	Max
1	0,00 - 7,00	1877,63	11,82	262,50	4,18	8,74
2	7,00 - 9,00	1540,88	24,45	921,20	6,56	13,92
3	9,00 - 13,00	1283,14	40,11	2064,16	2,39	6,18
4	13,00 - 25,00	1429,19	24,92	887,50	4,79	6,80
5	25,00 - 30,00	1838,86	30,61	1723,26	5,57	11,09

Table 41. Summary of the dynamic parameters of remolded samples from Zone I

Zone I (Remolded)						
Stratum	Depth (m)	γ (kg/m^3)	Vs (m/s)	Go (kPa)	Damping (%)	
					Min	Max
1	0,00 - 7,00	1964,82	37,95	2765,94	4,31	11,10
2	7,00 - 9,00	1912,63	67,42	8694,29	3,09	6,83
3	9,00 - 13,00	1633,79	25,34	1048,94	4,54	8,67
4	13,00 - 25,00	1475,13	26,49	1102,05	3,50	8,01
5	25,00 - 30,00	1877,86	62,79	7403,14	5,38	8,34

5.3. Evaluation and definition of the seismic input acting at the bedrock-soil interface.

5.3.1. Evaluation of the seismic action through type and depth of Quito´s fault system

The city of Quito can be affected by three types of earthquakes, mentioned by (Alfonso Naya et al. 2012b): First, due to the subduction zone located 200 km from the capital, with events of magnitude greater than 8. Second, surface events originating in the Cordillera de los Andes with magnitudes from 7 to 7.5. Finally, events that can be generated by local faults, with magnitudes between 6 and 7. Of these faults, the "Quito Fault" is the most dangerous, being under the city, with a probable maximum earthquake between 6.9 and 7.1 with a return period of 1500 to 4000 years (Alfonso Naya et al. 2012b).

The ”Quito fault” is a 60km long blind reverse fault system, in direction N-S, with 5 sub-segments capable of rupturing individually or simultaneously in a single event, with magnitudes from 5.7 to 7.1 (Alvarado et al. 2014; Yepes et al. 2016). In 2021, (Alvarado et al. 2021) described the distribution of seismicity along a perpendicular profile to the strike on the northern segment of the main Quito Fault System. The profile shows that seismicity mainly occurs below Quito, west of the fold segments and aligned on a well-defined single fault plane. The seismic zone dips ~55° to the west and extends down to 20–30 km. Based on the historic catalog, a maximum event of Mw = 6.6 is estimated (Alvarado et al. 2021).

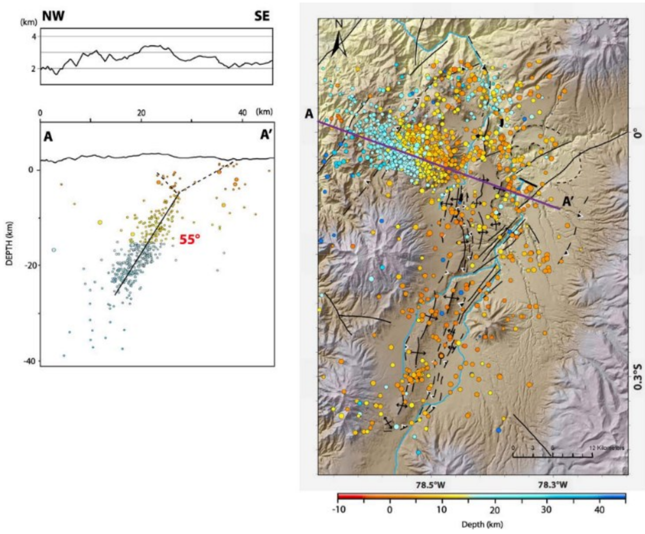

Figure 201. Cross-sectional and Longitudinal Geotechnical profiles, obtained from (Alvarado et al. 2021)

In 2022, a Seismic Risk Assessment for the Metropolitan District of Quito based on the Training and Communication for Earthquake Risk Assessment – TREQ Project was performed. Through a hazard disaggregation process, it was found that the most notable source of destructive seismicity is the Quito fault system, which is located approximately 5 to 10 km west of the city. The system is a complex structure of smaller faults that can produce earthquakes of magnitudes greater than Mw 7.0. These magnitudes, close to the city (5 to 10 km) together with a superficial depth (no greater than 20 km) govern the city's seismic hazard. In the project a depth of 8km was selected. (Calderon A, Yepes-Estrada C, Celi C, Marrero J, Yepes H, Alarcón F 2022).

Based on the presented literature, a search in the web-based Pacific Earthquake Engineering Research Center (PEER) ground motion database, NGA-West2 Shallow Crustal Earthquakes in Active Tectonic Regimes, was performed to find earthquakes with similar characteristics to run the numerical simulations. The input parameters were:

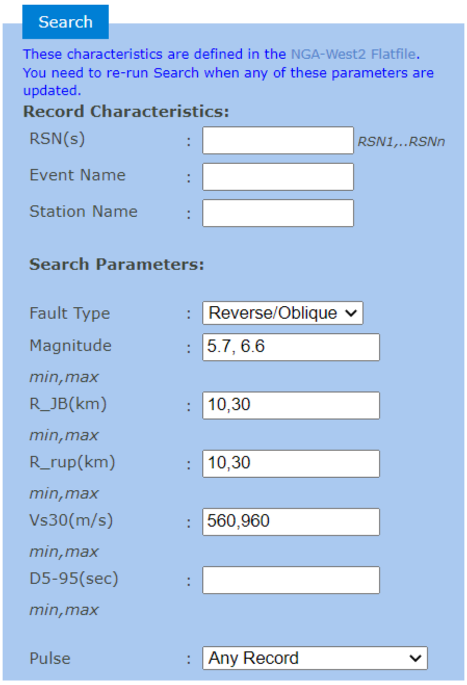

Figure 202. Search parameters, obtained from the PEER NGA-West2 database.

A total of 18 unscaled records were found:

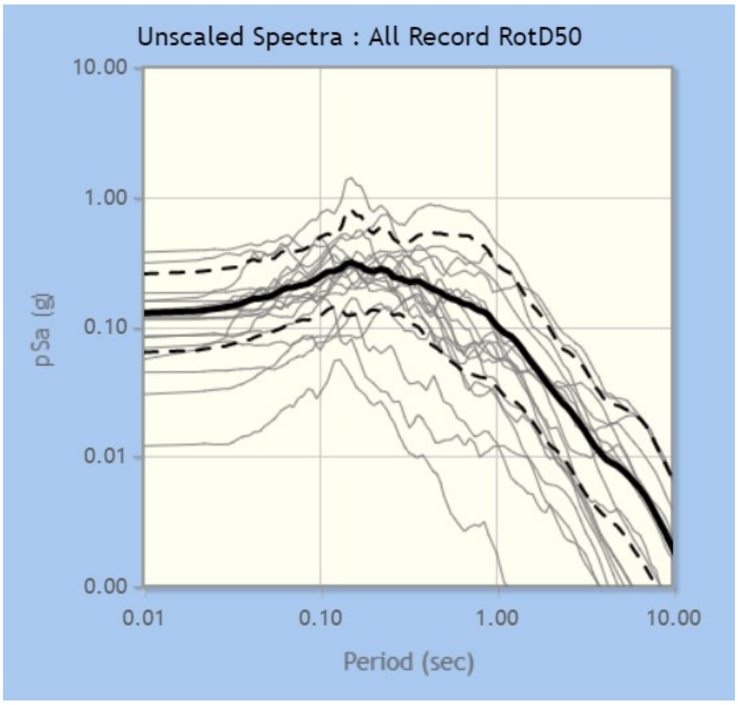

Figure 203. Unscaled records found, obtained from the PEER NGA-West2 database.

From this database, 7 records that are closer to the mean were selected, which can be seen in Table 42 and Figure 203.

Table 42. Summary of the 7 unscaled records to be used:

N.	Event	Year	Station	Mg.	Mech.	Rjb (km)	Rrup (km)	Vs30 (m/s)
1	Friuli, Italy-02	1976	San Rocco	5.91	Reverse	14.37	14.5	649.67
2	Coalinga, USA-01	1983	Slack Canyon	6.36	Reverse	25.98	27.46	648.09
3	N. Palm Springs, USA	1986	Sillent Valley - Poppet Flat	6.06	Reverse Oblique	16.55	17.03	659.09
4	Whittier Narrows, USA-01	1987	Mt. Wilson - CIT Seis Sta	5.99	Reverse Oblique	14.5	22.73	680.37
5	Chi-Chi, Taiwan-02	1999	TCU071	5.9	Reverse	20.1	21.11	624.85
6	Chi-Chi, Taiwan-03	1999	TCU071	6.2	Reverse	15.04	16.46	6485
7	Christchurch, New Zealand	2011	MQZ	6.2	Reverse Oblique	13.91	16.13	649.67

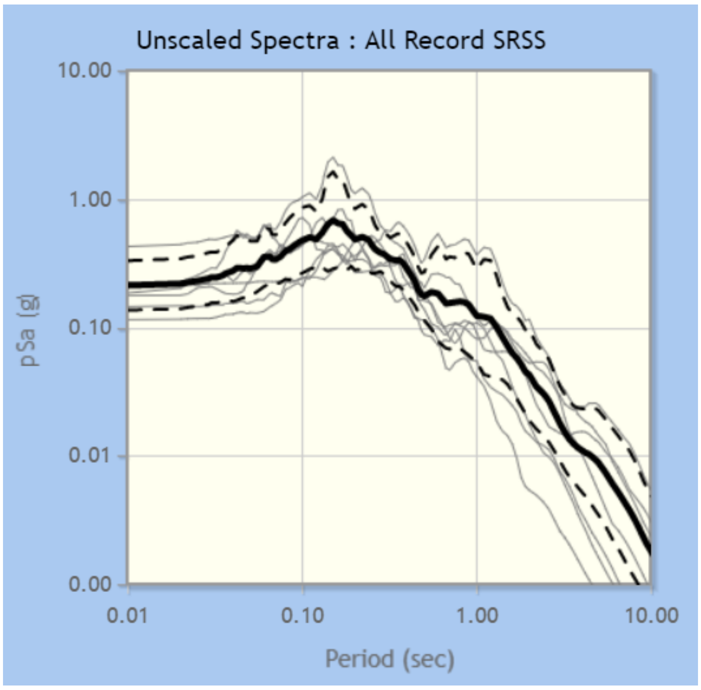

Figure 204. Unscaled records found, obtained from the PEER NGA-West2 database.

The detail of each motion is detailed in the following graphs:

5.3.1.1 Friuli, Italy-02, 1976, $\boldsymbol{M_w}$ **5.91**

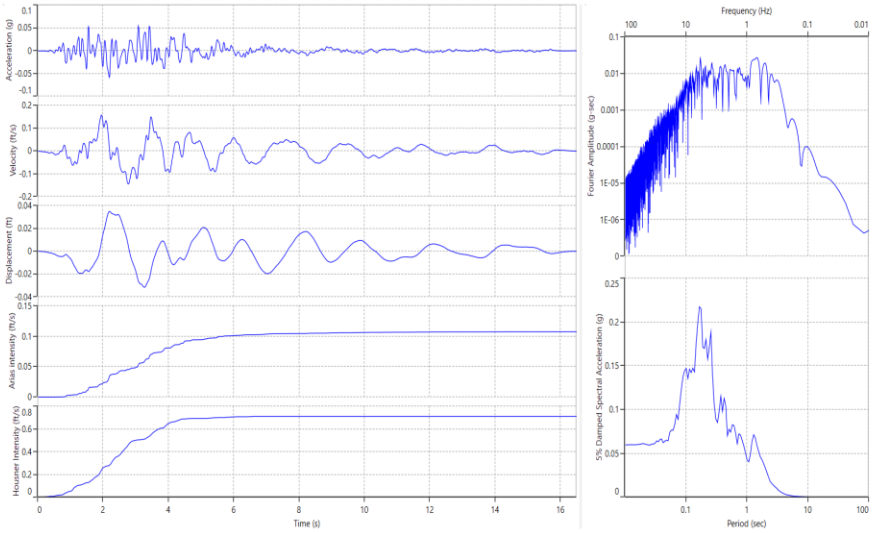

Figure 205. Input motion of Friuli, Italy-02, 1976. Mw=5.91.

5.3.1.2 Coalinga, USA-01, 1983, $\boldsymbol{M_w}$ **6.36**

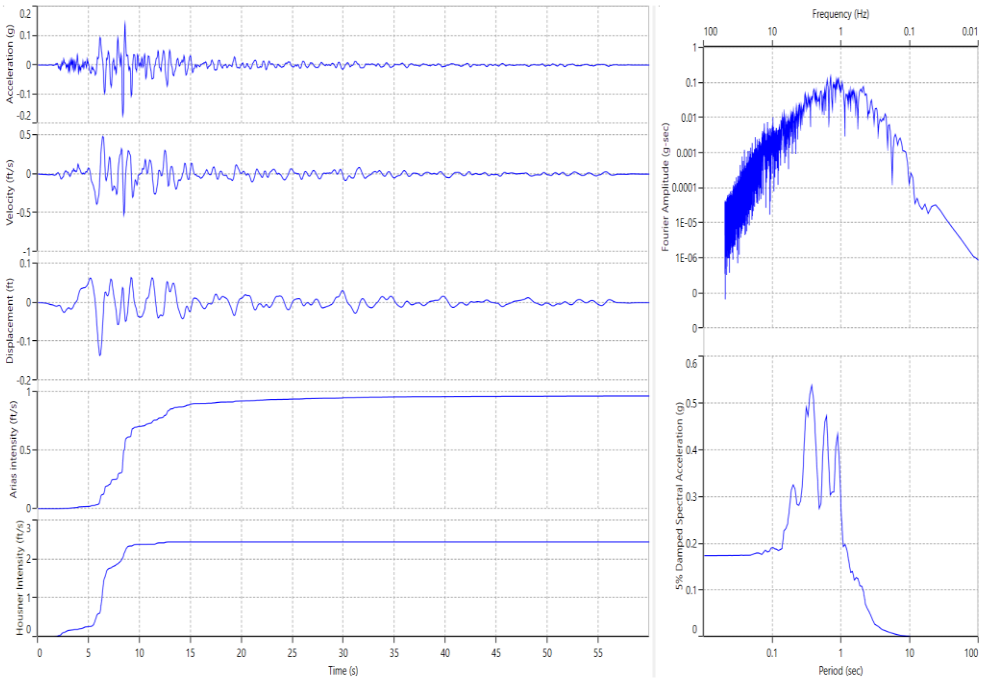

Figure 206. Input motion of Coalinga, USA-01, 1983. Mw=6.36.

5.3.1.3 N. Palm Springs, USA,1986, M_w 6.06

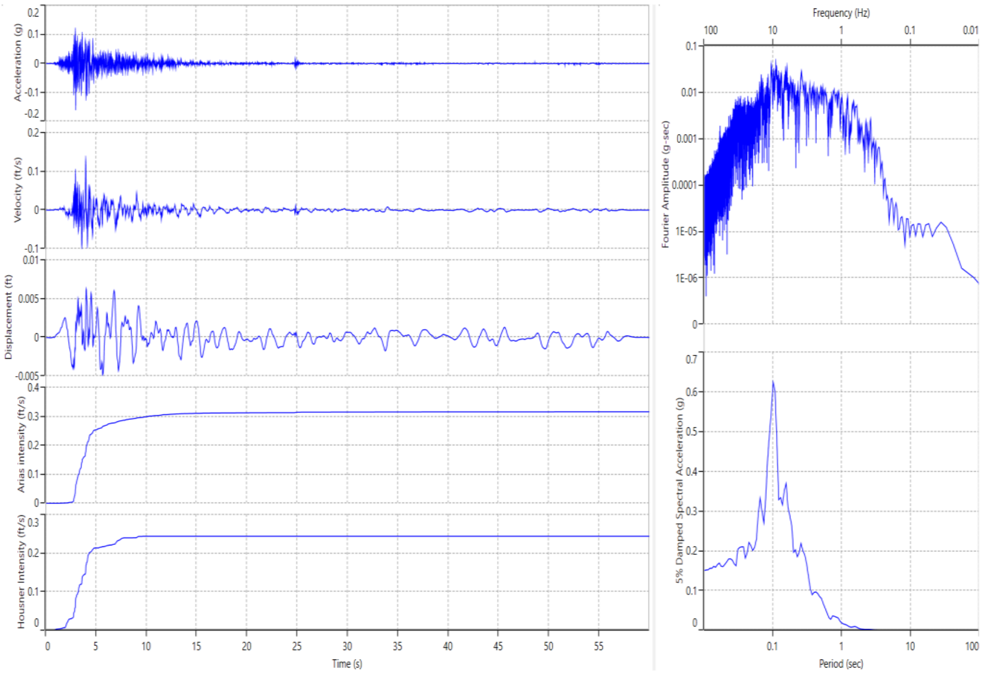

Figure 207. Input motion of N. Palm Springs, USA, 1986. Mw=6.06.

5.3.1.4 Whittier Narrows-01, USA, 1987, M_w 5.99

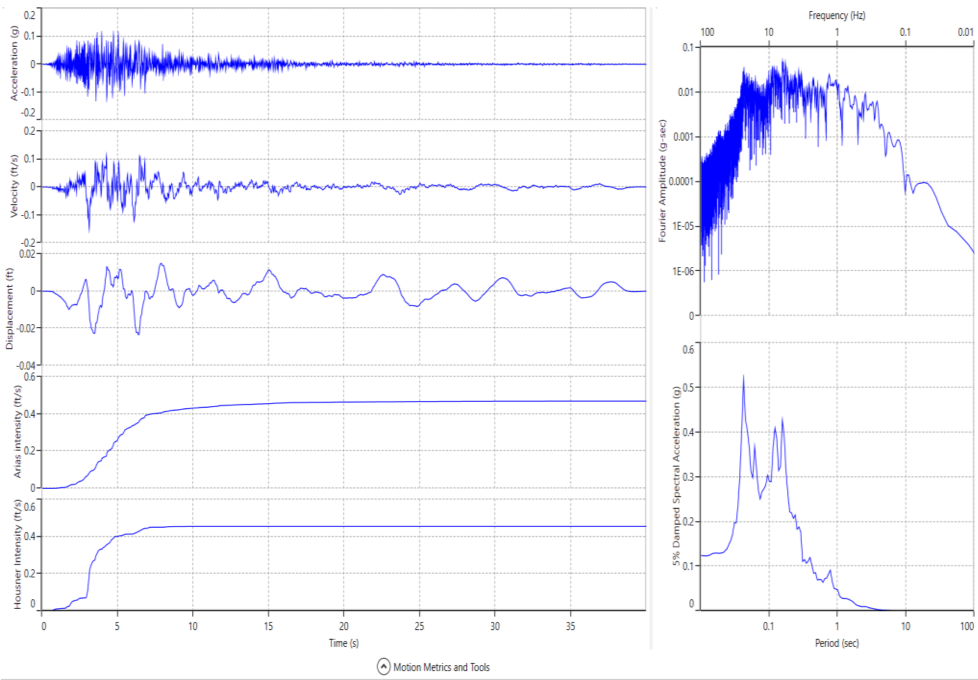

Figure 208. Input motion of Whittier Narrows-01, USA, 1987. Mw=5.99.

5.3.1.5 Chi-Chi, Taiwan-02, 1999, M_w 5.9

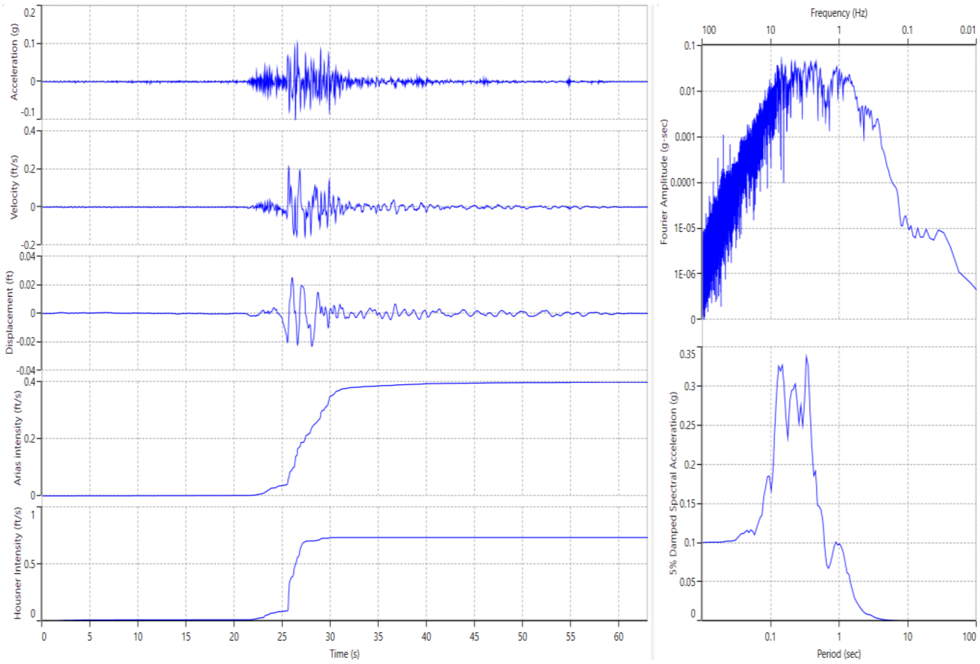

Figure 209. Input motion of Chi-Chi, Taiwan-02, 1999. Mw=5.9.

5.3.1.6 Chi-Chi, Taiwan-03, 1999, M_w 6.2

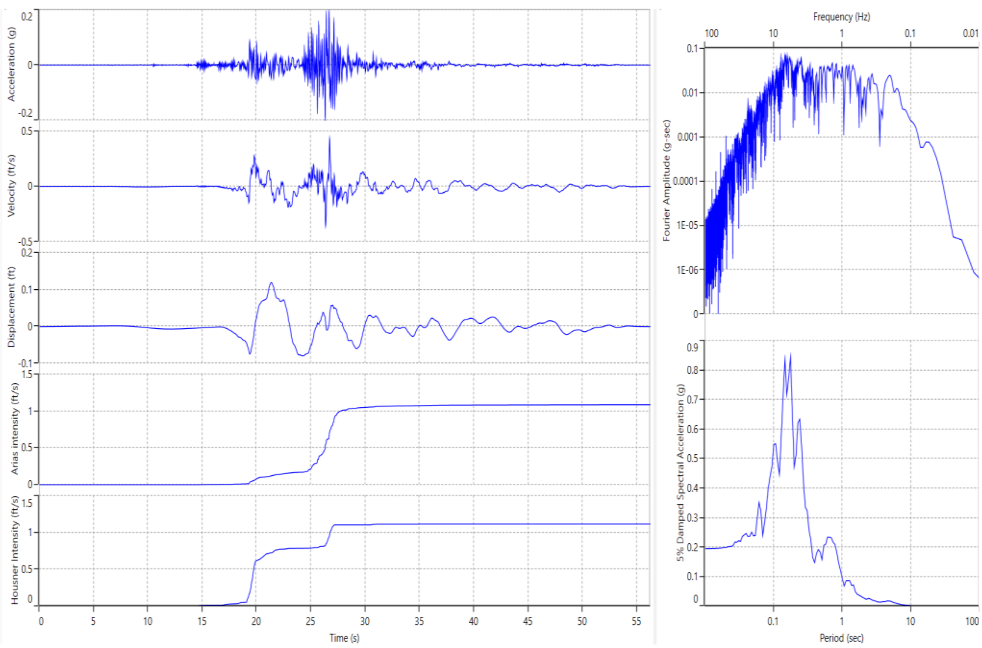

Figure 210. Input motion of Chi-Chi, Taiwan-03, 1999. Mw=6.2.

5.3.1.7 Christchurch, New Zeland, 2011, $\boldsymbol{M_w}$ **6.2**

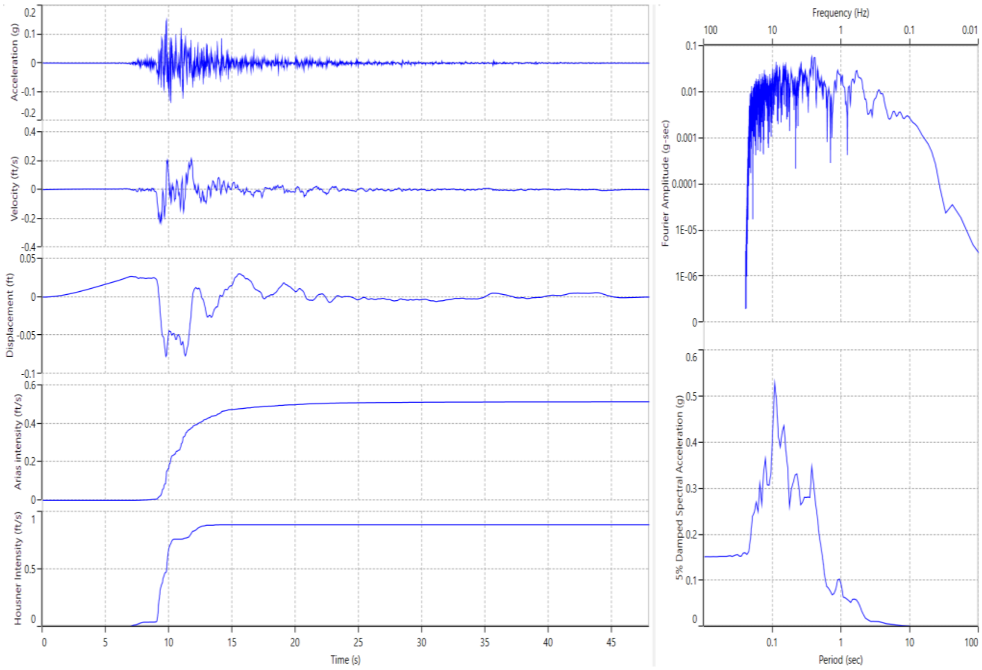

Figure 211. Input motion of Christchurch, New Zeland, 2011. Mw=6.2.

The procedure to define the input motion was based on information about the Quito fault system, such as depth, length and expected magnitude, which have been extensively studied in the last 10 years. Acceleration spectra based on probabilistic hazard analysis (PSHA) were not used, because these spectra generated by the Ecuadorian Construction Standard (NEC) are under revision and will be considered for use in the near future as part of the Seismic Microzonation of the Quito fault system.

5.4. Methods for numerical simulations.

Site response numerical analysis is commonly performed assuming one-dimensional wave propagation, which assumes that all the layers in the stratigraphy are horizontal, and that the soil deposit response is primarily caused by the SH-waves propagating vertically from the bedrock. For this reason, one-dimensional site response can´t model irregular soil surfaces, deep basins, and embedded structures. In such scenarios, two-dimensional and three-dimensional analysis have been used (Kramer 1996; Park et al. 2004a).

Analysis in two and three dimensions have been used to model basin effects using methods such as thin-layer, finite element, and finite difference to consider the topography and the structure of the basin, which is curved, and that can trap body waves causing some of them to propagate as surface waves. This effect can produce a stronger and longer shaking in comparison to a one-dimensional analysis (Hallal and Cox 2021; de la Torre, Bradley, and McGann 2021; Nautiyal et al. 2021; Park et al. 2004a; Primofiore et al. 2020).

Even though, considering that the south of Quito has over $100km^2$, it is not feasible to model the whole sector due to its size, and high frequency components of the ground motion could be filtered. Therefore, 1D approximation of wave propagation is acceptable for the analysis (Park et al. 2004a).

Based on (Carrer 2013; Kramer 1996), one-dimensional local response analysis assumes that all geologic boundaries are horizontal, and the response of soil deposits is predominantly caused by vertical wave propagation from the underlying bedrock. Because of this, one-dimensional computational codes are valid for modeling parallel layers along the vertical column, assuming homogeneous lateral stratigraphy. Therefore, under these assumptions, the main amplification factors of seismic motion are:

a) Impedance contrasts between underlying strata, particularly with bedrock.
b) Resonance effects due to the closeness between the frequencies of the substrate movement and the natural vibration of the deposit.

It is important to mention that, in order to quantify the seismic response and to evaluate the seismic amplification, as mentioned by (Shi 2019), the difference between soil stiffness and rocks stiffness determines the level of amplification: in general, the larger the difference, the larger the amplification. Therefore, to quantify site response, we need to quantitatively describe material stiffness at the locations of interest. However, the stiffness of soils is not a constant: it reduces with soil deformation. As soil deformation undoubtedly happens during ground shaking, the soils become softer, thus can further amplify seismic waves. To make things more complex, the energies in the seismic waves are partially absorbed by soil particles during shaking (referred to as damping). Damping decreases the wave amplitudes, counteracting the effects from soil softening. We refer to soil softening and damping effects as nonlinear site response (Shi 2019).

5.4.1. Types of Analysis for Ground Response Analysis

The calculation process considers, in the solution of the dynamic equilibrium of the system, the linear or nonlinear relationship through the following types of analysis:

- Linear analysis, where the material properties remain constant during shaking in the frequency domain with linear visco-elastic material behavior. It has been repeatedly shown that the linear method is not suitable for site response analyses to strong ground motions, except for hard rock sites (Hartzell, Bonilla, and Williams 2004; Kaklamanos 2012; Shi 2019)
- Equivalent linear analysis consists of performing a sequence of complete analyses, accounting for material yielding (modulus reduction) and hysteretic attenuation (damping) by iteratively matching the soil modulus and damping to a characteristic strain level. The parameters are dependent on the state of deformation of the soil. This method is essentially still a linear method because material properties remain constant throughout an iteration—although the stiffness is reduced, and damping is increased for subsequent iterations. This method yields satisfactory results for non-excessive ground deformations relative stiff sites subjected to intermediate levels of strain (< 0:1%) (Carrer 2013; Shi 2019)
- Non-linear analysis: is performed in the time domain, consists of the step-by-step integration of the equations of motion, while simultaneously changing the values of the stiffness and damping parameters (the material properties are adjusted instantaneously to the strain level and loading path). This analysis is used for high deformations. (Carrer 2013; Kramer 1996; Shi 2019)

5.4.2. Material constitutive model representation of cyclic soil behavior

To represent the behavior of a material, a constitutive model of the material is used, which relates stress to strain. The development of a constitutive model is complex, because it requires a convoluted simulation of phenomena such as:

a) Non-linearity
b) Hardening and softening
c) Anisotropy
d) Residual and initial stress
e) Volume change during cutting
f) History of stresses and stress path
g) Three-dimensional states of stress and deformation
h) Liquid in the pores

A simplification of soil behavior is usually necessary in site response analysis, since it is often not possible to run quality laboratory tests for in situ soil samples, so it is not possible to accurately determine soil behavior. In addition, the variation of soil characteristics is large and cannot be represented by selected soil samples. Because of the above, soil behavior should be simplified by using simple shear soil models or linear viscoelastic soil models in the site response analysis, mentioned below (Park et al. 2004b).

5.4.2.1. Linear Viscoelastic Model

The simplest way to model the dynamic response of geological materials is the linear viscoelastic model, where the stress-strain relationship is linear, but the energy dissipation characteristics of soils are considered. This type of model is valid only for limited applications, such as the propagation of weak ground motions through soil, or the propagation of motions through a very rigid material such as rock where the induced deformations are very small.

5.4.2.1.1. Kelvin-Voigt model

This model consists of a spring and a damper connected in parallel. The shear stress is calculated as follows:

$$\tau = G\gamma + \eta\dot{\gamma}$$

Equation 65. Equation to obtain the shear stress in the Kelvin-Voigt model.

Where:

G: spring shear modulus

η: viscosity of the shock absorber

For harmonic shear deformation:

$$\gamma = \gamma_0 \sin \omega t$$

Equation 66. Equation to calculate the harmonic shear deformation.

Where the energy dissipated in a single cycle is:

$$E_D = \int_{t_0}^{t_0+2\pi/\omega} \tau d\gamma = \int_{t_0}^{t_0+2\pi/\omega} \tau \frac{\partial \gamma}{\partial t} dt = \pi\eta\omega\gamma_0^2$$

Equation 67. Equation to calculate the energy dissipated in a single cycle.

The energy dissipated is a function of the loading frequency, however, the frequency-dependent nature of the viscous damping in this model means that it cannot disguise the damping of soils, which are nearly constant within the frequency range of interest in engineering applications (Kramer 1996; Park et al. 2004b)

5.4.2.1.2. Hysteretic model

This model incorporates a rate-independent dashpot to eliminate the frequency dependence of damping (so that the frequency is independent of the damping).

Viscosity is expressed in terms of equivalent damping:

$$\xi = \frac{E_D}{4\pi E_s} = \frac{\eta\omega}{2G}$$

Equation 68. Equation which describes the viscosity in terms of equivalent damping.

Where:

$E_S = \frac{1}{2} G_0^2$, where the equivalent damping ratio is assumed to be independent of the forcing frequency, $\frac{\omega}{\omega_n} = 1$

After a few fixes, assuming that the damping is small, an approximation of the complex shear modulus defined as:

$$G^* = G(1 - \xi^2 + i2\xi)$$

Equation 69. Equation of complex shear modulus, G*.

It is based on the approximate complex shear modulus (Kramer, 1996):

$$V_z^* = \sqrt{\frac{G^*}{\rho}} = \sqrt{\frac{G\,(1 + i2\xi)}{\rho}} \approx \sqrt{\frac{G}{\rho}}\,(1 + i\xi) = V_z\,(1 + i\xi)$$

Equation 70. Equation of Vz*, where the imaginary term represents the damping of soils.

Where the introduction of the imaginary term is necessary to represent the lag (damping of soils) (Park et al. 2004b)

5.4.2.1.3. Udaka Model

Udaka, in 1975, developed a complex modulus that results in a response amplitude identical to the Kelvin-Voigt model, having as complex shear modulus equation the following equation:

$$G^* = G\left(1 - 2\xi^2 + 2i\xi\sqrt{1 - \xi^2}\right)$$

Equation 71. Equation to calculate the complex modulus G* by Udaka, 1975.

This equation was obtained by back-calculation; however, the calculated phase angle does not match the Kelvin-Voigt model. This model represents an approximate solution to better simulate the Kelvin-Voigt model while retaining the convenience of using the complex shear modulus G*, keeping the defect of a frequency-dependent damping.(Park et al. 2004b)

5.4.2.2. Plasticity based models

These models require:

a) Yield surface represents the stress condition beyond which the material behaves plastically.
b) Rule of hardening describes the changes in the size and shape of the yield surface.
c) Flow rule relates increases in plastic deformation to increases in stress.

This type of model is rarely used for site response analysis (Hashash, M. Musgrove, et al. 2020; Park et al. 2004b).

5.4.3. Numerical formulation for one-dimensional site response analysis

The 1D equation of motion for vertically propagating shear waves through unbounded medium can be written as:

$$\rho \frac{\partial^2 u}{\partial z^2} = \frac{\partial \tau}{\partial z}$$

Equation 72. Equation of 1D motion for vertically propagating shear waves.

Where:

ρ: density of medium.

τ: shear stress

u: horizontal displacement

z: depth below ground surface

Soil behavior is commonly approximated as a Kelvin-Voigt solid. The shear stress-shear strain relationship is expressed as:

$$\tau = G\gamma + \eta \frac{\partial \gamma}{\partial t}$$

Equation 73. Equation that expresses the shear stress-shear strain relationship.

Where:

G: shear modulus

γ: shear strain

η: viscosity

Combining the two previous equations we obtain:

$$\rho\frac{\partial^2 u}{\partial t^2} = G\frac{\partial^2 u}{\partial z^2} + \eta\frac{\partial^3 u}{\partial z^2 \partial t}$$

Equation 74. Equation which can be solved in frequency domain.

This equation can be solved in frequency domain or in time domain.

5.4.3.1. Frequency domain solution for one-dimensional site response analysis

The equation 74 can be solved for a harmonic wave propagating through a multi-layered soil column (Schnabel, Lysmer, and Seed 1972). Introducing a local coordinate Z for each layer and solving the wave equation, the displacement at the top and bottom of a layer m becomes:

$$u(Z_m = 0, t) = u_m = (A_m + B_m)e^{i\omega t}$$

Equation 75. Equation to determine the displacement at top layer.

$$u(Z_m = h_m, t) = u_{m+1} = \left(A_m e^{ik_m^* h_m} + B_m e^{-ik_m^* h_m}\right)e^{i\omega t}$$

Equation 76. Equation to determine the displacement at bottom layer.

Where:

u: displacement

A_m, B_m: amplitudes of waves traveling upwards (-z) and downwards (z) at layer m.

h_m: thickness of a layer m.

k_m^*: is defined as (Kramer, 1996):

$$k_m^* = \frac{\omega}{(V_s^*)_m(1 + i\xi_m)}$$

Equation 77.Equation of k_m^* (Kramer, 1996).

Where:

ξ_m: damping ratio at layer m.

$(V_s^*)_m$: complex shear velocity. Is defined as:

$$(V_s^*)_m = \sqrt{\frac{G^*}{\rho}}$$

Equation 78. Equation to calculate the complex shear velocity.

Where:

G^*: complex shear modulus.

Applying the boundary conditions and compatibility requirements will result in the recursive formulae for successive layers:

$$A_{m+1} = \frac{1}{2}A_m(1+\alpha^*{}_m)e^{ik_m^* h_m} + \frac{1}{2}B_m(1-\alpha^*{}_m)e^{-ik_m^* h_m}$$

$$B_{m+1} = \frac{1}{2}A_m(1-\alpha^*{}_m)e^{ik_m^* h_m} + \frac{1}{2}B_m(1+\alpha^*{}_m)e^{-ik_m^* h_m}$$

$$\alpha^*{}_{m+1} = \frac{\rho_m (V_s)_m (1+i\xi_m)}{\rho_{m+1}(V_s)_{m+1}(1+i\xi_{m+1})}$$

Equation 79. The recursive formulae for successive layers.

Where:

ρ_m: density of layer m.

The motion at any layer can be easily computed from motion in any other layer using the transfer function, F_{ij}, that relates displacement amplitude at layer i to that at layer

$$F_{ij}(\omega) = \frac{|u_i|}{|u_j|} = \frac{A_i(\omega)+B_i(\omega)}{A_j(\omega)+B_j(\omega)}$$

Equation 80. Transfer function.

$$|\ddot{u}| = \omega$$

$$|\dot{u}| = \omega^2|u|$$

Since the solution for an arbitrary loading is performed by transforming the motion into a finite sum of harmonic motions using Fourier transform, the damping of the system becomes independent of the frequency of the input motion if the hysteretic model is used due to the frequency independent viscosity. However, the frequency domain solution becomes frequency dependent if the Udaka model is used.

This solution is not unique and depends on the type of the linear viscoelastic model or complex shear modulus incorporated and is possible based on the assumption that the modulus and damping properties are constant e independent of the strain level (Park et al. 2004b).

5.4.3.2. Equivalent linear analysis for one-dimensional site response analysis

This approximation method was developed to capture non-linear cyclic response of soil within the framework of the frequency domain solution, where the non-linear hysteretic stress-strain behavior is approximated by the modulus degradation and damping curves.

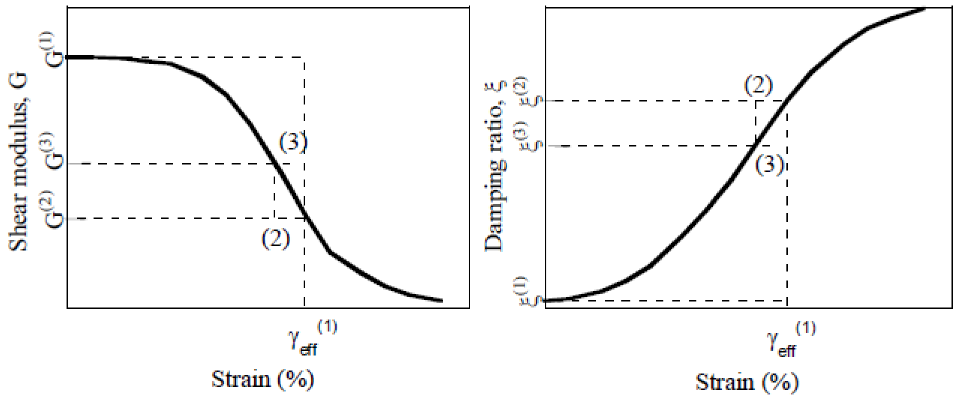

Figure 212. Representation of the iterative scheme used in Equivalent Linear Analysis, from (Park et al. 2004b)

For a given ground motion time history, the propagated ground motion is calculated using an initial estimate of small strain modulus and damping. This computation is performed in the frequency domain and then, the strain time histories for each layer, from which the maximum strain values are obtained, are calculated. An effective shear strain (equal to about 65% of peak strain) is computed for a given soil layer and corresponding estimates of shear modulus and damping is obtained from the shear modulus reduction and damping curves. This process is repeated until a converged solution is reached. (Park et al. 2004b)

The main limitation of this analysis is that constant shear modulus and damping is used throughout the analysis. It represents soil as a linear viscoelastic material. When a propagating strong ground motion, for which the effective strain would be large, using independent values of frequency throughout the ground motion record doesn't account for the variations of soil properties with change in strain levels experienced by soils. The constant linear modulus and damping overestimate the stiffness at large strain levels. That's why the use of frequency dependent modulus degradation and damping in equivalent linear analysis has been proposed (Assimaki, Kausel, and Whittle 2000; Park et al. 2004b).

Assimaki et al. 2000, proposes use of the smoothed strain Fourier spectrum to estimate the frequency dependent modulus and damping. The strain Fourier spectrum of each layer is calculated, normalized to peak strain, and then smoothed. The frequency dependent strain level is obtained, and corresponding shear modulus and damping is selected. The relationship between frequency and shear modulus and damping is not constant at a given frequency and therefore smoothed spectrum is only an approximation of the actual behavior. It is a phenomenological model developed as a mathematical convenience but does not reflect a real soil behavior.(Assimaki et al. 2000; Park et al. 2004b)

5.4.3.3. Quarter wavelength method (QWM)

It is a simple frequency domain analysis procedure assuming soil profile as an elastic medium. It is a simplified form of the frequency domain solution whereby the average properties up to a quarter wavelength are considered.

The soil amplification is modeled as:

$$Amp\ (f) = A(f)P(f)$$

$$A(f) = \sqrt{\frac{\rho^0 * V_s^0}{\bar{\rho}^s(f) * \bar{V_s}^s(f)}}$$

Equation 81. Equation for amplification function.

Where:

A(f): amplification function

P(f): attenuation function

ρ: density, g/cm^3.

V_s: shear velocity, m/s.

f: frequency

Note: superscript ^{0} denotes the source and ^{s} the site.

The frequency-dependent effective velocity $\overline{V_s}^{s}(f)$ is defined as the average shear wave velocity from the surface to a depth of a quarter wavelength for the given frequency f.

The travel time to the depth of a quarter wavelength can be calculated as:

$$tt_z(f) = \frac{1}{4f}$$

Equation 82. Equation of the travel time to the depth of a quarter wavelength.

The depth of the quarter wavelength z can be calculated as:

$$tt_z(f) = \sum_{i=1}^{m} \frac{h^{(i)}}{V_s^{(i)}}$$

$$z = \sum_{i=1}^{m} h^{(i)}$$

Equation 83. Equation to calculate the depth of the quarter wavelength.

Where:

$h^{(i)}$: thickness of the i-th layer

$V_s^{(i)}$: shear velocity of the i-th layer

The effective velocity at a given frequency is determined by:

$$\bar{\beta}_s(f) = \frac{z}{tt_z(f)}$$

$\bar{\rho}^s(f)$ is defined as:

$$\bar{\rho}^s(f) = \frac{1}{tt_z(f)} \left[\sum_{i=1}^{m} \frac{h^{(i)}}{V_s^{(i)}} * {\rho_s}^{(i)} \right]$$

The soil attenuation is modeled using the attenuation function P(f), which is defined as:

$$P(f) = e^{-\pi * k * f}$$

$$k = \sum_{i=1}^{N} \left[\int_{0}^{h^{(i)}} \frac{dz}{V_s^{(i)} * Q(h)} \right]$$

$$Q = \frac{1}{2\xi} \, for \; Q^{-1} \ll 1$$

Equation 84. Equation of quality factor, Q.

Where:

k: is a parameter that accounts for shear velocity and damping over the soil column.

N: number of soil layers

h: depth measured from the ground surface

Q: quality factor, it describes the energy dissipation.

ξ: damping ratio

5.4.3.4. Time domain solution

The nonlinear behavior can only be simulated via a time domain analysis using step-by-step integration scheme. In 1-D time domain analysis, the unbounded medium is idealized as discrete lumped mass system, so the wave propagation equation is written as:

$$[M]\{\ddot{u}\} + [C]\{\dot{u}\} + [K]\{u\} = -[M]\{I\}\ddot{u}_g$$

Equation 85. Wave propagation equation for nonlinear behavior.

Where:

[M]: mass matrix

[C]: viscous damping matrix

[K]: stiffness matrix

$\{\ddot{u}\}$: vector of nodal relative acceleration

$\{\dot{u}\}$: vector of nodal relative velocities

$\{u\}$: vector of nodal relative displacements

$\ddot{u}_g$: acceleration at the base of the soil column

$\{I\}$: unit vector

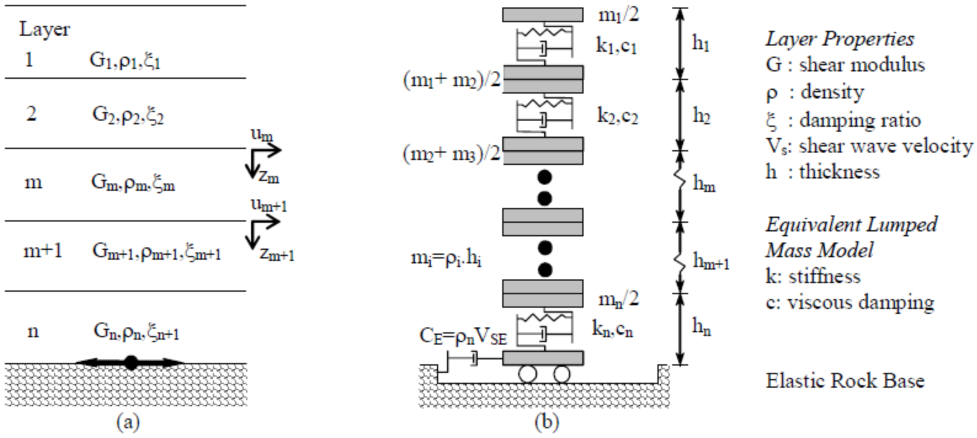

Figure 213. Idealized soil stratigraphy with a) frequency domain solution layered soil column, b) time domain solution, with multi-degree of freedom humped parameter idealization, from (Park et al. 2004b)

There are several numerical schemes available to solve the dynamic equation 85, which have two most important aspects: stability and accuracy. They are shown below:

- *Explicit methods:*

  Central difference: this method is only stable if the following requirement is satisfied:

$$\frac{\Delta t}{T_n} < \frac{1}{\pi}$$

- *Implicit methods:*
  - *Newmark β:* Newmark in 1959 developed various time-stepping methods based on the following equations:

$$\dot{u}_{i+1} = \dot{u}_i + [(1-\gamma)\Delta t]\ddot{u}_i + (\gamma\Delta t)\ddot{u}_{i+1} \qquad (B-2)$$

Equation 86. First equation to develop the time-stepping methods.

$$\dot{u}_{i+1} = u_i + (\Delta t)\dot{u}_i + [(0.5-\beta)(\Delta t)^2]\ddot{u}_i + [\beta(\Delta t)^2]\ddot{u}_{i+1}$$

Equation 87. Second equation to develop the time-stepping methods.

The parameters β, γ determine the variation of acceleration at a time step. The accuracy and stability depends on the value of the parameters selected.

This method has two special cases:

a. *Average acceleration:* In this method, the acceleration is constant over a time step.

$$\beta = \frac{1}{4} \text{ and } \gamma = \frac{1}{2}$$

To solve the equation 86 an iteration is required for a nonlinear system since unknown $\ddot{u}_{i+1}$ appears on the right side.

b. *Linear acceleration,* $\beta = \frac{1}{6}$ *and* $\gamma = \frac{1}{2}$

To solve the equation 86, it is possible to modify the equation and solve without iteration.

- *Wilson θ methods*

In figure 214 compares the accuracy of the three solution methods, in terms of amplitude decay (AD) and period elongation (PE). Linear and average acceleration.

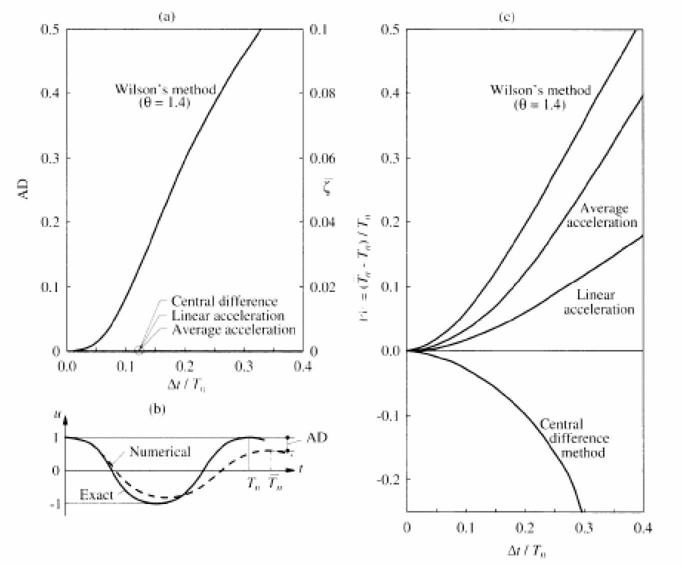

Figure B-1 Comparison of accuracy of numerical methods to solve dynamic equation of motion: a) AD (amplitude decay) versus Δt / T_n, b) definition of AD and PE (period elongation), c) period elongation versus Δt / T_n (Chopra, 1995).

Figure 214. Comparison of accuracy of numerical methods to solve dymanic equation of motion. (Chopra, 1995)

Note that in the time domain analysis, the motion is not decomposed into upwards and downwards components, as in frequency domain analysis. Instead, the calculated motions at the layers, $\{\ddot{u}\}$, and input motion at the base of the soil column, $\ddot{u}_g$, are the sum of both components. In 1D analysis, each individual layer i is represented by a corresponding mass, a spring, and a dashpot for viscous damping. Lumping half the mass of each of two consecutive layers at their common boundary forms the mass matrix. Since 1D model only considers vertical propagation of horizontal shear waves, a simple shear model is used.

The stiffness matrix is defined as:

$$k_i = \frac{G_i}{h_i}$$

Equation 88. Equation to define de stiffness matrix.

Where:

G_i: shear modulus of layer i. (For a linear-elastic material, it is constant)

h_i: thickness of layer i

When using a nonlinear soil model, k_i is the tangent stiffness of the shear model and updated at each time step. Viscous damping is added in the form of damping matrix [C], to represent damping at very small strains. There are two main numerical methods for solving the dynamic equation of motion used in site response analysis:

- Equivalent linear analysis method solved in frequency domain
- Nonlinear analysis performed in time domain

Although the equivalent linear analysis is widely used in engineering practice due to its simplicity, it is essentially a linear method that does not account for the change in soil properties throughout the duration of the ground motion. Nonlinear analysis, on the other hand, uses a step-by-step integration scheme and more accurately simulates the true nonlinear behavior of soils (Kramer 1996; Park et al. 2004a).

5.5. One dimensional linear equivalent analysis response using DEEPSOIL

To perform the One Dimensional (1-D) linear equivalent site response analysis, the software DEEPSOIL v7.0 (Hashash, M. I. Musgrove, et al. 2020) was used. The general quadratic hyperbolic model, implemented in DEEPSOIL, was used. First, the dynamic curves proposed by (Darendeli 2001) were adopted, secondly repeating the analysis with the dynamic curves obtained in the laboratory. To generate the nonlinear curves for each layer, the coefficient of lateral earth pressure (K_0), plasticity index (PI), number and frequency of cycles (N), loading frequency (f), and over consolidation ratio (OCR) were used, which previously were obtained in the field campaign detailed in Chapter 3. K_0 was calculated as 0.5 using the equation proposed by (Jaky 1944) based on the representative friction angle of each layer. Small strain damping (D_{min}) was also modeled using the functions of (Darendeli 2001), which usually predicts greater damping values near the ground surface, though keeps on decreasing along with the depth (Nguyen et al. 2020).

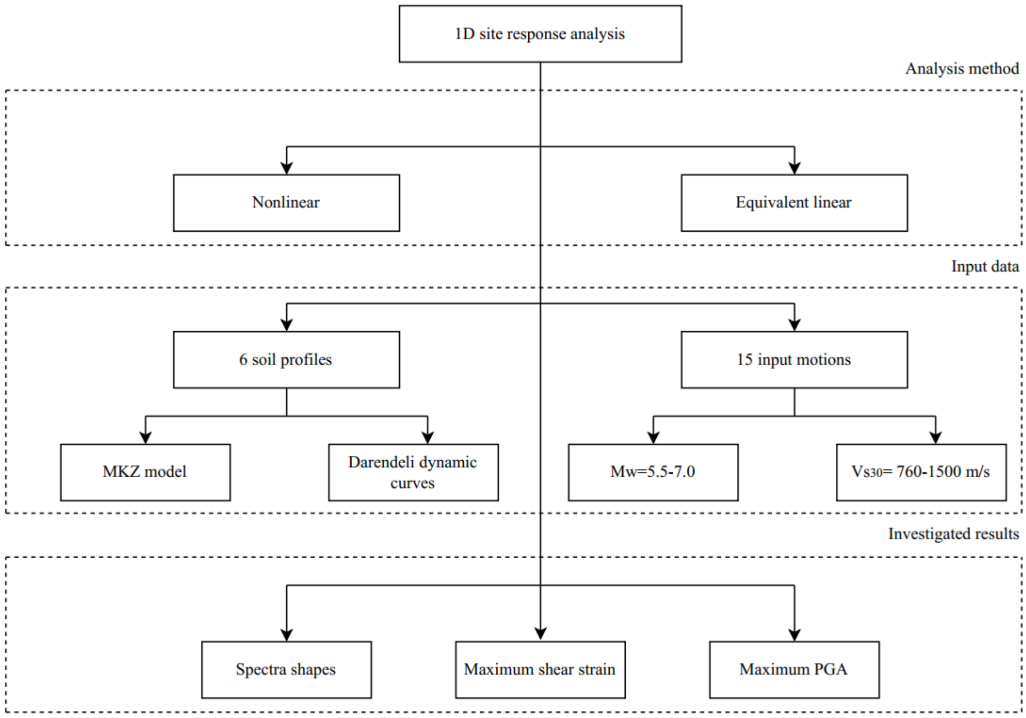

Figure 215. Description of the equivalent linear model.

The samples were obtained in 2019 prior to the start of the Covid-19 pandemic. Due to the worldwide quarantine for several months, the samples underwent changes in moisture content until they could be tested in 2022. With this background, 23 unaltered samples of the 25 required to perform the resonant column test were found. The state of these samples was dry, so the specimens were tested in this condition, however, they did not reflect the conditions in situ. For this reason, it was decided to elaborate remolded samples with the objective of simulating the in-situ conditions of density and moisture content, and later to analyze the effect of the change in moisture in the specimens on their dynamic behavior, as a secondary investigation of the main thesis project. For this reason, the analysis was performed for the following two cases:

a. Analysis with theoretical curves
b. Analysis with experimental curves
    b.1. Dry samples
    b.2. Remolded samples

The results are presented in Appendix C.2.

5.5.1. Results

The three highest values of the amplification factor results obtained by zone and by analysis are presented below:

Table 43. Amplification factor results for Zone A

Zone	Theoretical		Dry samples		Remolded samples	
	Amplification factor	**T (s)**	**Amplification factor**	**T (s)**	**Amplification factor**	**T (s)**
A	7.06	1.06	7.08	1.06	7.48	1.06
	6.99	0.99	7.01	0.99	7.21	0.99
	6.38	0.93	6.39	0.93	6.69	0.93

Table 44. Amplification factor results for Zone B

Zone	Theoretical		Dry samples		Remolded samples	
	Amplification factor	**T (s)**	**Amplification factor**	**T (s)**	**Amplification factor**	**T (s)**
B	2.90	1.63	2.19	2.69	3.07	1.63
	2.89	1.54	2.17	2.52	3.06	1.54
	2.89	10.00	2.15	2.86	2.97	2.52

Table 45. Amplification factor results for Zone C

Zone	Theoretical		Dry samples		Remolded samples	
	Amplification factor	T (s)	Amplification factor	T (s)	Amplification factor	T (s)
C	6.72	0.88	6.77	0.88	6.87	0.88
	6.42	0.82	6.55	0.82	6.81	0.93
	6.35	0.93	6.44	0.93	6.65	0.82

Table 46. Amplification factor results for Zone D

Zone	Theoretical		Dry samples		Remolded samples	
	Amplification factor	T (s)	Amplification factor	T (s)	Amplification factor	T (s)
D	7.68	1.06	7.68	1.06	7.74	1.06
	7.68	0.99	7.68	0.99	7.74	0.99
	6.89	0.93	6.89	0.93	6.97	0.93

Table 47. Amplification factor results for Zone E

Zone	Theoretical		Dry samples		Remolded samples	
	Amplification factor	T (s)	Amplification factor	T (s)	Amplification factor	T (s)
E	4.26	0.57	4.31	0.39	4.35	0.39
	4.15	0.60	4.30	0.42	4.32	0.42
	4.14	0.42	4.12	0.44	4.17	0.44

Table 48. Amplification factor results for Zone F

Zone	Theoretical		Dry samples		Remolded samples	
	Amplification factor	T (s)	Amplification factor	T (s)	Amplification factor	T (s)
F	5.08	0.73	5.08	0.73	5.28	0.73
	5.05	0.68	5.05	0.68	5.16	0.77
	5.05	0.77	5.05	0.77	5.09	0.68

Table 49. Amplification factor results for Zone G

Zone	Theoretical		Dry samples		Remolded samples	
	Amplification factor	T (s)	Amplification factor	T (s)	Amplification factor	T (s)
G	5.04	0.44	5.40	0.50	6.00	0.50
	5.02	0.57	5.10	0.64	5.36	0.53
	4.92	0.64	4.97	0.68	5.36	0.64

Table 50. Amplification factor results for Zone H

Zone	Theoretical		Dry samples		Remolded samples	
	Amplification factor	T (s)	Amplification factor	T (s)	Amplification factor	T (s)
H	5.21	0.20	5.21	0.20	5.16	0.20
	5.00	0.19	5.00	0.19	5.04	0.19
	4.75	0.22	4.75	0.22	4.86	0.17

Table 51. Amplification factor results for Zone I

Zone	Theoretical		Dry samples		Remolded samples	
	Amplification factor	T (s)	Amplification factor	T (s)	Amplification factor	T (s)
I	4.77	0.19	5.28	0.19	4.79	0.19
	4.23	0.20	4.74	0.17	4.31	0.20
	4.11	0.17	4.68	0.20	4.31	0.17

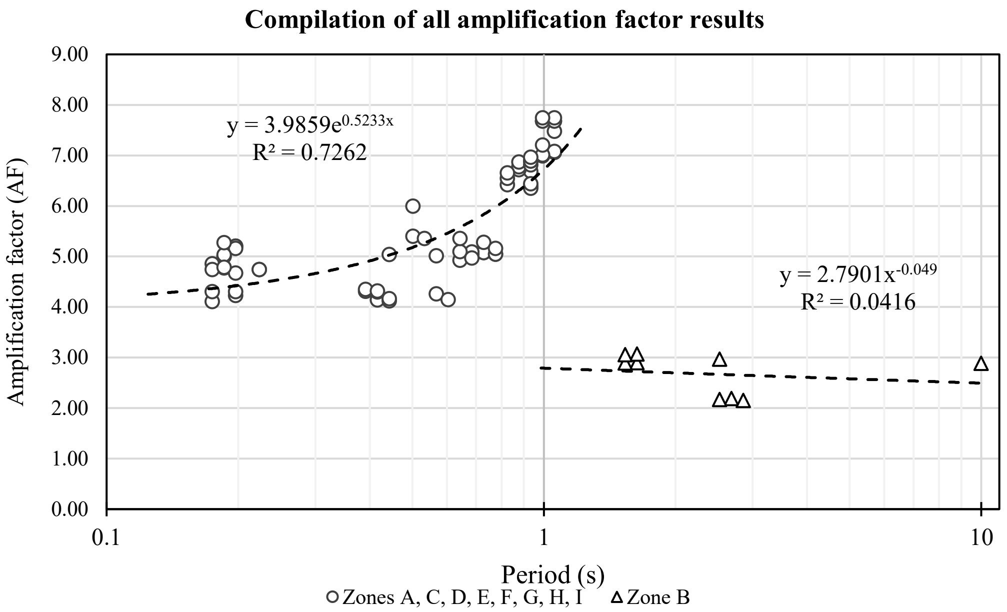

Figure 216. Compilation of all amplification factor results.

Figure 216 shows a compilation of the results obtained from section 5.5.1, where it is observed that the results obtained using the Darendeli (2001) curves, dry samples and remolded samples of all the zones, except zone B, present an exponential tendency in a range of periods between 0.1 and 1 s. Zone B presents a different behavior for the three types of analysis presented, having a potential tendency for a range of periods between 1 and 10 s. The different behavior of this zone can be related to the type of material present in this sector, which is composed of an organic stratum of high plasticity in the first 14 meters of depth (see section 3.3.1), where the water table is close to the surface, 1 meter deep (see section 5.2.1.2).

The Darendeli (2001) curves were used for the theoretical analysis since they consider the main effects throughout the entire range of deformation. When comparing the results of the maximum dynamic amplification factor, variations of 0.74 and 0.95 are obtained for comparing theoretical-dry and theoretical-remolded curves, respectively, which are less than unity.

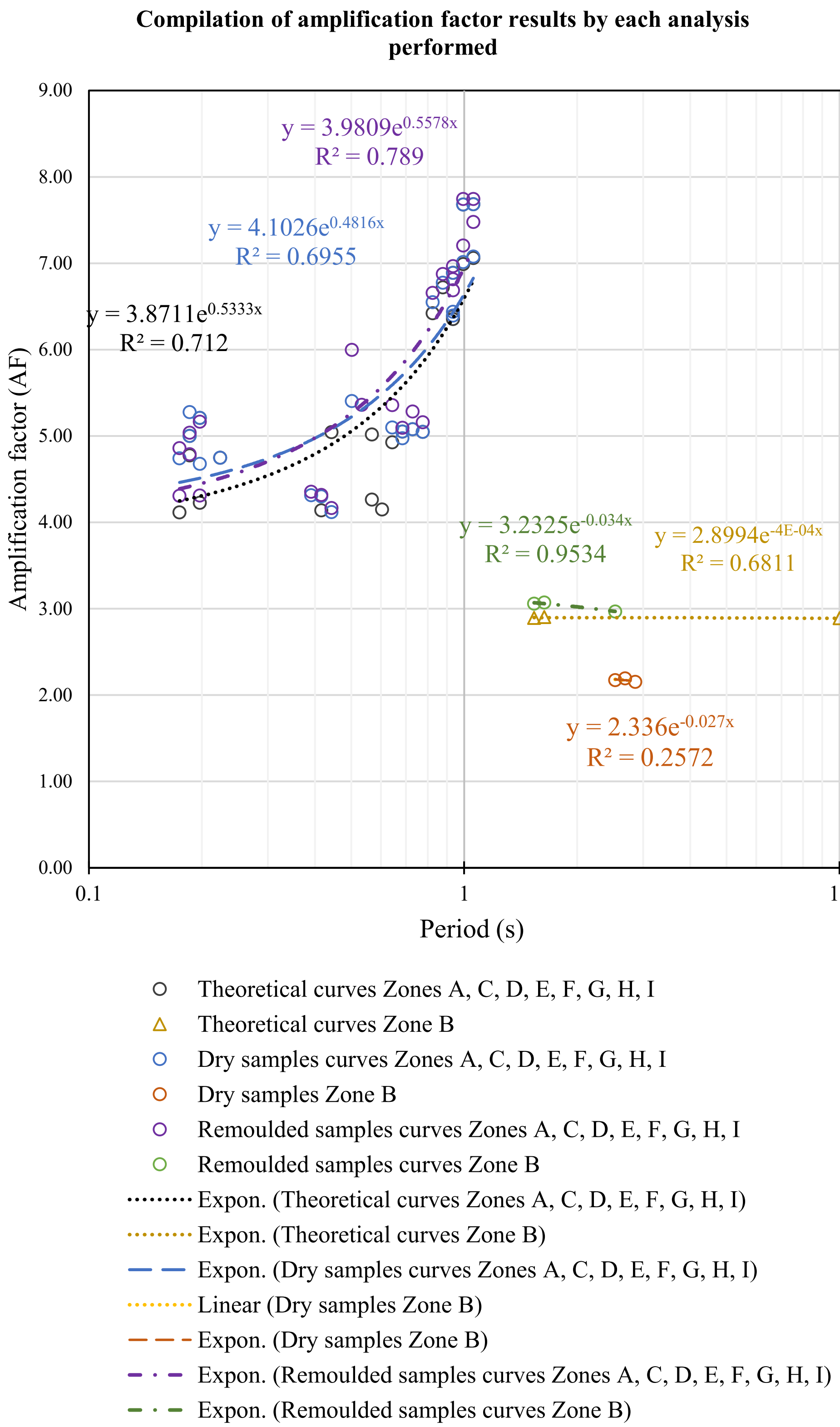

Figure 217. Compilation of amplification factor results by each analysis performed.

When comparing the curves generated by the peaks of the dynamic amplification factors with the theoretical curves, dry and remolded samples from each zone in figure 217, it is observed that zones A, C, D, E, F, G, H and I -where there are mainly mineral soils- exhibit a similar behavior of the trendline. The coefficient of determination R^2 values are close, with a minimum of 0.70 for the curves with dry samples, 0.71 for the theoretical curves, and a maximum of 0.79 for the remolded samples. On average it represents an R^2 of 0.73 with a standard deviation of 0.04.

In the case of zone B -where there are organic soils-, the change in R^2 is much more noticeable, with minimum values of 0.26 for the dry samples, 0.68 for the theoretical curves and 0.95 for the remolded samples. On average it represents an R^2 of 0.63 with a standard deviation of 0.29, which could be an indicator of the importance of humidity, as well as of the fabric and structure in this type of soil, which should be studied in greater depth in future research.

Table 52. Summary of analysis of the amplification factor results between dry and remolded samples.

Condition	Number of results	(%)
AF < 0.10	9	33.33
0.10 ≤ AF < 0.25	6	22.22
0.25 ≤ AF < 0.50	8	29.63
AF ≥ 0.50	4	14.81
Total	27	100.00

The geotechnical engineering problems have different uncertainties that can be studied based on safety factors and reliability. However, usually the laboratory specimens which are used to determine shear strength are prepared at water content and a dry density same as in the field conditions, but that conditions in the future might not remain the same. Furthermore, the durability of building structures is largely conditions by a proper foundation and the foundation is directly affected by unfavorable water relations in the soil, so excessive moisture content can bring permanent moistening of soil and it leads to significant changes in soil properties. (Bláhová, Ševelová, and Pilařová 2013; Shirgir et al. 2023; Ślusarek and Łupieżowiec 2020). According to the referenced literature, it was expected that as water content increases, shear strength decreases, but Bláhová et al. (2013) presented that this hypothesis was not proven for clayey soils, because the results had a considerable variability in the values obtained from shear tests of clayey soil, although they had a limited number of soil specimens, showed the necessity of taking moisture conditions into account, when processing stability analyses, in order to achieve reliable and safe constructions. Therefore, is important to investigate the effects the variability of mechanical and dynamic parameters which are dependent on moisture content, as the soil density, because from which we can obtain the shear wave velocity (Vs) and the shear modulus degradation (G/Go). (Minnucci et al. 2019).

In this research the results of amplification factor (AF) showed a total of 27 results from which the highest value of variation between dry and remolded samples is 0.89 with a period of 0.99 s, while the lowest value of variation is 0.02 for a period of 0.0 s. Furthermore, the 33.33%, belongs to the values of variation of AF of less than 10%, the 22.22% corresponds to the values of variation of AF between 10% to 25%, the 29.63% corresponds to the values of variation of AF between 25% to 50%, and the 14.81% belongs to the values of variation of AF that are higher than 50%. Therefore, this analysis of variations can show the highest percentaje of results corresponds to a variation lower than 10% for AF obtained between dry and remolded samples. In other words, the uncertainty in the definition of soils parameters affect the dynamic results, but in this case the uncertainty is limited to an analysis between dry and remolded samples obtaining the highest quantity of results with a variation lower than 10%. Consequently, the comparison of results between dry/remolded samples and unaltered samples is important to define the real uncertainty of the amplification factor, as the change in the water content in stored samples is an issue that can be found in soil mechanics laboratorories, and the research to determine these uncertainty with a higher accuracy, must be continued in the future with high quality unaltered samples.

CHAPTER 6

Final remarks and future research

- According to the Global Earthquake Model (GEM) Foundation (2022), the city of Quito is the capital of Ecuador, housing more than 15% of the national population and 87% of the population of the province of Pichincha, becoming the most important urban center in the country. It is located in a high seismic hazard zone, in a narrow valley of the Andes, from which most of the surface seismic events originate, which is also delimited by active faults. Furthermore, this has repercussions on the possible effects that may occur after an earthquake, for example, the local effect of amplification of seismic waves in the ground, due to the stratigraphy of the site. This phenomenon is critical for the city of Quito because the city is composed of more than 70% of buildings from 1 to 3 stories with a low level of seismic provisions. Therefore, within the study performed by the GEM Foundation in 2022, it was estimated that the city could have losses of 26 fatalities and 133 million dollars in an annual average, which can increase up to 74 fatalities and 311 million dollars considering the seismic amplification due to the quality of the soils present in the city. (Global Earthquake Model (GEM) Foundation 2022). For these reasons, the study of the potential amplification factors and dynamic behavior, especially in sectors with great heterogeneity in their soil types such as the south of Quito, should be studied, which is the main objective of this thesis, and which should continue to be studied in the future.
- The first 30 meters of 20 boreholes throughout southern Quito have been characterized by means of 1332 field tests and 2774 physical and mechanical laboratory tests. In addition to defining 6 cross-sectional profiles and 4 longitudinal profiles. Based on this information, 9 zones were defined according to their geographic location and physical and mechanical parameters.
- To define the depth of the bedrock, the information provided by the profiles and the information presented by (Pacheco et al. 2022) has been used. However, it is important to clarify that the depth of the basement is approximate, so it is recommended to elaborate a drilling campaign and additional studies with the objective of confirming the depth of the real bedrock.

- To define the 7 input motions (earthquakes), a literature review was performed, defining that the Quito fault is a 60 km long reverse blind fault system, with expected moment magnitudes between 5.2 and 6.6.
- To define the dynamic parameters, three types of analysis were established: theoretical curves, dry samples, and remolded samples. For which it was necessary to elaborate 9 soil columns according to the 9 predefined zones.
- Based on the soil columns, 25 similar strata were determined, thus defining the required number of resonant column tests for the analysis with dry and remolded samples. However, due to the absence of material, we were able to perform 23 tests for each analysis, and a total of 46 resonant column tests were performed.
- To perform the resonant column tests, the TSH-100 equipment developed by GCTS Testing Systems was used, by an iterative process in which the highest frequency must be found for a torque value applied to the specimen and increasing the torque value until the required deformation is reached, with the objective of obtaining a group of data that will help us to elaborate the degradation curve of the shear modulus and damping. MATLAB software was used to develop the shear modulus and damping degradation curves by means of parametric regression.
- Using the DEEPSOIL program, the transfer functions were calculated for the 9 soil columns for the three analyses proposed, obtaining the data of peak spectral acceleration (PSA), in function of gravity (g), from the superficial and basal layer for each recording of time in seconds. The spectral acceleration is a good index to hazard to buildings, because this value represents the maximum acceleration that a ground motion will cause in a linear oscillator with a specified natural period and damping level. Therefore, from these data the dynamic amplification factor is calculated as the ratio of the peak spectral acceleration of the superficial layer to the peak spectral acceleration of the basal layer for each recordind of time, obtaining the amplification factor curves for each soil column.
- Based on the results obtained which are presented in tables 43 to 51, it is observed that the maximum values of dynamic amplification factor are presented in the analysis with remolded samples in 7 of the 9 zones (A - G). However, in Zone H the same maximum value is presented for the theoretical analysis and with dry samples, while in Zone I the maximum value corresponds

to the analysis with dry samples. Moreover, the following conclusions are presented:

- In Zone A for the three types of analysis, the three highest amplification factor values range between 6.38 to 7.48 for periods between 0.93 to 1.06 s.

- The theoretical curves for Zone B the three highest amplification factor values range between 2.89 to 2.90 and period between 1.54 to 10 s, with dry samples, the values of amplification factor are between 2.15 to 2.19 and period between 2.52 to 2.86 s. However, for the analysis with dry samples, the amplification factor values range between 2.97 to 3.07 and period values between 1.54 to 2.52 s.

- In Zone C for the three types of analysis, the three highest amplification factor values ranged from 6.35 to 6.87 for periods between 0.82 to 0.93 s.

- The results corresponding to theoretical curves and dry samples analyses in Zone D are the same for the three highest values, having amplification factor values between 6.89 to 7.68 for periods between 0.93 and 1.06 s. However, for the analysis with remolded samples, the amplification factor values range between 6.97 to 7.74 for the same range of periods of those previously mentioned.

- In Zone E, the results corresponding to dry samples and remolded samples analyses are similar for the three highest amplification factor values, those range between 4.12 to 4.35 for periods between 0.39 to 0.44s. However, for the analysis with theoretical curves, the amplification factor values range between 4.14 to 4.26 for periods between 0.42 to 0.60s.

- In Zone F for the theoretical analysis and with dry samples, the amplification factor values range from 5.05 to 5.08, while in the analysis with remolded samples the amplification factor values range from 5.09 to 5.28. However, for the three types of analysis, period values are between 0.68 to 0.77 s.

- In Zone G, for the theoretical analysis, the amplification factor values range from 4.92 to 5.04, for period values between 0.44 to 0.64 s. In the analysis with dry samples, the amplification factor values range from 4.97 to 5.40, for period values between 0.50 to 0.68 s, while in the analysis with remolded samples the amplification factor values range from 5.36 to 6.00, for period values between 0.50 to 0.64 s.

- In Zone H, for the theoretical analysis and with dry samples, the amplification factor values range from 4.75 to 5.21 for period values between 0.19

to 0.22 s, while in the analysis with remolded samples the amplification factor values range from 4.86 to 5.16, for period values range from 0.17 to 0.20 s.

- In Zone I, for the theoretical analysis, the amplification factor values range from 4.11 to 4.77, for analysis with dry samples, the amplification factor values range from 4.68 to 5.28, while in the analysis with remolded samples the amplification factor values range from 4.31 to 4.79. For three analyses, period values were between 0.17 to 0.20 s.

- The results obtained show that the period values do not present a pattern of behavior, and therefore the following is obtained:

  - The period values present equal values for the three analyses in the following zones: A, C, D, F, H, I.
  - Zone B presents the highest period value for the analysis with dry samples, while for the other two the result is equal and the same.
  - Zone E presents the highest value of period in the theoretical analysis, while for the other two the value is equal and the same.
  - Zone G has the lowest period value in the theoretical analysis, while for the other two the value is the same and is the highest.

- To define the amplification factors for South Quito, we selected the results of remolded samples, as they can better represent field conditions than dry samples.

Table 53. Amplification factor for the South of Quito

Zone	Amplification factor	T (s)	H(z)
A	7.48	1.06	0.95
B	3.07	1.63	0.61
C	6.87	0.88	1.14
D	7.74	1.06	0.95
E	4.35	0.39	2.56
F	5.28	0.73	1.37
G	6.00	0.50	1.99
H	5.16	0.20	5.06
I	4.79	0.19	5.39

- Figures 218 and 219 show the following:
  1. For Zones A and D it is observed that the peak dynamic amplification is in a period close to 1 s (1 Hz), with a value of 1.06 s (0.95 Hz).

2. For Zones C, E, F, G, H, I it is observed that the dynamic amplification peaks have period values less than 1 s (1 Hz).
3. For Zone B it is observed that the dynamic amplification peak is at a period greater than 1 s (1 Hz). This change in behavior is analyzed in greater detail in figures 218-219, where the variation between the different theoretical analyses, with dry and remoulded samples, is much greater for zone B than for the rest of the zones, which could be an indicator of the importance of humidity, as well as of the fabric and structure in the dynamic behavior of organic soils, which should be studied in greater depth in future research.

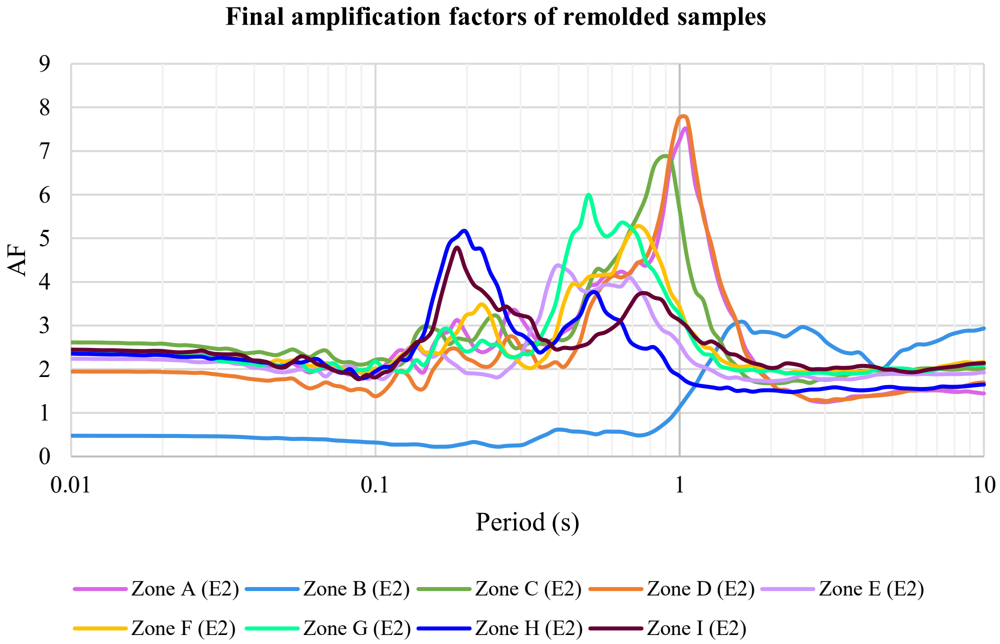

Figure 218. Compilation of amplification factor curves of remolded samples (Period)

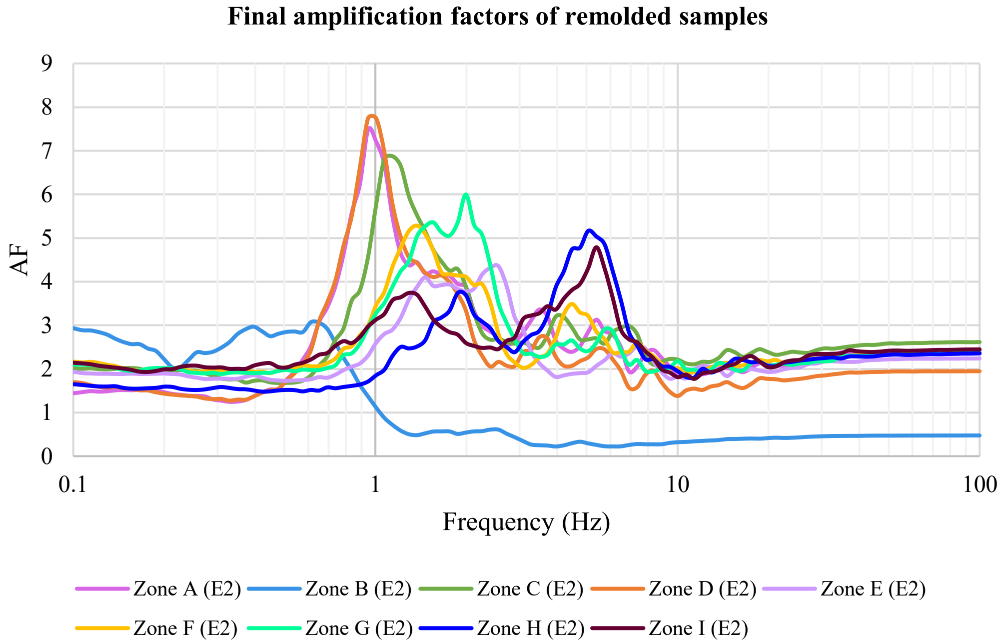

Figure 219. Compilation of amplification factor curves of remolded samples (Frequency)

- Figure 220 shows the Zoning Map of Southern Quito, which was based on all the data analyzed, the agrupation and location of the 21 boreholes for each zone.

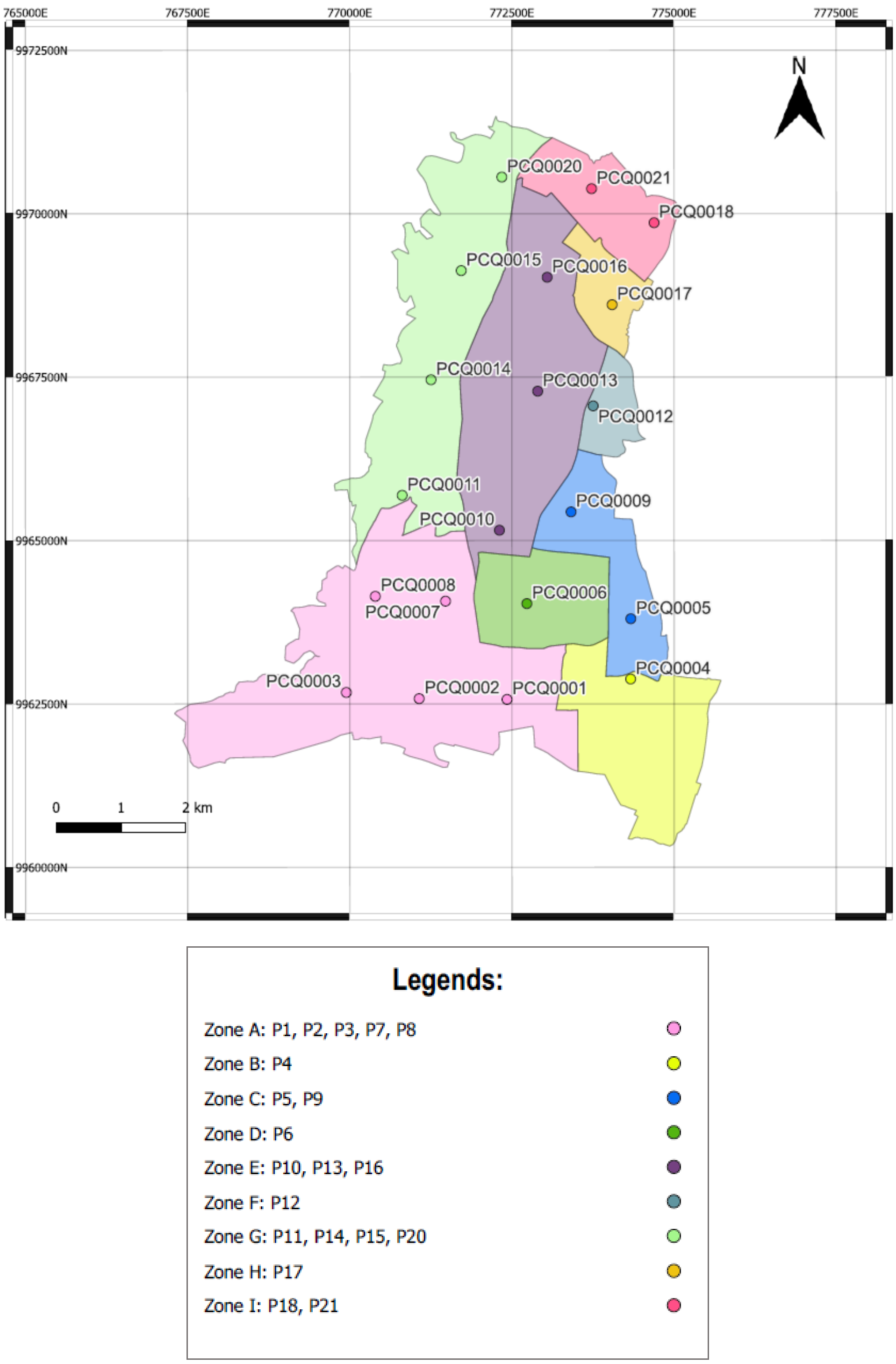

Figure 220. Map of South of Quito by geotechnical zones.

- Figure 221 shows the Hazard Map of South Quito by zones, which was based on the results of remolded samples because these samples can represent in-situ conditions better than dry samples. In addition, tables 43 to 51 shows that most of the amplification factor results, in 7 of 9 zones, are the highest for the remolded samples. Furthermore, four ranges of amplification factor can be distinguished and are represented by colors. The yellow colored zones have an amplification factor between 3.07 and 4.61, the light orange colored zones have an amplification factor between 4.61 and 5.18, the orange colored zones have an amplification factor between 5.18 and 5.86, the dark orange colored zones have an amplification factor between 5.86 and 7.11, and finally the red colored zones have an amplification factor between 7.11 and 7.74.

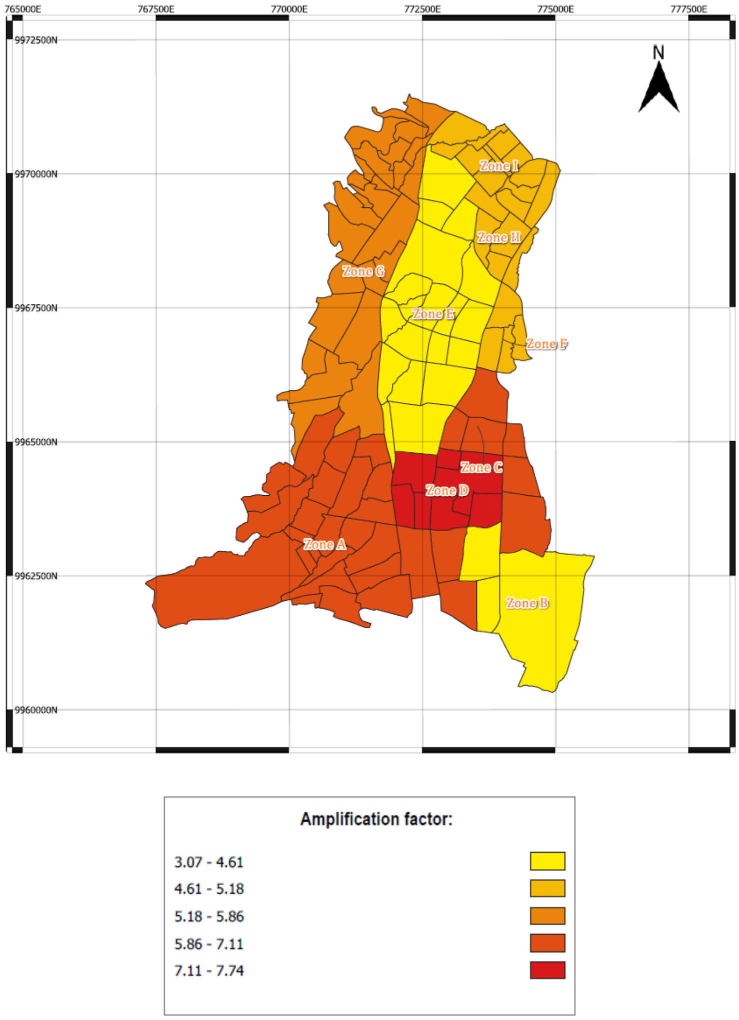

Figure 221. Hazard map by neighborhood of the South of Quito based on remolded samples.

BIBLIOGRAPHY

Aguiar, Roberto. 2013. "Microzonificación Sísmica de Quito." *Departamento de Ciencias de La Tierra y La Construcción ESPE* (August 2013).

Aguiar, Roberto. 2017. "Microzonificación Sísmica de Quito." *Departamento de Ciencias de La Tierra y La Construcción ESPE* 189.

Ahmed, Sayed M., Sherif W. Agaiby, and Ahmed H. Abdel-Rahman. 2013. "A Unified CPT-SPT Correlation for Non-Crushable and Crushable Cohesionless Soils." *Ain Shams Engineering Journal* 5(1):63–73. doi: 10.1016/j.asej.2013.09.009.

Aizprua, Carlos, C. Witt, M. Brönner, S. E. Johansen, D. Barba, and M. J. Hernandez. 2020. "Forearc Crustal Structure of Ecuador Revealed by Gravity and Aeromagnetic Anomalies and Their Geodynamic Implications." *Lithosphere* 2020(1):10707–21. doi: 10.2113/2020/2810692.

Albuja-Sánchez, Jorge. 2021. "Determination of the Undrained Shear Strength of Organic Soils Using the Cone Penetration Test and Marchetti´s Flat Dilatometer Test." Pp. 3–39 in *6th International Conference on Geotechnical and Geophysical Site Characterization*. Vol. 106.

Alfonso Naya, V., F. Courboulex, F. Bonilla, Mario Ruiz, Martin Vallée, and Hugo Yepes. 2012a. "A Large Earthquake in Quito (Ecuador): Ground Motion Simulations and Site Effects." *5th World Conference on Earthquake Engineering: Liboa (Portugal)* (1):10.

Alfonso Naya, V., F. Courboulex, F. Bonilla, Mario Ruiz, Martin Vallée, and Hugo Yepes. 2012b. "A Large Earthquake in Quito (Ecuador): Ground Motion Simulations and Site Effects." *5th World Conference on Earthquake Engineering: Liboa (Portugal)* (1):10.

Alvarado, A., L. Audin, J. M. Nocquet, S. Lagreulet, M. Segovia, Y. Font, G. Lamarque, H. Yepes, P. Mothes, F. Rolandone, P. Jarrín, and X. Quidelleur. 2014. "Active Tectonics in Quito, Ecuador, Assessed by Geomorphological Studies, GPS Data, and Crustal Seismicity." *Tectonics* 33(2):67–83. doi: 10.1002/2012TC003224.

Alvarado, A., L. Audin, J. M. Nocquet, Sandra Lagreulet, M. Segovia, Y. Font, G. Lamarque, H. Yepes, Patricia Mothes, Frédérique Rolandone, A. Alvadaro, L. Audin, J. M. Nocquet, Sandra Lagreulet, and M. Segovia. 2021. "Active Tectonics in Quito, Ecuador, Assessed by Geomorphological Studies, GPS Data, and Crustal Seismicity." doi: 10.1002/2012TC003224.Received.

Alvarado, Alexandra. 1996. "Evolución Geológica Cuaternaria y Paleosismicidad de La Cuenca de Quito (Ecuador)." Escuela Politécnica Nacional.

Alvarado, Alexandra. 2013. "Neotectonique et Cinematique de La Deformation Continentale En Equateur." 260.

Alvarado, Alexandra, Mario Ruiz, Patricia Mothes, Hugo Yepes, Mónica Segovia, Mayra Vaca, Cristina Ramos, Wilson Enríquez, Gabriela Ponce, Paul Jarrín, Jorge Aguilar, Wilson Acero, Sandro Vaca, Juan Carlos Singaucho, Daniel Pacheco, and Andrea Córdova. 2018. "Seismic, Volcanic, and Geodetic Networks in Ecuador: Building Capacity for Monitoring and Research." *Seismological Research Letters* 89(2A):432–39. doi: 10.1785/0220170229.

Arifuzzaman, and Md Anisuzzaman. 2022. "An Initiative to Correlate the SPT and CPT Data for an Alluvial Deposit of Dhaka City." *International Journal of Geo-Engineering* 13(1). doi: 10.1186/s40703-021-00170-3.

Assimaki, Dominic, Eduardo Kausel, and Andrew Whittle. 2000. "Model for Dynamic Shear Modulus and Damping for Granular Soils." *Journal of Geotechnical and Geoenvironmental Engineering* 126(10):859–69. doi: 10.1061/(ASCE)1090-0241(2000)126:10(859).

ASTM 2435/D2435M-11. 2020. "Standard Test Methods for One-Dimensional Consolidation Properties of Soils Using Incremental Loading." *Annual Book of ASTM Standards* i(Reapproved 2020):1–10. doi: 10.1520/D2435.

ASTM 2488-09a. 2009. "ASTMD 2488-09a Standard Practice for Description and Identification of Soils (Visual-Manual Procedure)." *Annual Book of ASTM Standards* (July):1–11. doi: 10.1520/D2488-09A.

ASTM C117 – 17. 2017. "Standard Test Method for Materials Finer than 75-Um (No.200) Sieve in Mineral Aggregates by Washing." (200):6–8.

ASTM D1586-11. 2011a. "Standard Test Method for Standard Penetration Test (SPT) and Split-Barrel Sampling of Soils." *ASTM International* 1–9.

ASTM D1586-11. 2011b. "Standard Test Method for Standard Penetration Test (SPT) and Split-Barrel Sampling of Soils." *ASTM International* 1–9.

ASTM D2216-10. 2010. "ASTM D2216-10 - Standard Test Methods for Laboratory Determination of Water (Moisture) Content of Soil and Rock by Mass." *ASTM International* (November 1988):1–7. doi: 10.1520/D2216-10.N.

ASTM D2216-19. 2019. "Standard Test Method for Laboratory Determination of Water (Moisture) Content of Soil and Rock by Mass." *ASTM International* (January):1–5. doi: 10.1520/D2216-19.

ASTM D2487-17. 2017. "ASTM D2487-17, Standard Practice for Classification of Soils for Engineering Purposes (Unified Soil Classification System), ASTM International, West Conshohocken, PA, 2017, Www.Astm.Org." 1–10. doi: 10.1520/D2487-17.

ASTM D3441-16. 2016. "Standard Test Method for Mechanical Cone Penetration Tests of Soil." *ASTM International* (July 2016):1–8. doi: 10.1520/D3441-16.2.

ASTM D4318, ASTM D 4318-10, and Astm D4318-05. 2005. "Standard Test Methods for Liquid Limit, Plastic Limit, and Plasticity Index of Soils." *Report* 04(March 2010):1–14. doi: 10.1520/D4318-10.

ASTM D4318-17. 2017. "Standard Test Methods for Liquid Limit, Plastic Limit, and Plasticity Index of Soils." *ASTM International* 04(March 2010):1–14. doi: 10.1520/D4318-17E01.

ASTM D6635-15. 2008. "Standard Test Method for Performing the Flat Plate Dilatometer." *Manual on Hydrocarbon Analysis, 6th Edition* 04:545-545–3. doi: 10.1520/D6635-15.2.

ASTM D6635-15. 2015. "Standard Test Method for Performing the Flat Plate Dilatometer." *ASTM International* 04:545-545–3. doi: 10.1520/D6635-15.2.

ASTM D6913-17. 2017. "Standard Test Methods for Particle-Size Distribution (Gradation) of Soils Using Sieve Analysis." *ASTM International* 04(Reapproved 2009). doi: 10.1520/D6913.

ASTM D7263. 2021. "Standard Test Methods for Laboratory Determination of Density and Unit Weight of Soil Specimens | Engineering360." *United States: American Society for Testing and Material.* i:1–7. doi: 10.1520/D7263-21.1.2.

ASTM D7263-21. 2021. "Standard Test Methods for Laboratory Determination of Density (Unit Weight) of Soil." *ASTM International* i:1–7. doi: 10.1520/D7263-21.1.2.

ASTM D7928-21. 2021. "Standard Test Method for Particle-Size Distribution (Gradation) of Fine-Grained Soils Using the Sedimentation (Hydrometer) Analysis." *ASTM International* 1–25. doi: 10.1520/D7928-21E01.

Avilés, Lucía. 2013. "Caracterización Geológica - Geotectónica Del Sur de La Ciudad de Quito." 190.

Barani, Simone, Roberto de Ferrari, and Gabriele Ferretti. 2013. "Influence of Soil Modeling Uncertainties on Site Response." *Earthquake Spectra* 29(3):705–32. doi: 10.1193/1.4000159.

Beauval, Céline, Hugo Yepes, William H. Bakun, José Egred, Alexandra Alvarado, and Juan Carlos Singaucho. 2010. "Locations and Magnitudes of Historical Earthquakes in the Sierra of Ecuador (1587-1996)." *Geophysical Journal International* 181(3):1613–33. doi: 10.1111/j.1365-246X.2010.04569.x.

Beauval, Céline, Hugo Yepes, Pablo Palacios, Monica Segovia, Alexandra Alvarado, Yvonne Font, Jorge Aguilar, Liliana Troncoso, and Sandro Vaca. 2013. "An Earthquake Catalog for Seismic Hazard Assessment in Ecuador." *Bulletin of the Seismological Society of America* 103(2 A):773–86. doi: 10.1785/0120120270.

Bernard, B., and D. Andrade. 2011. "Volcanes Cuaternarios Del Ecuador Continental." *IGEPN Poster Informativo* (January). doi: 10.13140/RG.2.1.3851.3683.

Bláhová, Kristýna, Lenka Ševelová, and Pavla Pilařová. 2013. "Influence of Water Content on the Shear Strength Parameters of Clayey Soil in Relation to Stability Analysis of a Hillside in BRNO Region." *Acta Universitatis Agriculturae et Silviculturae Mendelianae Brunensis* 61(6):1583–88. doi: 10.11118/actaun201361061583.

Bonnardot, M. A. 2003. "Modélisation Numérique Des Andes d'Equateur: Des Accrétions Océaniques à La Déformation Continentale (80-0 Ma)." *Mémoire DEA, Univirsité Savoie*.

Bonnefoy-Claudet, Sylvette, Cécile Cornou, Pierre Yves Bard, Fabrice Cotton, Peter Moczo, Jozef Kristek, and Donat Fäh. 2006. "H/V Ratio: A Tool for Site Effects Evaluation. Results from 1-D Noise Simulations." *Geophysical Journal International* 167(2):827–37. doi: 10.1111/j.1365-246X.2006.03154.x.

Borcherdt, R. D. 1970. "Effects of Local Geology on Ground Motion near San Francisco Bay*." *Bulletin of the Seismological Society of America* 60(1):29–61. doi: 10.1785/BSSA0600010029.

Burland, John, Tim Chapman, Hilary D. Skinner, and Michael Brown. 2012a. *ICE Manual of Geotechnical Engineering*.

Burland, John, Tim Chapman, Hilary D. Skinner, and Michael Brown. 2012b. *ICE Manual of Geotechnical Engineering*.

Bustos, J., Pastén, C., Pavez, D., Acevedo, M., Ruiz, S., & Astroza, R. (2023). Two-dimensional simulation of the seismic response of the Santiago Basin, Chile. Soil Dynamics and Earthquake Engineering, 164, 107569. https://doi.org/10.1016/J.SOILDYN.2022.107569

Calderon A, Yepes-Estrada C, Celi C, Marrero J, Yepes H, Alarcón F, Ordoñez J. 2022. *Evaluación de Riesgo Sísmico Para El Distrito Metropolitano de Quito. GEM-TREQ Reporte Técnico D2.6.1*.

Carrer, Michela. 2013. "Local Site Seismic Response in an Alpine Valley: Seismic Microzonation of the Castel Caldes Area (North-Western Trentino)."

Castelli, Francesco, and Valentina Lentini. 2017. "Dynamic Characterization of Municipal Solid Waste by In Situ and Laboratory Tests." *Journal of Geotechnical and Geoenvironmental Engineering* 143(5):06017002. doi: 10.1061/(asce)gt.1943-5606.0001641.

Cavallaro, Antonio, Piera Capilleri, and Salvatore Grasso. 2018. "Site Characterization by Dynamic In Situ and Laboratory Tests for Liquefaction Potential Evaluation during Emilia Romagna Earthquake." *Geosciences* 8(7):242. doi: 10.3390/geosciences8070242.

Celi, Carlos, and Juan Pantoja Moyano. 2017. "FINAL REPORT: CAPACITY CURVES AND FRAGILITY CURVES OF RESIDENTIAL BUILDINGS FOR THE CITY OF QUITO. Seismic Assessment of the Heritage Structures of Quito-Ecuador, through Incremental Dynamic Analysis. View Project Exposure Model and Vulnerability Functions of Residential Buildings for the City of Quito-South America Project (SARA Quito) View Project." doi: 10.13140/RG.2.2.28046.46402.

Chen, W. F., and E. Mizuno. 1990. *Nonlinear Analysis in Soil Mechanics: Theory and Implementation*. Elsevier.

Chetry, Viviana. 2018. "CARATTERIZZAZIONE DINAMICA DEI TERRENI DI ALCUNI COMUNI DELLE MARCHE PER LA MICROZONAZIONE SISMICA." Politecnico di Torino.

Chunga, Kervin, Franz Livio, Maurizio Mulas, Felipe Ochoa-Cornejo, Davide Besenzon, Maria Francesca Ferrario, and Alessandro Maria Michetti. 2018. "Earthquake Ground Effects and Intensity of the 16 April 2016 Mw 7.8 Pedernales, Ecuador, Earthquake: Implications for the Source Characterization of Large Subduction Earthquakes." *Bulletin of the Seismological Society of America* 108(6):3384–97. doi: 10.1785/0120180051.

Costa, Carlos, Alexandra Alvarado, Franck Audemard, Laurence Audin, Carlos Benavente, F. Hilario Bezerra, José Cembrano, Gabriel González, Myriam López, Estela Minaya, Isabel Santibañez, Julio Garcia, Mónica Arcila, Marco Pagani, Irene Pérez, Fabrizio Delgado, Mónica Paolini, and Hernán Garro. 2020. "Hazardous Faults of South America; Compilation and Overview." *Journal of South American Earth Sciences* 104(September). doi: 10.1016/j.jsames.2020.102837.

Courboulex, Francoise, David Alejandro Castro-Cruz, Aurore Laurendeau, Luis Fabian Bonilla, Alexandra Alvarado, and Etienne Bertrand. 2022. "Ground Motion Simulations in Quito (Ecuador) Due to Major Earthquakes from the Subduction Zone." *Geophysical Journal International* 229(3):2192–2208. doi: 10.1093/gji/ggac044.

Crespellani, Teresa, and Johann Facciorusso. 2014. *Dinamica Dei Terreni per Le Applicazioni Sismiche*.

Cuffaro, Livio. 2020. "Risposta Dei Terreni a Carichi Ciclici: Implementazione Di Un Database Di Prove Di Laboratorio." Politecnico di Torino.

D1587, ASTM. 2008. “Standard Practice for Thin-Walled Tube Sampling of Soils for Geotechnical Purposes.” *ASTM Standard Practice* D1587-08(Reapproved 2007):1–4.

Darendeli, Mehmet Baris. 2001. “Development of a New Family of Normalized Modulus Redction and Material Damping Curves.” The University of Texas at Austin.

Dobry, Ricardo, and Mladen Vucetic. 1987. “Dynamic Properties and Seismic Response of Soft Clay Deposits Liquefaction Analysis View Project.” (JANUARY 1987):39.

EEFIT. 2018. “The Muisne, Ecuador Earthquake of 16 April 2016. A Field Report by EEFIT.” (April):1–210.

ERN. 2012. *MICROZONIFICACIÓN SÍSMICA DEL DISTRITO METROPOLITANO DE QUITO: ESTUDIO DE LA AMENAZA SÍSMICA A NIVEL LOCAL. ECUADOR INFORME FINAL.*

Escribanoa, D. E., and D. F. T. Nashb. 2015. “Changing Anisotropy of G0 in Hostun Sand during Drained Monotonic and Cyclic Loading.”

Escuela Politecnica Nacional, GeoHazards International, Ilustre Municipo de Quito, ORSTOM Quito, and OYO Corporation. 1994. “The Quito, Ecuador, Risk Management Project - An Overview.” (January).

GCTS Testing Systems. 2007. “Resonant Column & Torsional Shear Test.” (1.85):105.

van Ginkel, Janneke, Elmer Ruigrok, Jan Stafleu, and Rien Herber. 2022. “Development of a Seismic Site-Response Zonation Map for the Netherlands.” *Natural Hazards and Earth System Sciences* 22(1):41–63. doi: 10.5194/nhess-22-41-2022.

Giretti, Daniela, and Vincenzo Fioravante. 2017. “A Correlation to Evaluate Cyclic Resistance from CPT Applied to a Case History.” *Bulletin of Earthquake Engineering* 15(5):1965–89. doi: 10.1007/s10518-016-0057-7.

Global Earthquake Model (GEM) Foundation. 2022. *Evaluación de Riesgo Sísmico Para El Distrito Metropolitano de Quito*.

Gobierno Autónomo Descentralizado del Distrito Metropolitano de Quito, Escuela Politécnica Nacional, and Pontificia Universidad Católica del Ecuador. 2019. *Informe 4: Caracterización Geológica, Geotécnica y Geofísica Del Subsuelo de Quito D.M., Fase 1*. Quito.

Goretti, Agostino, Carlos Molina Hutt, and Lida Hedelund. 2017. “Post-Earthquake Safety Evaluation of Buildings in Portoviejo, Manabí Province, Following the Mw7.8 Ecuador Earthquake of April 16, 2016.” *International Journal of Disaster Risk Reduction* 24(June):271–83. doi: 10.1016/j.ijdrr.2017.06.011.

Guéguen, P., J. L. Chatelain, B. Guillier, and H. Yepes. 2000. “2000_Gueguen_An Indication of the Soil Topmost Layer Response in Quito Ecuador Unsing Nois HV Spectral Ratio.Pdf.” *Soil Dynamics and Earthquake Engineering* 127–33.

Guerreiro, P., S. Kontoe, and D. Taborda. 2012. “Comparative Study of Stiffness Reduction and Damping Curves.” *15th World Conference on Earthquake Engineering* 2–11.

Hallal, Mohamad M., and Brady R. Cox. 2021. “An H/V Geostatistical Approach for Building Pseudo-3D Vs Models to Account for Spatial Variability in Ground Response Analyses Part I: Model Development.” *Earthquake Spectra* 37(3):2013–40. doi: 10.1177/8755293020981989.

Hao, Gang-Lai, and Thomas M. H. Lok. 2008. “Study of Shear Wave Velocity of Macao Marine Clay under Anisotropic Stress Condition.”

Hardin, Bobby O., and Vincent P. Drnevich. 1972a. “Shear Modulus and Damping in Soils: Design Equations and Curves.” *Journal of the Soil Mechanics and Foundations Division* 98(7):667–92. doi: 10.1061/jsfeaq.0001760.

Hardin, Bobby O., and Vincent P. Drnevich. 1972b. “Shear Modulus and Damping in Soils: Measurement and Parameter Effects (Terzaghi Leture).” *Journal of the Soil Mechanics and Foundations Division* 98(6):603–24. doi: 10.1061/jsfeaq.0001756.

Hartzell, S., L. F. Bonilla, and R. A. Williams. 2004. “Prediction of Nonlinear Soil Effects.” *Bulletin of the Seismological Society of America* 94(5):1609–29. doi: 10.1785/012003256.

Hashash, Youssef M. A., Michael Musgrove, Joseph Harmon, O. Ilhan, G. Xing, O. Numanoglu, D. R. Groholski, C. A. Phillips, and D. Park. 2020. “Deepsoil 7.” 1–170.

Hashash, Youssef M. A., Michael I. Musgrove, Joseph A. Harmon, Okan Ilhan, Guangchao Xing, Ozgun Numanoglu, David Groholski, Camilo A. Phillips, and Duhee Park. 2020. *DEEPSOIL V7.0, User Manual*. Urbana, IL: Board of Trustees of University of Illinois at Urbana-Champaign.

Huang, Xin, Xiaoguang Cai, Jingshan Bo, Sihan Li, and Wenhao Qi. 2021. “Experimental Study of the Influence of Gradation on the Dynamic Properties of Centerline Tailings Sand.” *Soil Dynamics and Earthquake Engineering* 151(January):106993. doi: 10.1016/j.soildyn.2021.106993.

Hughes, Richard A., and Luis F. Pilatasig. 2002. “Cretaceous and Tertiary Terrane Accretion in the Cordillera Occidental of the Andes of Ecuador.” *Tectonophysics* 345(1–4):29–48. doi: 10.1016/S0040-1951(01)00205-0.

Hungerbühler, Dominik, Michael Steinmann, Wilfried Winkler, Diane Seward, Arturo Egüez, Dawn E. Peterson, Urs Helg, and Cliff Hammer. 2002. “Neogene Stratigraphy and Andean Geodynamics of Southern Ecuador.” *Earth-Science Reviews* 57(1–2):75–124. doi: 10.1016/S0012-8252(01)00071-X.

INEC. 2022. “Proyección de La Población Ecuatoriana, Por 2010-2020.” Retrieved (https://www.ecuadorencifras.gob.ec/proyecciones-poblacionales/).

Jaillard, Etienne. 2022. “Earth-Science Reviews Late Cretaceous-Paleogene Orogenic Build-up of the Ecuadorian Andes : Review and Discussion.” *Earth-Science Reviews* 230(April):104033. doi: 10.1016/j.earscirev.2022.104033.

Jaillard, Etienne, M. Caron, A. Dhondt, M. Ordoñez, R. Andrade, P. Bengtson, L. Bulot, H. Cappetta, C. Dávila, and R. Díaz. 1997. “Síntesis Estratigráfica y Sedimentológica Del Cretáceo y Paleógeno de La Cuenca Oriental Del Ecuador.” *Orstom-Petroproduccion Eds* 164.

Jaky, J. 1944. “The Coefficient of Earth Pressure at Rest.” *Journal of the Society of Hungarian Architects and Engineers* 355–58.

Jiang, P.-L., Jiang, H., Yu, T.-Y., Sun, T.-Y., & Zhang, L. (2020). Influence of 3D Urban Dense Building Groups on Magnification of Ground Motion in Homogeneous Sedimentary Basin. Shock and Vibration, 2020. https://doi.org/10.1155/2020/8812424

Kaklamanos, James. 2012. “Quantifying Uncertainty in Earthquake Site Response Models Using the KiK-Net Database.” (November).

Kendrick, Eric, Michael Bevis, Robert Smalley, Benjamin Brooks, Rodrigo Barriga Vargas, Eduardo Lauría, and Luiz Paulo Souto Fortes. 2003. "The Nazca-South America Euler Vector and Its Rate of Change." *Journal of South American Earth Sciences* 16(2):125–31. doi: 10.1016/S0895-9811(03)00028-2.

Kramer, Steven. 1996. *Geotechnical Earthquake Engineering*.

de la Torre, Christopher A., Brendon A. Bradley, and Christopher R. McGann. 2021. "2D Geotechnical Site-Response Analysis Including Soil Heterogeneity and Wave Scattering." *Earthquake Spectra* 38(2):1124–47. doi: 10.1177/87552930211056667.

Lanzo, G., and F. Silvestri. 1999. *Risposta Sismica Locale, Teoria Ed Esperienze*.

Laurendeau, A, L-f Bonilla, D. Mercerat, F. Courboulex, A. Alvarado, and J. C. Singaucho. 2017. "Seismic Response of the Basin of Quito From Continuous Accelerometric Records of RENAC-Quito." *16th World Conference on Earthquake Engineering* (January):1–12.

Laurendeau, Aurore, Françoise Courboulex, Luis Fabian Bonilla, Alexandra Alvarado, Victor Alfonso Naya, Philippe Guéguen, E. Diego Mercerat, Juan Carlos Singaucho, Etienne Bertrand, Matthieu Perrault, Juan Gabriel Barros, and Mario Ruiz. 2017. "Low-Frequency Seismic Amplification in the Quito Basin (Ecuador) Revealed by Accelerometric Recordings of the RENAC Network." *Bulletin of the Seismological Society of America* 107(6):2917–26. doi: 10.1785/0120170134.

Lavenu, A., C. Noblet, M. G. Bonhomme, A. Egüez, F. Dugas, and G. Vivier. 1992. "New K□Ar Age Dates of Neogene and Quaternary Volcanic Rocks from the Ecuadorian Andes: Implications for the Relationship between Sedimentation, Volcanism, and Tectonics." *Journal of South American Earth Sciences* 5(3):309–20. doi: https://doi.org/10.1016/0895-9811(92)90028-W.

Lopez J., Vera-Grunauer X., Rollins K., Salvatierra G. 2018. "Gravelly Soil Liquefaction after the 2016 Ecuador Earthquake." *Geotechnical Earthquake Engineering and Soil Dynamics V GSP 290*.

Lunne, T., P. Robertson, and J. Powell. 1997. "Cone Penetration Testing in Geotechnical Practice."

Marchetti, S. 1980. "In Situ Tests by Flat Dilatometer." *Journal of the Geotechnical Engineering Division, ASCE* 106(GT3, Proc.).

Marchetti, S., and D. Crapps. 1981. "Flat Dilatometer Manual."

Marchetti, Silvano, Diego Marchetti, and Felipe Villalobos. 2013. "El Dilatómetro Sísmico SDMT Para Ensayos de Suelos in Situ." *Obras y Proyectos* (13):20–29. doi: 10.4067/s0718-28132013000100002.

Mariniere, J., J. M. Nocquet, C. Beauval, J. Champenois, L. Audin, A. Alvarado, S. Baize, and A. Socquet. 2020. "Geodetic Evidence for Shallow Creep along the Quito Fault, Ecuador." *Geophysical Journal International* 220(3):2039–55. doi: 10.1093/gji/ggz564.

Marjiyono, I. Setiadi, and J. Setiawan. 2021. "The Estimation of Seismic Site Amplification of Bukittinggi City, West Sumatera, Indonesia." *IOP Conference Series: Earth and Environmental Science* 873(1). doi: 10.1088/1755-1315/873/1/012009.

de Martin, Florent. 2010. "Influence of the Nonlinear Behaviour of Soft Soils on Strong Ground Motions." *Earth Sciences* 214.

McGann, C. R., Bradley, B. A., Wotherspoon, L. M., & Lee, R. L. (2021). Basin effects and limitations of 1D site response analysis from 2D numerical models

of the Thorndon basin. Bulletin of the New Zealand Society for Earthquake Engineering, 54(1), 21–30. https://doi.org/10.5459/bnzsee.54.1.21-30
Mégard, Francois. 1987. “Cordilleran Andes and Marginal Andes: A Review of Andean Geology North of the Arica Elbow (18 (S.” *Circum-Pacific Orogenic Belts and Evolution of the Pacific Ocean Basin* 18:71–95.
Mégard, Francois. 1989. “The Evolution of the Pacific Ocean Margin in South America North of Arica Elbow (18°S).” *The Evolution of the Pacific Ocean Margins* 208–30.
Mera, Walter, Xavier Vera, Antonio La Tegola, and Guillermo Ponce. 2017. “April 2016 Ecuador Earthquake of Moment Magnitude M_w7.8: Overview and Damage Report.” *Key Engineering Materials* 747:662–69. doi: 10.4028/www.scientific.net/kem.747.662.
Minnucci, L., F. Dezi, S. Carbonari, M. Morici, F. Gara, and G. Leoni. 2019. “Effects of Uncertainties of Soil and Pile Mechanical Properties on the Dynamic Stiffness of Single Piles in Homogenous Deposits.” Pp. 4157–65 in *COMPDYN Proceedings*. Vol. 3.
Muñoz, Andrés. 2017. “Laboratory Manual to Determine Dynamic Parameters in Soils, with the Use of the Following Equipment: Cyclic Triaxial, Resonant Column and Piezoelectric Bender Elements.” Pontificia Universidad Católica del Ecuador.
Naik, Sambit Prasanajit, Nihar Ranjan Patra, and Javed N. Malik. 2022. “Cyclic Behavior of Late Quaternary Alluvial Soil along Indo-Gangetic Plain: Northern India.” *International Journal of Geo-Engineering* 13(1). doi: 10.1186/s40703-021-00167-y.
Nautiyal, Praveen, Dhiraj Raj, M. Bharathi, and Ramanand Dubey. 2021. “Ground Response Analysis: Comparison of 1D, 2D and 3D Approach BT - Proceedings of the Indian Geotechnical Conference 2019.” Pp. 607–19 in, edited by S. Patel, C. H. Solanki, K. R. Reddy, and S. K. Shukla. Singapore: Springer Singapore.
Nguyen, Van-quang, Muhammad Aaqib, Duy-duan Nguyen, Nguyen-vu Luat, and Duhee Park. 2020. “Applied Sciences A Site-Specific Response Analysis : A Case Study In.” *Applied Sciences (Switzerland)* 10(11).
Ocaña, Doménica. 2019. “Implementación Del Método de Calibración de La Energía de Penetración Dinámica Según La Normativa ASTM D4633 – 16, Con Aplicación al Análisis Del Potencial de Licuefacción En Suelos Granulares En Una Zona Específica de Manabí.”
Ozaslan, B., Iyisan, R., Hasal, M. E., Khanbabazadeh, H., & Yamanaka, H. (2022). Assessment of the design spectrum with aggravation factors by 2D nonlinear numerical analyses: a case study in the Gemlik Basin, Turkey. Bulletin of Earthquake Engineering, 20(3), 1371–1395. https://doi.org/10.1007/s10518-021-01296-6
Pacheco, D., E. D. Mercerat, F. Courboulex, L. F. Bonilla, A. Laurendeau, and A. Alvarado. 2022. “Profiling the Quito Basin (Ecuador) Using Seismic Ambient Noise.” *Geophysical Journal International* 228(2):1419–37. doi: 10.1093/gji/ggab408.
Panzera, F., Alber, J., Imperatori, W., Bergamo, P., & Fäh, D. (2022). Reconstructing a 3D model from geophysical data for local amplification

modelling: The study case of the upper Rhone valley, Switzerland. Soil Dynamics and Earthquake Engineering, 155. https://doi.org/10.1016/j.soildyn.2022.107163

Park, Duhee, Youssef M. A. Hashash, D. Ph, and Youssef M. A. Hashash. 2004a. “Estimation of Non-Linear Seismic Site Effects for Deep Deposits of the Mississippi Embayment.” (October).

Park, Duhee, Youssef M. A. Hashash, D. Ph, and Youssef M. A. Hashash. 2004b. “Estimation of Non-Linear Seismic Site Effects for Deep Deposits of the Mississippi Embayment.” (October).

Peñafiel, Lilia. 2008. “Geología y Análisis Del Recurso Hídrico Subterráneo de La Subcuenca Del Sur de Quito.” Escuela Politécnica Nacional.

Petersen, Mark D., Stephen C. Harmsen, Kishor S. Jaiswal, Kenneth S. Rukstales, Nicolas Luco, Kathleen M. Haller, Charles S. Mueller, and Allison M. Shumway. 2018. “Seismic Hazard, Risk, and Design for South America.” *Bulletin of the Seismological Society of America* 108(2):781–800. doi: 10.1785/0120170002.

del Pino, Inés, and Hugo Yepes. 1990. *1990 Apuntes Para Una Historia Sísmica de Quito*. Quito.

Potts, D. M., L. Zdravkovic, and L. Zdravković. 1999. *Finite Element Analysis in Geotechnical Engineering: Theory*. Thomas Telford.

Pousse-Beltran, Lea, Riccardo Vassallo, Franck Audemard, François Jouanne, Julien Carcaillet, Erwan Pathier, and Matthieu Volat. 2017. “Pleistocene Slip Rates on the Boconó Fault along the North Andean Block Plate Boundary, Venezuela.” *Tectonics* 36(7):1207–31. doi: https://doi.org/10.1002/2016TC004305.

Pratt, Warren T., Pablo Duque, and Miguel Ponce. 2005. “An Autochthonous Geological Model for the Eastern Andes of Ecuador.” *Tectonophysics* 399(1):251–78. doi: https://doi.org/10.1016/j.tecto.2004.12.025.

Primofiore, Ilaria, Julie Baron, Peter Klin, Giovanna Laurenzano, Cristina Muraro, Franco Capotorti, Marco Amanti, and Giovanna Vessia. 2020. “3D Numerical Modelling for Interpreting Topographic Effects in Rocky Hills for Seismic Microzonation: The Case Study of Arquata Del Tronto Hamlet.” *Engineering Geology* 279:105868. doi: https://doi.org/10.1016/j.enggeo.2020.105868.

Pua, Lina María, Jorge Macedo, Juan P. Villacreses, Bernardo Caicedo, and Fabricio Yépez. 2021. “A Homogenization Approach to Estimate the Shear Modulus of Spatially Variable Soil Materials.” *Soil Dynamics and Earthquake Engineering* 151(April). doi: 10.1016/j.soildyn.2021.106970.

Robertson, P. K. 2009. “Interpretation of Cone Penetration Tests - A Unified Approach.” *Canadian Geotechnical Journal* 46(11). doi: 10.1139/T09-065.

Robertson, P. K., R. G. Campanella, D. Gillespie, and J. Greig. 1986. “USE OF PIEZOMETER CONE DATA.”

Robertson, Peter K. 2016. “Cone Penetration Test (CPT)-Based Soil Behaviour Type (SBT) Classification System — An Update.” *Canadian Geotechnical Journal* 0615(May):1–18. doi: 10.1139/cgj-2016-0044.

Rodriguez-Plata, R., Ozcebe, A. G., Smerzini, C., & Lai, C. G. (2021). Aggravation factors for 2D site effects in sedimentary basins: The case of Norcia, central Italy. Soil Dynamics and Earthquake Engineering, 149, 106854. https://doi.org/10.1016/J.SOILDYN.2021.106854

Rogers, J. D. 2006. "Subsurface Exploration Using the Standard Penetration Test and the Cone Penetrometer Test." *Environmental and Engineering Geoscience* 12(2):161–79. doi: 10.2113/12.2.161.
Rollins, Kyle M., Mark D. Evans, Diehl B. Nathan, and William D. Daily III. 1998. "Shear Modulos and Damping Relationships for Gravel." *Journal of Geotechnical and Geoenvironmental Engineering* 124(11141):396–405.
Rollins, Kyle M., Manali Singh, and Jashod Roy. 2020. "Simplified Equations for Shear-Modulus Degradation and Damping of Gravels." *Journal of Geotechnical and Geoenvironmental Engineering* 146(9):04020076. doi: 10.1061/(asce)gt.1943-5606.0002300.
S. Gundersen, Aleksander, Pasquale Carotenuto, Tom Lunne, Axel Walta, and Per M. Sparrevik. 2019. "Field Verification Tests of the Newly Developed Flow Cone Tool—In-Situ Measurements of Hydraulic Soil Properties." *AIMS Geosciences* 5(4):784–803. doi: 10.3934/geosci.2019.4.784.
Santander, Pamela. 2013. *Informe Técnico de Inspección Provincial Pichincha - Quito Sector Turubamba.Pdf.*
Schnabel, Per B., John Lysmer, and H. Bolton Seed. 1972. "Shake-91." *SHAKE: A Computer Program for Earthquake Response Analysis of Horizontally Layered Sites.* (December).
Seed, Bolton, Wong Robert T., Idriss I. M., and Tokimatsu K. 1986. "Moduli and Damping Factors for Dynamic Analyses of Cohesionless Soils." *Journal of Geotechnical Engineering* 112(11):1016–32. doi: 10.1061/(ASCE)0733-9410(1986)112:11(1016).
Seed, H. Bolton, and I. M. Idriss. 1970. "Soil Moduli and Damping Factors for Dynamic Analysis." *Earthquake Engineering Research Center, EERC* (70–10):41.
Senetakis, Kostas, Anastasios Anastasiadis, and Kyriazis Pitilakis. 2012. "The Small-Strain Shear Modulus and Damping Ratio of Quartz and Volcanic Sands." *Geotechnical Testing Journal* 35(6). doi: 10.1520/GTJ20120073.
Senetakis, Kostas, Anastasios Anastasiadis, and Kyriazis Pitilakis. 2013. "Normalized Shear Modulus Reduction and Damping Ratio Curves of Quartz Sand and Rhyolitic Crushed Rock." *Soils and Foundations* 53(6):879–93. doi: 10.1016/j.sandf.2013.10.007.
Shi, Jian. 2019. "Improving Site Response Analysis for Earthquake Ground Motion Modeling."
Shinde, Ninad Sanjeev, and Jyant Kumar. 2022. "Assessing the Liquefaction Potential of a Sand Specimen by Using Resonant Column Test." *Soil Dynamics and Earthquake Engineering* 159(August 2021):107343. doi: 10.1016/j.soildyn.2022.107343.
Shirgir, Sina, Amir Shamsaddinlou, Reza Najafi Zare, Sorour Zehtabiyan, and Masoud Hajialilue Bonab. 2023. "An Efficient Double-Loop Reliability-Based Optimization with Metaheuristic Algorithms to Design Soil Nail Walls under Uncertain Condition." *Reliability Engineering & System Safety* 232:109077. doi: 10.1016/J.RESS.2022.109077.
Skempton, A. W. 1987. "Standard Penetration Test Procedures and the Effects in Sands of Overburden Pressure, Relative Density, Particle Size, Ageing and

Overconsolidation." *Geotechnique* 37(3):411–12. doi: 10.1680/geot.1987.37.3.411.
Ślusarek, J., and M. Łupieżowiec. 2020. "Analysis of the Influence of Soil Moisture on the Stability of a Building Based on a Slope." *Engineering Failure Analysis* 113. doi: 10.1016/j.engfailanal.2020.104534.
Stokoe, K. H., M. B. Darendeli, R. D. Andrus, L. T. Brown, Portuguese Society for Geotechnique (SPG), and International Society for Soil Mechanics and Geotechnical Engineering. 1999. "Dynamic Soil Properties: Laboratory, Field and Correlation Studies." Pp. 811–46 in *International conference; 2nd, Earthquake geotechnical engineering*. Vol. 3. Lisbon: A A Balkema;
Stokoe, Kenneth H., S. H. Lee, and David P. Knox. 1985. "Shear Moduli Measurements under True Triaxial Stresses."
Tamay, José, Jesús Galindo-Zaldivar, John Soto, and Antonio J. Gil. 2021. "GNSS Constraints to Active Tectonic Deformations of the South American Continental Margin in Ecuador." doi: 10.3390/s21124003.
Trenkamp, Robert, James N. Kellogg, Jeffrey T. Freymueller, and Hector P. Mora. 2002. "Wide Plate Margin Deformation, Southern Central America and Northwestern South America, CASA GPS Observations." *Journal of South American Earth Sciences* 15(2):157–71. doi: 10.1016/S0895-9811(02)00018-4.
Trujillo Tamayo, Santiago Fernando. 2015. "Espectro de Control Para El Centro Norte de Quito." ESPE.
Uzielli, M., Facciorusso, J., & Madiai, C. (2022). Statistical calibration of two-dimensional seismic aggravation effects for homogeneous basins. Soil Dynamics and Earthquake Engineering, 163, 107533. https://doi.org/10.1016/J.SOILDYN.2022.107533
Vaca, Sandro, Martin Vallée, Jean-Mathieu Nocquet, and Alexandra Alvarado. 2019. "Active Deformation in Ecuador Enlightened by a New Waveform-Based Catalog of Earthquake Focal Mechanisms." *Journal of South American Earth Sciences* 93(June 2018):449–61. doi: 10.1016/j.jsames.2019.05.017.
Valverde, Jorge, Jeannette Fernández, Elianna Jiménez, Tany Vca, and Fausto Alarcón. 2001. *Microzonificación Sísmica de Los Suelos Del Distrito Metropolitano de Quito*.
Villagómez, Diego. 2003. "Evolución Geológica Plio-Cuaternaria Del Valle Interandino Central En Ecuador (Zona de Quito- Guayllabamba-San..." (May).
Villalobos, Enrique, Chungwook Sim, J. Paul Smith-Pardo, Pedro Rojas, Santiago Pujol, and Michael E. Kreger. 2018. "The 16 April 2016 Ecuador Earthquake Damage Assessment Survey." *Earthquake Spectra* 34(3):1201–17. doi: 10.1193/060217EQS106M.
Vinale, F., C. Mancuso, and F. Silvestri. 1996. *Dinamica Dei Terreni. Manuale Di Ingegneria Civile, Vol. 1. Ed. Scientifiche A. Cremonese.*
Vucetic, M. 1992. "Soil Properties and Seismic Response." in *Earthquake Engineering, Tenth World Conference*.
Watson, C. Scott, John R. Elliott, Susanna K. Ebmeier, María Antonieta Vásquez, Camilo Zapata, Santiago Bonilla-bedoya, Paulina Cubillo, Diego Francisco Orbe, Marco Córdova, and Elisa Sevilla. 2022. "Enhancing Disaster Risk Resilience Using Greenspace in Urbanising Quito , Ecuador." (January):1–37.
White, Scott M., Robert Trenkamp, and James N. Kellogg. 2003. "Recent Crustal Deformation and the Earthquake Cycle along the Ecuador-Colombia

Subduction Zone." *Earth and Planetary Science Letters* 216(3):231–42. doi: 10.1016/S0012-821X(03)00535-1.

Yepes, Hugo, Laurence Audin, Alexandra Alvarado, Céline Beauval, Jorge Aguilar, Yvonne Font, and Fabrice Cotton. 2016. "A New View for the Geodynamics of Ecuador: Implication in Seismogenic Source Definition and Seismic Hazard Assessment." *Tectonics* 35(5):1249–79. doi: 10.1002/2015TC003941.

Yoshimoto, Masahiro, Hiroyuki Kumagai, Wilson Acero, Gabriela Ponce, Freddy Vásconez, Santiago Arrais, Mario Ruiz, Alexandra Alvarado, Patricia Pedraza García, Viviana Dionicio, Orlando Chamorro, Yuta Maeda, and Masaru Nakano. 2017. "Depth-Dependent Rupture Mode along the Ecuador-Colombia Subduction Zone." *Geophysical Research Letters* 44(5):2203–10. doi: 10.1002/2016GL071929.

Zhang, Jianfeng, Ronald D. Andrus, and C. Hsein Juang. 2005. "Normalized Shear Modulus and Material Damping Ratio Relationships." *Journal of Geotechnical and Geoenvironmental Engineering* 131(4):453–64. doi: 10.1061/(asce)1090-0241(2005)131:4(453).

APPENDIXES

APPENDIX A – Test Methods

A.1. Field Tests

- **Standard Penetration Test (SPT)**

The SPT test method is to drive a split barrel sampler to obtain a representative sample of disturbed soil for identification purposes and measure the resistance of the soil to penetration by the sampler. (ASTM D1586-11 2011b). Penetration resistance tests are normally performed at 1.5 m depth intervals or when significant change in materials is observed, this test method is limited to use in unlithified soils whose maximum particle size is approximately less than one-half the diameter of the sampler. It is widely used in a variety of geotechnical exploration projects, which relate the blow count, or N value, and the engineering behavior of earthworks and foundations. (ASTM D1586-11 2011b).

Below are 9 groups of boreholes based on geographic location and similar physical and mechanical properties, representing each zone defined in Figure 23.

- **Zone A (P1-P2-P3-P7-P8)**

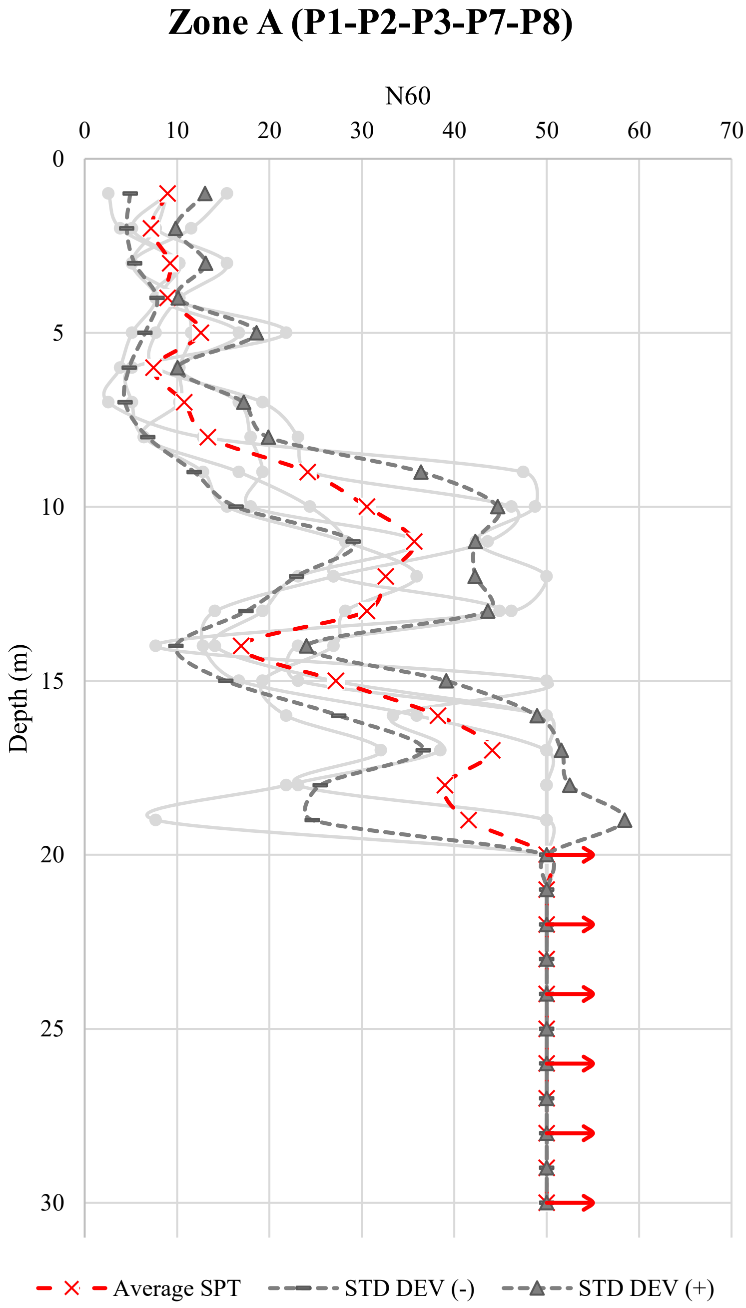

Figure 222. N SPT Test Results Summary for Zone A.

- **Zone B (P4)**

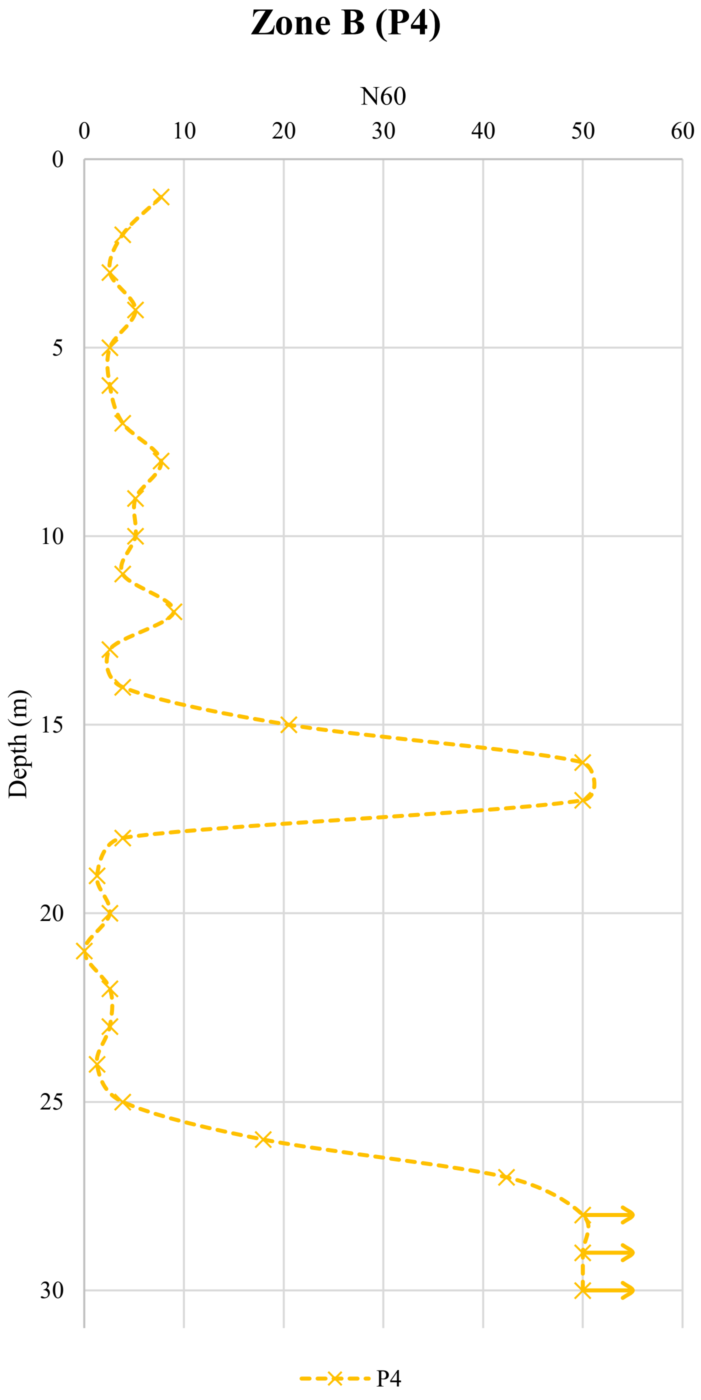

Figure 223. N SPT Test Results Summary for Zone B.

- **Zone C (P5-P9)**

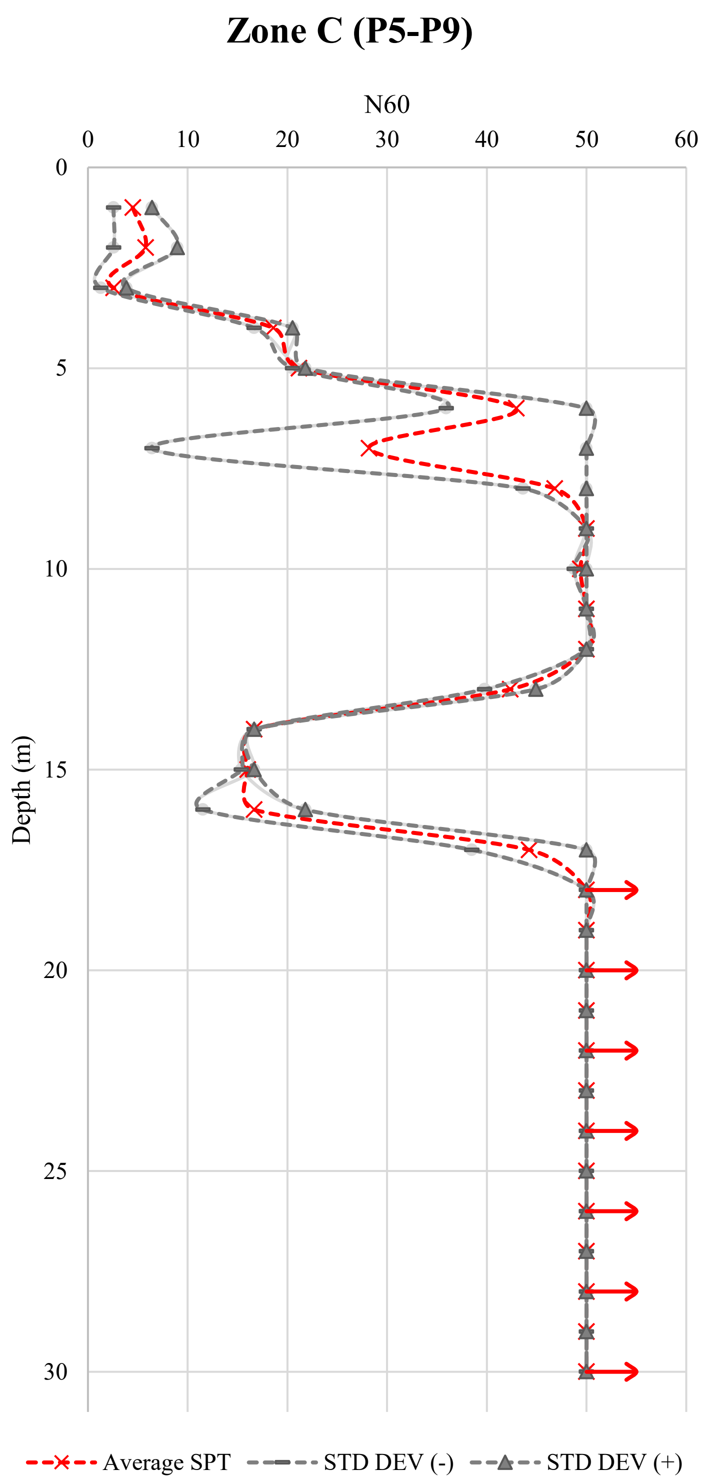

Figure 224. N SPT Test Results Summary for Zone C.

- **Zone D (P6)**

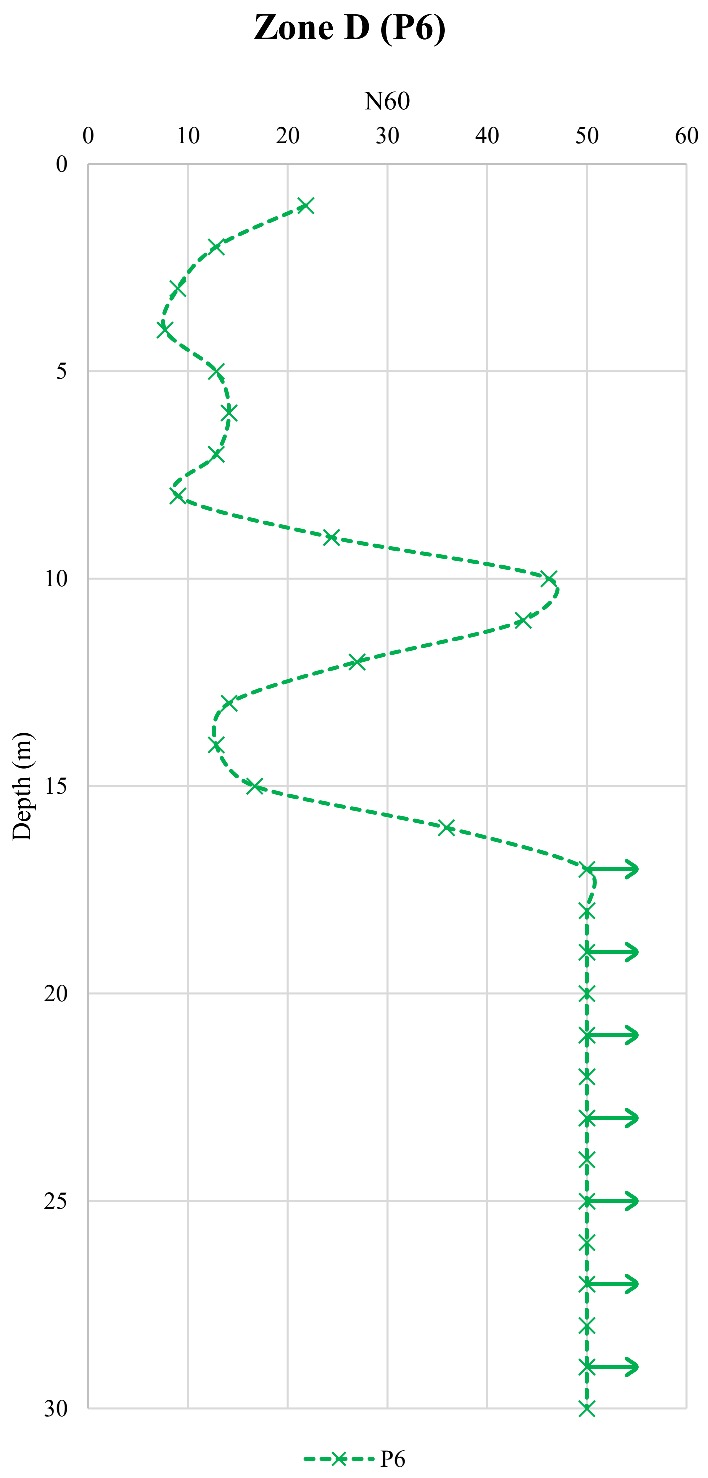

Figure 225. N SPT Test Results Summary for Zone D.

- **Zone E (P10-P13-P16)**

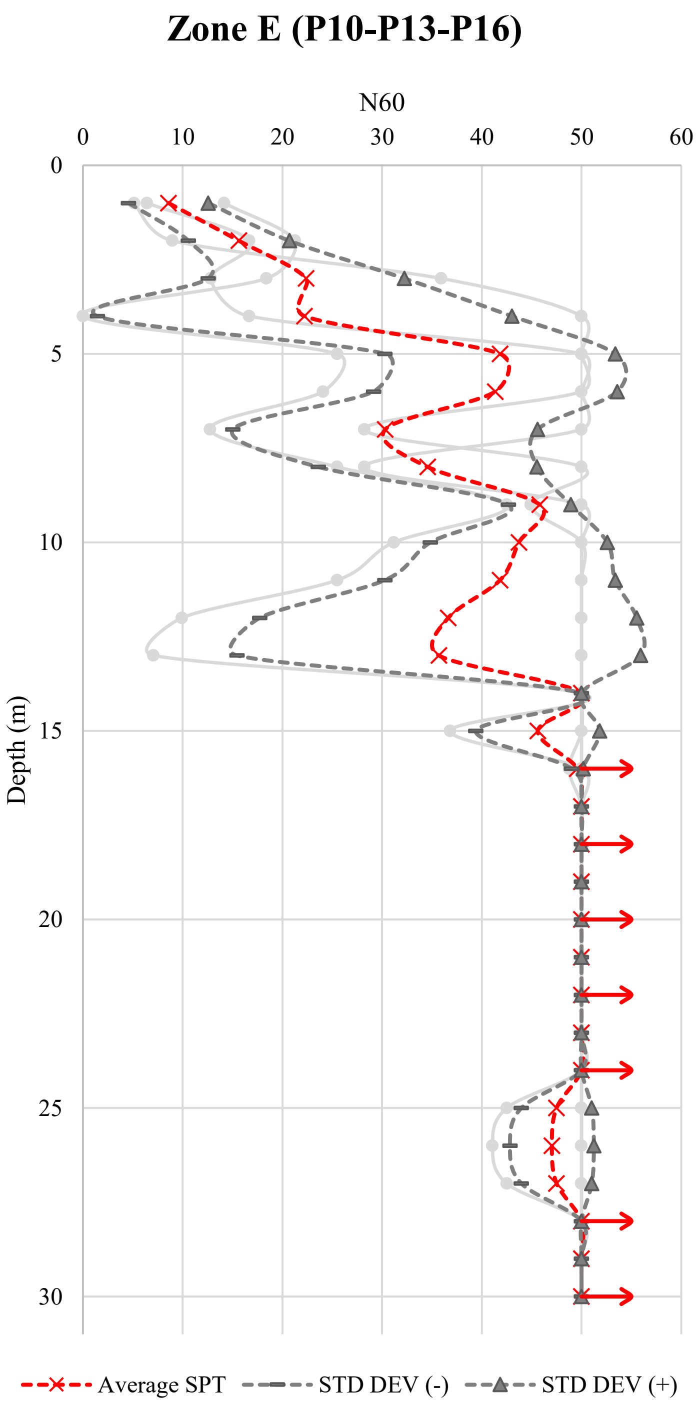

Figure 226. N SPT Test Results Summary for Zone E.

- **Zone F (P12)**

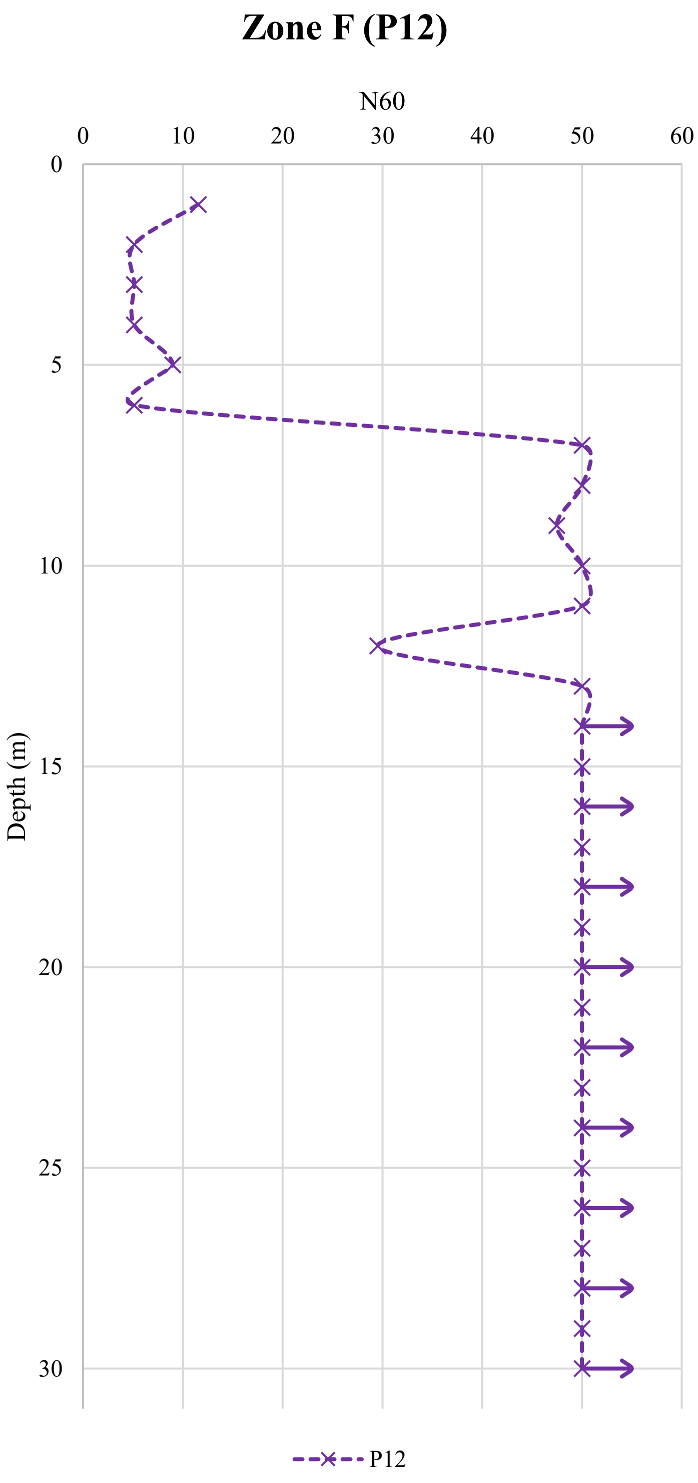

Figure 227. N SPT Test Results Summary for Zone F.

- **Zone G (P11-P14-P15-P20)**

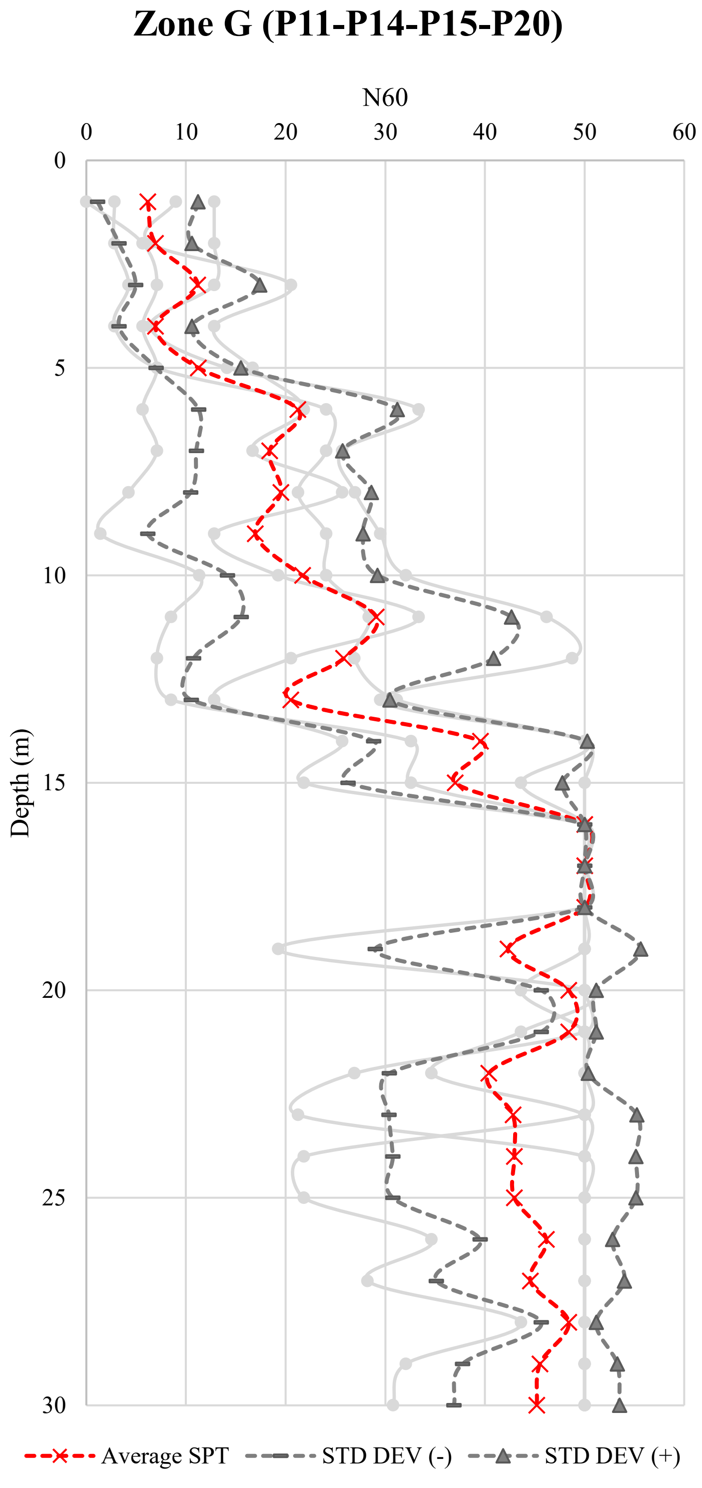

Figure 228. N SPT Test Results Summary for Zone G.

- **Zone H (P17)**

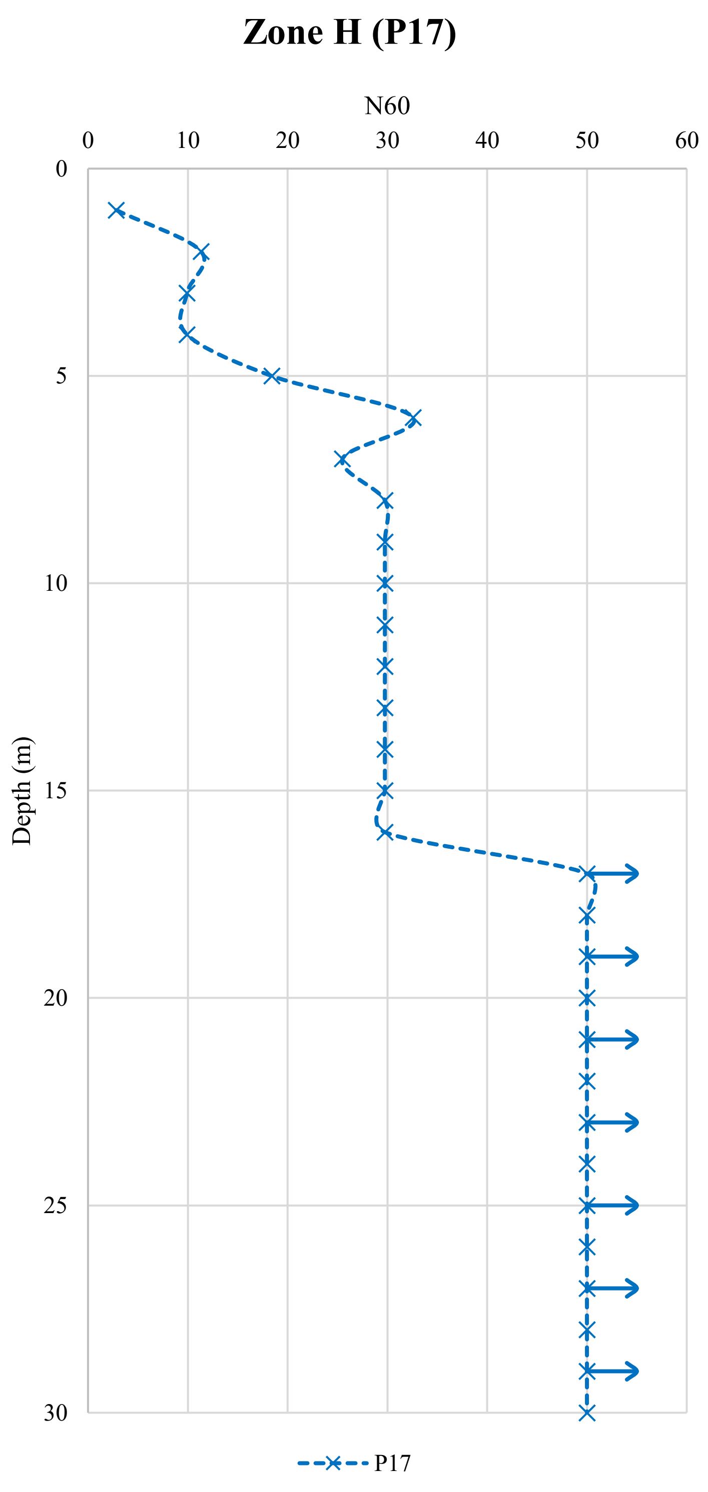

Figure 229. N SPT Test Results Summary for Zone H.

- **Zone I (P18-P21)**

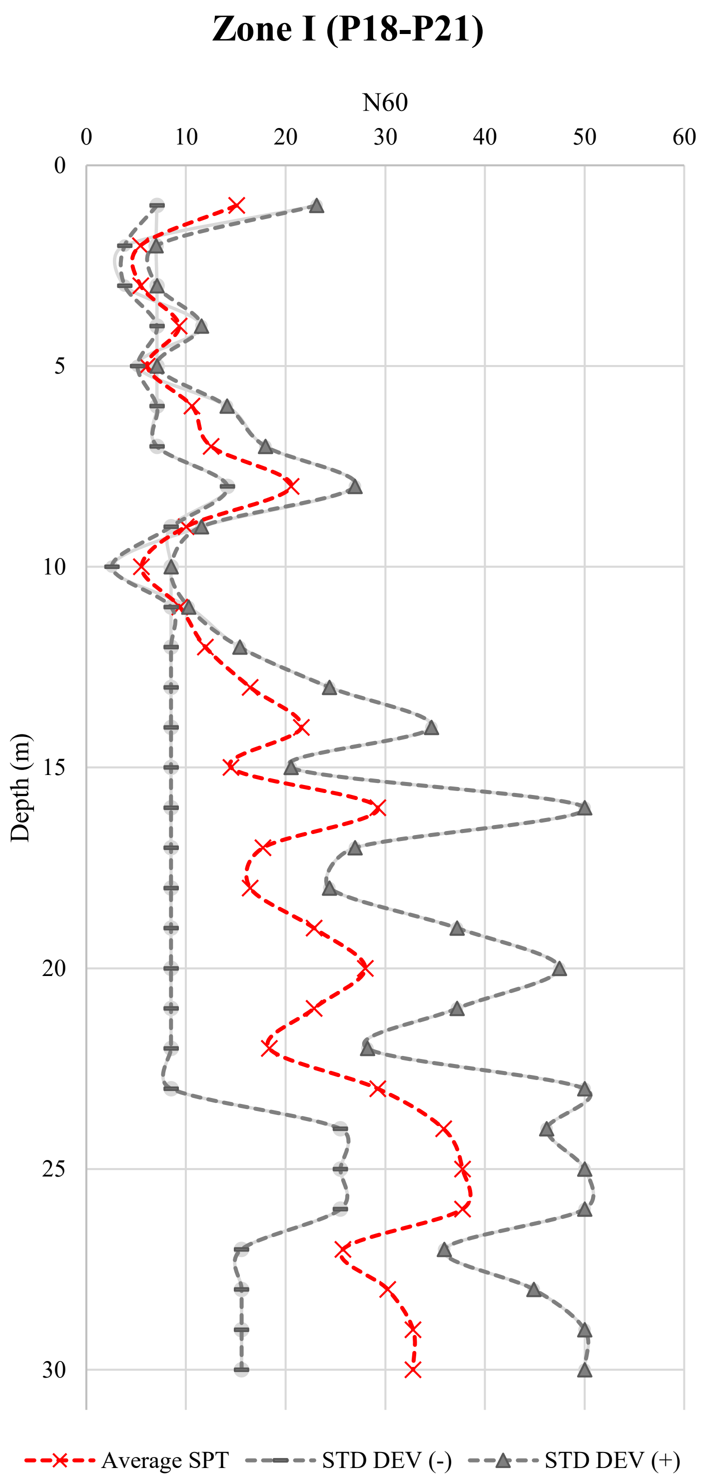

Figure 230. N SPT Test Results Summary for Zone I.

- **Cone Penetration Test (CPT)**

This test method explains the procedure to determine the resistance that has the fine soil during the penetration of a conical-shaped penetrometer as a steady rate, also, for determine the frictional resistance of a cylindrical sleeve. The cone penetration data helps to interpret subsurface stratigraphy, homogeneity and depth to firm layers, voids or cavities, and other discontinuities. Also, we can design the foundations for structures and preset earthworks with correlations. (ASTM D3441-16 2016).

Below are 9 groups of CPTs based on geographic location and similar physical and mechanical properties, representing each zone defined in Figure 23.

- **Zone A (P1-P2-P3-P7-P8)**

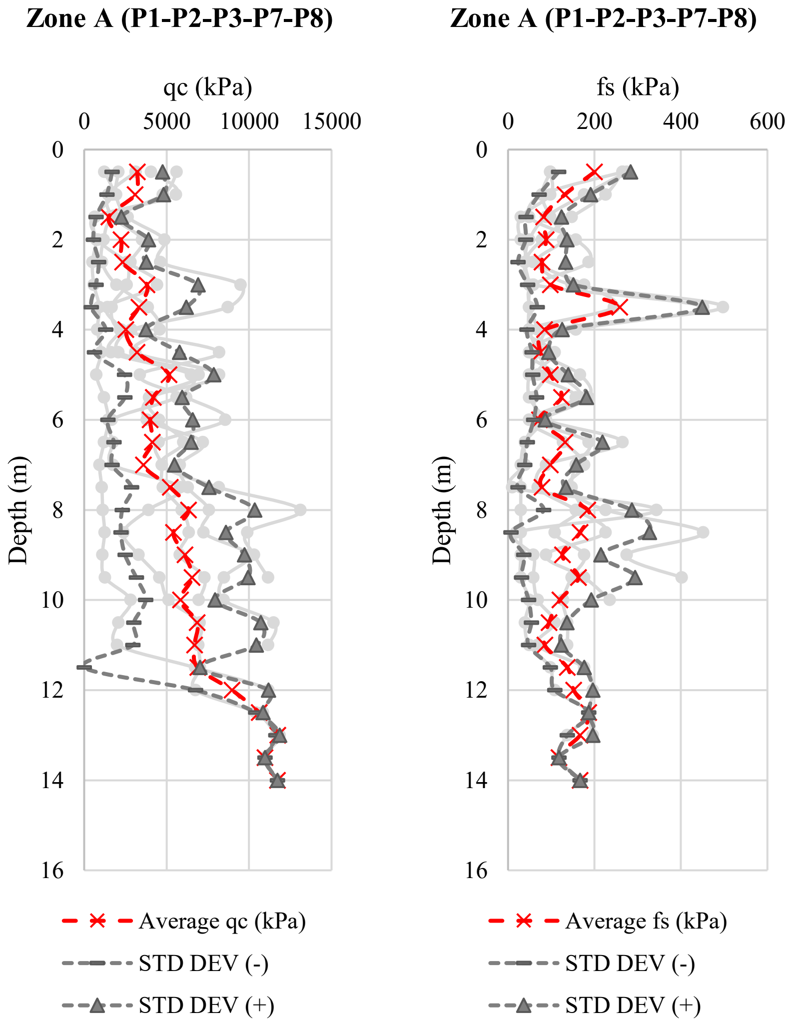

Figure 231. CPT Test Results Summary for Zone A.1.

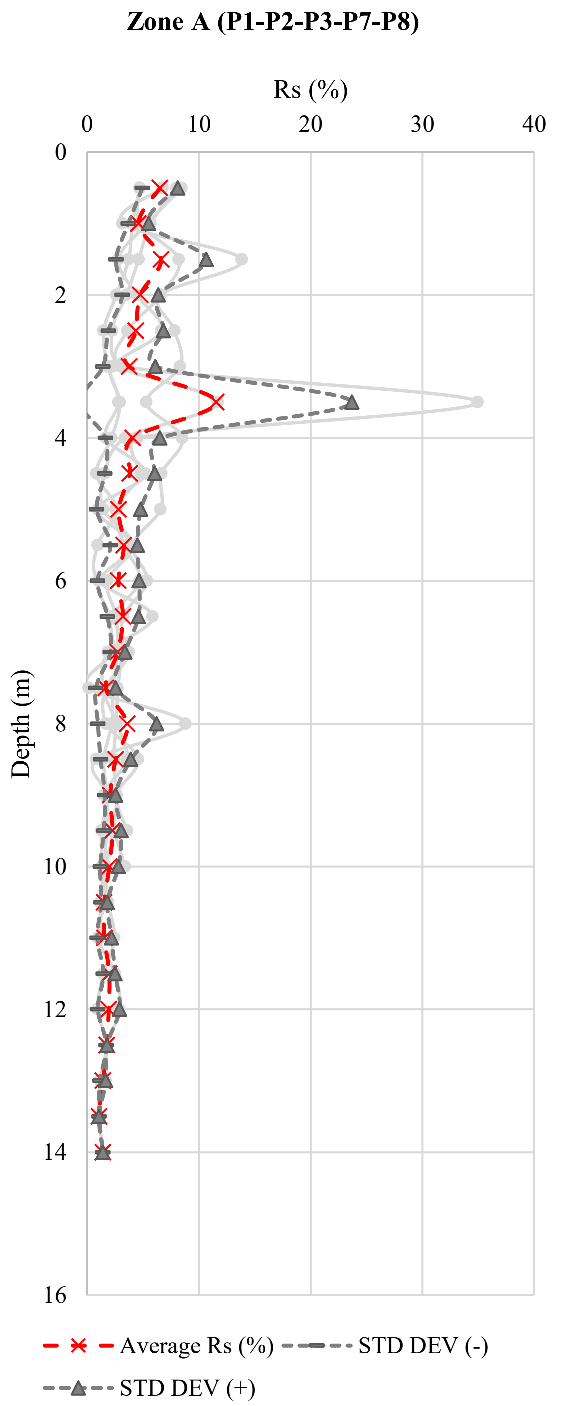

Figure 232. CPT Test Results Summary for Zone A.2.

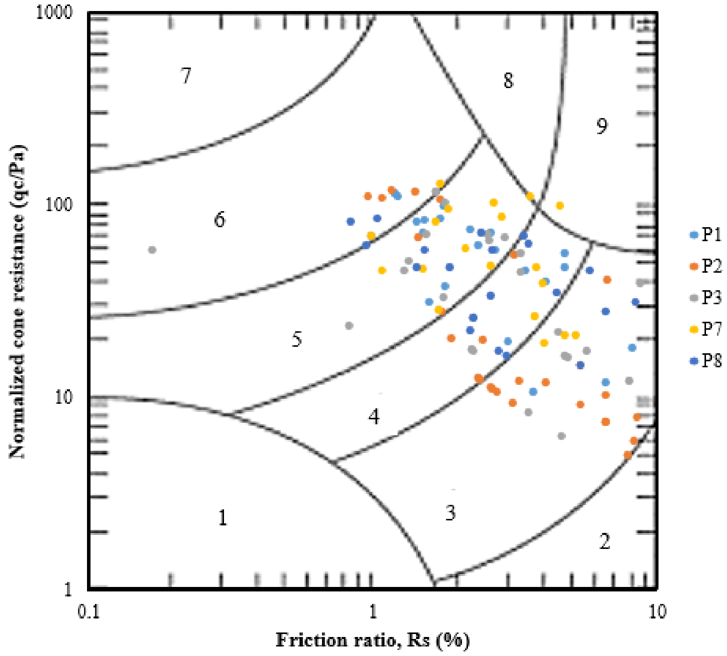

Figure 233. CPT Test Results Summary for Zone A.3.

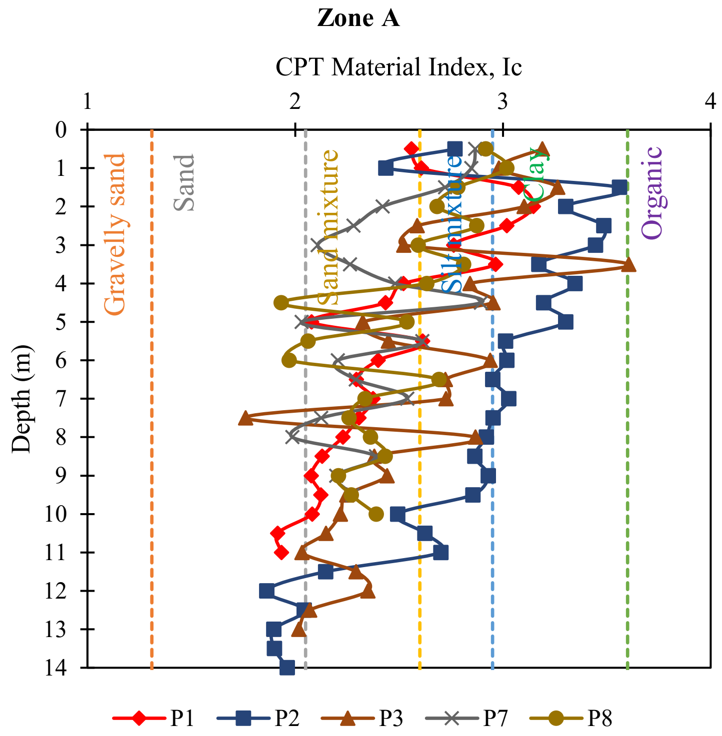

Figure 234. CPT Test Results Summary for Zone A.4.

- **Zone B (P4)**

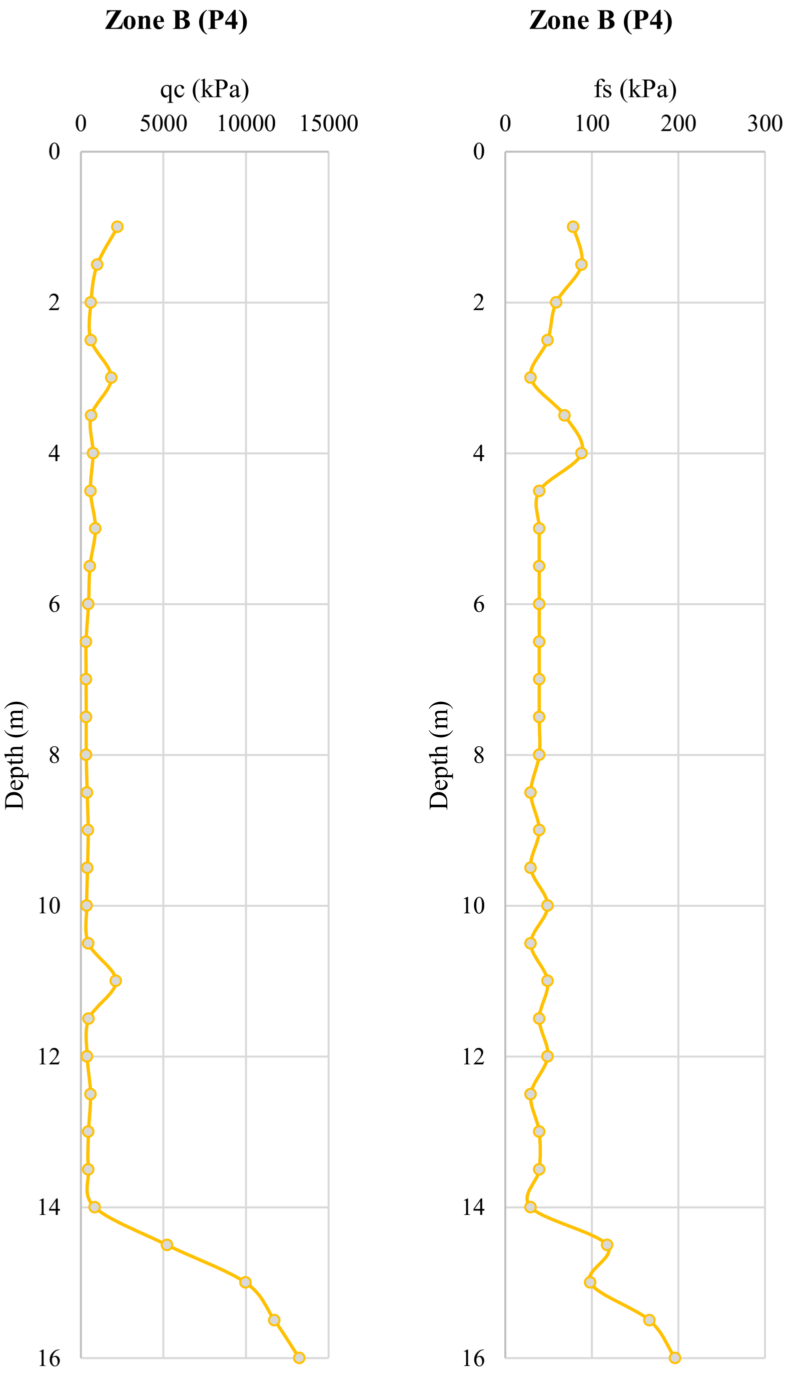

Figure 235. CPT Test Results Summary for Zone B.1.

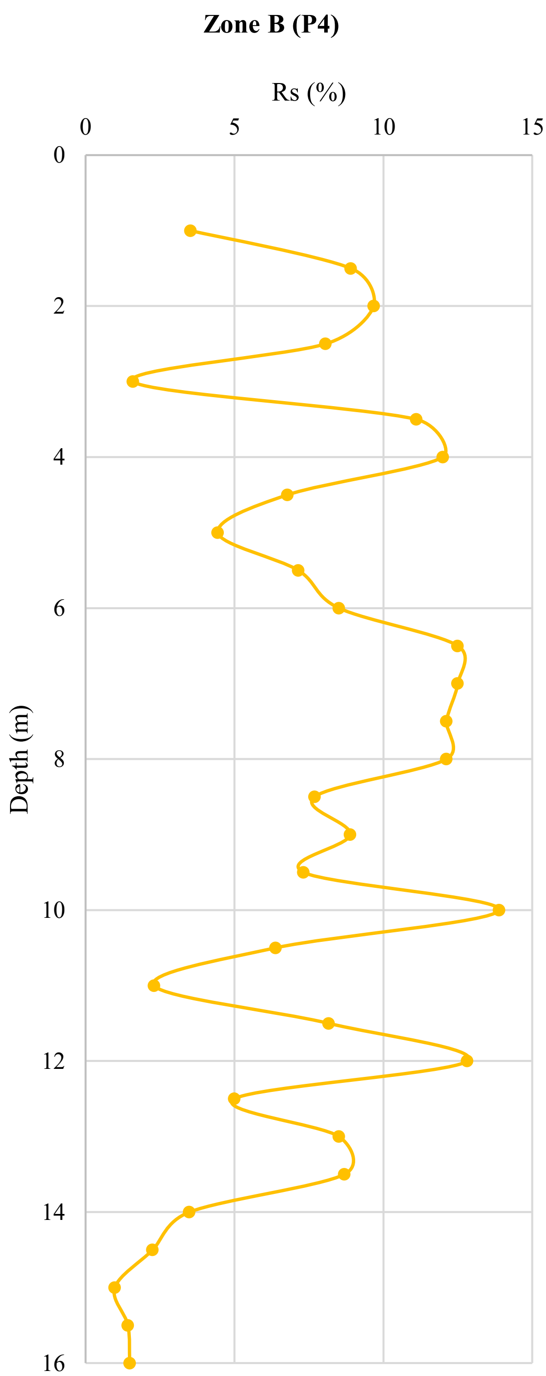

Figure 236. CPT Test Results Summary for Zone B.2.

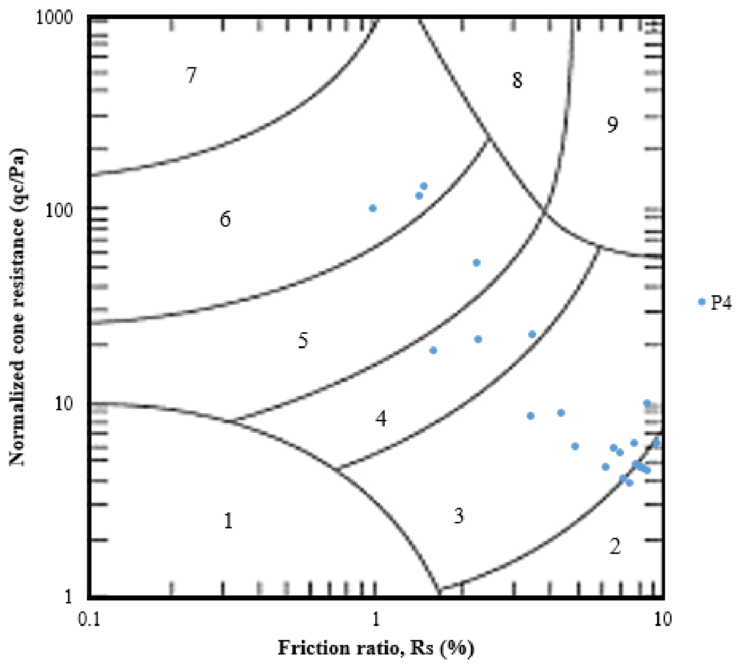

Figure 237. CPT Test Results Summary for Zone B.3

Zone B

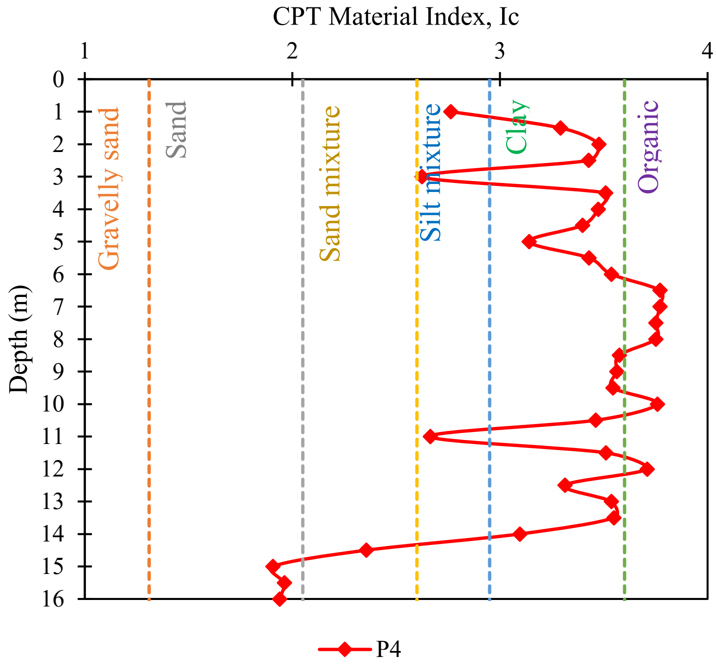

Figure 238. CPT Test Results Summary for Zone B.4

- **Zone C (P5-P9)**

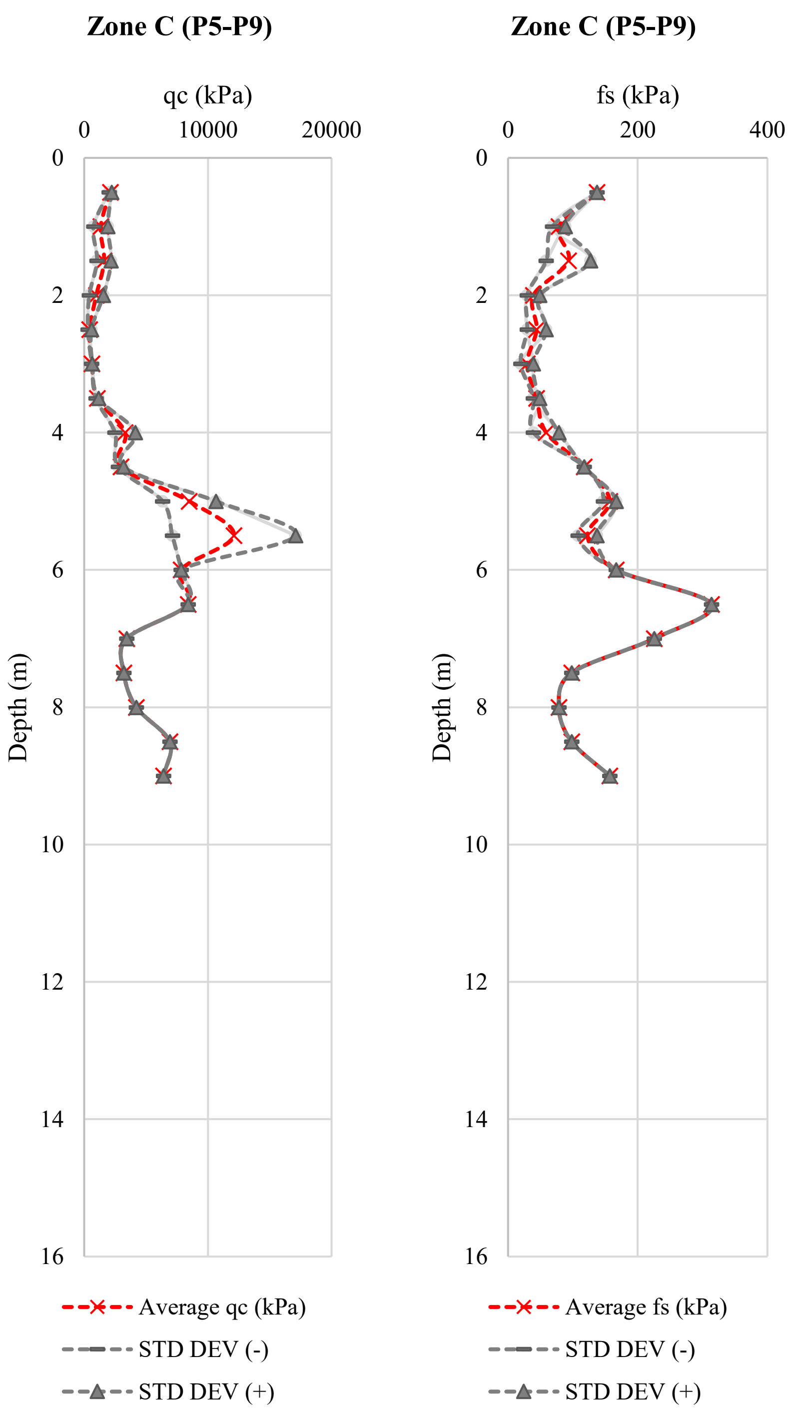

Figure 239. CPT Test Results Summary for Zone C.1

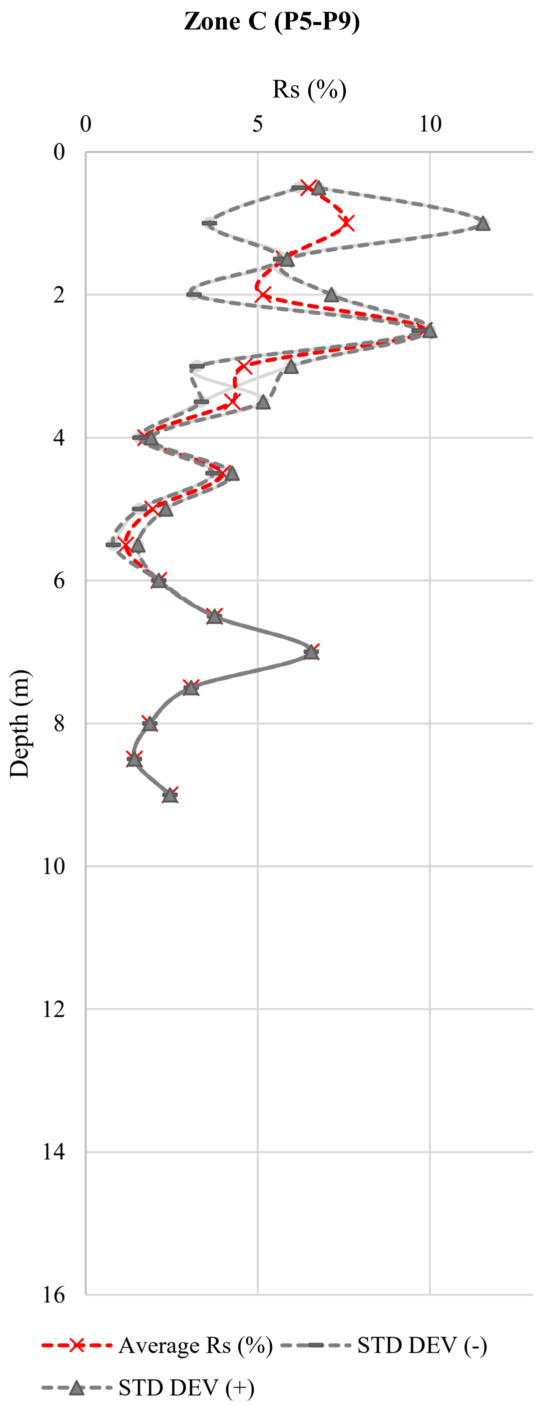

Figure 240. CPT Test Results Summary for Zone C.2

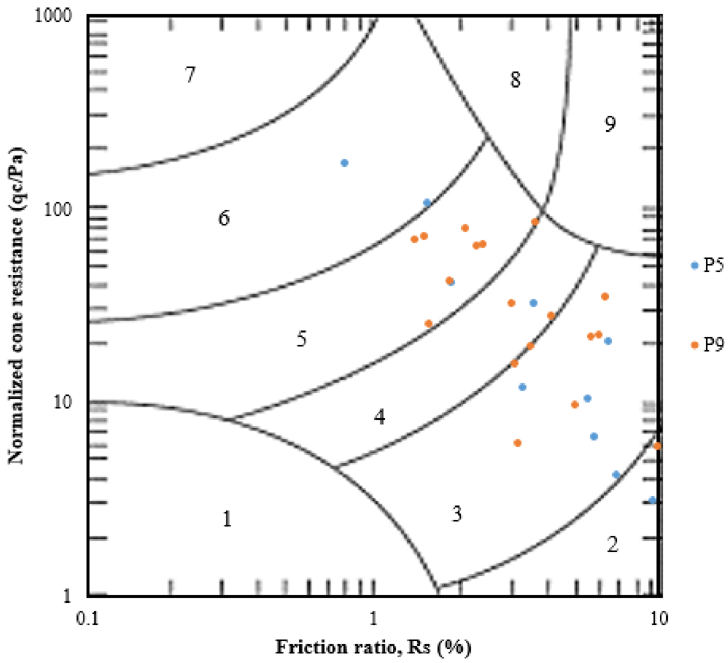

Figure 241. CPT Test Results Summary for Zone C.3

Zone C

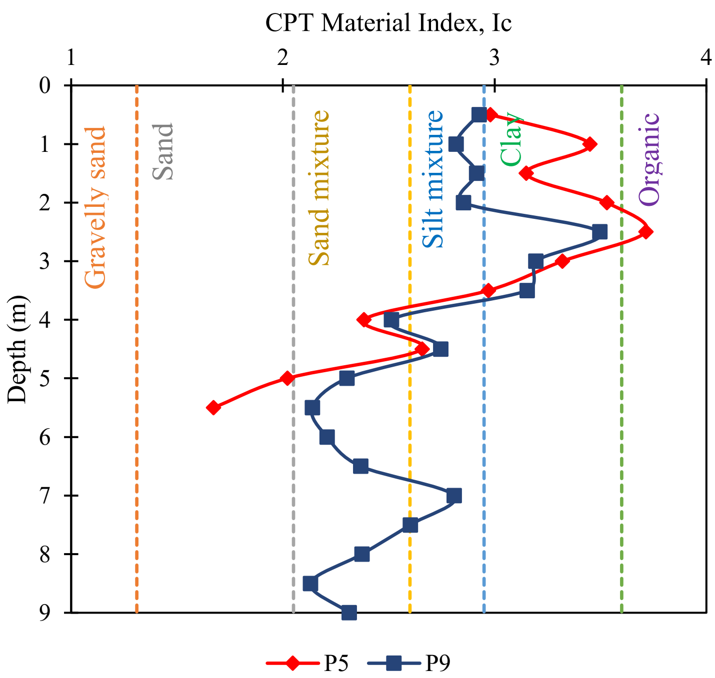

Figure 242. CPT Test Results Summary for Group C.4

- **Zone D (P6)**

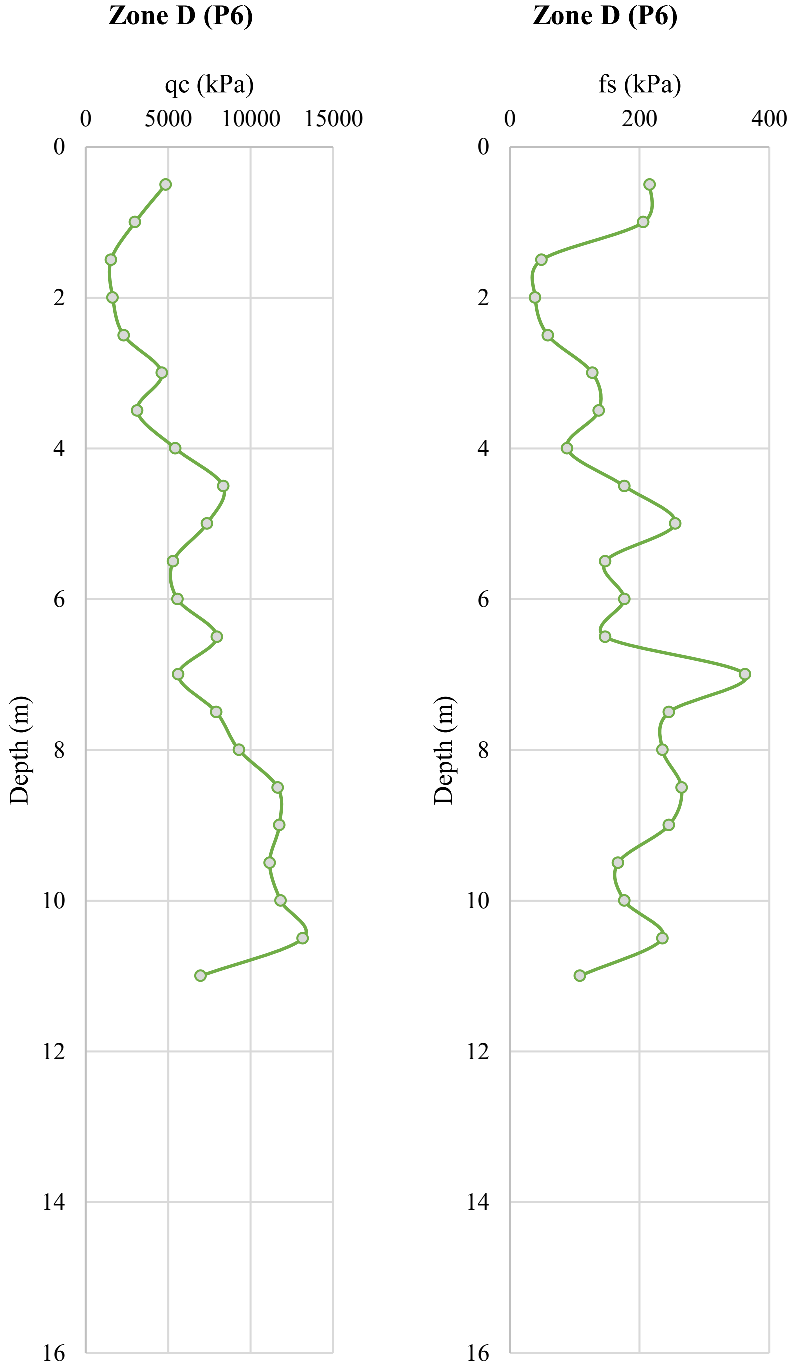

Figure 243. CPT Test Results Summary for Zone D.1

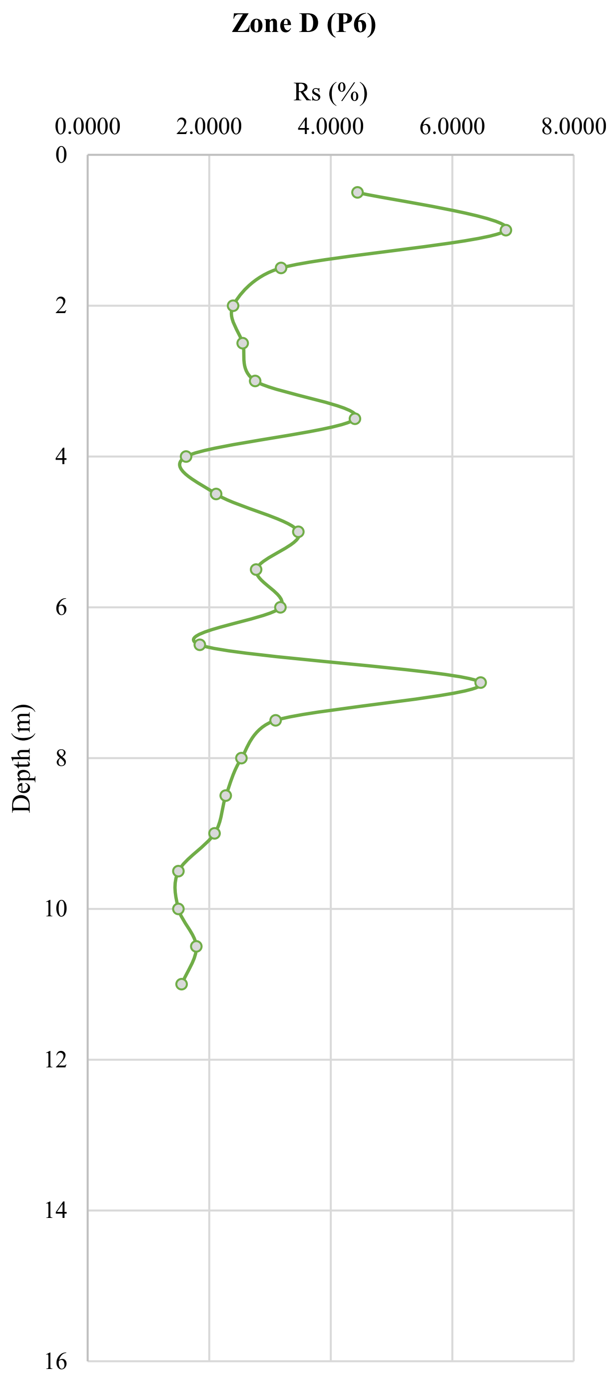

Figure 244. CPT Test Results Summary for Zone D.2

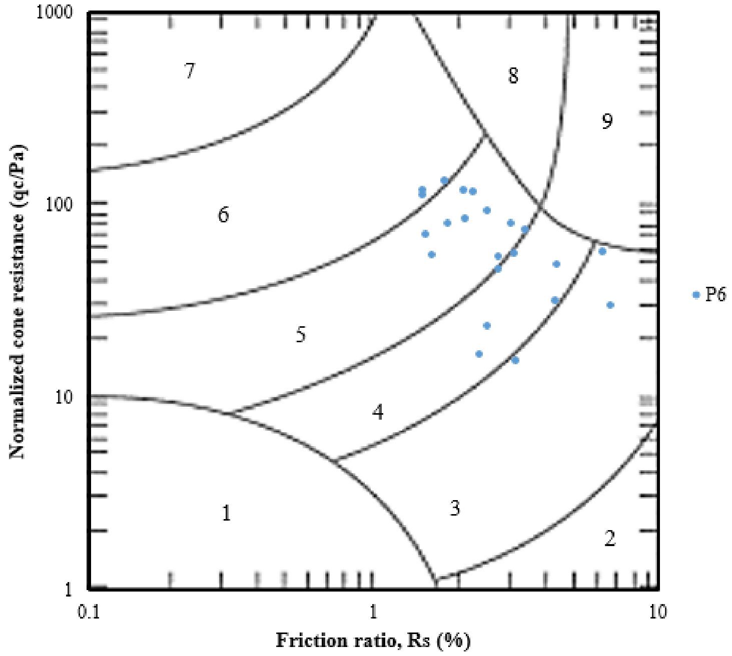

Figure 245. CPT Test Results Summary for Zone D.3

Group D

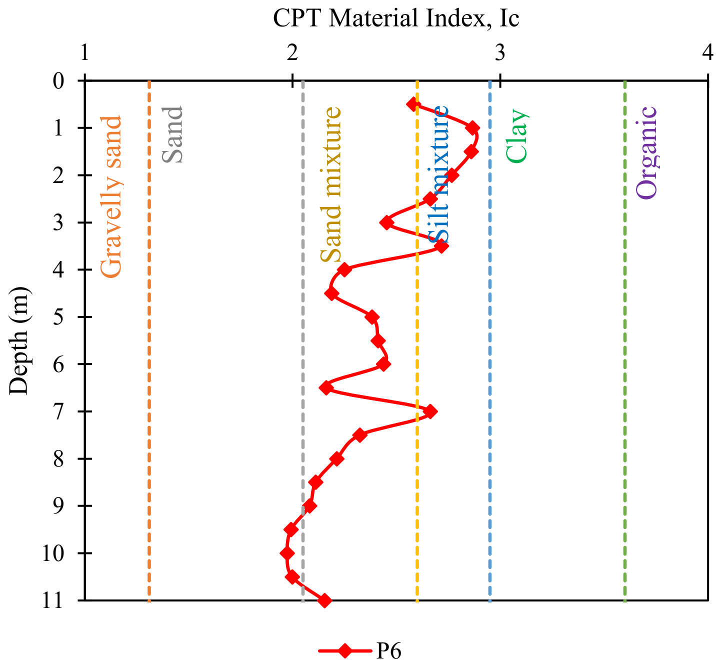

Figure 246. CPT Test Results Summary for Zone D.4

- **Zone E (P10-P13-P16)**

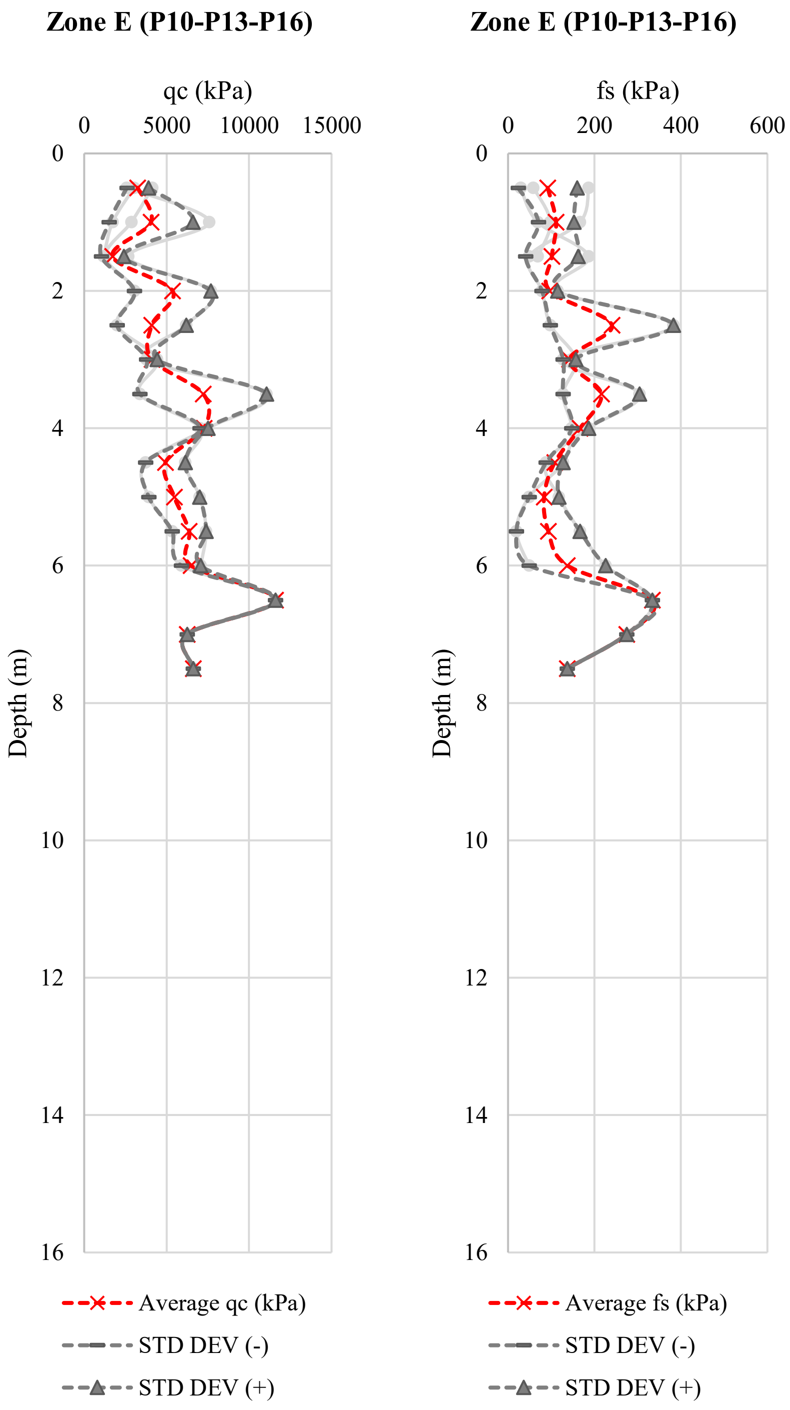

Figure 247. CPT Test Results Summary for Zone E.1

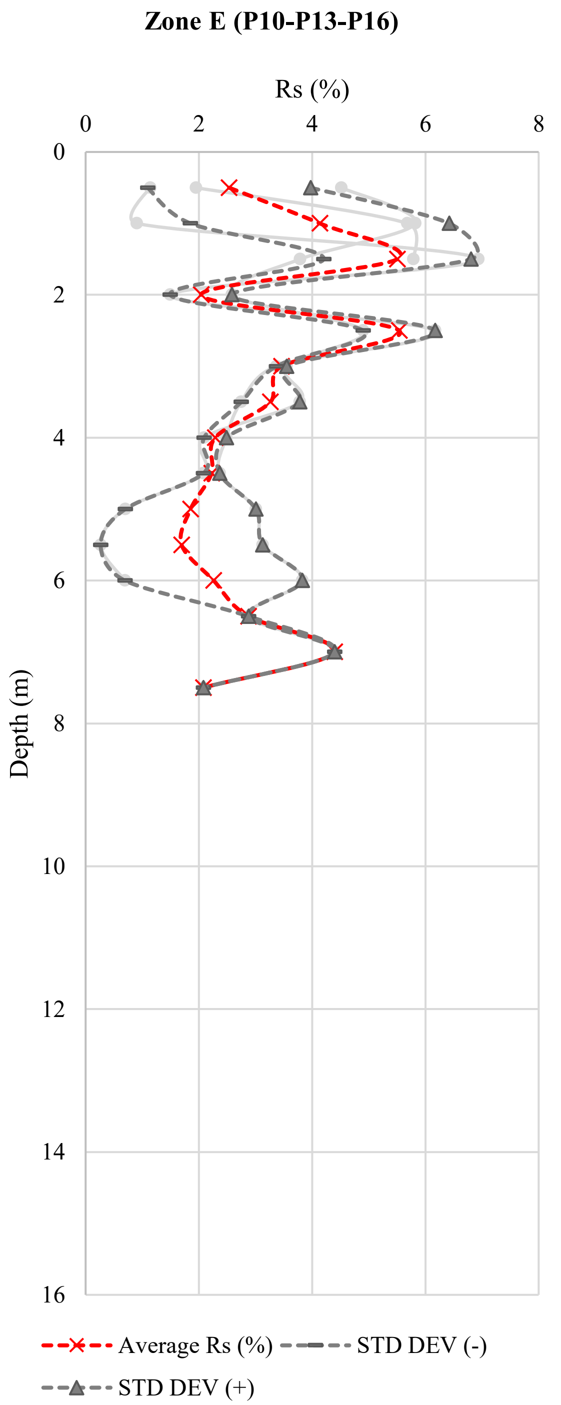

Figure 248. CPT Test Results Summary for Zone E.2

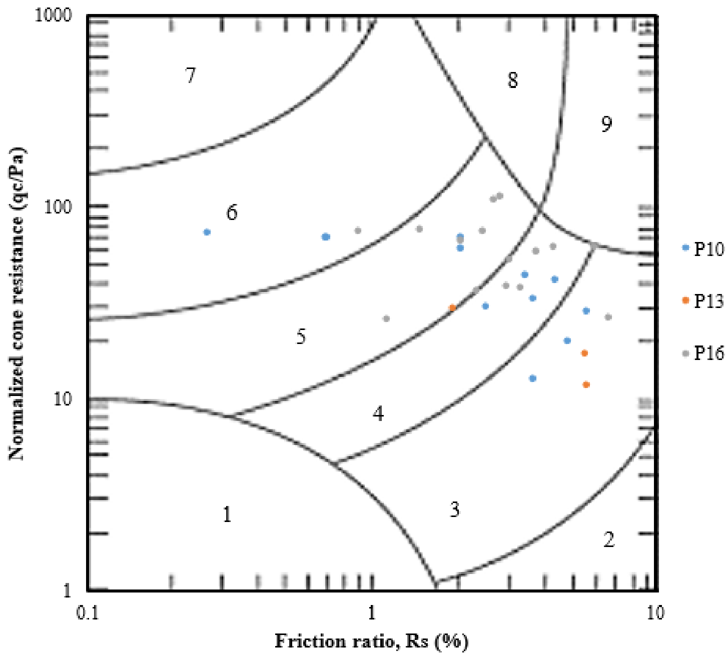

Figure 249. CPT Test Results Summary for Zone E.3

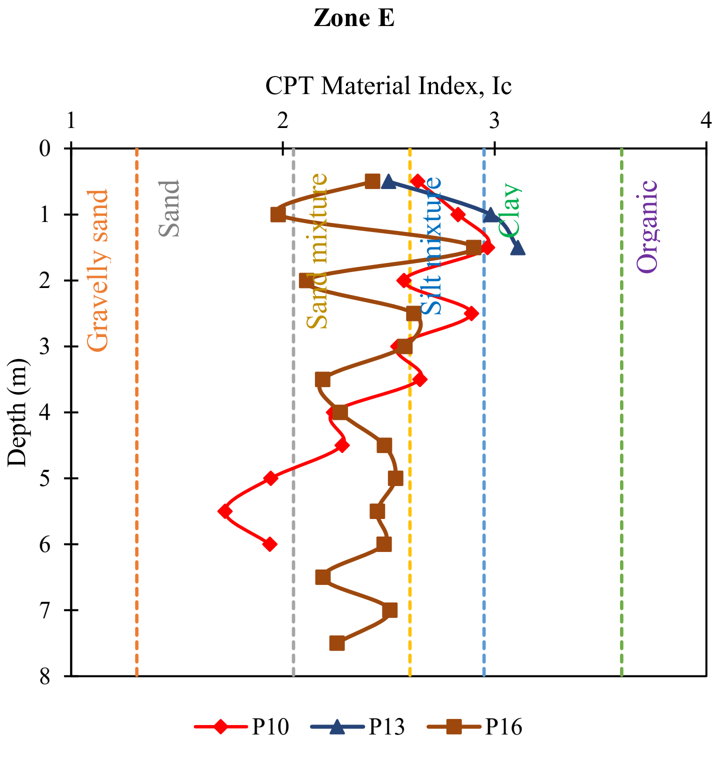

Figure 250. CPT Test Results Summary for Zone E.4

- **Zone F (P12)**

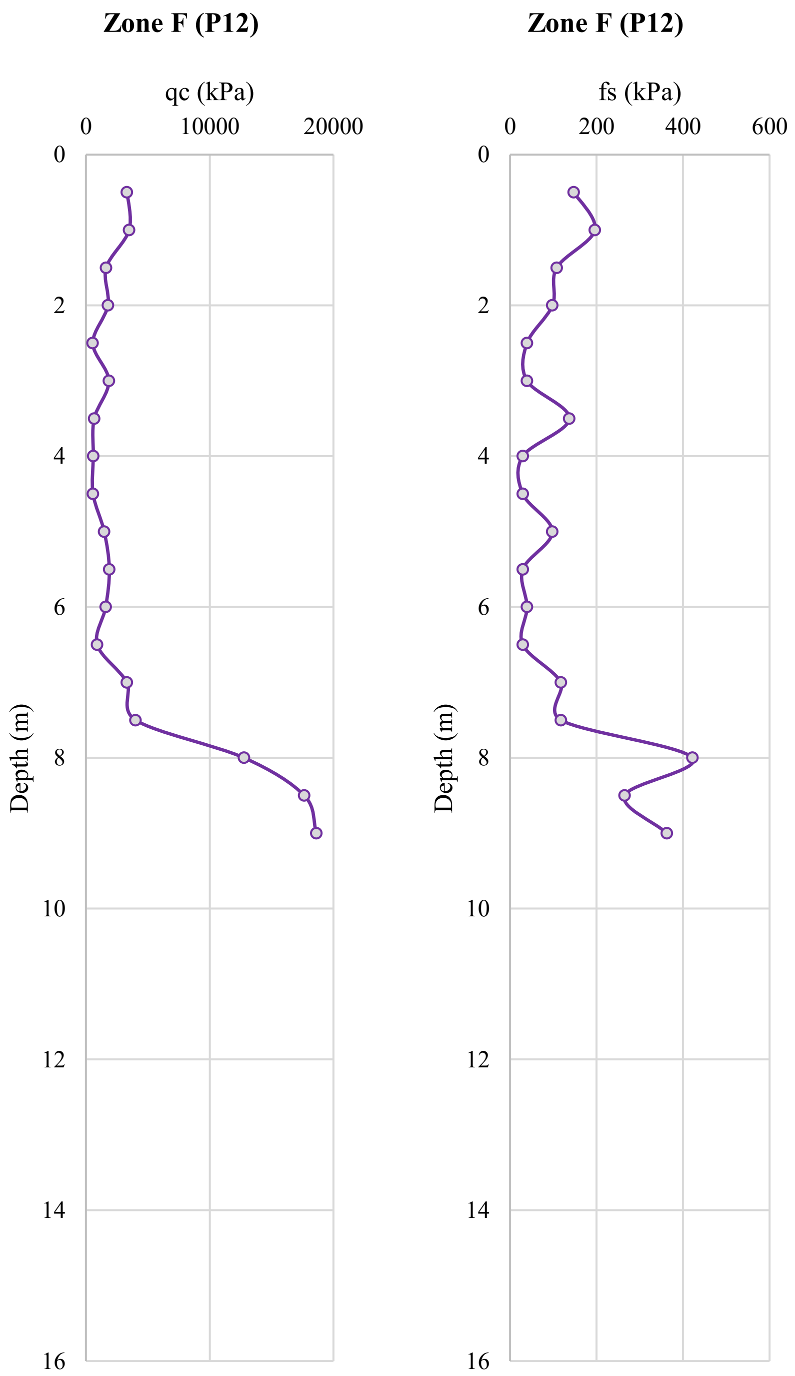

Figure 251. CPT Test Results Summary for Zone F.1

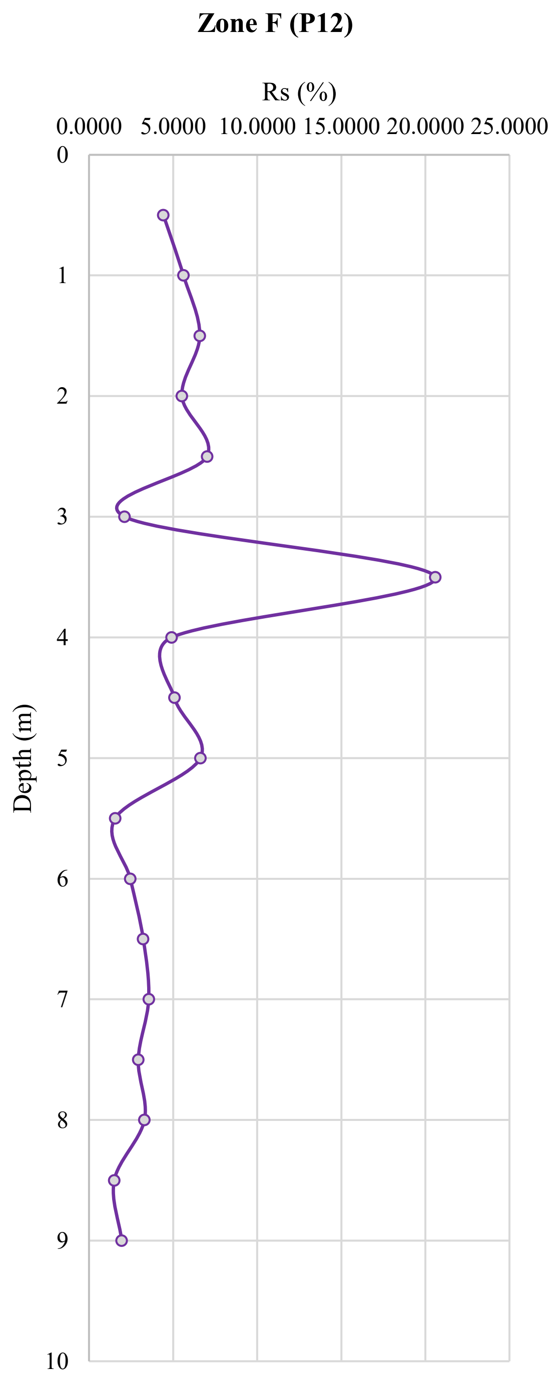

Figure 252. CPT Test Results Summary for Zone F.2

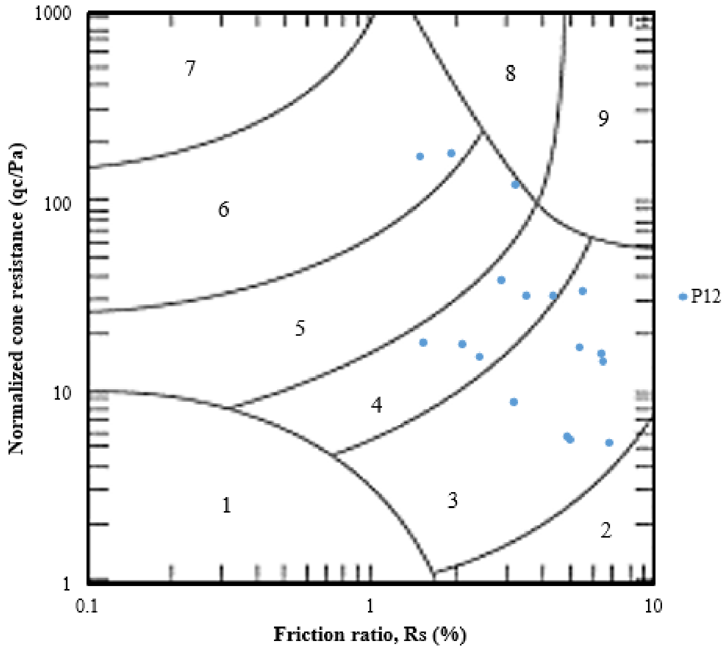

Figure 253. CPT Test Results Summary for Zone F.3

Zone F

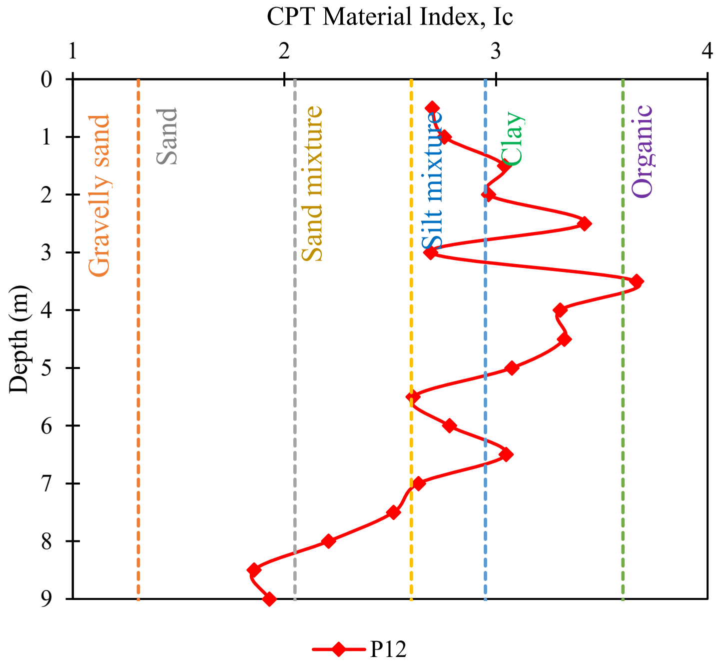

Figure 254. CPT Test Results Summary for Zone F.4

- **Zone G (P11-P14-P15-P20)**

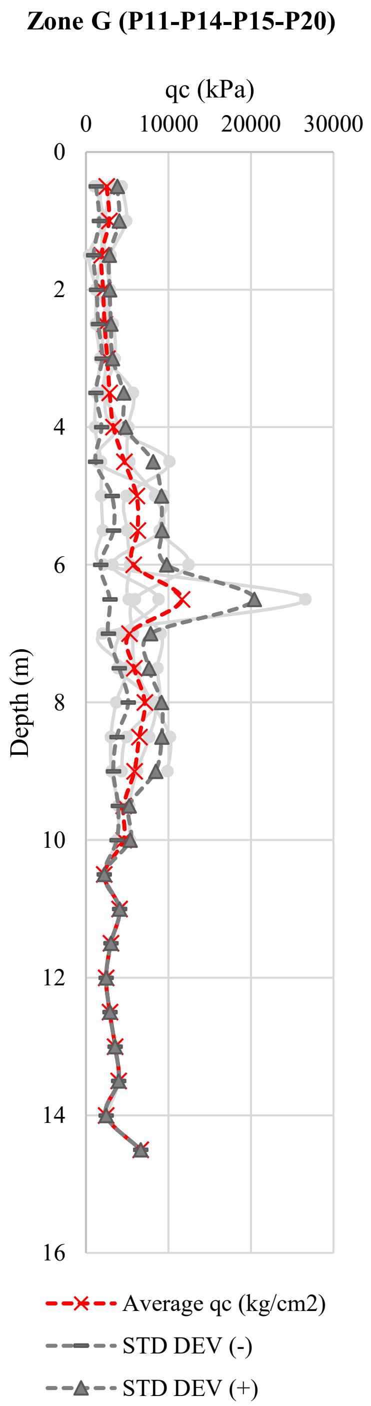

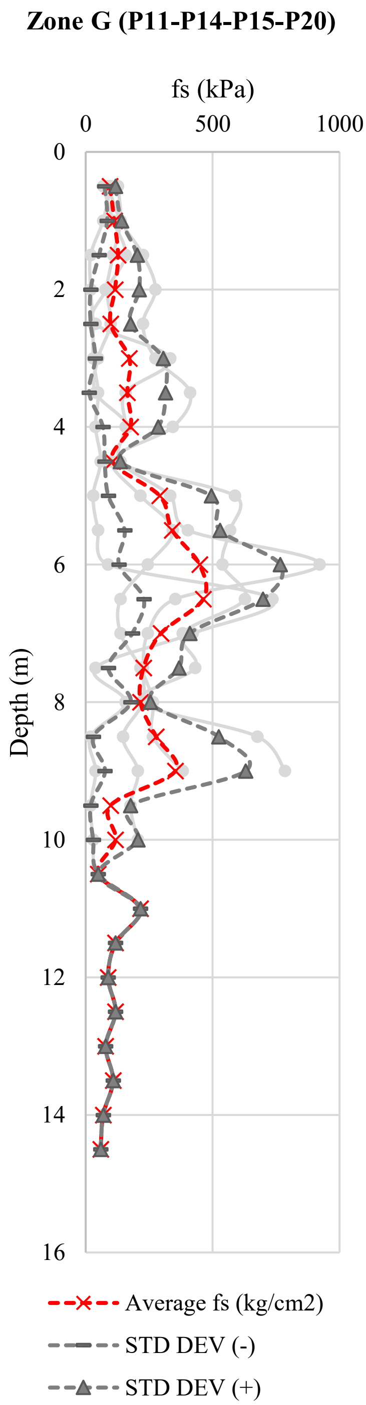

Figure 255. CPT Test Results Summary for Zone G.1

Zone G (P11-P14-P15-P20)

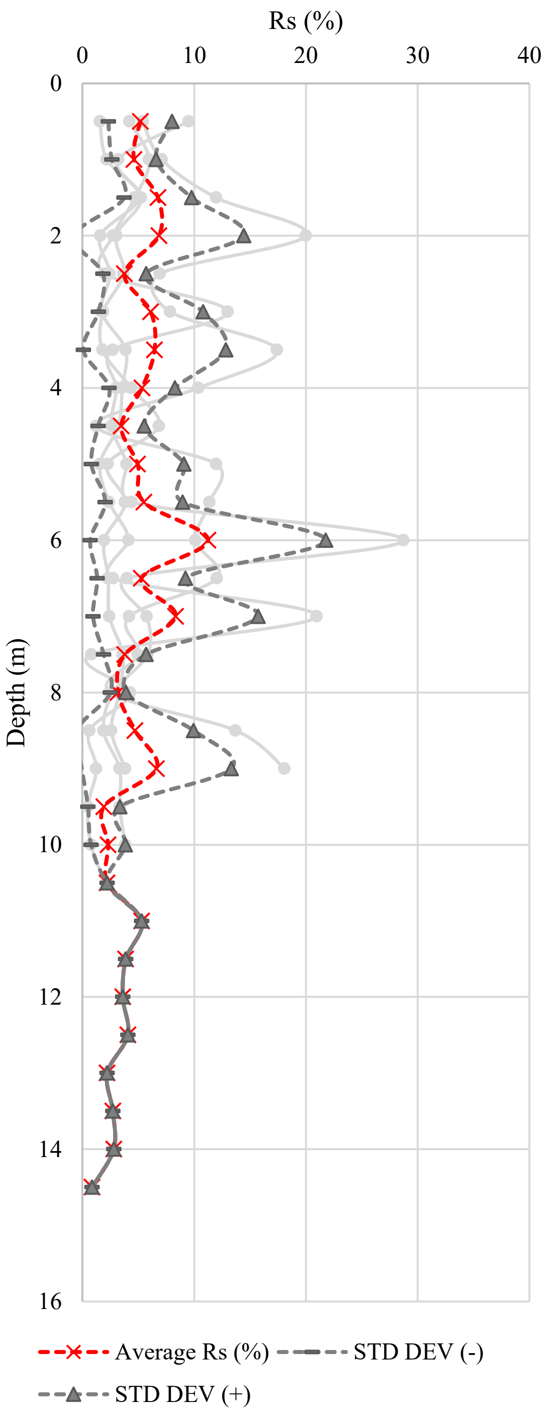

Figure 256. CPT Test Results Summary for Zone G.2

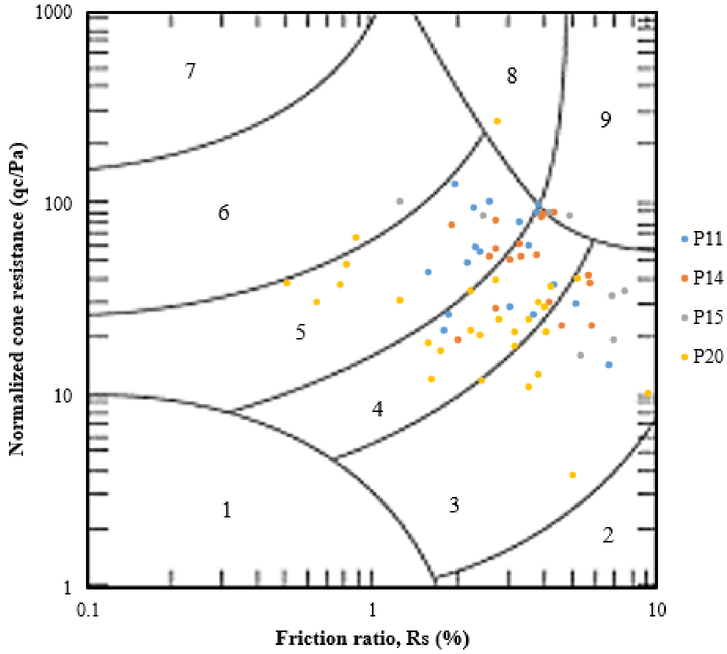

Figure 257. CPT Test Results Summary for Zone G.3

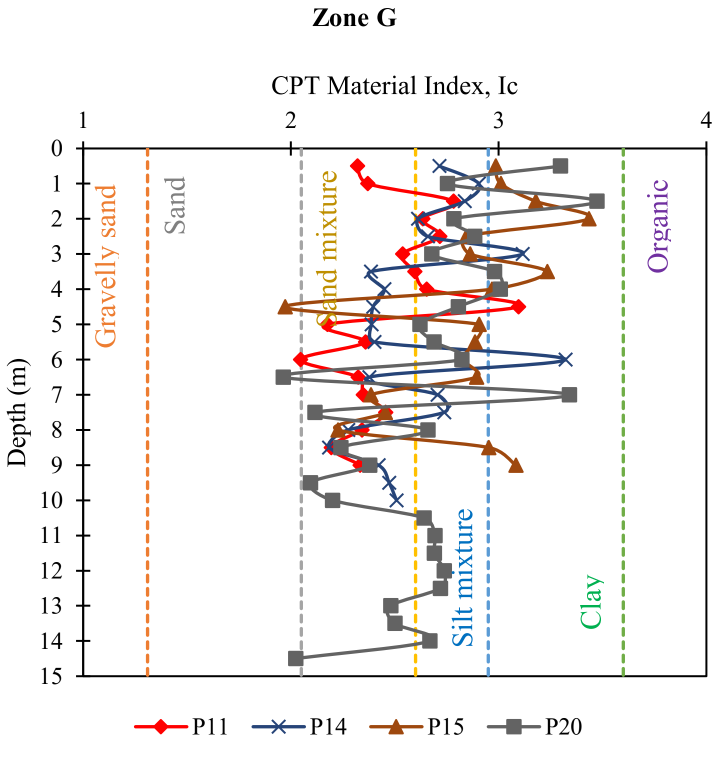

Figure 258. CPT Test Results Summary for Zone G.4

- **Zone H (P17)**

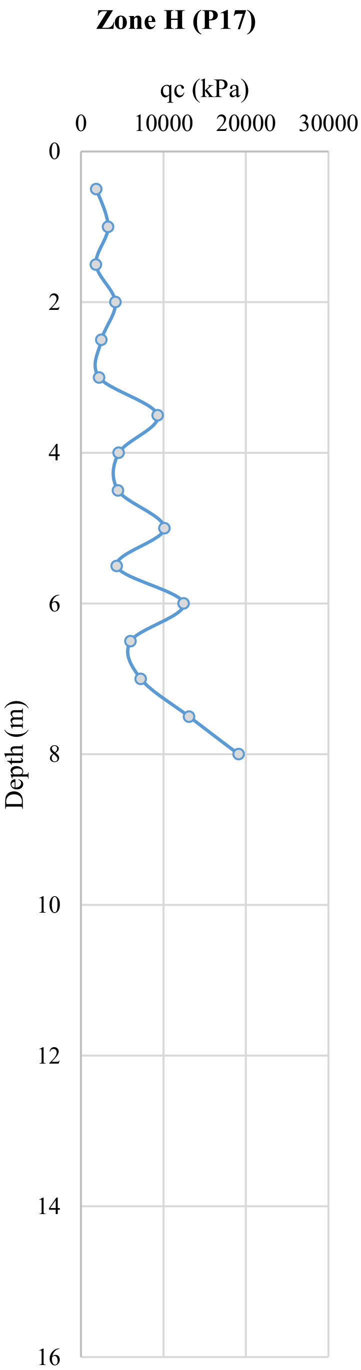

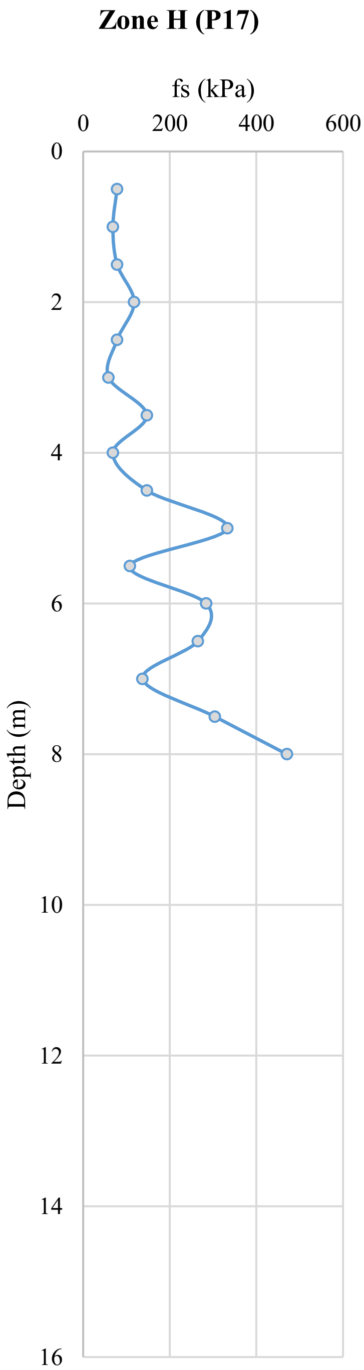

Figure 259. CPT Test Results Summary for Zone H.1

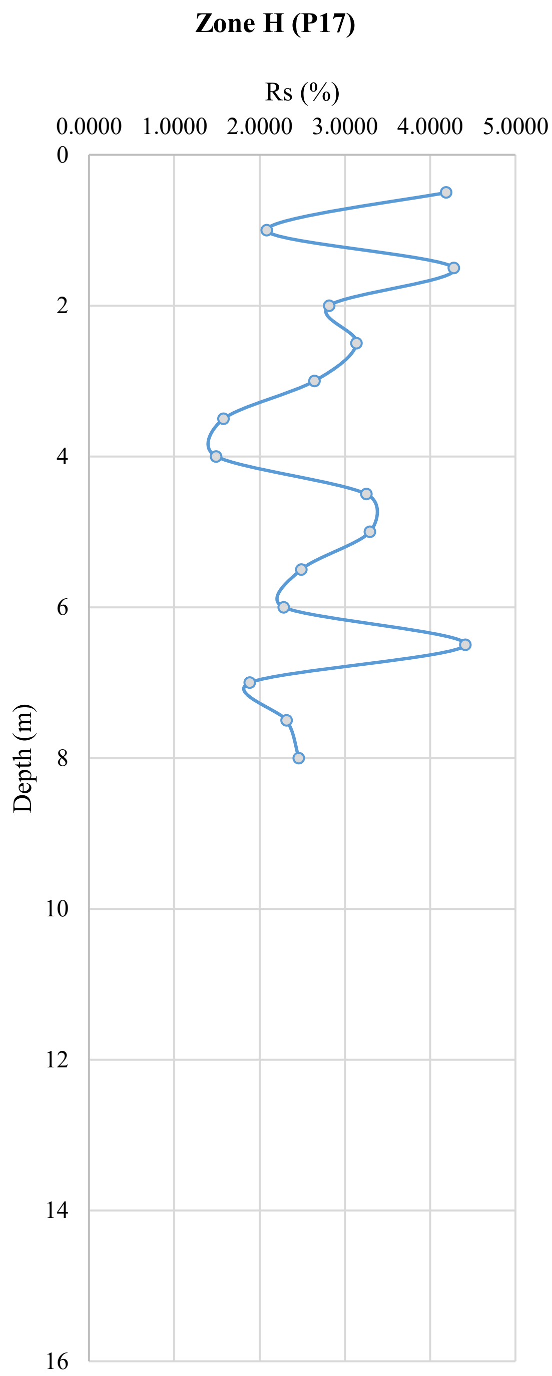

Figure 260. CPT Test Results Summary for Zone H.2

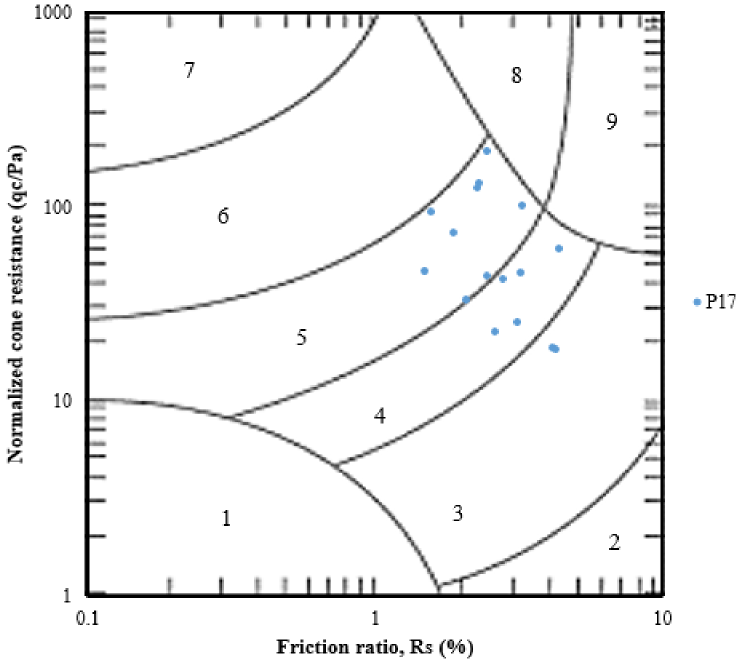

Figure 261. CPT Test Results Summary for Zone H.3

Zone H

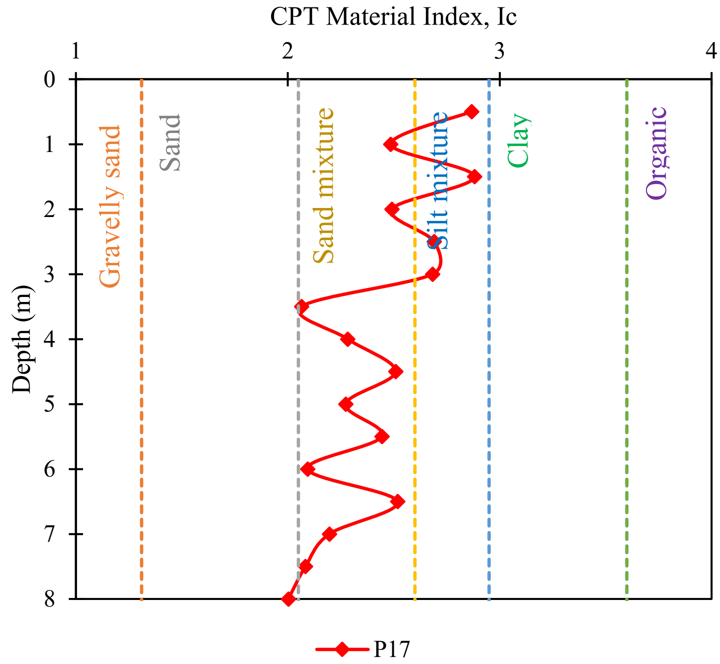

Figure 262. CPT Test Results Summary for Zone H.4

- **Zone I (P18-P21)**

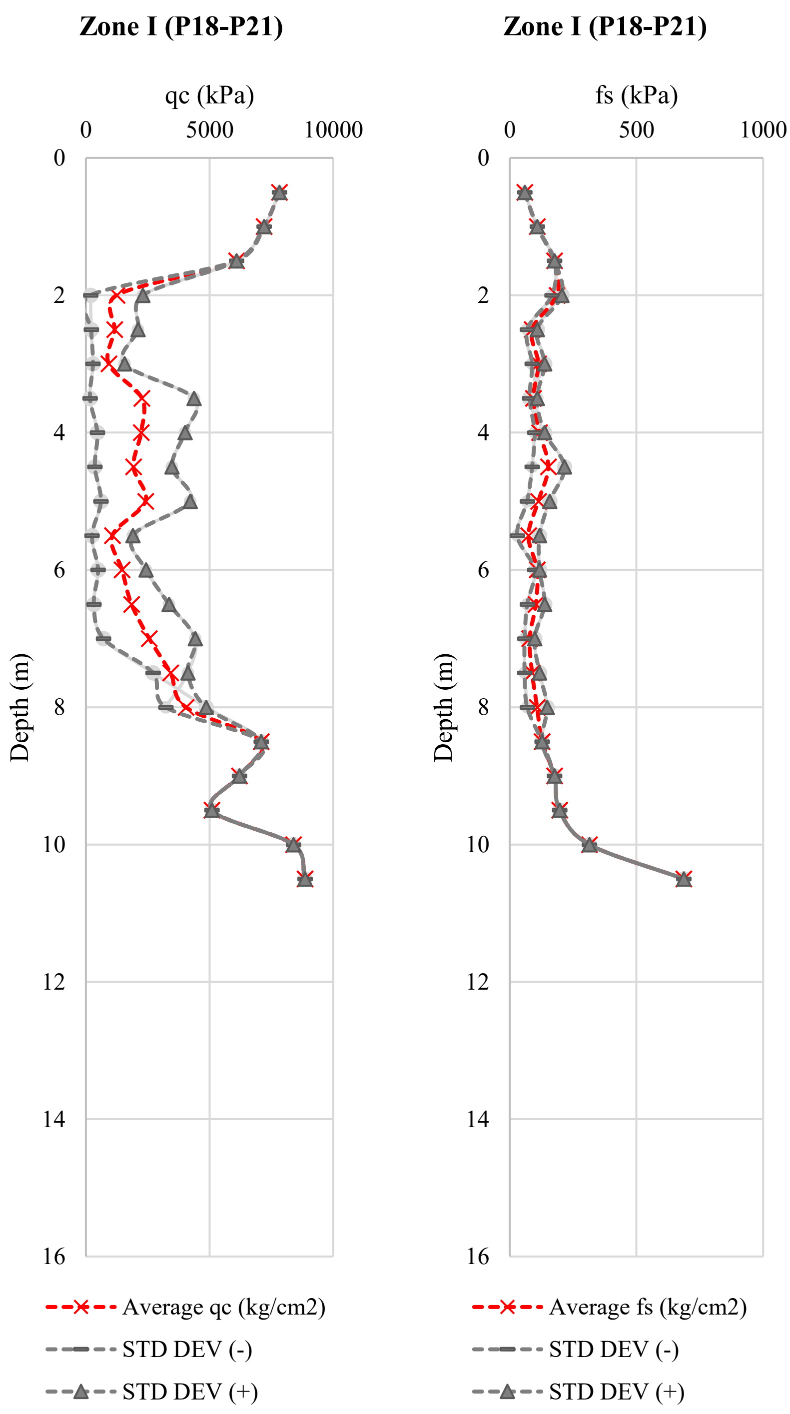

Figure 263. CPT Test Results Summary for Zone I.1

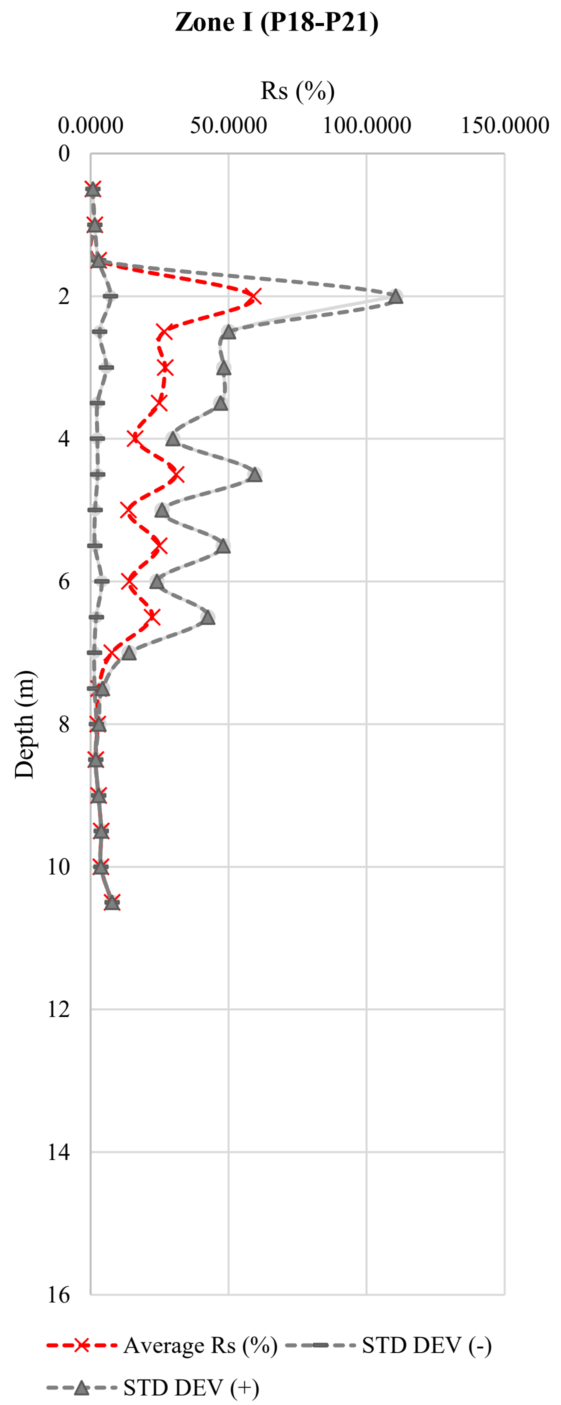

Figure 264. CPT Test Results Summary for Zone I.2

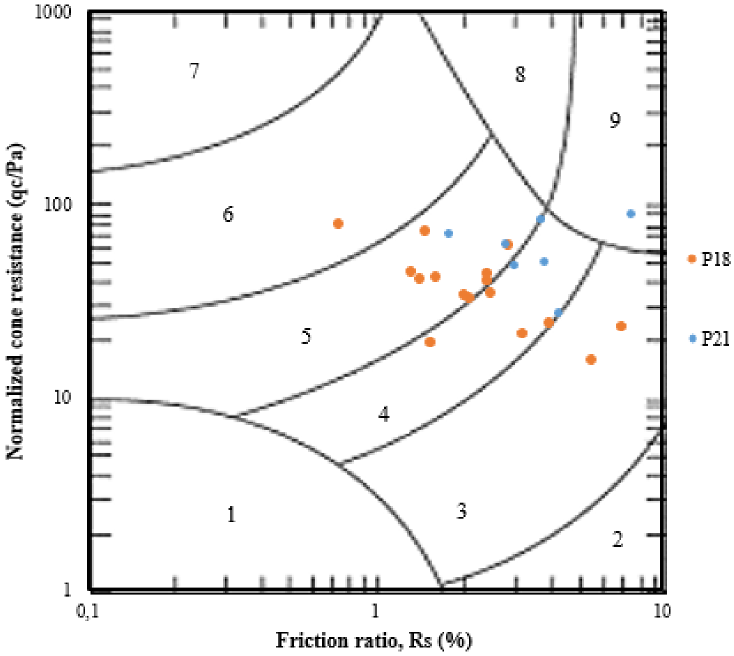

Figure 265. CPT Test Results Summary for Zone I.3

Zone I

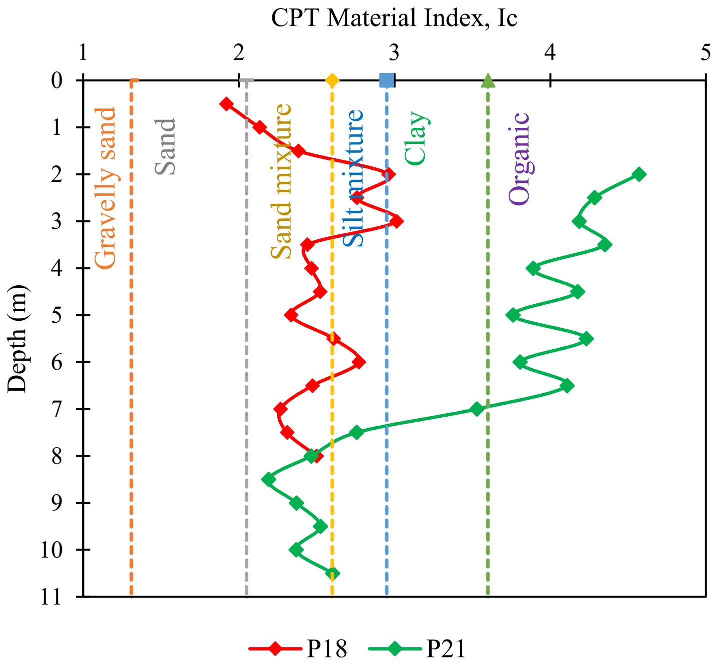

Figure 266. CPT Test Results Summary for Zone I.4

- **Seismic Marchetti Dilatometer Test (SDMT)**

This standard test method describes a penetration and expansion trial in situ test, it is beginning forcing the steel, flat plate, dilatometer blade with sharp cutting edge into a soil. Each one of the test consist in an increment of penetration, in majority of cases they are vertical and is follow by flat expansion into the surrounding soil. It is important because provides us information about the soil´s in situ stratigraphy, stress, strength, compressibility and pore water pressure, this information is special widely used for designing the foundations. It is applied to sands, silts, clays, and organic soils that can be readily penetrated with the dilatometer blade, is not recommended use on soils that can´t be penetrated by the dilatometer. (ASTM D6635-15 2015).

Below are groups of boreholes based on geographic location and similar physical and mechanical properties, representing some of the zones defined in Figure 23.

- **Zone A (P1-P2-P7)**

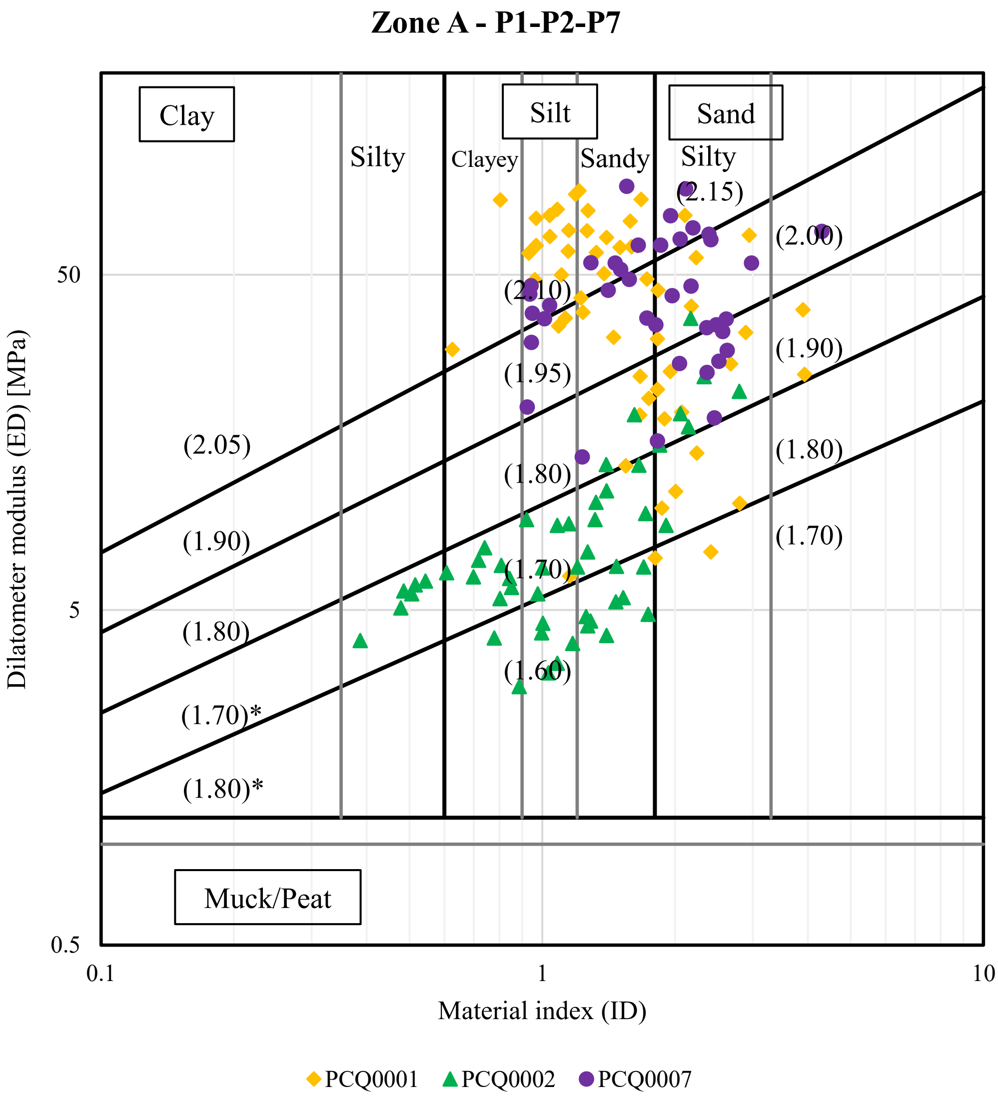

Figure 267. Zone A Dilatometer modulus (ED) [MPa]

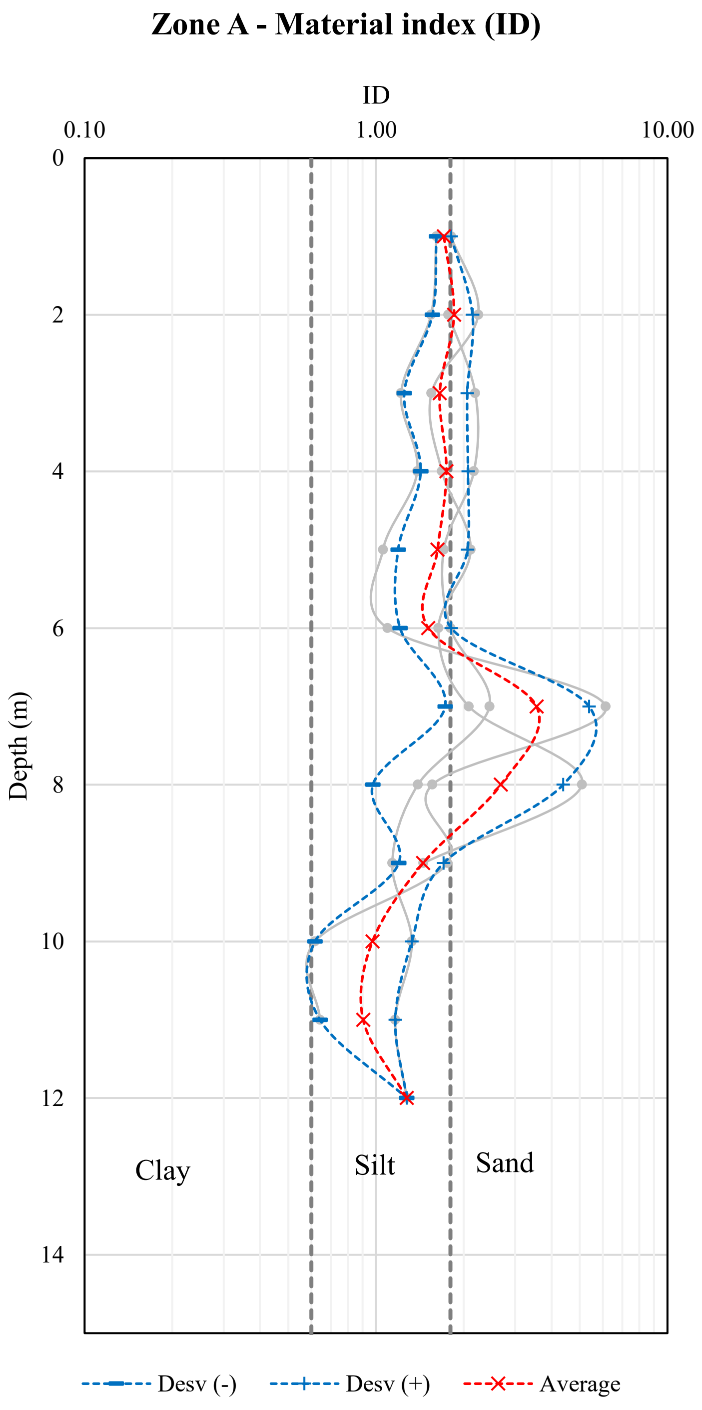

Figure 268. Zone A - Material index (ID)

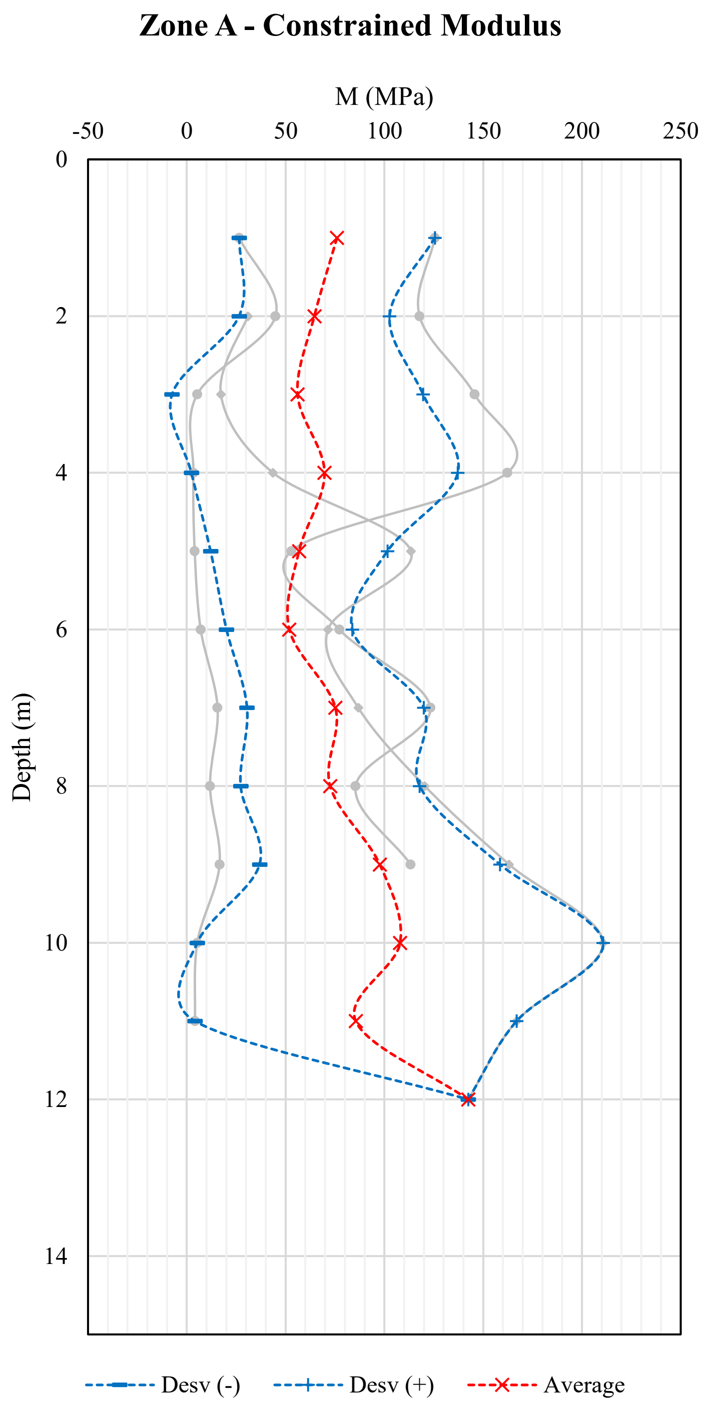

Figure 269. Zone A - Constrained Modulus

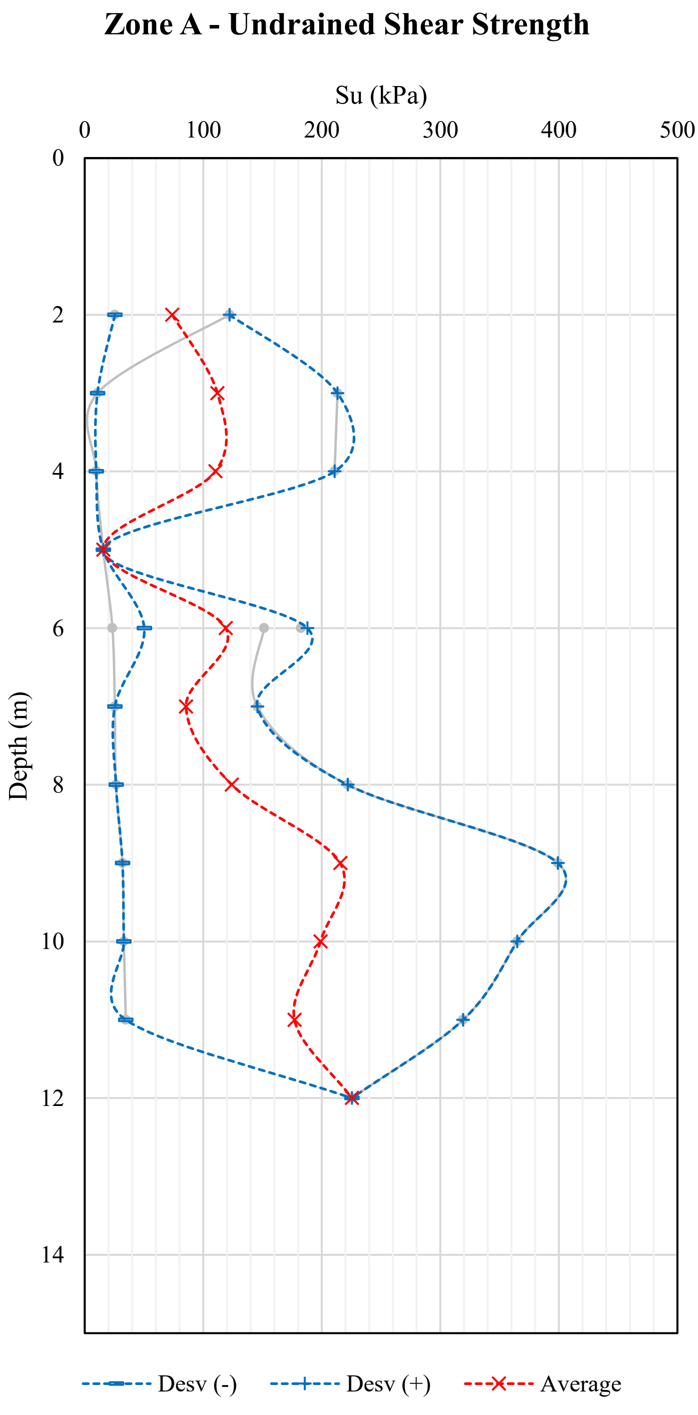

Figure 270. Zone A - Undrained Shear Strength

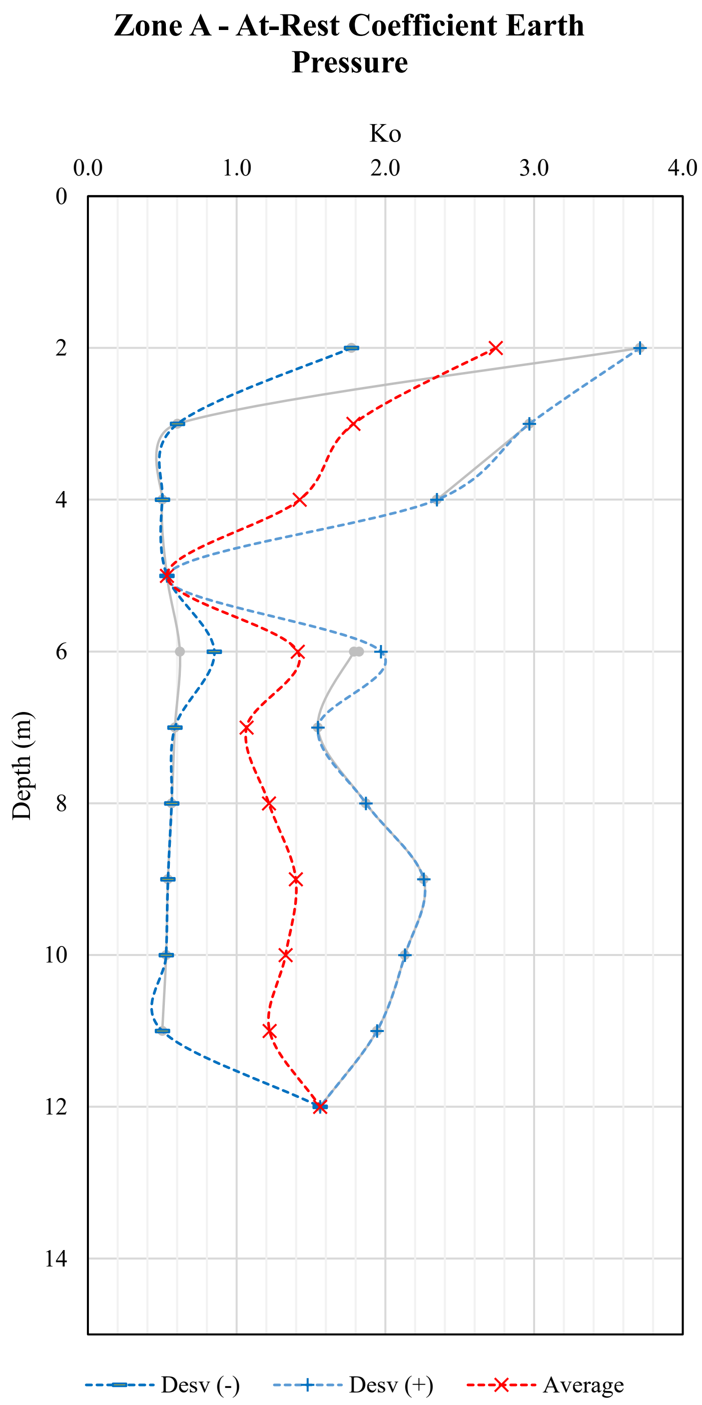

Figure 271. Zone A - At-Rest Coefficient Earth Pressure

- **Zone B (P4)**

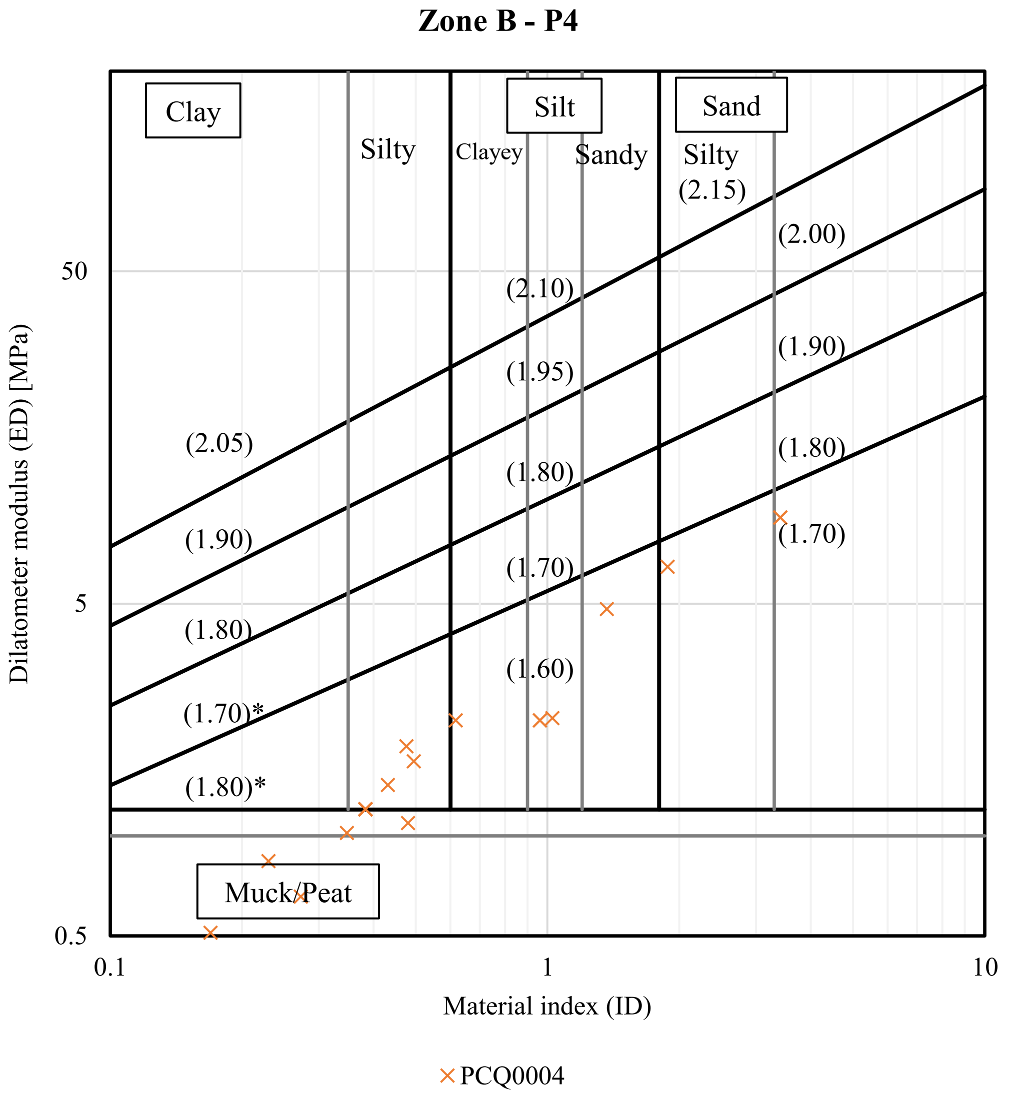

Figure 272. DMT results – Zone B

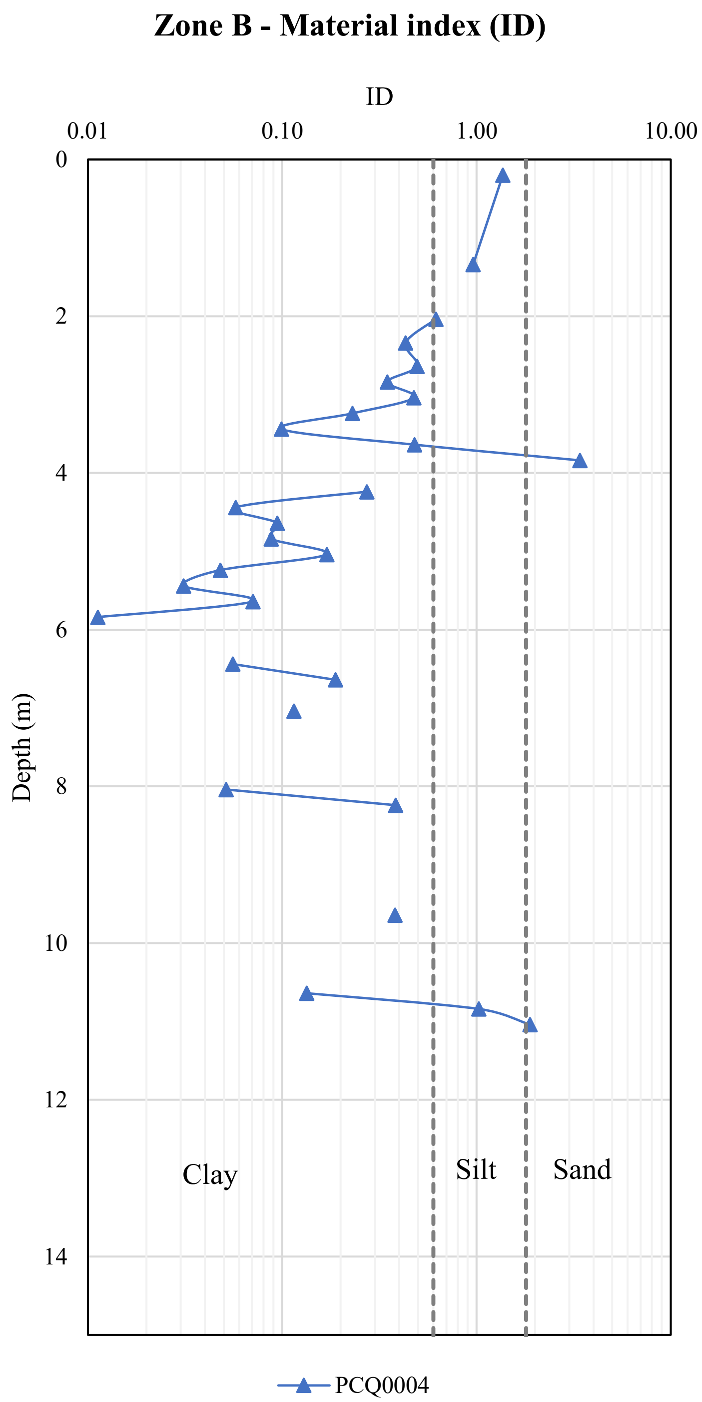

Figure 273. Material index (I_D) results – Zone B.

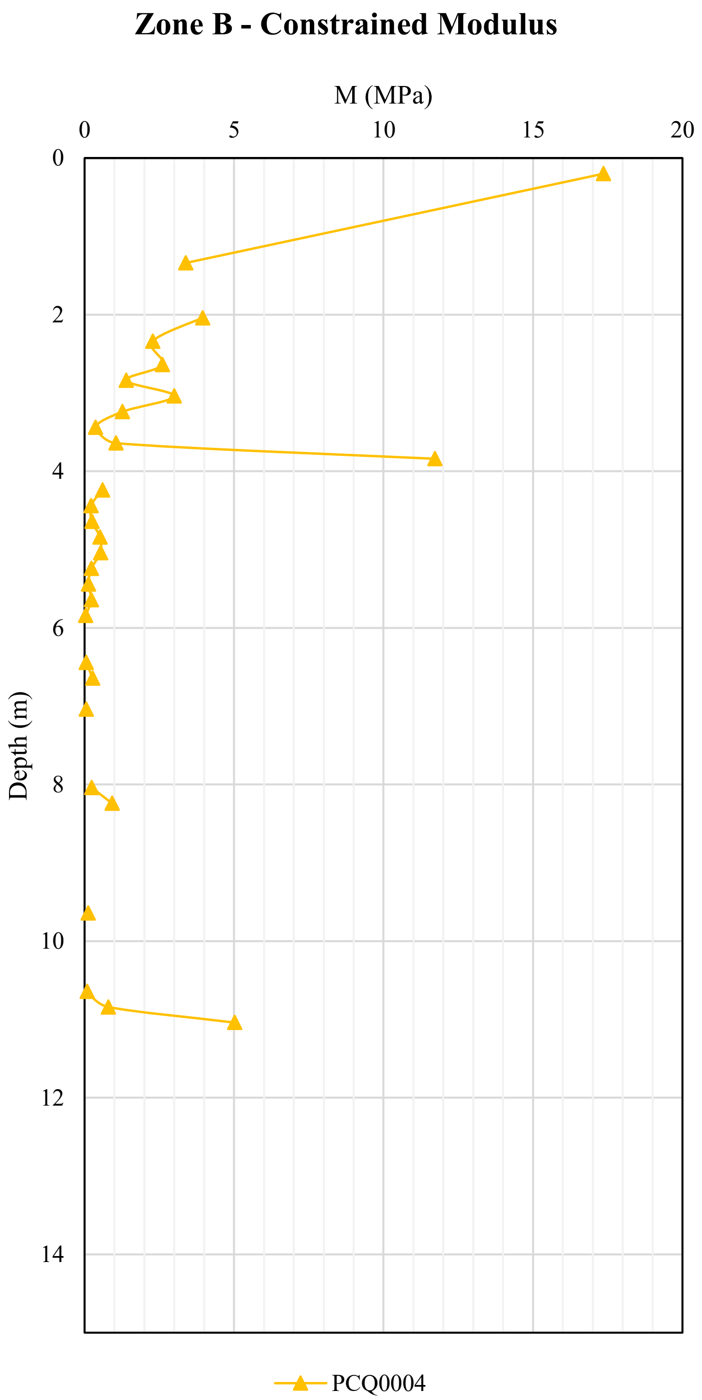

Figure 274. Constrained Modulus (M) results – Zone B.

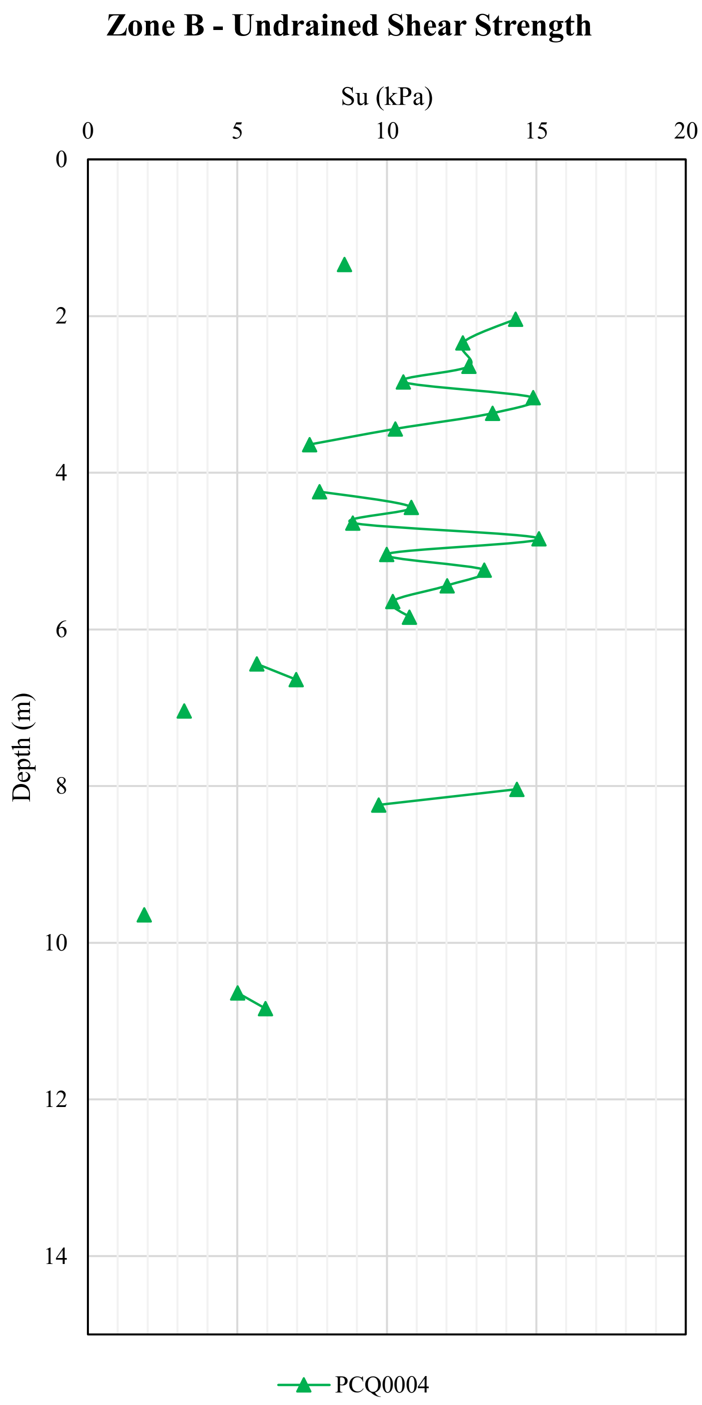

Figure 275. Undrained Shear Strength (Su) results – Zone B.

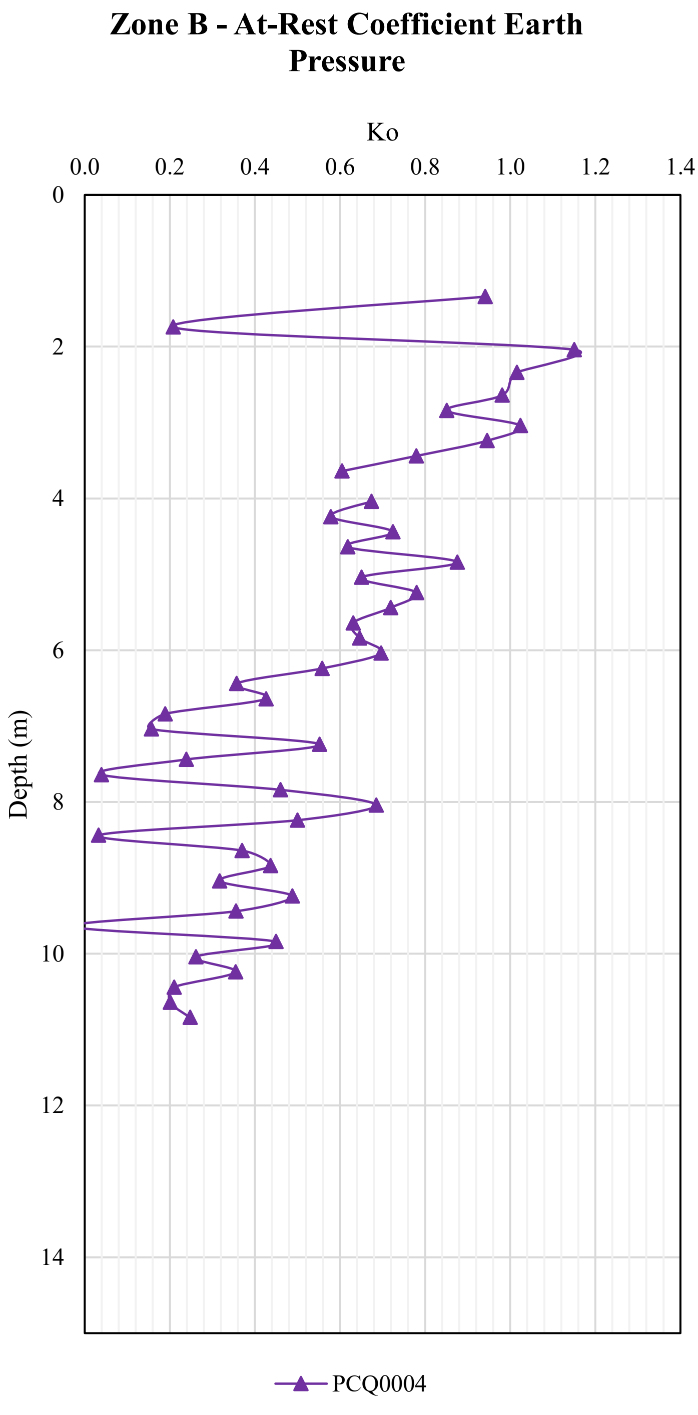

Figure 276. At-Rest Coefficient Earth Pressure (Ko) results – Zone B.

- **Zone C (P5-P9)**

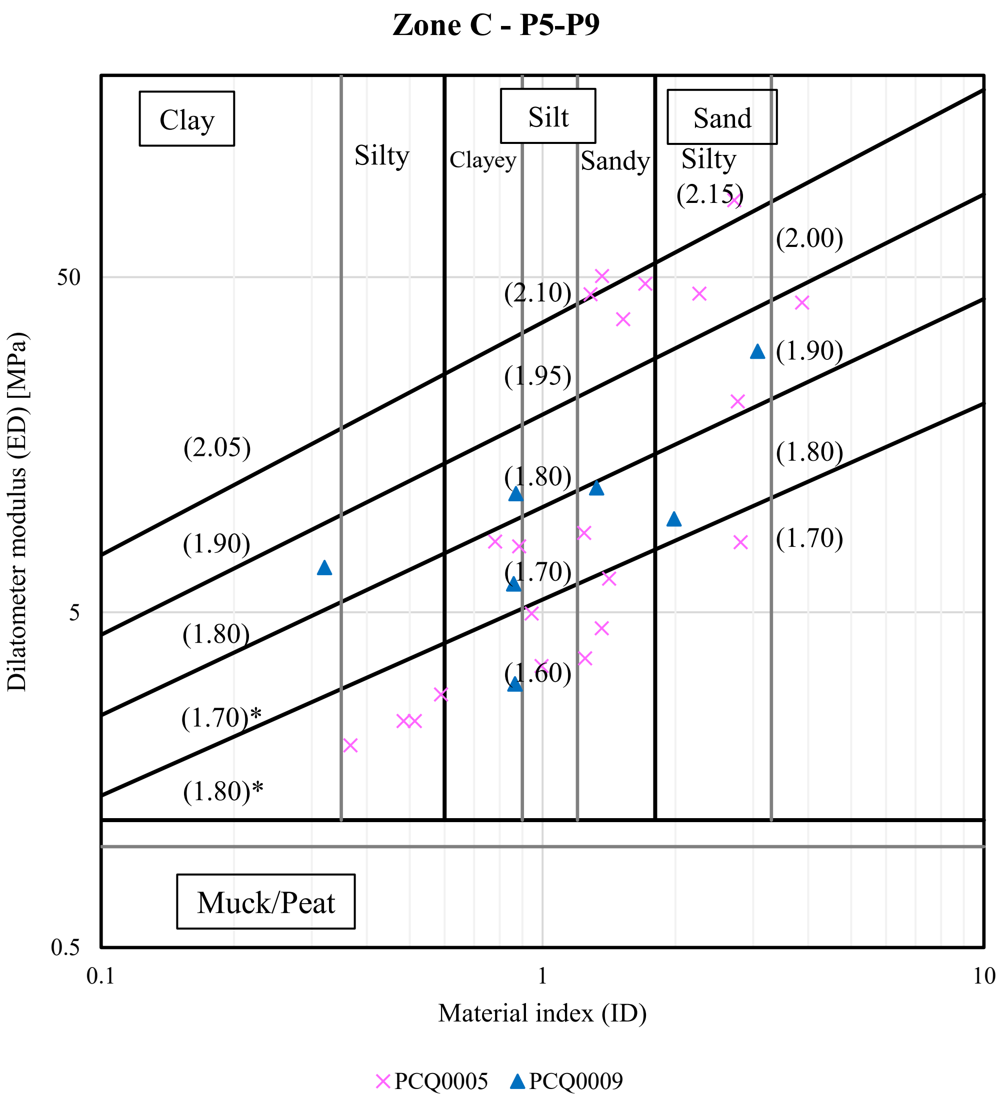

Figure 277. DMT results – Zone C

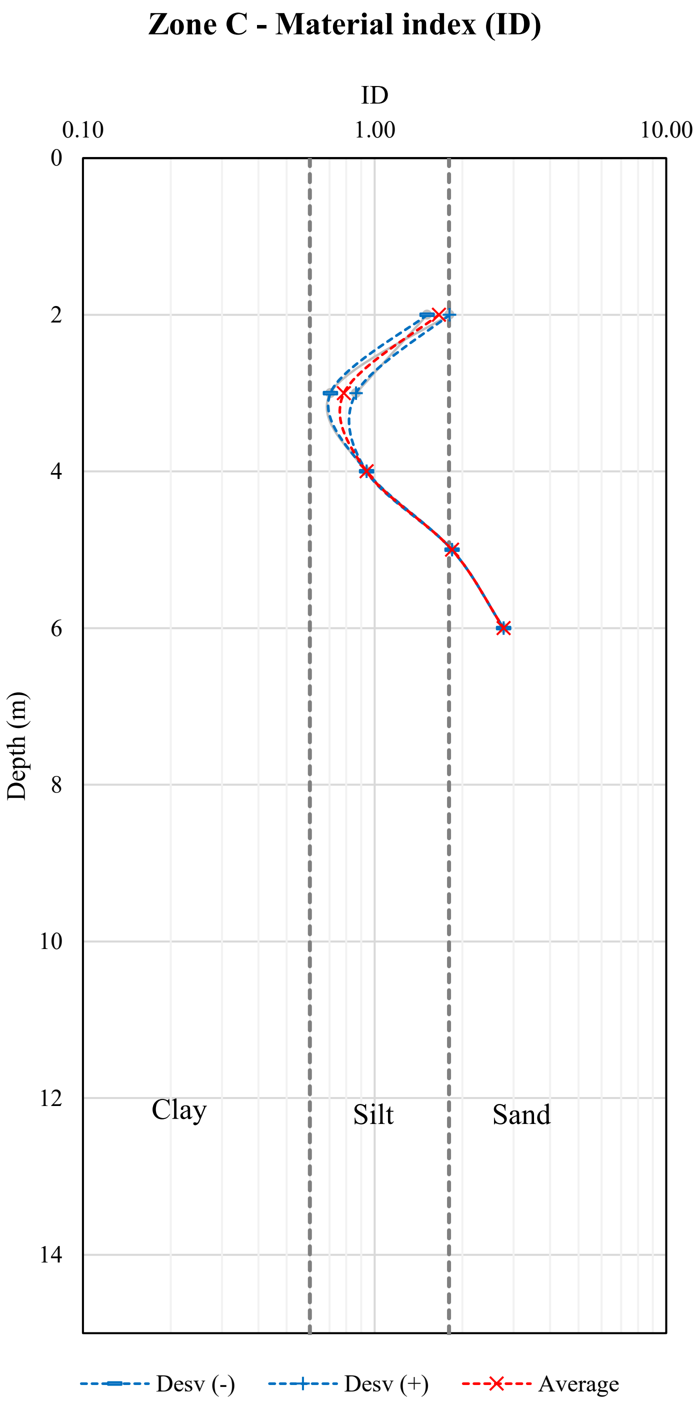

Figure 278. Material index (I_D) results – Zone C.

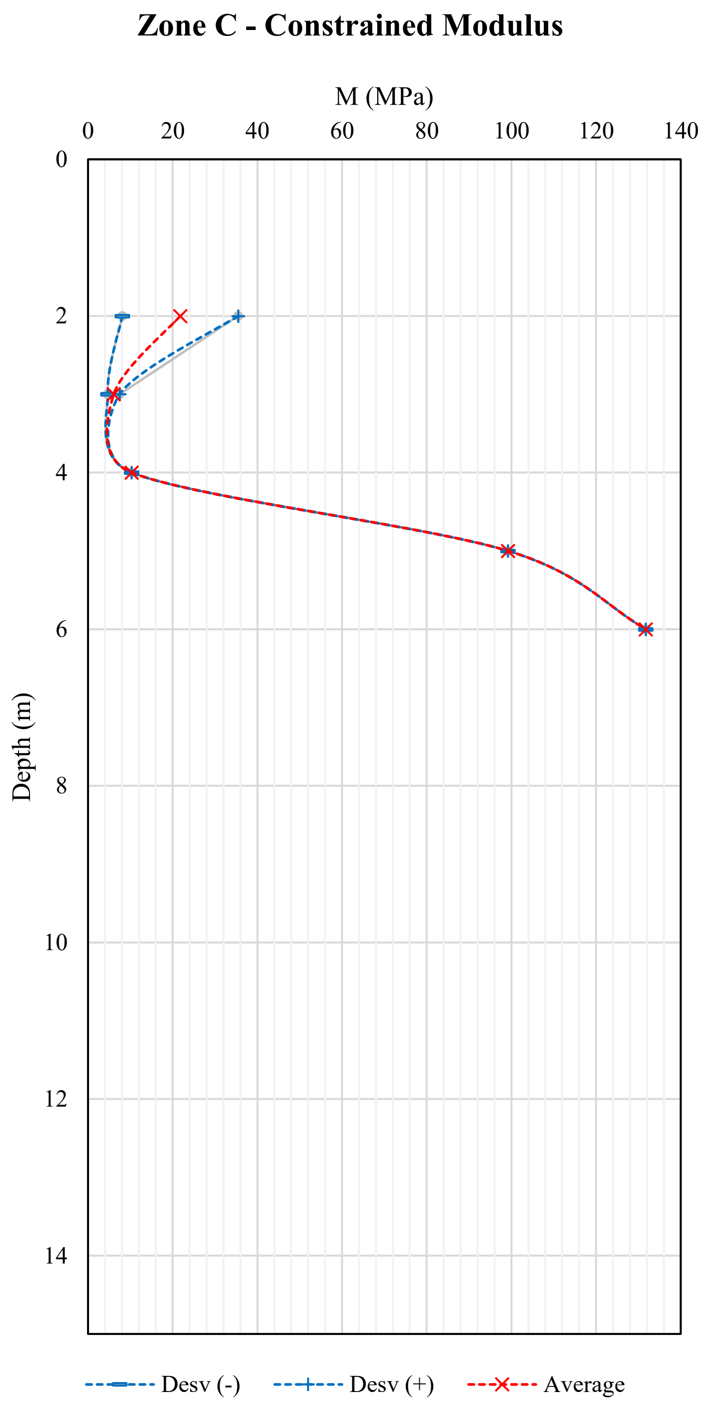

Figure 279. Constrained Modulus (M) results – Zone C.

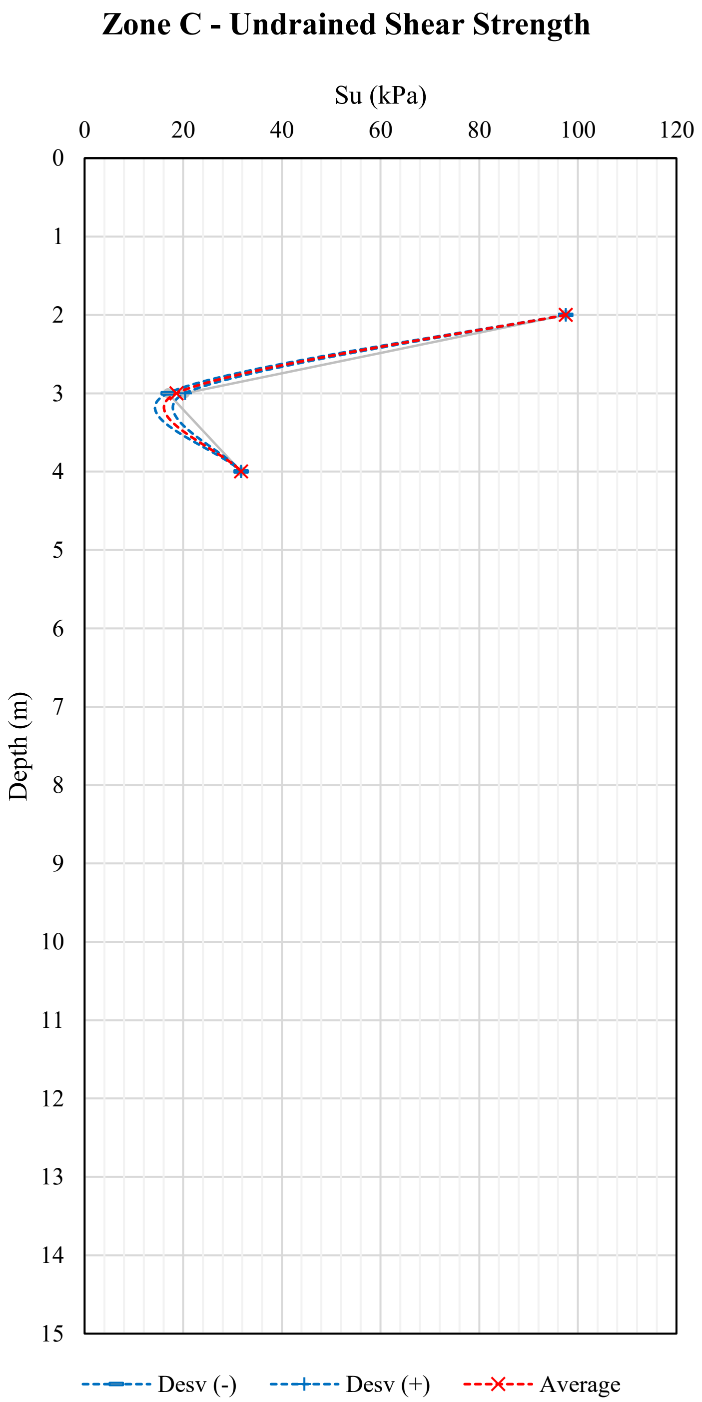

Figure 280. Undrained Shear Strength (Su) results – Zone C.

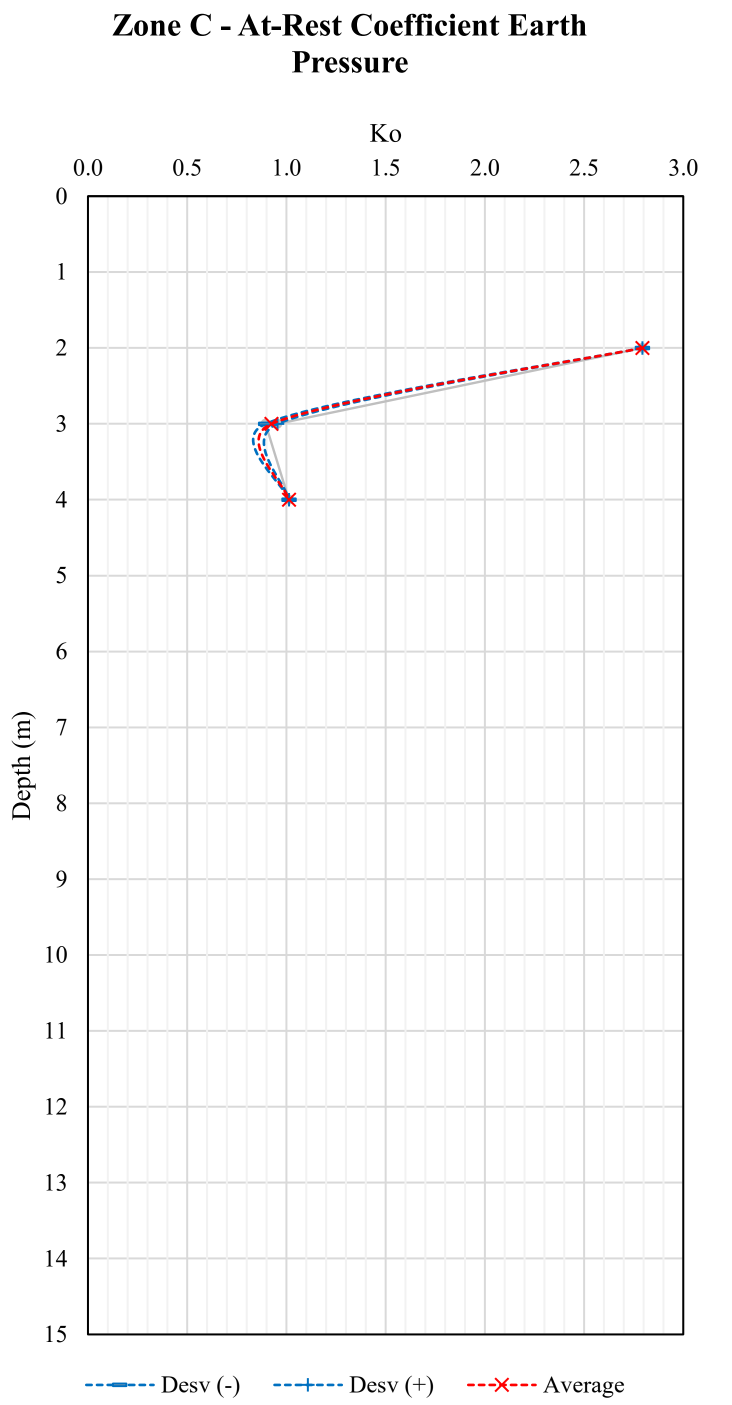

Figure 281. At-Rest Coefficient Earth Pressure (Ko) results – Zone C.

- **Zone D (P6)**

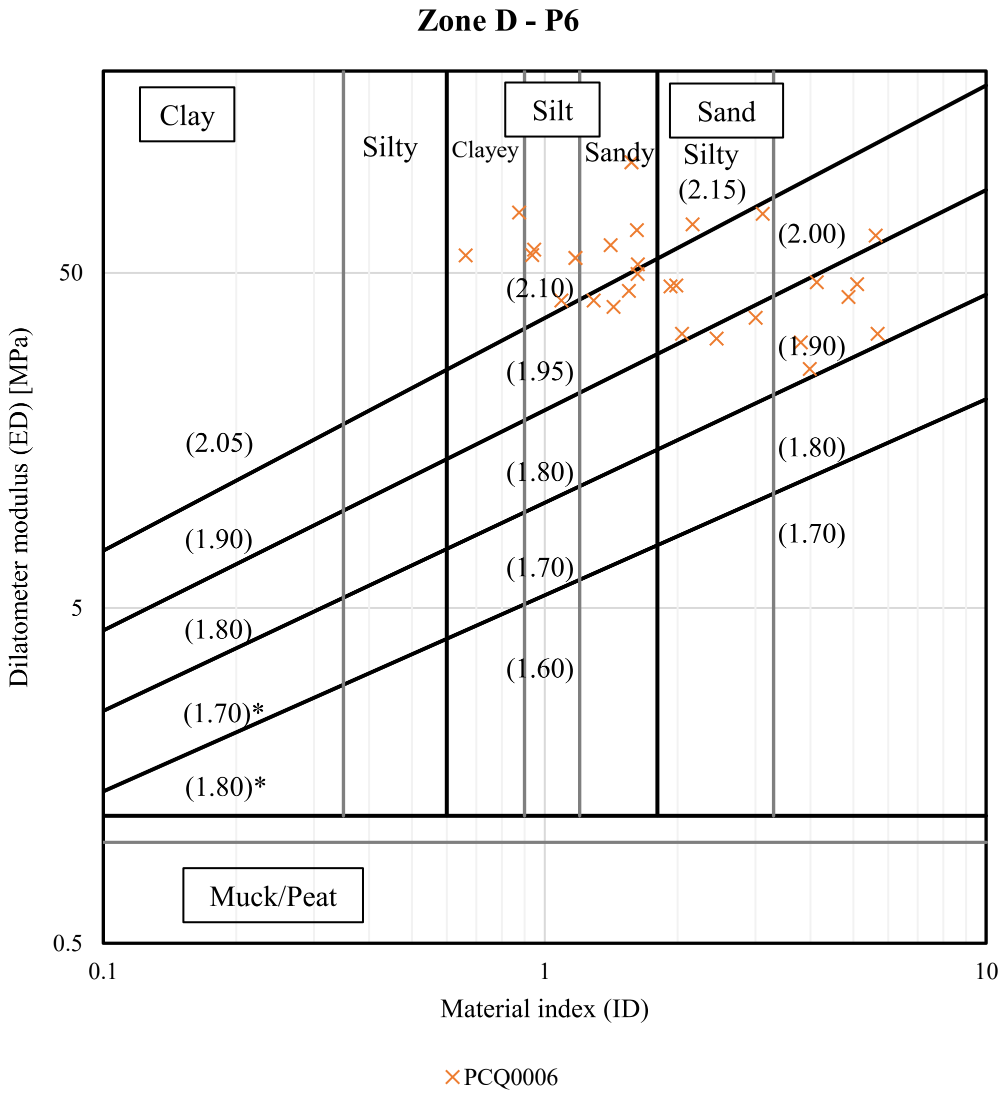

Figure 282. DMT results – Zone D

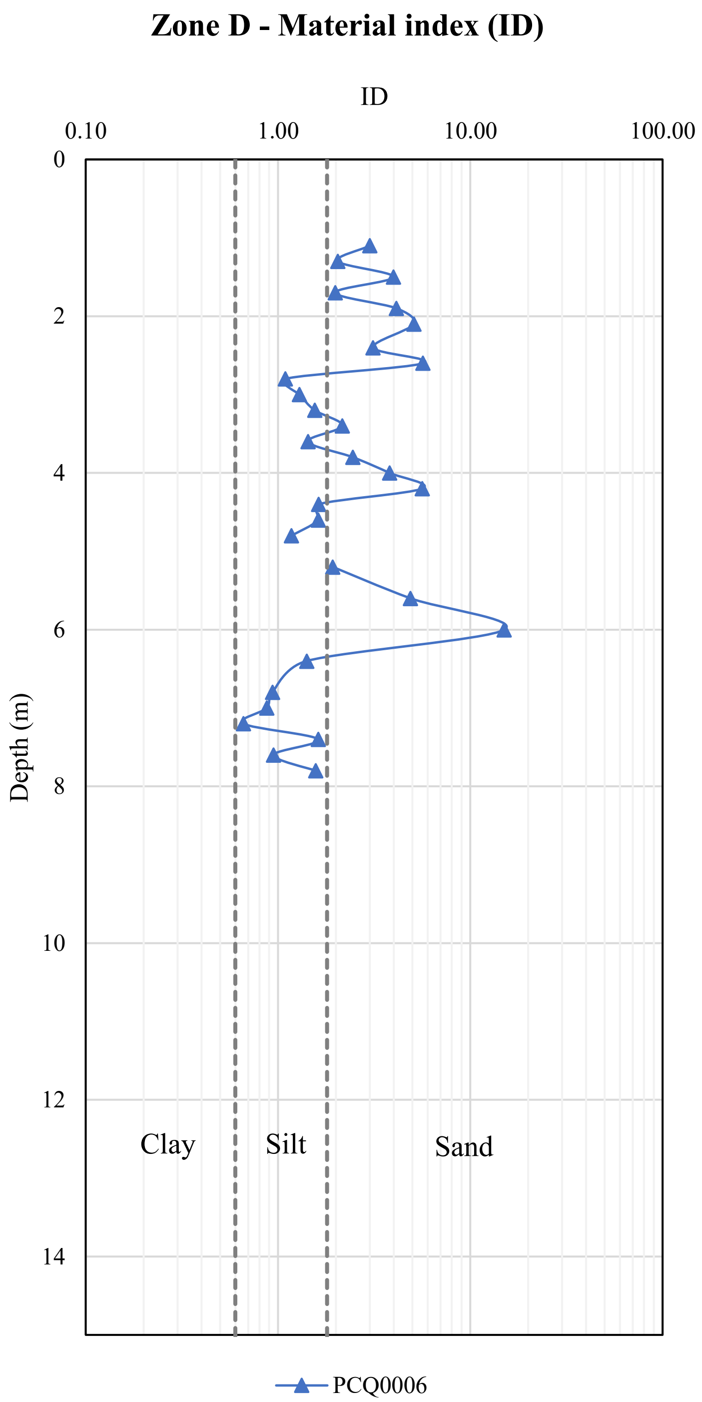

Figure 283. Material index (I_D) results – Zone D.

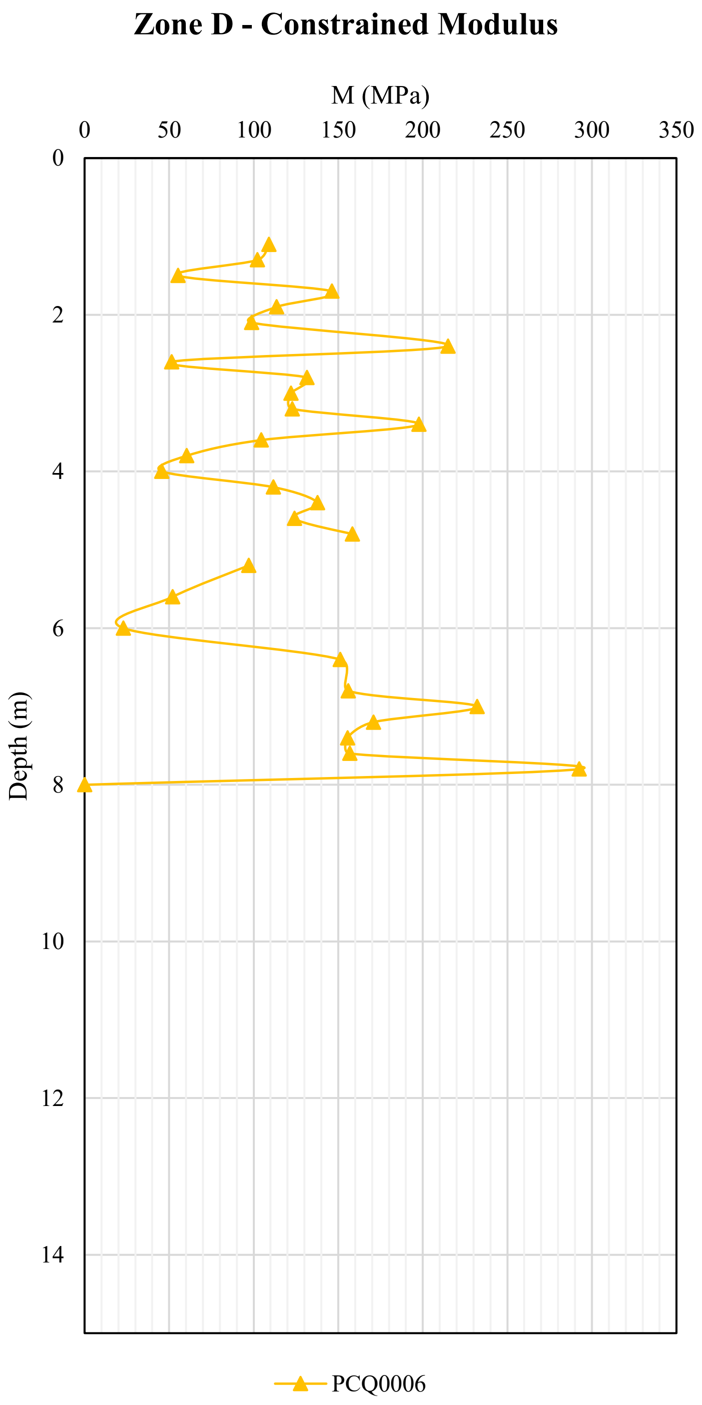

Figure 284. Constrained Modulus (M) results – Zone D.

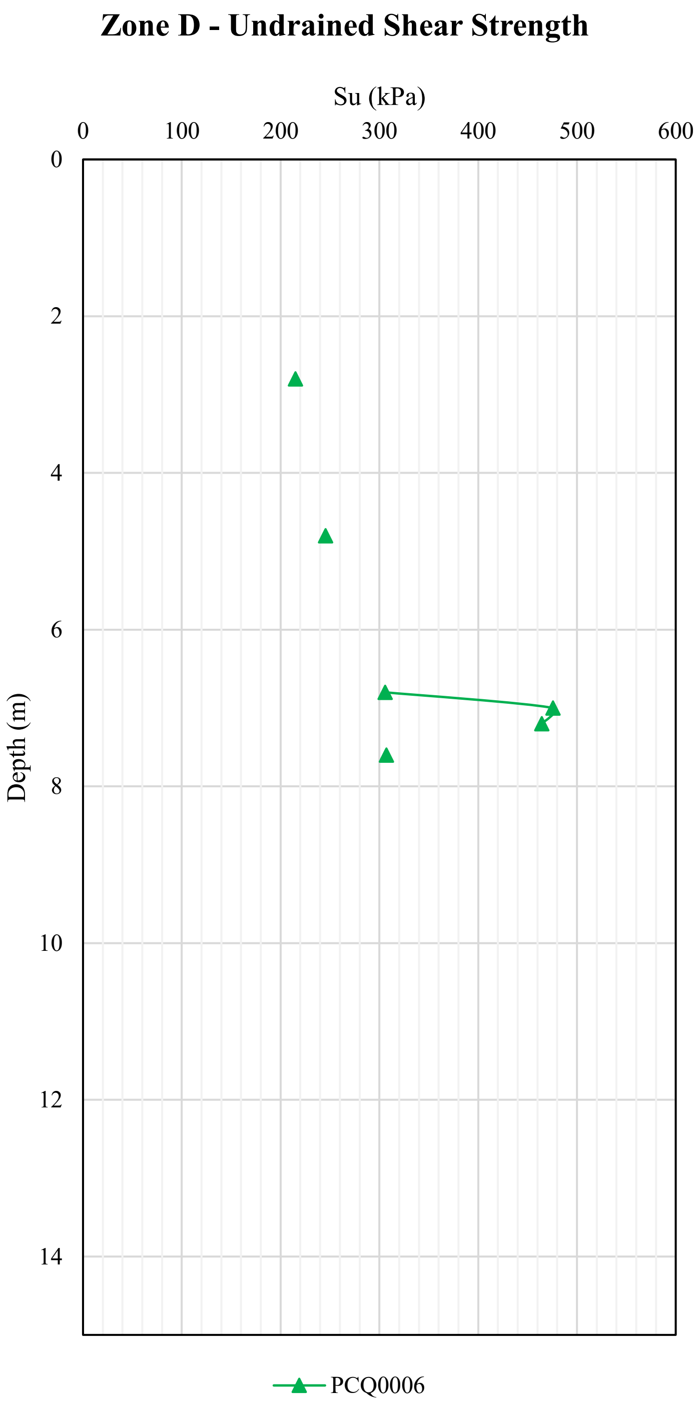

Figure 285. Undrained Shear Strength (Su) results – Zone D.

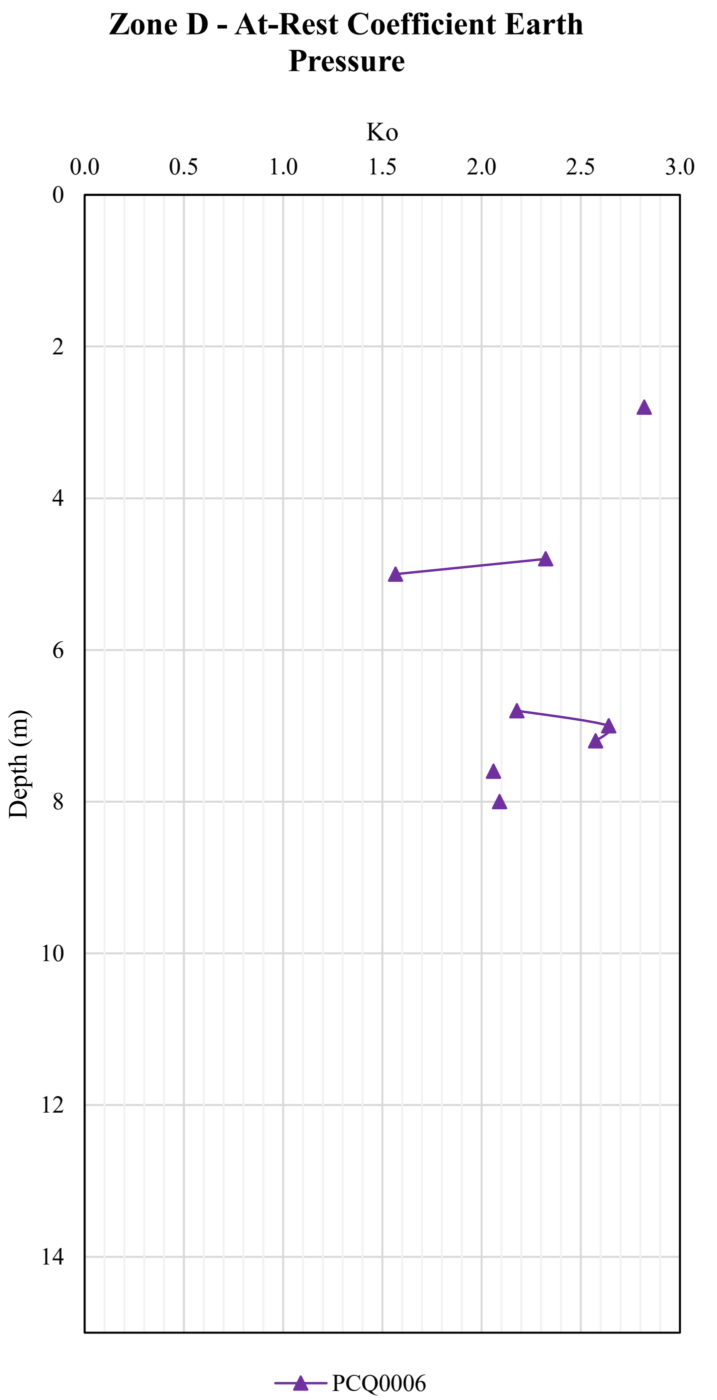

Figure 286. At-Rest Coefficient Earth Pressure (Ko) results – Zone D.

- **Zone E (P10)**

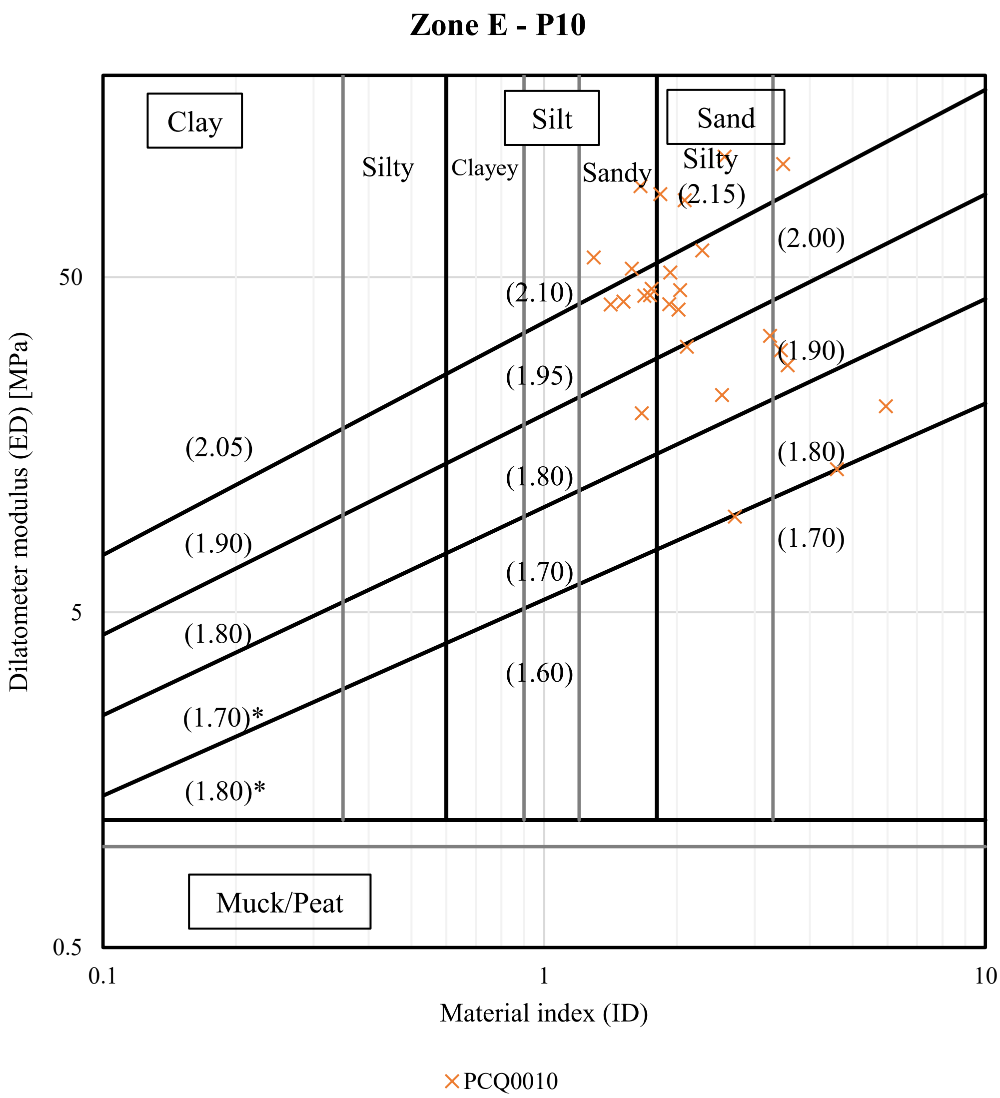

Figure 287. DMT results – Zone E

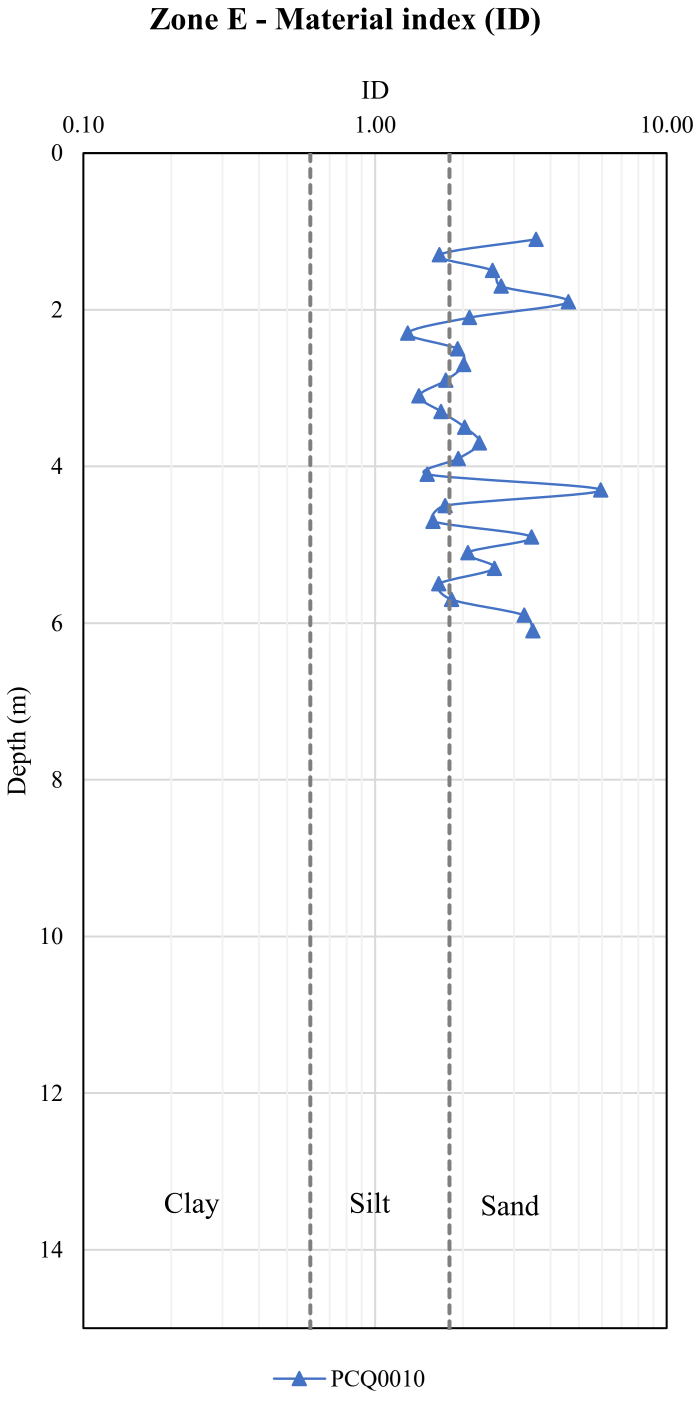

Figure 288. Material index (I_D) results – Zone E.

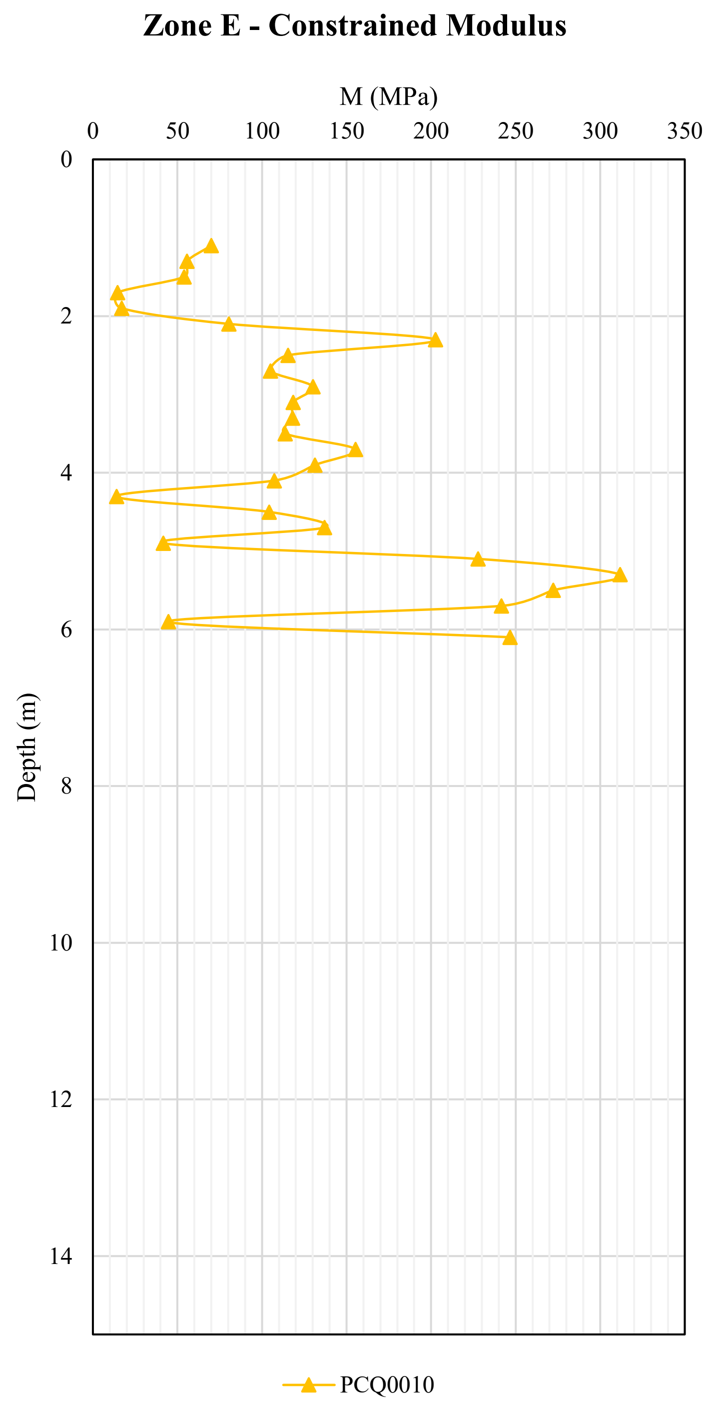

Figure 289. Constrained Modulus (M) results – Zone E.

No results were obtained for Su and Ko in this borehole.

- **Zone G (P11)**

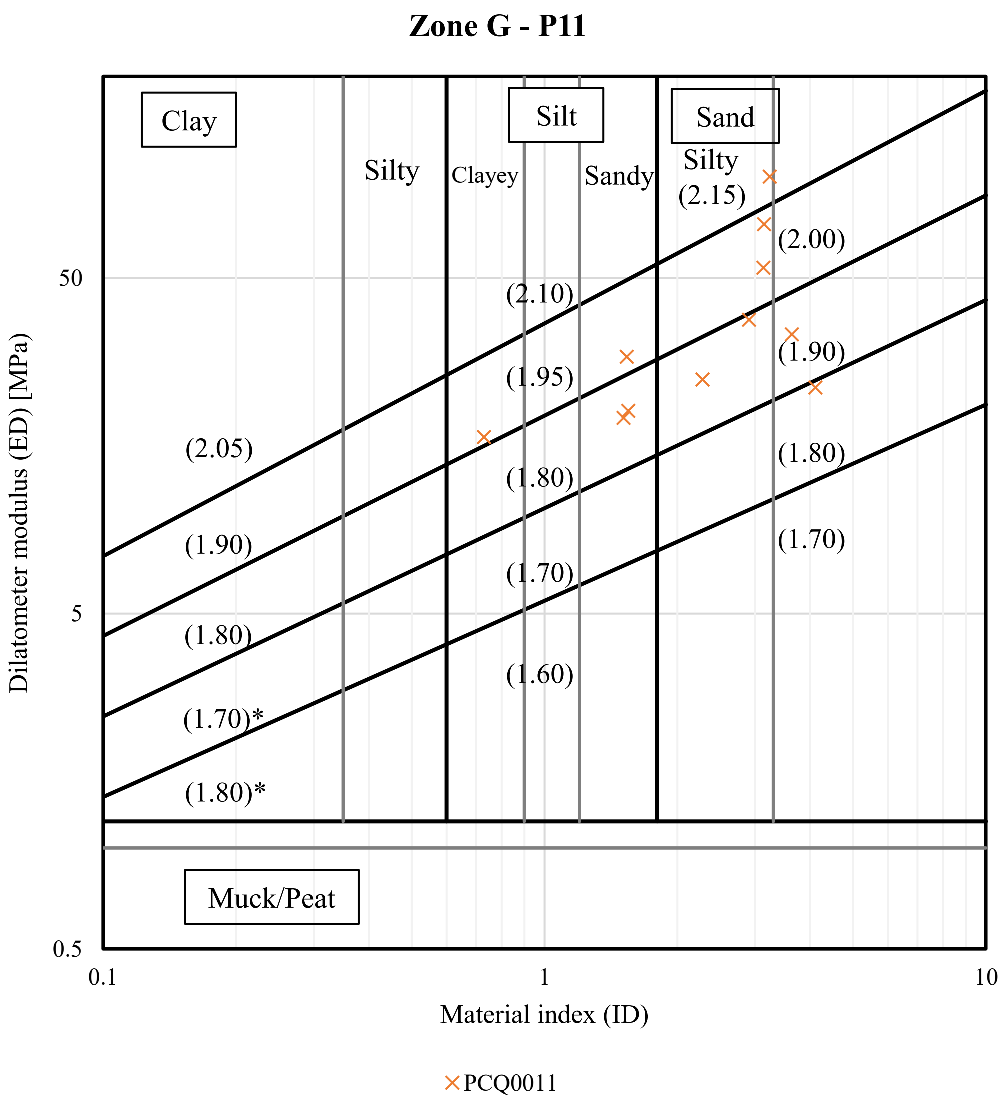

Figure 290. DMT results – Zone G

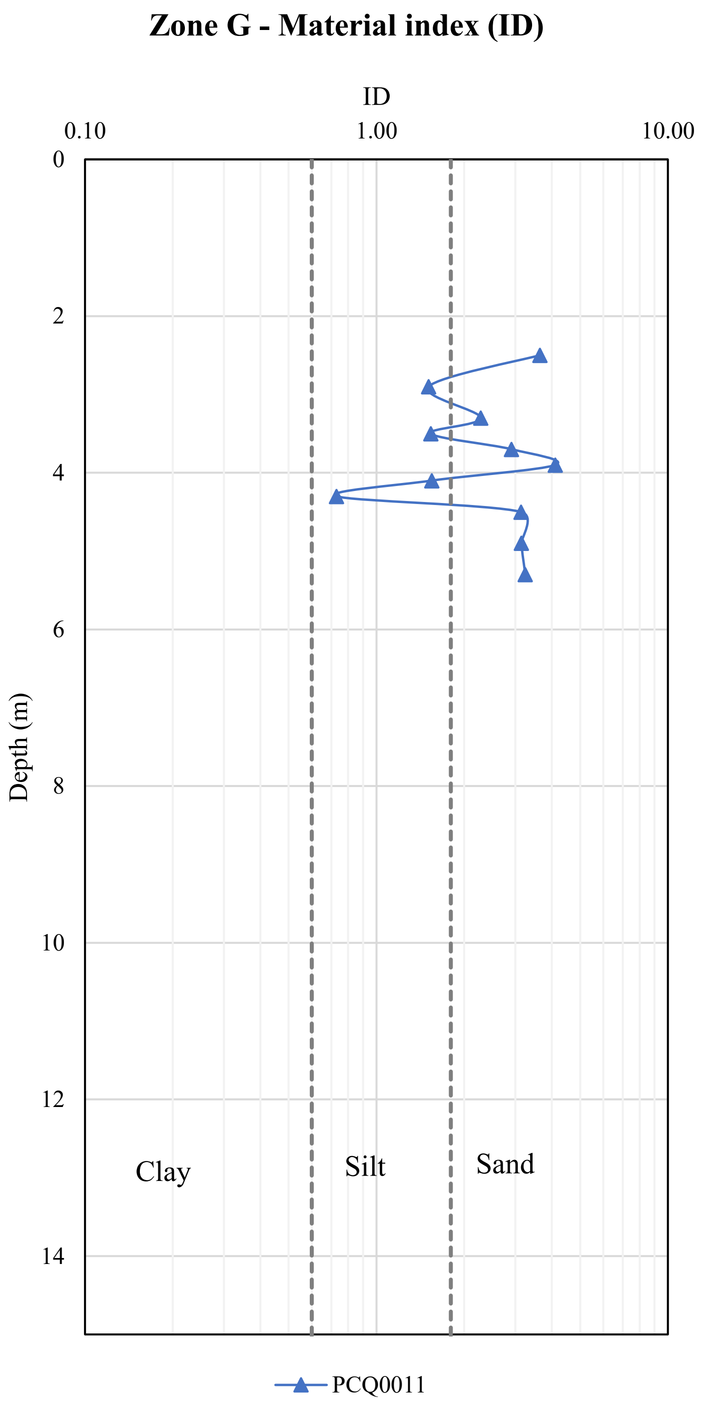

Figure 291. Material index (I_D) results – Zone G.

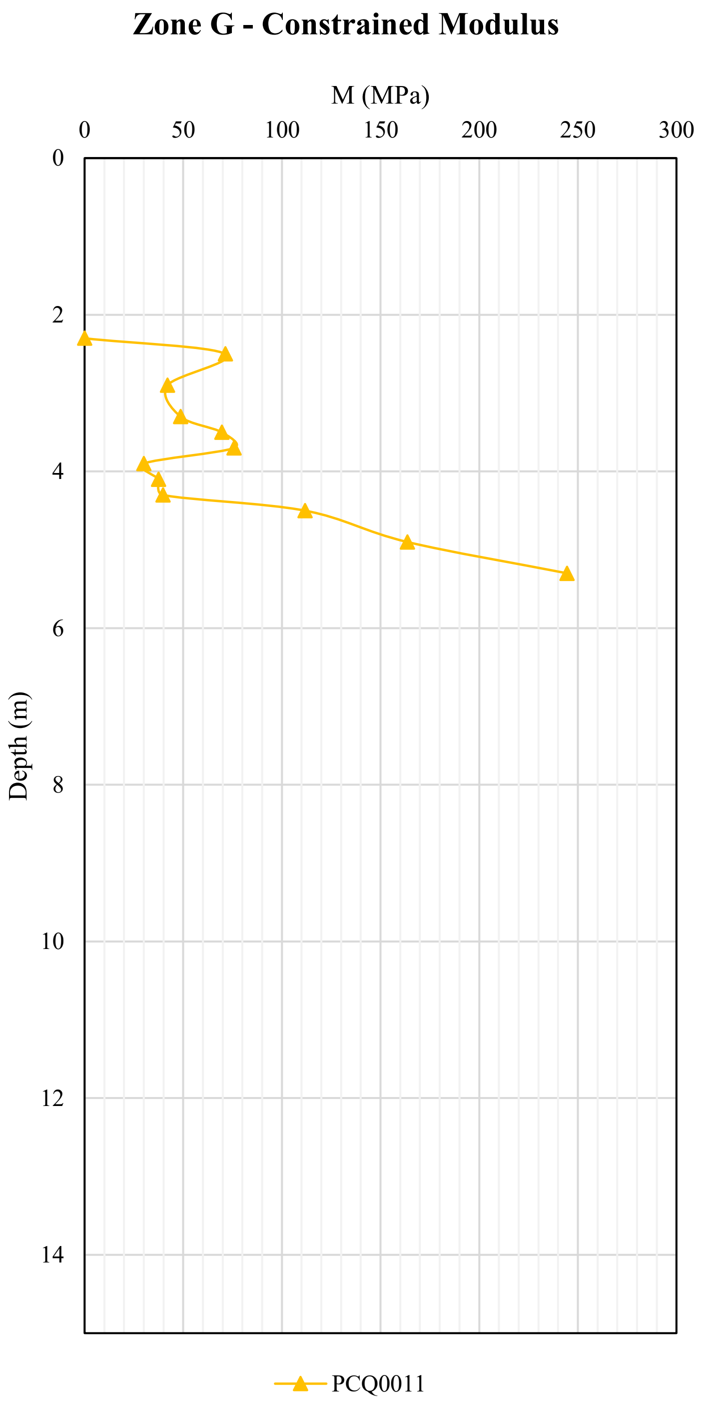

Figure 292. Constrained Modulus (M) results – Zone G.

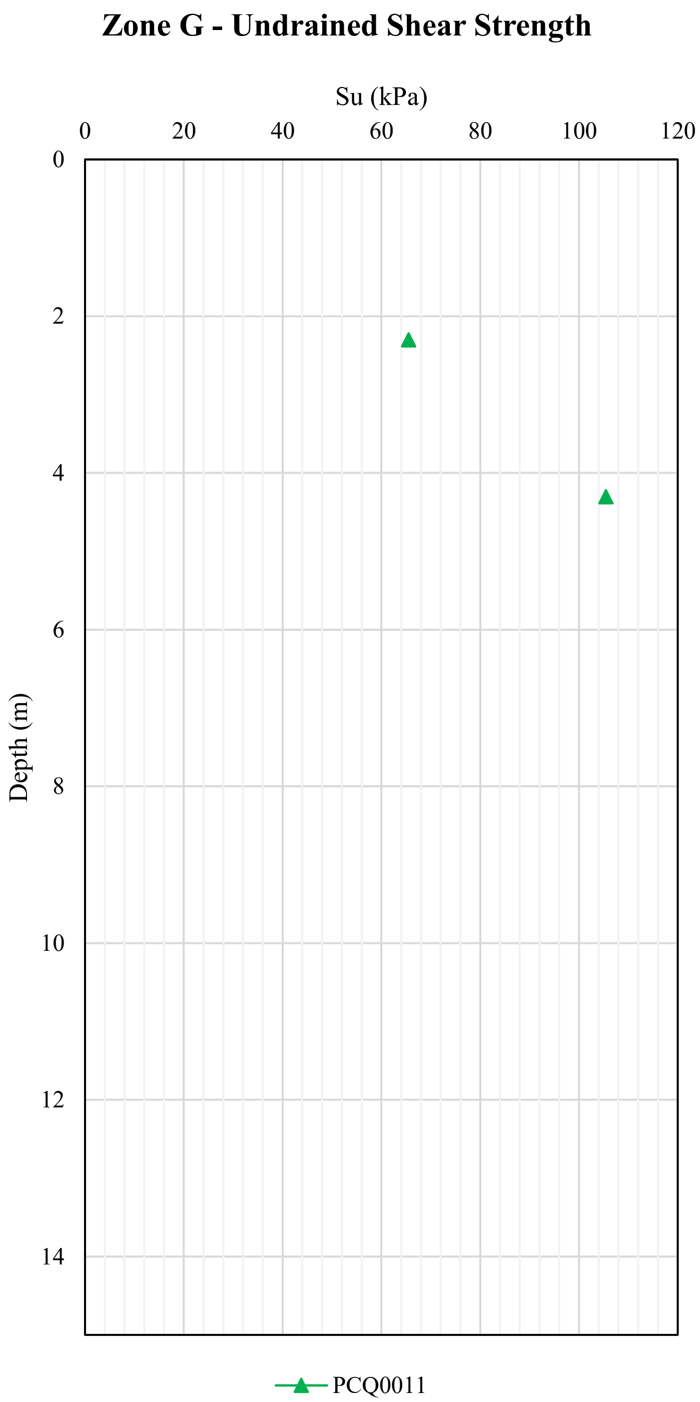

Figure 293. Undrained Shear Strength (Su) results – Zone G.

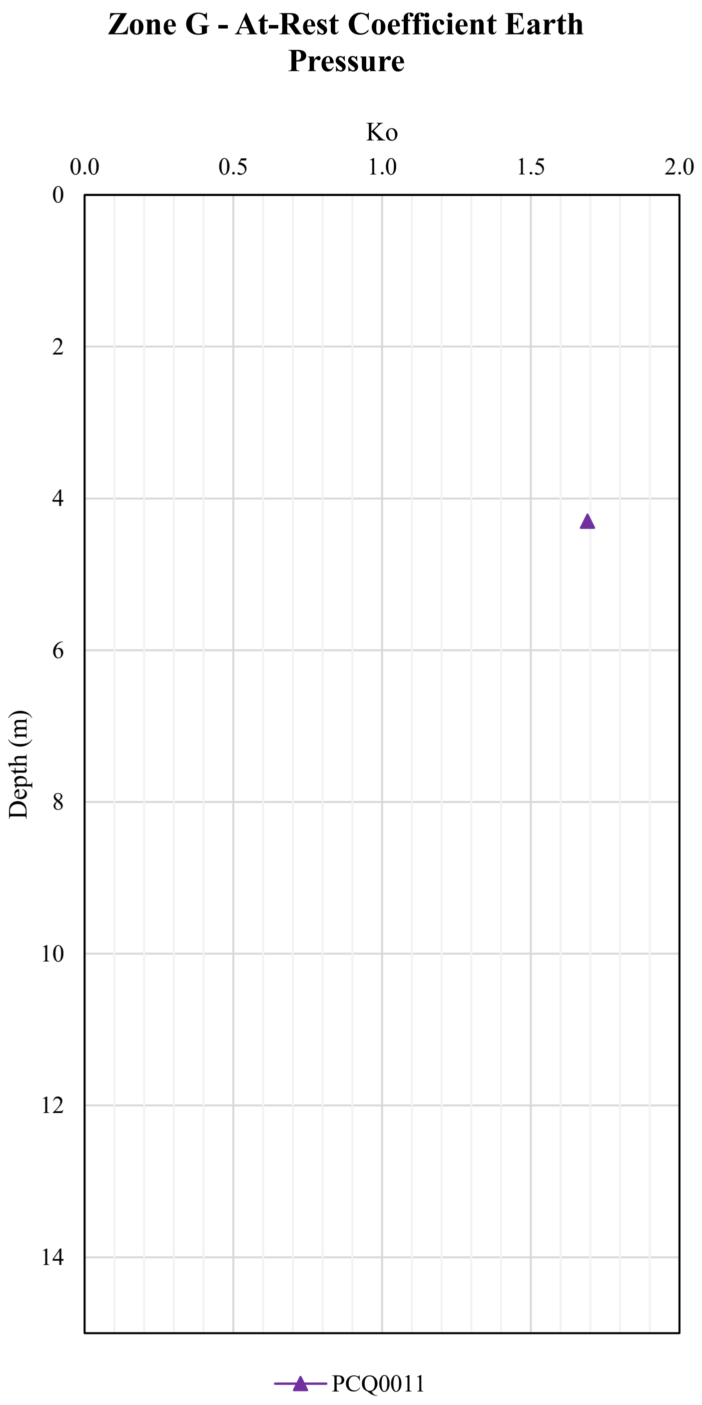

Figure 294. At-Rest Coefficient Earth Pressure (Ko) results – Zone G.

A.2. Laboratory Tests

- **Water Content**

These test methods cover the laboratory determination of water (moisture) content by mass of soils, rocks and similar materials where the reduction in mass by drying is due to water loss. This test standard requires several hours for proper drying of the water content sample. This standard provides two test methods, which are as follows: Method A. The water content by mass is recorded to an accuracy of 1%. and Method B, where the water content by mass is recorded to an accuracy of 0.1%. (ASTM D2216-19 2019).

Figure 295. Moisture content test.

- **Liquid Limit**

This standard test methods is used for classified fine soils, USCS (liquid limit, plastic limit, and index plastic) are used for correlate with engineering behavior such as compressibility, hydraulic conductivity or permeability, compatibility, shrink-swell and shear strength. The liquid and plastic limit and the water content of a soil can be used for express soil relative consistency or liquid index. In addition to these trials, the plastic index, and the percentage fine than $2-\mu m$ particle size can be used to determine the activity number. Sometimes, these trials are used for evaluating the weathering characteristics of clay-shale materials. We can use two methods: the first one is the dry preparation method and the second one is the dry preparation method. (ASTM D4318-17 2017).

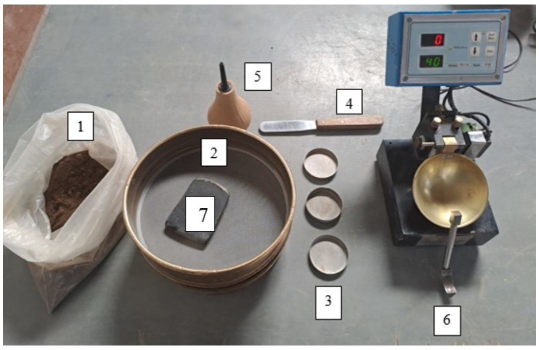

1. Sample specimen
2. No.40 Sieve
3. Water content containers
4. Spatula
5. Wash bottle
6. Motor drive
7. Rubber feet

Figure 296. Materials used for this test.

Figure 297. Procedure to obtain liquid limit.

- **Plastic Limit**

The Plastic Limit test is performed on material prepared for liquid limit test. We have two procedures for rolling. In this case we used the procedure 1 (Hand Rolling). We need to select 20g or more portion of soil. This procedure consists of reduce water content of the soil to a consistency at which it can be rolled without sticking to the hands until the diameter reaches 3.2mm (1/8 in). (ASTM D4318-17 2017)

Figure 298. Procedure to perform plastic limit test

- **Material Passing Sieve N°200**

This test method covers the determination of the amount material finer than a 75-µm (No. 200) sieve in aggregate by washing. Clay particles and other aggregate particles that are dispersed by the wash water, as well as water-soluble materials, will be removed from the aggregate during the test. (ASTM C117 – 17 2017)

- **Sieving test**

This test method covers the quantitative determination of the distribution of particle sizes in soils. The distribution of particle sizes larger than 75 µm, retained on the No. 200 sieve, is determined by sieving, while the distribution of particle sizes smaller than 75 µm is determined by a sedimentation process, using a hydrometer to secure the necessary data. (ASTM D6913-17 2017)

- **Hydrometer test**

The present test method concerns the quantitative determination of the particle size distribution of the fine-grained part of soils. The sedimentation or hydrometer method is used to determine the particle size distribution of material that is finer than the No. 200 sieve. The test is performed on the finer material and the results are presented as the percentage of finer mass versus the logarithm of the particle diameter, this method can be used to evaluate the fine-grained fraction of a soil with a wide range of particle sizes by sedimentation results with a granulometric analysis resulting in the complete gradation curve. (ASTM D7928-21 2021).

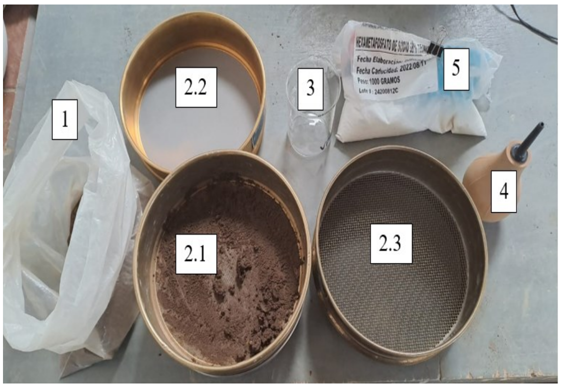

1. Sample specimen
2.1 Sieve N°40
2.2 Sieve N°200
2.3 Sieve N° 10
3. Glass cup
4. Destilled water
5. Sodium Hexametaphosphate

Figure 299. Materials used for hydrometer test.

Figure 300. Process to perform hydrometer test

- **Total and Dry Unit Weight Test**

The standard test methods for laboratory determination of density and unit weight of soil describe two ways of determining the moist and dry densities and unit weights of intact, disturbed, remolded, and reconstituted soil specimens. The method A covers the procedure for measuring the volume of wax coated specimens by determining the quantity of water displaced, and the method B covers the procedure by means of the direct measurement of the dimensions and mass of a specimen. (ASTM D7263-21 2021).

1. Stove
2. Waxe
3. Blade
4. Balance
5. Sample

Figure 301. Materials to perform laboratory determination of density

Figure 302. Process to perform laboratory determination of density (Method A)

- **Consolidaded Undrained Triaxial Test**

This test method covers the determination of strength and stress-strain relationships of cylindric specimens of either an intact, reconstituted, or remolded saturated cohesive soil. (ASTM D4767-11 2020). This method provides the calculation of total and effective stresses and axial compression by measurement of axial deformation, axial load, and pore pressure. With this test we can determine the strength envelopes to obtain shear parameters of soil.

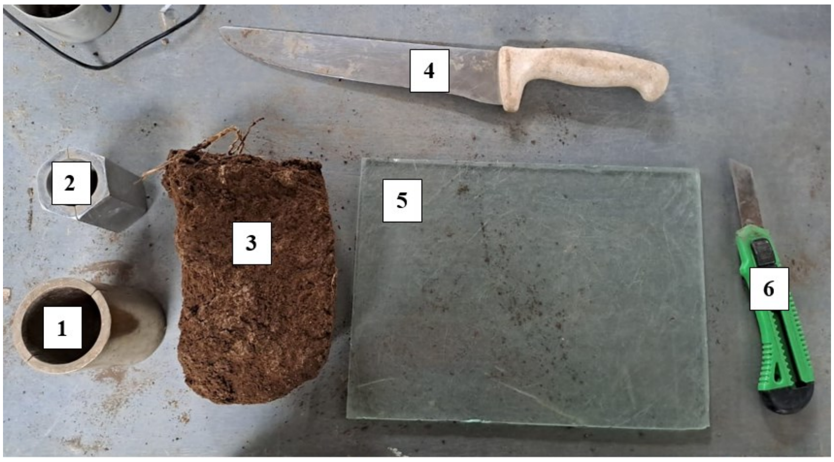

1. 50mm diameter mold
2. 35mm diameter mold
3. Unaltered sample
4. Knife
5. Glass plate
6. Stiletto

Figure 303. Materials to perform a cylindrical specimen

(a) (b)

Figure 304. (a) Process to perform a cylindrical unaltered specimen, (b) Sample after testing.

- **Oedometer Test**

These test methods cover the determination of magnitude and rate of consolidation of soil, which is restrained laterally and drained axially while subjected to incrementally applied controlled-stress loading. (ASTM 2435/D2435M-11 2020). Method A is performed with constant load increment duration of 24h and covers the determination of compression curve of the specimen. The method B measure time-deformation readings with successive loads are applied after 100% primary consolidation is reached, this method provides the compression curve with explicit data of secondary compression. (ASTM 2435/D2435M-11 2020).

Figure 305. Consolidation chamber

Figure 306. Consolidation test

APPENDIX B – Resonant Column Tests

B.1. Dry Samples

Zone A

AREA SOIL MECHANICS AND GEOTECHNICS

Resonant Column Test

Borehole:	PCQ0008	**Type of sample:**	Remolded
Zone:	A	**Stratum:**	1
Depth (m):	2,00-3,00	**Number of test:**	2

Dimensions and properties of sample

Height:	118.84	mm	σ_3 **:**	46.00	kPa
Diameter:	58.83	mm	**Saturated unit weight:**	17.69	kN/m^3
Initial wet weight:	596.72	g	**Dry unit weight:**	17.30	kN/m^3
Dry weight:	569.66	g	**Gs:**	2.60	-
Wet unit weight:	18.12	kN/m^3	**e:**	0.992	-
Initial water content:	4.75	%	**n:**	49.80	%
Final water content:	14.29	%	**S:**	12.45	%
PI:	11	%	w_{sat}**:**	4.75	%

Results

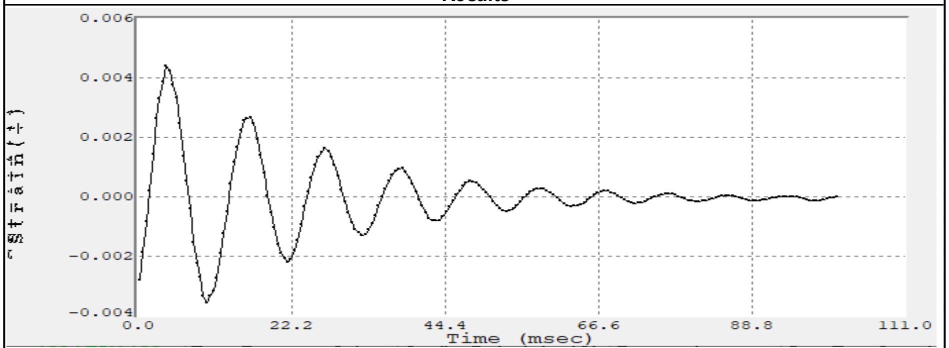

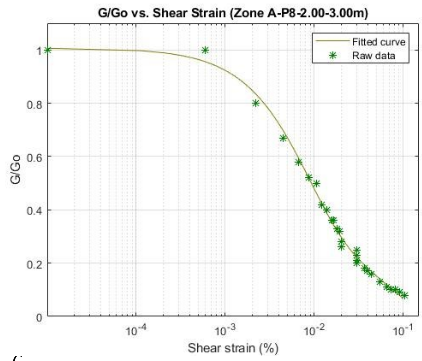

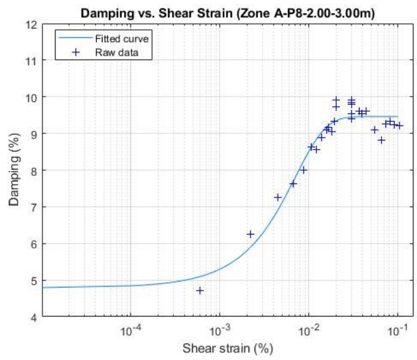

$$\frac{G}{Go} = 0{,}6765 * \exp(-123{,}6 * x) + 0{,}3304 * \exp(-15{,}72 * x)$$

$$D = 9{,}693/(1 + \exp(-217{,}2 * x) + 0{,}02455)$$

Shear Modulus vs. Shear Strain

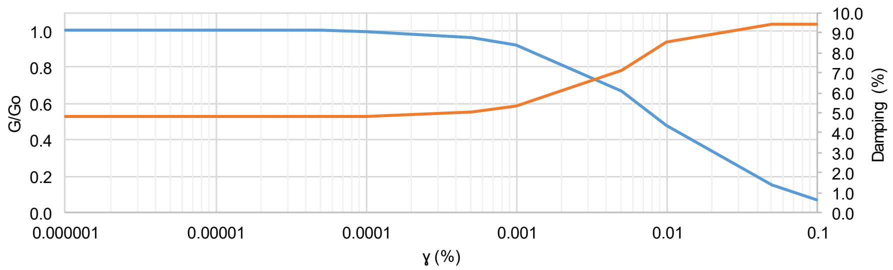

General observations: To obtain the points it is required to perform an iterative process. For each torque valve applied to the specimen, the highest frequency must be searched in different fequency ranges. This process should be excecuted by increasing the applied torque valves until the required deformation is reached.

AREA SOIL MECHANICS AND GEOTECHNICS

Resonant Column Test

Borehole:	PCQ0002	**Type of sample:**	Unaltered
Zone:	A	**Stratum:**	2
Depth (m):	11,00-12,00	**Number of test:**	1

Dimensions and properties of sample

Height:	126.04	mm	**σ_3 :**	112.00	kPa
Diameter:	60.31	mm	**Saturated unit weight:**	17.32	kN/m^3
Initial wet weight:	554.79	g	**Dry unit weight:**	14.53	kN/m^3
Dry weight:	533.20	g	**Gs:**	2.60	-
Wet unit weight:	15.12	kN/m^3	**e:**	1.091	-
Initial water content:	4.05	%	**n:**	52.18	%
Final water content:	4.05	%	**S:**	9.65	%
PI:	9	%	**w_{sat}:**	4.05	%

Results

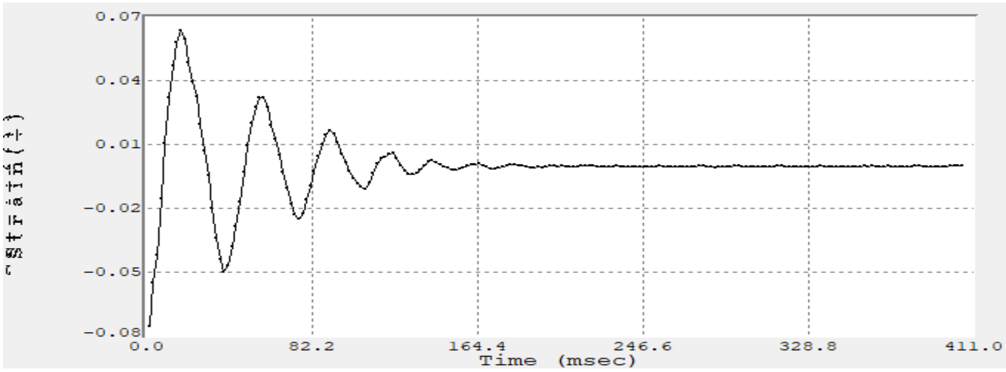

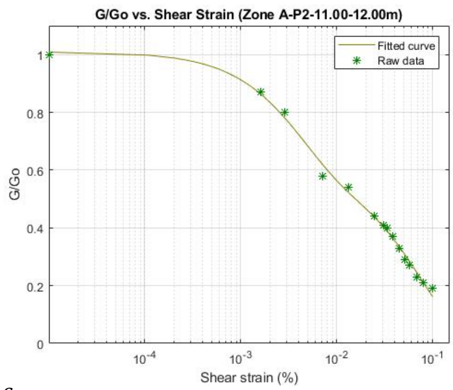

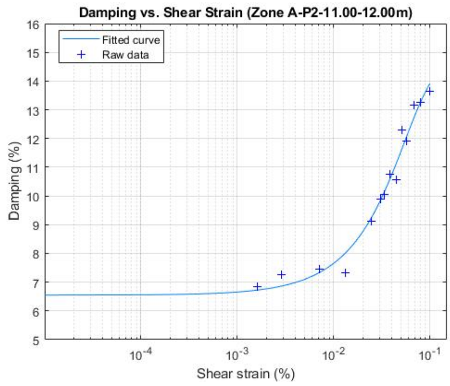

$$\frac{G}{Go} = 0{,}405 * \exp(-248{,}4 * x) + 0{,}6046 * \exp(-13{,}2 * x)$$

$$D = 11.76/(1 + \exp(-30{,}09 * x) - 0{,}2043)$$

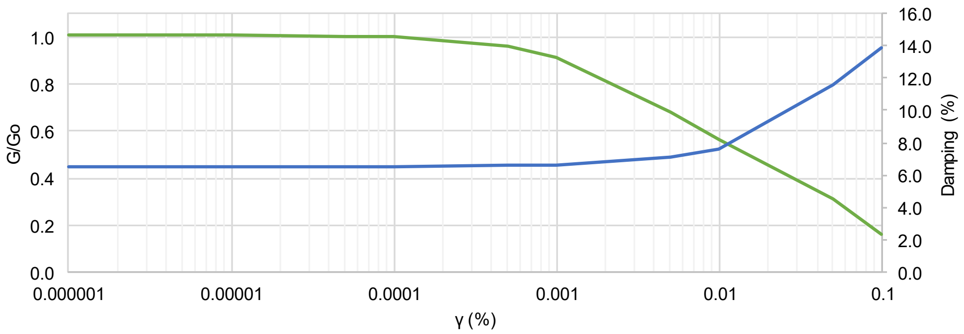

General observations: To obtain the points it is required to perform an iterative process. For each torque valve applied to the specimen, the highest frequency must be searched in different fequency ranges. This process should be excecuted by increasing the applied torque valves until the required deformation is reached.

AREA SOIL MECHANICS AND GEOTECHNICS

Resonant Column Test

Borehole:	PCQ0002	**Type of sample:**	Unaltered
Zone:	A	**Stratum:**	3
Depth (m):	12,00-13,00	**Number of test:**	1

Dimensions and properties of sample

Height:	121.34	mm	**σ_3 :**	130.00	kPa
Diameter:	60.18	mm	**Saturated unit weight:**	16.92	kN/m^3
Initial wet weight:	504.28	g	**Dry unit weight:**	13.71	kN/m^3
Dry weight:	482.56	g	**Gs:**	2.60	-
Wet unit weight:	14.33	kN/m^3	**e:**	1.208	-
Initial water content:	4.50	%	**n:**	54.71	%
Final water content:	4.50	%	**S:**	9.69	%
PI:	6	%	**w_{sat}:**	4.50	%

Results

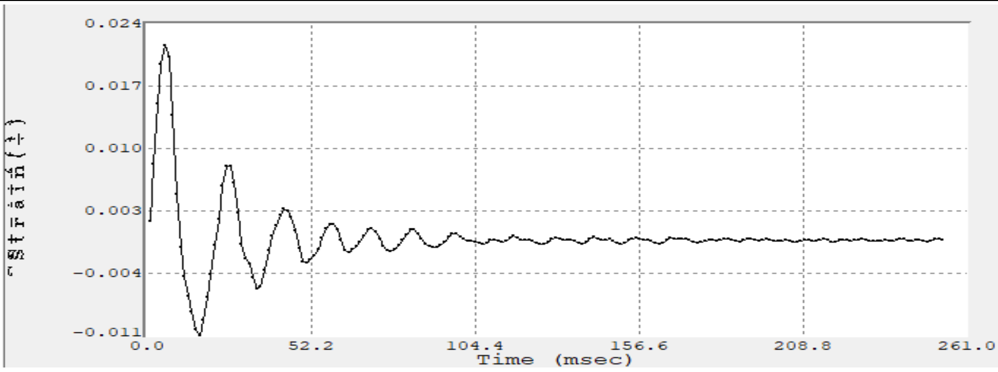

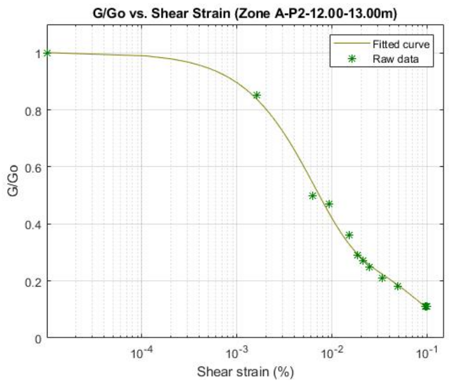

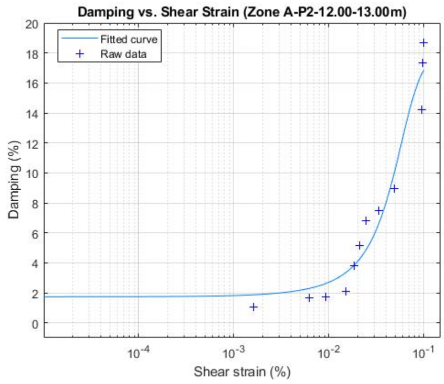

$\frac{G}{Go} = 0{,}6779 * \exp(-165{,}2 * x) + 0{,}3241 * \exp(-11{,}41 * x)$ $\quad D = 1{,}92/(1 + \exp(-50{,}59 * x) - 0{,}8924)$

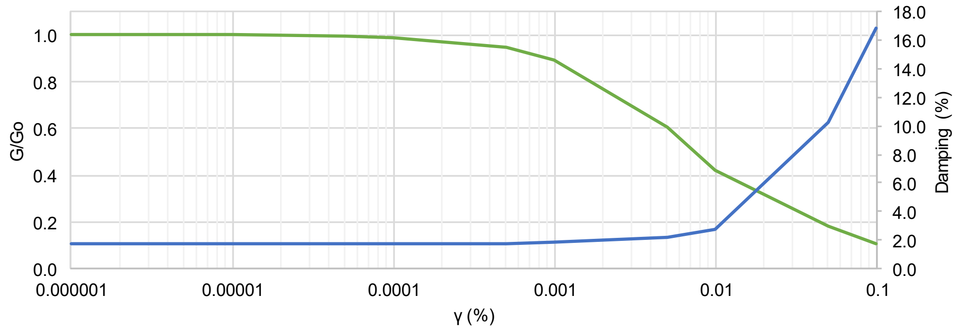

General observations: To obtain the points it is required to perform an iterative process. For each torque valve applied to the specimen, the highest frequency must be searched in different fequency ranges. This process should be excecuted by increasing the applied torque valves until the required deformation is reached.

AREA SOIL MECHANICS AND GEOTECHNICS

Resonant Column Test

Borehole:	PCQ0002	**Type of sample:**	Unaltered
Zone:	A	**Stratum:**	4
Depth (m):	17,00-18,00	**Number of test:**	2

Dimensions and properties of sample

Height:	119.49	mm	**σ_3 :**	182.00	kPa
Diameter:	60.64	mm	**Saturated unit weight:**	16.52	kN/m^3
Initial wet weight:	524.46	g	**Dry unit weight:**	14.32	kN/m^3
Dry weight:	503.71	g	**Gs:**	2.60	-
Wet unit weight:	14.91	kN/m^3	**e:**	1.340	-
Initial water content:	4.12	%	**n:**	57.26	%
Final water content:	4.12	%	**S:**	7.99	%
PI:	3	%	**w_{sat}:**	4.12	%

Results

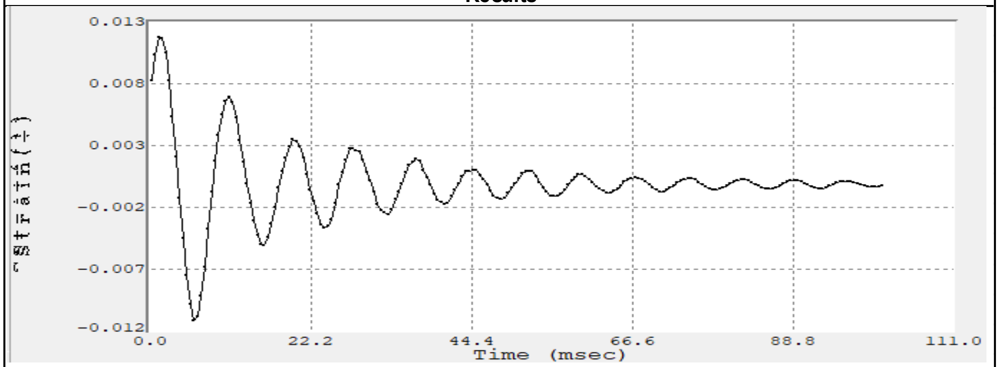

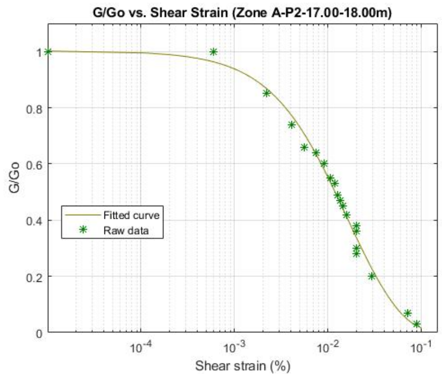

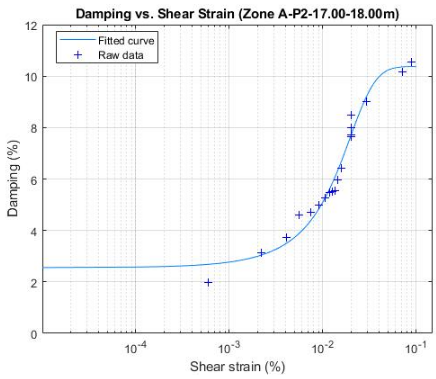

$$\frac{G}{Go} = 0{,}3496 * \exp(-123{,}2 * x) + 0{,}6528 * \exp(-37{,}15 * x) \quad D = 3{,}392/(1 + exp(-108{,}2 * x) - 0{,}673)$$

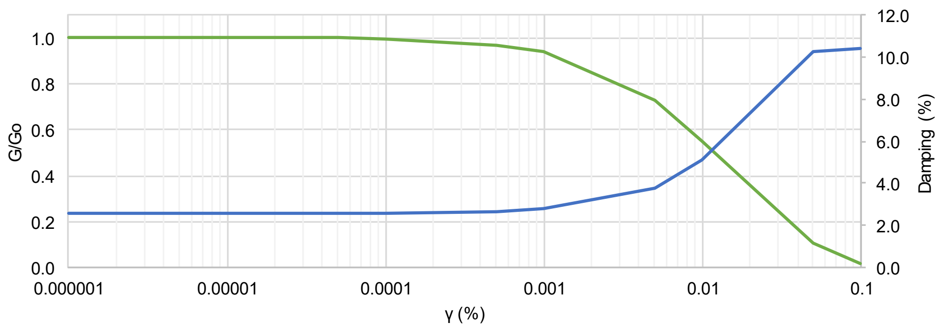

General observations: To obtain the points it is required to perform an iterative process. For each torque valve applied to the specimen, the highest frequency must be searched in different fequency ranges. This process should be excecuted by increasing the applied torque valves until the required deformation is reached.

Zone B

AREA SOIL MECHANICS AND GEOTECHNICS

Resonant Column Test

Borehole:	PCQ0004	**Type of sample:**	Unaltered
Zone:	B	**Stratum:**	1
Depth (m):	3,00-4,00	**Number of test:**	2

Dimensions and properties of sample

Height:	113.16	mm	**σ_3 :**	112.00	kPa
Diameter:	61.53	mm	**Saturated unit weight:**	12.20	kN/m^3
Initial wet weight:	446.04	g	**Dry unit weight:**	12.43	kN/m^3
Dry weight:	426.38	g	**Gs:**	2.60	-
Wet unit weight:	13.00	kN/m^3	**e:**	5.562	-
Initial water content:	4.61	%	**n:**	84.76	%
Final water content:	4.61	%	**S:**	2.15	%
PI:	64	%	**w_{sat}:**	4.61	%

Results

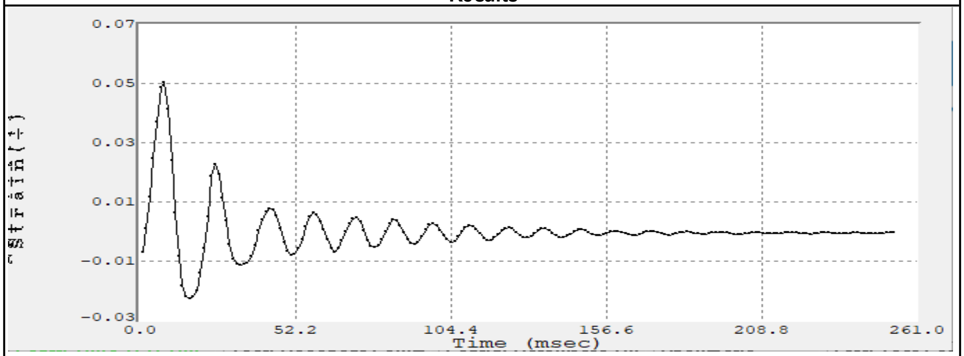

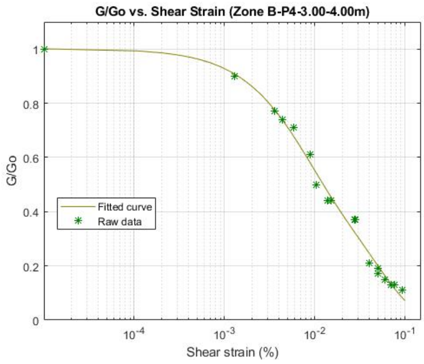

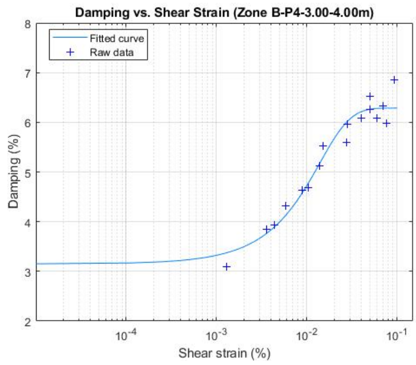

$\frac{G}{Go} = 0{,}4406 * \exp(-153 * x) + 0{,}5611 * \exp(-20{,}65 * x)$ $\quad D = 6{,}312/(1+\exp(-110{,}3*x)+0{,}003928)$

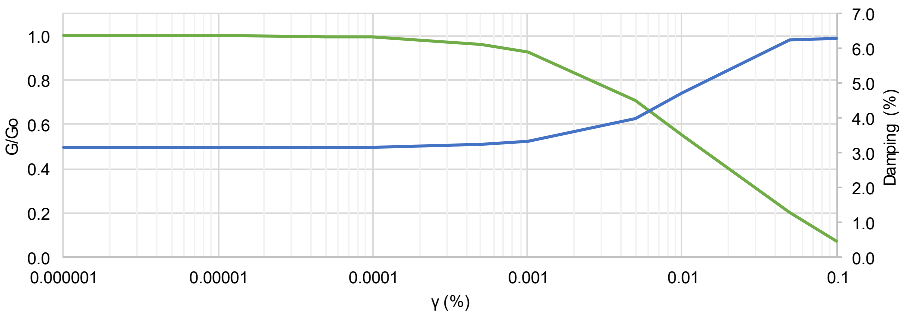

General observations: To obtain the points it is required to perform an iterative process. For each torque valve applied to the specimen, the highest frequency must be searched in different fequency ranges. This process should be excecuted by increasing the applied torque valves until the required deformation is reached.

AREA SOIL MECHANICS AND GEOTECHNICS

Resonant Column Test

Borehole:	PCQ0004	**Type of sample:**	Unaltered
Zone:	B	**Stratum:**	2
Depth (m):	16,00-17,00	**Number of test:**	1

Dimensions and properties of sample

Height:	112.01	mm	**σ_3 :**	141.00	kPa
Diameter:	59.99	mm	**Saturated unit weight:**	16.21	kN/m^3
Initial wet weight:	394.49	g	**Dry unit weight:**	11.72	kN/m^3
Dry weight:	378.15	g	**Gs:**	2.60	-
Wet unit weight:	12.22	kN/m^3	**e:**	1.452	-
Initial water content:	4.32	%	**n:**	59.22	%
Final water content:	4.32	%	**S:**	7.74	%
PI:	39	%	**w_{sat}:**	4.32	%

Results

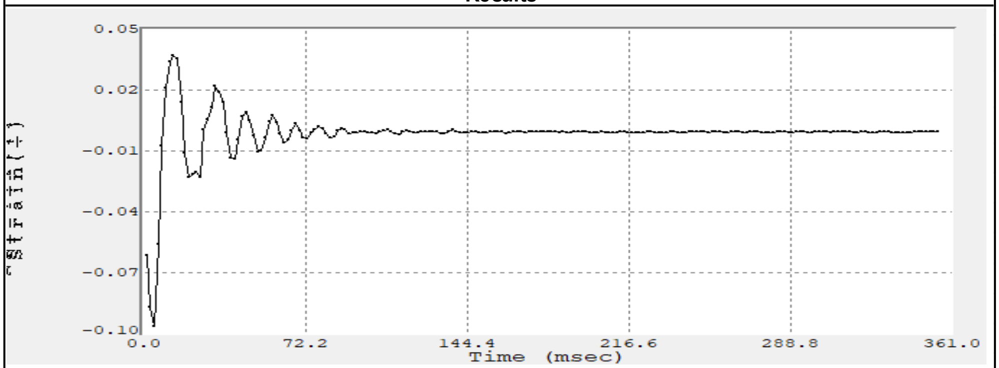

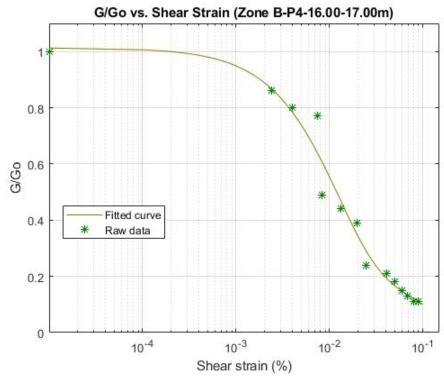

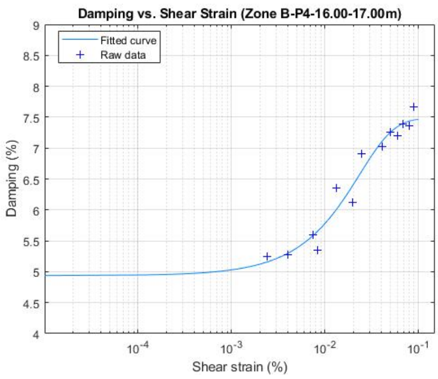

$$\frac{G}{Go} = 0{,}7732 * \exp(-83{,}95 * x) + 0{,}2401 * \exp(-8{,}76 * x) \qquad D = 14{,}52/(1 + \exp(-56{,}09 * x) + 0{,}9419)$$

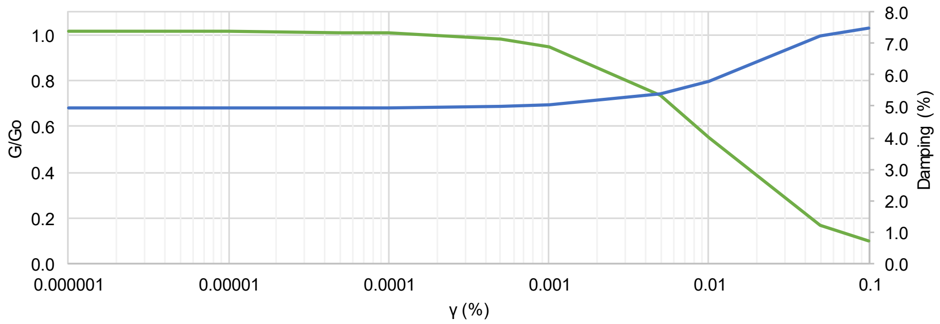

General observations: To obtain the points it is required to perform an iterative process. For each torque valve applied to the specimen, the highest frequency must be searched in different fequency ranges. This process should be excecuted by increasing the applied torque valves until the required deformation is reached.

AREA SOIL MECHANICS AND GEOTECHNICS

Resonant Column Test

Borehole:	PCQ0004	**Type of sample:**	Unaltered
Zone:	B	**Stratum:**	3
Depth (m):	20,00-21,00	**Number of test:**	1

Dimensions and properties of sample

Height:	121.10	mm	**σ_3 :**	190.00	kPa
Diameter:	59.93	mm	**Saturated unit weight:**	13.74	kN/m^3
Initial wet weight:	511.47	g	**Dry unit weight:**	14.26	kN/m^3
Dry weight:	496.33	g	**Gs:**	2.60	-
Wet unit weight:	14.69	kN/m^3	**e:**	2.993	-
Initial water content:	3.05	%	**n:**	74.96	%
Final water content:	3.05	%	**S:**	2.65	%
PI:	44	%	**w_{sat}:**	3.05	%

Results

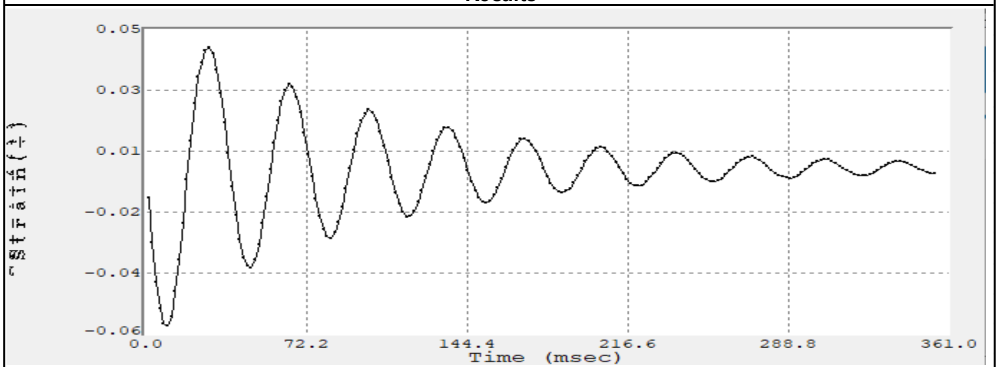

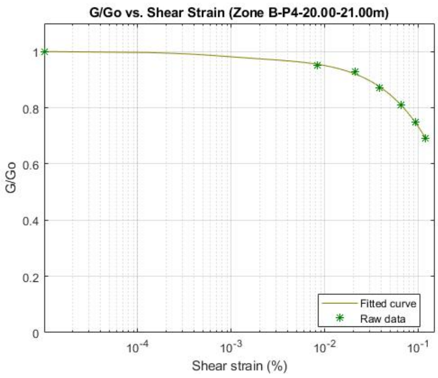

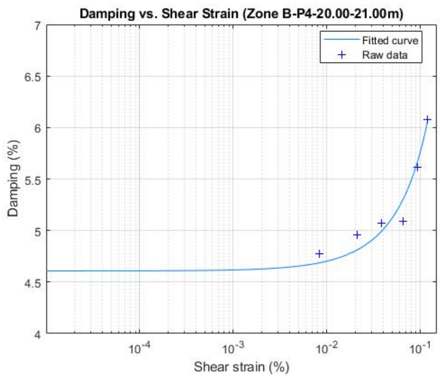

$\frac{G}{Go} = 0{,}9781 * \exp(-2{,}902 * x) + 0{,}02225 * \exp(-1304 * x)$ $D = 14{,}52/(1+\exp(-56{,}09*x)+0{,}9419)$

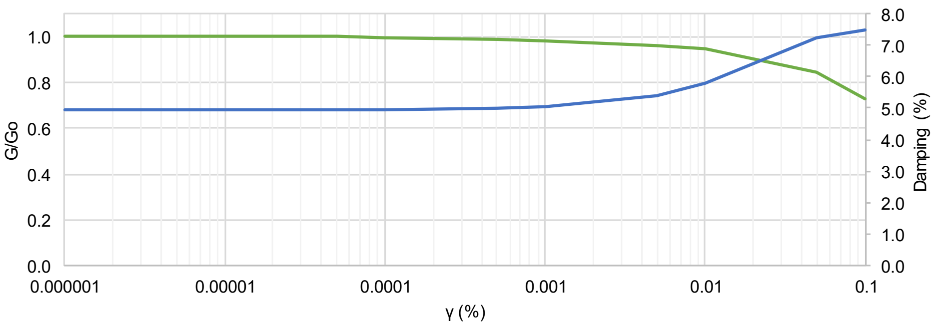

General observations: To obtain the points it is required to perform an iterative process. For each torque valve applied to the specimen, the highest frequency must be searched in different fequency ranges. This process should be excecuted by increasing the applied torque valves until the required deformation is reached.

AREA SOIL MECHANICS AND GEOTECHNICS

Resonant Column Test

Borehole:	PCQ0004	**Type of sample:**	Remolded
Zone:	B	**Stratum:**	4
Depth (m):	25,00-26,00	**Number of test:**	2

Dimensions and properties of sample

Height:	119.51	mm	**σ_3 :**	237.00	kPa
Diameter:	59.23	mm	**Saturated unit weight:**	15.74	kN/m^3
Initial wet weight:	540.62	g	**Dry unit weight:**	13.68	kN/m^3
Dry weight:	459.07	g	**Gs:**	2.60	-
Wet unit weight:	16.10	kN/m^3	**e:**	1.646	-
Initial water content:	17.76	%	**n:**	62.21	%
Final water content:	22.51	%	**S:**	28.06	%
PI:	11	%	**w_{sat}:**	17.76	%

Results

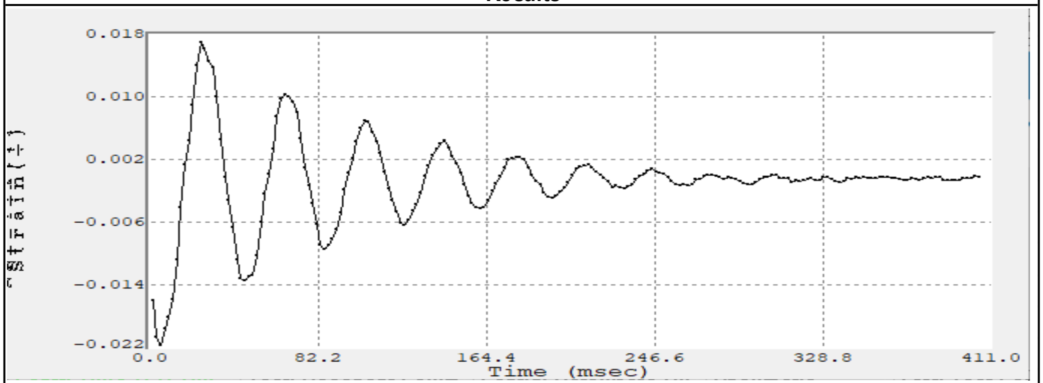

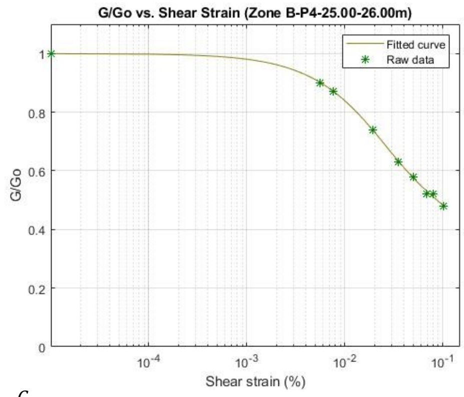

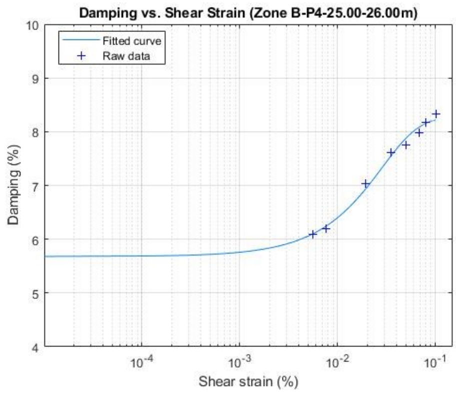

$$\frac{G}{Go} = 0{,}4023 * \exp(-45{,}82 * x) + 0{,}5974 * \exp(-2{,}208 * x)$$

$$D = 18{,}18/(1 + \exp(-44{,}81 * x) + 1{,}201$$

Shear Modulus vs. Shear Strain

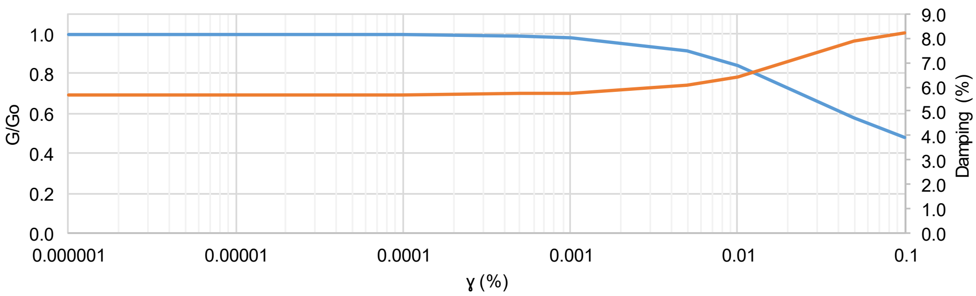

General observations: To obtain the points it is required to perform an iterative process. For each torque valve applied to the specimen, the highest frequency must be searched in different fequency ranges. This process should be excecuted by increasing the applied torque valves until the required deformation is reached.

Zone C

AREA SOIL MECHANICS AND GEOTECHNICS

Resonant Column Test

Borehole:	PCQ0009	**Type of sample:**	Remolded
Zone:	C	**Stratum:**	1
Depth (m):	1,00-2,00	**Number of test:**	1

Dimensions and properties of sample

Height:	120.20	mm	**σ_3 :**	30.00	kPa
Diameter:	58.77	mm	**Saturated unit weight:**	15.00	kN/m^3
Initial wet weight:	566.77	g	**Dry unit weight:**	15.28	kN/m^3
Dry weight:	507.77	g	**Gs:**	2.60	-
Wet unit weight:	17.05	kN/m^3	**e:**	2.023	-
Initial water content:	11.62	%	**n:**	66.92	%
Final water content:	25.64	%	**S:**	14.93	%
PI:	23	%	**w_{sat}:**	11.62	%

Results

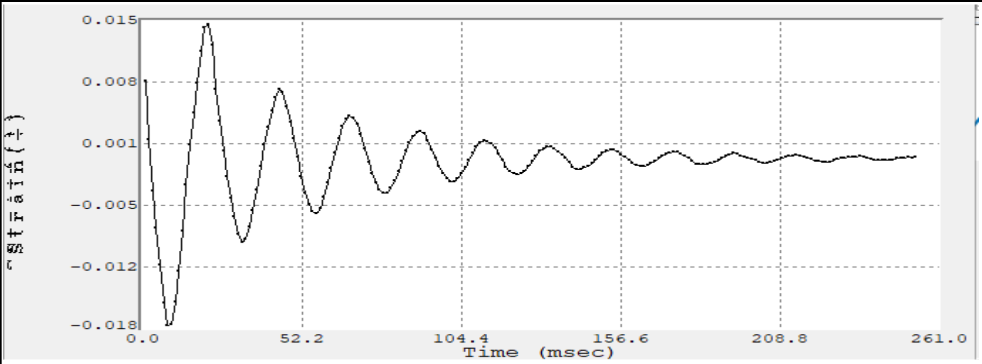

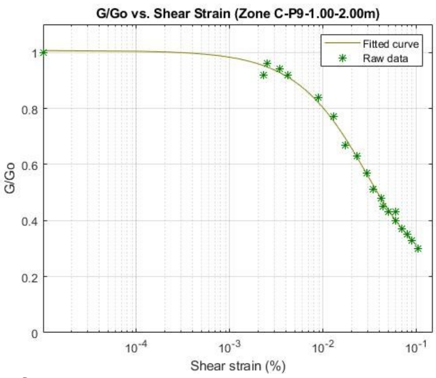

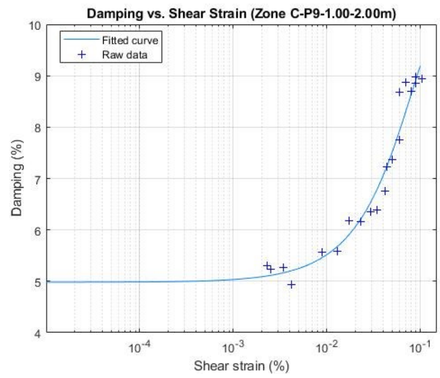

$$\frac{G}{Go} = 0{,}5833 * \exp(-39{,}52 * x) + 0{,}4233 * \exp(-3{,}385 * x) \qquad D = 9{,}471/(1 + \exp(-20{,}51 * x) + 0{,}0983$$

Shear Modulus vs. Shear Strain

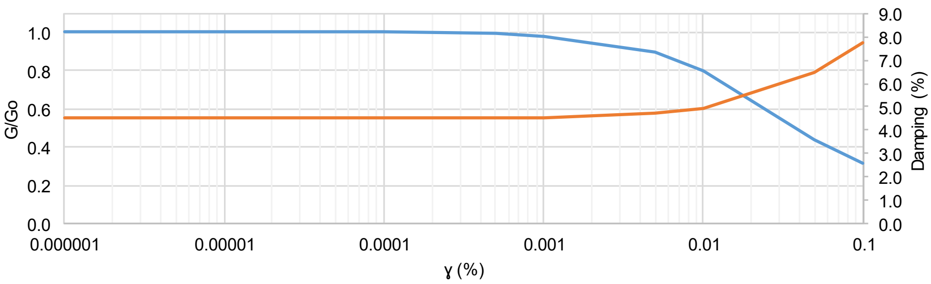

General observations: To obtain the points it is required to perform an iterative process. For each torque valve applied to the specimen, the highest frequency must be searched in different fequency ranges. This process should be excecuted by increasing the applied torque valves until the required deformation is reached.

AREA SOIL MECHANICS AND GEOTECHNICS

Resonant Column Test

Borehole:	PCQ0005	**Type of sample:**	Unaltered
Zone:	C	**Stratum:**	2
Depth (m):	6,00-7,00	**Number of test:**	1

Dimensions and properties of sample

Height:	119.14	mm	**σ_3 :**	63.00	kPa
Diameter:	60.27	mm	**Saturated unit weight:**	17.56	kN/m^3
Initial wet weight:	541.86	g	**Dry unit weight:**	15.01	kN/m^3
Dry weight:	520.27	g	**Gs:**	2.60	-
Wet unit weight:	15.64	kN/m^3	**e:**	1.024	-
Initial water content:	4.15	%	**n:**	50.59	%
Final water content:	4.15	%	**S:**	10.54	%
PI:	16	%	**w_{sat}:**	4.15	%

Results

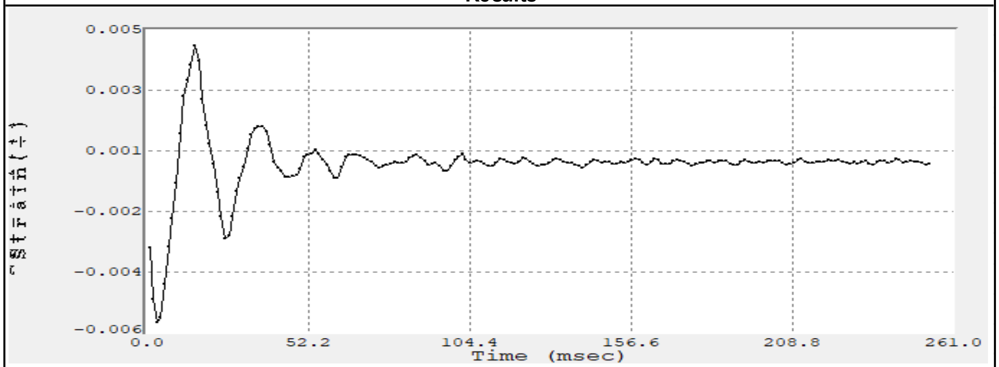

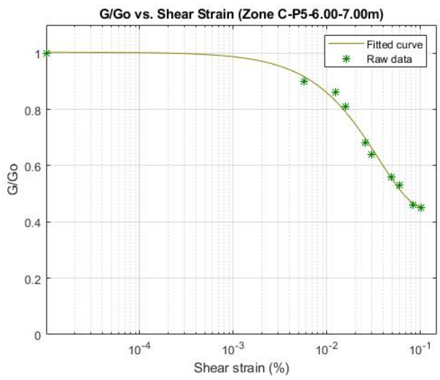

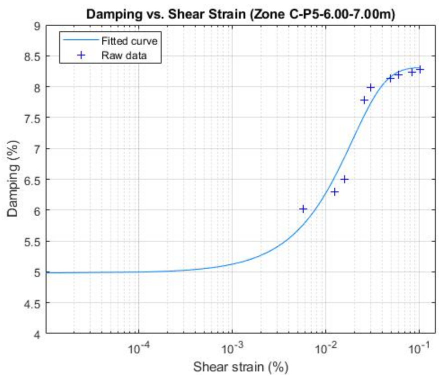

$$\frac{G}{Go} = 0{,}6819 * \exp(-25{,}02 * x) + 0{,}3214 * \exp(2{,}058 * x) \qquad D = 12{,}43/(1 + \exp(-72{,}66 * x) + 0{,}4952)$$

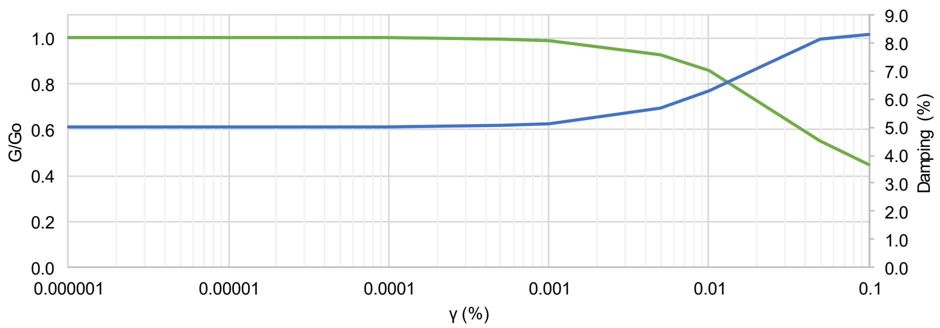

General observations: To obtain the points it is required to perform an iterative process. For each torque valve applied to the specimen, the highest frequency must be searched in different fequency ranges. This process should be excecuted by increasing the applied torque valves until the required deformation is reached.

AREA SOIL MECHANICS AND GEOTECHNICS

Resonant Column Test

Borehole:	PCQ0005	**Type of sample:**	Unaltered
Zone:	C	**Stratum:**	3
Depth (m):	7,00-8,00	**Number of test:**	1

Dimensions and properties of sample

Height:	121.07	mm	**σ_3 :**	116.00	kPa
Diameter:	61.79	mm	**Saturated unit weight:**	17.55	kN/m^3
Initial wet weight:	530.98	g	**Dry unit weight:**	13.79	kN/m^3
Dry weight:	510.21	g	**Gs:**	2.60	-
Wet unit weight:	14.35	kN/m^3	**e:**	1.027	-
Initial water content:	4.07	%	**n:**	50.67	%
Final water content:	4.07	%	**S:**	10.30	%
PI:	9	%	**w_{sat}:**	4.07	%

Results

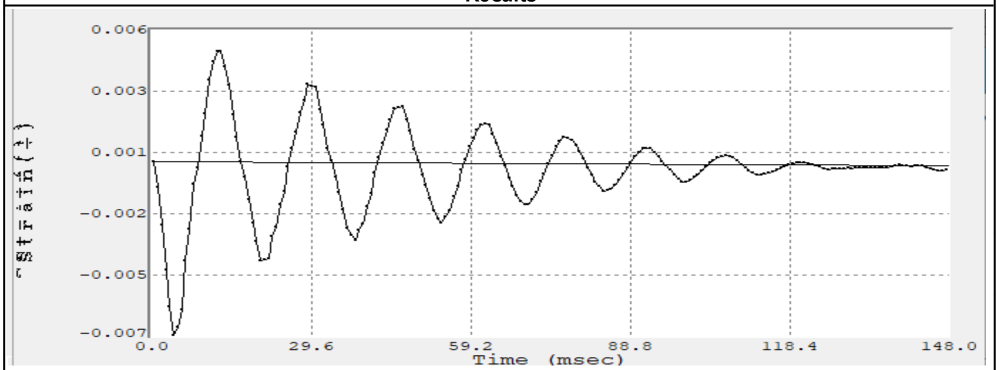

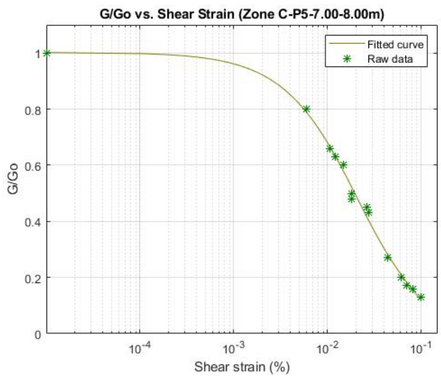

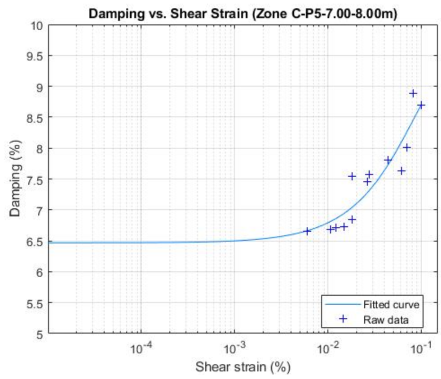

$$\frac{G}{Go} = 0{,}5501 * \exp(-65{,}82 * x) + 0{,}452 * \exp(-13{,}36 * x)$$

$$D = 20{,}24/(1 + \exp(-16{,}35 * x) + 1{,}13)$$

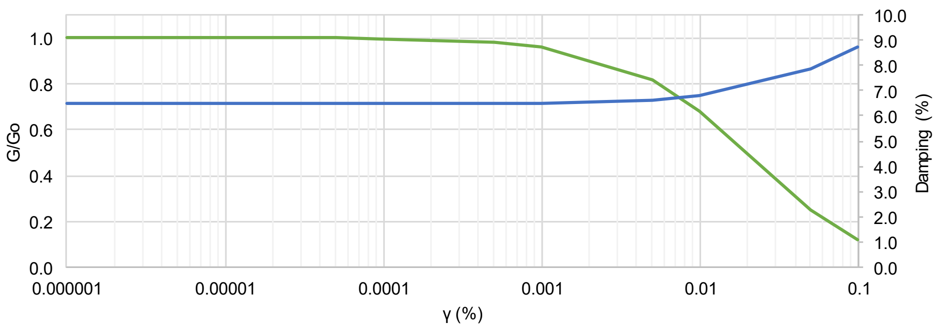

General observations: To obtain the points it is required to perform an iterative process. For each torque valve applied to the specimen, the highest frequency must be searched in different fequency ranges. This process should be excecuted by increasing the applied torque valves until the required deformation is reached.

AREA SOIL MECHANICS AND GEOTECHNICS

Resonant Column Test

Borehole:	PCQ0005	**Type of sample:**	Unaltered
Zone:	C	**Stratum:**	4
Depth (m):	12,00-13,00	**Number of test:**	1

Dimensions and properties of sample

Height:	117.45	mm	**σ_3 :**	141.00	kPa
Diameter:	60.59	mm	**Saturated unit weight:**	16.33	kN/m^3
Initial wet weight:	455.91	g	**Dry unit weight:**	12.68	kN/m^3
Dry weight:	437.79	g	**Gs:**	2.60	-
Wet unit weight:	13.21	kN/m^3	**e:**	1.409	-
Initial water content:	4.14	%	**n:**	58.49	%
Final water content:	4.14	%	**S:**	7.64	%
PI:	13	%	**w_{sat}:**	4.14	%

Results

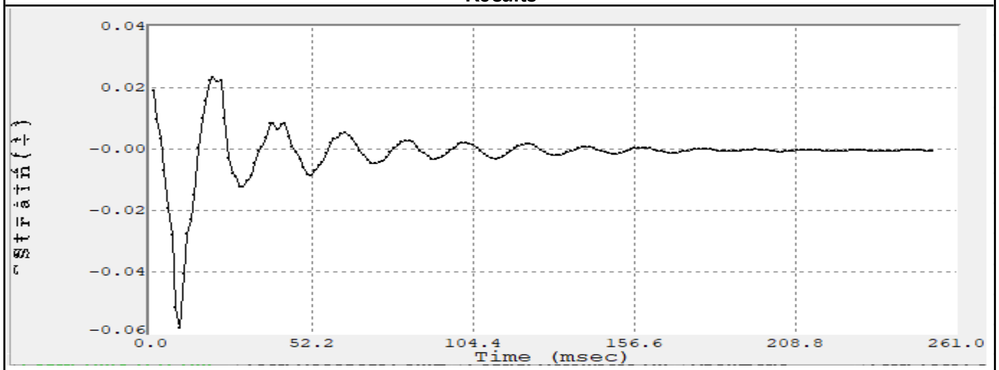

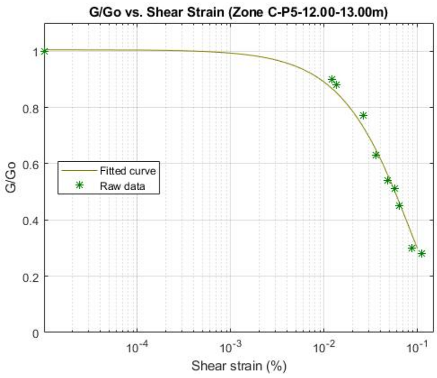

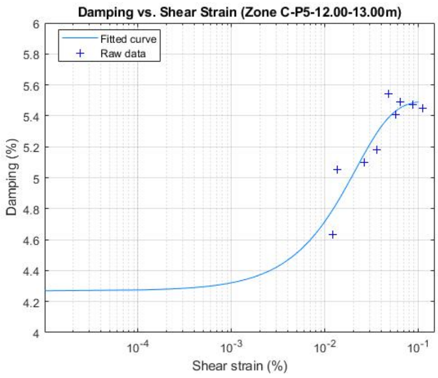

$$\frac{G}{Go} = (1{,}334e - 16) * \exp(293 * x) + 1{,}005 * \exp(-12{,}17 * x) \qquad D = 19{,}13/(1 + \exp(-55{,}61 * x) + 2{,}48)$$

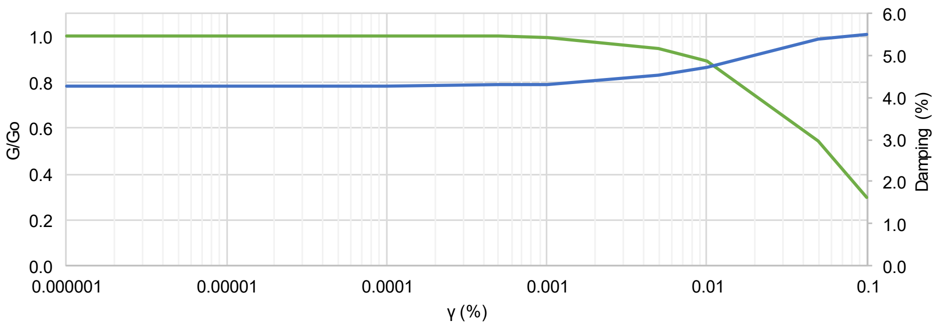

General observations: To obtain the points it is required to perform an iterative process. For each torque valve applied to the specimen, the highest frequency must be searched in different fequency ranges. This process should be excecuted by increasing the applied torque valves until the required deformation is reached.

Zone D

AREA SOIL MECHANICS AND GEOTECHNICS

Resonant Column Test

Borehole:	PCQ0006	**Type of sample:**	Unaltered
Zone:	D	**Stratum:**	4
Depth (m):	13,00-14,00	**Number of test:**	1

Dimensions and properties of sample

Height:	125.84	mm	**σ_3 :**	151.00	kPa
Diameter:	60.20	mm	**Saturated unit weight:**	17.30	kN/m^3
Initial wet weight:	614.81	g	**Dry unit weight:**	12.35	kN/m^3
Dry weight:	450.87	g	**Gs:**	2.60	-
Wet unit weight:	16.84	kN/m^3	**e:**	1.095	-
Initial water content:	36.36	%	**n:**	52.27	%
Final water content:	0.00	%	**S:**	86.34	%
PI:	3	%	**w_{sat}:**	36.36	%

Results

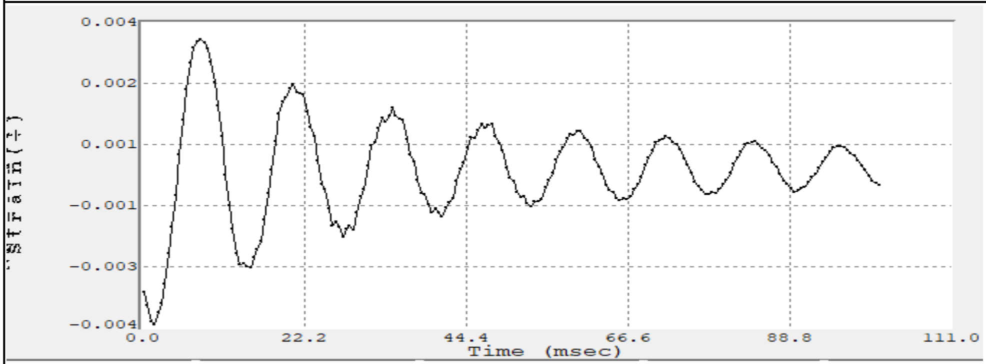

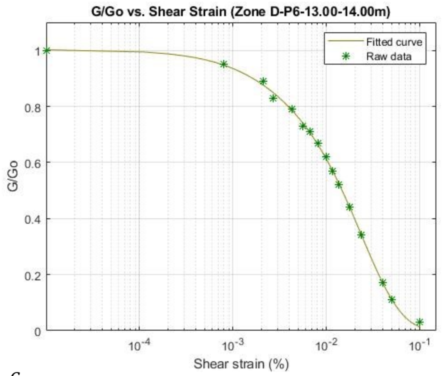

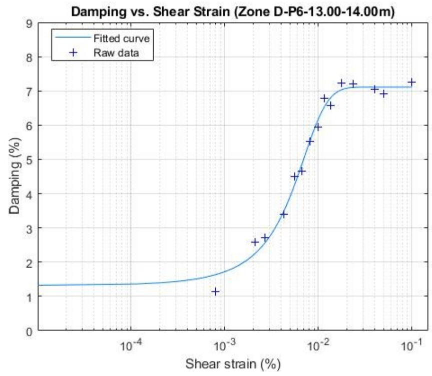

$$\frac{G}{Go} = 0{,}935 * \exp(-42{,}54 * x) + 0{,}06775 * \exp(-551{,}6 * x)$$

$$D = 1{,}622/(1 + \exp(-336{,}2 * x) - 0{,}7719)$$

Shear Modulus vs. Shear Strain

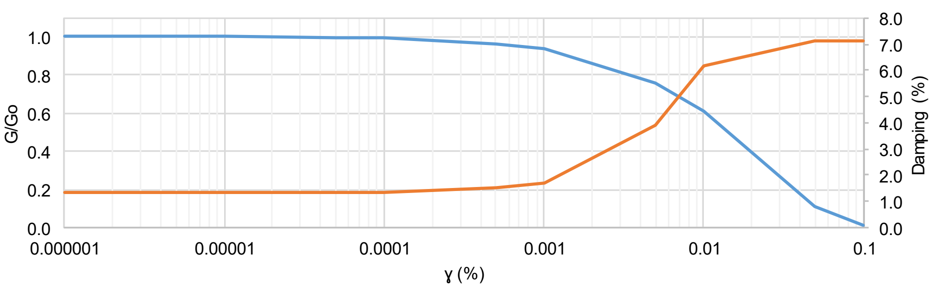

General observations: To obtain the points it is required to perform an iterative process. For each torque valve applied to the specimen, the highest frequency must be searched in different fequency ranges. This process should be excecuted by increasing the applied torque valves until the required deformation is reached.

Zone E

AREA SOIL MECHANICS AND GEOTECHNICS

Resonant Column Test

Borehole:	PCQ0013	**Type of sample:**	Unaltered
Zone:	E	**Stratum:**	3
Depth (m):	9,00-10,00	**Number of test:**	1

Dimensions and properties of sample

Height:	132.92	mm	σ_3 **:**	128.00	kPa
Diameter:	60.90	mm	**Saturated unit weight:**	18.13	kN/m^3
Initial wet weight:	639.40	g	**Dry unit weight:**	15.57	kN/m^3
Dry weight:	614.45	g	**Gs:**	2.60	-
Wet unit weight:	16.20	kN/m^3	**e:**	0.887	-
Initial water content:	4.06	%	**n:**	47.01	%
Final water content:	4.06	%	**S:**	11.90	%
PI:	4	%	w_{sat}**:**	4.06	%

Results

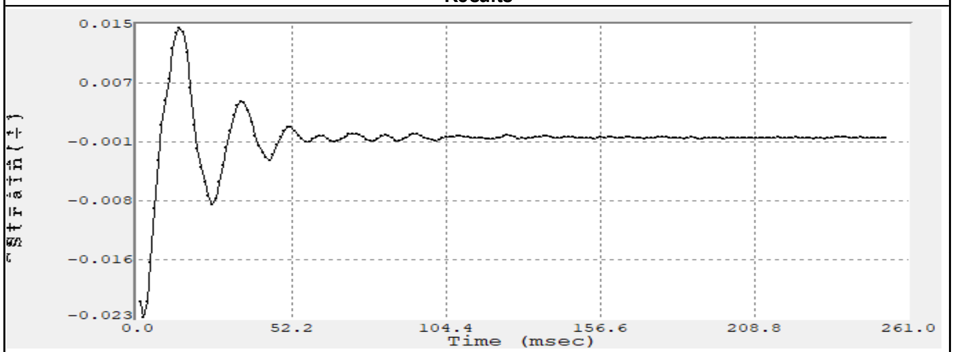

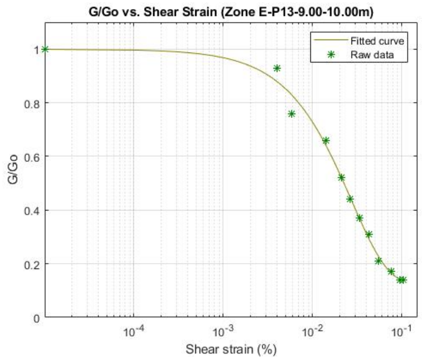

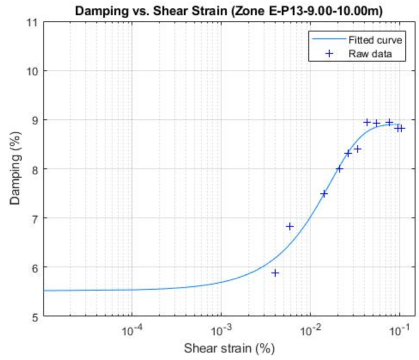

$$\frac{G}{Go} = 0{,}9242 * \exp(-35{,}3 * x) + 0{,}07521 * \exp(4{,}053 * x)$$

$$D = 14{,}53/(1 + \exp(-83{,}11 * x) + 0{,}6319)$$

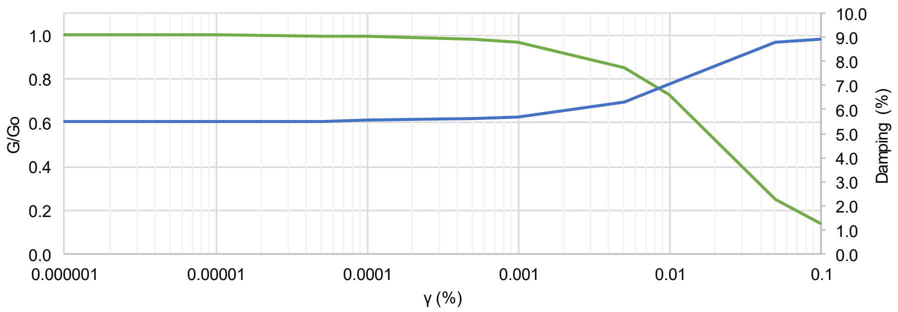

General observations: To obtain the points it is required to perform an iterative process. For each torque valve applied to the specimen, the highest frequency must be searched in different fequency ranges. This process should be excecuted by increasing the applied torque valves until the required deformation is reached.

Zone F

AREA SOIL MECHANICS AND GEOTECHNICS

Resonant Column Test

Borehole:	PCQ0012	**Type of sample:**	Remolded
Zone:	F	**Stratum:**	1
Depth (m):	5,00-6,00	**Number of test:**	1

Dimensions and properties of sample

Height:	112.54	mm	**σ_3 :**	63.00	kPa
Diameter:	58.39	mm	**Saturated unit weight:**	15.47	kN/m^3
Initial wet weight:	548.06	g	**Dry unit weight:**	12.93	kN/m^3
Dry weight:	397.08	g	**Gs:**	2.60	-
Wet unit weight:	17.84	kN/m^3	**e:**	1.772	-
Initial water content:	38.02	%	**n:**	63.92	%
Final water content:	15.23	%	**S:**	55.79	%
PI:	27	%	**w_{sat}:**	38.02	%

Results

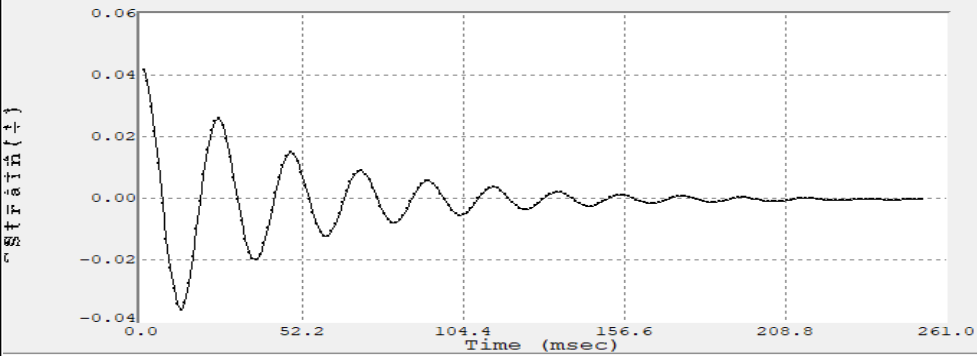

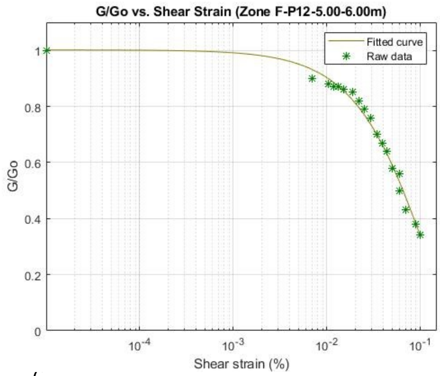

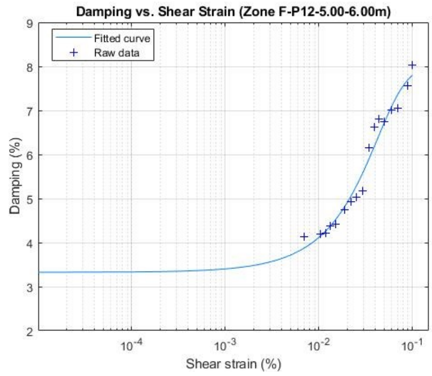

$$\frac{G}{Go} = 21{,}79 * \exp(-7{,}561 * x) - 20{,}79 * \exp(-7{,}427 * x) \qquad D = 5{,}689/(1 + \exp(-39{,}96 * x) - 0{,}2888$$

Shear Modulus vs. Shear Strain

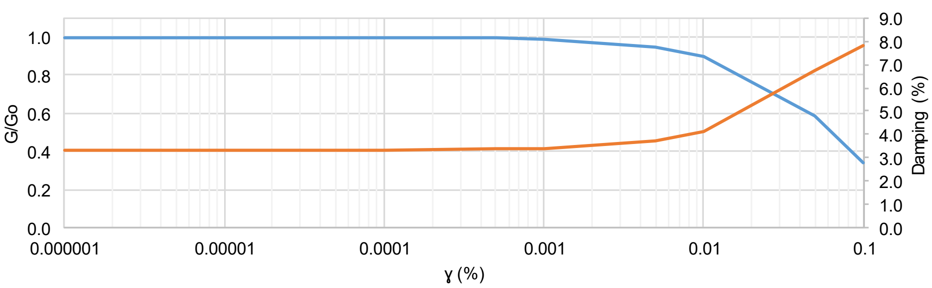

General observations: To obtain the points it is required to perform an iterative process. For each torque valve applied to the specimen, the highest frequency must be searched in different fequency ranges. This process should be excecuted by increasing the applied torque valves until the required deformation is reached.

AREA SOIL MECHANICS AND GEOTECHNICS

Resonant Column Test

Borehole:	PCQ0012	**Type of sample:**	Remolded
Zone:	F	**Stratum:**	2
Depth (m):	7,00-8,00	**Number of test:**	2

Dimensions and properties of sample

Height:	106.40	mm	**σ_3 :**	124.00	kPa
Diameter:	58.85	mm	**Saturated unit weight:**	18.58	kN/m^3
Initial wet weight:	583.15	g	**Dry unit weight:**	17.10	kN/m^3
Dry weight:	504.36	g	**Gs:**	2.60	-
Wet unit weight:	19.77	kN/m^3	**e:**	0.790	-
Initial water content:	15.62	%	**n:**	44.13	%
Final water content:	19.15	%	**S:**	51.41	%
PI:	15	%	**w_{sat}:**	15.62	%

Results

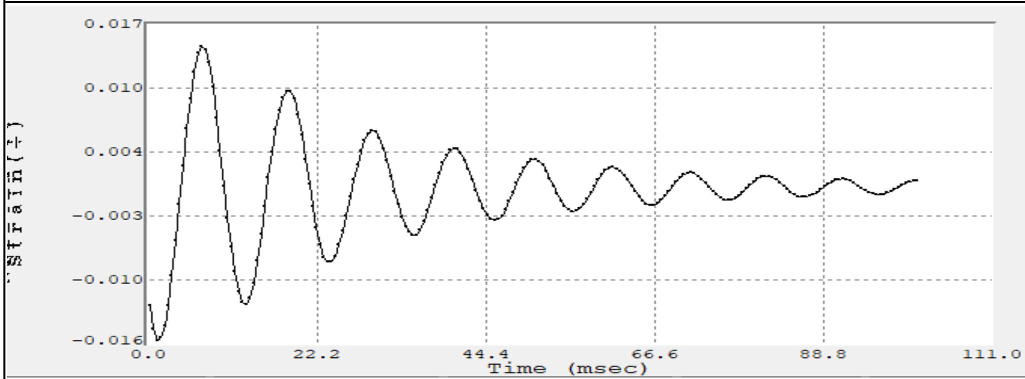

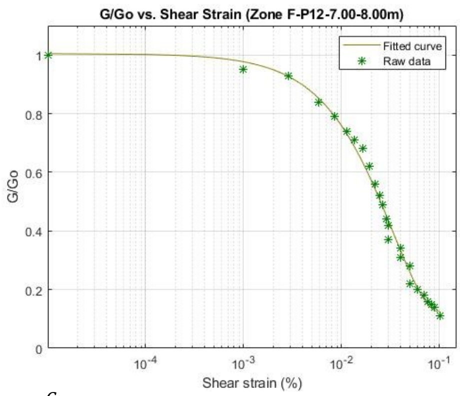

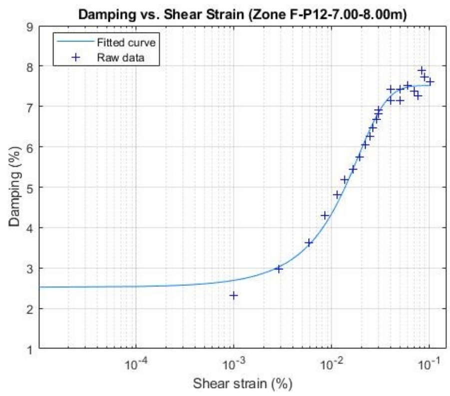

$$\frac{G}{Go} = 0{,}004552 * \exp(26{,}81 * x) + 1 * \exp(-28{,}38 * x)$$

$$D = 3{,}796/(1 + \exp(-99{,}91 * x) - 0{,}495$$

Shear Modulus vs. Shear Strain

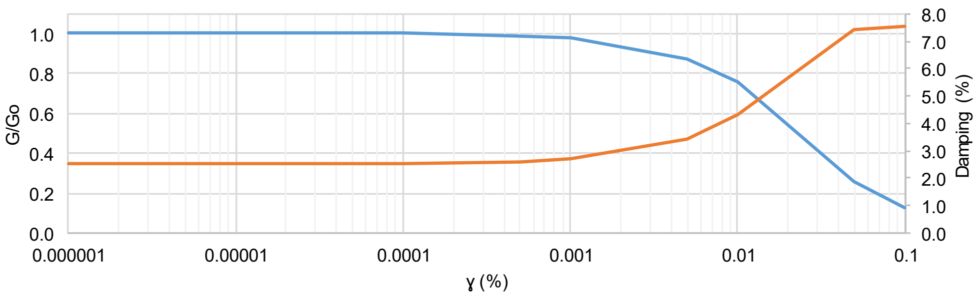

General observations: To obtain the points it is required to perform an iterative process. For each torque valve applied to the specimen, the highest frequency must be searched in different fequency ranges. This process should be excecuted by increasing the applied torque valves until the required deformation is reached.

Zone G

AREA SOIL MECHANICS AND GEOTECHNICS

Resonant Column Test

Borehole:	PCQ0015	**Type of sample:**	Unaltered
Zone:	G	**Stratum:**	4
Depth (m):	16,00-17,00	**Number of test:**	1

Dimensions and properties of sample

Height:	126.27	mm	**σ_3 :**	230.00	kPa
Diameter:	60.48	mm	**Saturated unit weight:**	18.33	kN/m^3
Initial wet weight:	602.32	g	**Dry unit weight:**	16.29	kN/m^3
Dry weight:	602.32	g	**Gs:**	2.60	-
Wet unit weight:	16.29	kN/m^3	**e:**	0.843	-
Initial water content:	0.00	%	**n:**	45.74	%
Final water content:	0.00	%	**S:**	0.00	%
PI:	3	%	**w_{sat}:**	0.00	%

Results

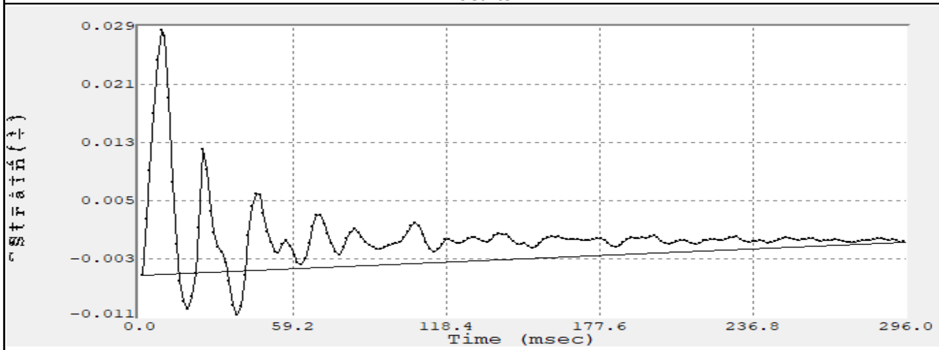

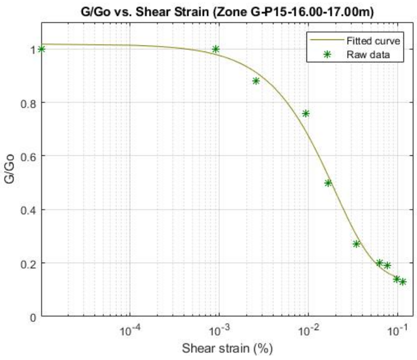

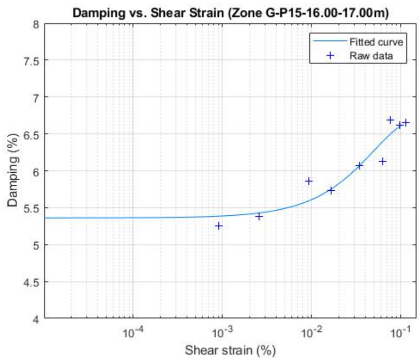

$$\frac{G}{Go} = 0{,}8469 * \exp(-51{,}76 * x) + 0{,}1713 * \exp(-1{,}909 * x) \qquad D = 25{,}72/(1 + \exp(-23{,}89 * x) + 2{,}798)$$

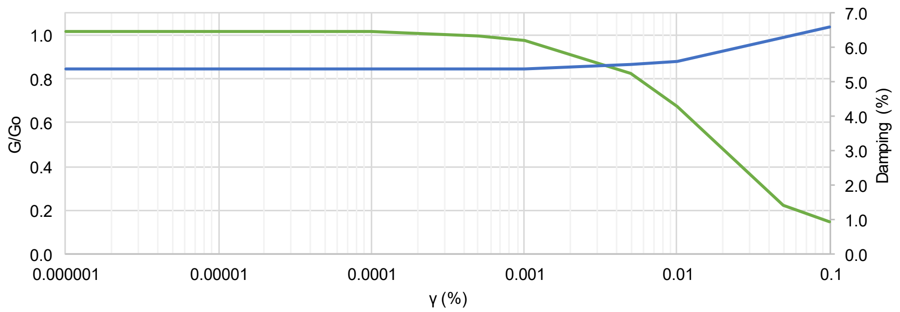

General observations: To obtain the points it is required to perform an iterative process. For each torque valve applied to the specimen, the highest frequency must be searched in different fequency ranges. This process should be excecuted by increasing the applied torque valves until the required deformation is reached.

AREA SOIL MECHANICS AND GEOTECHNICS

Resonant Column Test

Borehole:	PCQ0020	**Type of sample:**	Remolded
Zone:	G	**Stratum:**	5
Depth (m):	26,00-27,00	**Number of test:**	1

Dimensions and properties of sample

Height:	118.36	mm	**σ_3 :**	275.00	kPa
Diameter:	59.41	mm	**Saturated unit weight:**	18.58	kN/m^3
Initial wet weight:	566.04	g	**Dry unit weight:**	15.94	kN/m^3
Dry weight:	533.05	g	**Gs:**	2.60	-
Wet unit weight:	16.92	kN/m^3	**e:**	0.790	-
Initial water content:	6.19	%	**n:**	44.13	%
Final water content:	17.02	%	**S:**	20.37	%
PI:	3	%	**w_{sat}:**	6.19	%

Results

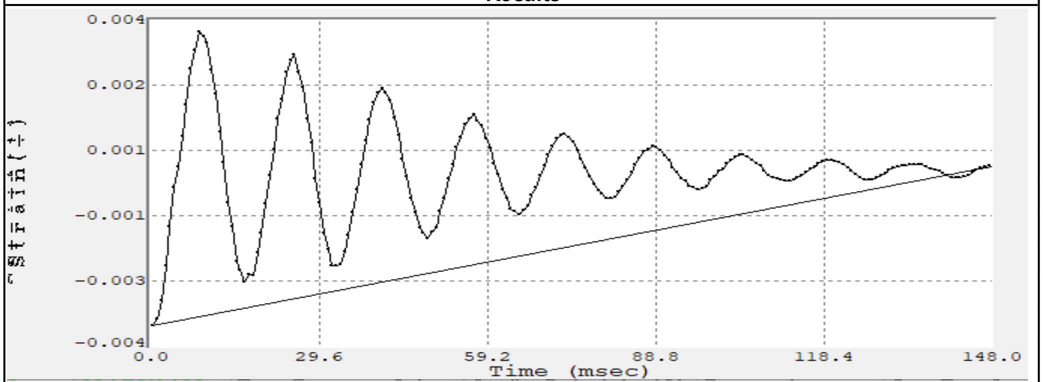

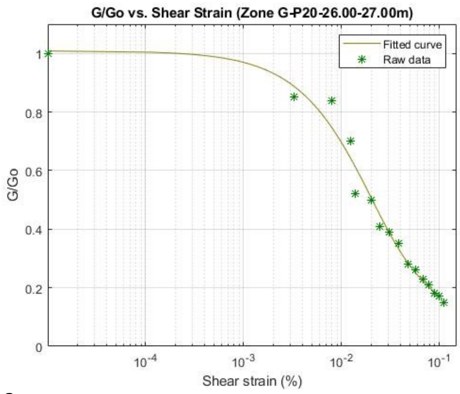

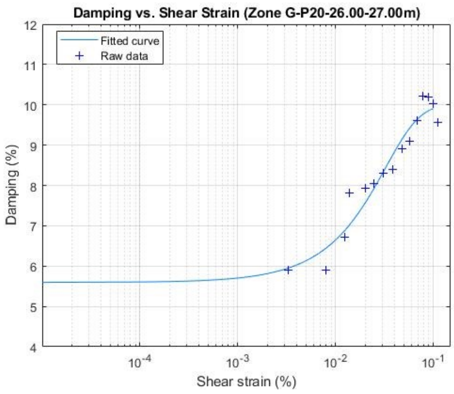

$$\frac{G}{Go} = 0{,}3228 * \exp(-6{,}533 * x) + 0{,}6858 * \exp(-55{,}57 * x)$$

$$D = 12{,}7/(1 + \exp(-44{,}62 * x) + 0{,}2703$$

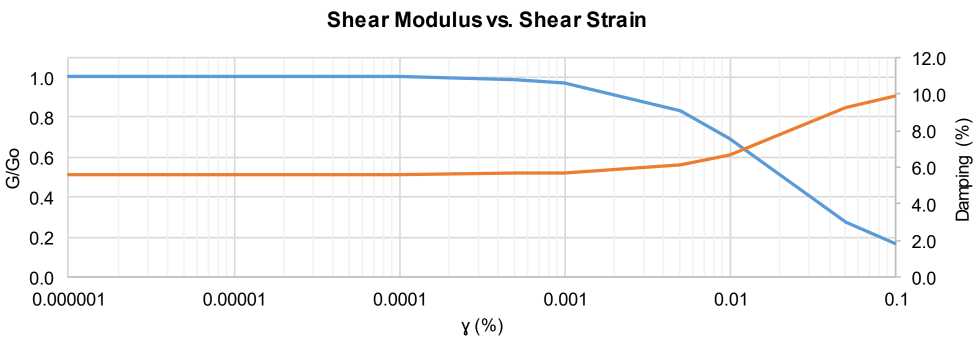

General observations: To obtain the points it is required to perform an iterative process. For each torque valve applied to the specimen, the highest frequency must be searched in different fequency ranges. This process should be excecuted by increasing the applied torque valves until the required deformation is reached.

Zone H

AREA SOIL MECHANICS AND GEOTECHNICS

Resonant Column Test

Borehole:	PCQ0017	**Type of sample:**	Unaltered
Zone:	H	**Stratum:**	3
Depth (m):	9.00-10.00	**Number of test:**	1

Dimensions and properties of sample

Height:	121.31	mm	**σ_3 :**	180.00	kPa
Diameter:	59.56	mm	**Saturated unit weight:**	18.11	kN/m^3
Initial wet weight:	538.95	g	**Dry unit weight:**	15.03	kN/m^3
Dry weight:	517.67	g	**Gs:**	2.60	-
Wet unit weight:	15.64	kN/m^3	**e:**	0.890	-
Initial water content:	4.11	%	**n:**	47.09	%
Final water content:	4.11	%	**S:**	12.01	%
PI:	0	%	**w_{sat}:**	4.11	%

Results

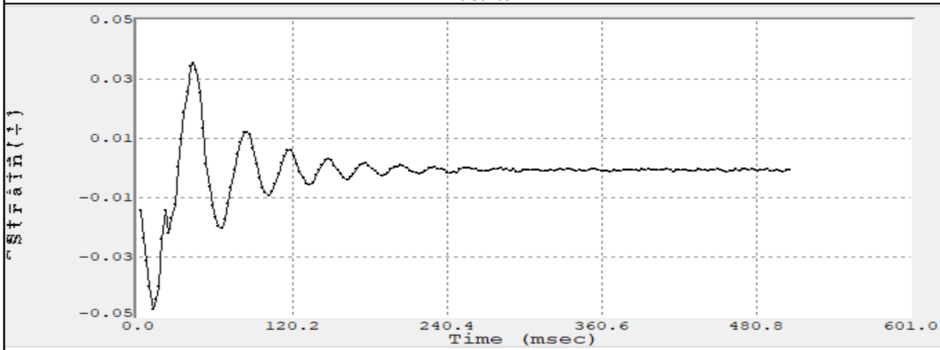

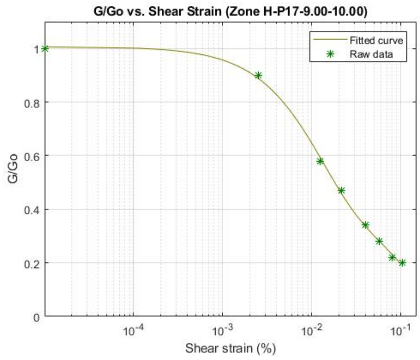

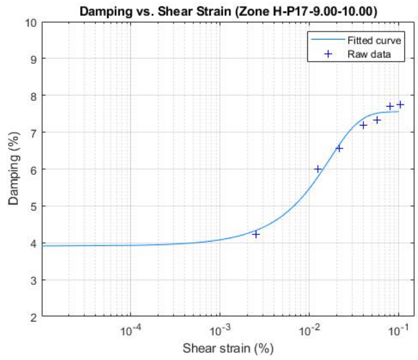

$$\frac{G}{Go} = 0{,}568 * \exp(-85{,}5 * x) + 0{,}4386 * \exp(-8{,}048 * x) \qquad D = 8{,}111/(1 + \exp(-89{,}85 * x) + 0{,}07339)$$

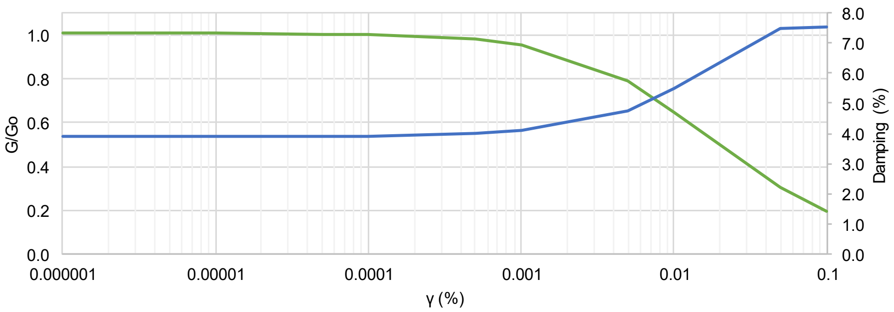

General observations: To obtain the points it is required to perform an iterative process. For each torque valve applied to the specimen, the highest frequency must be searched in different fequency ranges. This process should be excecuted by increasing the applied torque valves until the required deformation is reached.

Zone I

AREA SOIL MECHANICS AND GEOTECHNICS			
Resonant Column Test			
Borehole:	PCQ0021	**Type of sample:**	Remolded
Zone:	I	**Stratum:**	1
Depth (m):	3,00-4,00	**Number of test:**	2

Dimensions and properties of sample

Height:	113.69	mm	**σ_3 :**	65.00	kPa
Diameter:	59.65	mm	**Saturated unit weight:**	15.66	kN/m^3
Initial wet weight:	596.62	g	**Dry unit weight:**	17.28	kN/m^3
Dry weight:	559.58	g	**Gs:**	2.60	-
Wet unit weight:	18.42	kN/m^3	**e:**	1.682	-
Initial water content:	6.62	%	**n:**	62.71	%
Final water content:	12.81	%	**S:**	10.23	%
PI:	5	%	**w_{sat}:**	6.62	%

Results

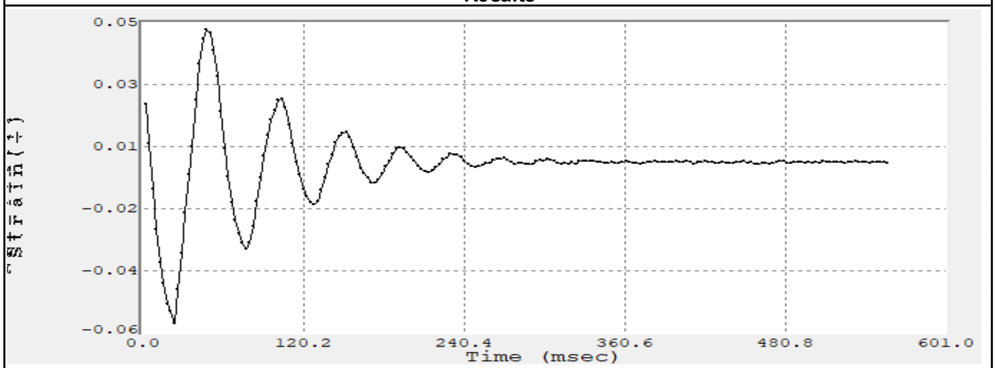

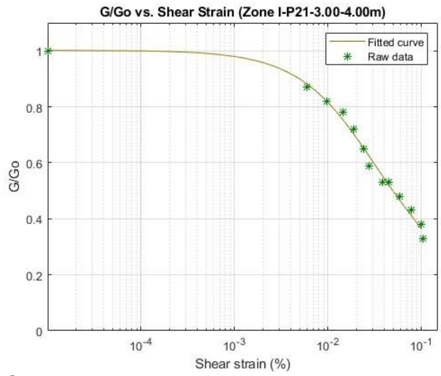

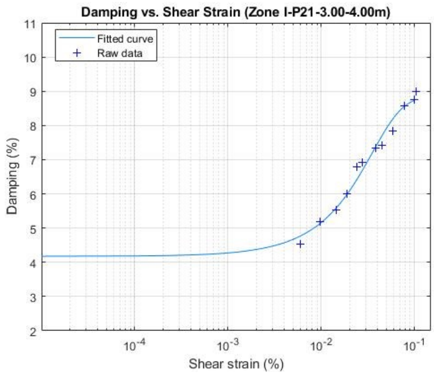

$$\frac{G}{Go} = 0{,}5961 * \exp(-5{,}027 * x) + 0{,}406 * \exp(-49{,}15 * x) \qquad D = 7{,}907/(1 + \exp(-45{,}01 * x) - 0{,}1061$$

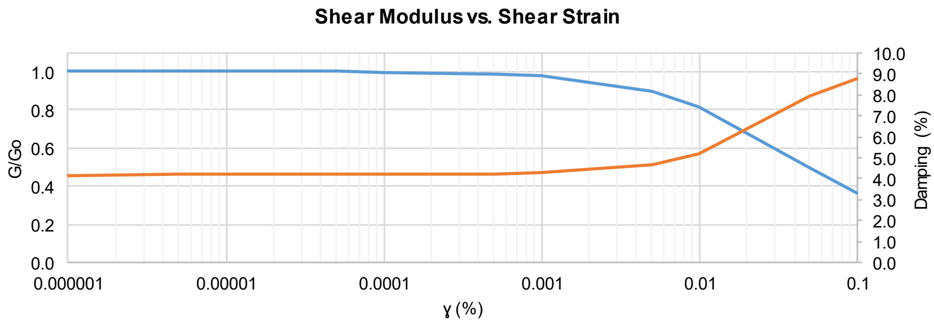

General observations: To obtain the points it is required to perform an iterative process. For each torque valve applied to the specimen, the highest frequency must be searched in different fequency ranges. This process should be excecuted by increasing the applied torque valves until the required deformation is reached.

AREA SOIL MECHANICS AND GEOTECHNICS

Resonant Column Test

Borehole:	PCQ0018	**Type of sample:**	Unaltered
Zone:	I	**Stratum:**	3
Depth (m):	12,00-13,00	**Number of test:**	1

Dimensions and properties of sample

Height:	119.37	mm	**σ_3 :**	113.00	kPa
Diameter:	59.53	mm	**Saturated unit weight:**	16.51	kN/m^3
Initial wet weight:	426.34	g	**Dry unit weight:**	12.08	kN/m^3
Dry weight:	409.31	g	**Gs:**	2.60	-
Wet unit weight:	12.59	kN/m^3	**e:**	1.342	-
Initial water content:	4.16	%	**n:**	57.29	%
Final water content:	4.16	%	**S:**	8.06	%
PI:	6	%	**w_{sat}:**	4.16	%

Results

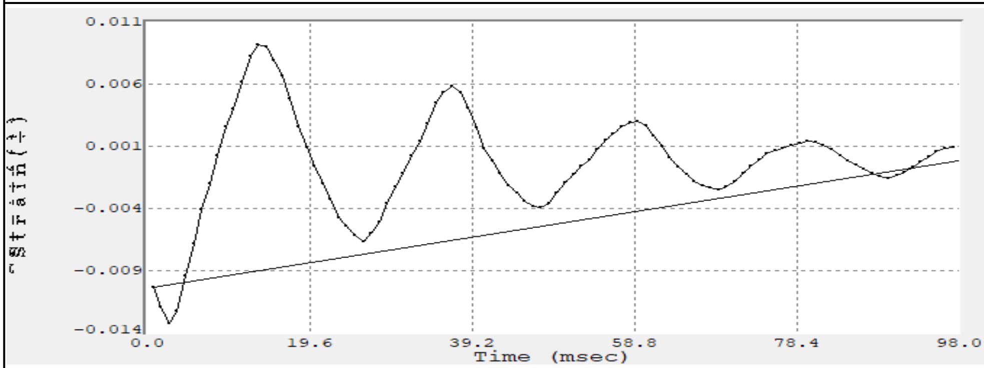

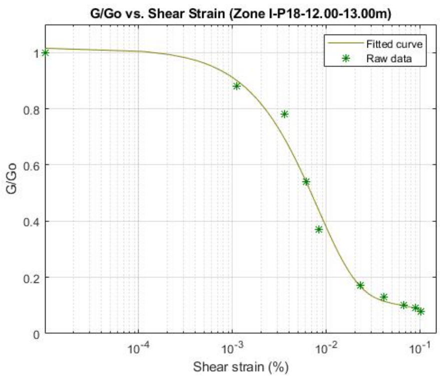

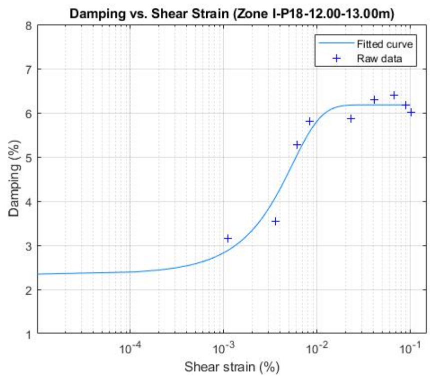

$$\frac{G}{Go} = 0{,}8859 * \exp(-125{,}5 * x) + 0{,}1304 * \exp(-4{,}14 * x) \qquad D = 3{,}77/(1 + \exp(-325{,}1 * x) - 0{,}39)$$

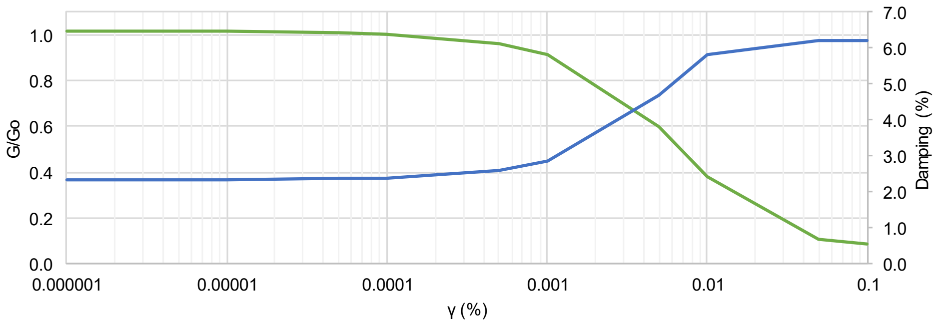

General observations: To obtain the points it is required to perform an iterative process. For each torque valve applied to the specimen, the highest frequency must be searched in different fequency ranges. This process should be excecuted by increasing the applied torque valves until the required deformation is reached.

AREA SOIL MECHANICS AND GEOTECHNICS

Resonant Column Test

Borehole:	PCQ0018	**Type of sample:**	Unaltered
Zone:	I	**Stratum:**	4
Depth (m):	14,00-15,00	**Number of test:**	1

Dimensions and properties of sample

Height:	117.55	mm	**σ_3 :**	205.00	kPa
Diameter:	60.41	mm	**Saturated unit weight:**	16.94	kN/m^3
Initial wet weight:	481.48	g	**Dry unit weight:**	13.44	kN/m^3
Dry weight:	461.50	g	**Gs:**	2.60	-
Wet unit weight:	14.02	kN/m^3	**e:**	1.202	-
Initial water content:	4.33	%	**n:**	54.58	%
Final water content:	4.33	%	**S:**	9.37	%
PI:	10	%	**w_{sat}:**	4.33	%

Results

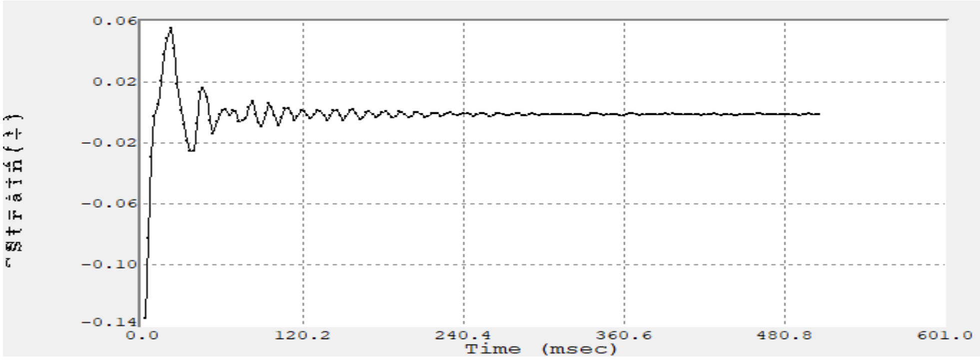

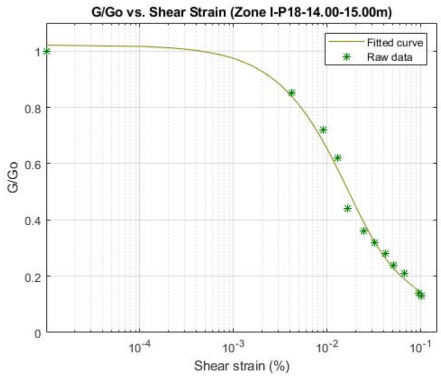

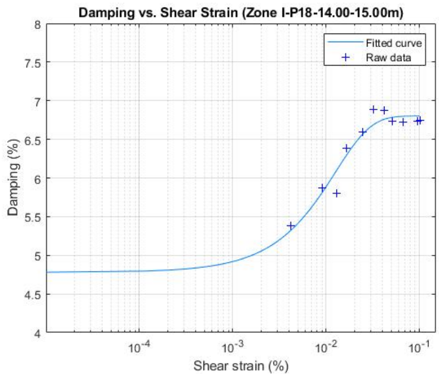

$$\frac{G}{Go} = 0{,}7275 * \exp(-65{,}2 * x) + 0{,}2943 * \exp(-7{,}338 * x) \quad D = 16{,}07/(1 + \exp(-100{,}3 * x) + 1{,}362)$$

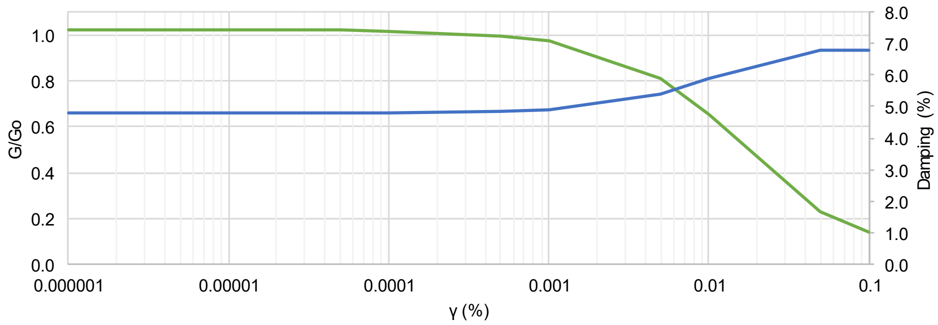

General observations: To obtain the points it is required to perform an iterative process. For each torque valve applied to the specimen, the highest frequency must be searched in different fequency ranges. This process should be excecuted by increasing the applied torque valves until the required deformation is reached.

AREA SOIL MECHANICS AND GEOTECHNICS

Resonant Column Test

Borehole:	PCQ0018	**Type of sample:**	Unaltered
Zone:	I	**Stratum:**	5
Depth (m):	29,00-30,00	**Number of test:**	1

Dimensions and properties of sample

Height:	123.44	mm	σ_3 **:**	244.00	kPa
Diameter:	60.05	mm	**Saturated unit weight:**	17.93	kN/m^3
Initial wet weight:	642.82	g	**Dry unit weight:**	14.16	kN/m^3
Dry weight:	504.49	g	**Gs:**	2.60	-
Wet unit weight:	18.04	kN/m^3	**e:**	0.933	-
Initial water content:	27.42	%	**n:**	48.25	%
Final water content:	0.00	%	**S:**	76.45	%
PI:	22	%	w_{sat}**:**	27.42	%

Results

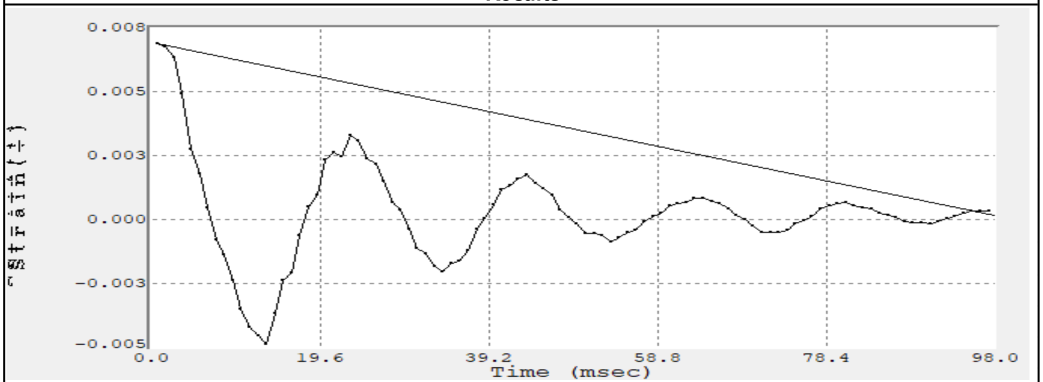

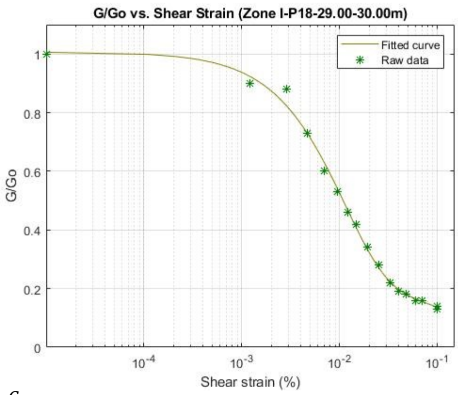

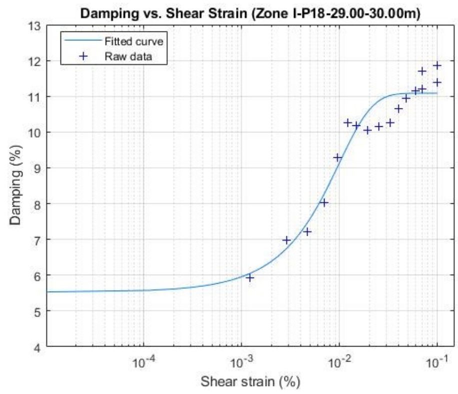

$$\frac{G}{Go} = 0{,}7982 * \exp(-89{,}57 * x) + 0{,}2083 * \exp(-4{,}286 * x)$$

$$D = 11{,}03/(1 + \exp(-155{,}7 * x) - 0{,}005316)$$

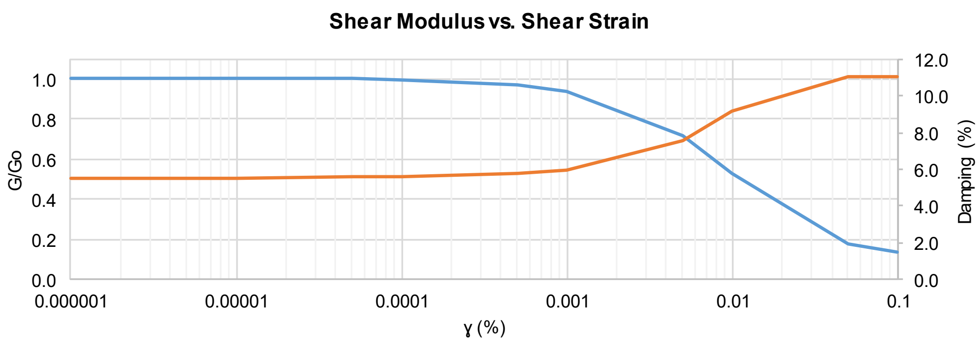

General observations: To obtain the points it is required to perform an iterative process. For each torque valve applied to the specimen, the highest frequency must be searched in different fequency ranges. This process should be excecuted by increasing the applied torque valves until the required deformation is reached.

B.2. Remolded Samples

Zone A

AREA SOIL MECHANICS AND GEOTECHNICS

Resonant Column Test

Borehole:	PCQ0003	**Type of sample:**	Remolded
Zone:	A	**Stratum:**	1
Depth (m):	1.00-2.00	**Number of test:**	1

Dimensions and properties of sample

Height:	140,65	mm	σ_3 **:**	46,00	kPa
Diameter:	70,84	mm	**Saturated unit weight:**	19,51	kN/m^3
Initial wet weight:	1062,45	g	**Dry unit weight:**	15,76	kN/m^3
Dry weight:	1017,77	g	**Gs:**	2,60	-
Wet unit weight:	18,80	kN/m^3	**e:**	0,619	-
Initial water content:	4,39	%	**n:**	38,23	%
Final water content:	19,33	%	**S:**	81,22	%
PI:	11	%	w_{sat}**:**	19,33	%

Results

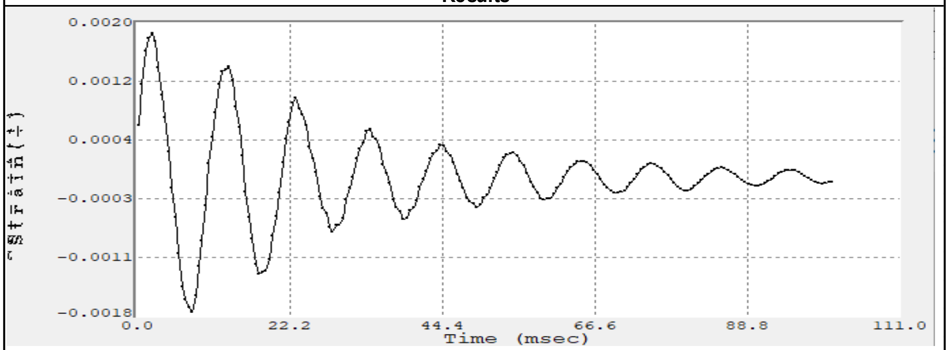

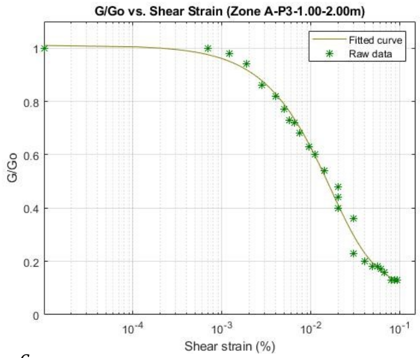

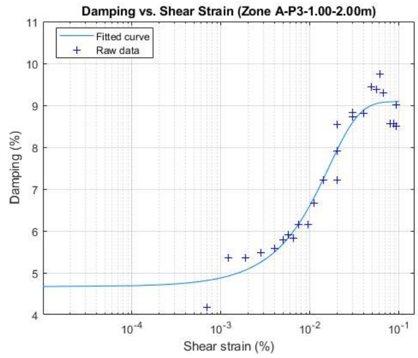

$$\frac{G}{Go} = 0{,}8005 * \exp(-62{,}73 * x) + 0{,}21 * \exp(-5{,}779 * x)$$

$$D = 9{,}603/(1 + \exp(-92{,}71 * x) + 0{,}05678)$$

Shear Modulus vs. Shear Strain

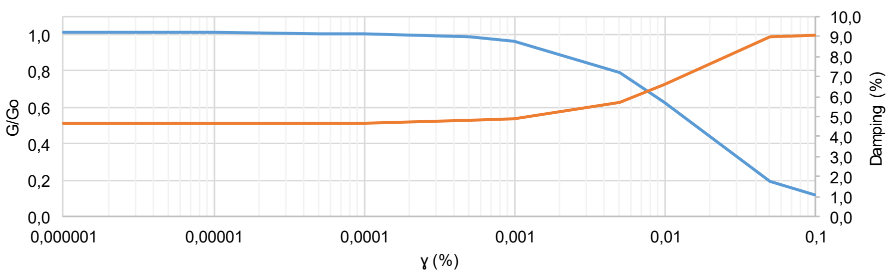

General observations: To obtain the points it is required to perform an iterative process. For each torque valve applied to the specimen, the highest frequency must be searched in different fequency ranges. This process should be excecuted by increasing the applied torque valves until the required deformation is reached.

AREA SOIL MECHANICS AND GEOTECHNICS

Resonant Column Test

Borehole:	PCQ0008	**Type of sample:**	Remolded
Zone:	A	**Stratum:**	2
Depth (m):	6.00-7.00	**Number of test:**	1

Dimensions and properties of sample

Height:	137,04	mm	**σ_3 :**	112,00	kPa
Diameter:	70,26	mm	**Saturated unit weight:**	19,00	kN/m^3
Initial wet weight:	1016,09	g	**Dry unit weight:**	14,93	kN/m^3
Dry weight:	959,14	g	**Gs:**	2,60	-
Wet unit weight:	18,76	kN/m^3	**e:**	0,708	-
Initial water content:	5,94	%	**n:**	41,46	%
Final water content:	25,67	%	**S:**	94,22	%
PI:	9	%	**w_{sat}:**	25,67	%

Results

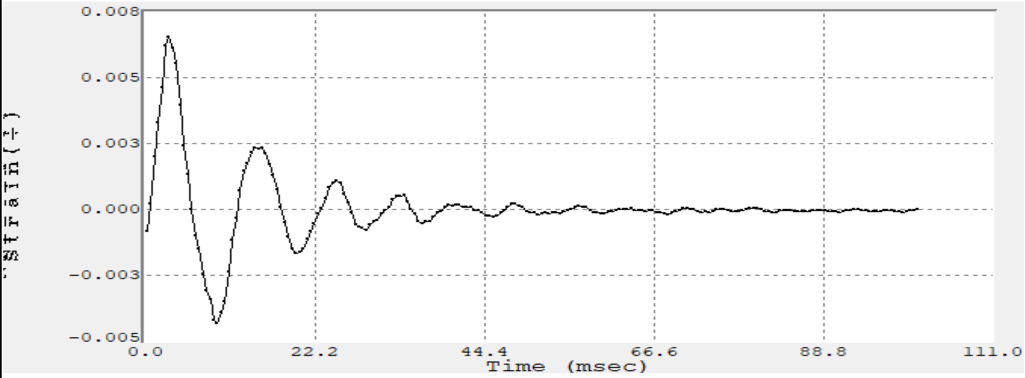

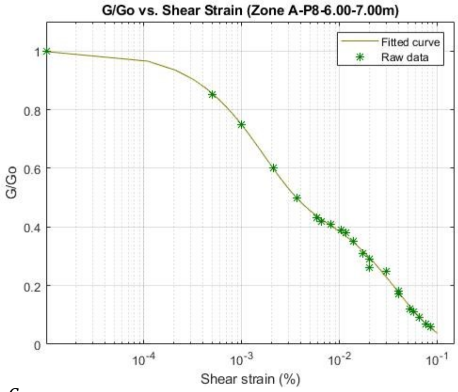

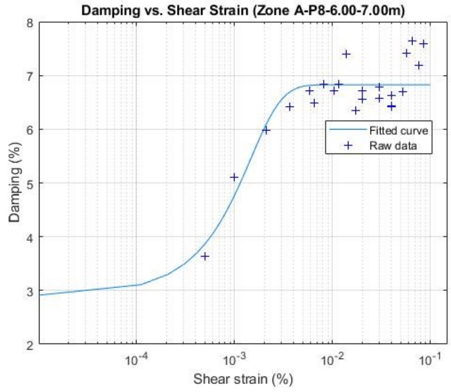

$$\frac{G}{Go} = 0{,}5061 * \exp(-647{,}6 * x) + 0{,}4953 * \exp(-25{,}66 * x)$$

$$D = 5{,}022/(1 + \exp(-1148 * x) - 0{,}2643)$$

Shear Modulus vs. Shear Strain

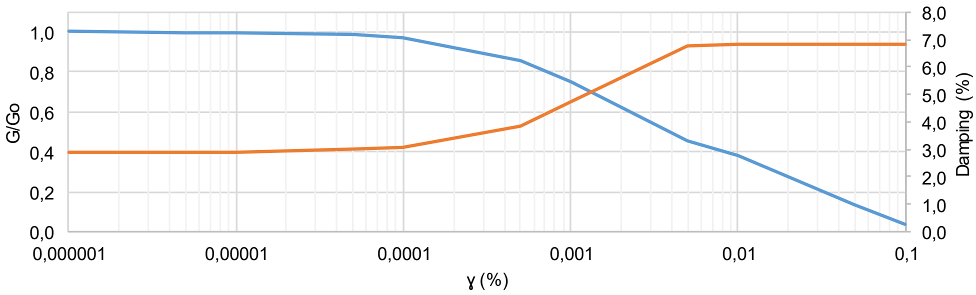

General observations: To obtain the points it is required to perform an iterative process. For each torque valve applied to the specimen, the highest frequency must be searched in different fequency ranges. This process should be excecuted by increasing the applied torque valves until the required deformation is reached.

AREA SOIL MECHANICS AND GEOTECHNICS

Resonant Column Test

Borehole:	PCQ0002	**Type of sample:**	Remolded
Zone:	A	**Stratum:**	3
Depth (m):	15.00-16.00	**Number of test:**	1

Dimensions and properties of sample

Height:	133,70	mm	**σ_3 :**	130,00	kPa
Diameter:	70,59	mm	**Saturated unit weight:**	18,92	kN/m^3
Initial wet weight:	955,66	g	**Dry unit weight:**	14,80	kN/m^3
Dry weight:	916,06	g	**Gs:**	2,60	-
Wet unit weight:	17,92	kN/m^3	**e:**	0,723	-
Initial water content:	4,32	%	**n:**	41,97	%
Final water content:	21,04	%	**S:**	75,66	%
PI:	6	%	**w_{sat}:**	21,04	%

Results

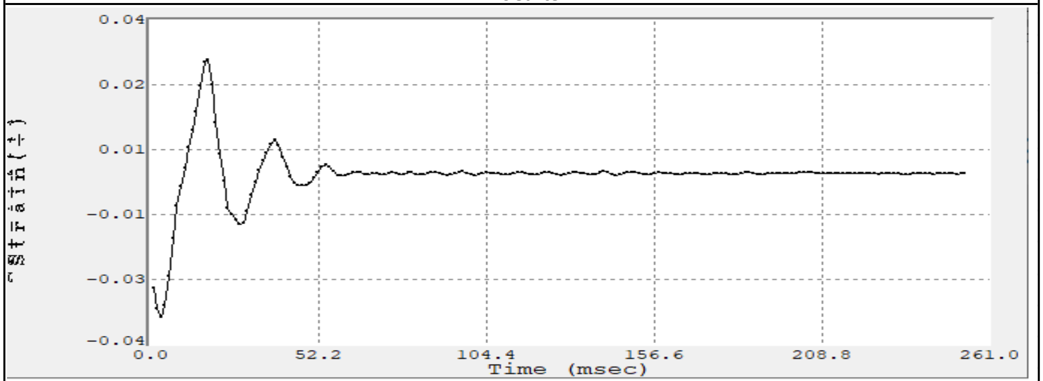

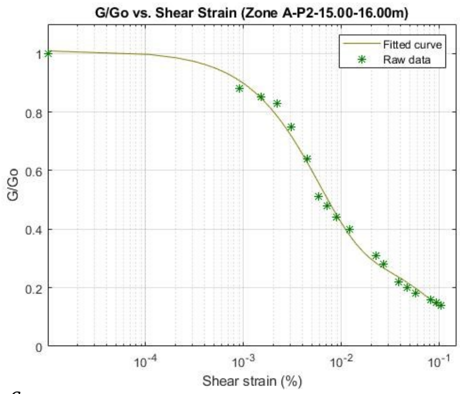

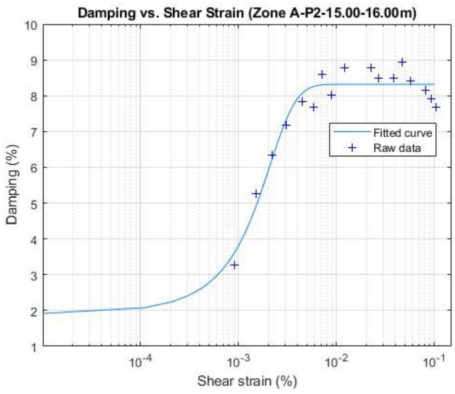

$$\frac{G}{Go} = 0{,}6752 * \exp(-176{,}4 * x) + 0{,}3345 * \exp(-9{,}157 * x) \qquad D = 2{,}466/(1 + \exp(-1048 * x) - 0{,}7035)$$

Shear Modulus vs. Shear Strain

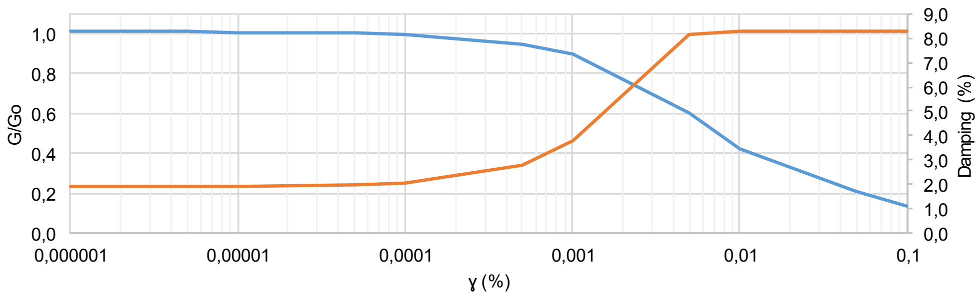

General observations: To obtain the points it is required to perform an iterative process. For each torque valve applied to the specimen, the highest frequency must be searched in different fequency ranges. This process should be excecuted by increasing the applied torque valves until the required deformation is reached.

AREA SOIL MECHANICS AND GEOTECHNICS

Resonant Column Test

Borehole:	PCQ0002	**Type of sample:**	Remolded
Zone:	A	**Stratum:**	4
Depth (m):	17.00-18.00	**Number of test:**	1

Dimensions and properties of sample

Height:	140,38	mm	**σ_3 :**	182,00	kPa
Diameter:	69,71	mm	**Saturated unit weight:**	17,14	kN/m^3
Initial wet weight:	797,60	g	**Dry unit weight:**	11,92	kN/m^3
Dry weight:	709,89	g	**Gs:**	2,60	-
Wet unit weight:	14,60	kN/m^3	**e:**	1,140	-
Initial water content:	12,35	%	**n:**	53,28	%
Final water content:	22,53	%	**S:**	51,38	%
PI:	3	%	**w_{sat}:**	22,53	%

Results

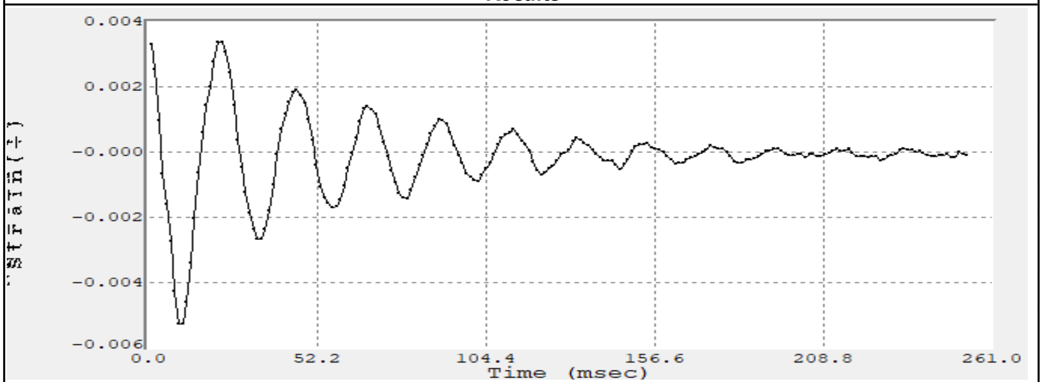

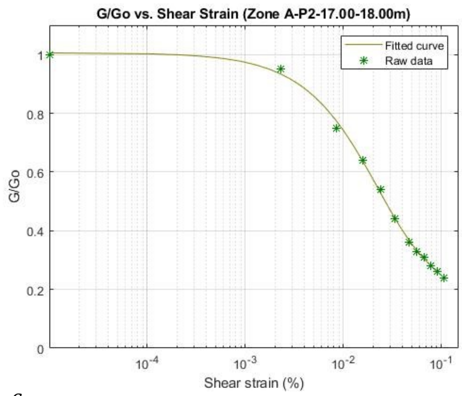

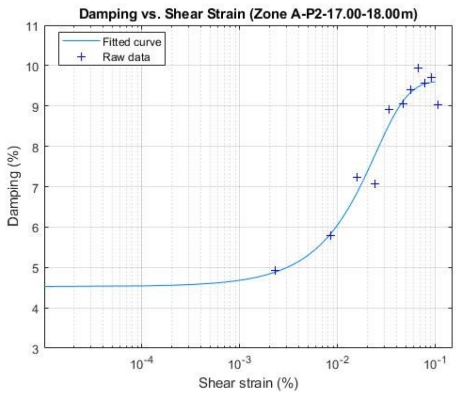

$$\frac{G}{Go} = 0{,}6223 * \exp(-50{,}67 * x) + 0{,}3836 * \exp(-4{,}548 * x)$$

$$D = 8{,}551/(1 + \exp(-64{,}88 * x) - 0{,}1107)$$

Shear Modulus vs. Shear Strain

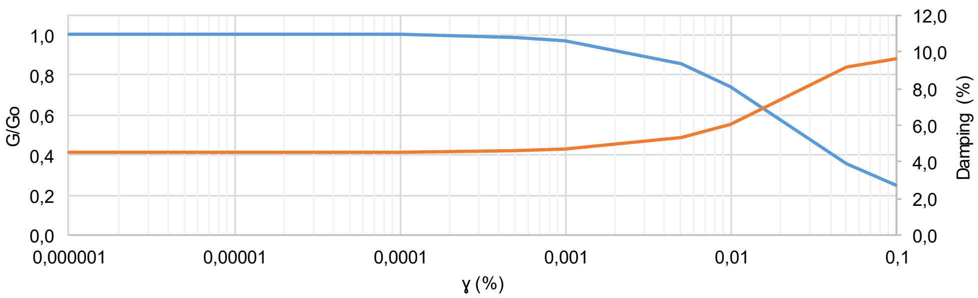

General observations: To obtain the points it is required to perform an iterative process. For each torque valve applied to the specimen, the highest frequency must be searched in different fequency ranges. This process should be excecuted by increasing the applied torque valves until the required deformation is reached.

Zone B

AREA SOIL MECHANICS AND GEOTECHNICS

Resonant Column Test

Borehole:	PCQ0004	**Type of sample:**	Remolded
Zone:	B	**Stratum:**	1
Depth (m):	3.00-4.00	**Number of test:**	1

Dimensions and properties of sample

Height:	139,45	mm	**σ_3 :**	112,00	kPa
Diameter:	70,50	mm	**Saturated unit weight:**	16,32	kN/m^3
Initial wet weight:	720,34	g	**Dry unit weight:**	10,58	kN/m^3
Dry weight:	593,37	g	**Gs:**	2,60	-
Wet unit weight:	12,98	kN/m^3	**e:**	1,410	-
Initial water content:	21,40	%	**n:**	58,50	%
Final water content:	22,66	%	**S:**	41,79	%
PI:	64	%	**w_{sat}:**	22,66	%

Results

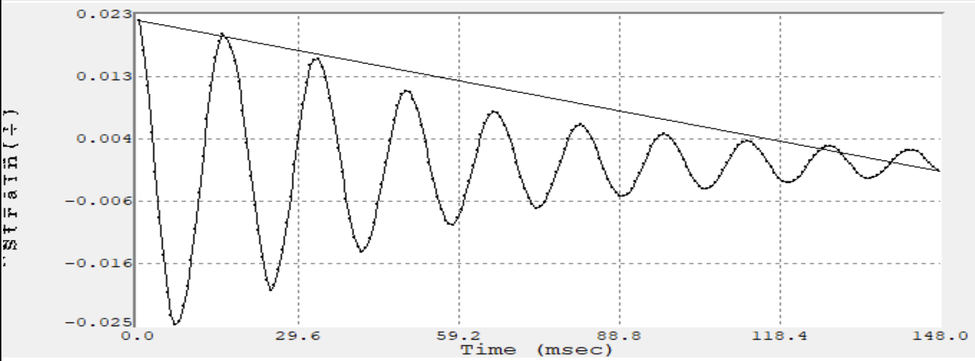

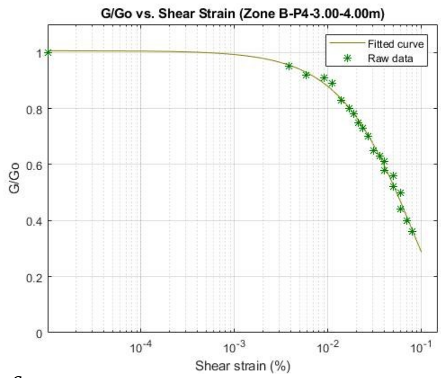

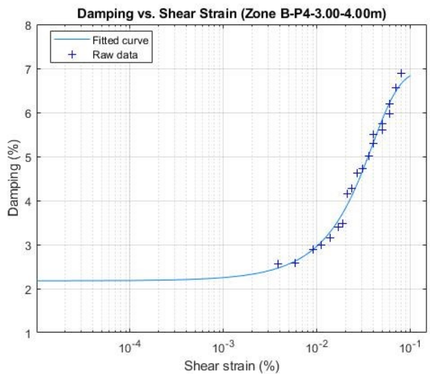

$$\frac{G}{Go} = 0{,}07462 * \exp(-38{,}95 * x) + 0{,}9314 * \exp(-11{,}8 * x)$$

$$D = 3{,}169/(1 + \exp(-48{,}94 * x) - 0{,}5438)$$

Shear Modulus vs. Shear Strain

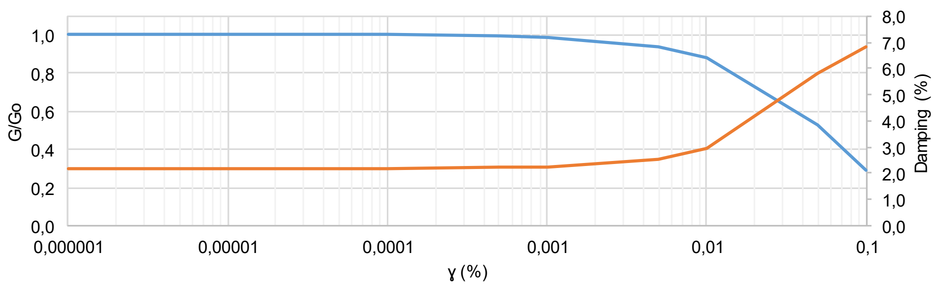

General observations: To obtain the points it is required to perform an iterative process. For each torque valve applied to the specimen, the highest frequency must be searched in different fequency ranges. This process should be excecuted by increasing the applied torque valves until the required deformation is reached.

AREA SOIL MECHANICS AND GEOTECHNICS

Resonant Column Test

Borehole:	PCQ0004	**Type of sample:**	Remolded
Zone:	B	**Stratum:**	2
Depth (m):	16.00-17.00	**Number of test:**	1

Dimensions and properties of sample

Height:	125,75	mm	σ_3 **:**	141,00	kPa
Diameter:	70,60	mm	**Saturated unit weight:**	16,49	kN/m^3
Initial wet weight:	798,21	g	**Dry unit weight:**	10,86	kN/m^3
Dry weight:	537,72	g	**Gs:**	2,60	-
Wet unit weight:	15,91	kN/m^3	**e:**	1,349	-
Initial water content:	48,44	%	**n:**	57,42	%
Final water content:	46,47	%	**S:**	89,59	%
PI:	39	%	w_{sat}**:**	46,47	%

Results

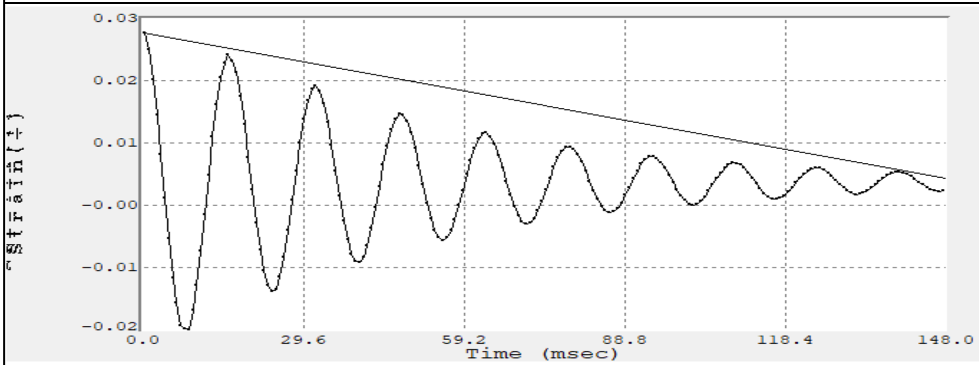

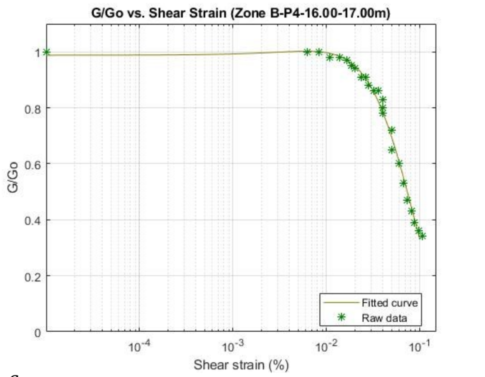

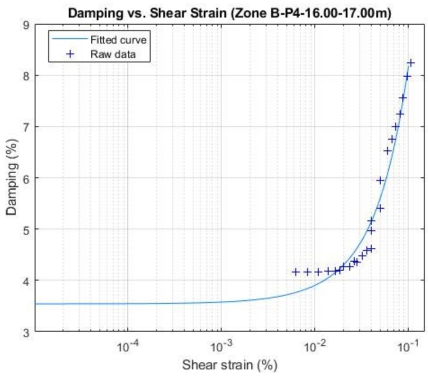

$$\frac{G}{Go} = -0{,}9658 * \exp(-40{,}02 * x) + 1{,}954 * \exp(-17{,}26 * x)$$

$$D = 4{,}419/(1 + \exp(-12{,}29 * x) - 0{,}7523)$$

Shear Modulus vs. Shear Strain

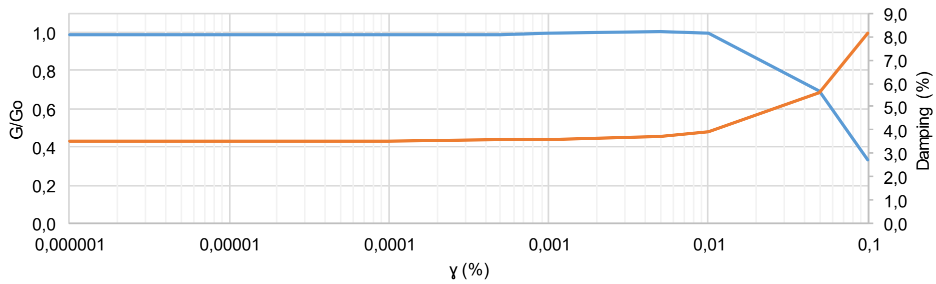

General observations: To obtain the points it is required to perform an iterative process. For each torque valve applied to the specimen, the highest frequency must be searched in different fequency ranges. This process should be excecuted by increasing the applied torque valves until the required deformation is reached.

AREA SOIL MECHANICS AND GEOTECHNICS

Resonant Column Test

Borehole:	PCQ0004	**Type of sample:**	Remolded
Zone:	B	**Stratum:**	3
Depth (m):	20.00-21.00	**Number of test:**	1

Dimensions and properties of sample

Height:	147,89	mm	**σ_3 :**	190,00	kPa
Diameter:	70,26	mm	**Saturated unit weight:**	18,01	kN/m^3
Initial wet weight:	965,50	g	**Dry unit weight:**	13,33	kN/m^3
Dry weight:	903,03	g	**Gs:**	2,60	-
Wet unit weight:	16,52	kN/m^3	**e:**	0,914	-
Initial water content:	6,92	%	**n:**	47,76	%
Final water content:	23,97	%	**S:**	68,16	%
PI:	44	%	**w_{sat}:**	23,97	%

Results

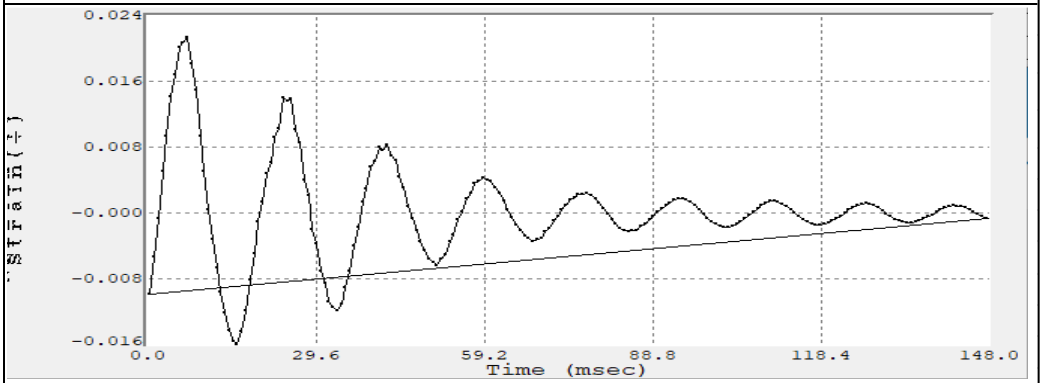

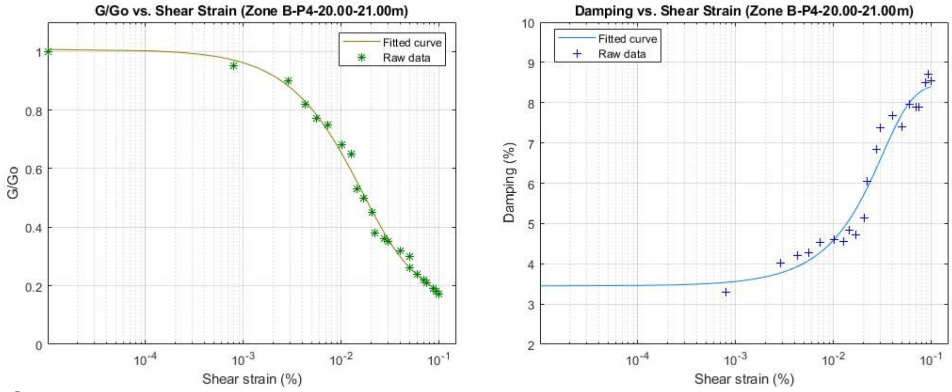

$$\frac{G}{Go} = 0{,}6907 * \exp(-66{,}47 * x) + 0{,}3165 * \exp(-5{,}816 * x) \qquad D = 5{,}828/(1 + \exp(-54{,}32 * x) - 0{,}3104)$$

Shear Modulus vs. Shear Strain

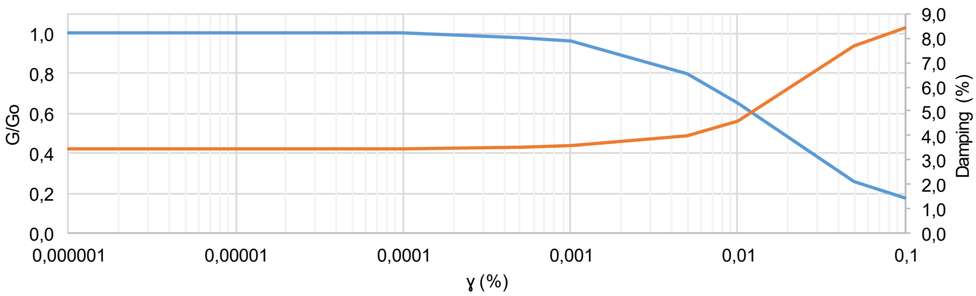

General observations: To obtain the points it is required to perform an iterative process. For each torque valve applied to the specimen, the highest frequency must be searched in different fequency ranges. This process should be excecuted by increasing the applied torque valves until the required deformation is reached.

AREA SOIL MECHANICS AND GEOTECHNICS

Resonant Column Test

Borehole:	PCQ0004	**Type of sample:**	Remolded
Zone:	B	**Stratum:**	4
Depth (m):	25.00-26.00	**Number of test:**	1

Dimensions and properties of sample

Height:	127,44	mm	**σ_3 :**	237,00	kPa
Diameter:	70,83	mm	**Saturated unit weight:**	18,21	kN/m^3
Initial wet weight:	901,85	g	**Dry unit weight:**	13,66	kN/m^3
Dry weight:	714,74	g	**Gs:**	2,60	-
Wet unit weight:	17,62	kN/m^3	**e:**	0,868	-
Initial water content:	26,18	%	**n:**	46,46	%
Final water content:	29,03	%	**S:**	86,97	%
PI:	11	%	**w_{sat}:**	29,03	%

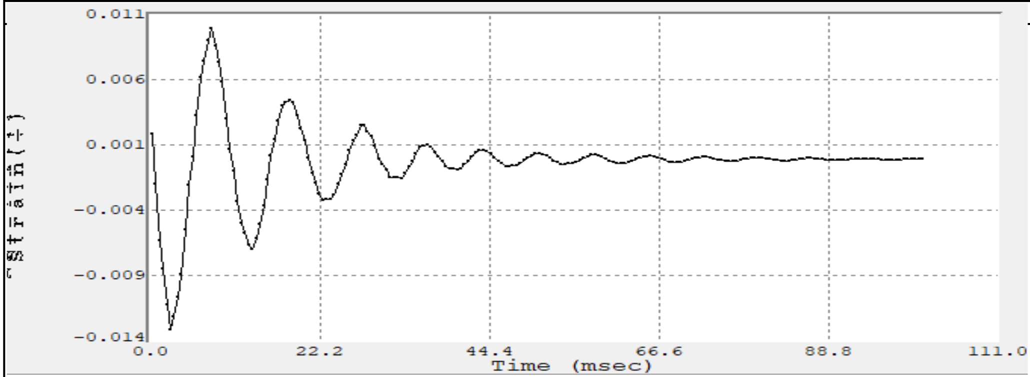

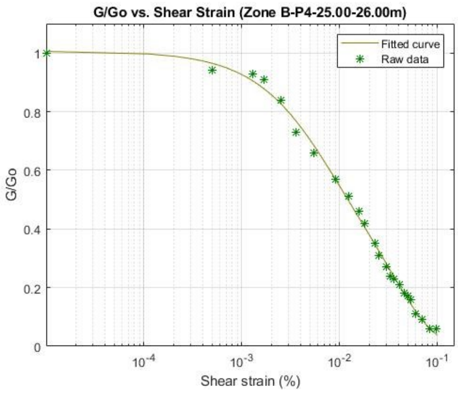

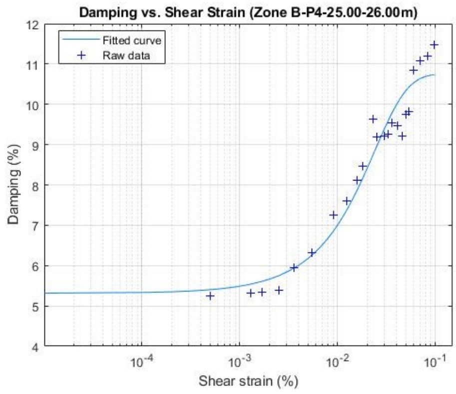

$$\frac{G}{Go} = 0{,}343 * \exp(-196{,}8 * x) + 0{,}6632 * \exp(-28{,}57 * x) \qquad D = 10{,}51/(1 + \exp(-64{,}85 * x) - 0{,}02246)$$

Shear Modulus vs. Shear Strain

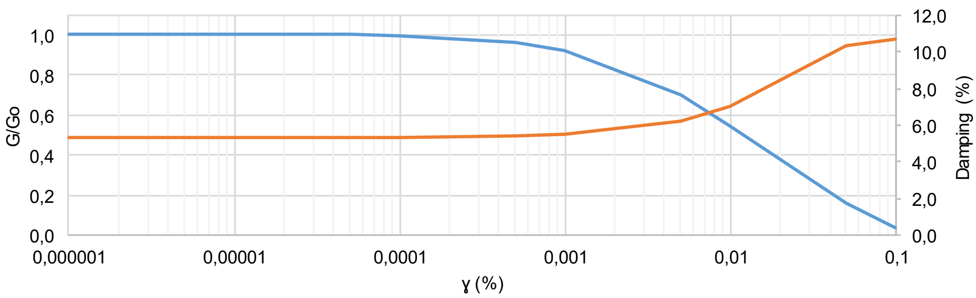

General observations: To obtain the points it is required to perform an iterative process. For each torque valve applied to the specimen, the highest frequency must be searched in different fequency ranges. This process should be excecuted by increasing the applied torque valves until the required deformation is reached.

Zone C

AREA SOIL MECHANICS AND GEOTECHNICS

Resonant Column Test

Borehole:	PCQ0009	**Type of sample:**	Remolded
Zone:	C	**Stratum:**	1
Depth (m):	3.00-4.00	**Number of test:**	1

Dimensions and properties of sample

Height:	135,68	mm	**σ_3 :**	30,00	kPa
Diameter:	70,61	mm	**Saturated unit weight:**	17,68	kN/m^3
Initial wet weight:	935,47	g	**Dry unit weight:**	12,79	kN/m^3
Dry weight:	817,20	g	**Gs:**	2,60	-
Wet unit weight:	17,27	kN/m^3	**e:**	0,995	-
Initial water content:	14,47	%	**n:**	49,87	%
Final water content:	35,10	%	**S:**	91,72	%
PI:	23	%	**w_{sat}:**	35,10	%

Results

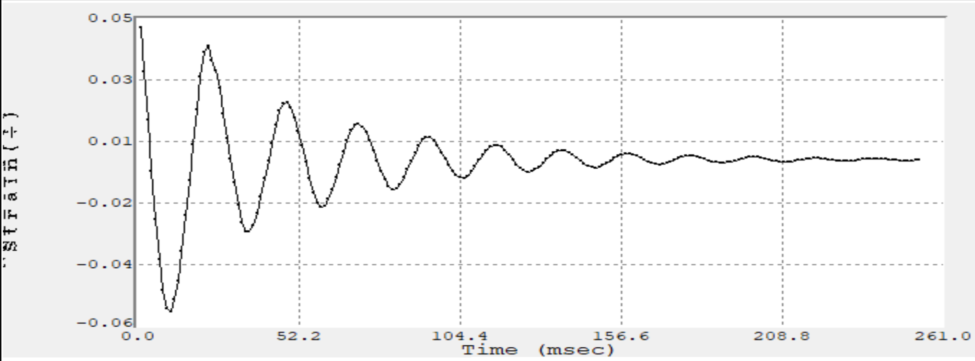

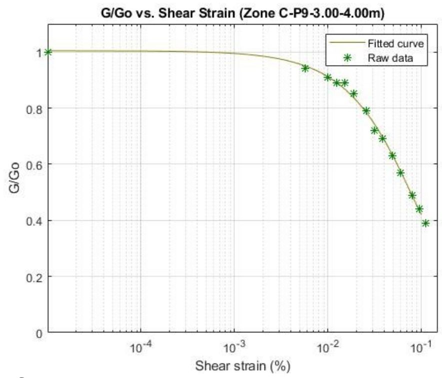

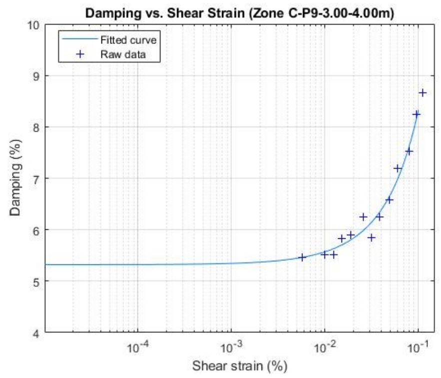

$\frac{G}{Go} = 0,9878 * \exp(-10,14 * x) + 0,01662 * \exp(13,15 * x)$ $\quad D = 5,882/(1 + \exp(-5,093 * x) - 0,8944)$

Shear Modulus vs. Shear Strain

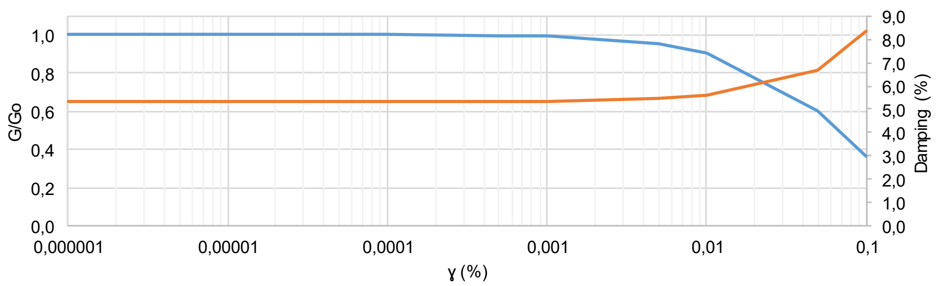

General observations: To obtain the points it is required to perform an iterative process. For each torque valve applied to the specimen, the highest frequency must be searched in different fequency ranges. This process should be excecuted by increasing the applied torque valves until the required deformation is reached.

AREA SOIL MECHANICS AND GEOTECHNICS

Resonant Column Test

Borehole:	PCQ0005	**Type of sample:**	Remolded
Zone:	C	**Stratum:**	2
Depth (m):	6.00-7.00	**Number of test:**	1

Dimensions and properties of sample

Height:	147,77	mm	**σ_3 :**	63,00	kPa
Diameter:	70,86	mm	**Saturated unit weight:**	19,39	kN/m^3
Initial wet weight:	1120,78	g	**Dry unit weight:**	15,57	kN/m^3
Dry weight:	1060,34	g	**Gs:**	2,60	-
Wet unit weight:	18,87	kN/m^3	**e:**	0,638	-
Initial water content:	5,70	%	**n:**	38,96	%
Final water content:	21,19	%	**S:**	86,30	%
PI:	16	%	**w_{sat}:**	21,19	%

Results

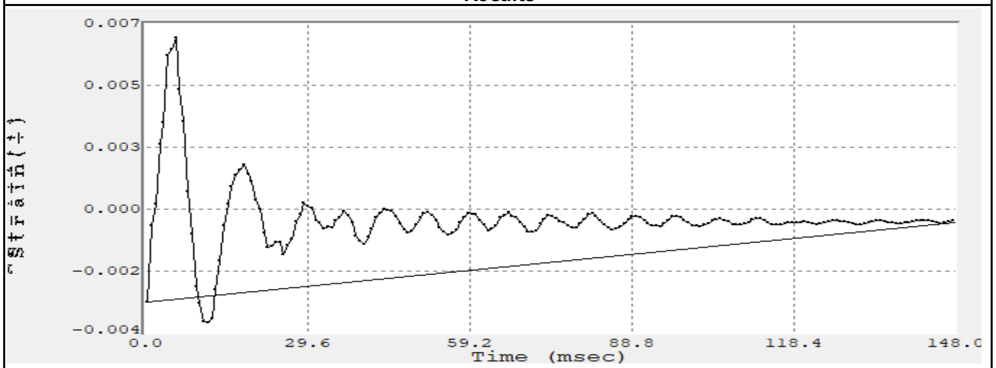

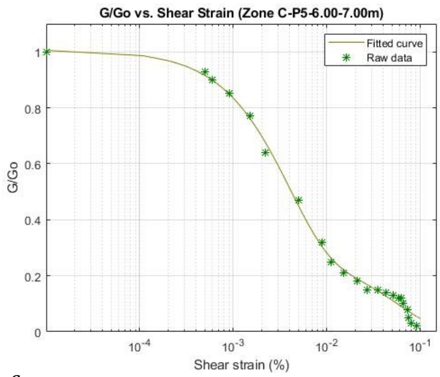

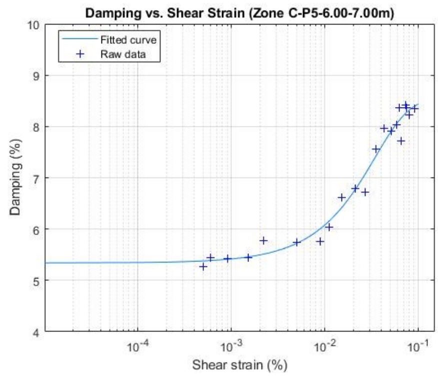

$$\frac{G}{Go} = 0{,}7387 * \exp(-258{,}5 * x) + 0{,}2685 * \exp(-17{,}47 * x)$$

$$D = 14{,}27/(1 + \exp(-39{,}4 * x) + 0{,}672)$$

Shear Modulus vs. Shear Strain

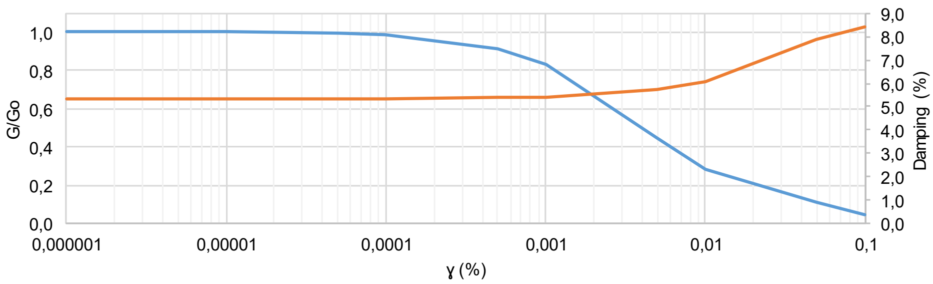

General observations: To obtain the points it is required to perform an iterative process. For each torque valve applied to the specimen, the highest frequency must be searched in different fequency ranges. This process should be excecuted by increasing the applied torque valves until the required deformation is reached.

AREA SOIL MECHANICS AND GEOTECHNICS

Resonant Column Test

Borehole:	PCQ0005	**Type of sample:**	Remolded
Zone:	C	**Stratum:**	3
Depth (m):	9.00-10.00	**Number of test:**	1

Dimensions and properties of sample

Height:	146,82	mm	**σ_3 :**	116,00	kPa
Diameter:	70,75	mm	**Saturated unit weight:**	18,81	kN/m^3
Initial wet weight:	1080,50	g	**Dry unit weight:**	14,63	kN/m^3
Dry weight:	1004,16	g	**Gs:**	2,60	-
Wet unit weight:	18,37	kN/m^3	**e:**	0,744	-
Initial water content:	7,60	%	**n:**	42,66	%
Final water content:	25,57	%	**S:**	89,38	%
PI:	9	%	**w_{sat}:**	25,57	%

Results

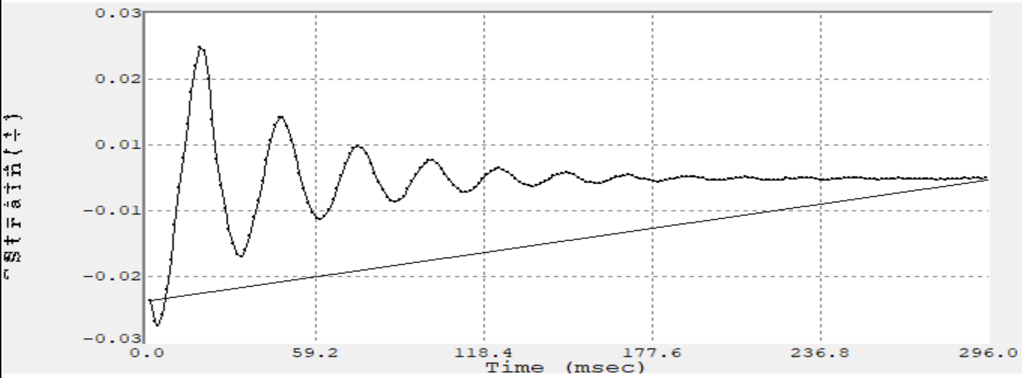

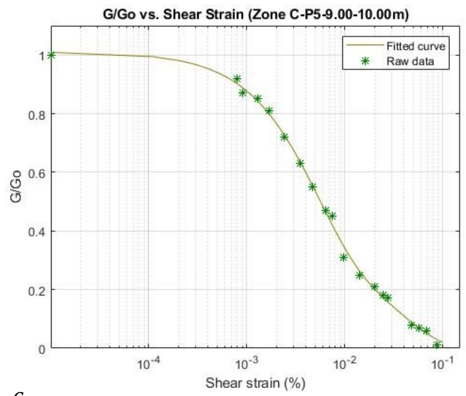

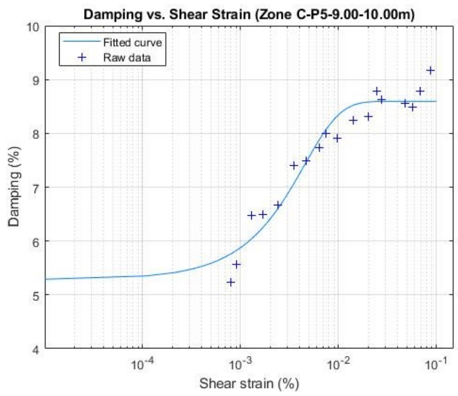

$$\frac{G}{Go} = 0{,}6791 * \exp(-202{,}3 * x) + 0{,}3312 * \exp(-27{,}52 * x)$$

$$D = 13{,}72/(1 + \exp(-303{,}8 * x) + 0{,}5961)$$

Shear Modulus vs. Shear Strain

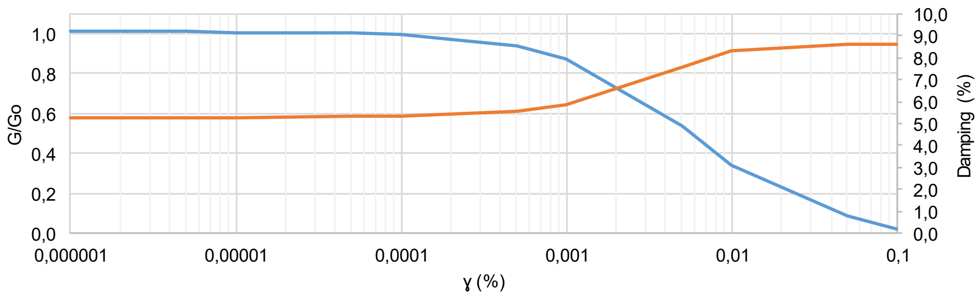

General observations: To obtain the points it is required to perform an iterative process. For each torque valve applied to the specimen, the highest frequency must be searched in different fequency ranges. This process should be excecuted by increasing the applied torque valves until the required deformation is reached.

AREA SOIL MECHANICS AND GEOTECHNICS

Resonant Column Test

Borehole:	PCQ0005	**Type of sample:**	Remolded
Zone:	C	**Stratum:**	4
Depth (m):	12.00-13.00	**Number of test:**	1

Dimensions and properties of sample

Height:	130,92	mm	σ_3 **:**	141,00	kPa
Diameter:	69,92	mm	**Saturated unit weight:**	18,37	kN/m^3
Initial wet weight:	886,54	g	**Dry unit weight:**	13,91	kN/m^3
Dry weight:	849,62	g	**Gs:**	2,60	-
Wet unit weight:	17,30	kN/m^3	**e:**	0,833	-
Initial water content:	4,35	%	**n:**	45,45	%
Final water content:	24,35	%	**S:**	76,00	%
PI:	13	%	w_{sat}**:**	24,35	%

Results

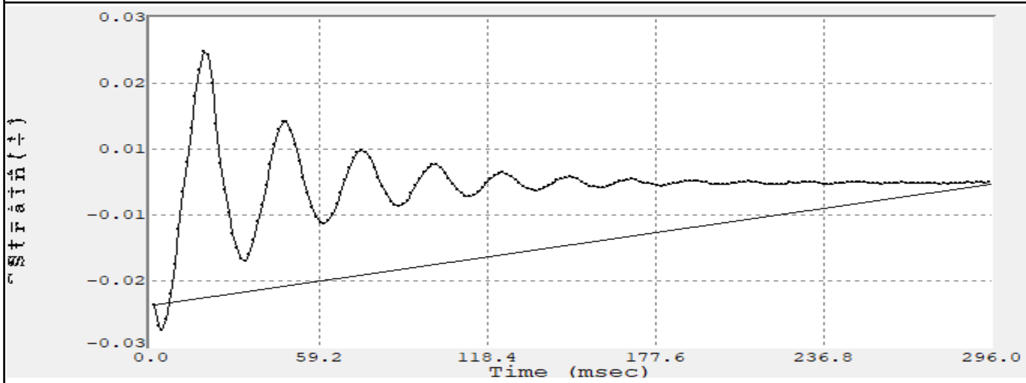

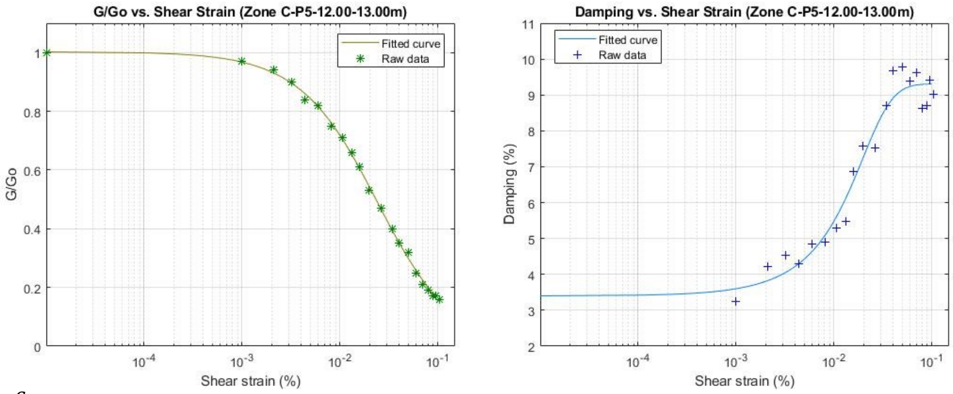

$$\frac{G}{Go} = 0{,}5224 * \exp(-59{,}06 * x) + 0{,}4802 * \exp(-11{,}4 * x) \qquad D = 5{,}36/(1 + \exp(-91{,}2 * x) - 0{,}424)$$

Shear Modulus vs. Shear Strain

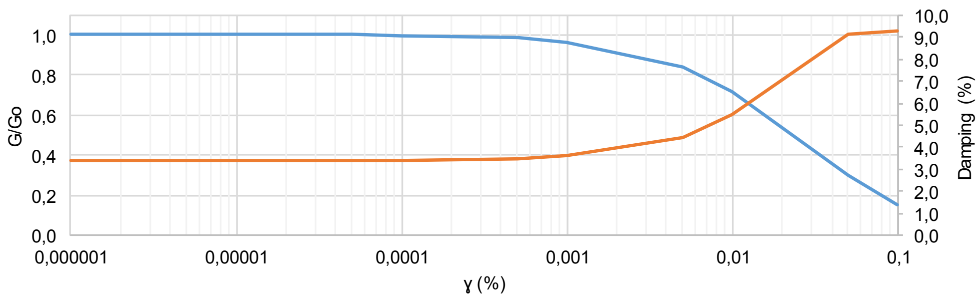

General observations: To obtain the points it is required to perform an iterative process. For each torque valve applied to the specimen, the highest frequency must be searched in different fequency ranges. This process should be excecuted by increasing the applied torque valves until the required deformation is reached.

Zone D

AREA SOIL MECHANICS AND GEOTECHNICS

Resonant Column Test

Borehole:	PCQ0006	**Type of sample:**	Remolded
Zone:	D	**Stratum:**	4
Depth (m):	15.00-16.00	**Number of test:**	1

Dimensions and properties of sample

Height:	142,82	mm	**σ_3 :**	151,00	kPa
Diameter:	70,15	mm	**Saturated unit weight:**	18,12	kN/m^3
Initial wet weight:	977,65	g	**Dry unit weight:**	13,50	kN/m^3
Dry weight:	766,35	g	**Gs:**	2,60	-
Wet unit weight:	17,38	kN/m^3	**e:**	0,889	-
Initial water content:	27,57	%	**n:**	47,06	%
Final water content:	28,71	%	**S:**	83,94	%
PI:	3	%	**w_{sat}:**	28,71	%

Results

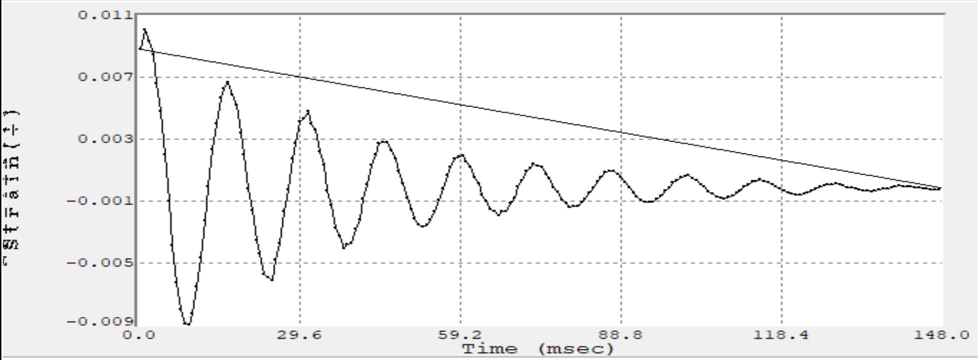

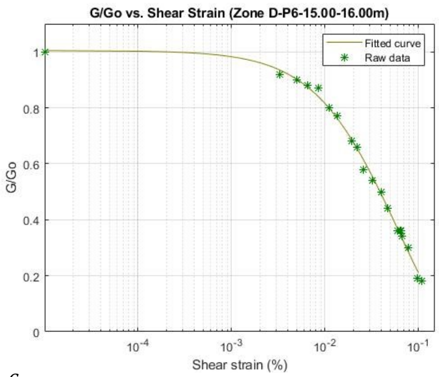

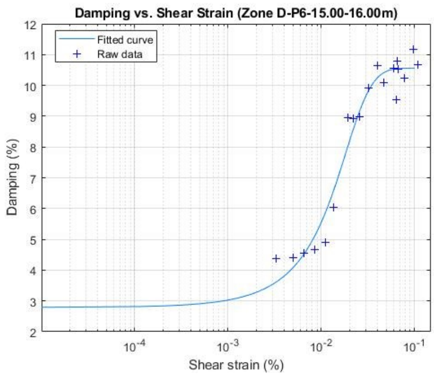

$$\frac{G}{Go} = 0{,}1869 * \exp(-61{,}19 * x) + 0{,}8177 * \exp(-13{,}58 * x) \qquad D = 3{,}793/(1 + \exp(-112{,}6 * x) - 0{,}6408)$$

Shear Modulus vs. Shear Strain

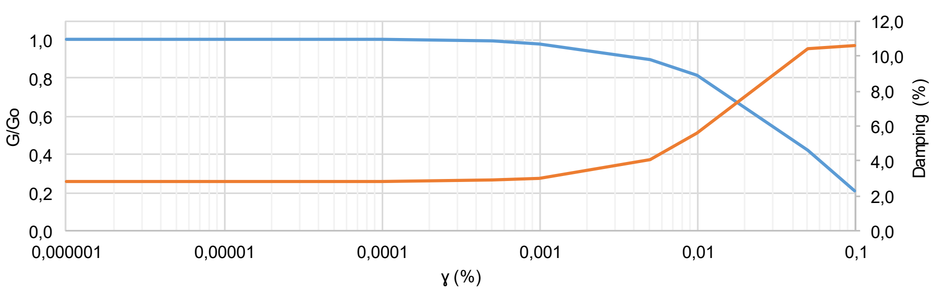

General observations: To obtain the points it is required to perform an iterative process. For each torque valve applied to the specimen, the highest frequency must be searched in different fequency ranges. This process should be excecuted by increasing the applied torque valves until the required deformation is reached.

Zone E

AREA SOIL MECHANICS AND GEOTECHNICS			
Resonant Column Test			
Borehole:	PCQ0010	**Type of sample:**	Remolded
Zone:	E	**Stratum:**	3
Depth (m):	7.00-8.00	**Number of test:**	1

Dimensions and properties of sample

Height:	140,65	mm	σ_3 **:**	128,00	kPa
Diameter:	70,47	mm	**Saturated unit weight:**	19,41	kN/m^3
Initial wet weight:	1010,88	g	**Dry unit weight:**	15,60	kN/m^3
Dry weight:	959,62	g	**Gs:**	2,60	-
Wet unit weight:	18,08	kN/m^3	**e:**	0,635	-
Initial water content:	5,34	%	**n:**	38,83	%
Final water content:	15,89	%	**S:**	65,06	%
PI:	4	%	w_{sat}**:**	15,89	%

Results

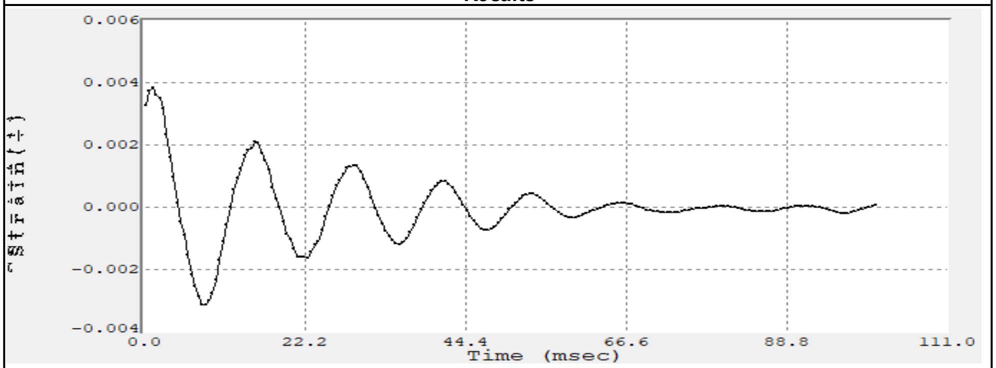

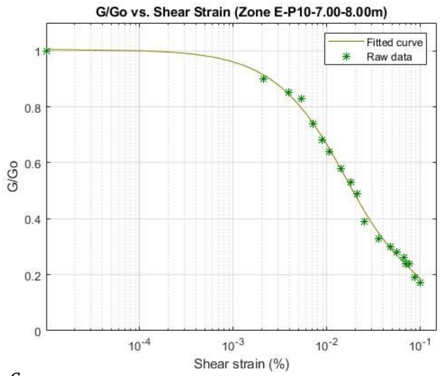

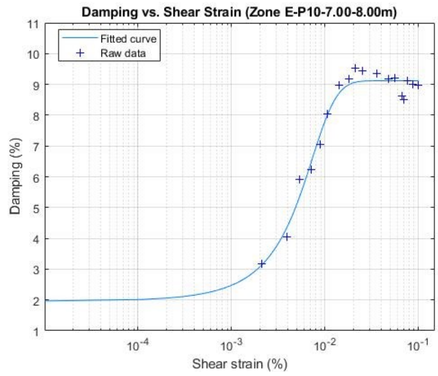

$$\frac{G}{Go} = 0{,}6059 * \exp(-71{,}82 * x) + 0{,}3992 * \exp(-7{,}739 * x)$$

$$D = 2{,}499/(1 + \exp(-307{,}5 * x) - 0{,}726)$$

Shear Modulus vs. Shear Strain

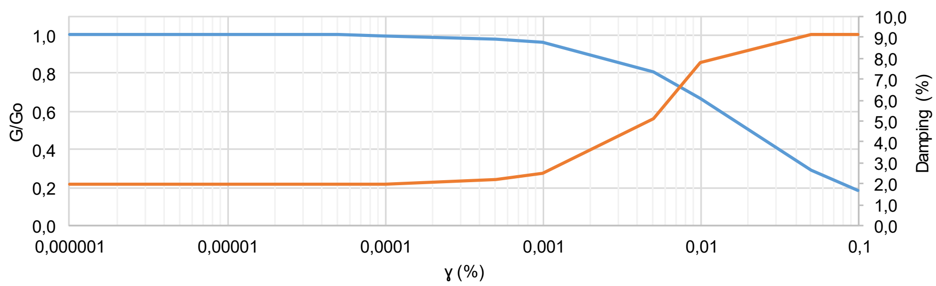

General observations: To obtain the points it is required to perform an iterative process. For each torque valve applied to the specimen, the highest frequency must be searched in different fequency ranges. This process should be excecuted by increasing the applied torque valves until the required deformation is reached.

Zone F

AREA SOIL MECHANICS AND GEOTECHNICS

Resonant Column Test

Borehole:	PCQ0012	**Type of sample:**	Remolded
Zone:	F	**Stratum:**	1
Depth (m):	5.00-6.00	**Number of test:**	1

Dimensions and properties of sample

Height:	129,86	mm	**σ_3 :**	63,00	kPa
Diameter:	70,50	mm	**Saturated unit weight:**	17,61	kN/m^3
Initial wet weight:	895,43	g	**Dry unit weight:**	12,68	kN/m^3
Dry weight:	750,25	g	**Gs:**	2,60	-
Wet unit weight:	17,33	kN/m^3	**e:**	1,012	-
Initial water content:	19,35	%	**n:**	50,29	%
Final water content:	36,67	%	**S:**	94,26	%
PI:	27	%	**w_{sat}:**	36,67	%

Results

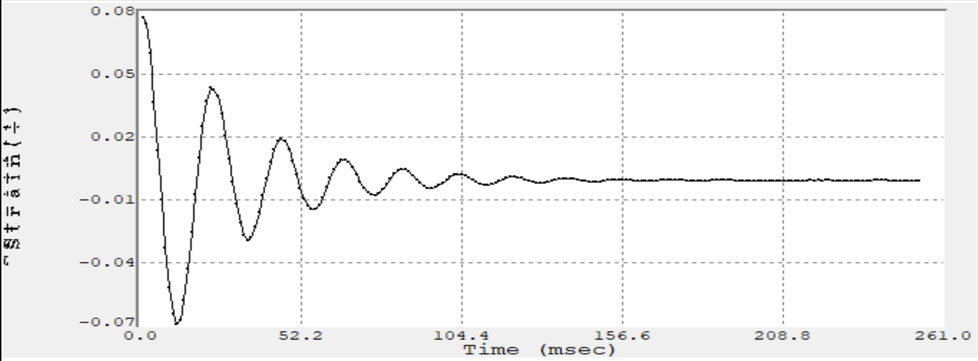

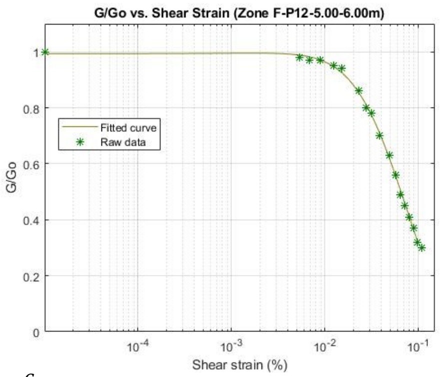

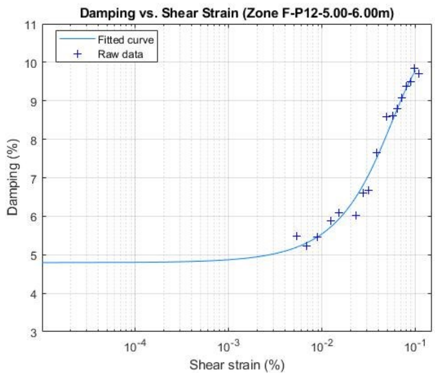

$$\frac{G}{Go} = 1{,}199 * \exp(-13{,}41 * x) - 0{,}206 * \exp(-88{,}7 * x)$$

$$D = 8{,}879/(1 + \exp(-28{,}84 * x) - 0{,}1485)$$

Shear Modulus vs. Shear Strain

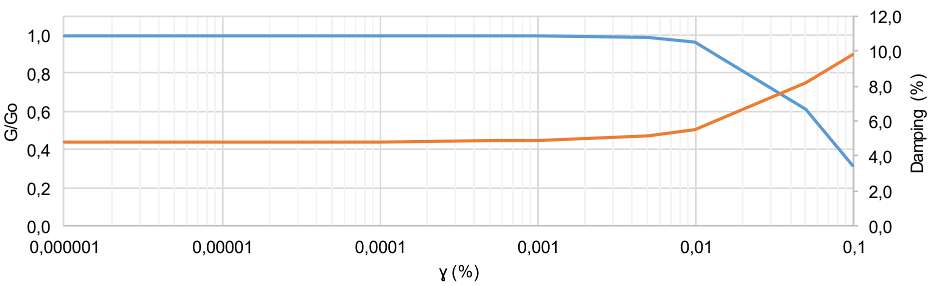

General observations: To obtain the points it is required to perform an iterative process. For each torque valve applied to the specimen, the highest frequency must be searched in different fequency ranges. This process should be excecuted by increasing the applied torque valves until the required deformation is reached.

AREA SOIL MECHANICS AND GEOTECHNICS

Resonant Column Test

Borehole:	PCQ0012	**Type of sample:**	Remolded
Zone:	F	**Stratum:**	2
Depth (m):	11.00-12.00	**Number of test:**	1

Dimensions and properties of sample

Height:	149,62	mm	**σ_3 :**	124,00	kPa
Diameter:	69,43	mm	**Saturated unit weight:**	19,00	kN/m^3
Initial wet weight:	1038,58	g	**Dry unit weight:**	14,93	kN/m^3
Dry weight:	962,15	g	**Gs:**	2,60	-
Wet unit weight:	17,99	kN/m^3	**e:**	0,708	-
Initial water content:	7,94	%	**n:**	41,45	%
Final water content:	20,45	%	**S:**	75,12	%
PI:	15	%	**w_{sat}:**	20,45	%

Results

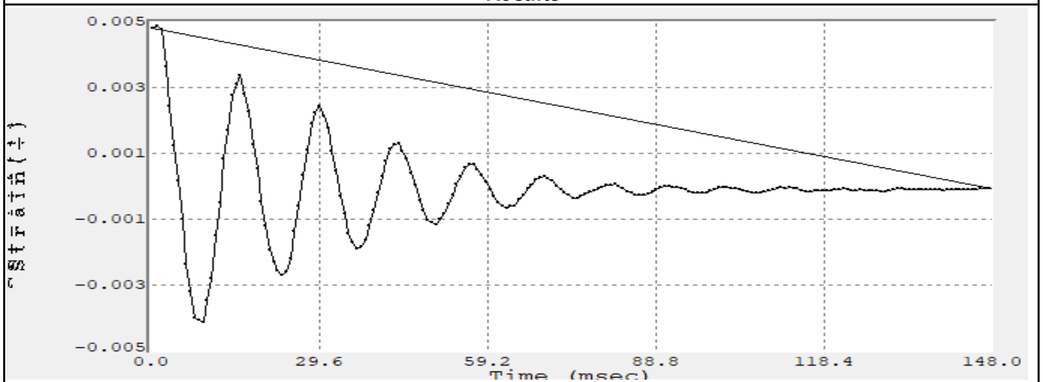

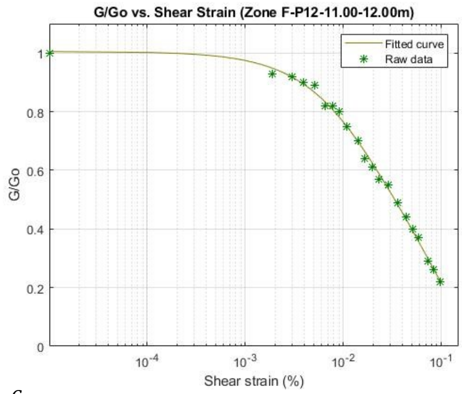

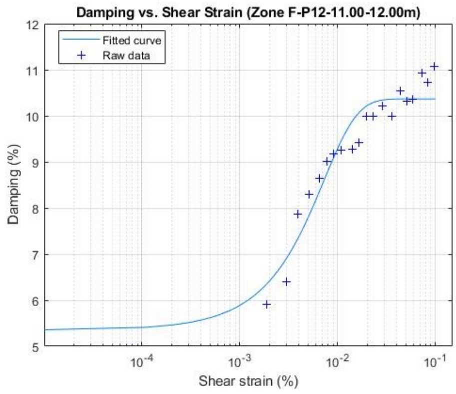

$$\frac{G}{Go} = 0{,}2823 * \exp(-82{,}04 * x) + 0{,}7229 * \exp(-12{,}14 * x)$$

$$D = 11{,}06/(1 + \exp(-208{,}9 * x) - 0{,}06706)$$

Shear Modulus vs. Shear Strain

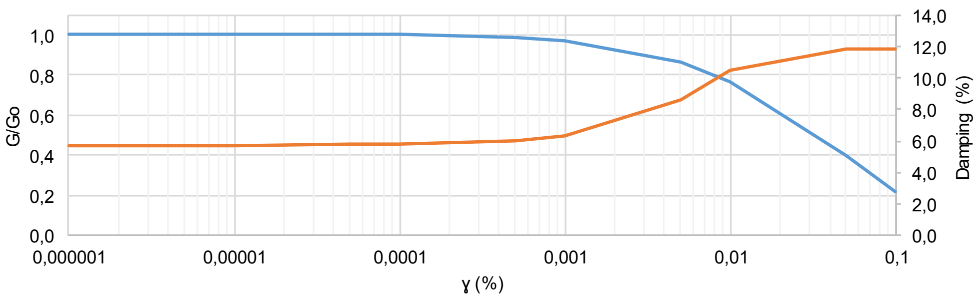

General observations: To obtain the points it is required to perform an iterative process. For each torque valve applied to the specimen, the highest frequency must be searched in different fequency ranges. This process should be excecuted by increasing the applied torque valves until the required deformation is reached.

Zone G

AREA SOIL MECHANICS AND GEOTECHNICS

Resonant Column Test

Borehole:	PCQ0015	**Type of sample:**	Remolded
Zone:	G	**Stratum:**	4
Depth (m):	17.00-18.00	**Number of test:**	1

Dimensions and properties of sample

Height:	142,77	mm	**σ_3 :**	230,00	kPa
Diameter:	71,01	mm	**Saturated unit weight:**	19,30	kN/m^3
Initial wet weight:	1077,91	g	**Dry unit weight:**	15,42	kN/m^3
Dry weight:	1011,63	g	**Gs:**	2,60	-
Wet unit weight:	18,70	kN/m^3	**e:**	0,654	-
Initial water content:	6,55	%	**n:**	39,53	%
Final water content:	21,26	%	**S:**	84,59	%
PI:	3	%	**w_{sat}:**	21,26	%

Results

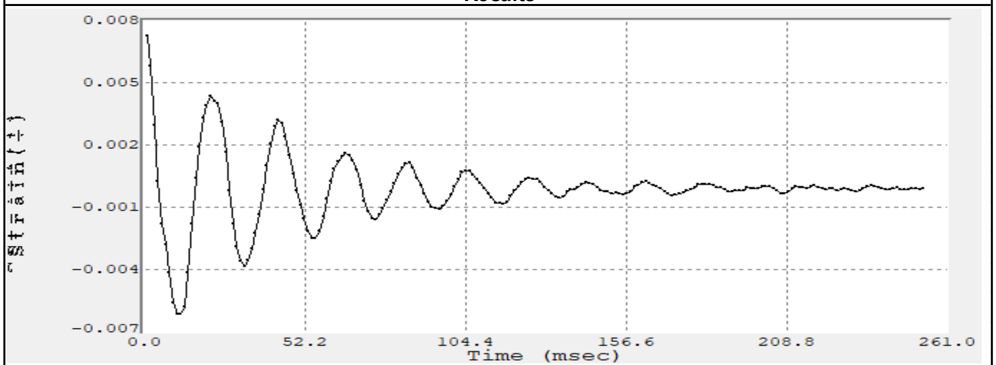

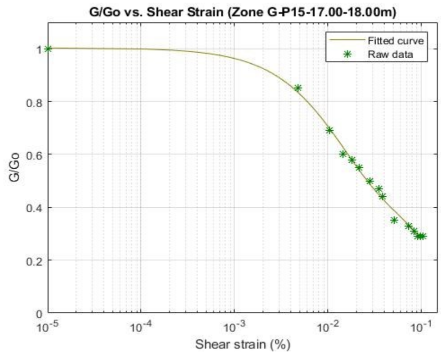

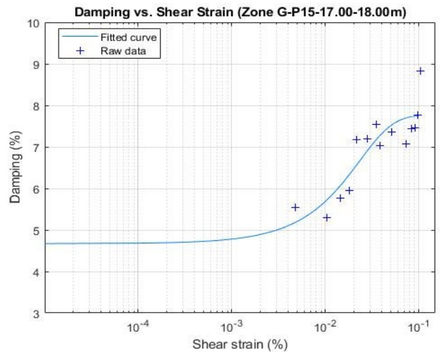

$$\frac{G}{Go} = 0{,}4873 * \exp(-79{,}41 * x) + 0{,}516 * \exp(-6{,}044 * x)$$

$$D = 11{,}72/(1 + \exp(-59{,}55 * x) + 0{,}51)$$

Shear Modulus vs. Shear Strain

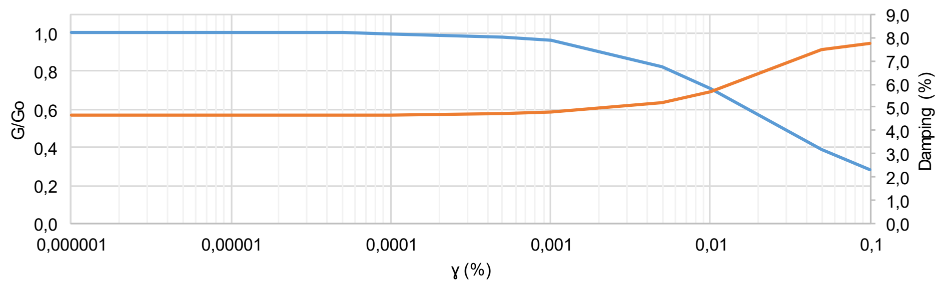

General observations: To obtain the points it is required to perform an iterative process. For each torque valve applied to the specimen, the highest frequency must be searched in different fequency ranges. This process should be excecuted by increasing the applied torque valves until the required deformation is reached.

AREA SOIL MECHANICS AND GEOTECHNICS			
Resonant Column Test			
Borehole:	PCQ0020	**Type of sample:**	Remolded
Zone:	G	**Stratum:**	5
Depth (m):	25.00-26.00	**Number of test:**	1

Dimensions and properties of sample

Height:	133,78	mm	**σ_3 :**	276,00	kPa
Diameter:	70,82	mm	**Saturated unit weight:**	17,80	kN/m^3
Initial wet weight:	850,71	g	**Dry unit weight:**	12,98	kN/m^3
Dry weight:	778,59	g	**Gs:**	2,60	-
Wet unit weight:	15,84	kN/m^3	**e:**	0,966	-
Initial water content:	9,26	%	**n:**	49,12	%
Final water content:	22,04	%	**S:**	59,35	%
PI:	3	%	**w_{sat}:**	22,04	%

Results

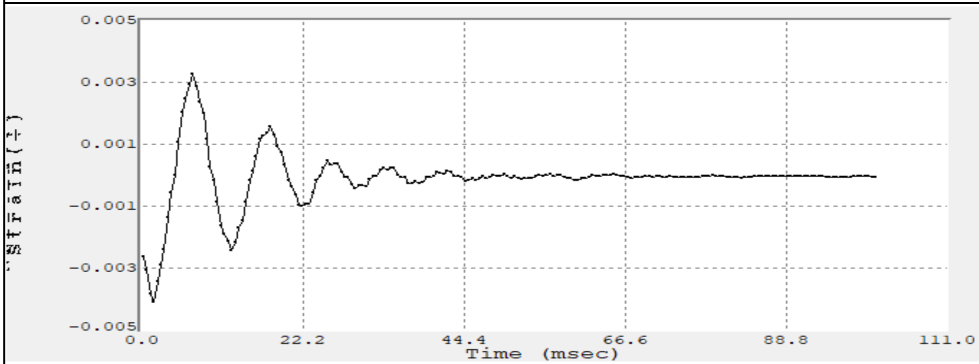

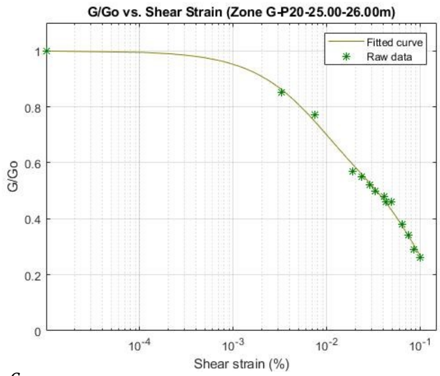

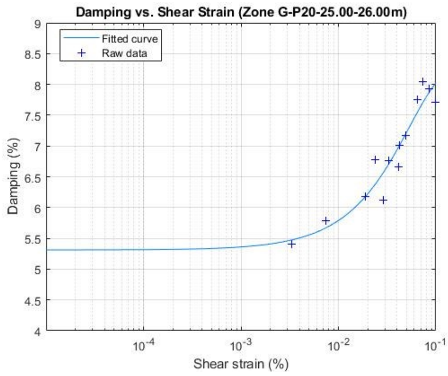

$$\frac{G}{Go} = 0{,}3148 * \exp(-142{,}6 * x) + 0{,}6851 * \exp(-9{,}455 * x)$$

$$D = 14{,}48/(1 + \exp(-25{,}56 * x) + 0{,}7275)$$

Shear Modulus vs. Shear Strain

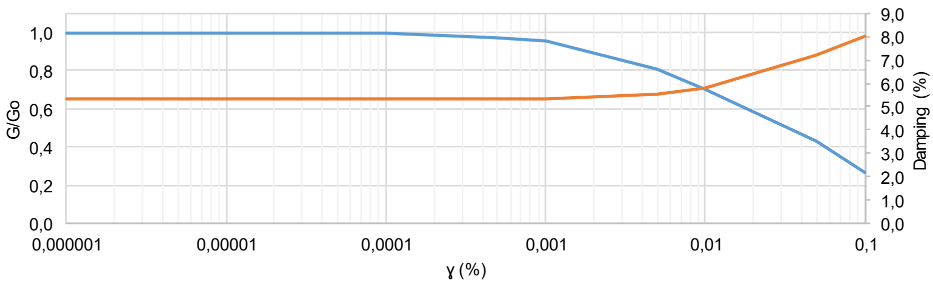

General observations: To obtain the points it is required to perform an iterative process. For each torque valve applied to the specimen, the highest frequency must be searched in different fequency ranges. This process should be excecuted by increasing the applied torque valves until the required deformation is reached.

Zone H

AREA SOIL MECHANICS AND GEOTECHNICS			
Resonant Column Test			
Borehole:	PCQ0017	**Type of sample:**	Remolded
Zone:	H	**Stratum:**	3
Depth (m):	9.00-10.00	**Number of test:**	1

Dimensions and properties of sample

Height:	141,18	mm	σ_3 **:**	270,00	kPa
Diameter:	70,17	mm	**Saturated unit weight:**	19,24	kN/m^3
Initial wet weight:	999,89	g	**Dry unit weight:**	15,33	kN/m^3
Dry weight:	940,81	g	**Gs:**	2,60	-
Wet unit weight:	17,97	kN/m^3	**e:**	0,664	-
Initial water content:	6,28	%	**n:**	39,89	%
Final water content:	17,21	%	**S:**	67,41	%
PI:	0	%	w_{sat}**:**	17,21	%

Results

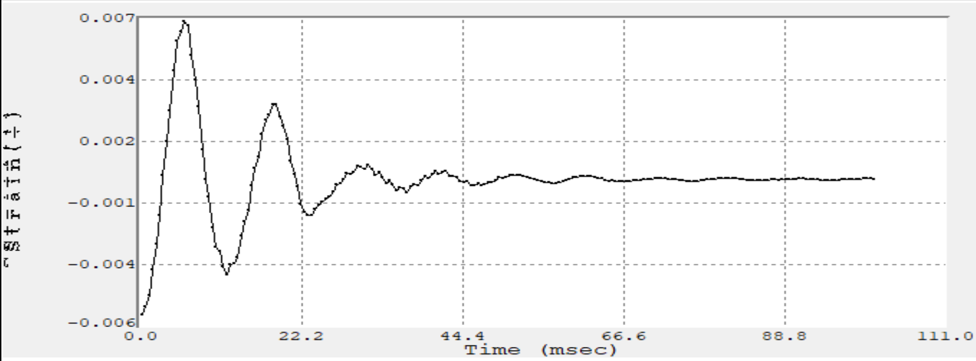

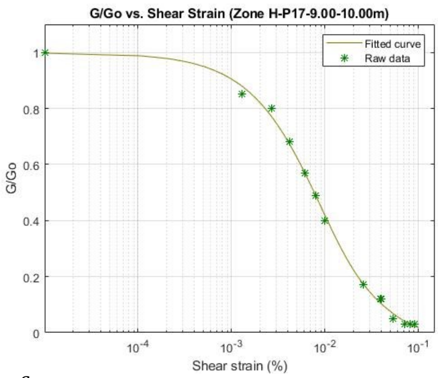

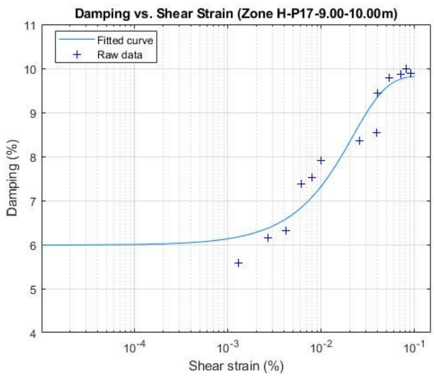

$$\frac{G}{Go} = 0{,}682 * \exp(-132{,}5 * x) + 0{,}3164 * \exp(-28{,}8 * x)$$

$$D = 15{,}31/(1 + \exp(-63{,}07 * x) + 0{,}5576)$$

Shear Modulus vs. Shear Strain

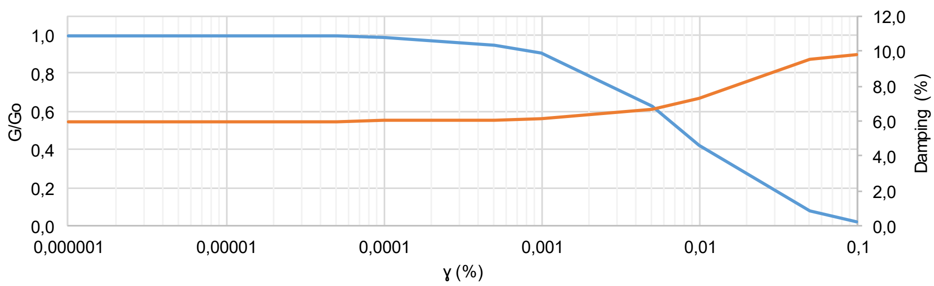

General observations: To obtain the points it is required to perform an iterative process. For each torque valve applied to the specimen, the highest frequency must be searched in different fequency ranges. This process should be excecuted by increasing the applied torque valves until the required deformation is reached.

Zone I

AREA SOIL MECHANICS AND GEOTECHNICS

Resonant Column Test

Borehole:	PCQ0021	**Type of sample:**	Remolded
Zone:	I	**Stratum:**	1
Depth (m):	3.00-4.00	**Number of test:**	1

Dimensions and properties of sample

Height:	139.51	mm	**σ_3 :**	65.00	kPa
Diameter:	70.96	mm	**Saturated unit weight:**	19.67	kN/m^3
Initial wet weight:	1084.05	g	**Dry unit weight:**	16.03	kN/m^3
Dry weight:	1024.52	g	**Gs:**	2.60	-
Wet unit weight:	19.27	kN/m^3	**e:**	0.591	-
Initial water content:	5.81	%	**n:**	37.16	%
Final water content:	20.25	%	**S:**	89.05	%
PI:	5	%	**w_{sat}:**	20.25	%

Results

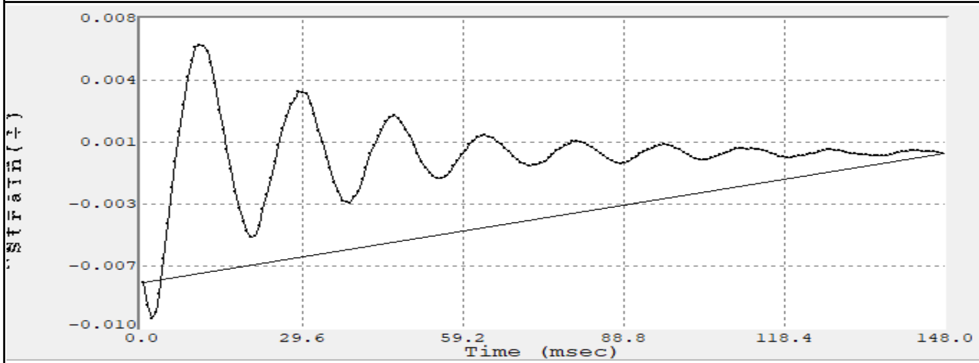

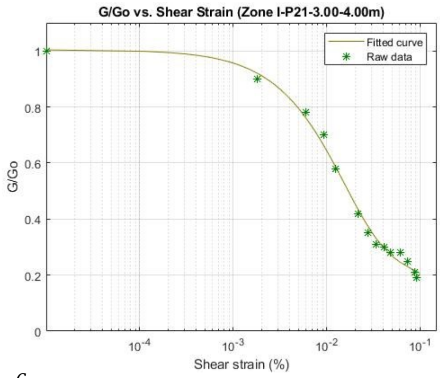

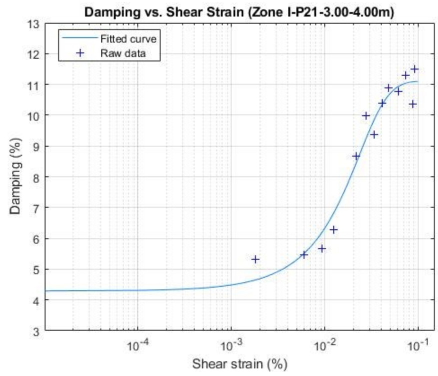

$$\frac{G}{Go} = 0{,}7158 * \exp(-67{,}5 * x) + 0{,}2883 * \exp(-3{,}393 * x)$$

$$D = 6{,}984/(1 + \exp(-74{,}84 * x) - 0{,}3715)$$

Shear Modulus vs. Shear Strain

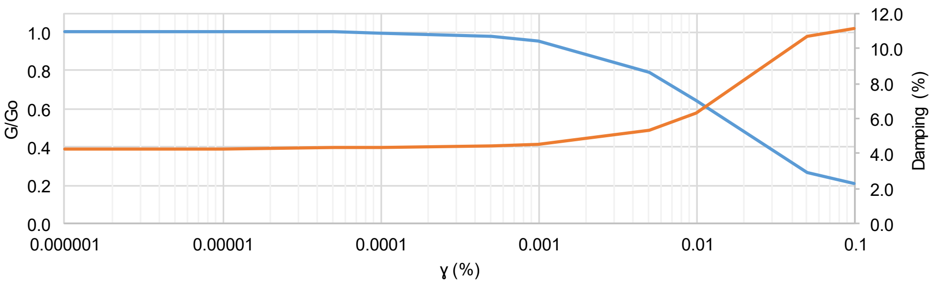

General observations: To obtain the points it is required to perform an iterative process. For each torque valve applied to the specimen, the highest frequency must be searched in different fequency ranges. This process should be excecuted by increasing the applied torque valves until the required deformation is reached.

AREA SOIL MECHANICS AND GEOTECHNICS

Resonant Column Test

Borehole:	PCQ0018	**Type of sample:**	Remolded
Zone:	I	**Stratum:**	3
Depth (m):	12.00-13.00	**Number of test:**	1

Dimensions and properties of sample

Height:	140,77	mm	**σ_3 :**	113,00	kPa
Diameter:	68,98	mm	**Saturated unit weight:**	18,02	kN/m^3
Initial wet weight:	859,40	g	**Dry unit weight:**	13,34	kN/m^3
Dry weight:	778,14	g	**Gs:**	2,60	-
Wet unit weight:	16,03	kN/m^3	**e:**	0,912	-
Initial water content:	10,44	%	**n:**	47,70	%
Final water content:	20,15	%	**S:**	57,44	%
PI:	6	%	**w_{sat}:**	20,15	%

Results

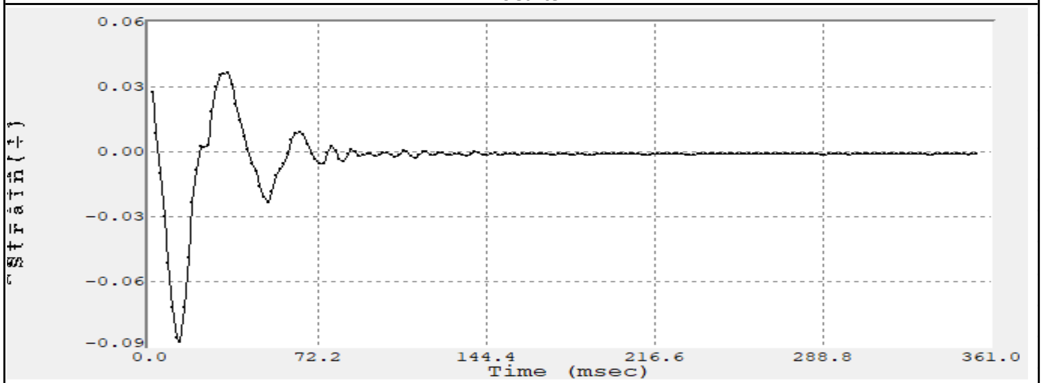

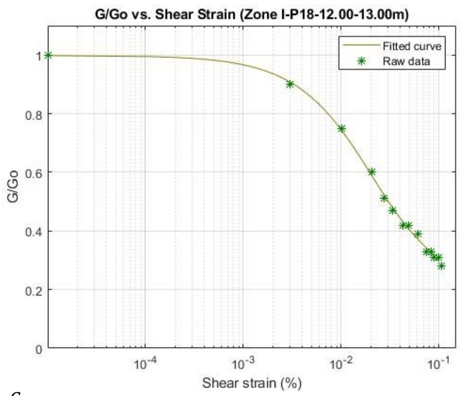

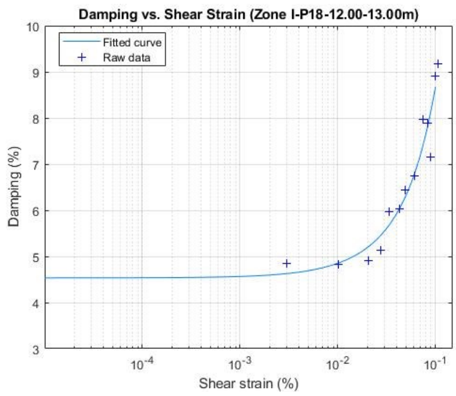

$$\frac{G}{Go} = 0{,}5244 * \exp(-58{,}18 * x) + 0{,}4738 * \exp(-4{,}658 * x)$$

$$D = 5{,}029/(1 + \exp(-7{,}537 * x) - 0{,}8907)$$

Shear Modulus vs. Shear Strain

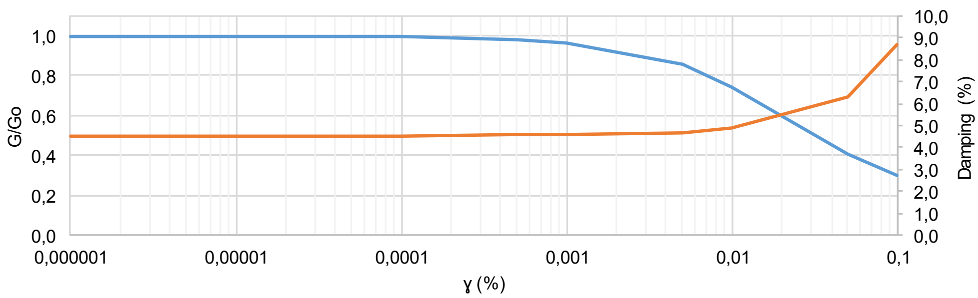

General observations: To obtain the points it is required to perform an iterative process. For each torque valve applied to the specimen, the highest frequency must be searched in different fequency ranges. This process should be excecuted by increasing the applied torque valves until the required deformation is reached.

AREA SOIL MECHANICS AND GEOTECHNICS

Resonant Column Test

Borehole:	PCQ0018	**Type of sample:**	Remolded
Zone:	I	**Stratum:**	4
Depth (m):	14.00-15.00	**Number of test:**	1

Dimensions and properties of sample

Height:	137,97	mm	**σ_3 :**	206,00	kPa
Diameter:	70,15	mm	**Saturated unit weight:**	16,84	kN/m^3
Initial wet weight:	786,64	g	**Dry unit weight:**	11,43	kN/m^3
Dry weight:	680,32	g	**Gs:**	2,60	-
Wet unit weight:	14,47	kN/m^3	**e:**	1,232	-
Initial water content:	15,63	%	**n:**	55,20	%
Final water content:	26,64	%	**S:**	56,22	%
PI:	10	%	**w_{sat}:**	26,64	%

Results

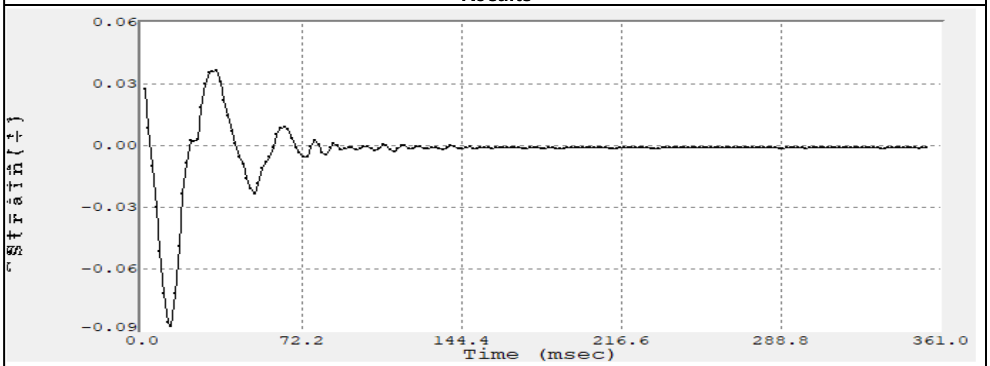

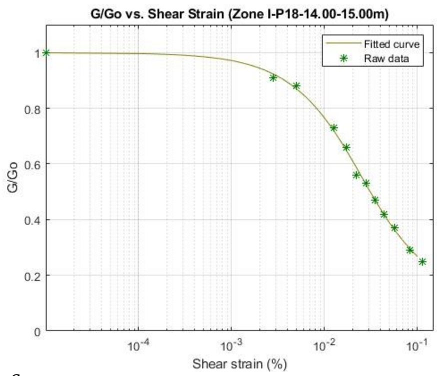

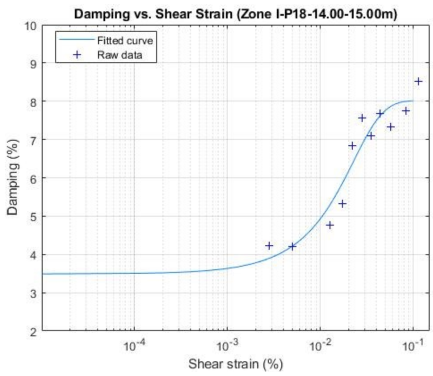

$$\frac{G}{Go} = 0{,}5751 * \exp(-46{,}51 * x) + 0{,}4241 * \exp(-4{,}824 * x) \qquad D = 6{,}174/(1 + \exp(-72{,}98 * x) - 0{,}2302)$$

Shear Modulus vs. Shear Strain

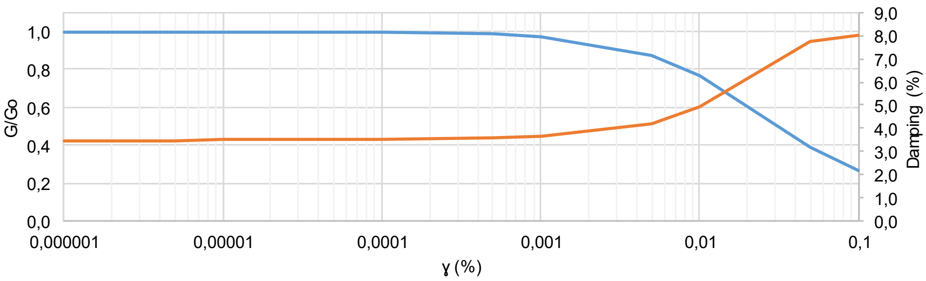

General observations: To obtain the points it is required to perform an iterative process. For each torque valve applied to the specimen, the highest frequency must be searched in different fequency ranges. This process should be excecuted by increasing the applied torque valves until the required deformation is reached.

AREA SOIL MECHANICS AND GEOTECHNICS

Resonant Column Test

Borehole:	PCQ0018	**Type of sample:**	Remolded
Zone:	I	**Stratum:**	4
Depth (m):	28.00-29.00	**Number of test:**	1

Dimensions and properties of sample

Height:	140.15	mm	**σ_3 :**	244.00	kPa
Diameter:	71.02	mm	**Saturated unit weight:**	18.96	kN/m^3
Initial wet weight:	1042.54	g	**Dry unit weight:**	14.88	kN/m^3
Dry weight:	831.73	g	**Gs:**	2.60	-
Wet unit weight:	18.42	kN/m^3	**e:**	0.715	-
Initial water content:	25.35	%	**n:**	41.68	%
Final water content:	23.84	%	**S:**	86.74	%
PI:	22	%	**w_{sat}:**	23.84	%

Results

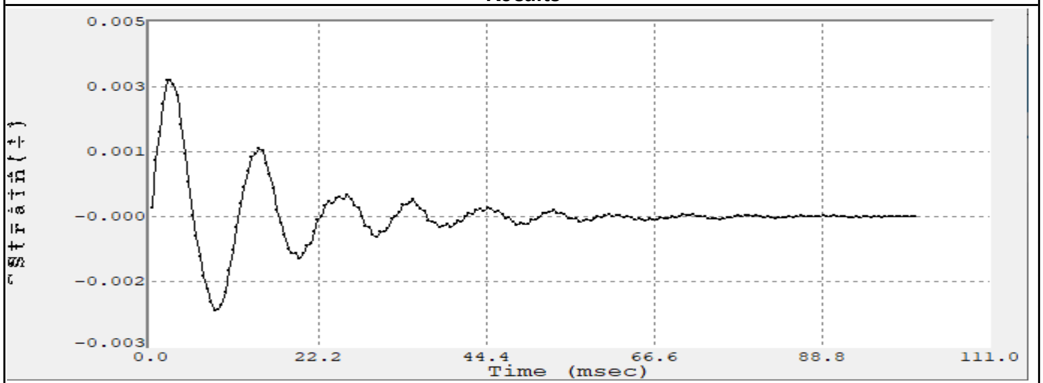

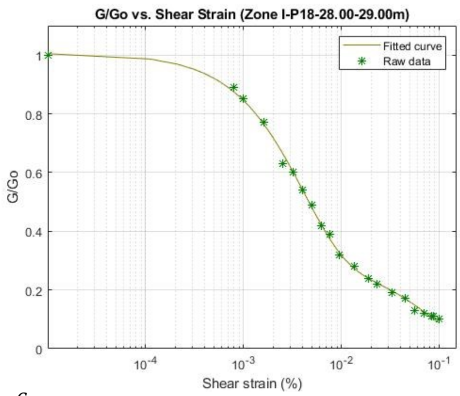

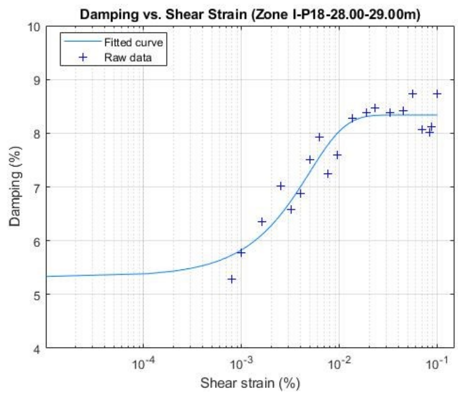

$$\frac{G}{Go} = 0{,}713 * \exp(-250{,}1 * x) + 0{,}2933 * \exp(-12{,}18 * x)$$

$$D = 14{,}76/(1 + \exp(-271{,}6 * x) + 0{,}7707)$$

Shear Modulus vs. Shear Strain

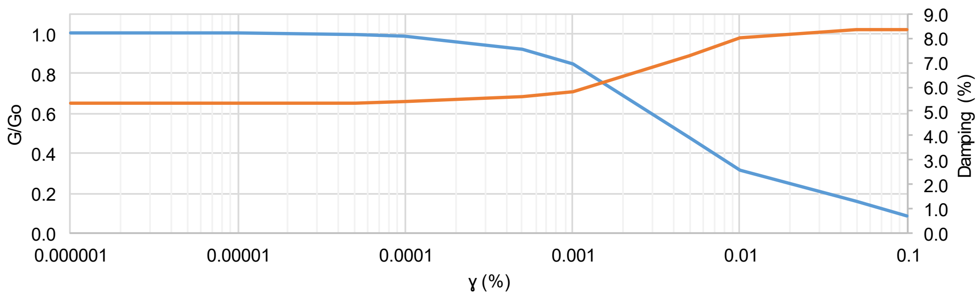

General observations: To obtain the points it is required to perform an iterative process. For each torque valve applied to the specimen, the highest frequency must be searched in different fequency ranges. This process should be excecuted by increasing the applied torque valves until the required deformation is reached.

APPENDIX C – DEEPSOIL software analysis and results

C.1. Use of DEEPSOIL software

To start using DeepSoil we must first define the soil columns to be analyzed (see chapter 5.2.1).

The first step to create a new profile in DEEPSOIL is defining the following information:

- Analysis method
- Solution type
- Default soil model
- Default hysteretic Re/Unloading formulation
- Unit system

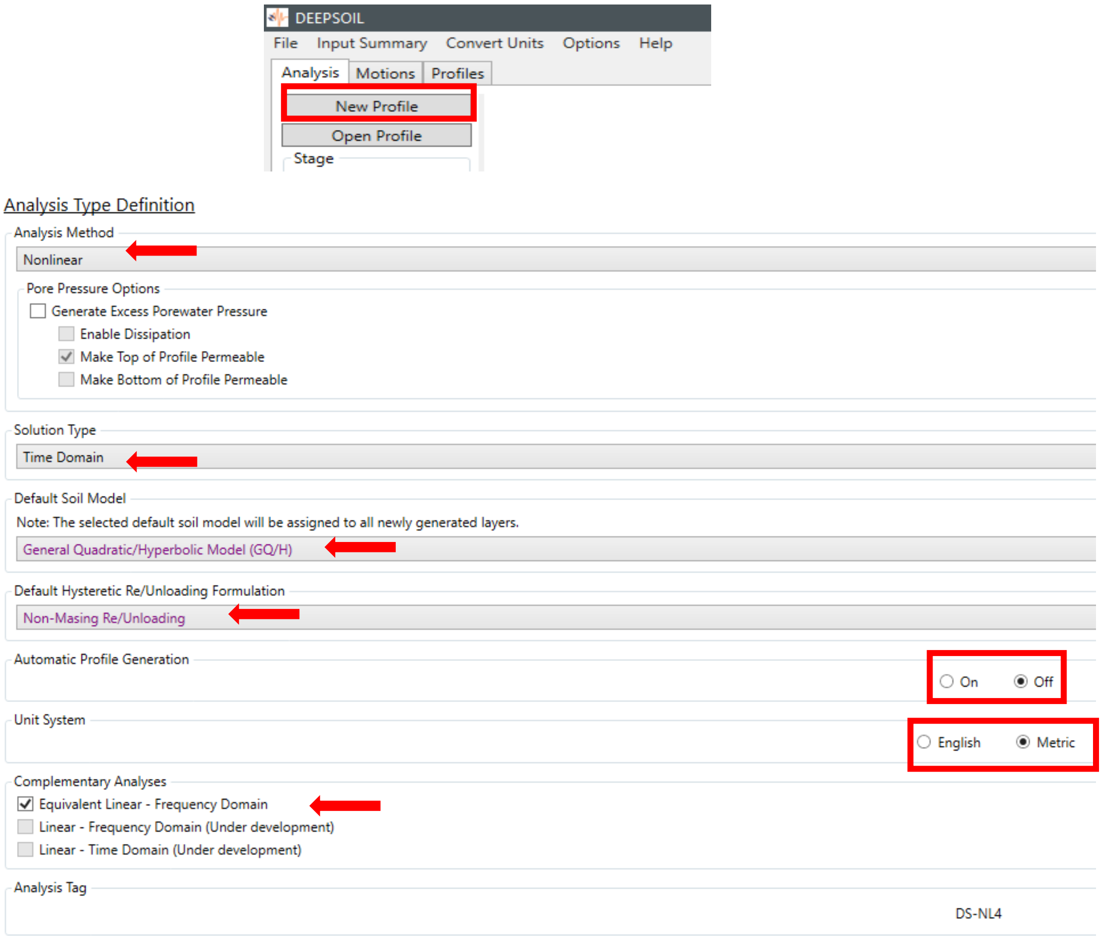

Figure 307. First step to use DEEPSOIL.

To describe the steps to follow to enter the information from a soil column in DEEPSOIL, we used the soil column of Zone A.

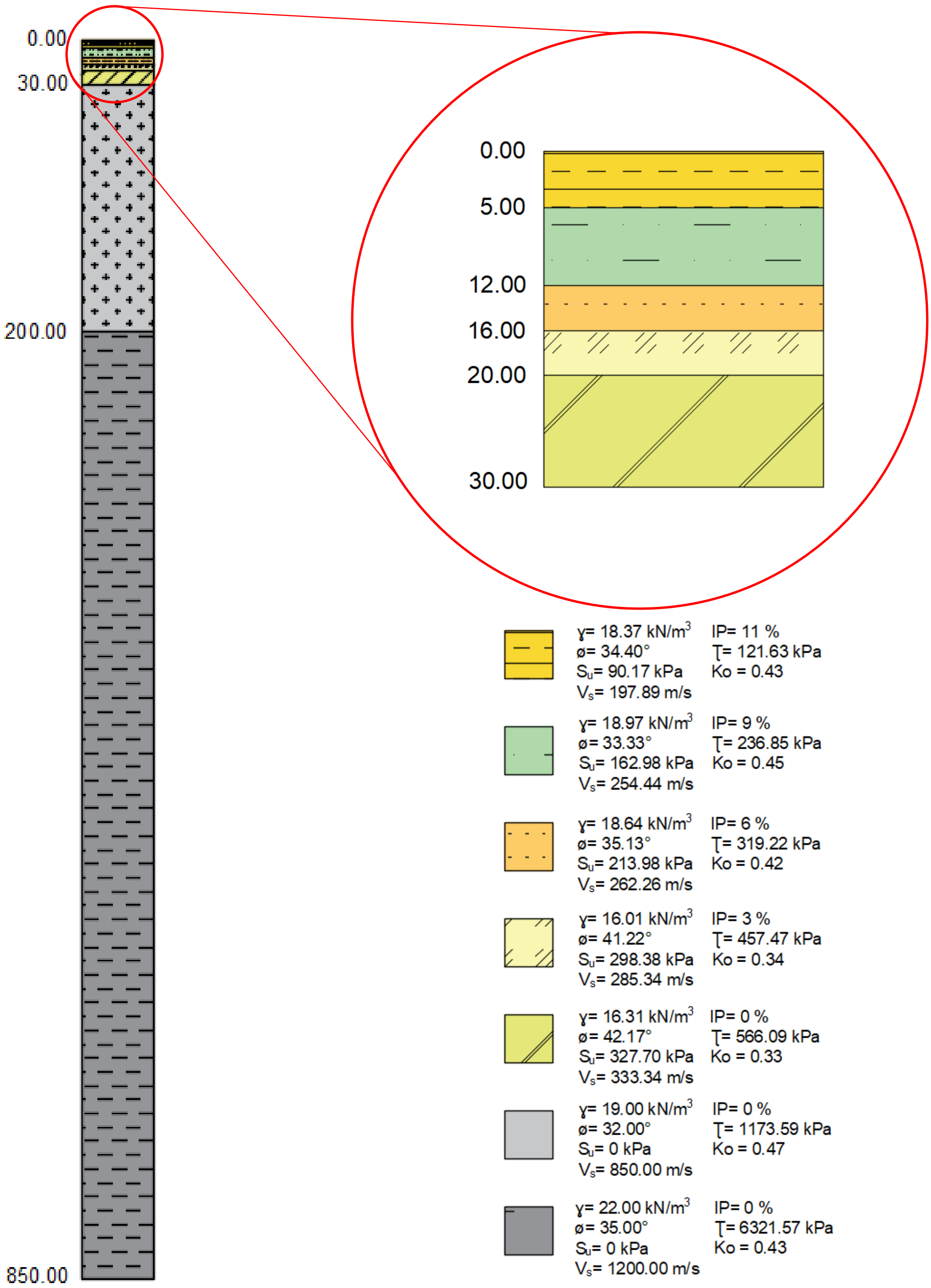

Figure 308. Profile of soil column of Zone A

Table 54. Information about soil colum of Zone A

Zone A									
Depth (m)	**Width (m)**	**γ (kN/m^3)**	**φ (°)**	**Su (kPa)**	**Vs (m/s)**	**$\sigma_{m\ prom}$ (kPa)**	**τ (kPa)**	**Ko**	**PI (%)**
1.00	5.00	18.37	34.40	90.17	197.89	45.94	121.63	0.43	11
5.00									
6.00	7.00	18.97	33.33	162.98	254.44	112.32	236.85	0.45	9
12.00									
13.00	4.00	18.64	35.13	213.98	262.26	149.60	319.22	0.42	6
16.00									
17.00	4.00	16.01	41.22	298.38	285.34	181.61	457.47	0.34	3
20.00									
21.00	10.00	16.31	42.17	327.70	333.34	263.14	566.09	0.33	0
30.00									
31.00	170.00	19.00	32.00	0.00	850.00	1878.14	1173.59	0.47	0
200.00									
201.00	650.00	22.00	35.00	0.00	1200.00	9028.14	6321.57	0.43	0
850.00									

Once the first step is completed, we have to enter the basic soil properties about each stratum composing the soil column.

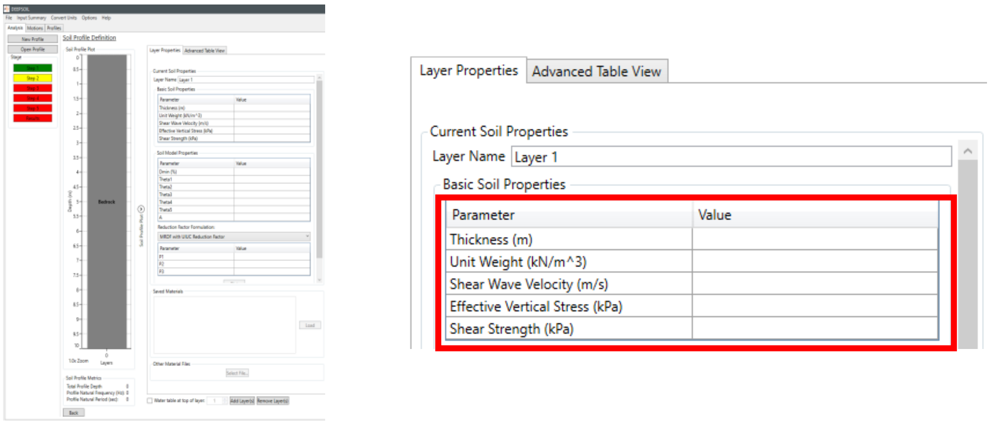

Figure 309. Data input in DEEPSOIL per each stratum.

Next, we must generate or enter the reference curve to define the dynamic properties of each layer. We can choose between theoretical or user-defined reference curves. Depending on the analysis we consider, we can select one of them for the analysis.

For this case we considered a user defined reference curve and obtained the following information, after this step we have to do a curve fitting to determine the dynamic properties of the soil that we will use during the analysis for this stratum.

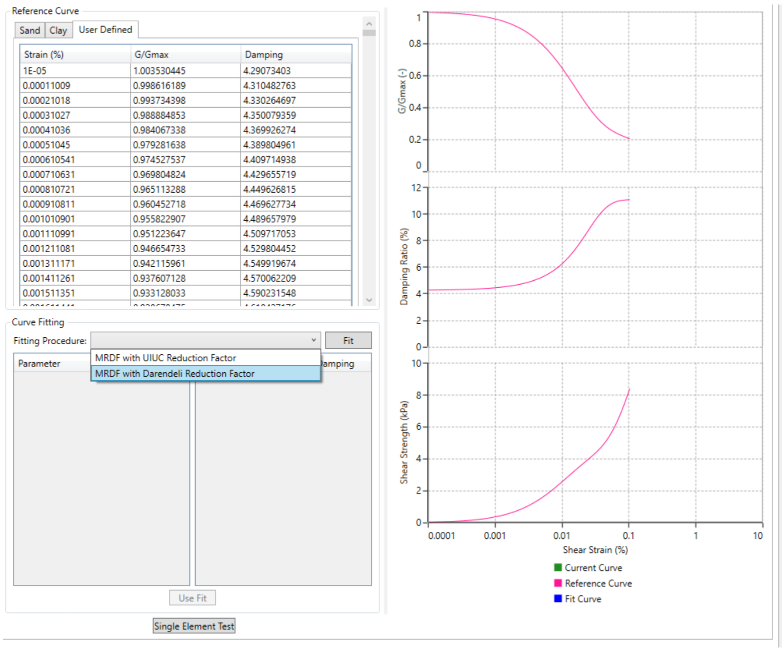

Figure 310. User-defined data input.

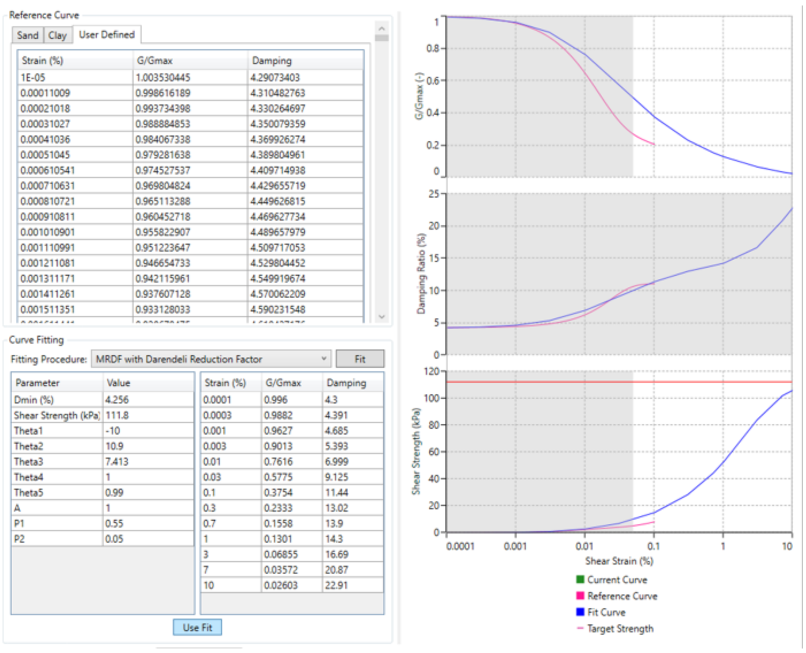

Figure 311. Results after curve fitting.

Once the curve fitting results have been obtained, select *"Use Fitting"* to define the Soil Model properties for each stratum. And continue this process for each stratum until the soil column is completed.

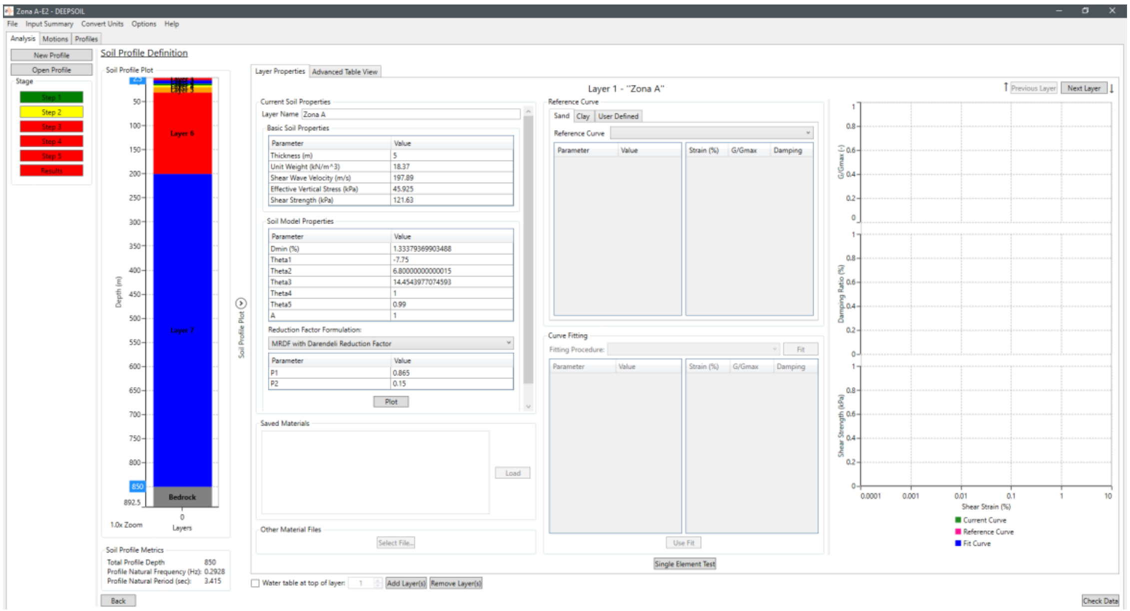

Figure 312. Soil column completed.

Before checking the data, we have to select the *"Rigid halfspace"* for the bedrock, then we press *"Check data"* to obtain the following information:

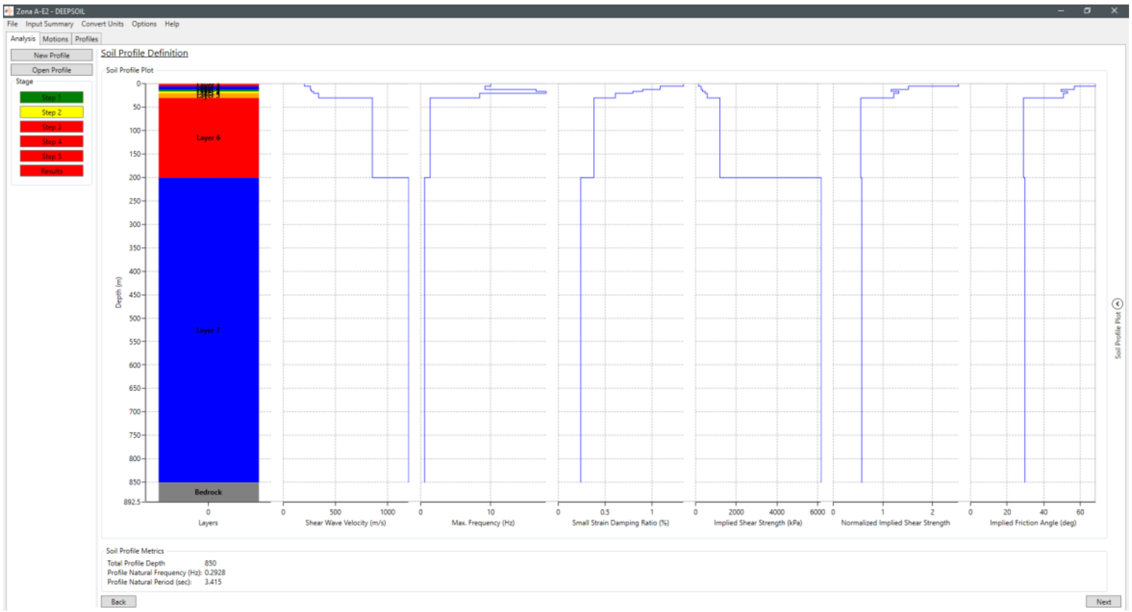

Figure 313. Soil profile definition

Then, we have to select the input motions that we consider during the analysis. These input flows are defined in section 5.3. We obtain the following screen:

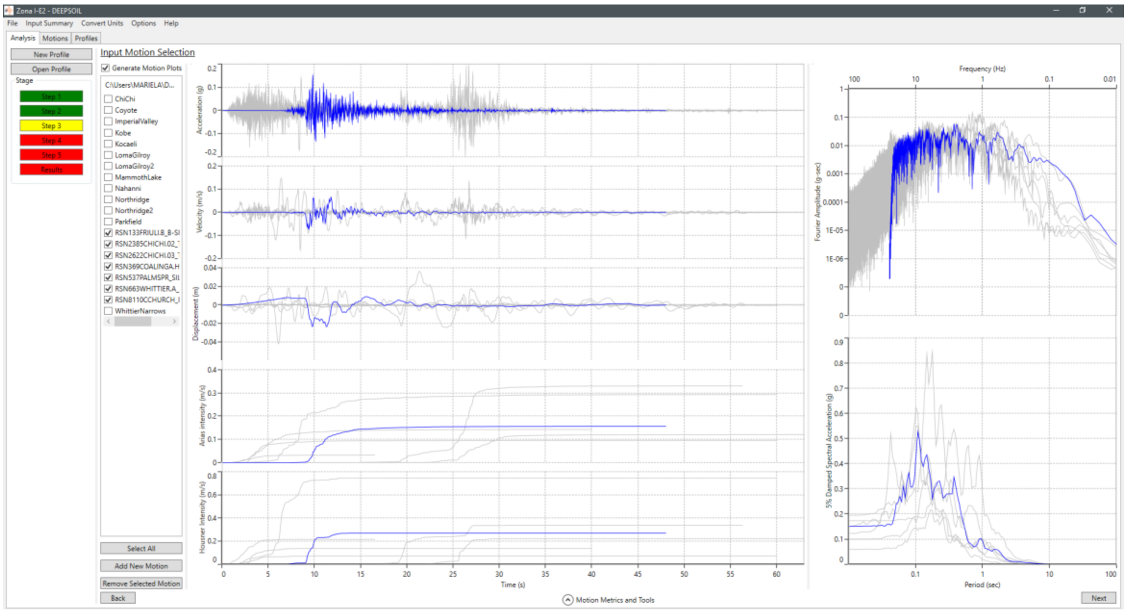

Figure 314. Selection of input motions for analysis

Summary results of response spectra for each input motion selected for analysis are also presented.

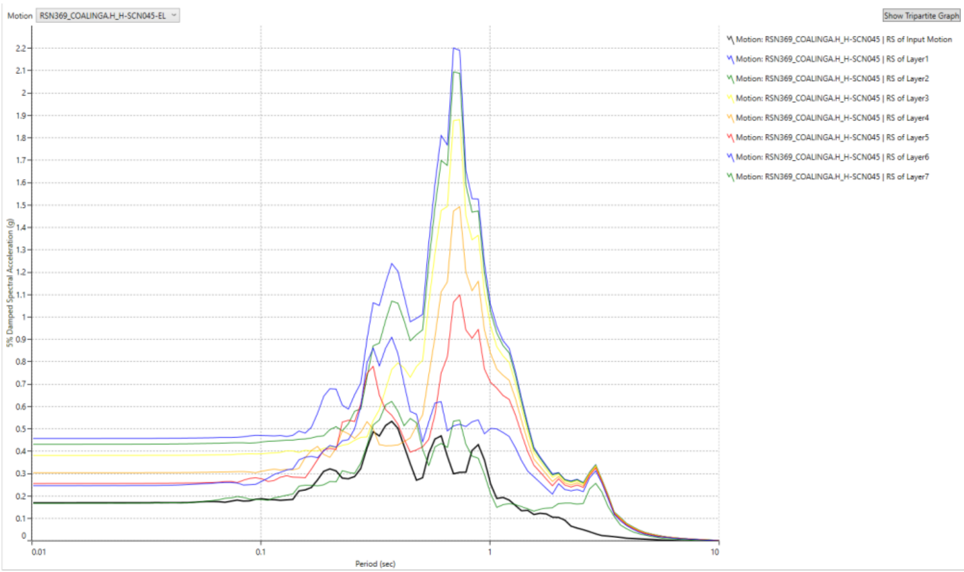

Figure 315. Responde spectra summary of all layers for one input motion.

Finally, we analyze all layers for each input movement and obtain the results. These results can be exported to EXCEL.

The results obtained in zone A are as follows:

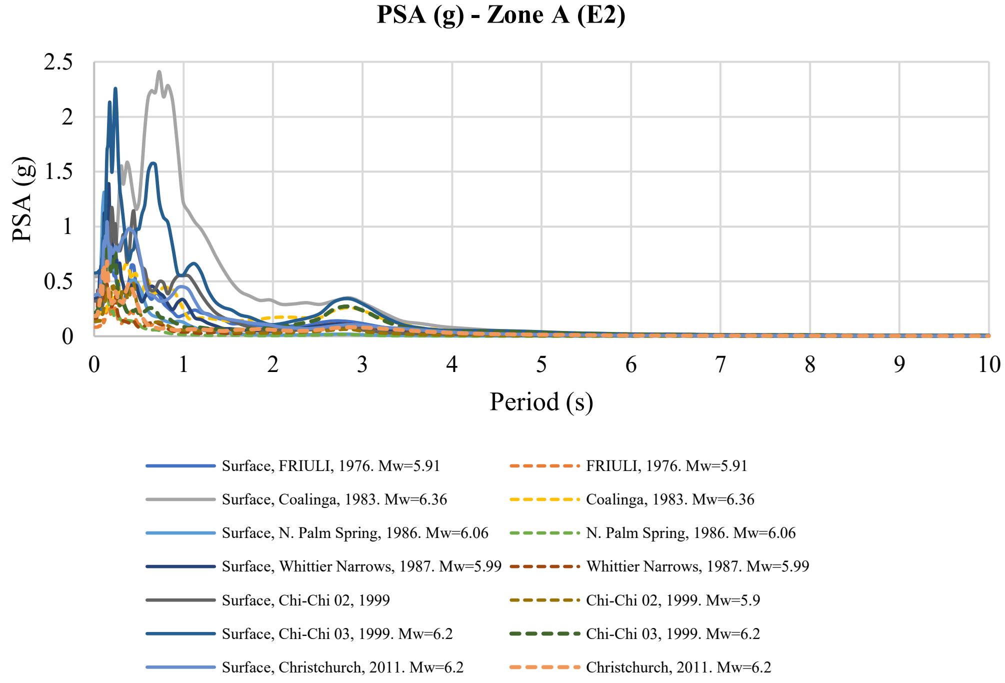

Figure 316. PSA (g) results of Zone A for each input motion.

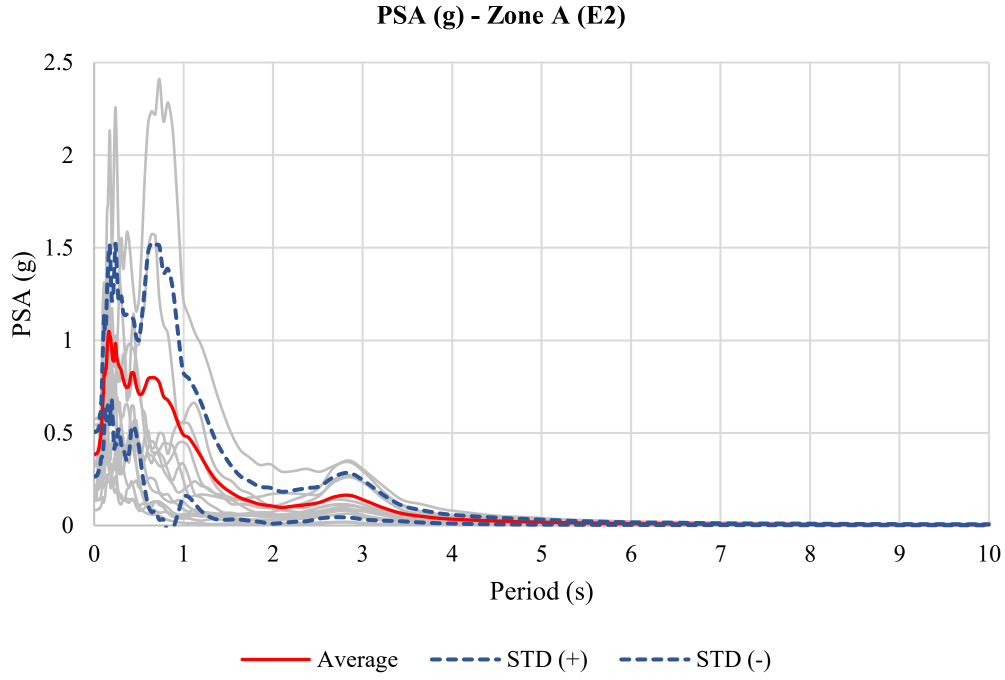

Figure 317. Average of PSA (g) - Zone A

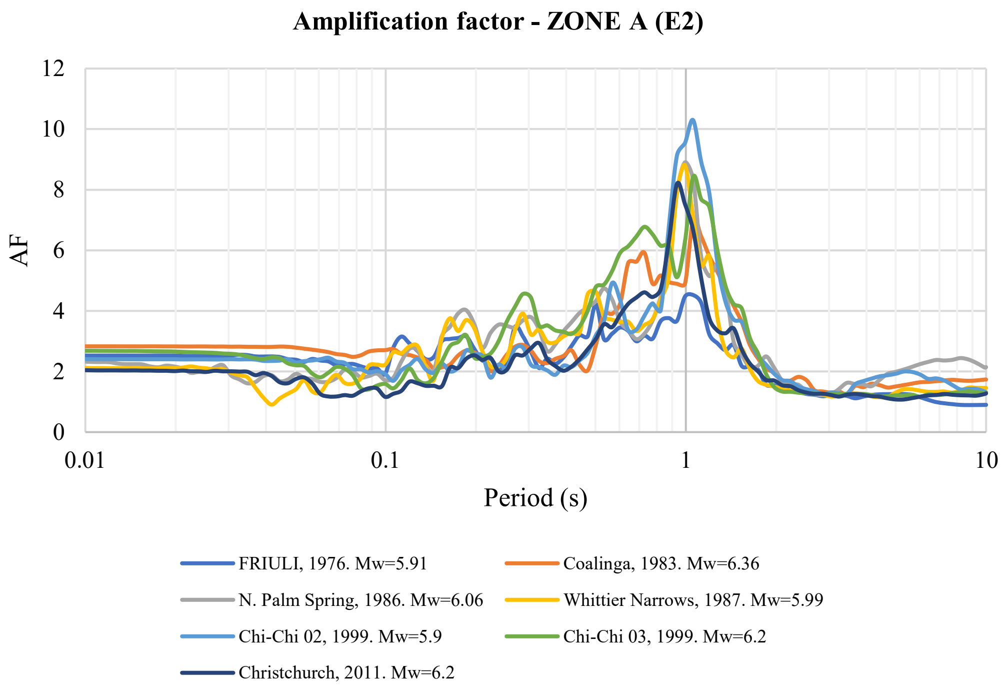

Figure 318. Amplification factor results for Zone A for each input motion

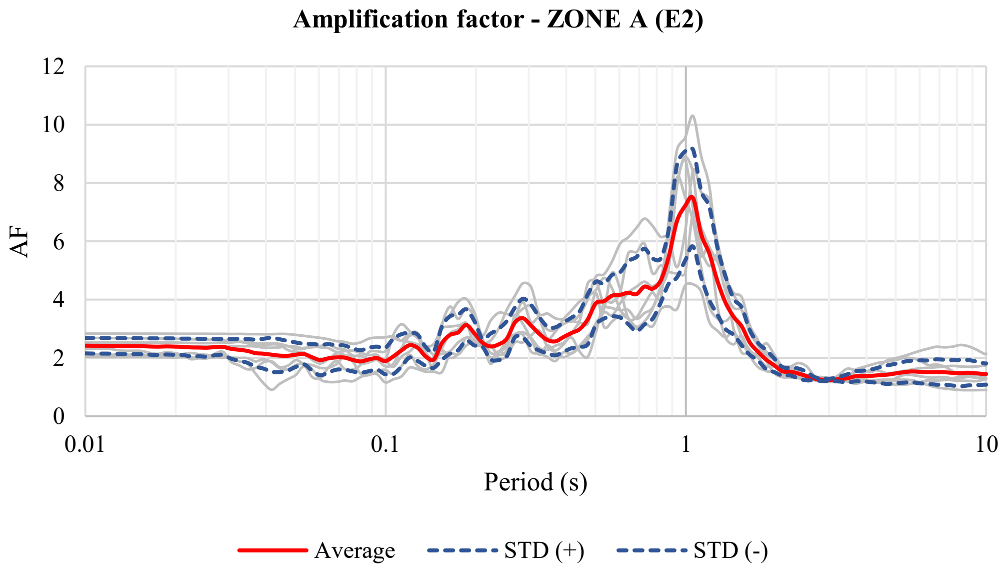

Figure 319. Average of Amplification factor for Zone A (Period)

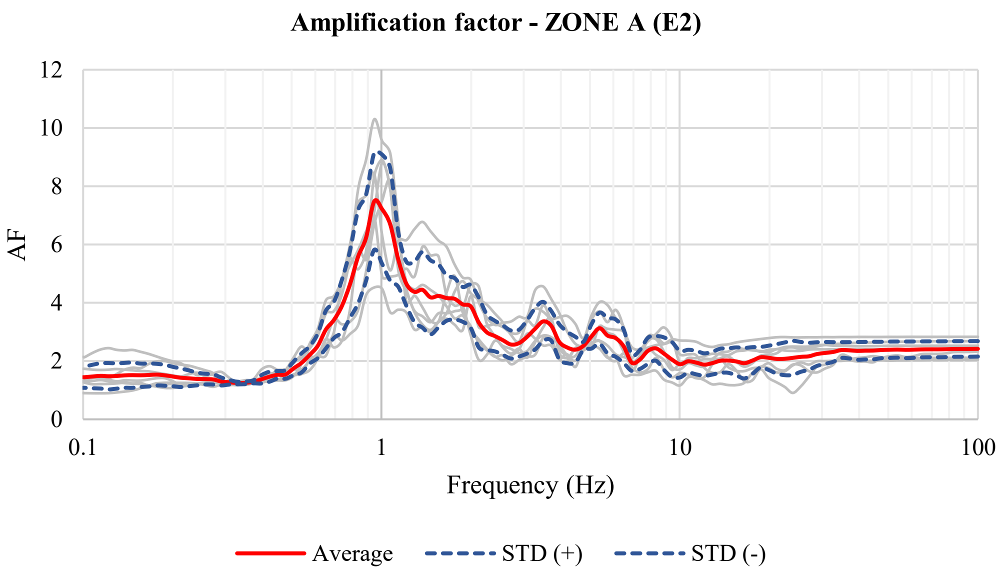

Figure 320. Average of Amplification factor for Zone A (Frequency)

C.2. Results for theoretical and experimental curves

C.2.1. Analysis with theoretical curves

- Zone A

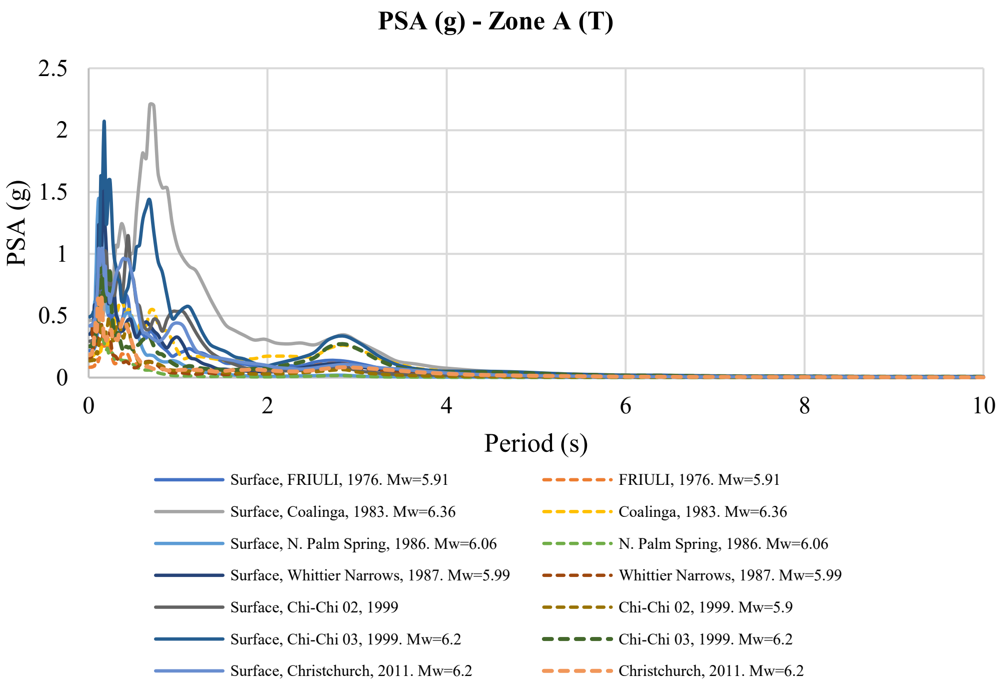

Figure 321. PSA (g) for theoretical curves of Zone A

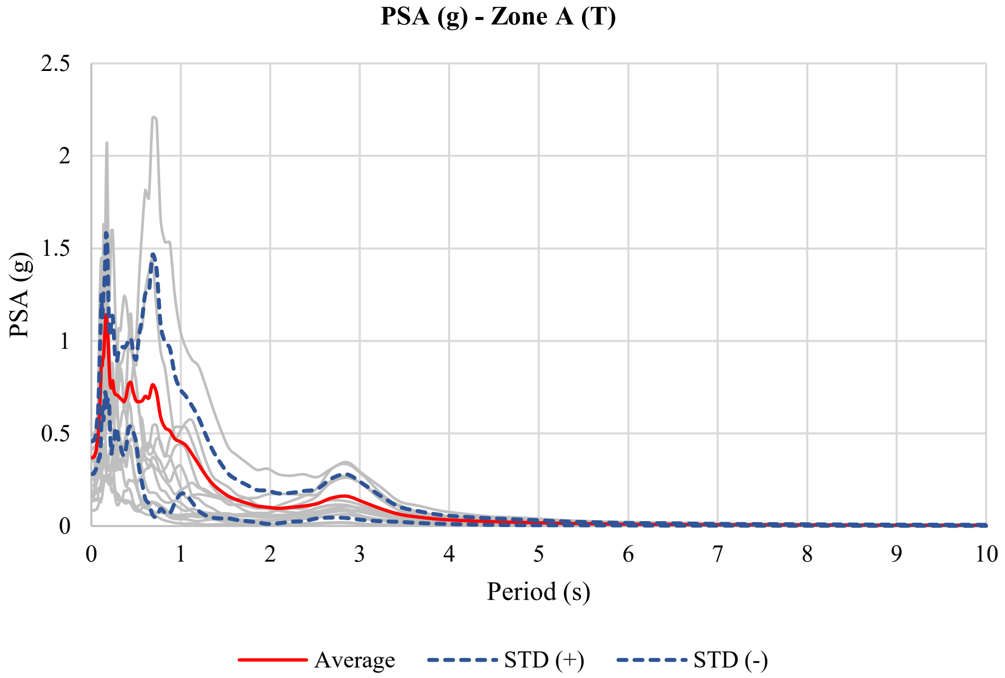

Figure 322. PSA (g) average for theoretical curves of Zone A

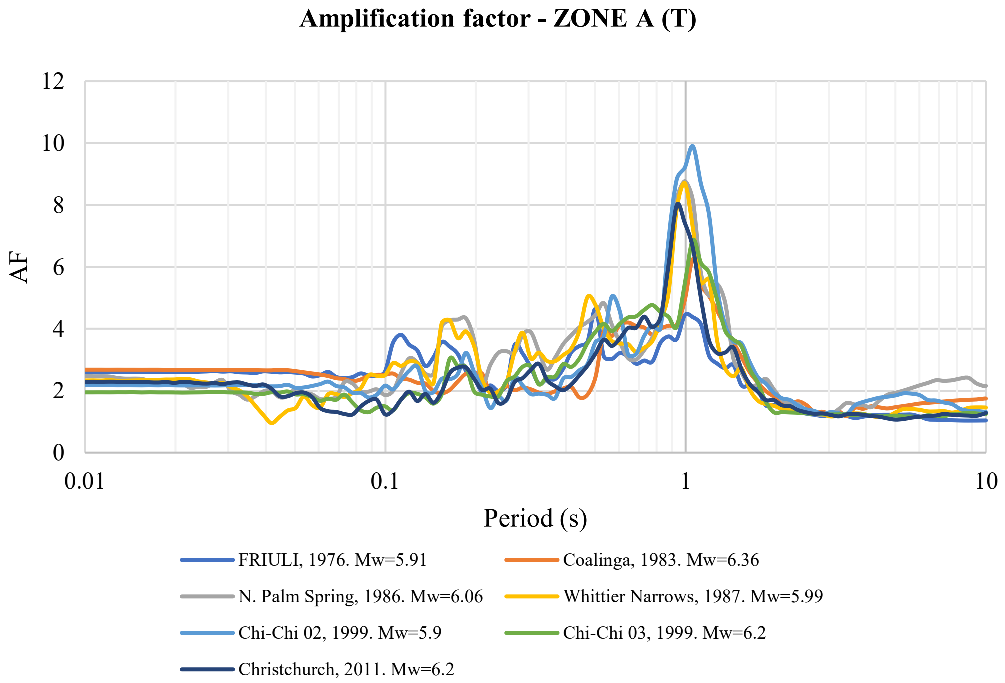

Figure 323. Amplification factor for theoretical curves of Zone A

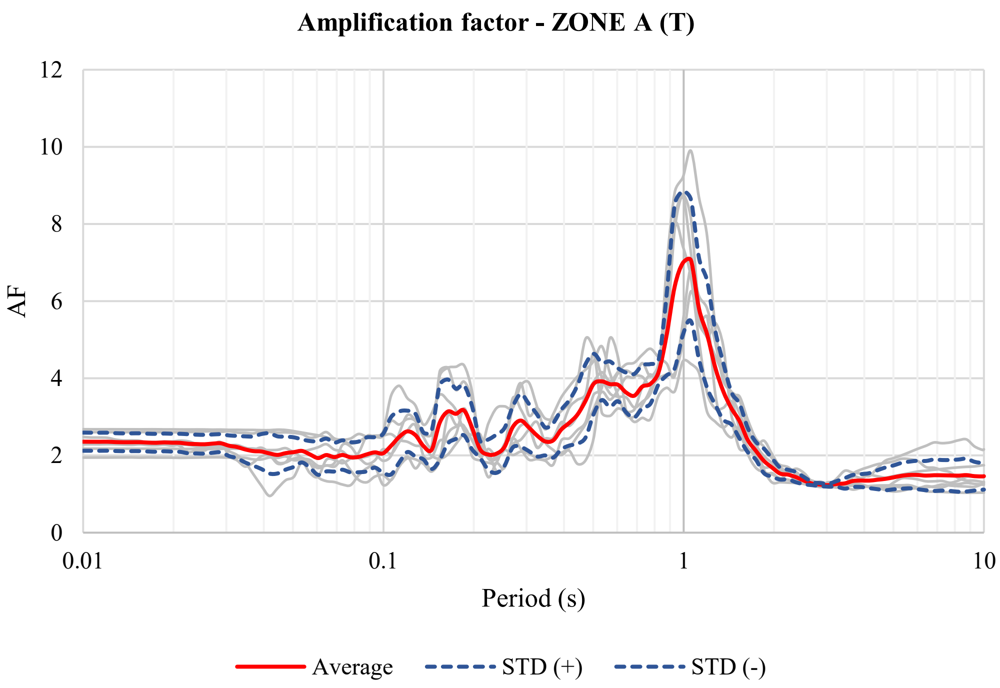

Figure 324. Amplification factor average for theoretical curves of Zone A (Period)

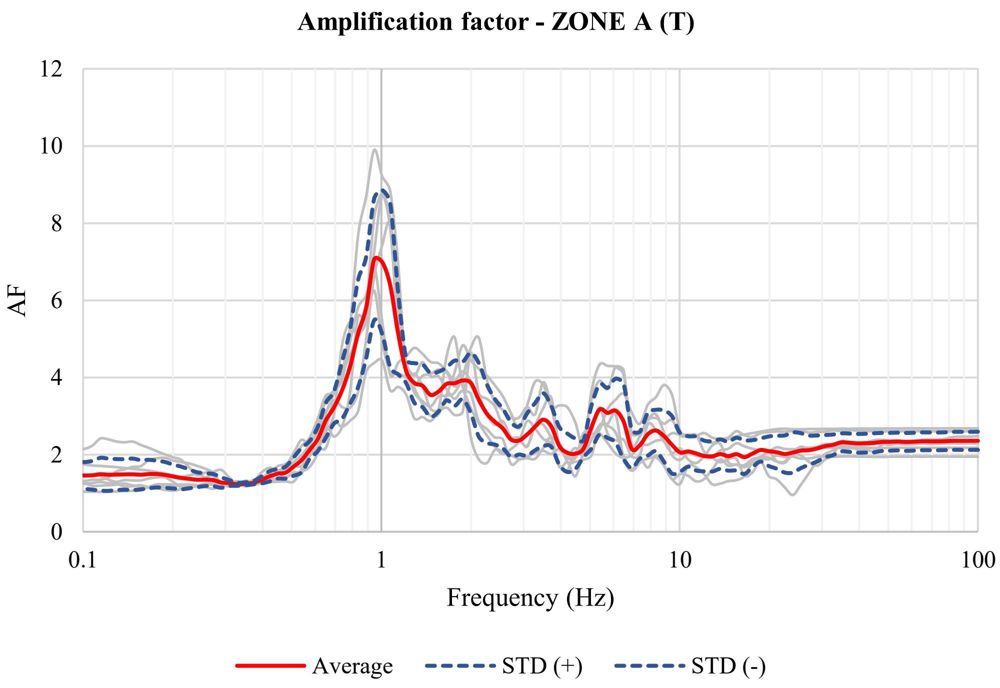

Figure 325. Amplification factor average for theoretical curves of Zone A (Frequency)

Table 55. Maximun values of Amplification factor for theoretical curves of Zone A

Zone A (T)			
	Amplification factor	T (s)	F (Hz)
1	7.06	1.06	0.95
2	6.99	0.99	1.01
3	6.38	0.93	1.07

- Zone B

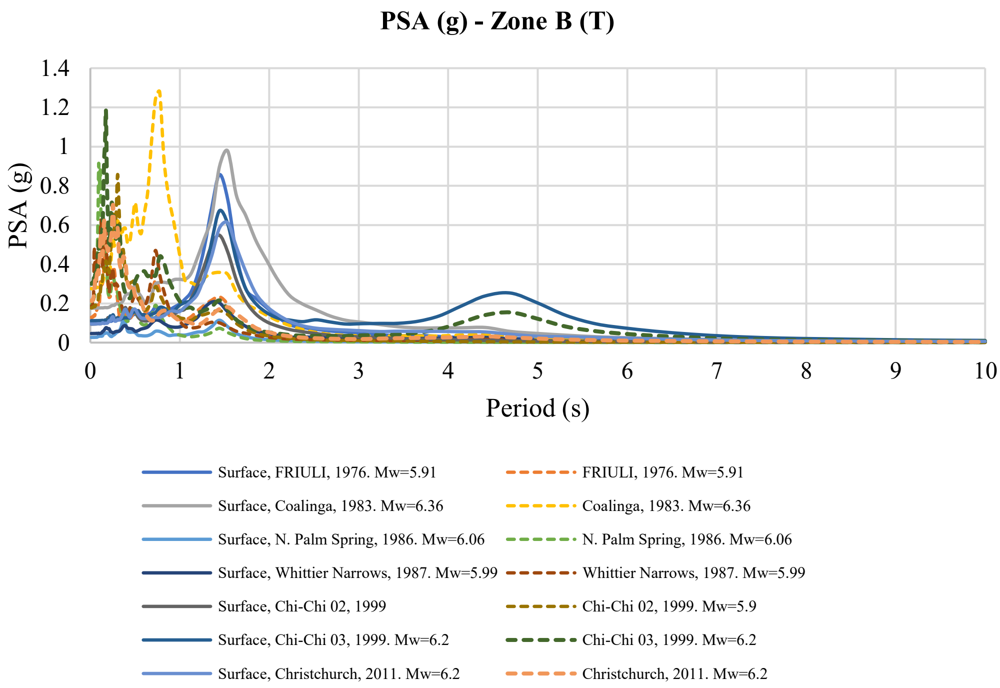

Figure 326. PSA (g) for theoretical curves of Zone B

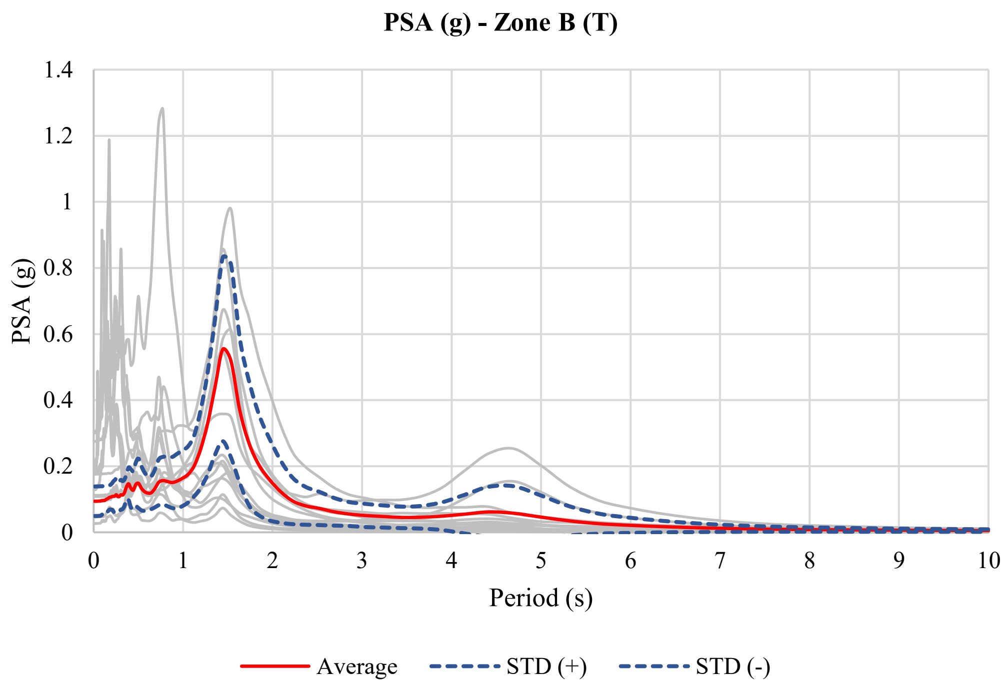

Figure 327. PSA (g) average for theoretical curves of Zone B

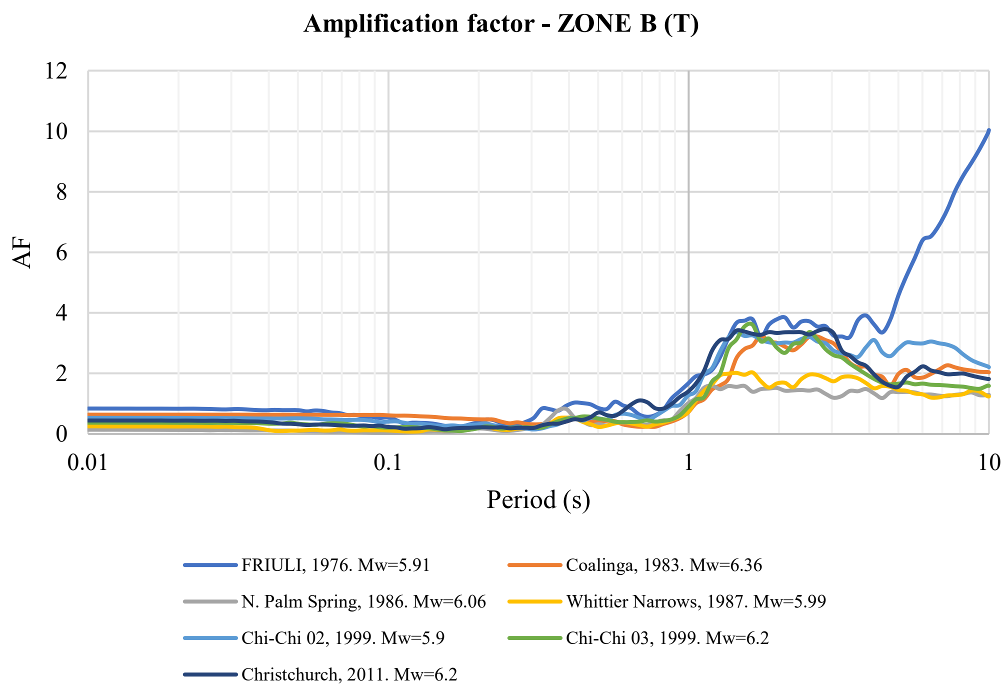

Figure 328. Amplification factor for theoretical curves of Zone B

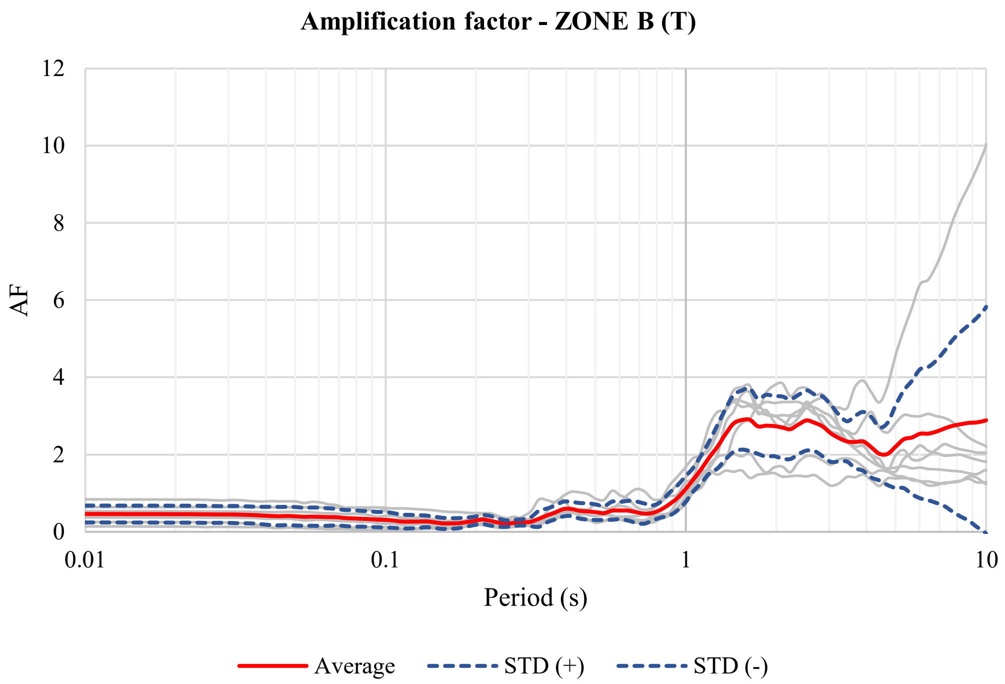

Figure 329. Amplification factor average for theoretical curves of Zone B (Period)

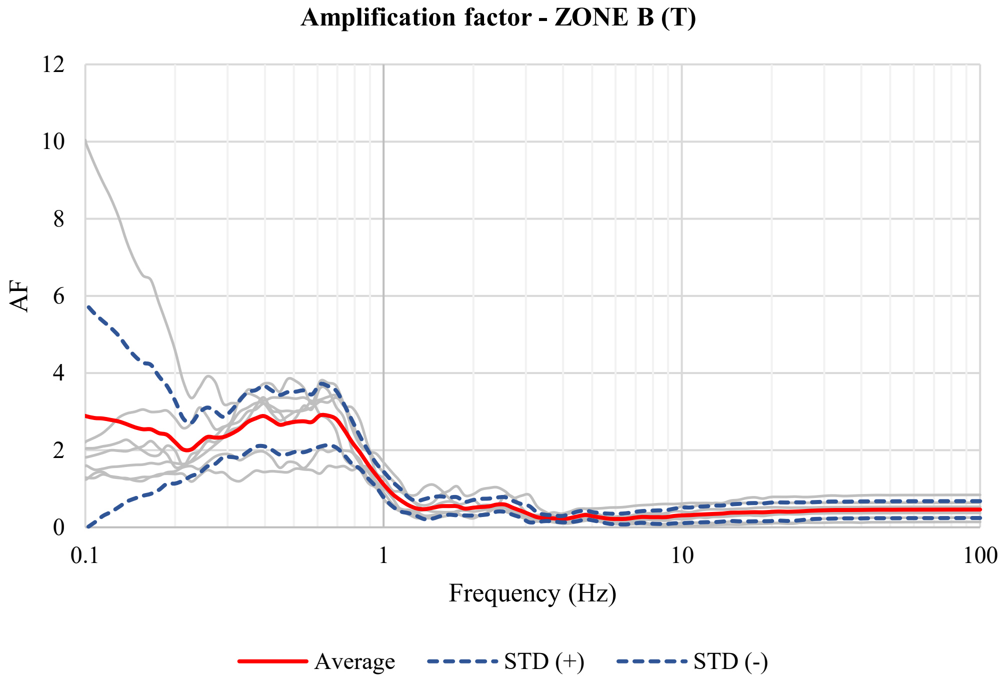

Figure 330. Amplification factor average for theoretical curves of Zone B (Frequency)

Table 56. Maximun values of Amplification factor for theoretical curves of Zone B

Zone B (T)			
	Amplification factor	T (s)	F (Hz)
1	2.90	1.63	0.61
2	2.89	1.54	0.65
3	2.89	10.00	0.10

➢ Zone C

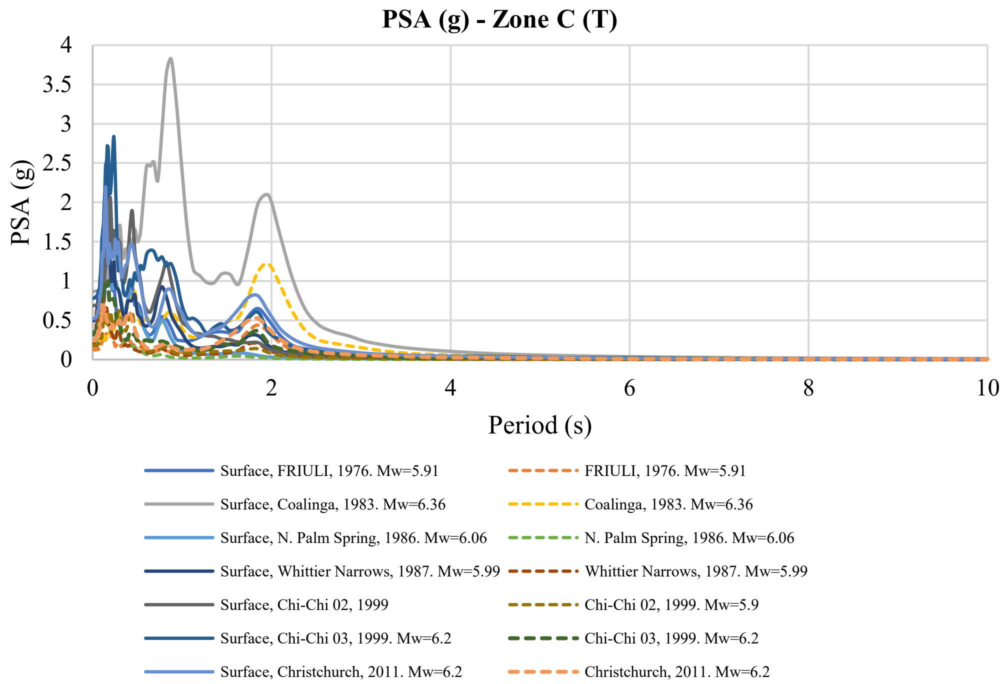

Figure 331. PSA (g) for theoretical curves of Zone C

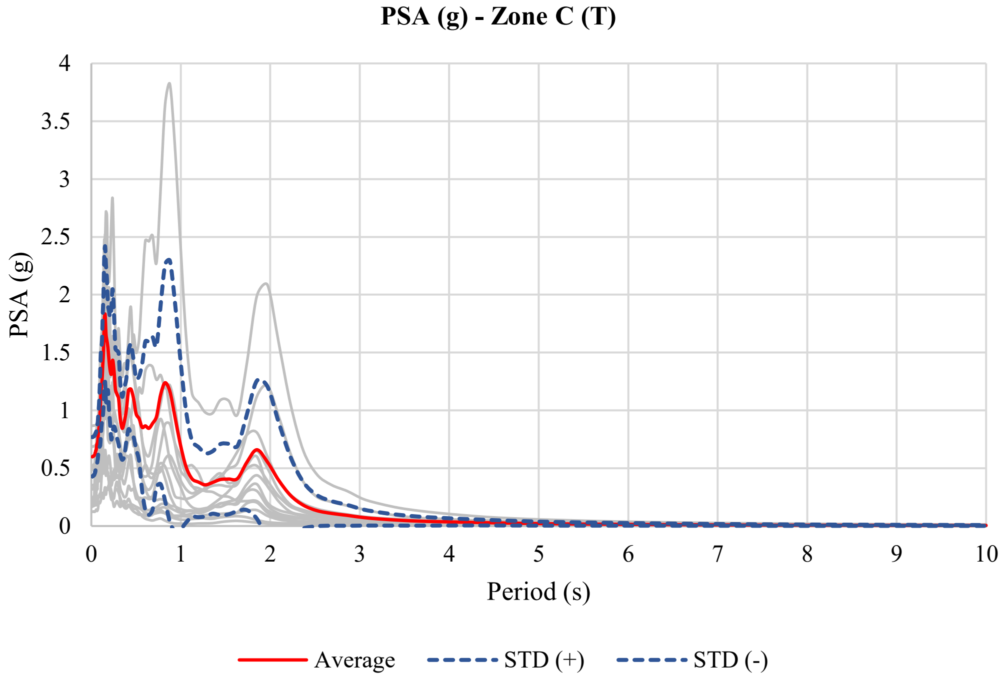

Figure 332. PSA (g) average for theoretical curves of Zone C

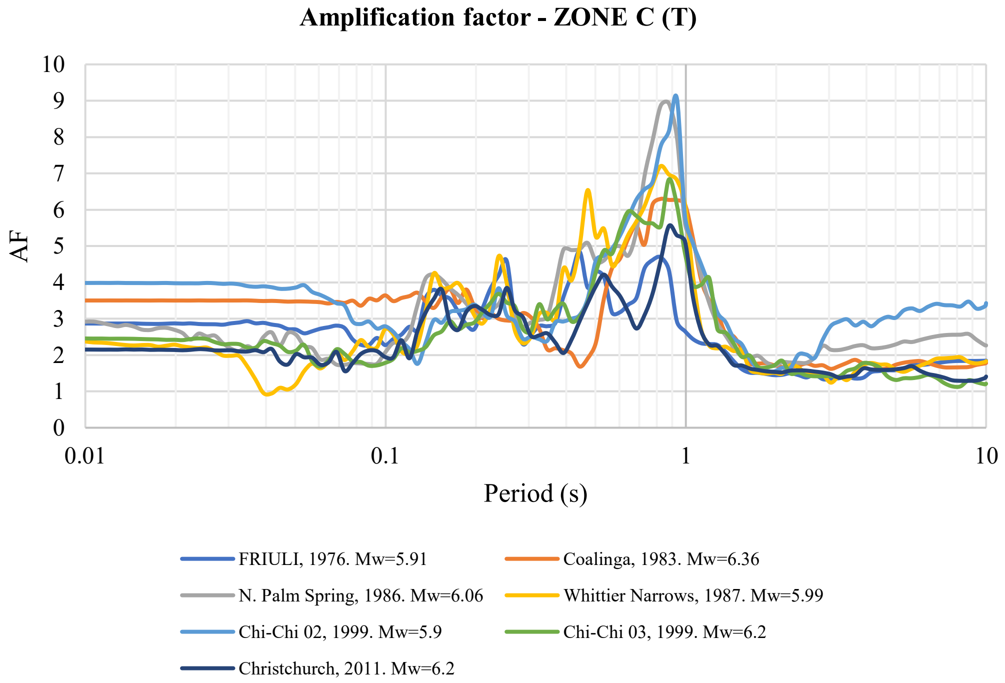

Figure 333. Amplification factor for theoretical curves of Zone C

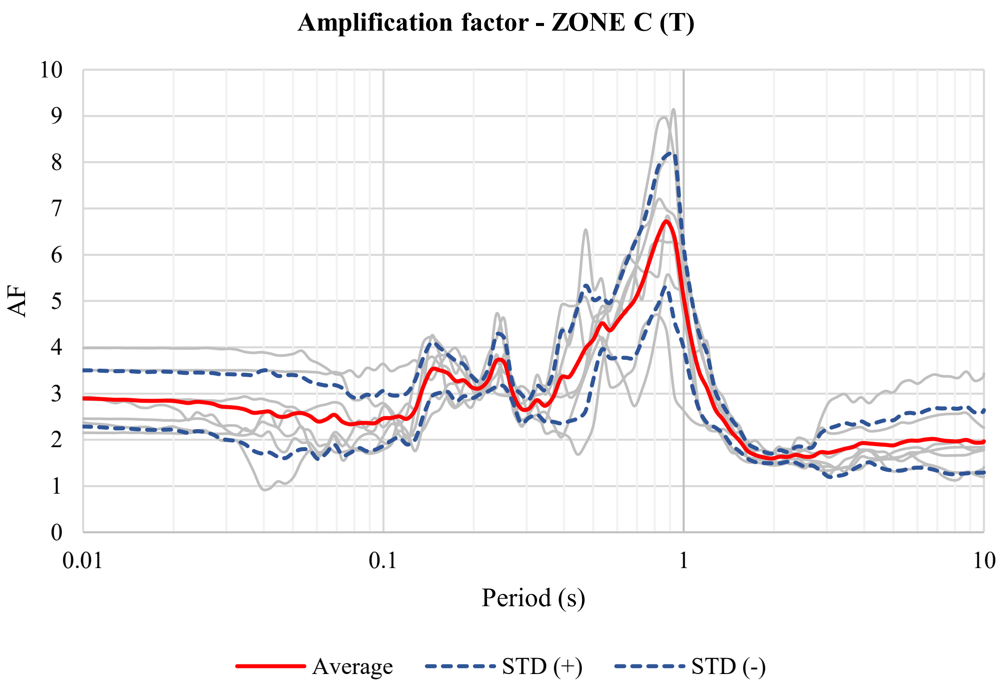

Figure 334. Amplification factor average for theoretical curves of Zone C (Period)

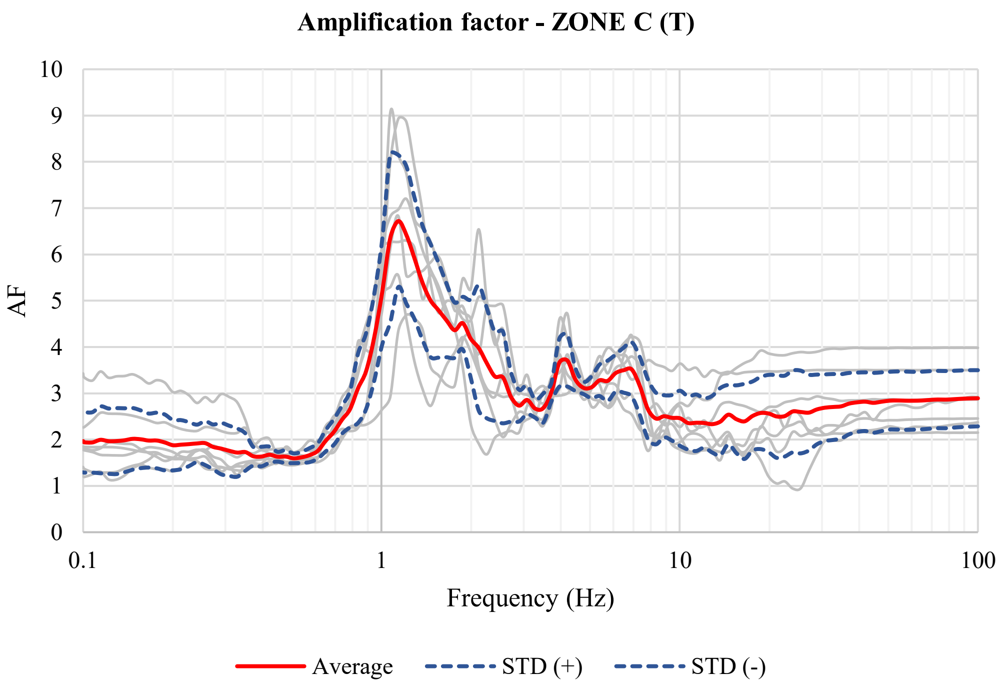

Figure 335. Amplification factor average for theoretical curves of Zone C (Frequency)

Table 57. Maximun values of Amplification factor for theoretical curves of Zone C

Zone C (T)			
	Amplification factor	**T (s)**	**F (Hz)**
1	6.72	0.88	1.14
2	6.42	0.82	1.21
3	6.35	0.93	1.07

- Zone D

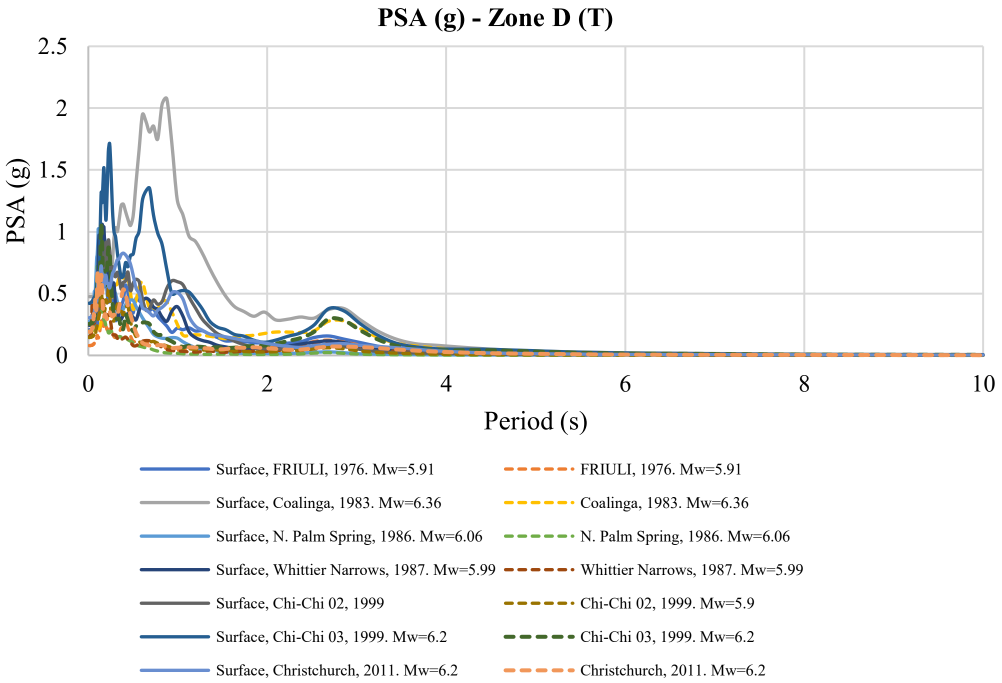

Figure 336. PSA (g) for theoretical curves of Zone D

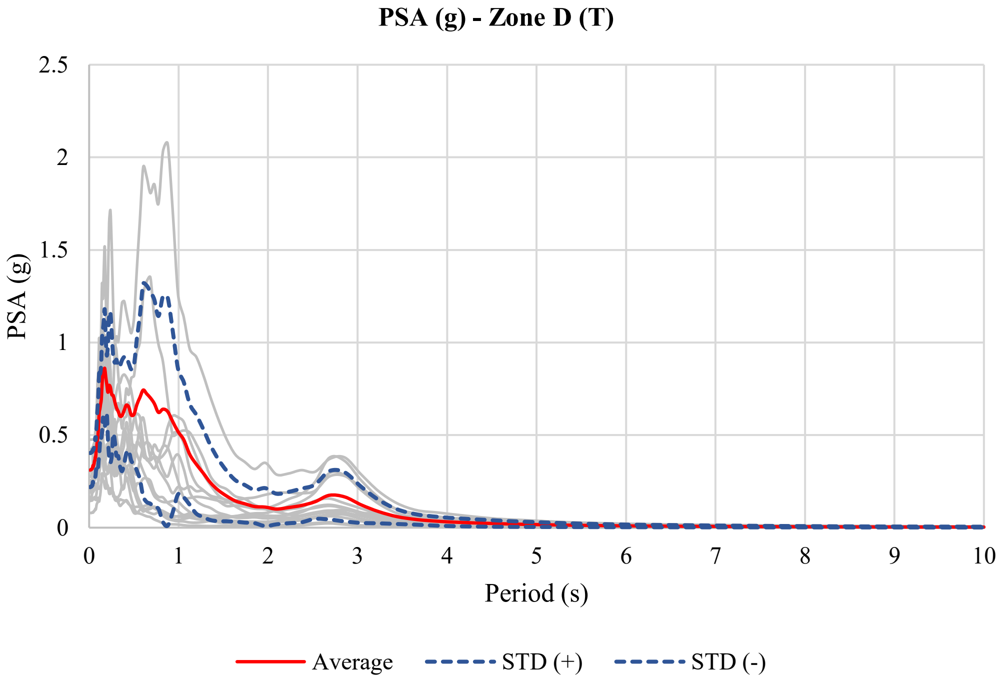

Figure 337. PSA (g) average for theoretical curves of Zone D

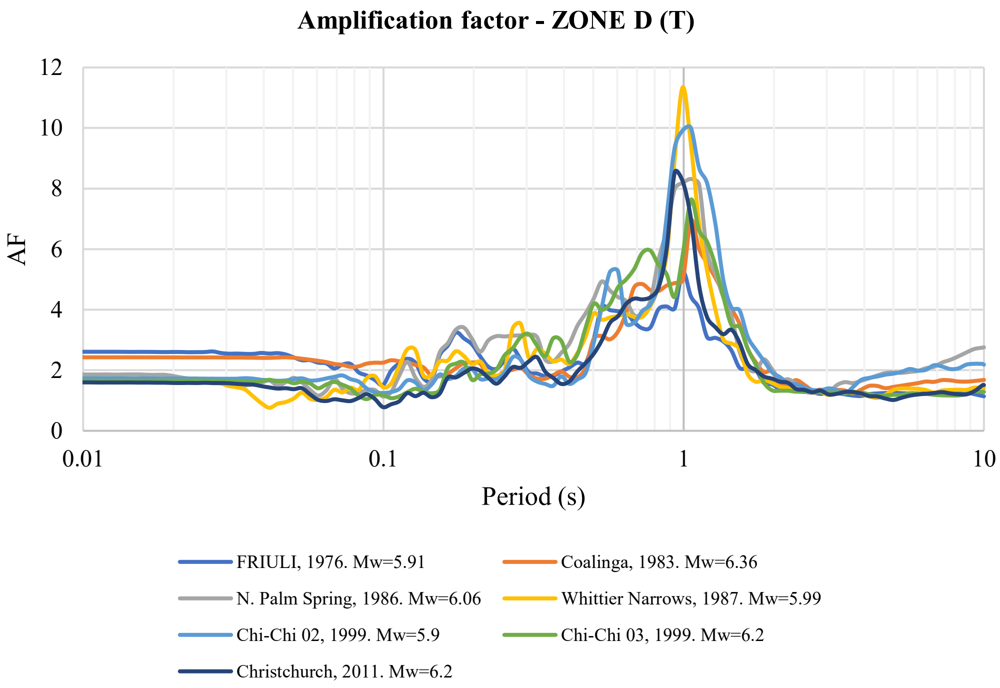

Figure 338. Amplification factor for theoretical curves of Zone D

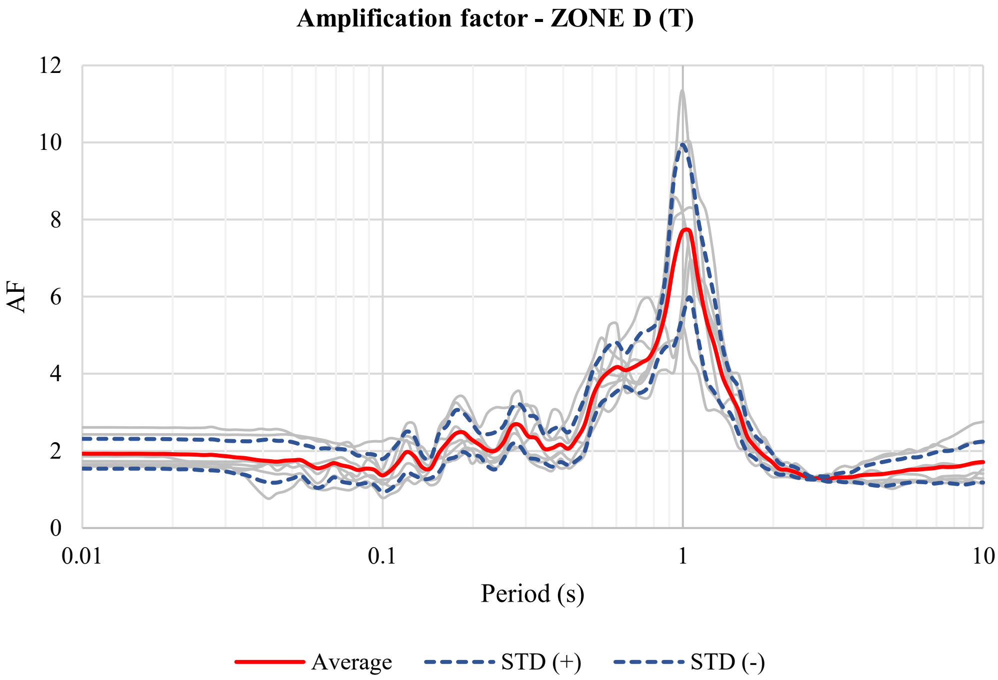

Figure 339. Amplification factor average for theoretical curves of Zone D (Period)

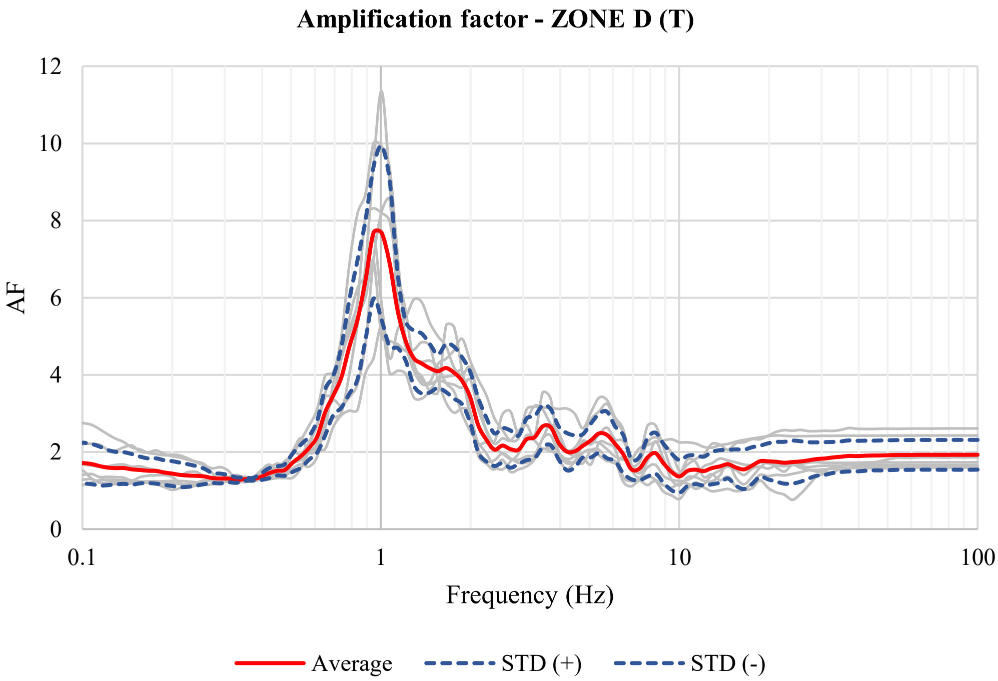

Figure 340. Amplification factor average for theoretical curves of Zone D (Frequency)

Table 58. Maximun values of Amplification factor for theoretical curves of Zone D

Zone D (T)			
	Amplification factor	T (s)	F (Hz)
1	7.68	1.06	0.95
2	7.68	0.99	1.01
3	6.89	0.93	1.07

- Zone E

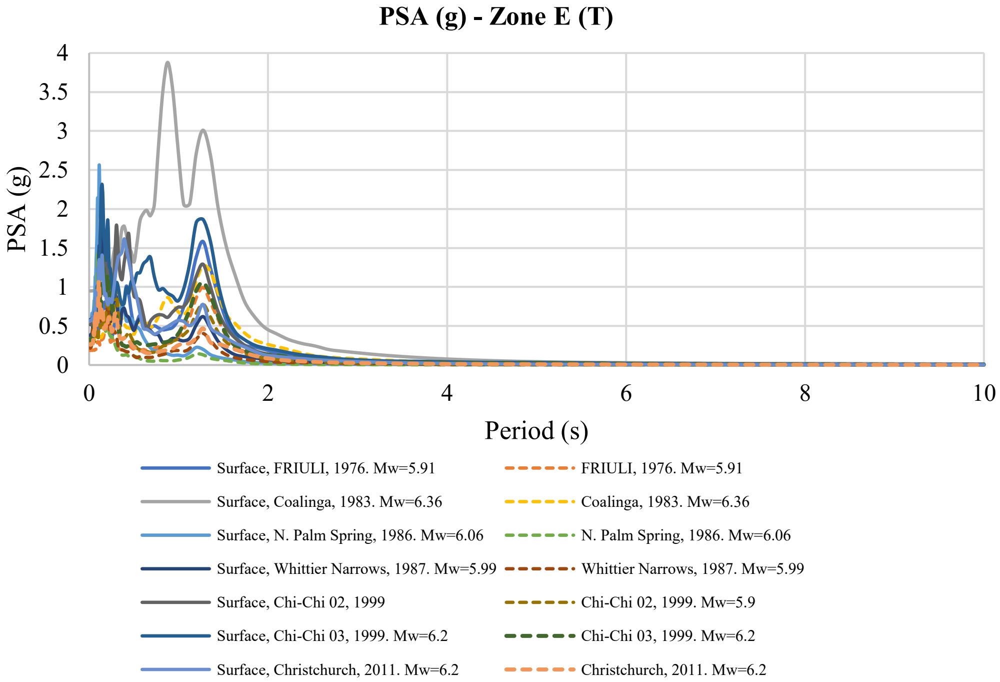

Figure 341. PSA (g) for theoretical curves of Zone E

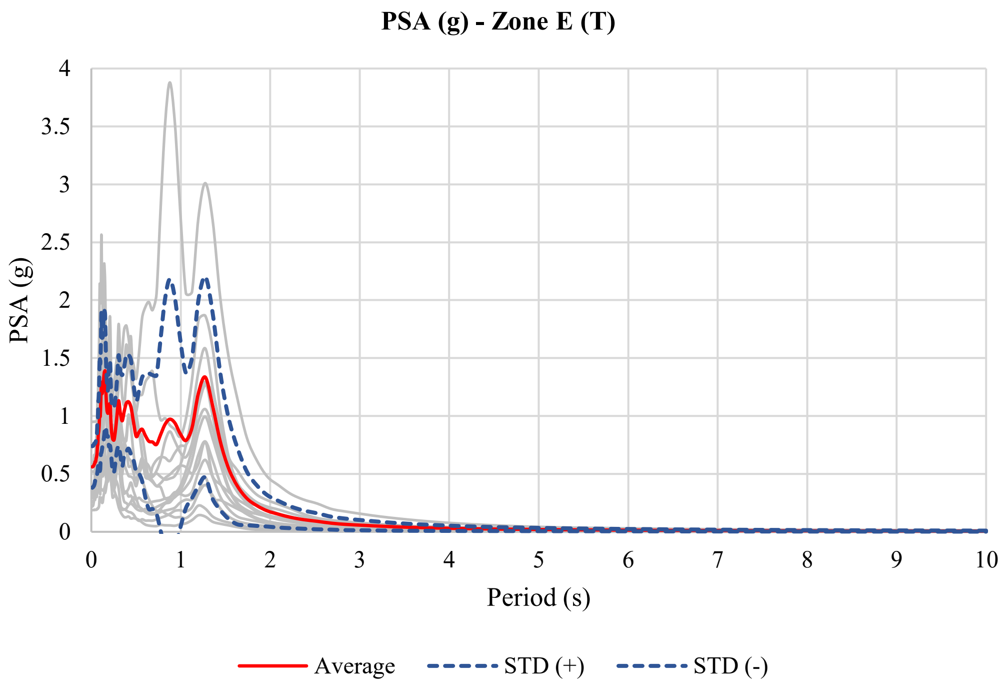

Figure 342. PSA (g) average for theoretical curves of Zone E

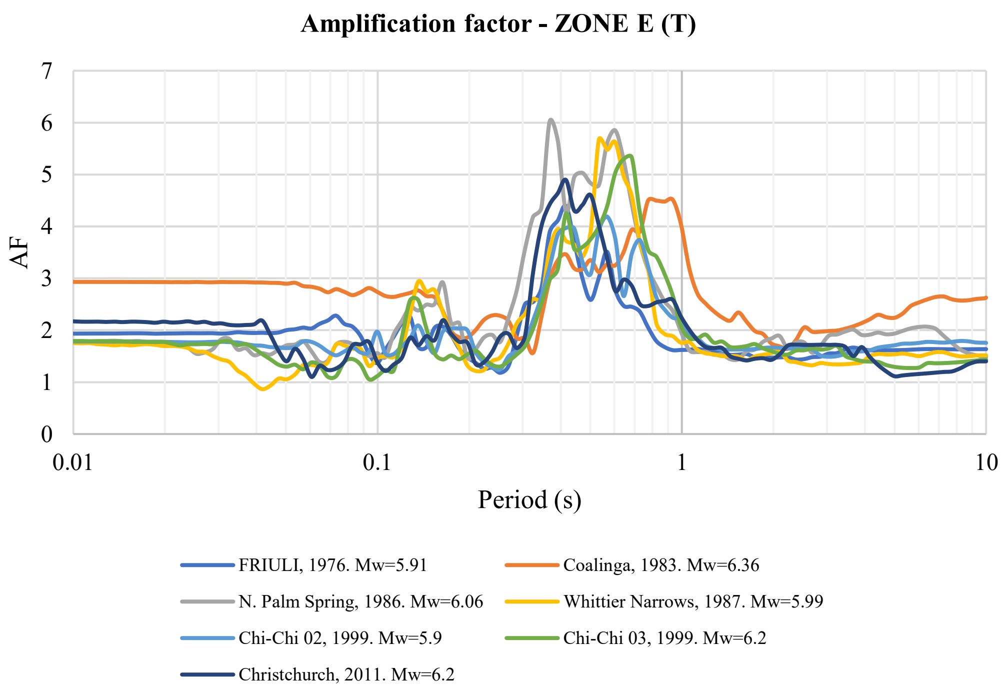

Figure 343. Amplification factor for theoretical curves of Zone E

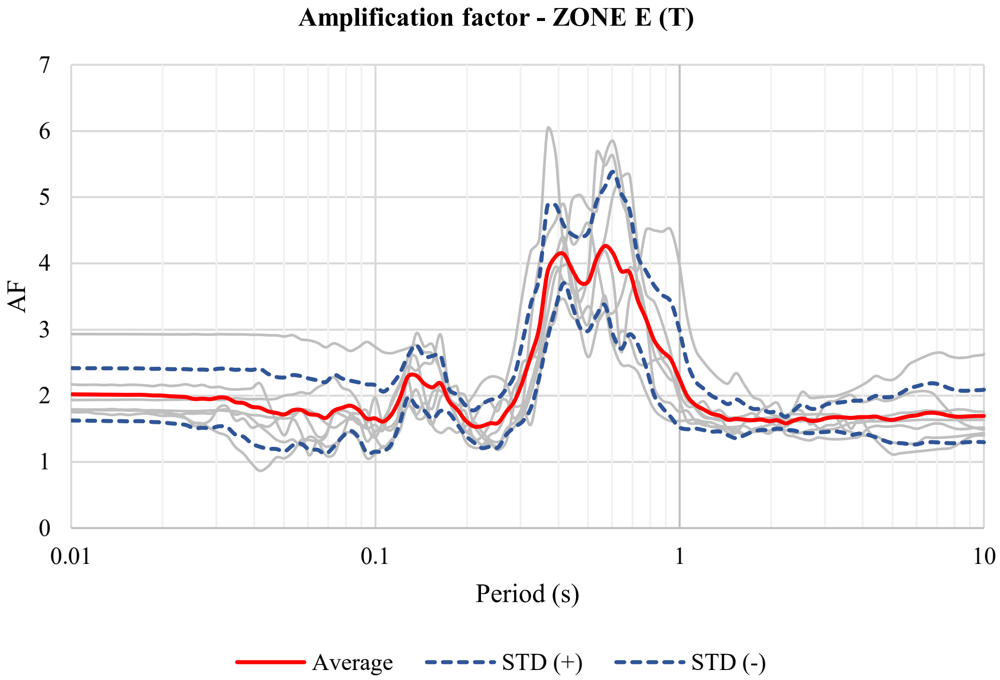

Figure 344. Amplification factor average for theoretical curves of Zone E (Period)

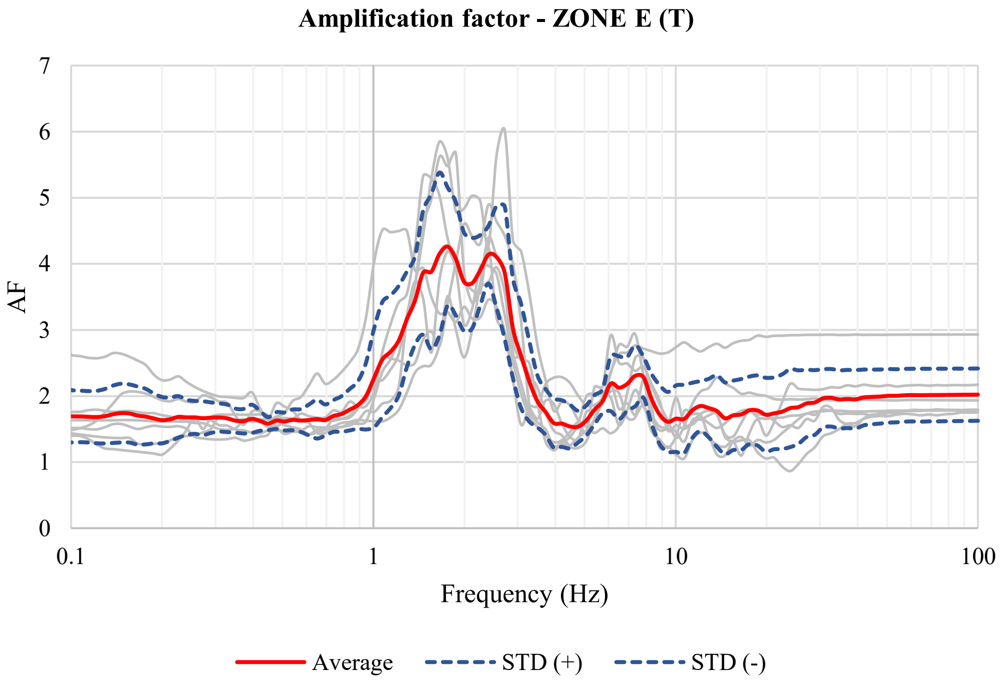

Figure 345. Amplification factor average for theoretical curves of Zone E (Frequency)

Table 59. Maximun values of Amplification factor for theoretical curves of Zone E

Zone E (T)			
	Amplification factor	**T (s)**	**F (Hz)**
1	4.26	0.57	1.76
2	4.15	0.60	1.65
3	4.14	0.42	2.40

- Zone F

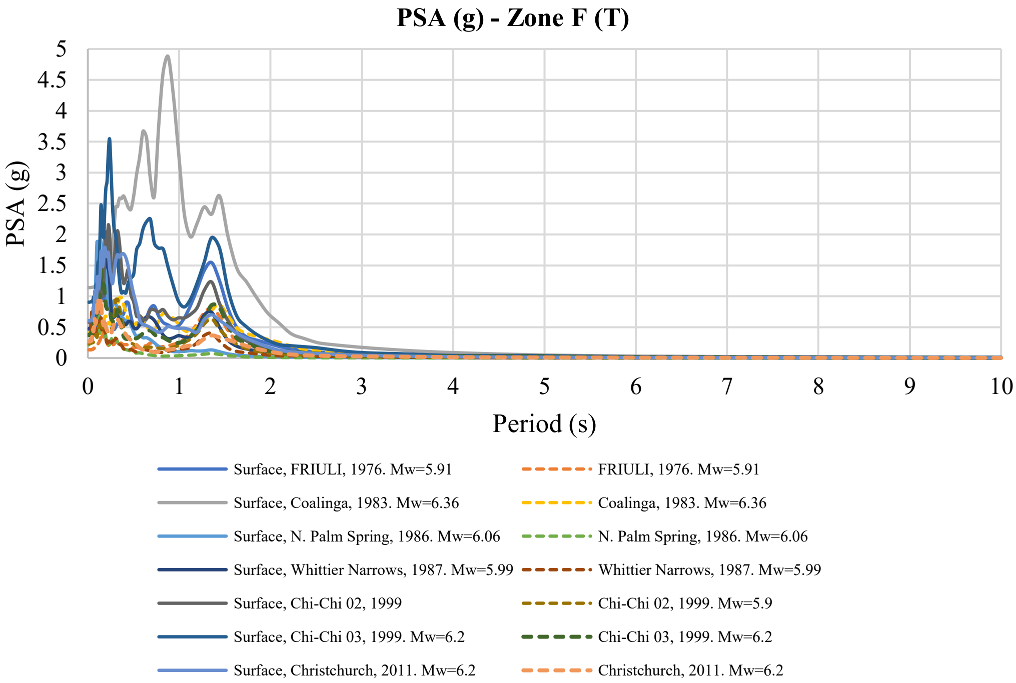

Figure 346. PSA (g) for theoretical curves of Zone F

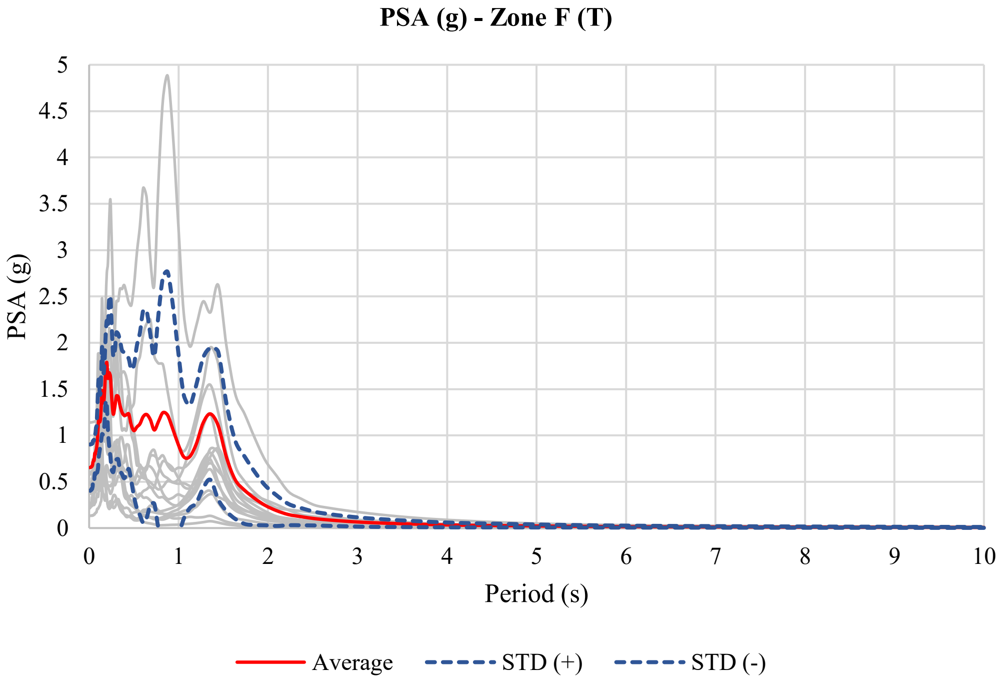

Figure 347. PSA (g) average for theoretical curves of Zone F

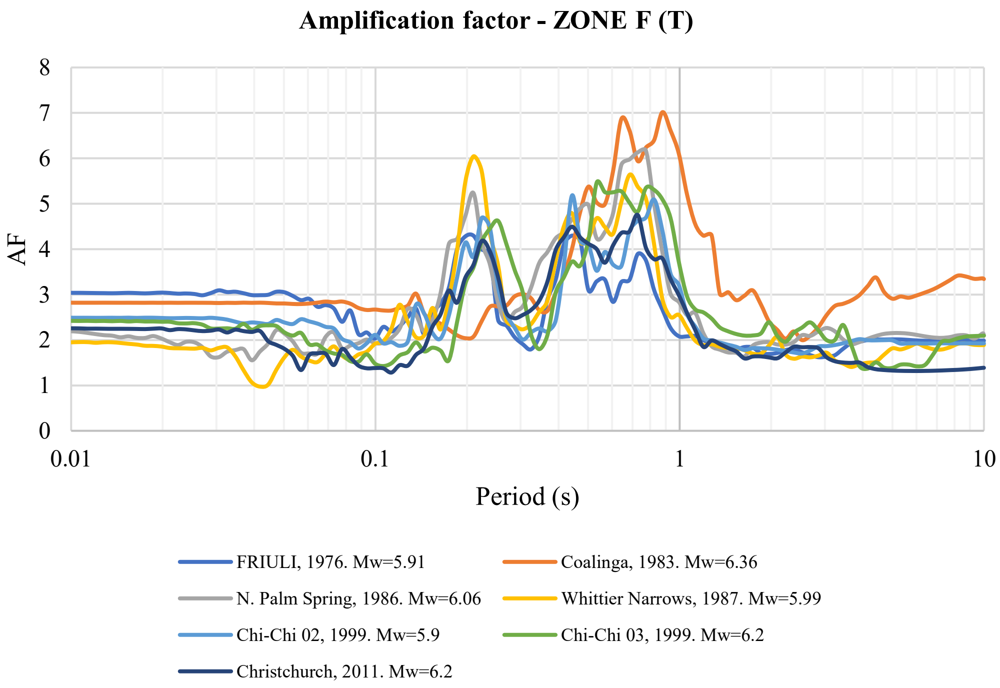

Figure 348. Amplification factor for theoretical curves of Zone F

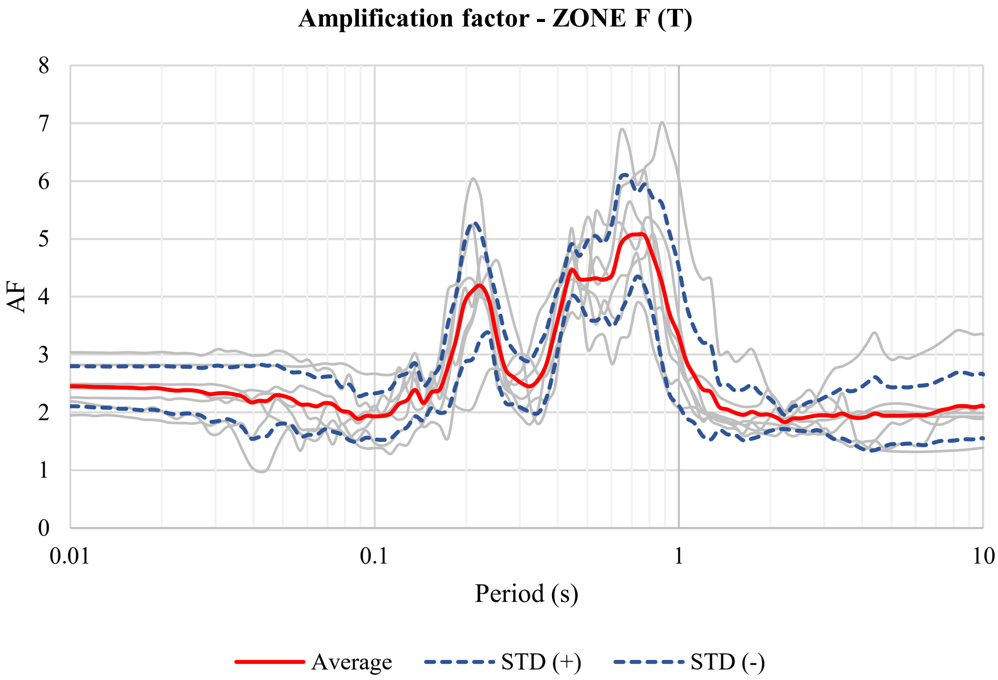

Figure 349. Amplification factor average for theoretical curves of Zone F (Period)

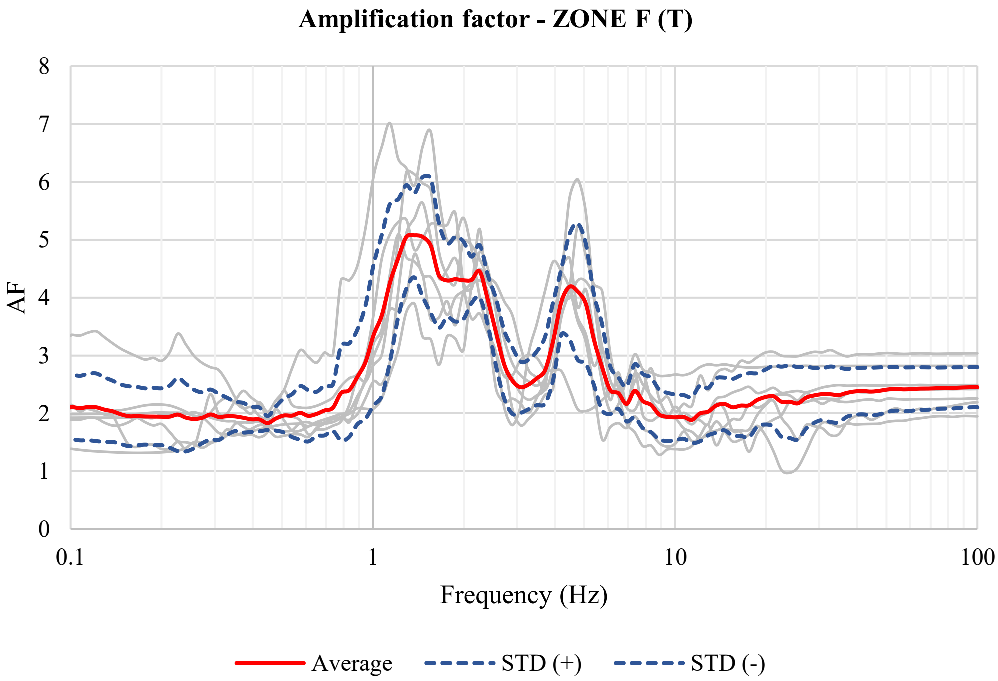

Figure 350. Amplification factor average for theoretical curves of Zone F (Frequency)

Table 60. Maximun values of Amplification factor for theoretical curves of Zone F

Zone F (T)			
	Amplification factor	T (s)	F (Hz)
1	5.08	0.73	1.37
2	5.05	0.68	1.46
3	5.05	0.77	1.29

- Zone G

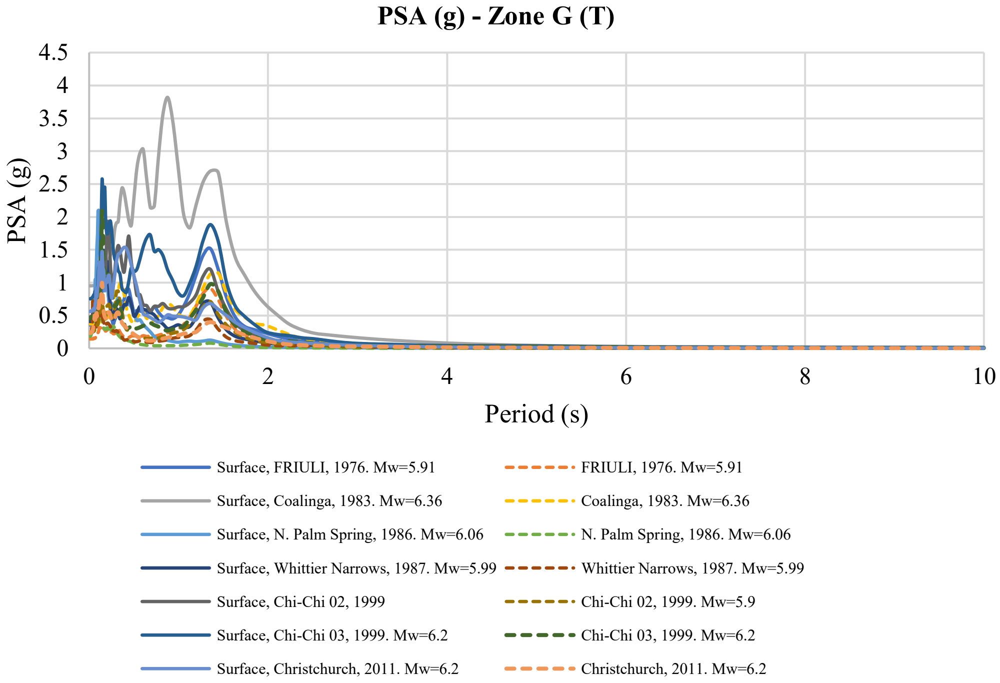

Figure 351. PSA (g) for theoretical curves of Zone G

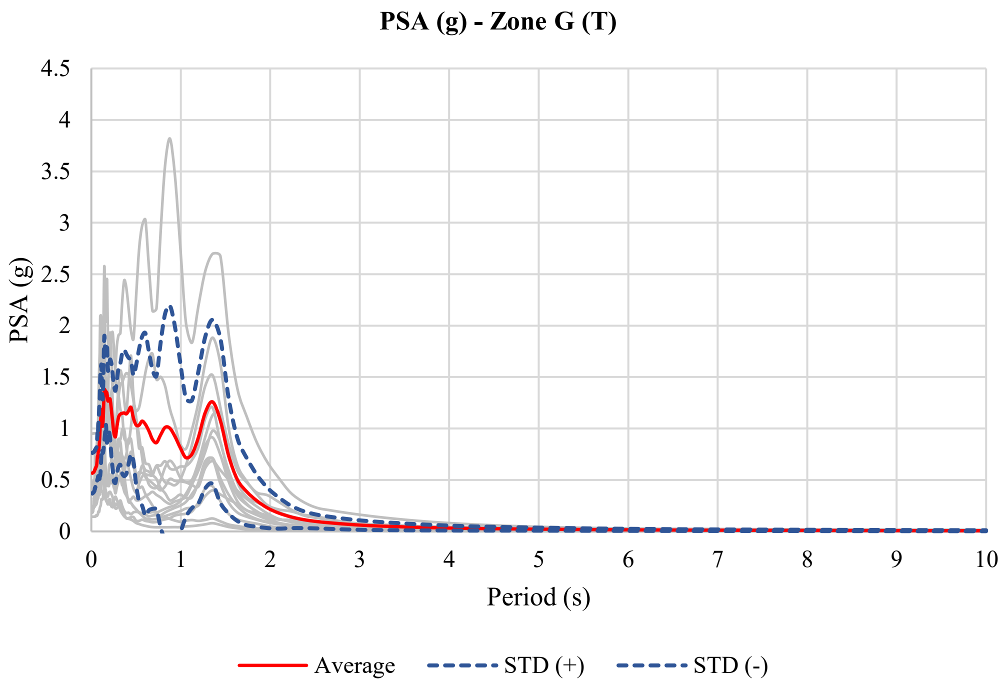

Figure 352. PSA (g) average for theoretical curves of Zone G

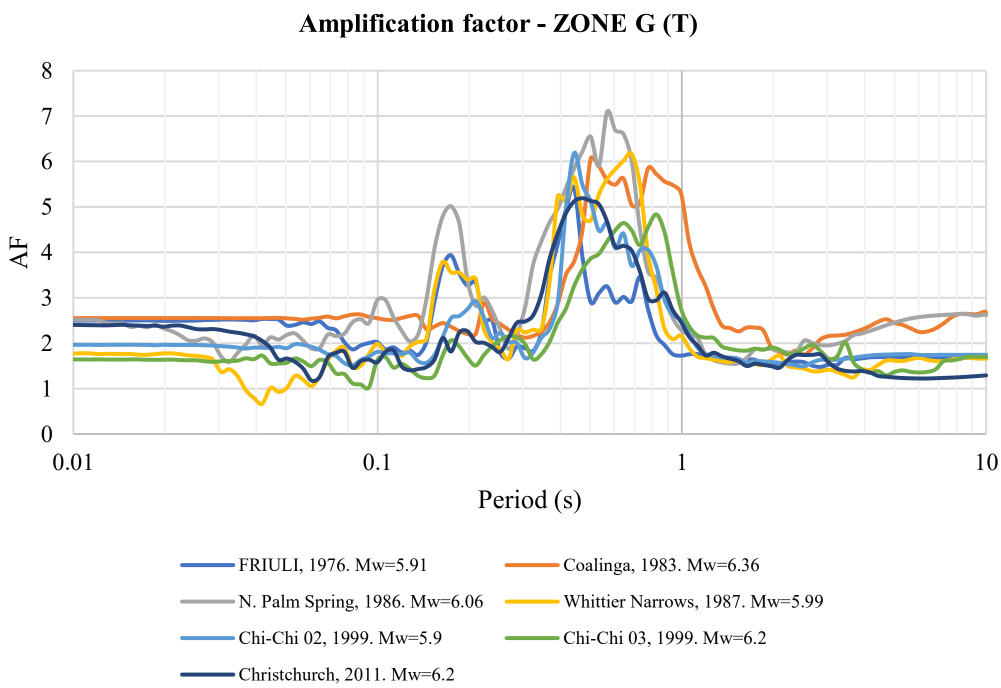

Figure 353. Amplification factor for theoretical curves of Zone G

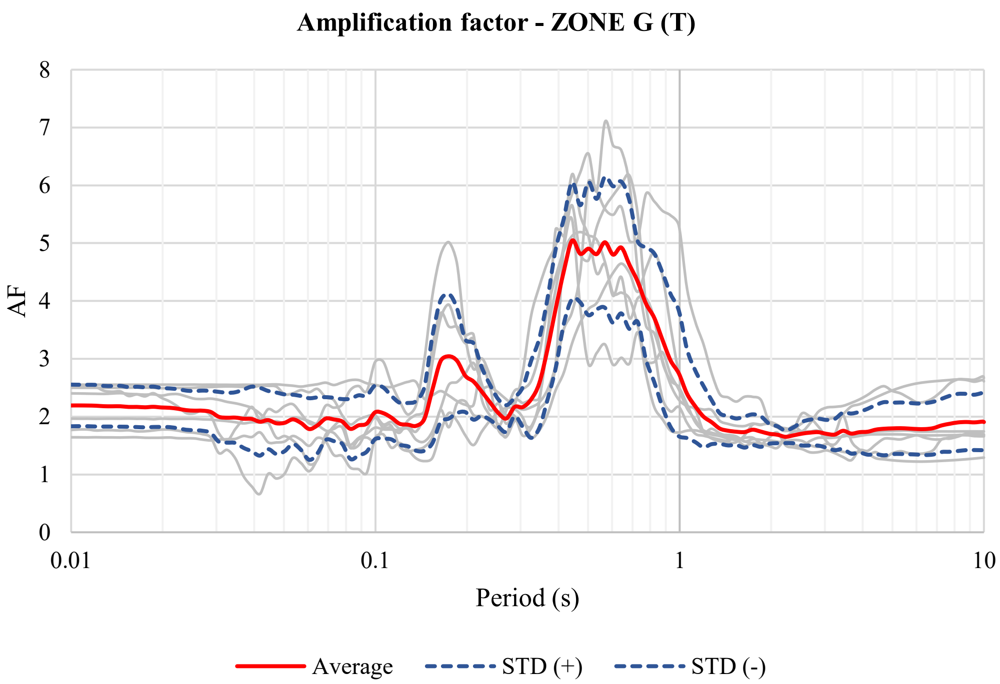

Figure 354. Amplification factor average for theoretical curves of Zone G (Period)

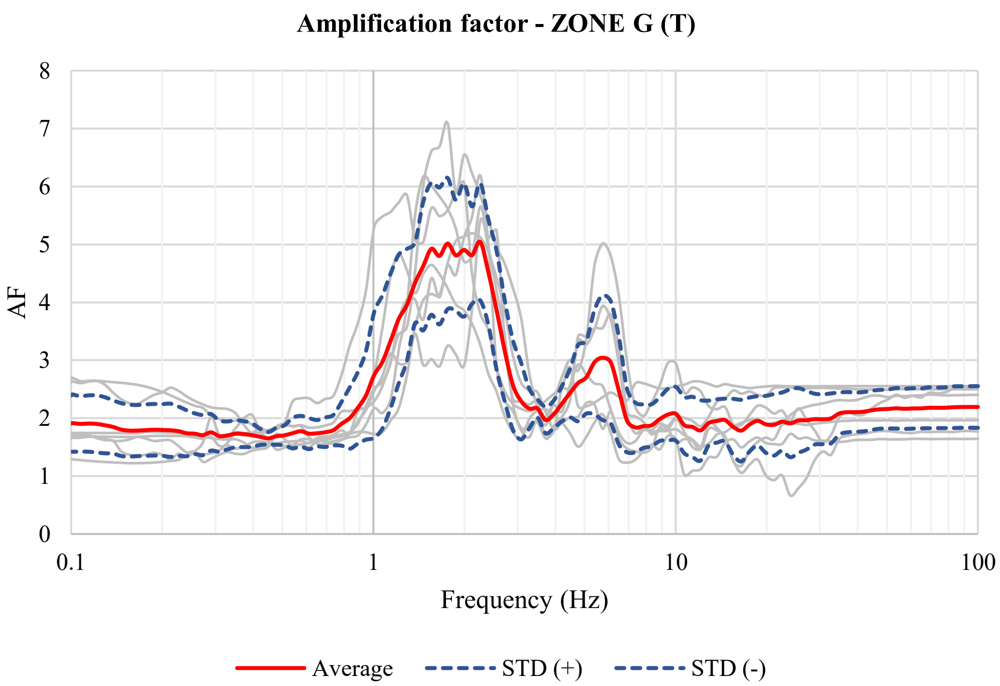

Figure 355. Amplification factor average for theoretical curves of Zone G (Frequency)

Table 61. Maximun values of Amplification factor for theoretical curves of Zone G

Zone G (T)			
	Amplification factor	**T (s)**	**F (Hz)**
1	5.04	0.44	2.26
2	5.02	0.57	1.76
3	4.92	0.64	1.55

➢ Zone H

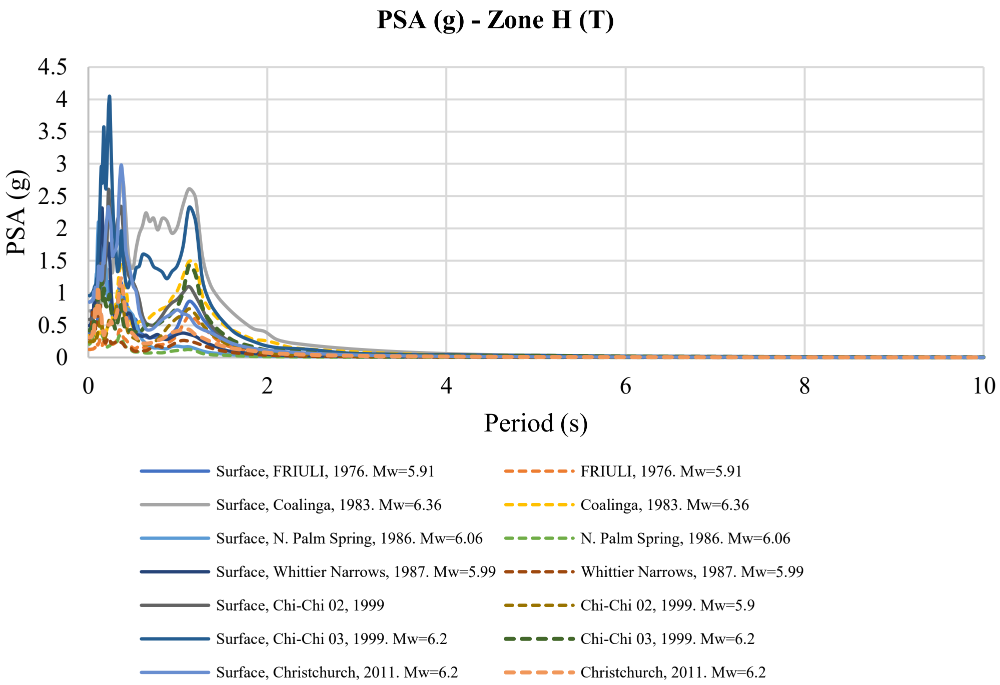

Figure 356. PSA (g) for theoretical curves of Zone H

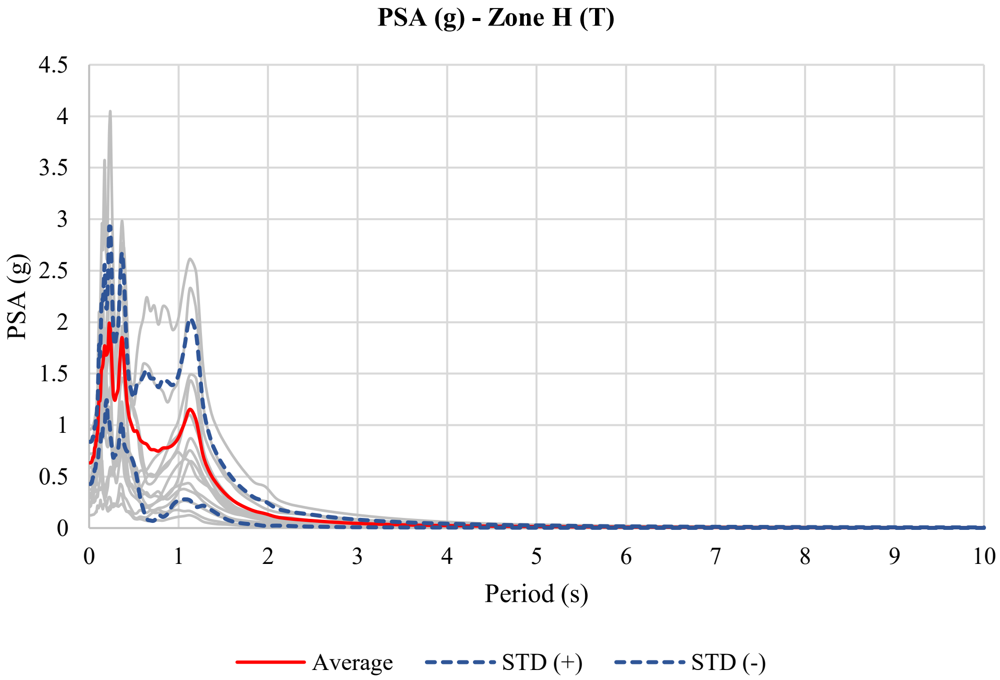

Figure 357. PSA (g) average for theoretical curves of Zone H

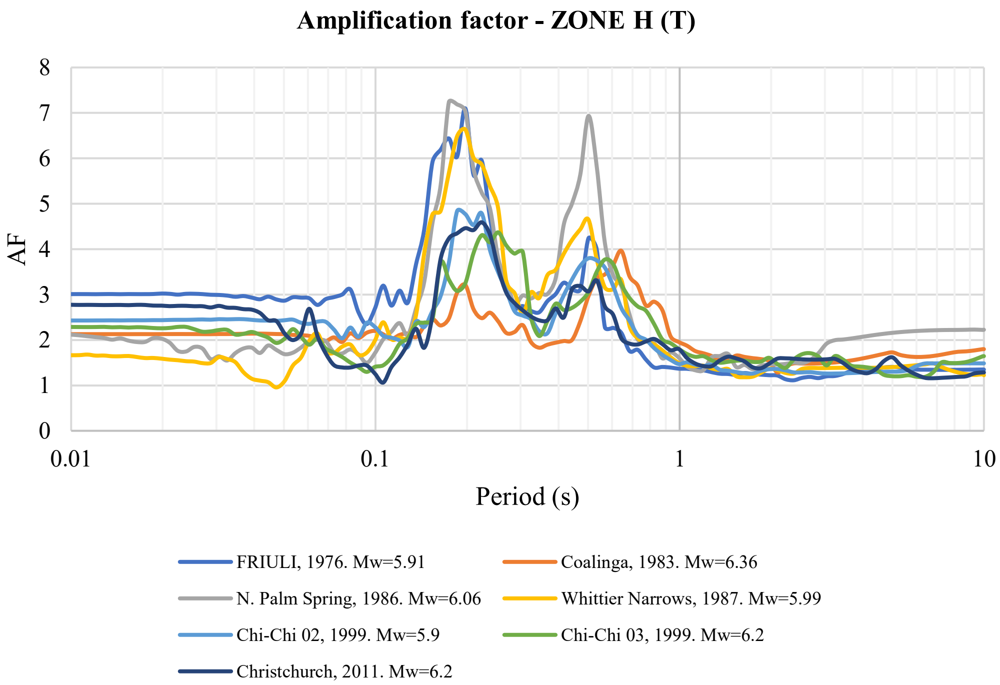

Figure 358. Amplification factor for theoretical curves of Zone H

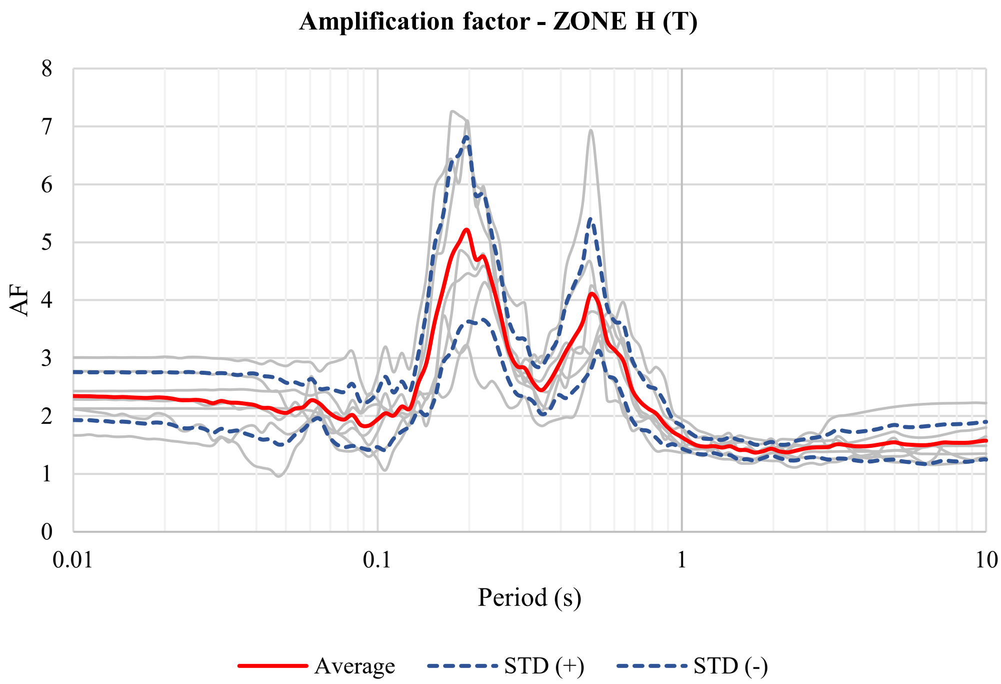

Figure 359. Amplification factor average for theoretical curves of Zone H (Period)

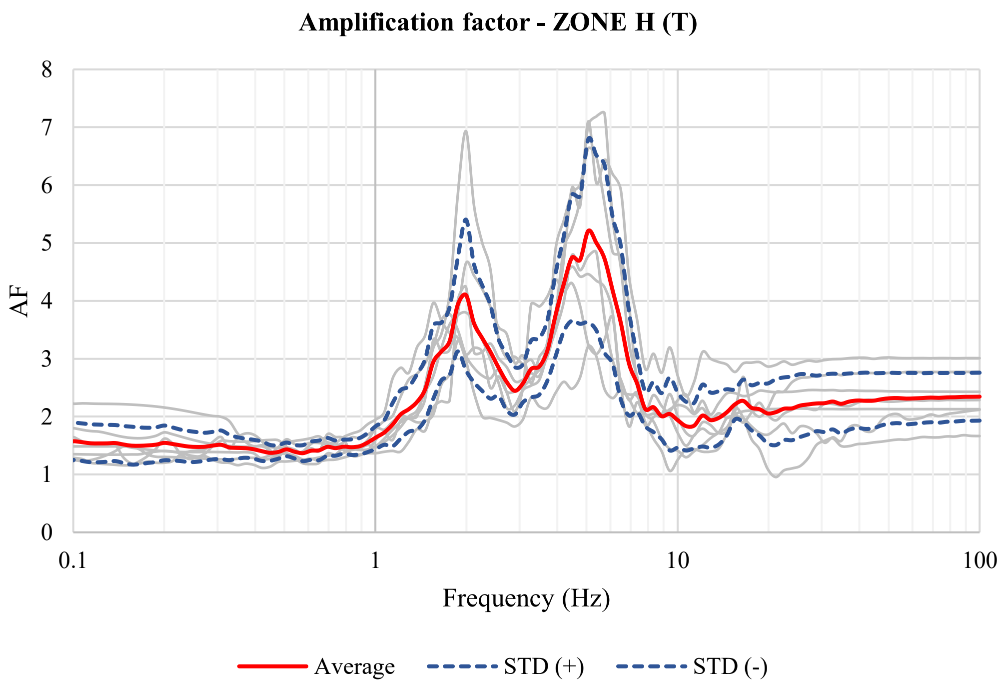

Figure 360. Amplification factor average for theoretical curves of Zone H (Frequency)

Table 62. Maximun values of Amplification factor for theoretical curves of Zone H

Zone H (T)			
	Amplification factor	T (s)	F (Hz)
1	5.21	0.20	5.06
2	5.00	0.19	5.39
3	4.75	0.22	4.47

➢ Zone I

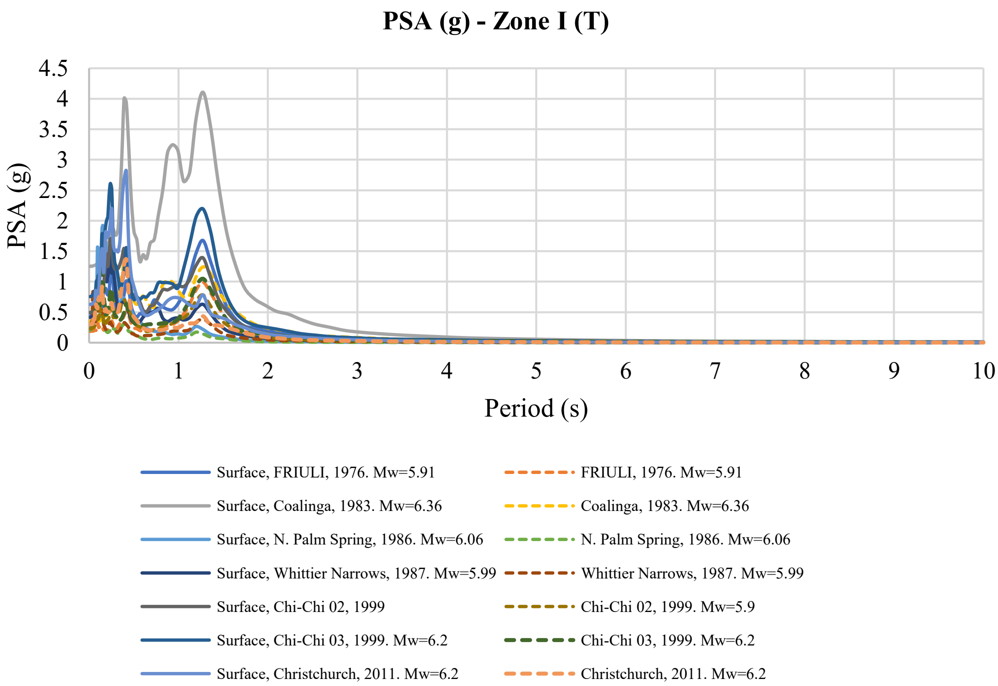

Figure 361. PSA (g) for theoretical curves of Zone I

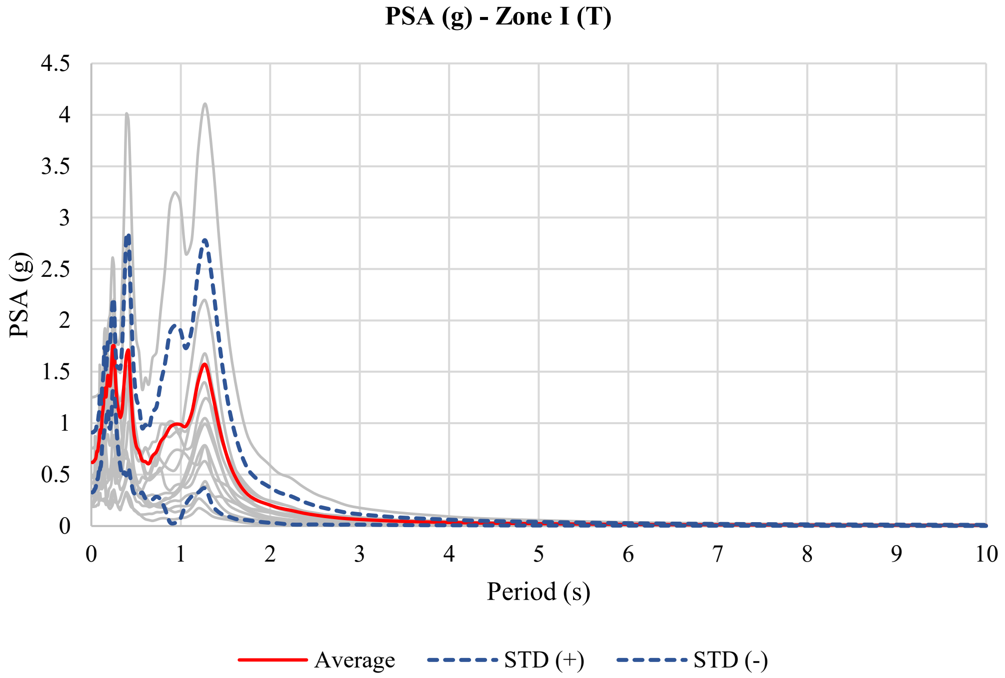

Figure 362. PSA (g) average for theoretical curves of Zone I

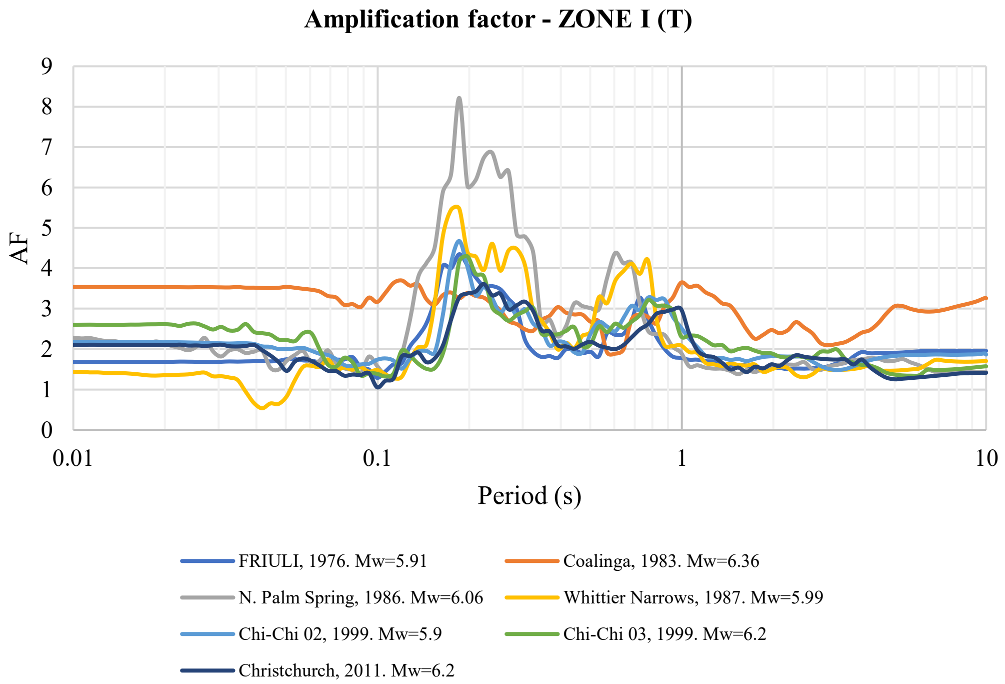

Figure 363. Amplification factor for theoretical curves of Zone I

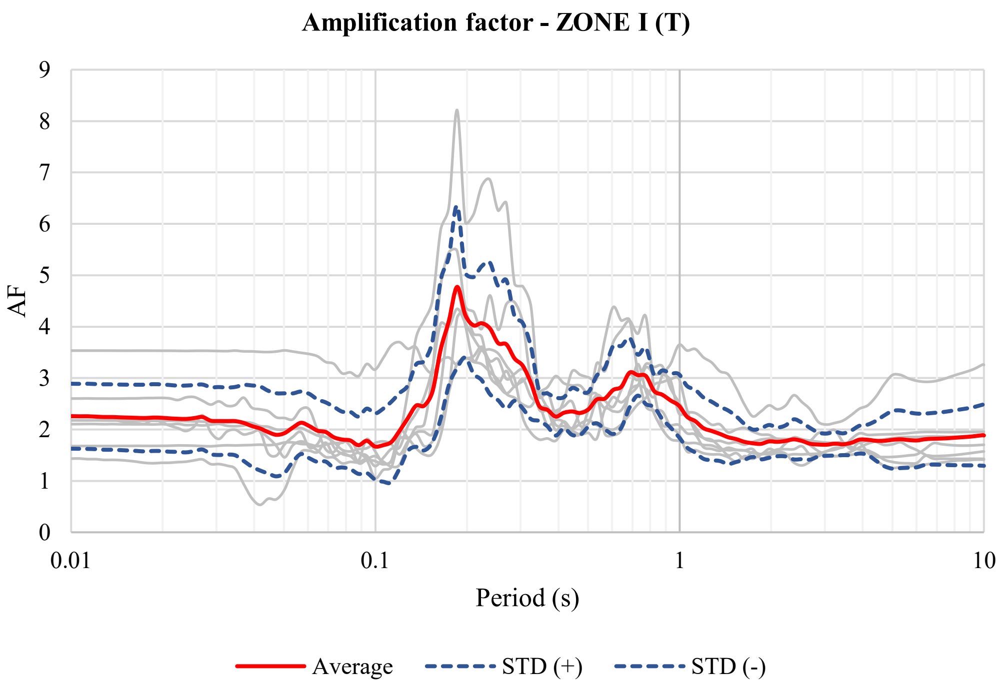

Figure 364. Amplification factor average for theoretical curves of Zone I (Period)

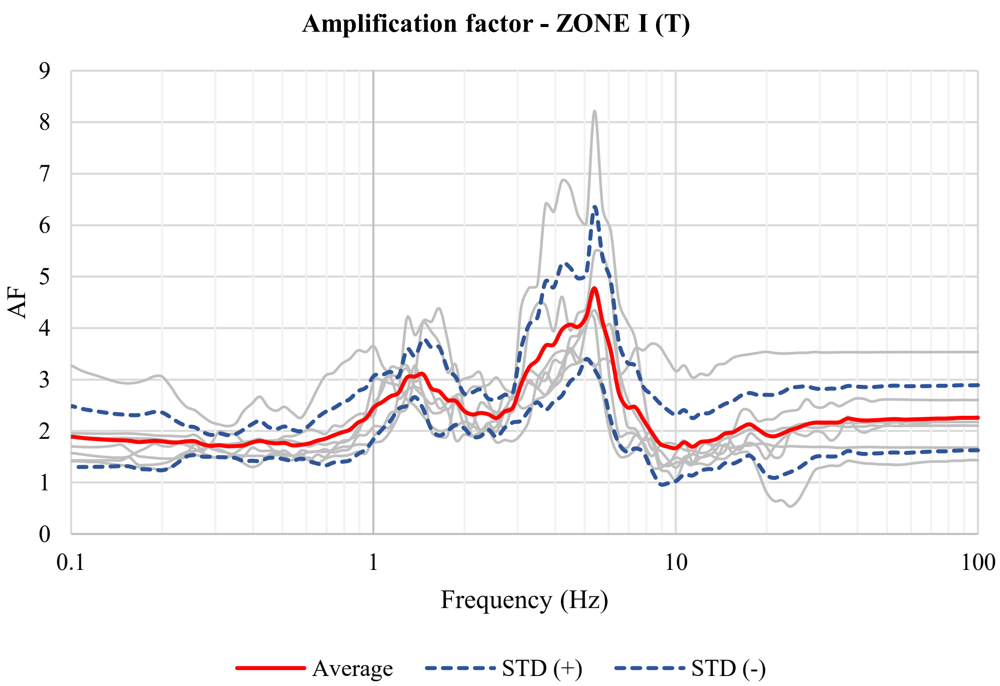

Figure 365. Amplification factor average for theoretical curves of Zone I (Frequency)

Table 63. Maximun values of Amplification factor for theoretical curves of Zone I

Zone I (T)			
	Amplification factor	**T (s)**	**F (Hz)**
1	4.77	0.19	5.39
2	4.23	0.20	5.06
3	4.11	0.17	5.73

C.2.2. Analysis with dry samples

- Zone A

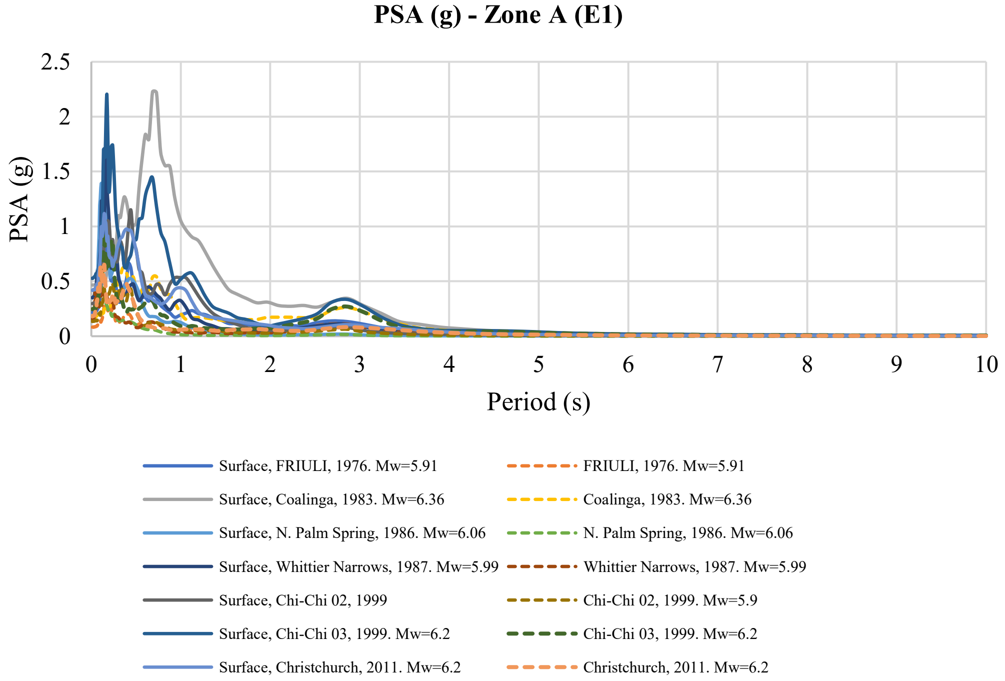

Figure 366. PSA (g) curves for dry samples of Zone A

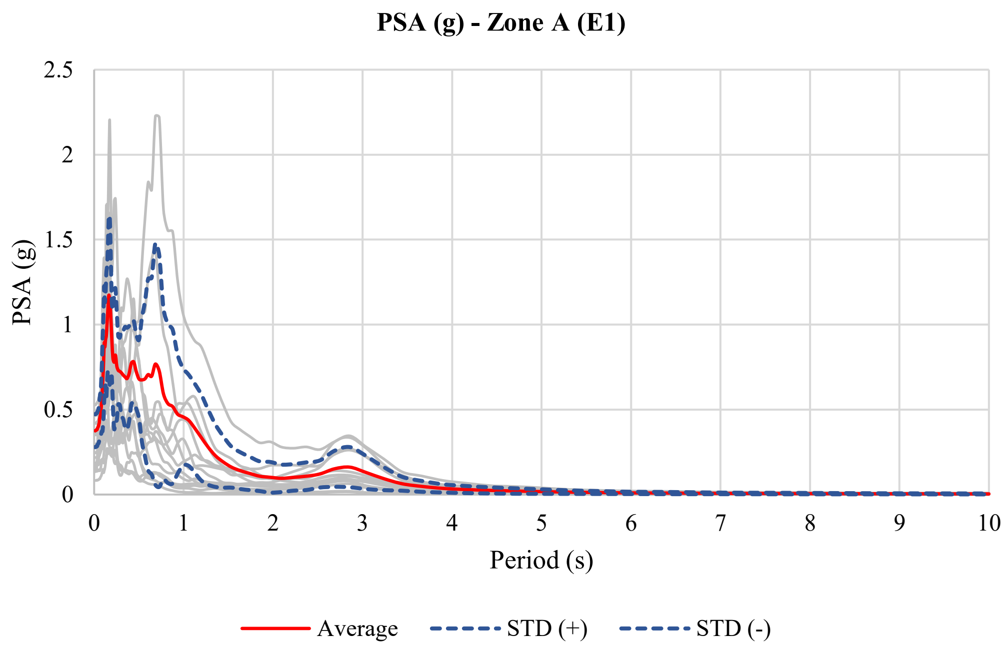

Figure 367. PSA (g) average curves for dry samples of Zone A

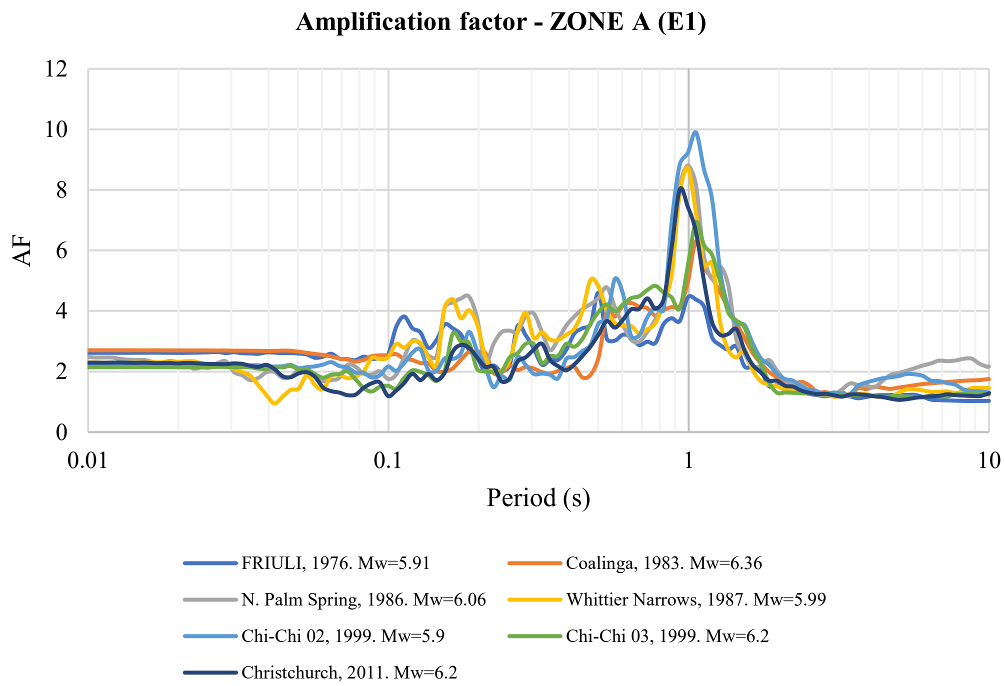

Figure 368. Amplification factor curves for dry samples of Zone A

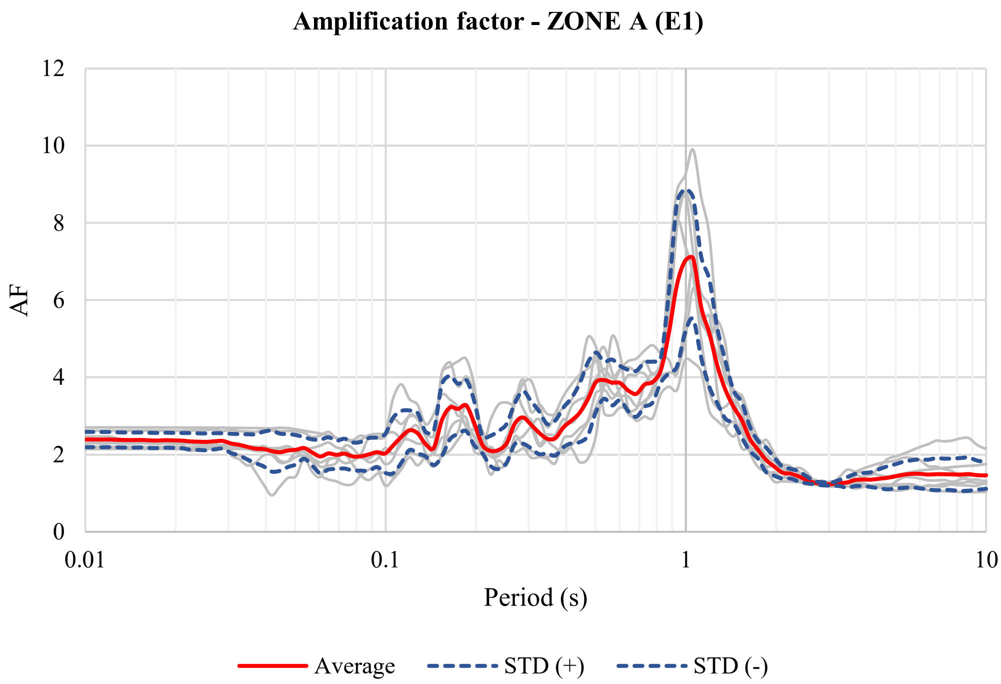

Figure 369. Amplification factor average curves for dry samples of Zone A (Period)

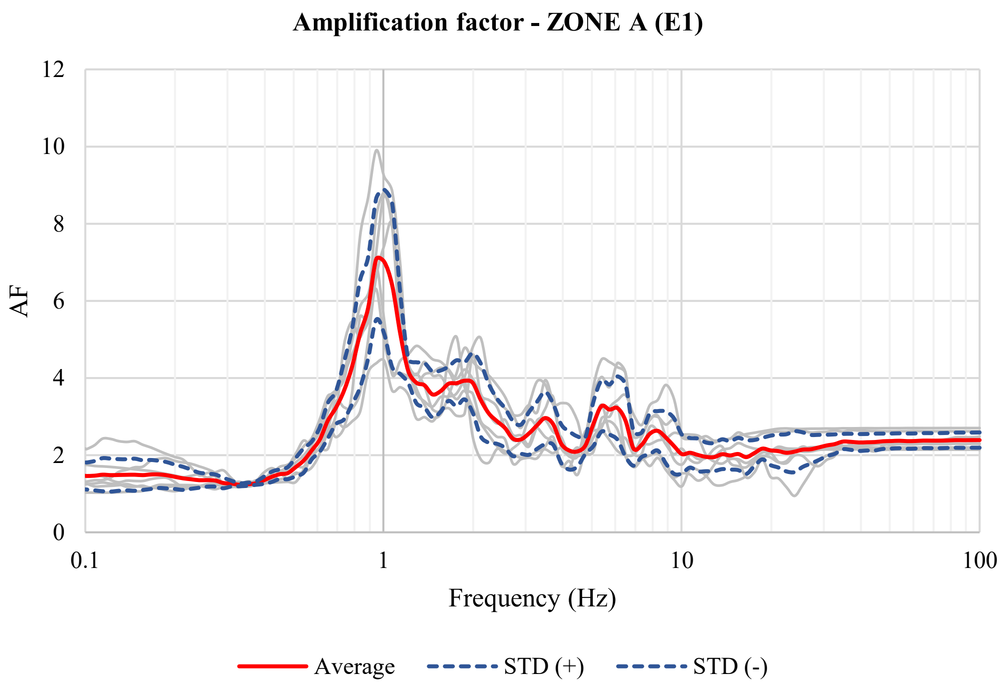

Figure 370. Amplification factor average curves for dry samples of Zone A (Frequency)

Table 64. Maximun values of Amplification factor for dry samples of Zone A

Zoom A (E1)			
	Amplification factor	**T (s)**	**F (Hz)**
1	7.08	1.06	0.95
2	7.01	0.99	1.01
3	6.39	0.93	1.07

- Zone B

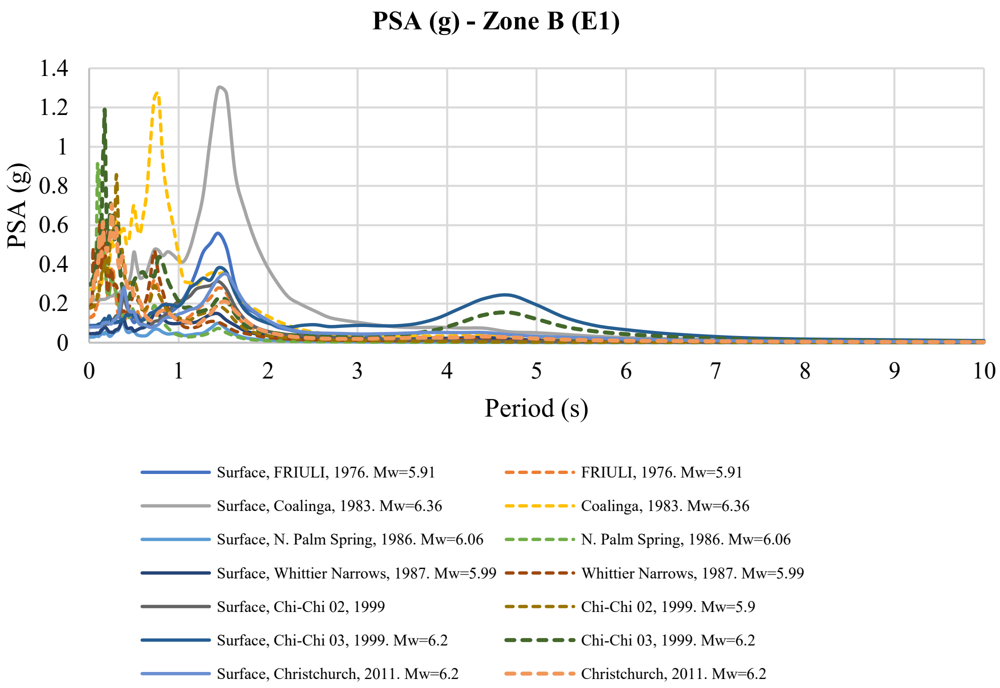

Figure 371. PSA (g) curves for dry samples of Zone B

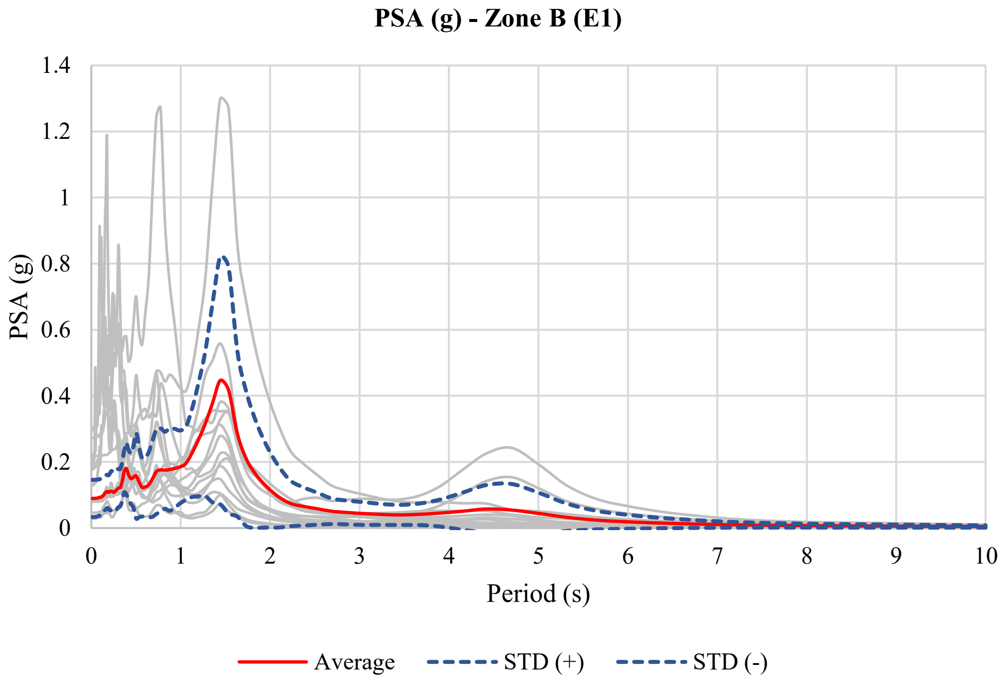

Figure 372. PSA (g) average curves for dry samples of Zone B

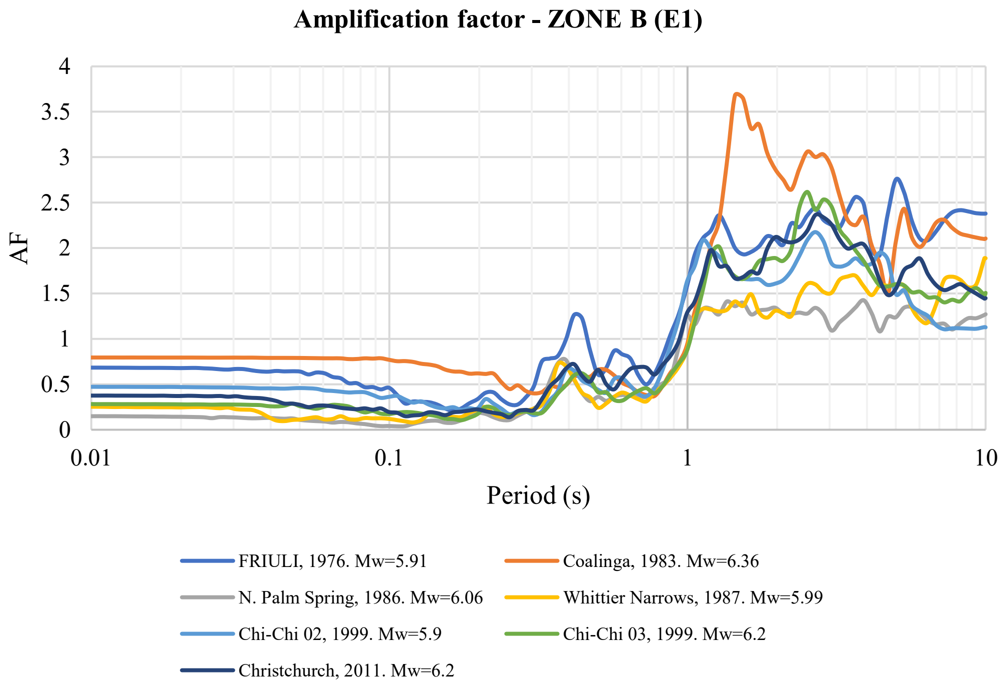

Figure 373. Amplification factor curves for dry samples of Zone B

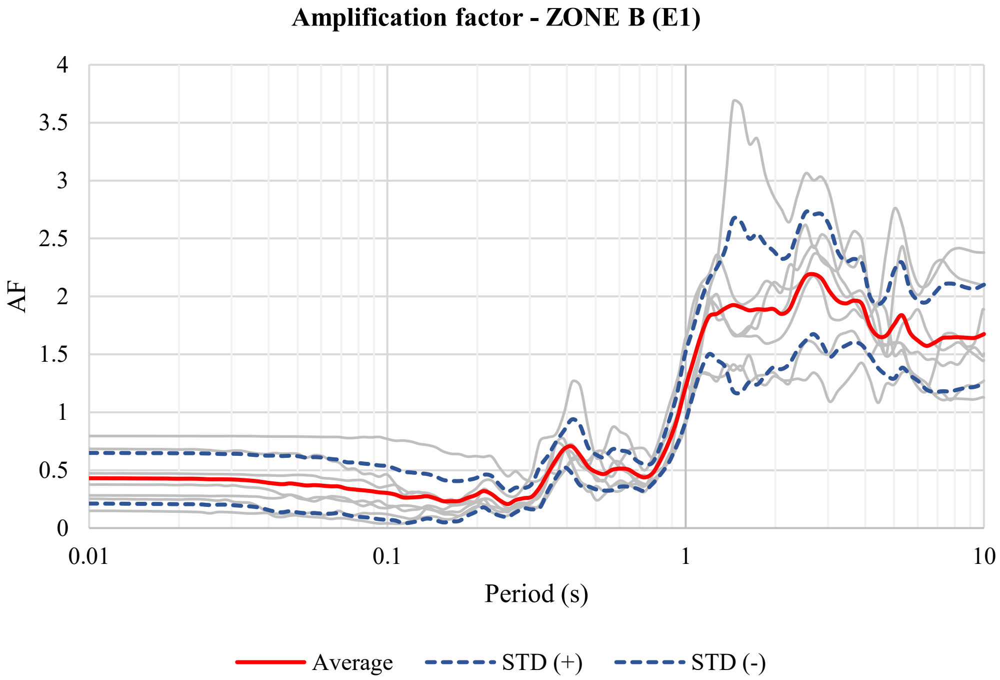

Figure 374. Amplification factor average curves for dry samples of Zone B (Period)

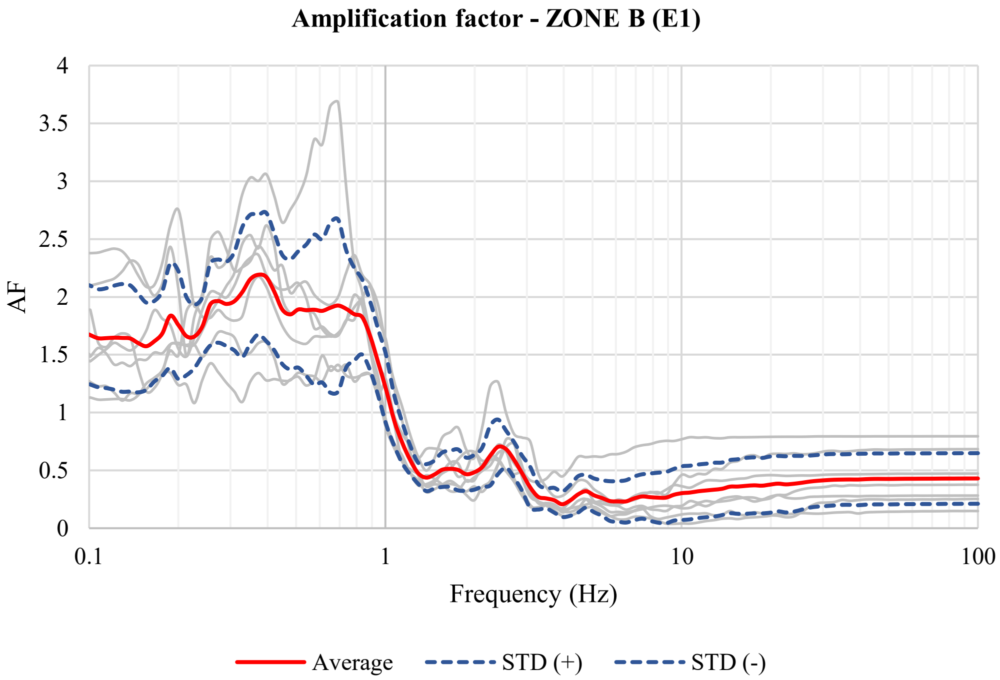

Figure 375. Amplification factor average curves for dry samples of Zone B (Frequency)

Table 65. Maximun values of Amplification factor for dry samples of Zone B

Zone B (E1)			
	Amplification factor	**T (s)**	**F (Hz)**
1	2.19	2.69	0.37
2	2.17	2.52	0.40
3	2.15	2.86	0.35

- Zone C

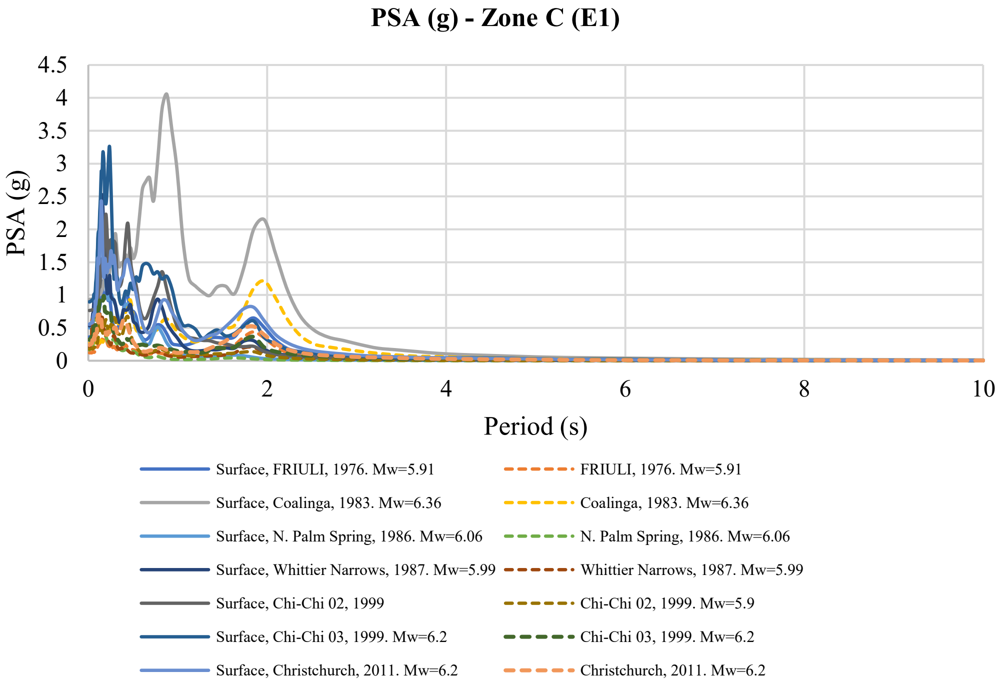

Figure 376. PSA (g) curves for dry samples of Zone C

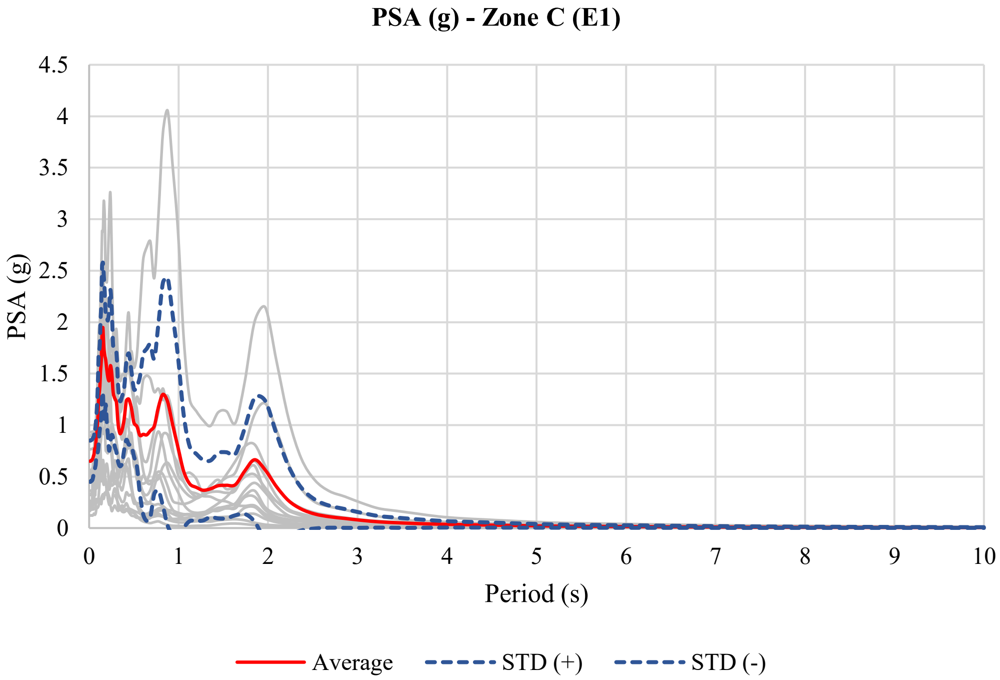

Figure 377. PSA (g) average curves for dry samples of Zone C

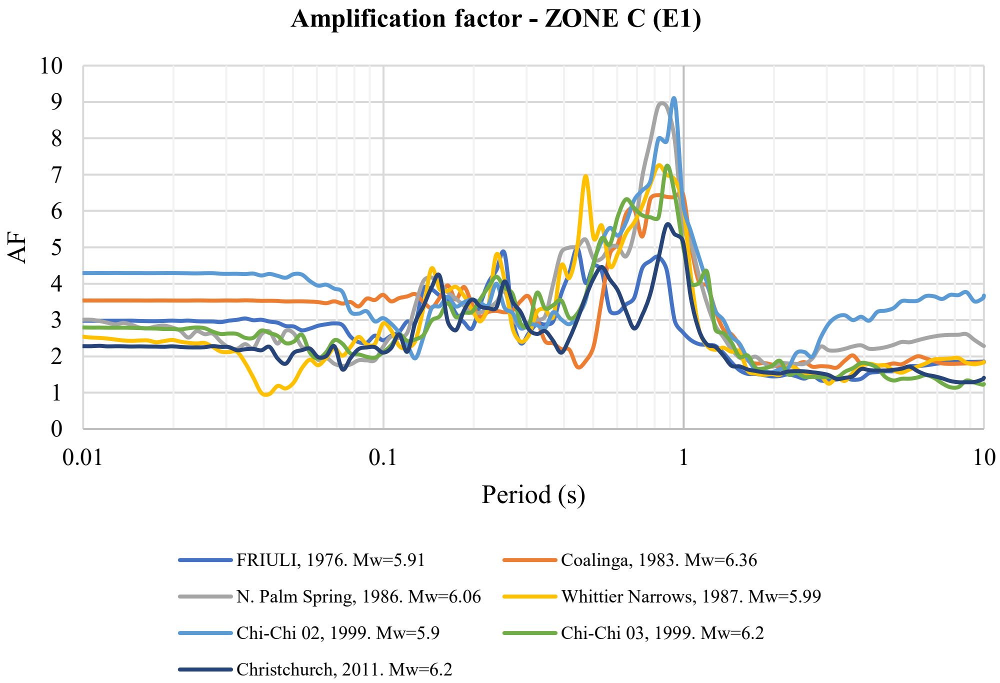

Figure 378. Amplification factor curves for dry samples of Zone C

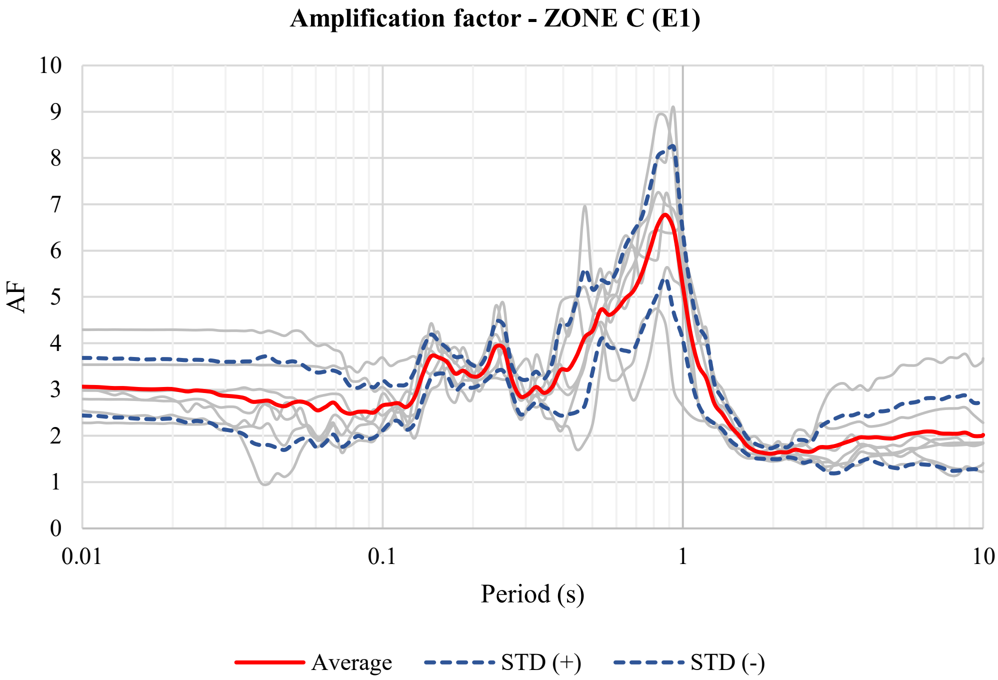

Figure 379. Amplification factor average curves for dry samples of Zone C (Period)

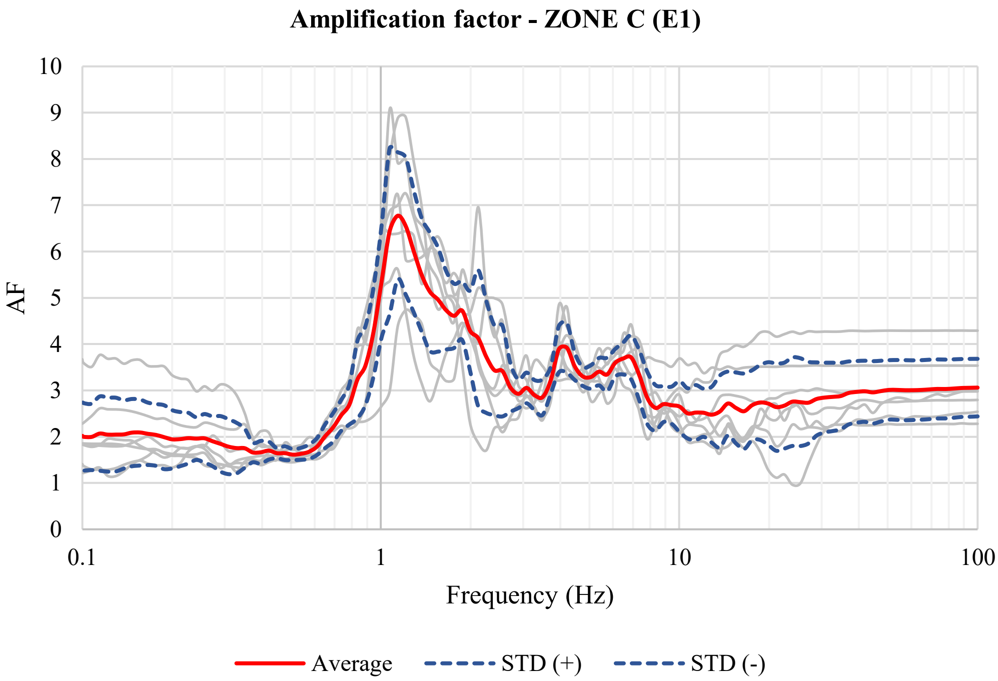

Figure 380. Amplification factor average curves for dry samples of Zone C (Frequency)

Table 66. Maximun values of Amplification factor for dry samples of Zone C

Zone C (E1)			
	Amplification factor	T (s)	F (Hz)
1	6.77	0.88	1.14
2	6.55	0.82	1.21
3	6.44	0.93	1.07

- Zone D

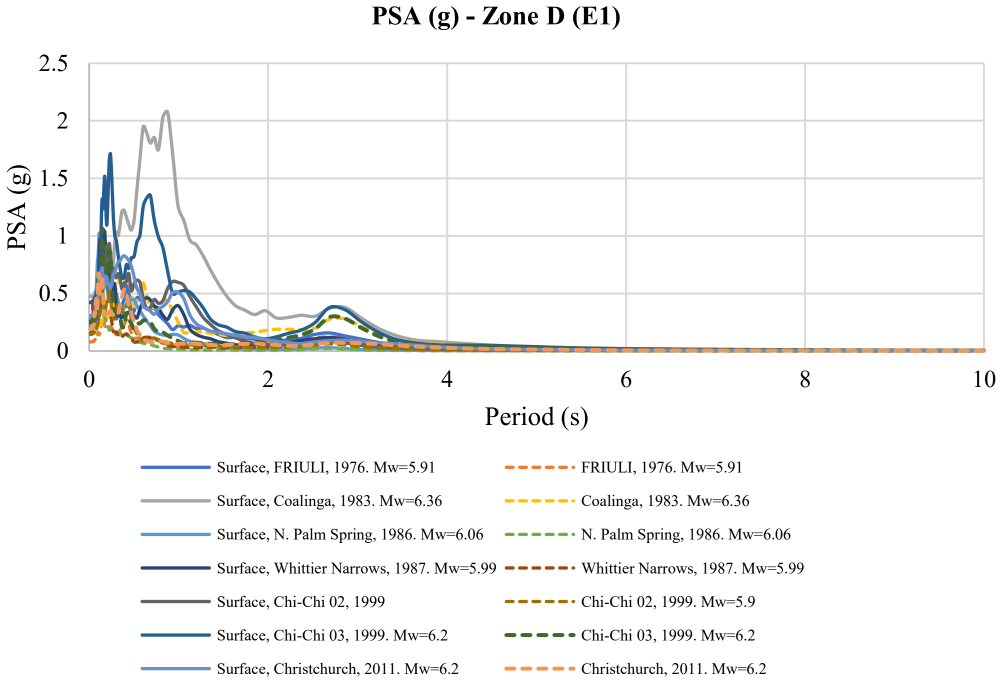

Figure 381. PSA (g) curves for dry samples of Zone D

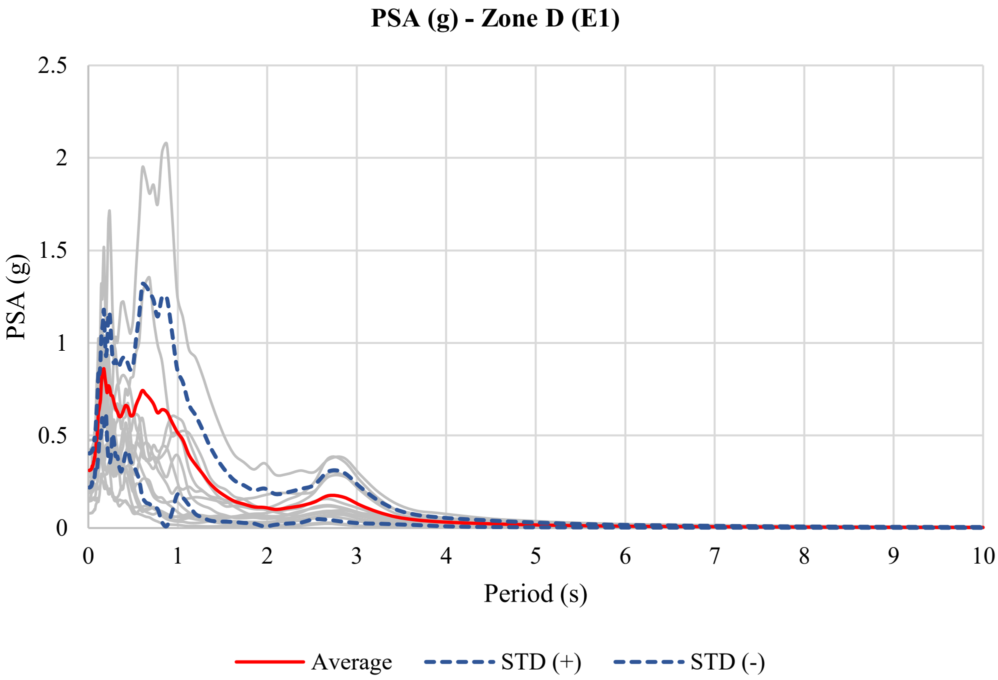

Figure 382. PSA (g) average curves for dry samples of Zone D

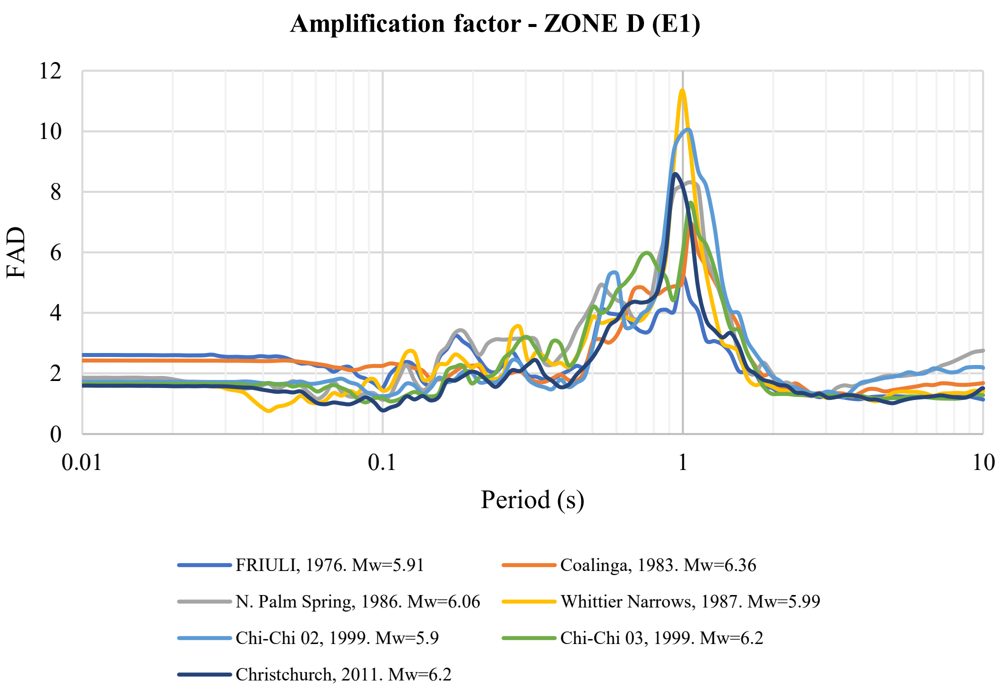

Figure 383. Amplification factor curves for dry samples of Zone D

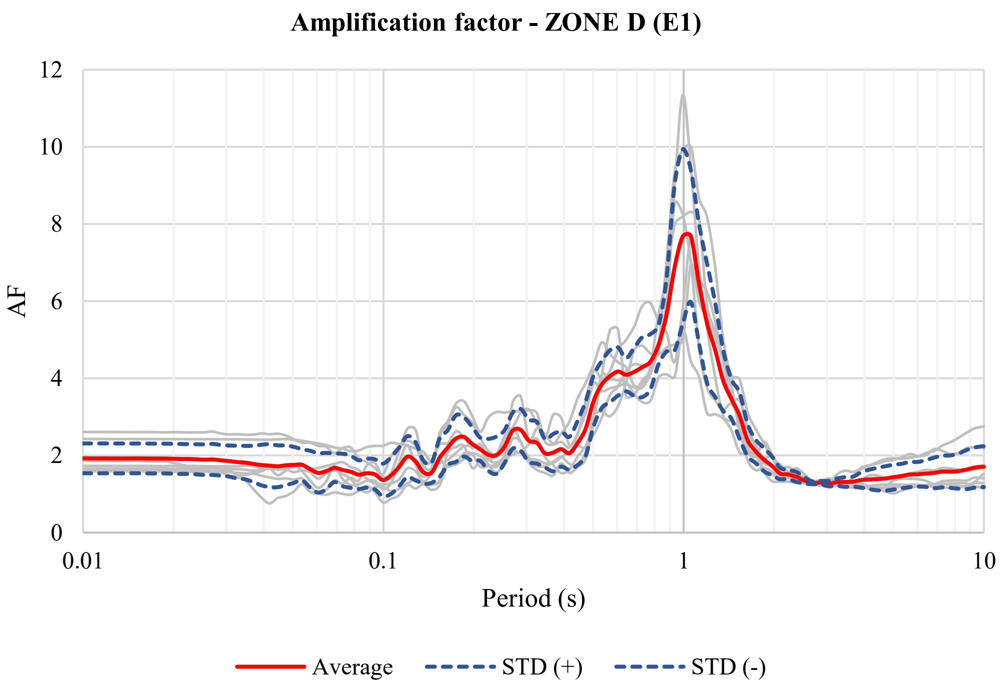

Figure 384. Amplification factor average curves for dry samples of Zone D (Period)

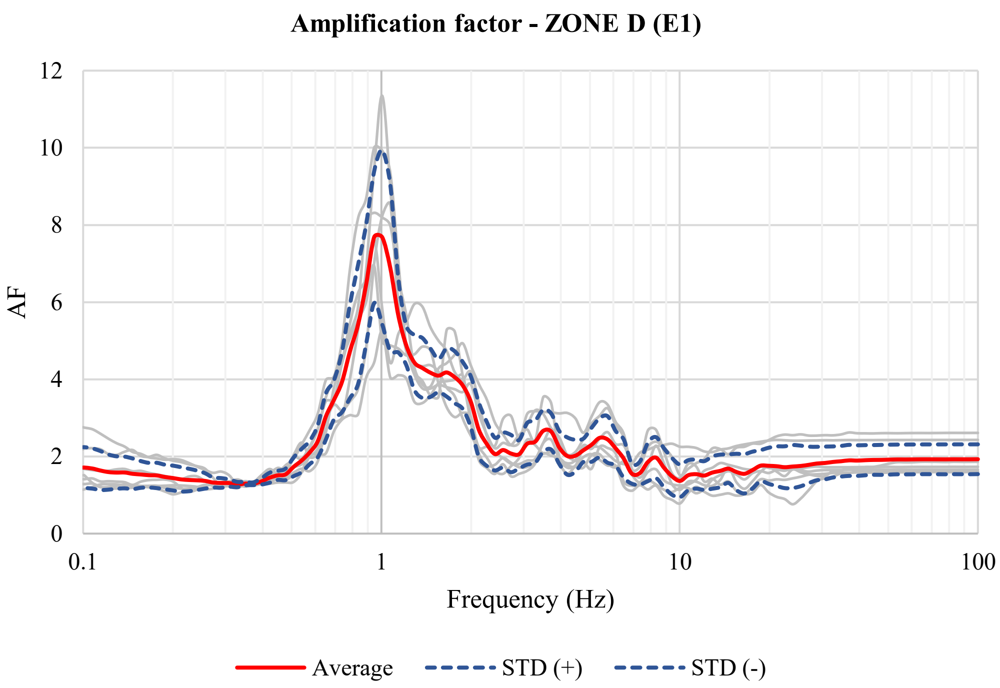

Figure 385. Amplification factor average curves for dry samples of Zone D (Frequency)

Table 67. Maximun values of Amplification factor for dry samples of Zone D

Zone D (E1)			
	Amplification factor	**T (s)**	**F (Hz)**
1	7.68	1.06	0.95
2	7.68	0.99	1.01
3	6.89	0.93	1.07

➢ Zone E

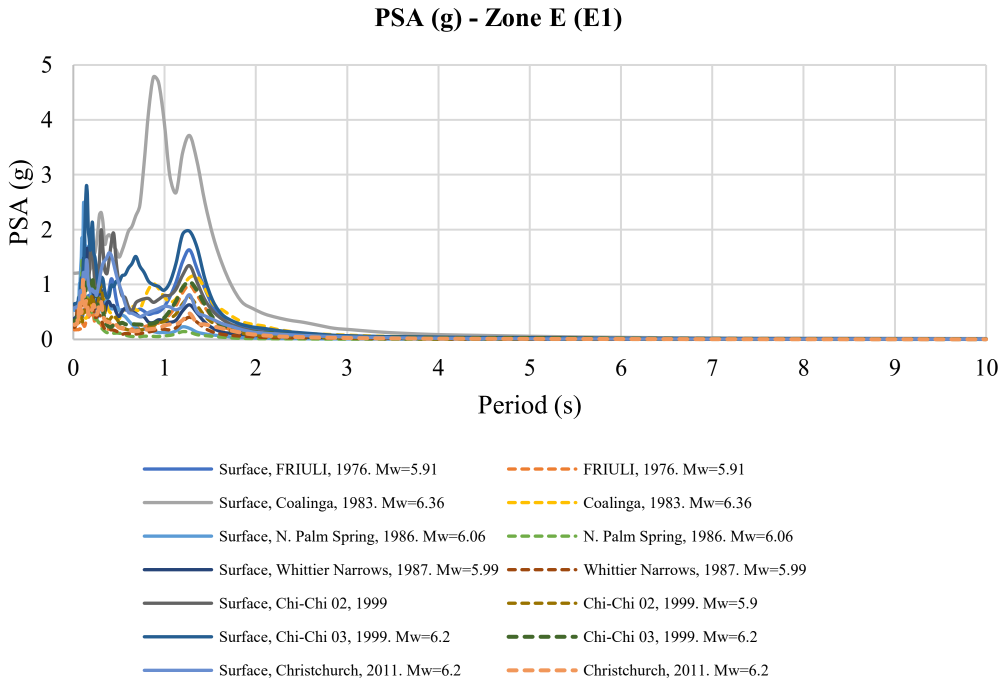

Figure 386. PSA (g) curves for dry samples of Zone E

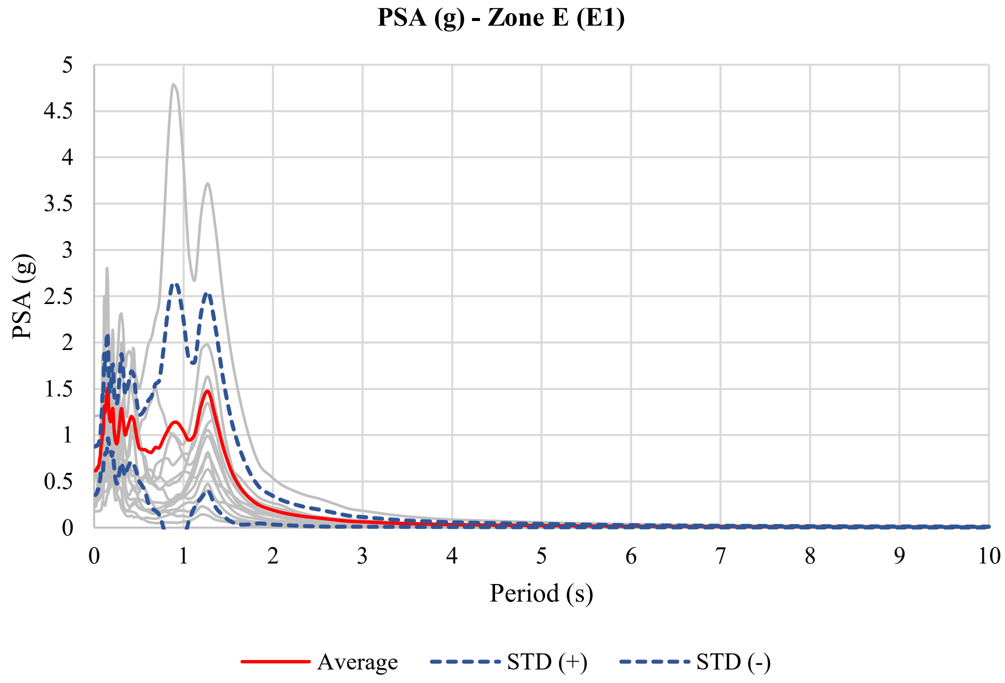

Figure 387. PSA (g) average curves for dry samples of Zone E

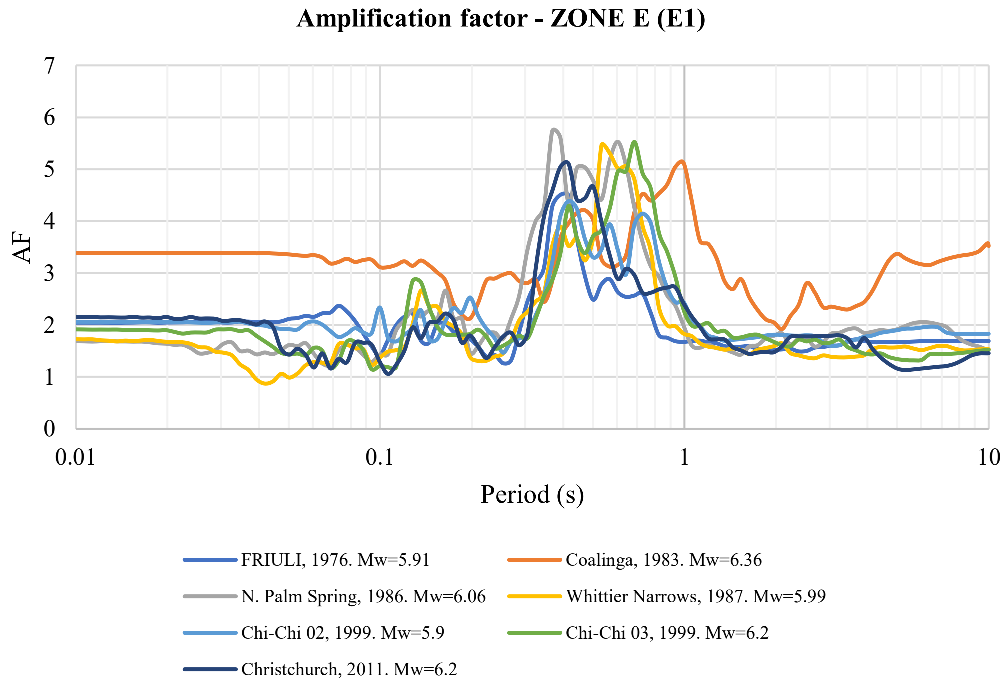

Figure 388. Amplification factor curves for dry samples of Zone E

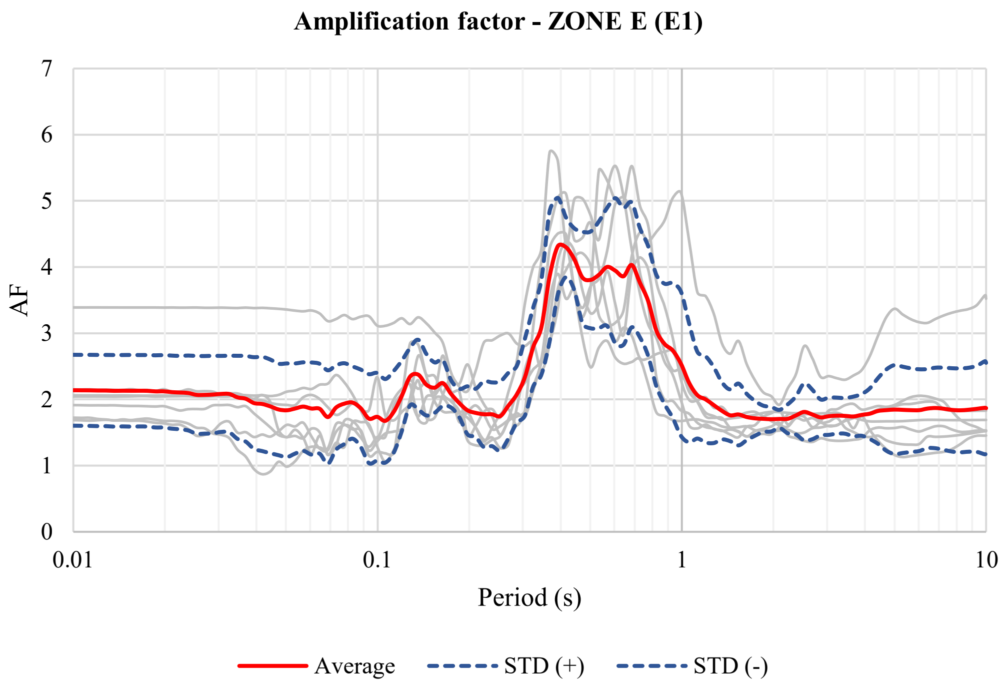

Figure 389. Amplification factor average curves for dry samples of Zone E (Period)

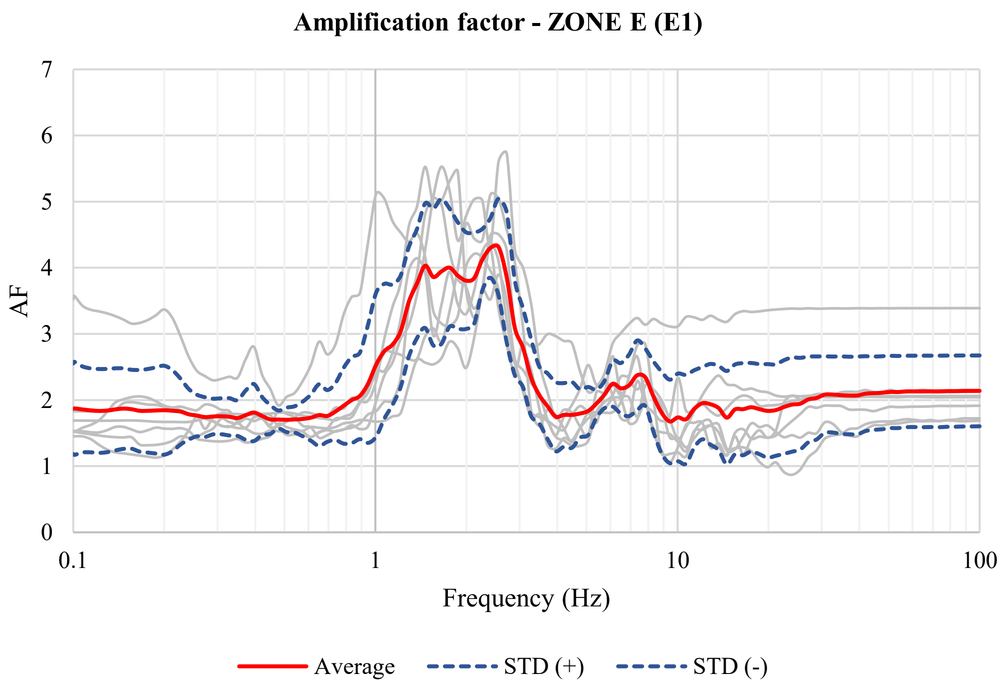

Figure 390. Amplification factor average curves for dry samples of Zone E (Frequency)

Table 68. Maximun values of Amplification factor for dry samples of Zone E

Zone E (E1)			
	Amplification factor	**T (s)**	**F (Hz)**
1	4.31	0.39	2.56
2	4.30	0.42	2.40
3	4.12	0.44	2.26

- Zone F

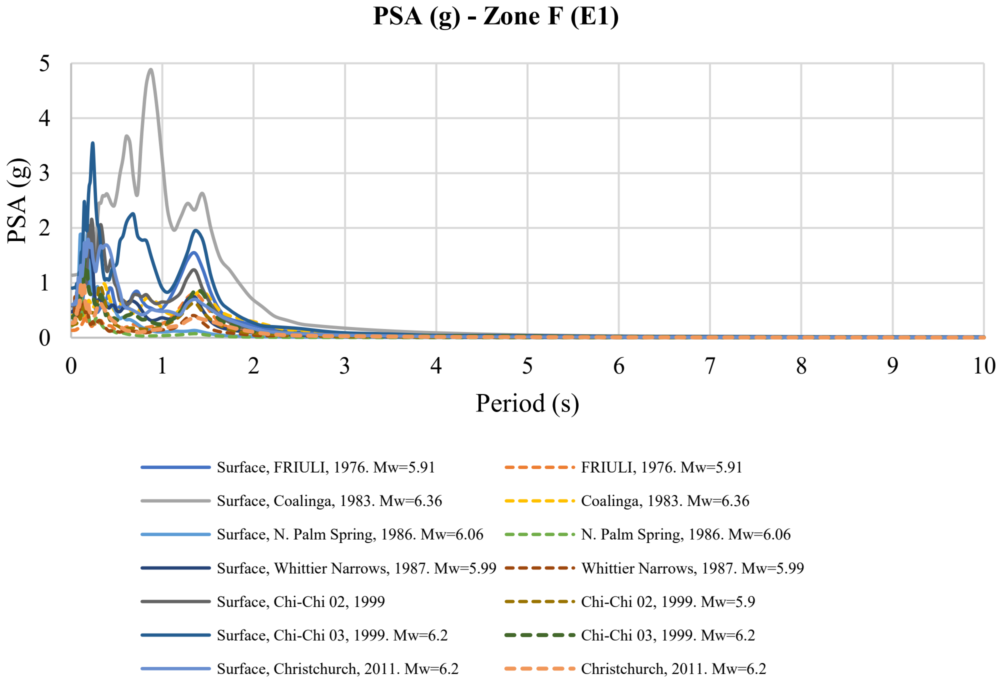

Figure 391. PSA (g) curves for dry samples of Zone F

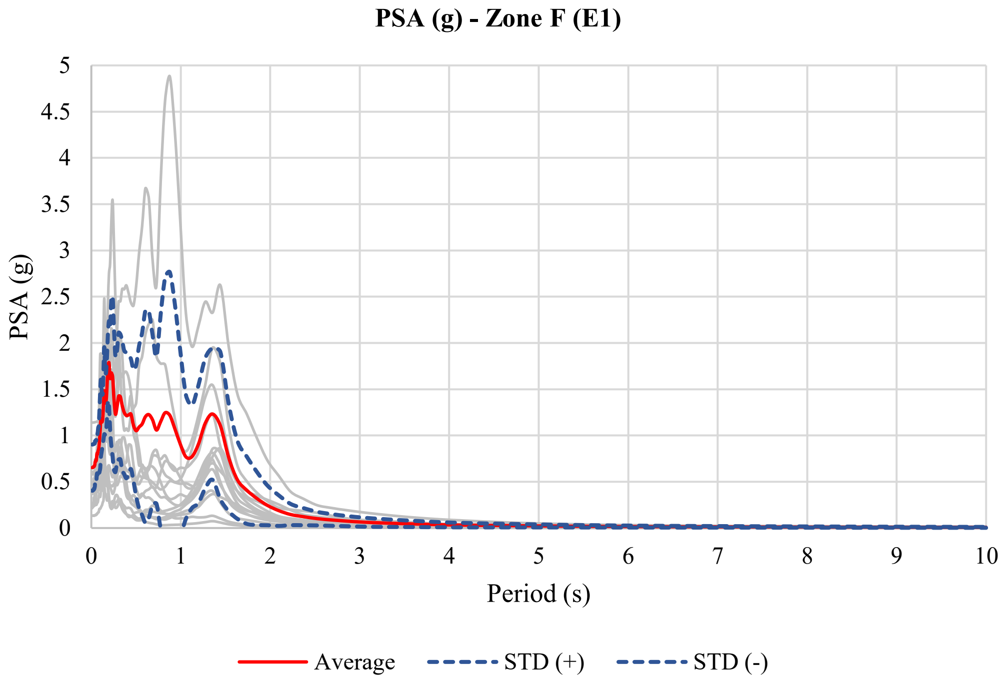

Figure 392. PSA (g) average curves for dry samples of Zone F

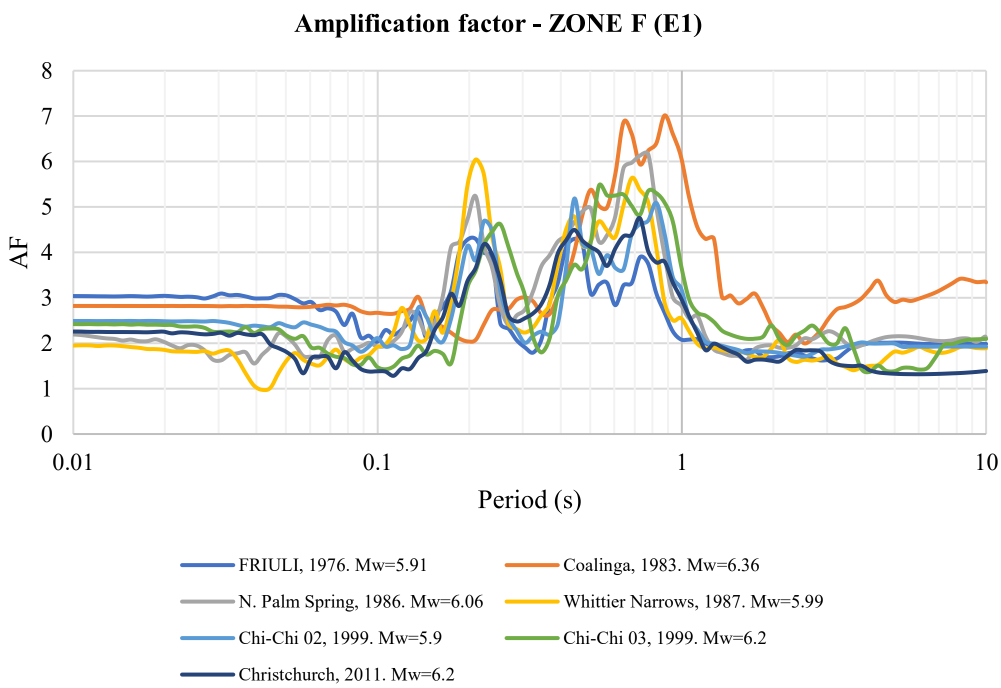

Figure 393. Amplification factor curves for dry samples of Zone F

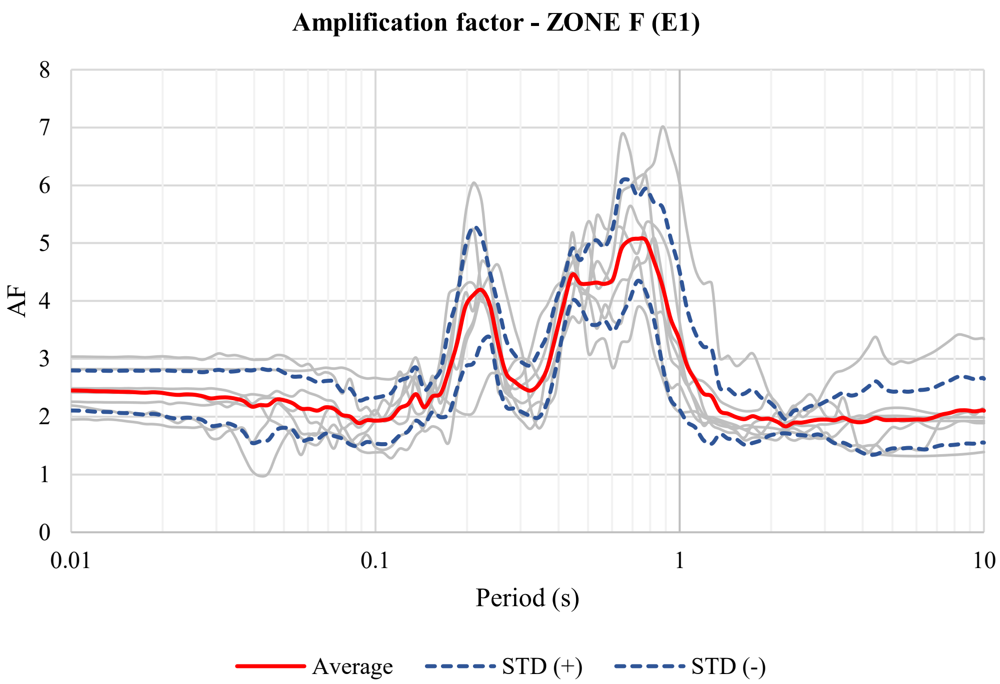

Figure 394. Amplification factor average curves for dry samples of Zone F (Period)

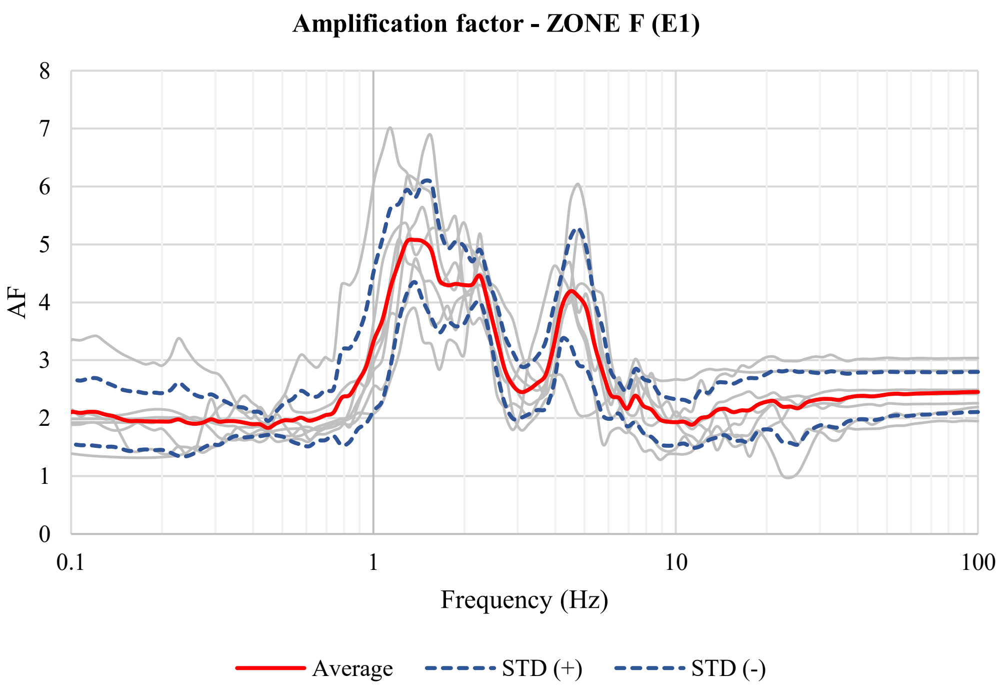

Figure 395. Amplification factor average curves for dry samples of Zone F (Frequency)

Table 69. Maximun values of Amplification factor for dry samples of Zone F

Zone F (E1)			
	Amplification factor	**T (s)**	**F (Hz)**
1	5.08	0.73	1.37
2	5.05	0.68	1.46
3	5.05	0.77	1.29

➢ Zone G

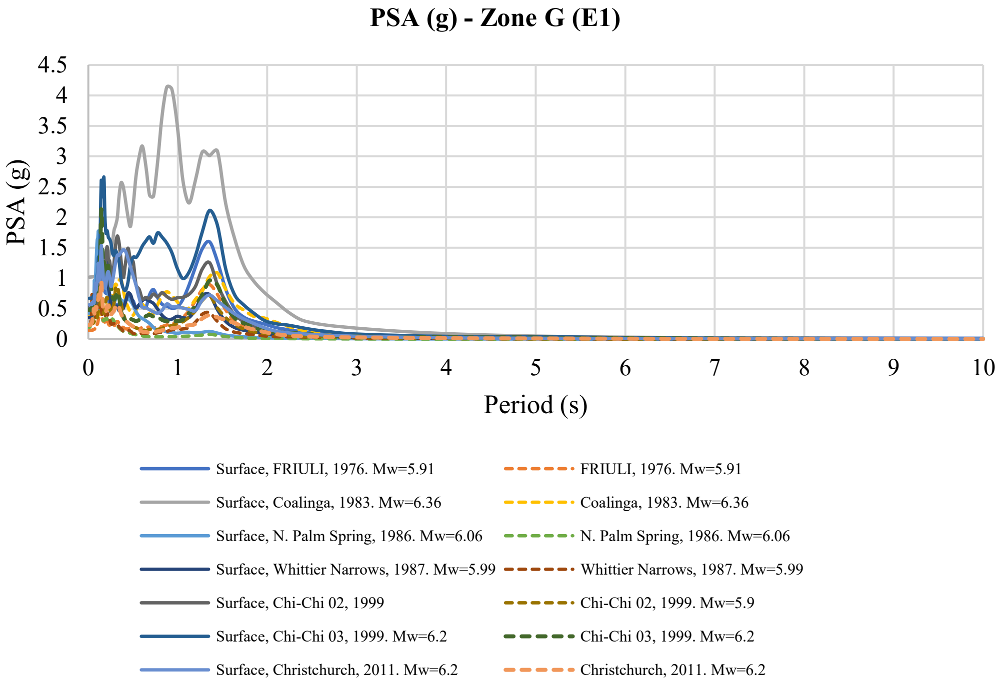

Figure 396. PSA (g) curves for dry samples of Zone G

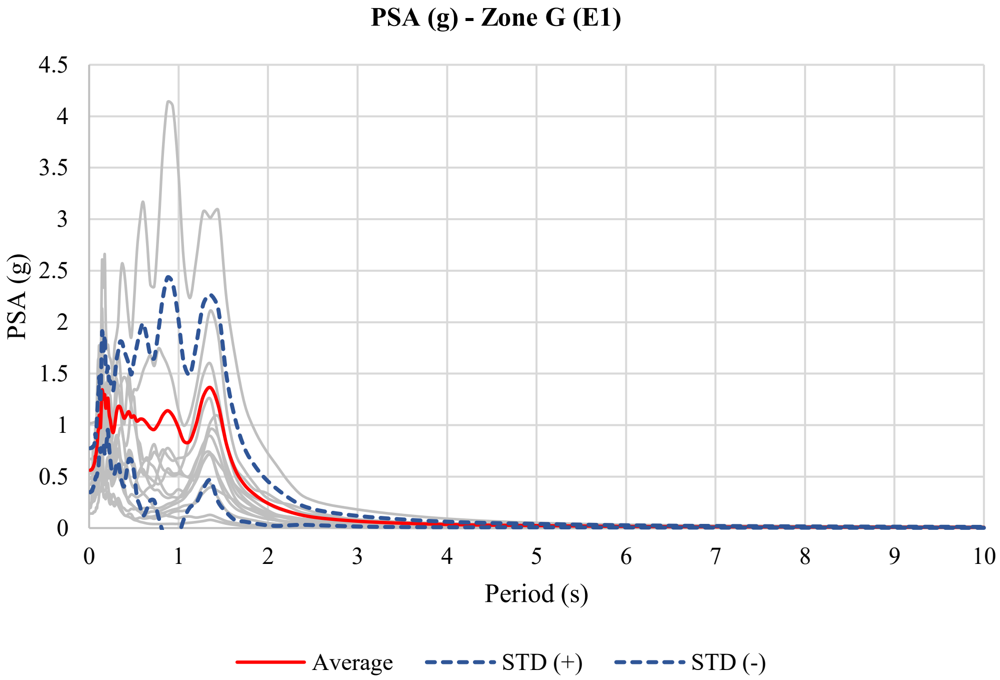

Figure 397. PSA (g) average curves for dry samples of Zone G

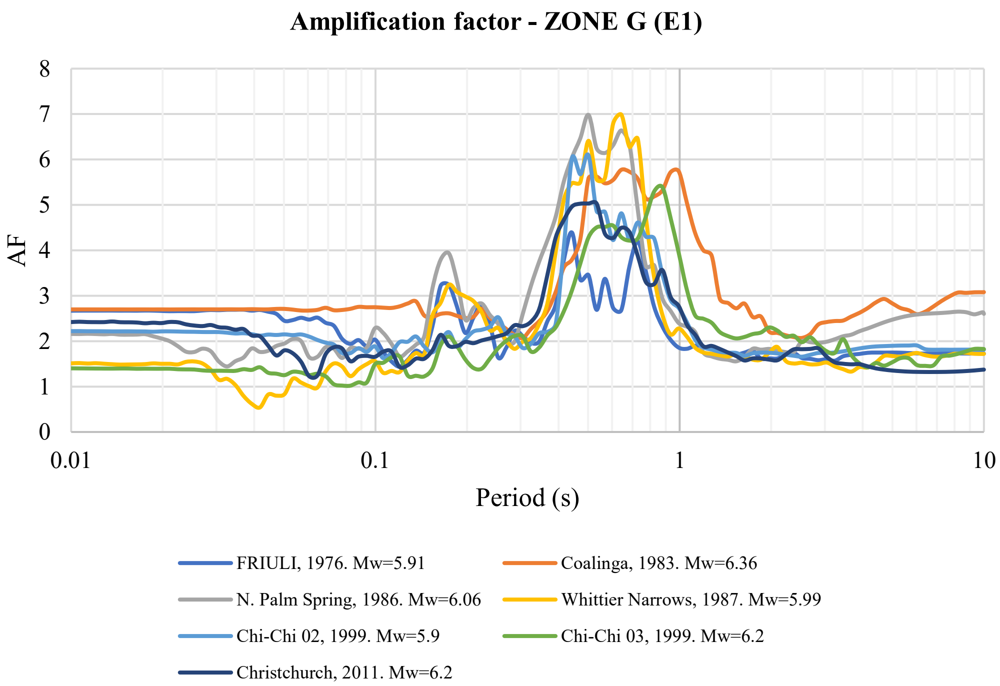

Figure 398. Amplification factor curves for dry samples of Zone G

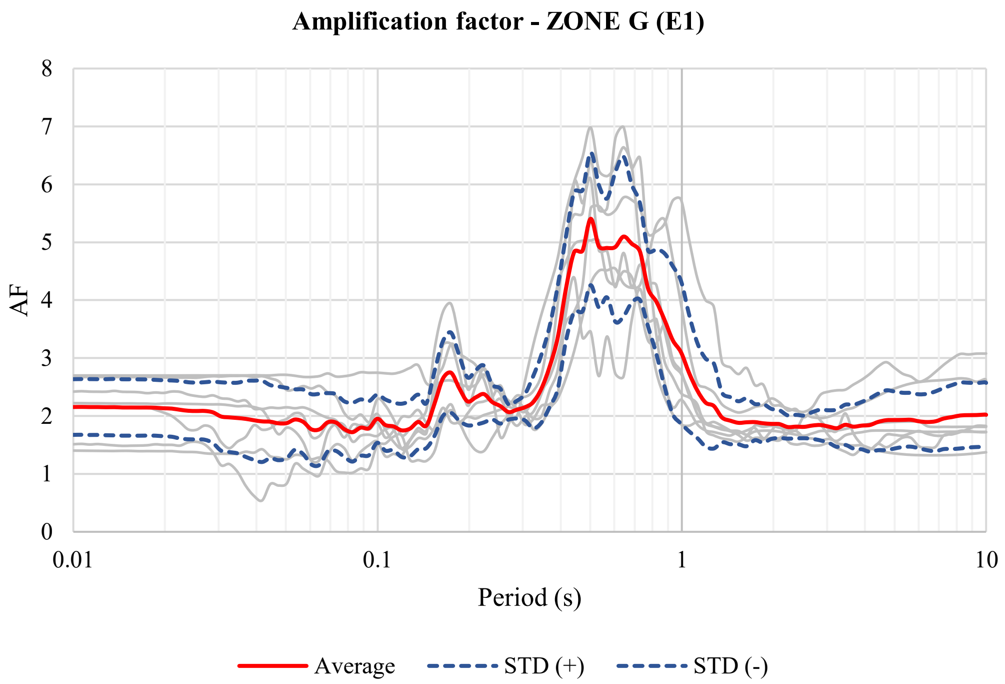

Figure 399. Amplification factor average curves for dry samples of Zone G (Period)

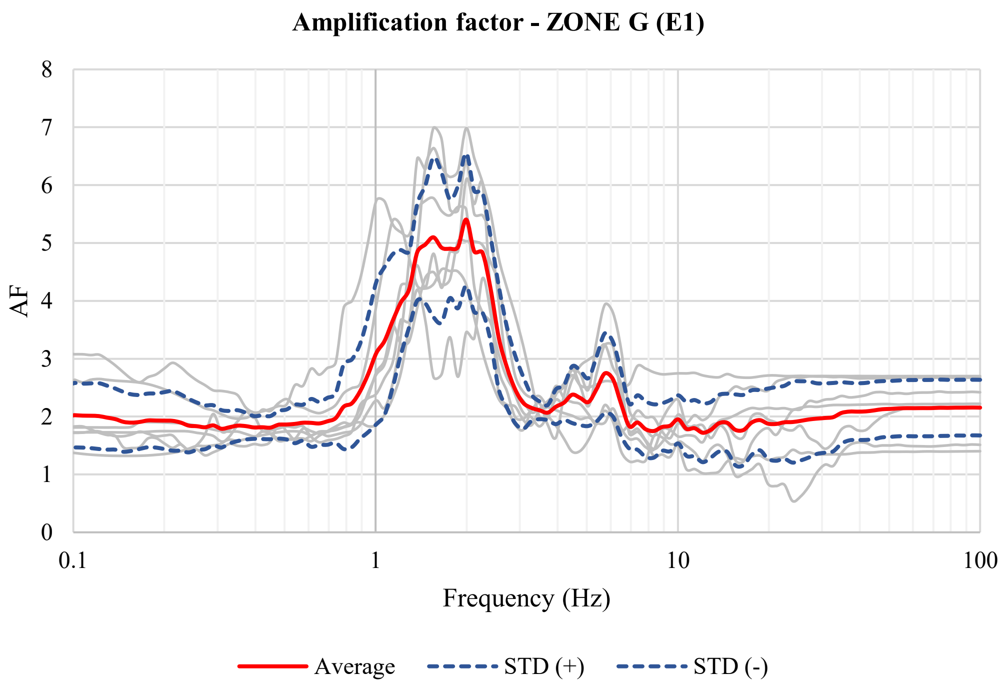

Figure 400. Amplification factor average curves for dry samples of Zone G (Frequency)

Table 70. Maximun values of Amplification factor for dry samples of Zone G

Zone G (E1)			
	Amplification factor	**T (s)**	**F (Hz)**
1	5.40	0.50	1.99
2	5.10	0.64	1.55
3	4.97	0.68	1.46

➢ Zone H

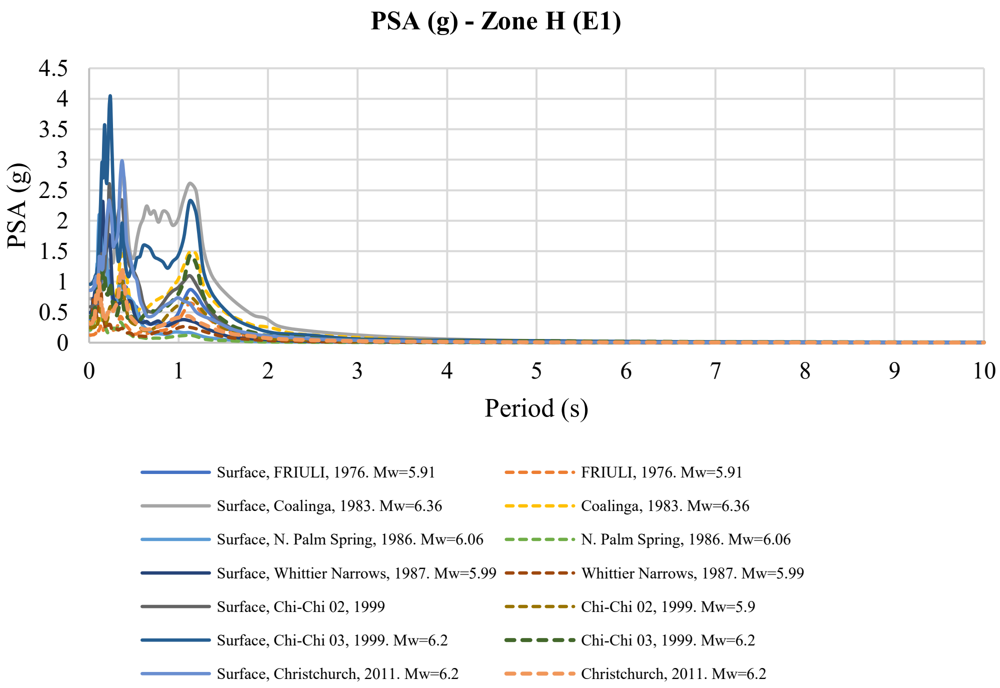

Figure 401. PSA (g) curves for dry samples of Zone H

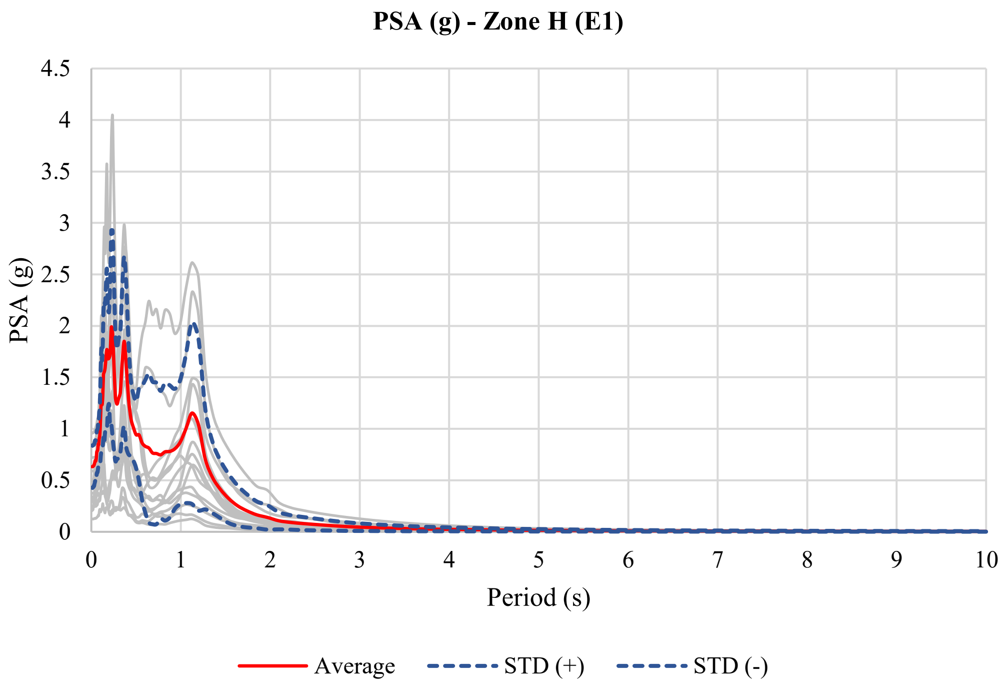

Figure 402. PSA (g) average curves for dry samples of Zone H

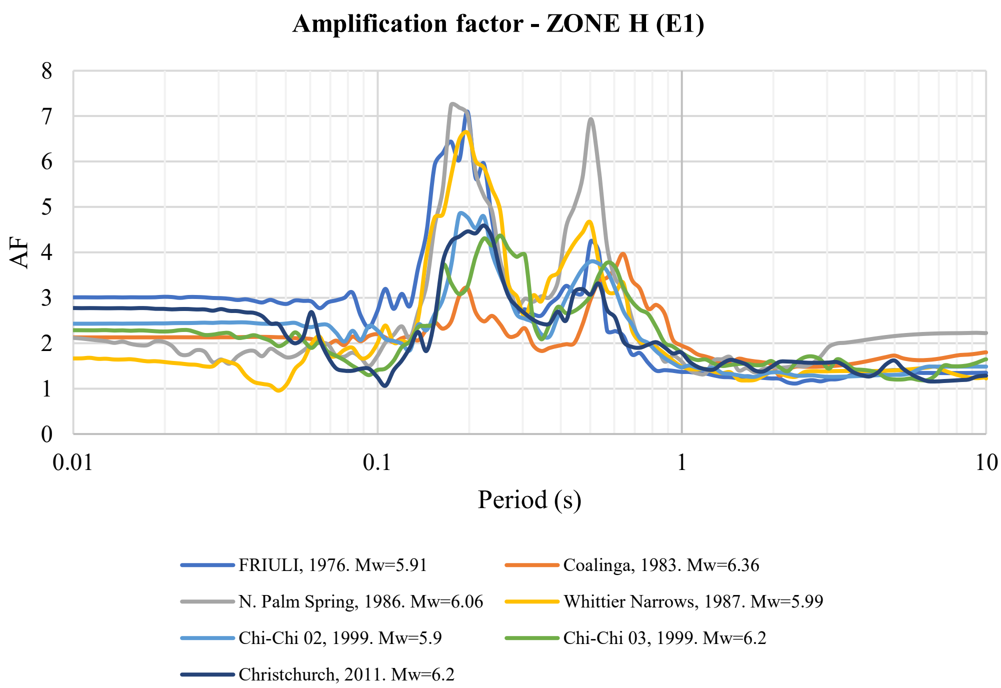

Figure 403. Amplification factor curves for dry samples of Zone H

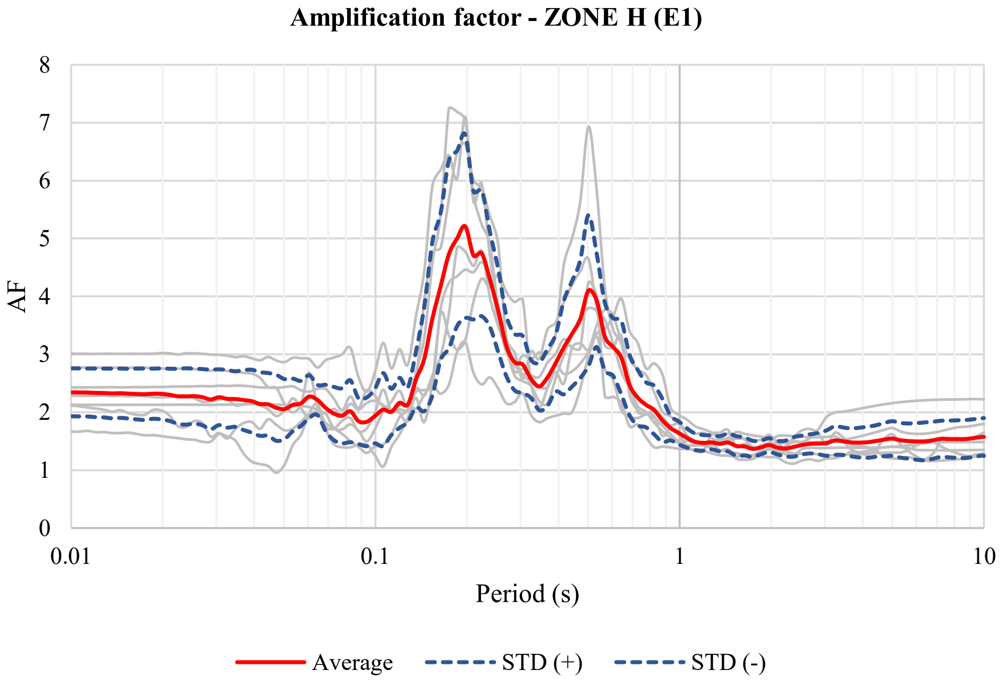

Figure 404. Amplification factor average curves for dry samples of Zone H (Period)

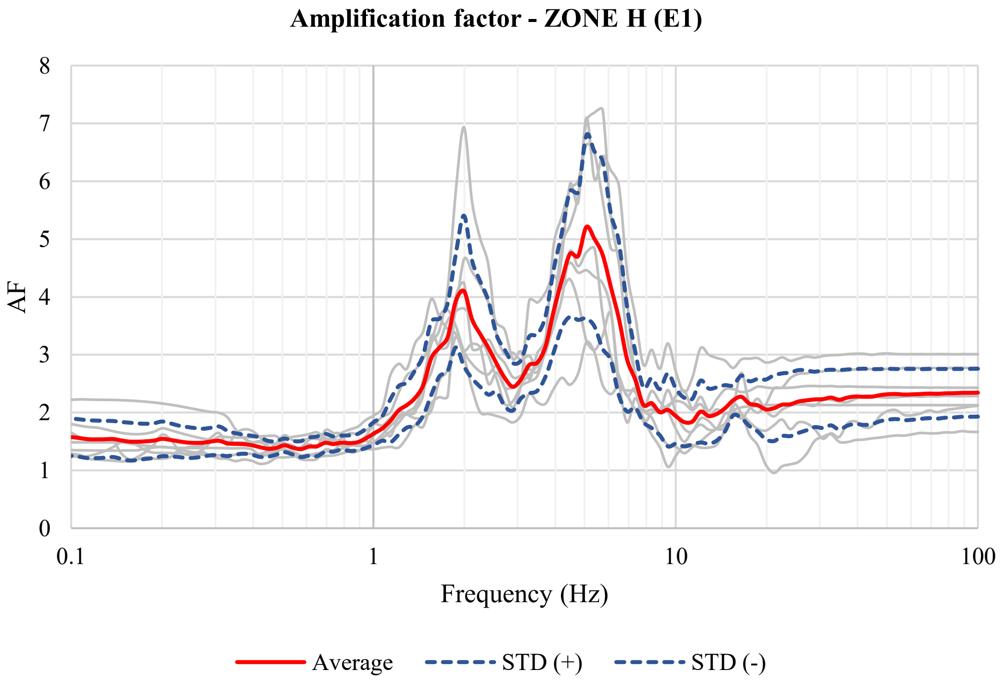

Figure 405. Amplification factor average curves for dry samples of Zone H (Frequency)

Table 71. Maximun values of Amplification factor for dry samples of Zone H

Zone H (E1)			
	Amplification factor	T (s)	F (Hz)
1	5.21	0.20	5.06
2	5.00	0.19	5.39
3	4.75	0.22	4.47

- Zone I

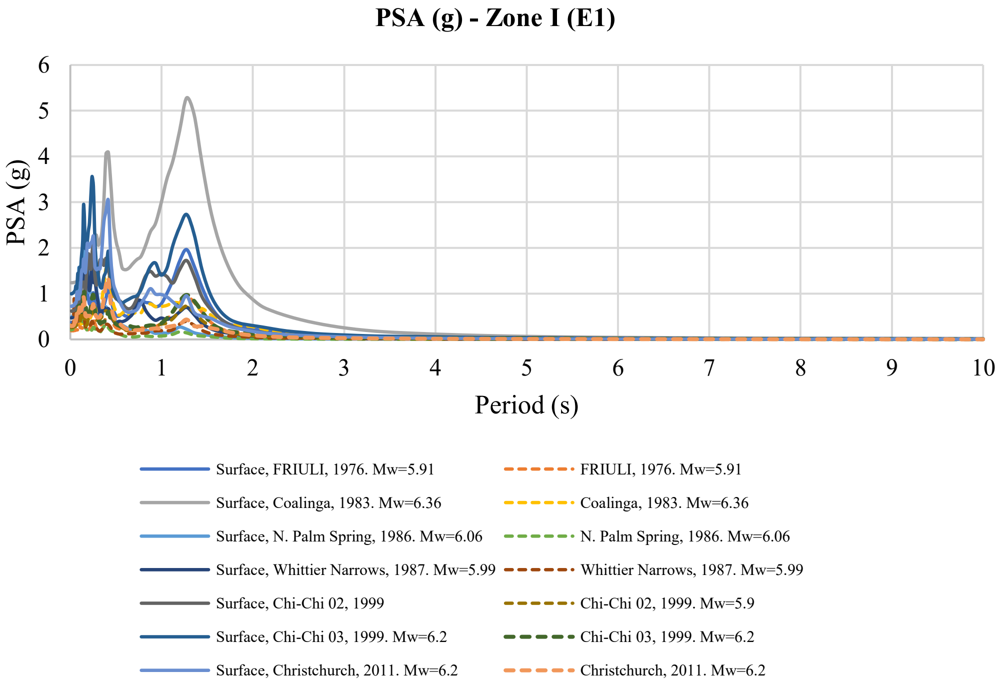

Figure 406. PSA (g) curves for dry samples of Zone I

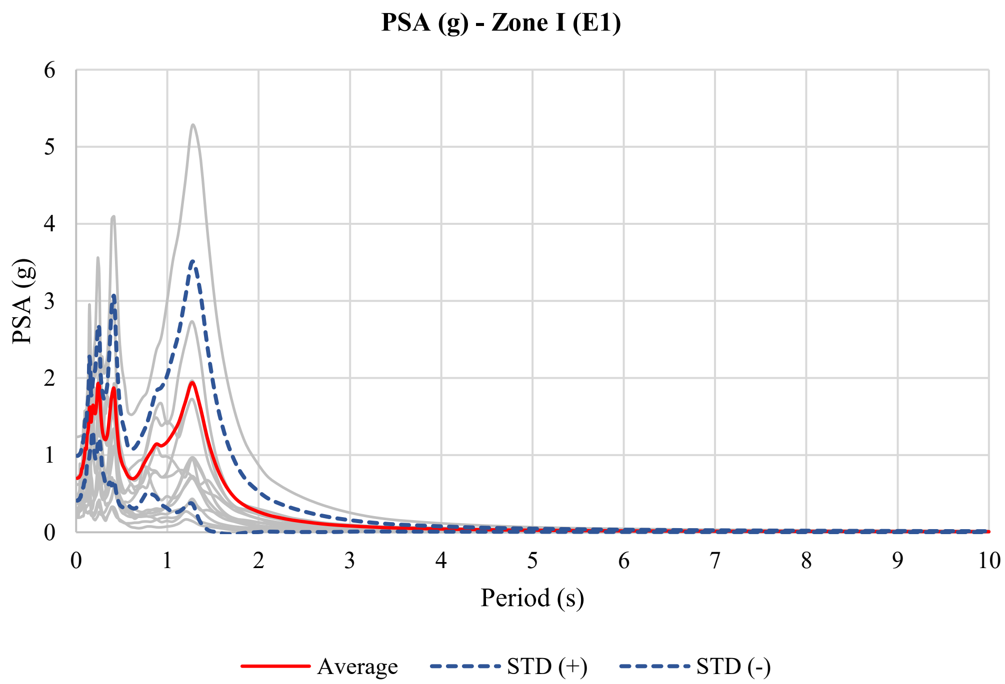

Figure 407. PSA (g) average curves for dry samples of Zone I

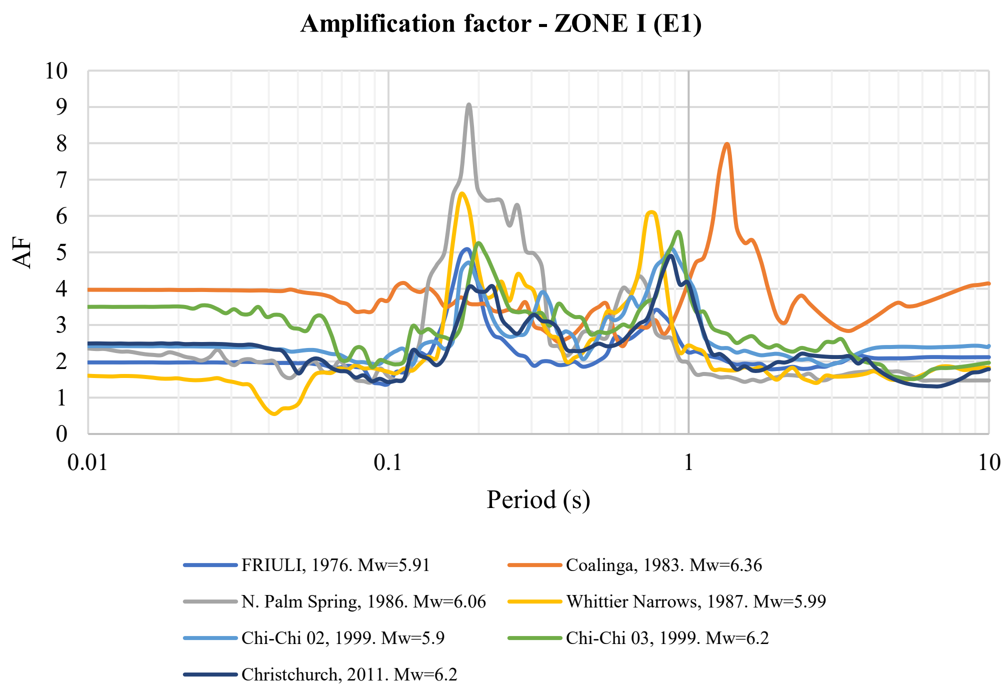

Figure 408. Amplification factor curves for dry samples of Zone I

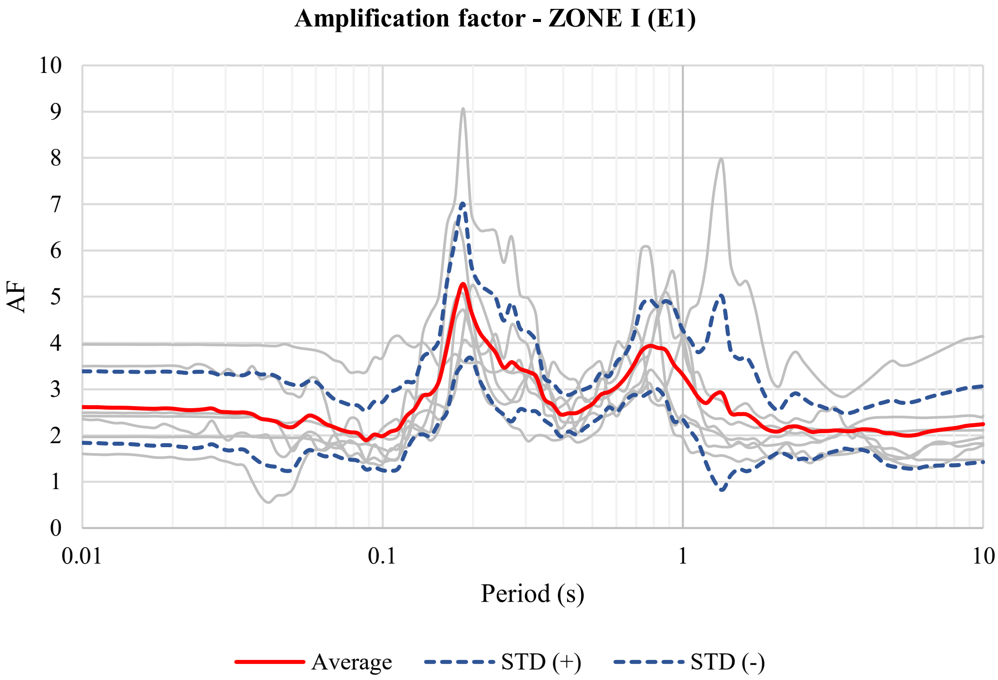

Figure 409. Amplification factor average curves for dry samples of Zone I (Period)

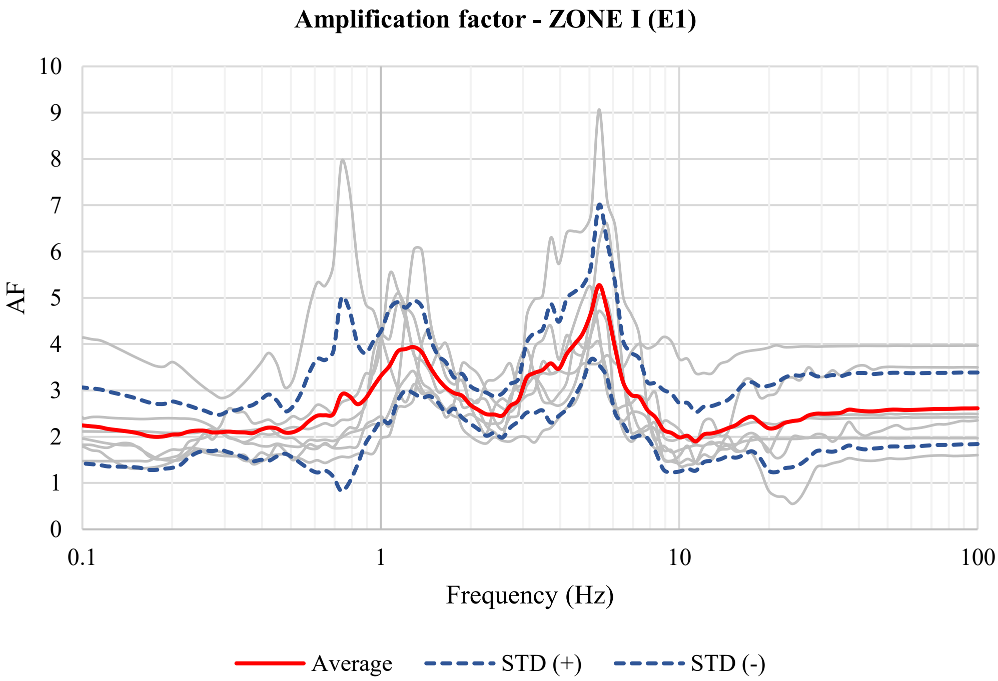

Figure 410. Amplification factor average curves for dry samples of Zone I (Frequency)

Table 72. Maximun values of Amplification factor for dry samples of Zone I

Zone I (E1)			
	Amplification factor	**T (s)**	**F (Hz)**
1	5.28	0.19	5.39
2	4.74	0.17	5.73
3	4.68	0.20	5.06

C.2.3. Analysis with remolded samples

- Zone A

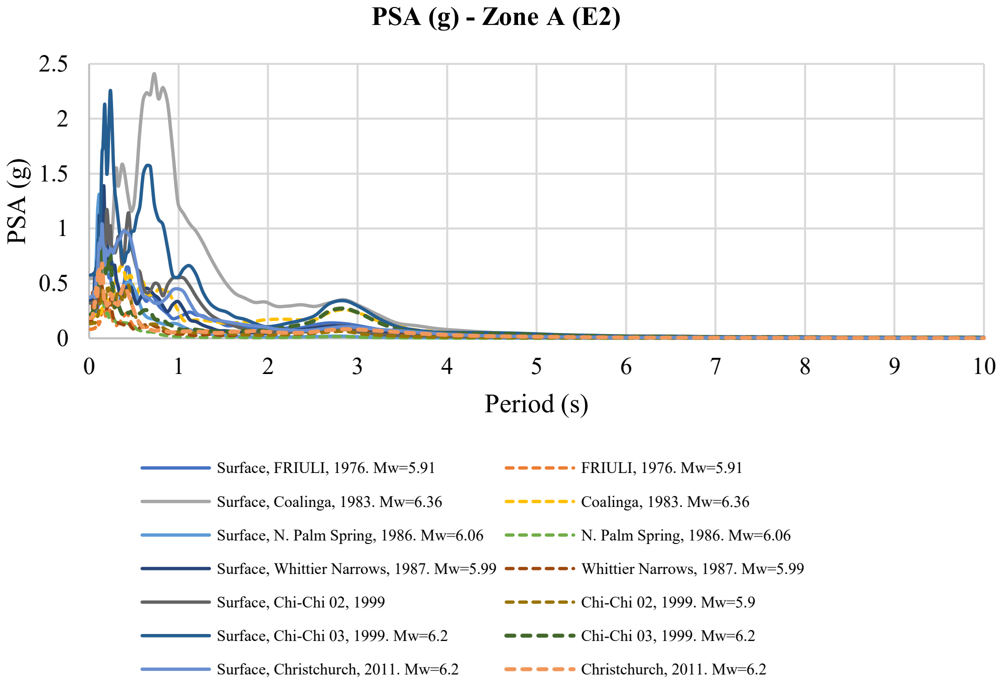

Figure 411. PSA (g) curves for remolded samples of Zone A

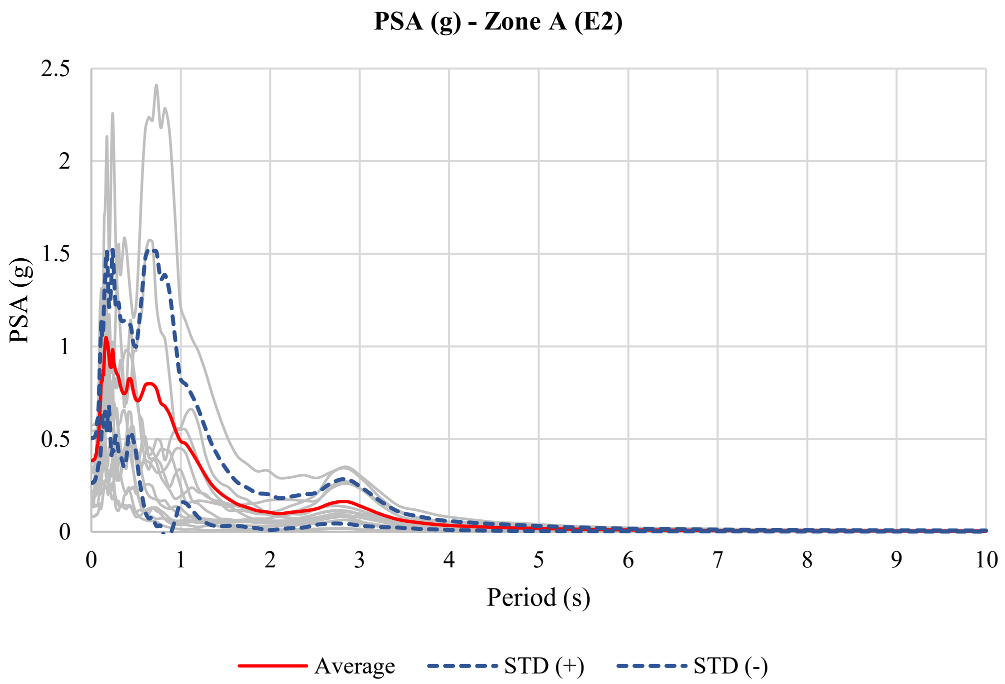

Figure 412. PSA (g) average curves for remolded samples of Zone A

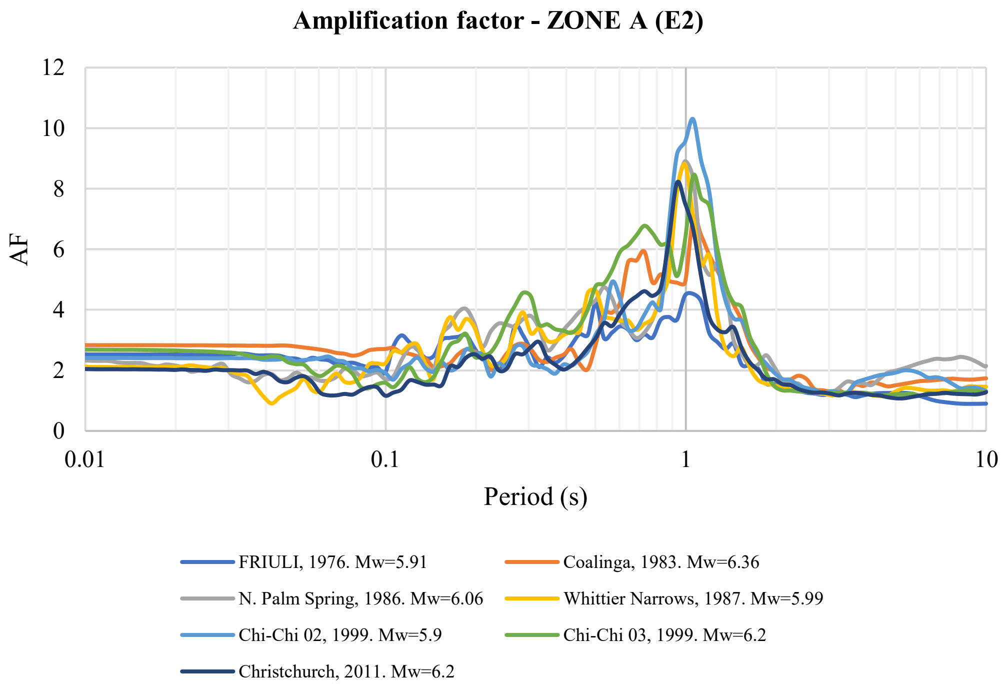

Figure 413. Amplification factor curves for remolded samples of Zone A

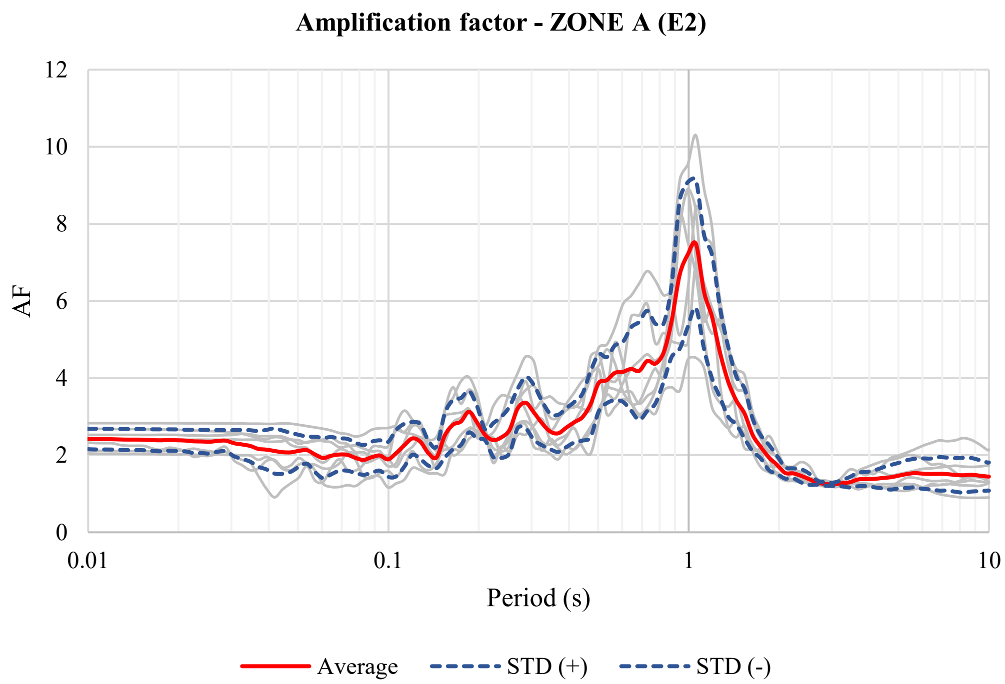

Figure 414. Amplification factor average curves for remolded samples of Zone A (Period)

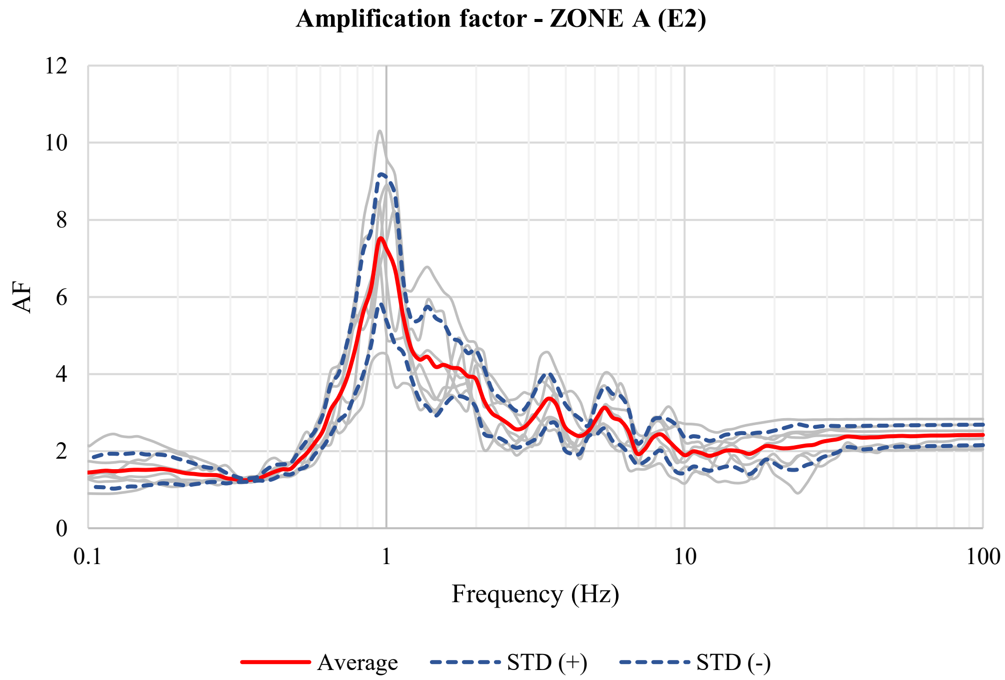

Figure 415. Amplification factor average curves for remolded samples of Zone A (Frequency)

Table 73. Maximun values of Amplification factor for remolded samples of Zone A

Zone A (E2)			
	Amplification factor	T (s)	F (Hz)
1	7.48	1.06	0.95
2	7.21	0.99	1.01
3	6.69	0.93	1.07

➢ Zone B

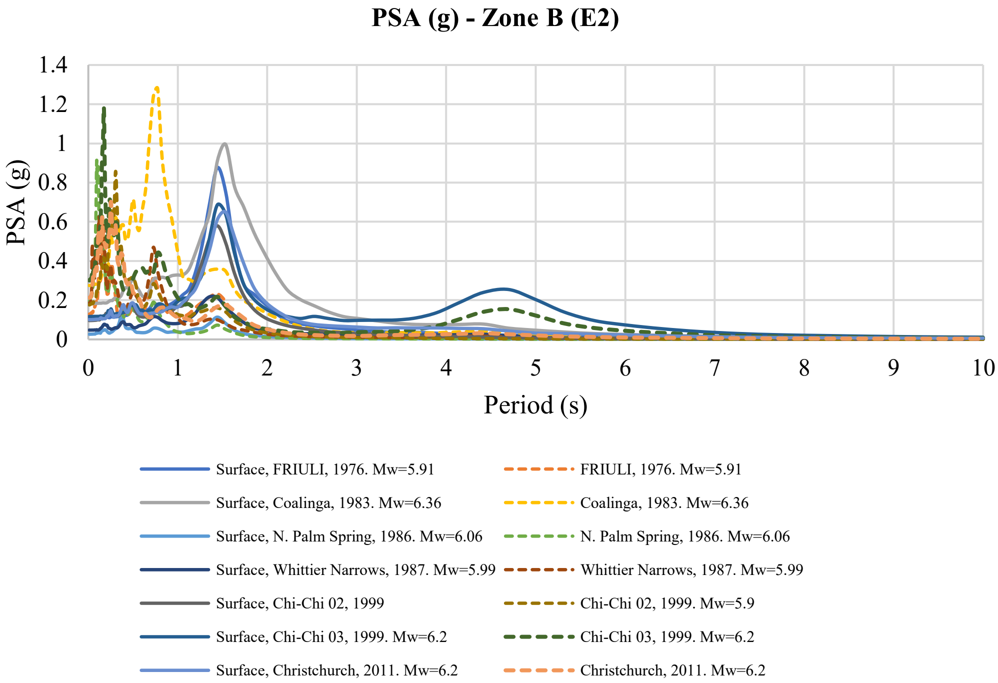

Figure 416. PSA (g) curves for remolded samples of Zone B

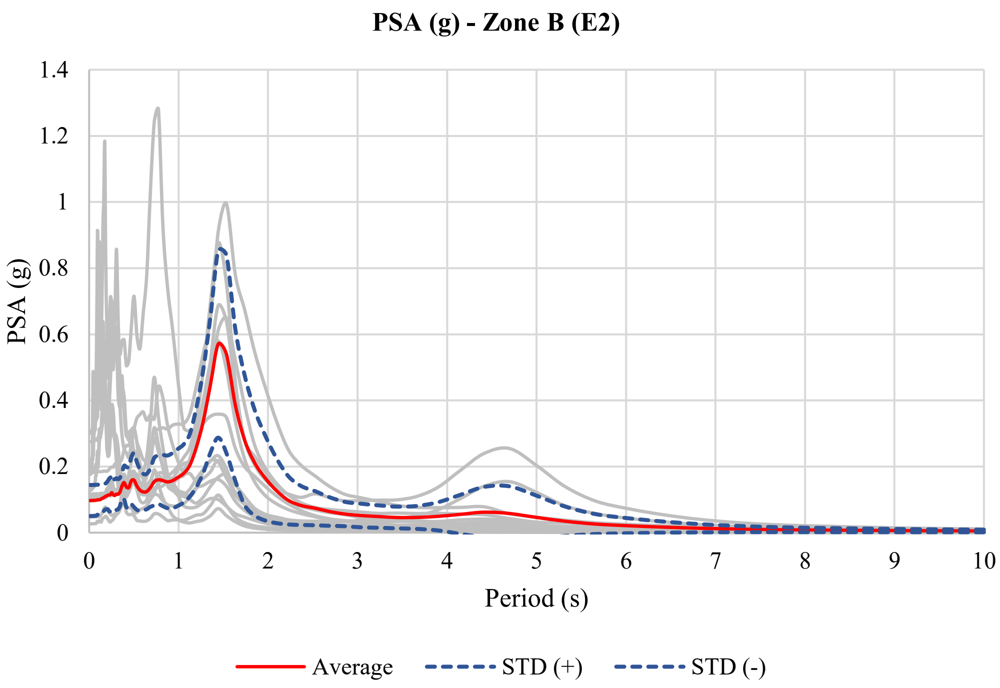

Figure 417. PSA (g) average curves for remolded samples of Zone B

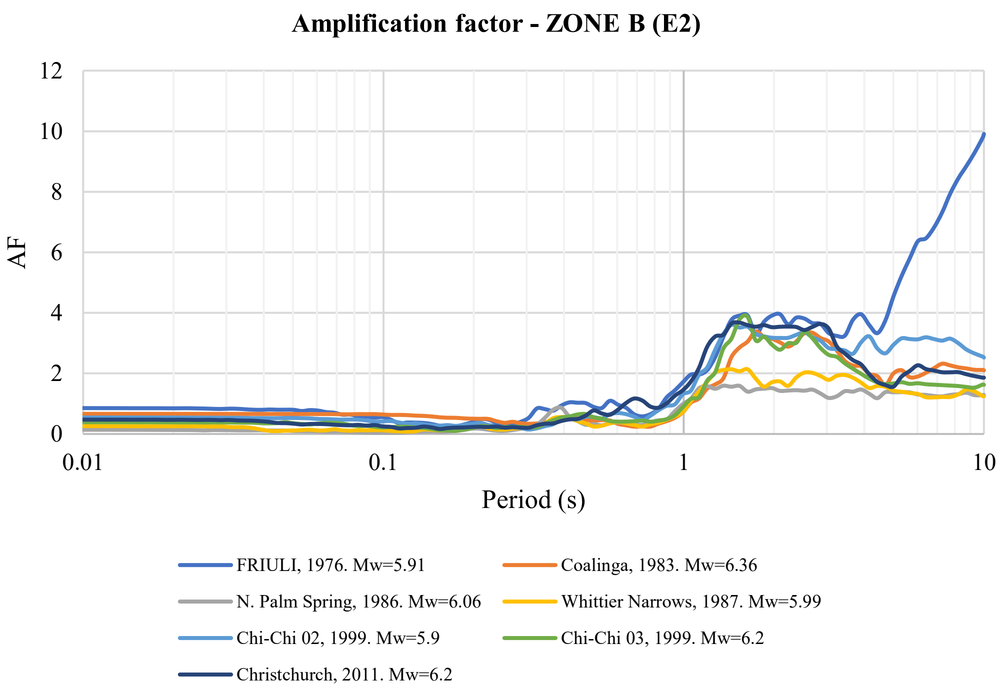

Figure 418. Amplification factor curves for remolded samples of Zone B

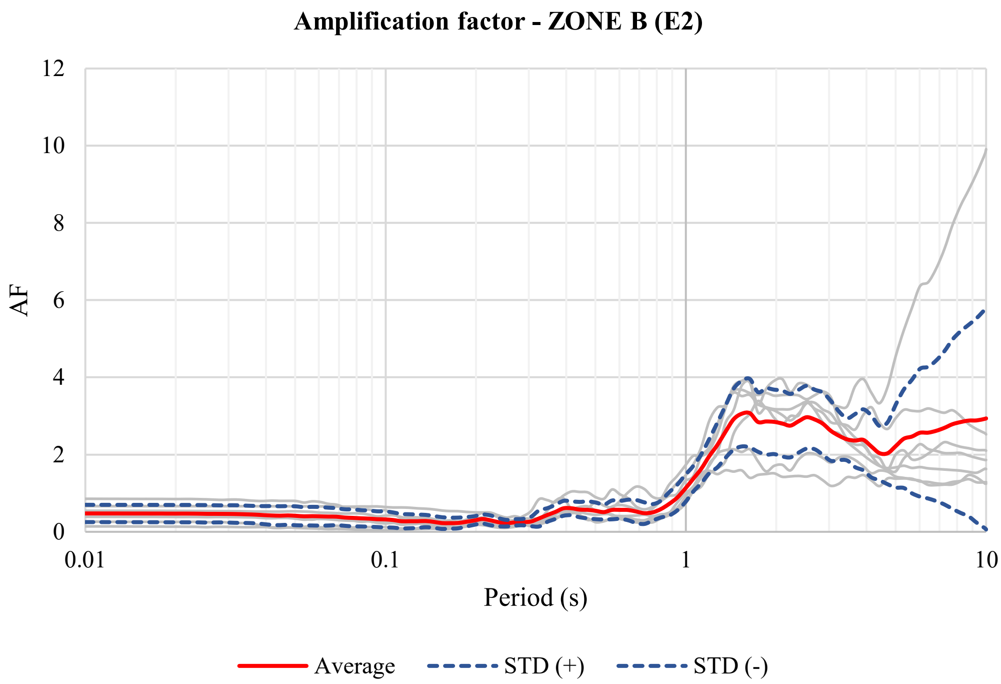

Figure 419. Amplification factor average curves for remolded samples of Zone B (Period)

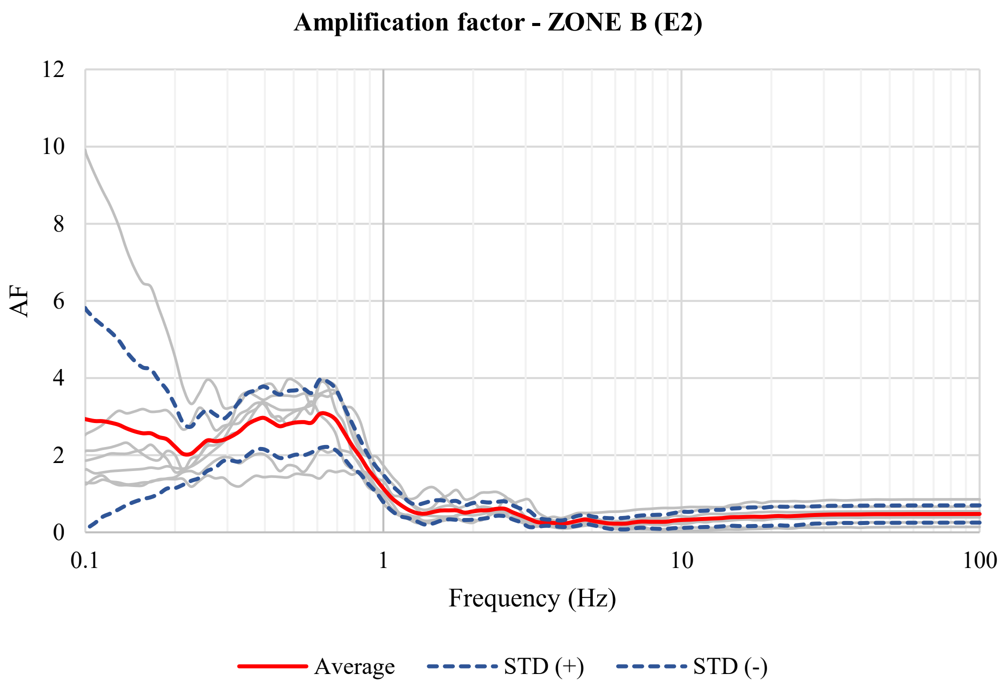

Figure 420. Amplification factor average curves for remolded samples of Zone B (Frequency)

Table 74. Maximun values of Amplification factor for remolded samples of Zone B

Zone B (E2)			
	Amplification factor	T (s)	F (Hz)
1	3.07	1.63	0.61
2	3.06	1.54	0.65
3	2.97	2.52	0.40

- Zone C

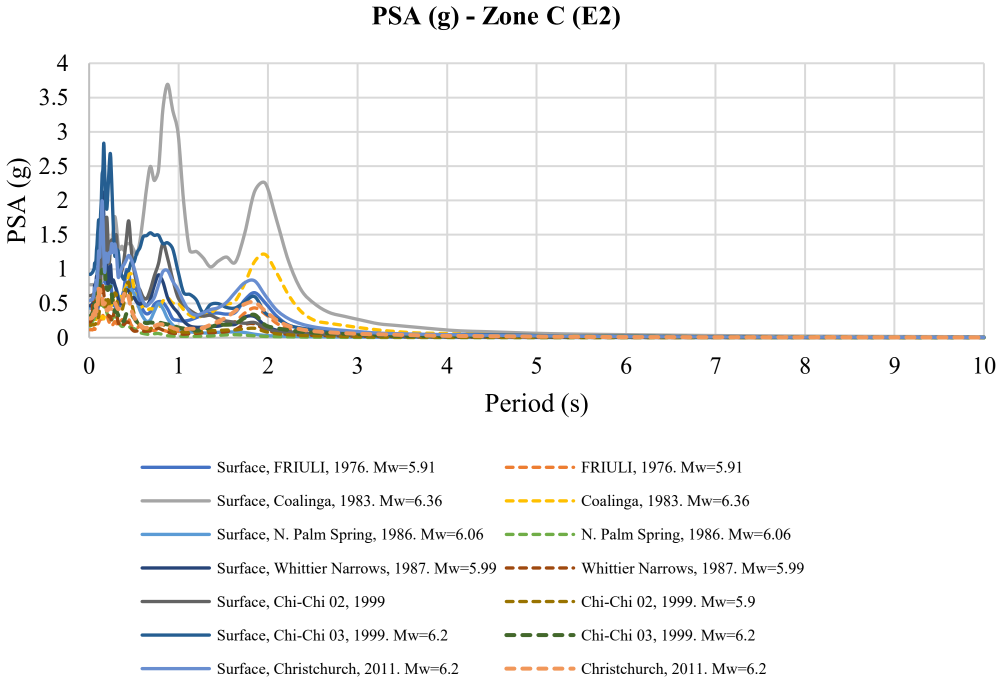

Figure 421. PSA (g) curves for remolded samples of Zone C

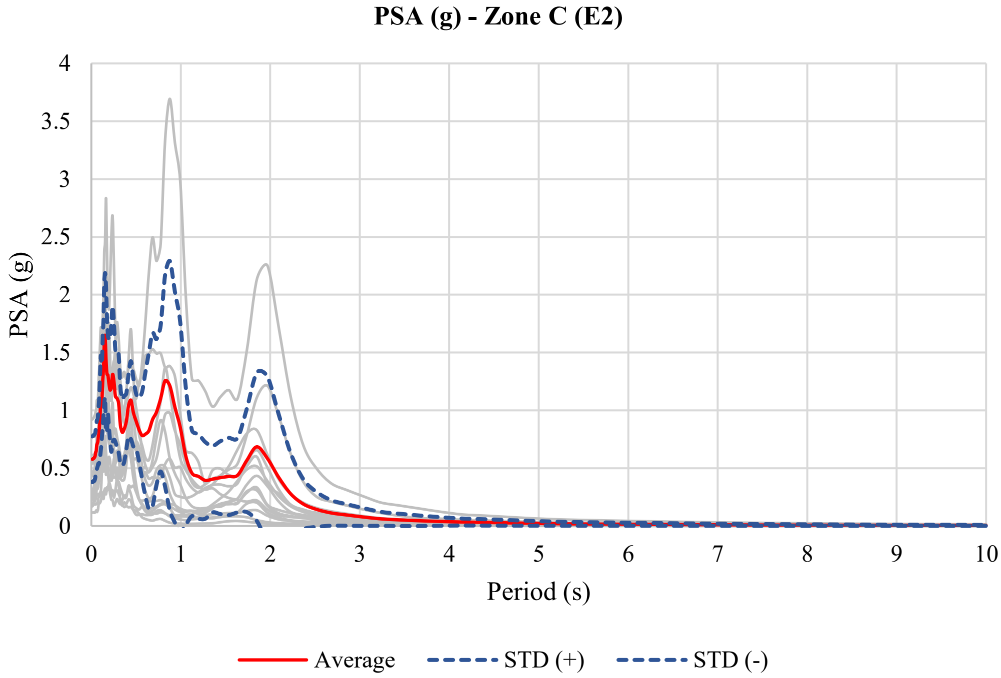

Figure 422. PSA (g) average curves for remolded samples of Zone C

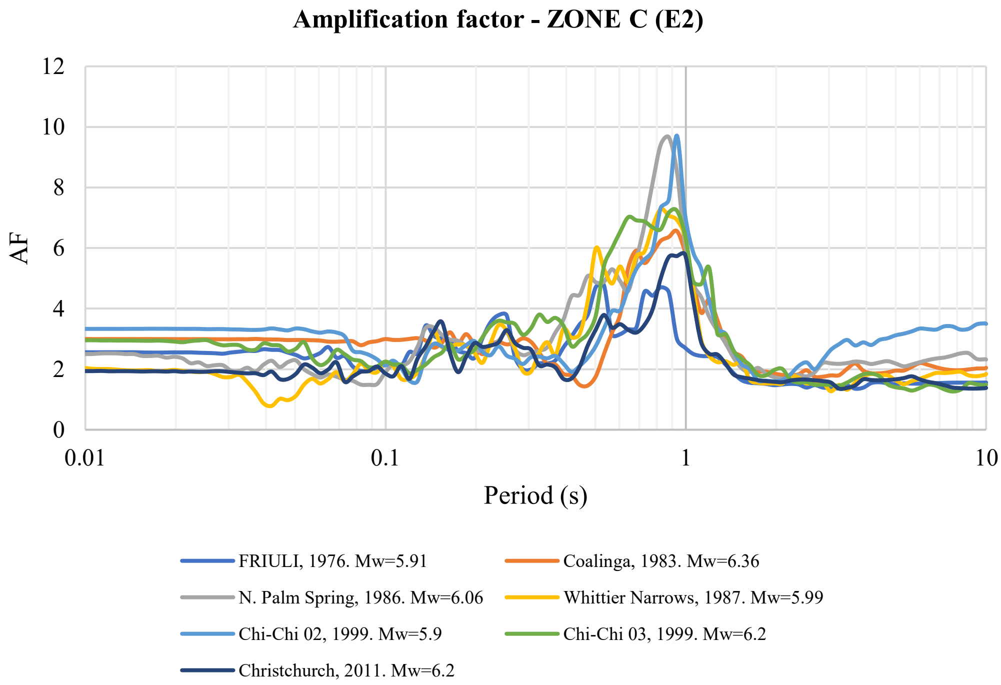

Figure 423. Amplification factor curves for remolded samples of Zone C

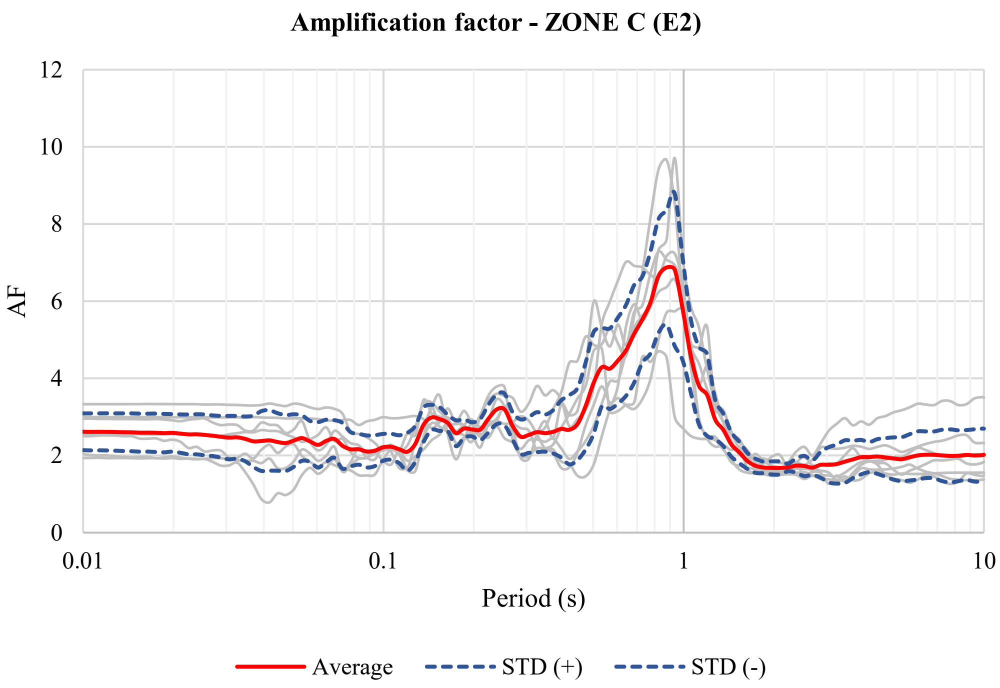

Figure 424. Amplification factor average curves for remolded samples of Zone C (Period)

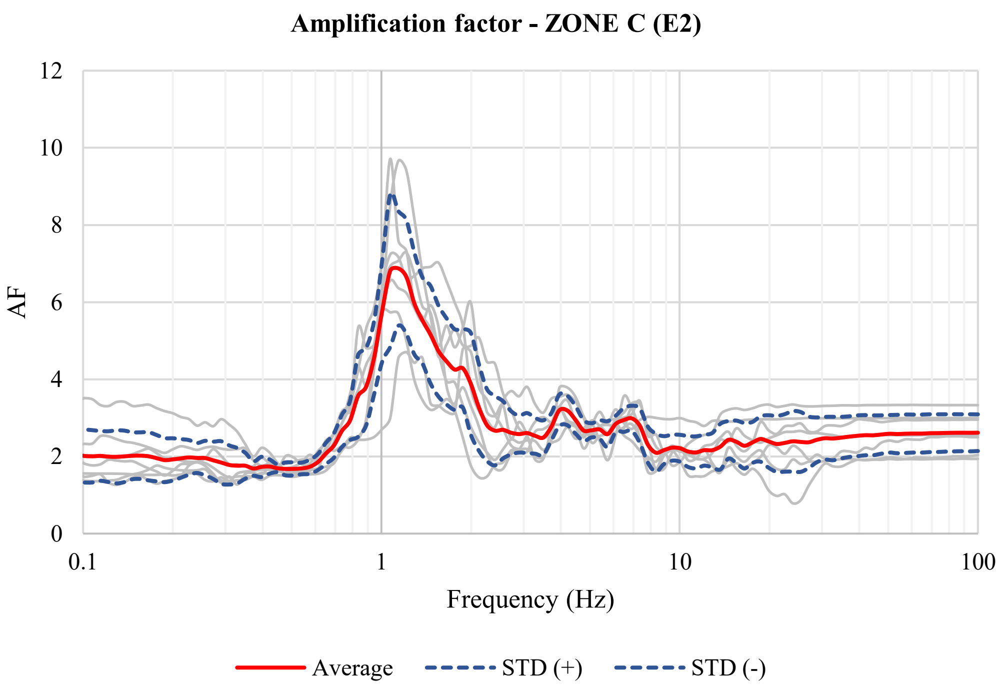

Figure 425. Amplification factor average curves for remolded samples of Zone C (Frequency)

Table 75. Maximun values of Amplification factor for remolded samples of Zone C

Zone C (E2)			
	Amplification factor	**T (s)**	**F (Hz)**
1	6.87	0.88	1.14
2	6.81	0.93	1.07
3	6.65	0.82	1.21

➢ Zone D

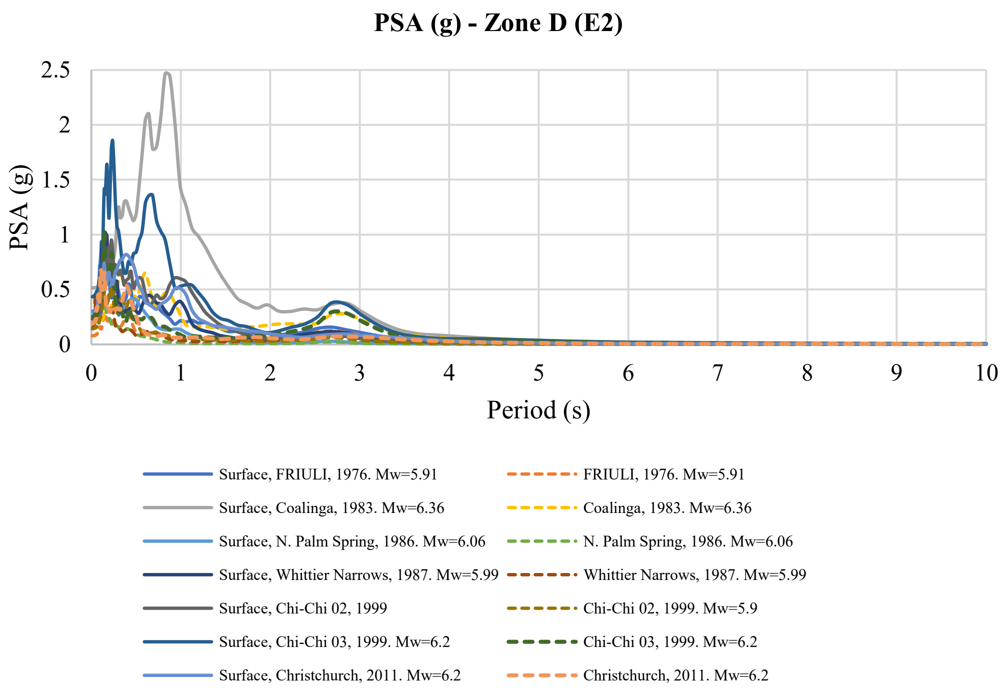

Figure 426. PSA (g) curves for remolded samples of Zone D

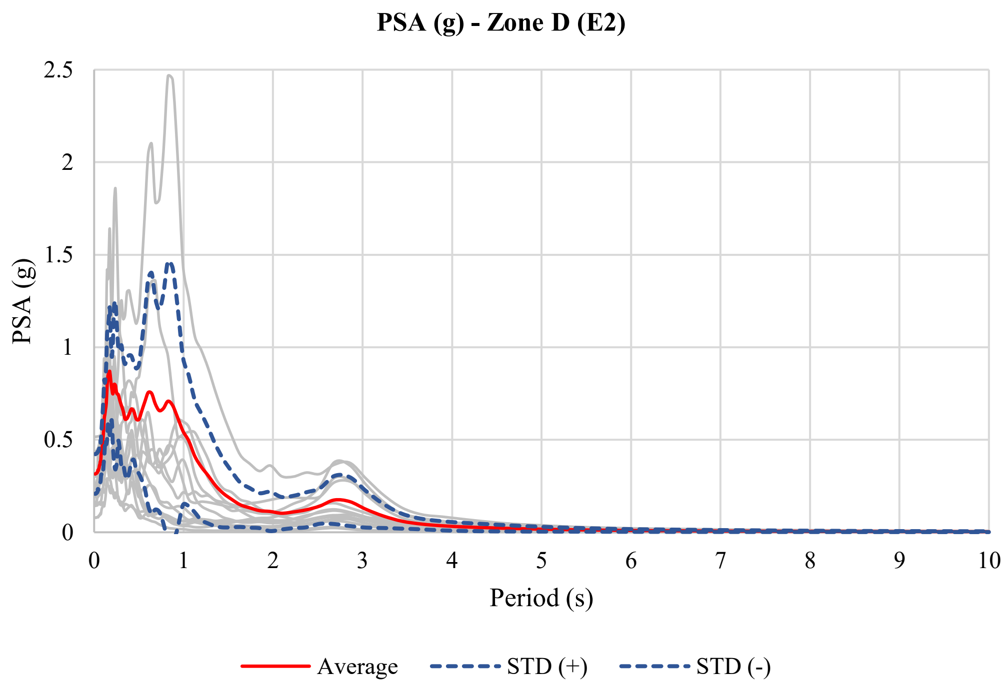

Figure 427. PSA (g) average curves for remolded samples of Zone D

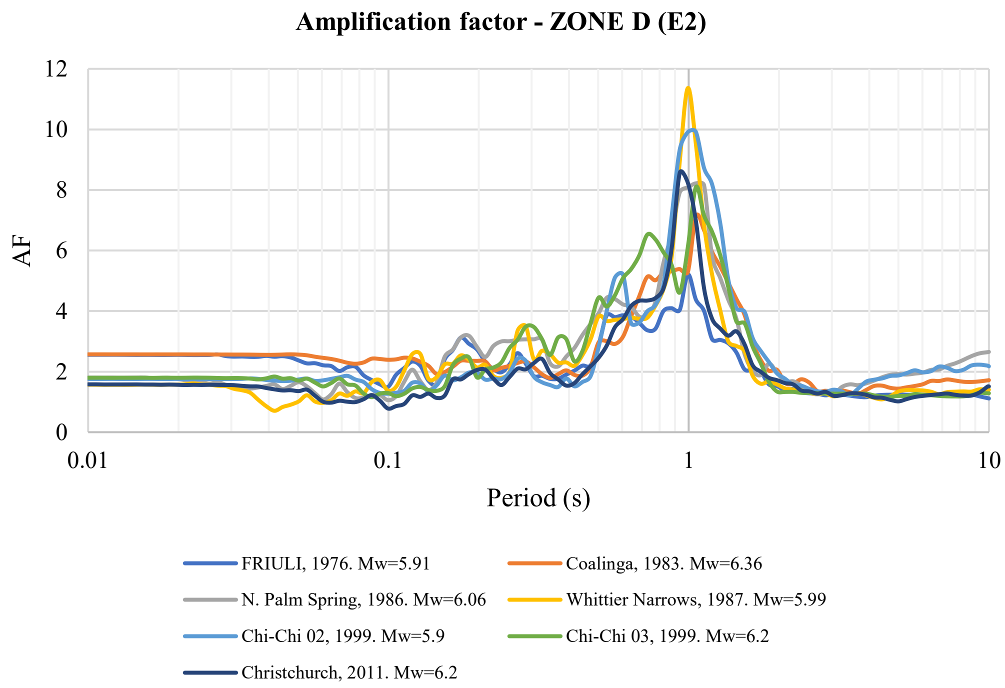

Figure 428. Amplification factor curves for remolded samples of Zone D

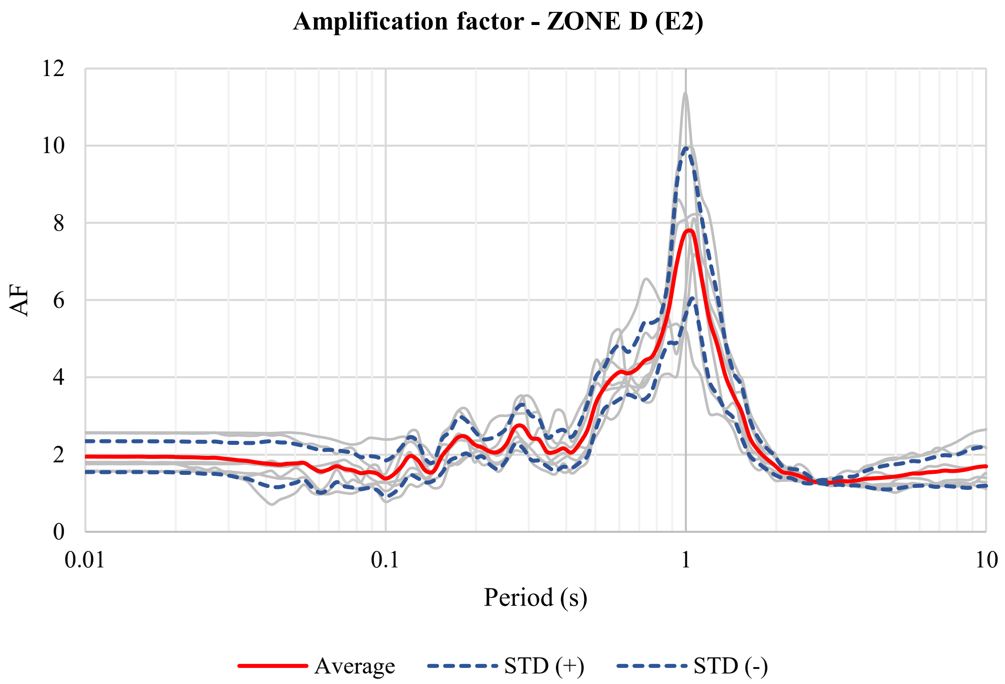

Figure 429. Amplification factor average curves for remolded samples of Zone D (Period)

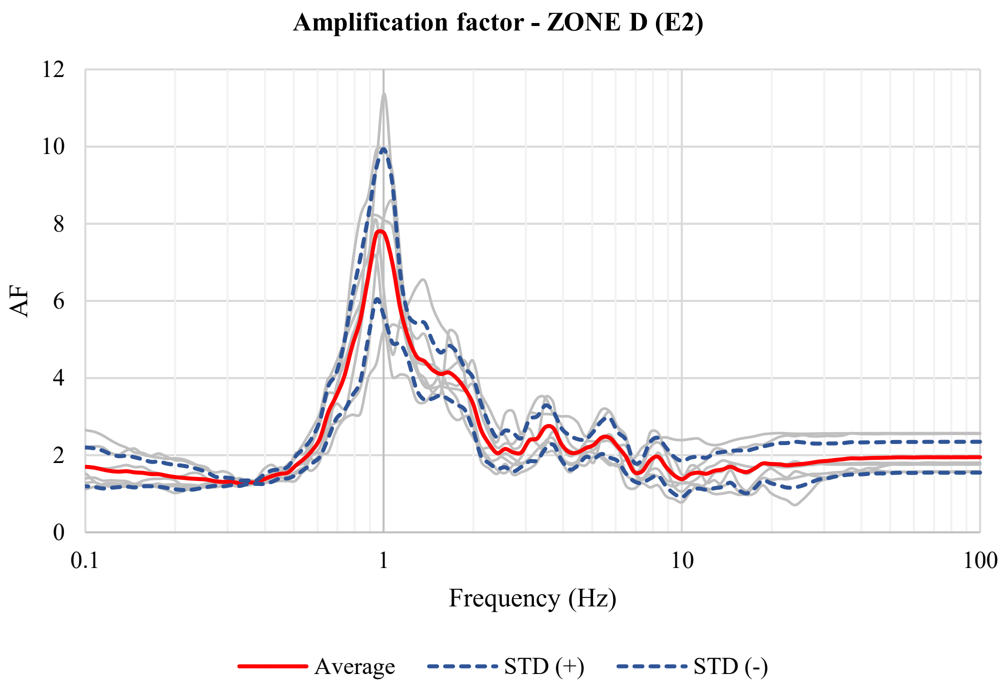

Figure 430. Amplification factor average curves for remolded samples of Zone D (Frequency)

Table 76. Maximun values of Amplification factor for remolded samples of Zone D

Zone D (E2)			
	Amplification factor	T (s)	F (Hz)
1	7.74	1.06	0.95
2	7.74	0.99	1.01
3	6.97	0.93	1.07

- Zone E

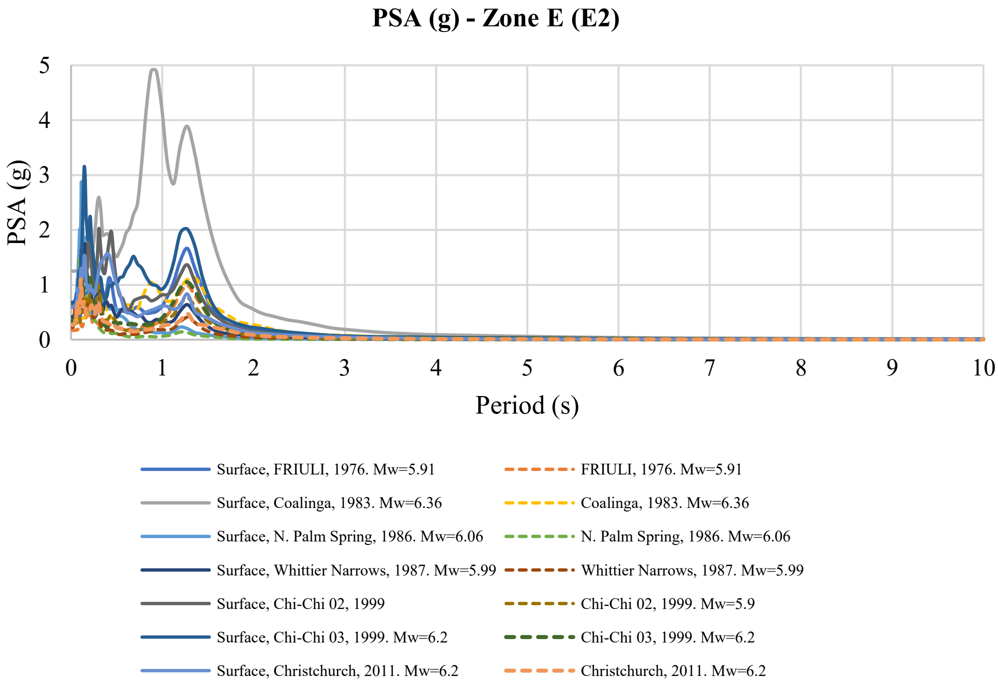

Figure 431. PSA (g) curves for remolded samples of Zone E

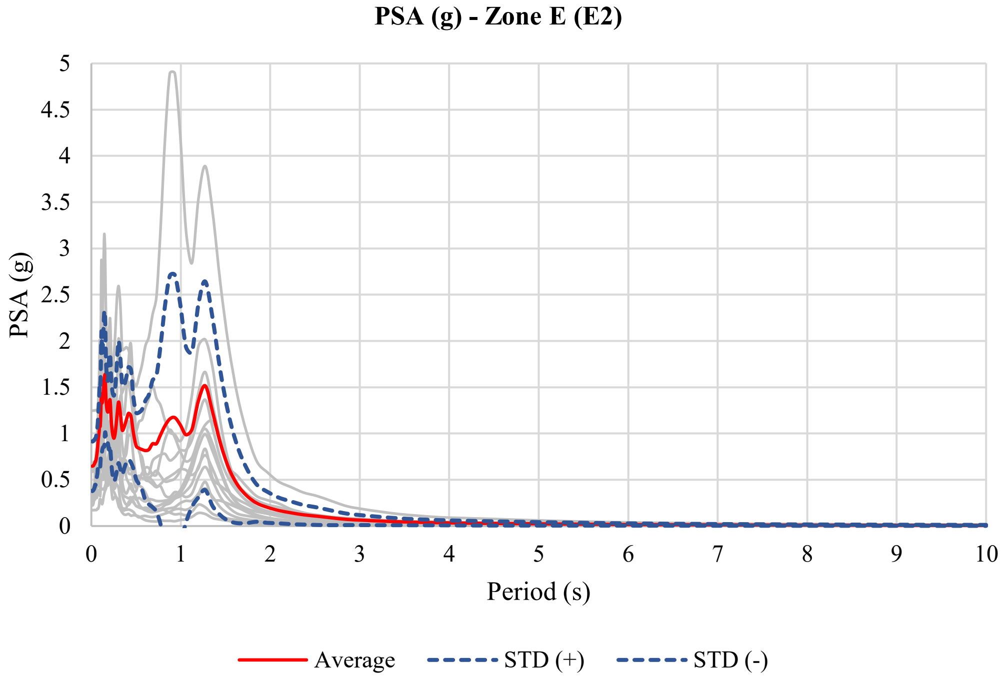

Figure 432. PSA (g) average curves for remolded samples of Zone E

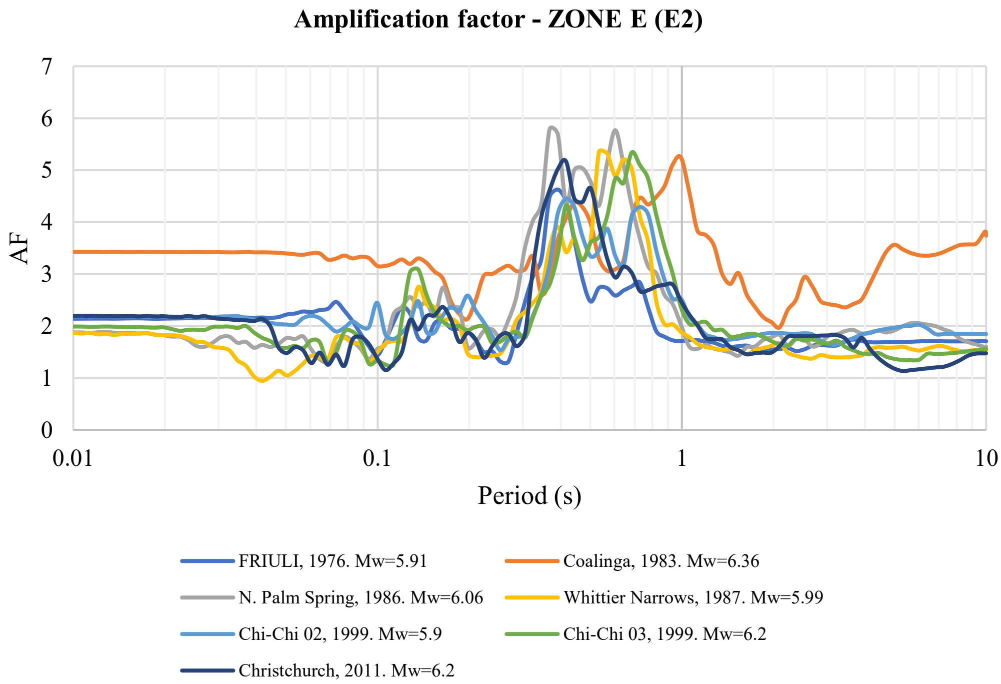

Figure 433. Amplification factor curves for remolded samples of Zone E

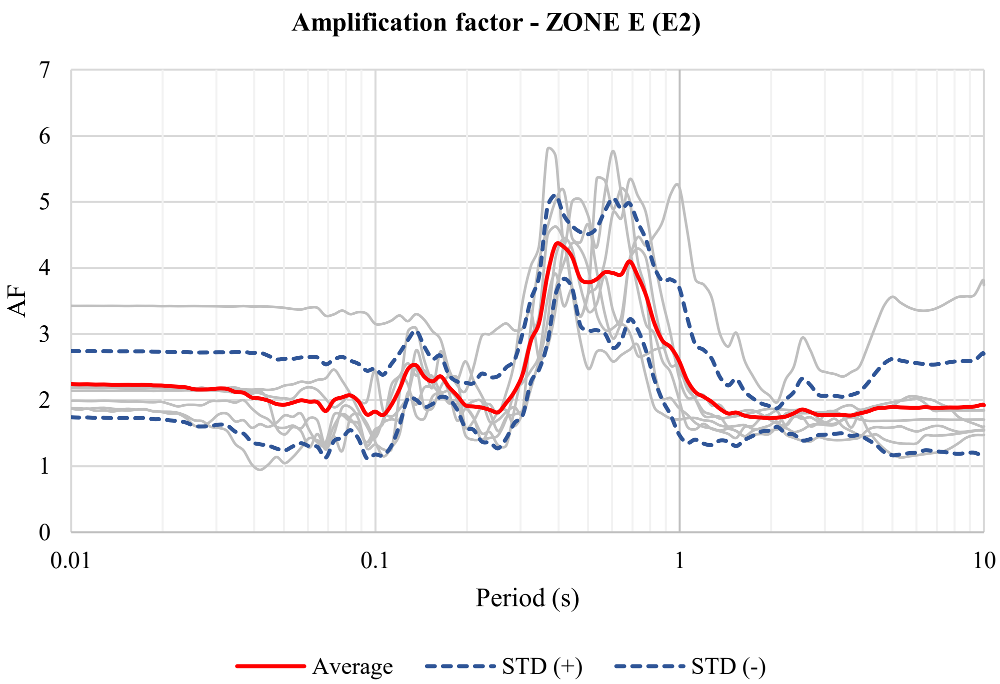

Figure 434. Amplification factor average curves for remolded samples of Zone E (Period)

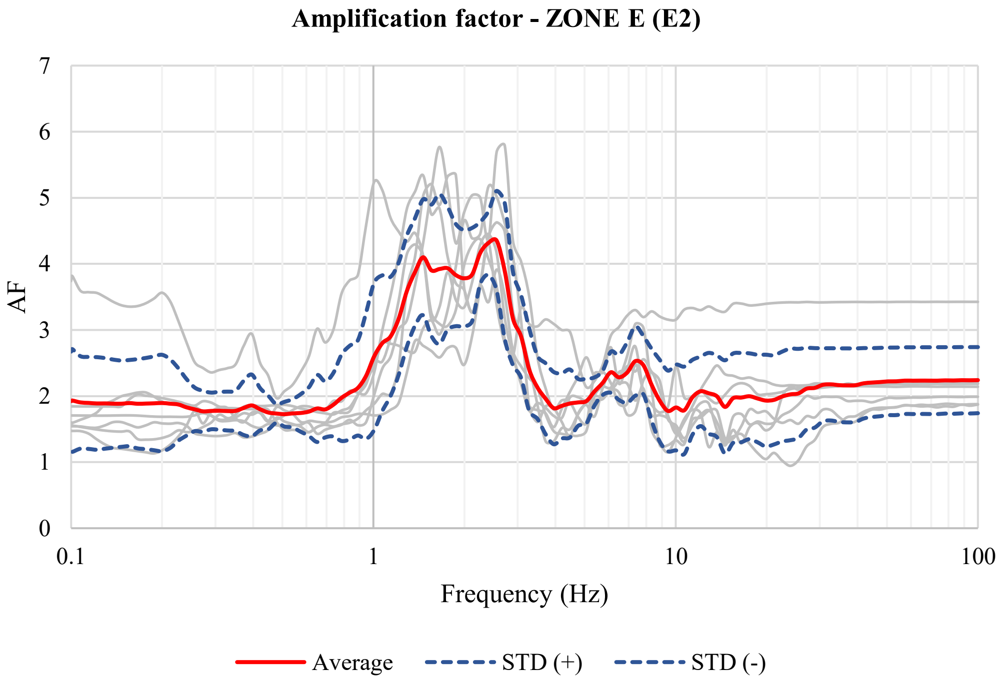

Figure 435. Amplification factor average curves for remolded samples of Zone E (Frequency)

Table 77. Maximun values of Amplification factor for remolded samples of Zone E

Zone E (E2)			
	Amplification factor	**T (s)**	**F (Hz)**
1	4.35	0.39	2.56
2	4.32	0.42	2.40
3	4.17	0.44	2.26

- Zone F

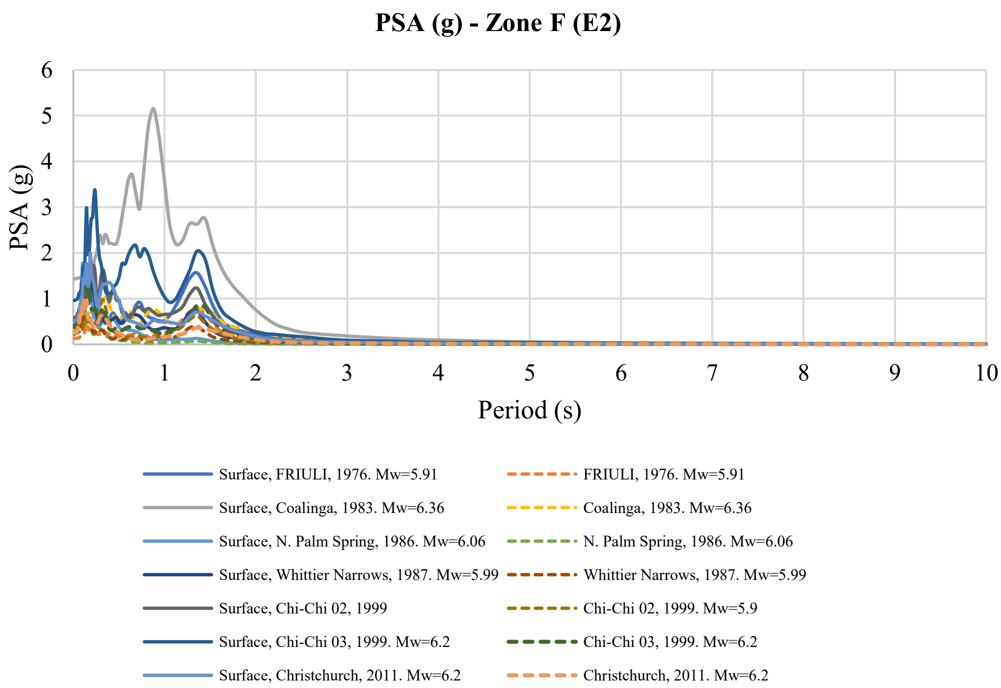

Figure 436. PSA (g) curves for remolded samples of Zone F

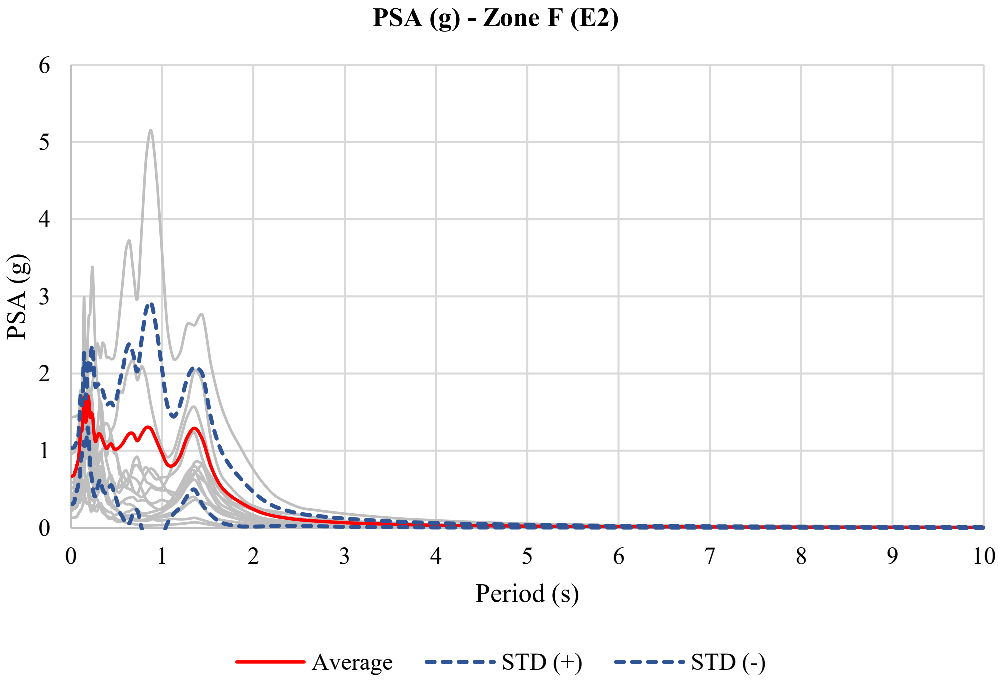

Figure 437. PSA (g) average curves for remolded samples of Zone F

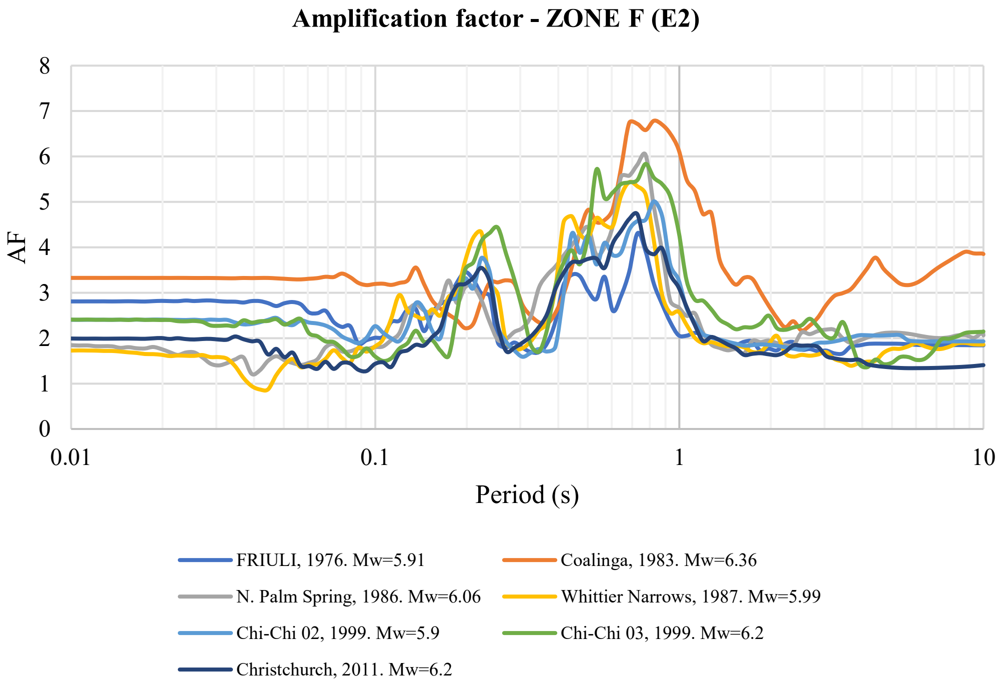

Figure 438. Amplification factor curves for remolded samples of Zone F

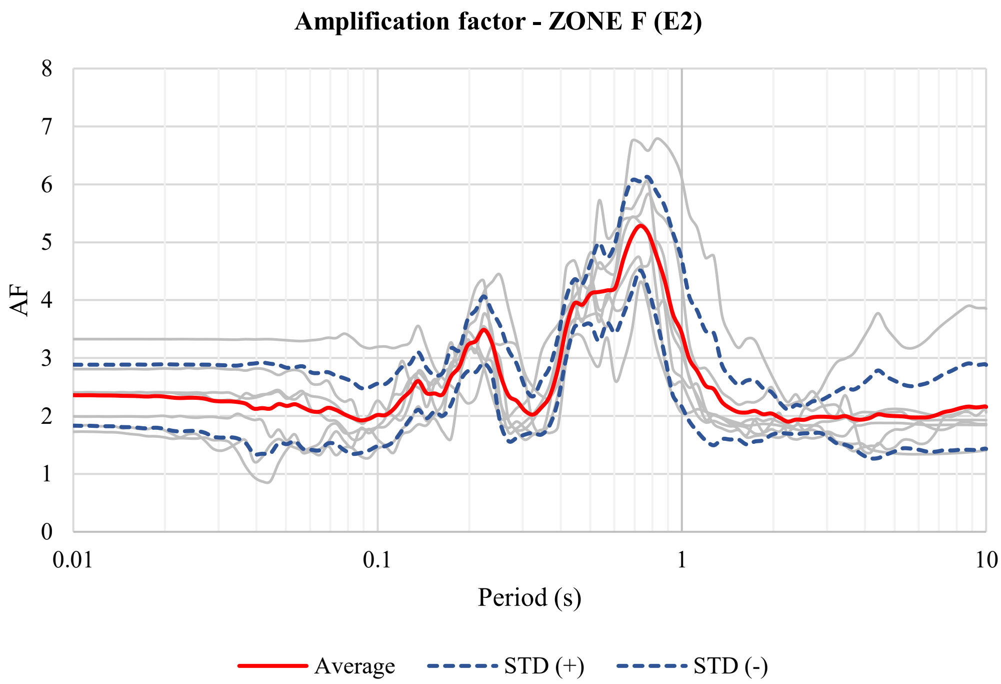

Figure 439. Amplification factor average curves for remolded samples of Zone F (Period)

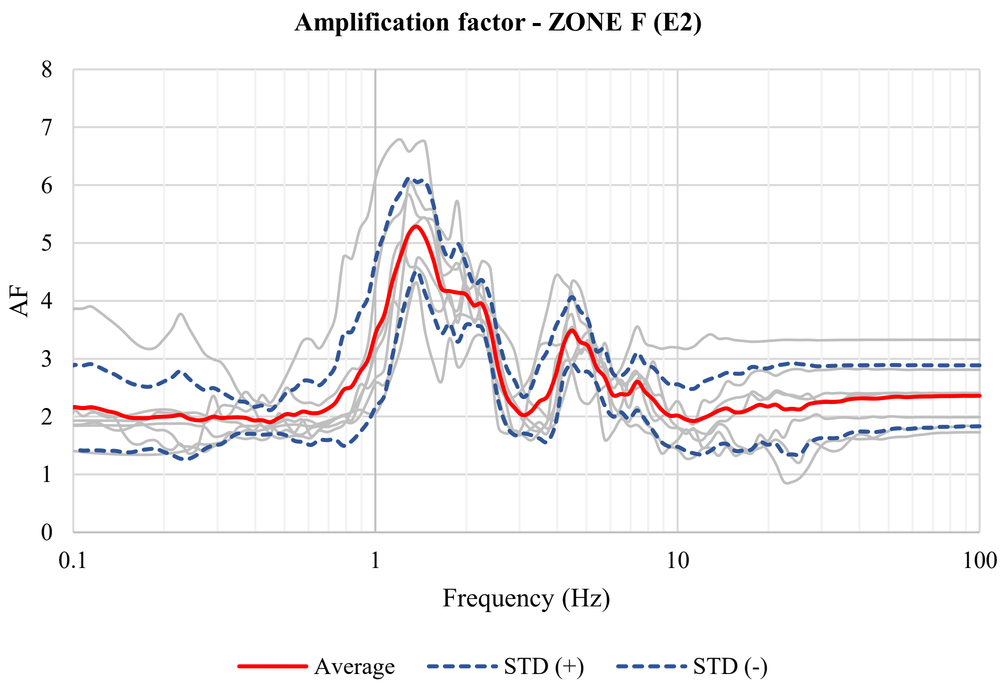

Figure 440. Amplification factor average curves for remolded samples of Zone F (Frequency)

Table 78. Maximun values of Amplification factor for remolded samples of Zone F

Zone F (E2)			
	Amplification factor	T (s)	F (Hz)
1	5.28	0.73	1.37
2	5.16	0.77	1.29
3	5.09	0.68	1.46

- Zone G

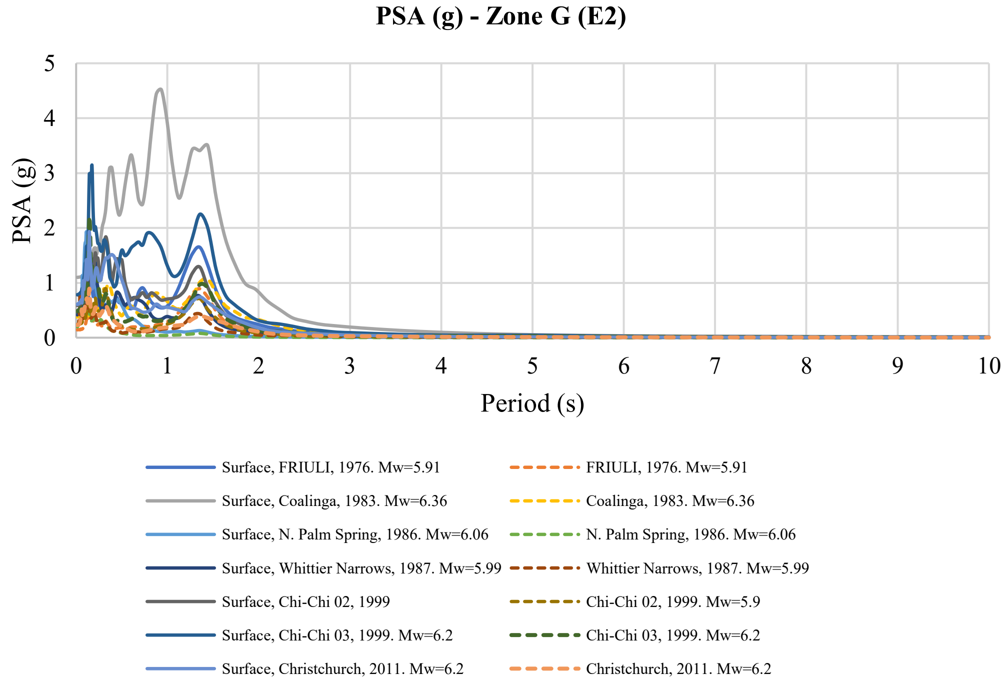

Figure 441. PSA (g) curves for remolded samples of Zone G

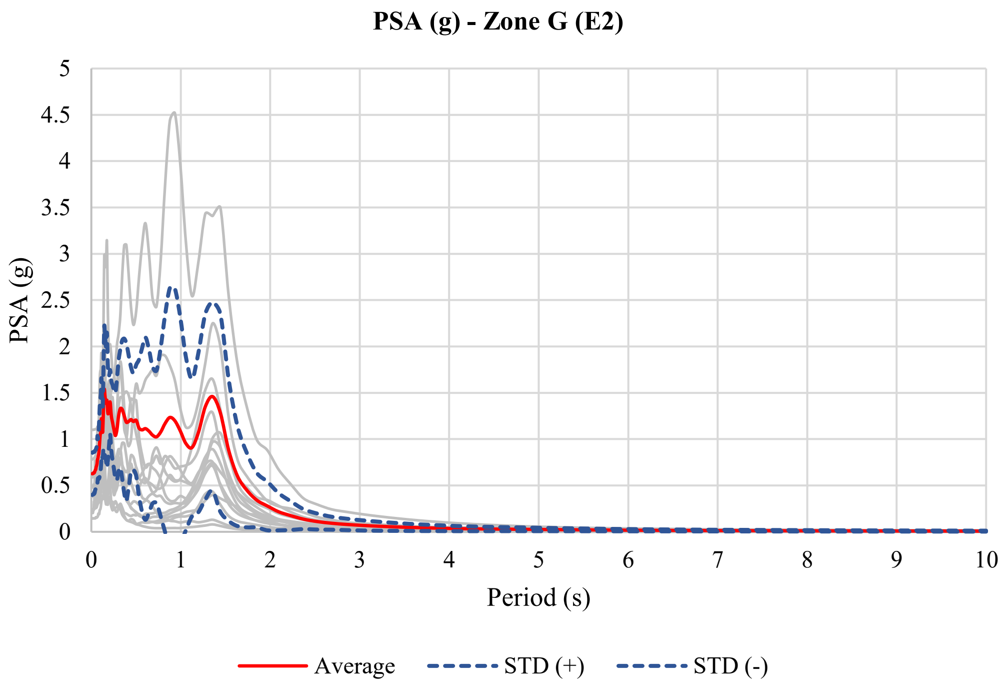

Figure 442. PSA (g) average curves for remolded samples of Zone G

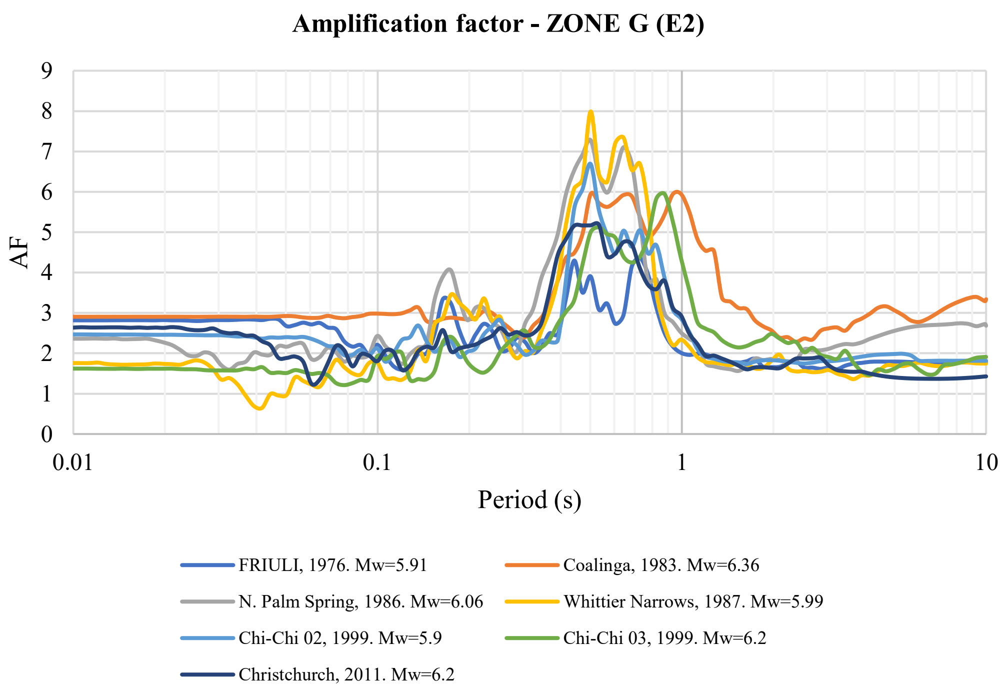

Figure 443. Amplification factor curves for remolded samples of Zone G

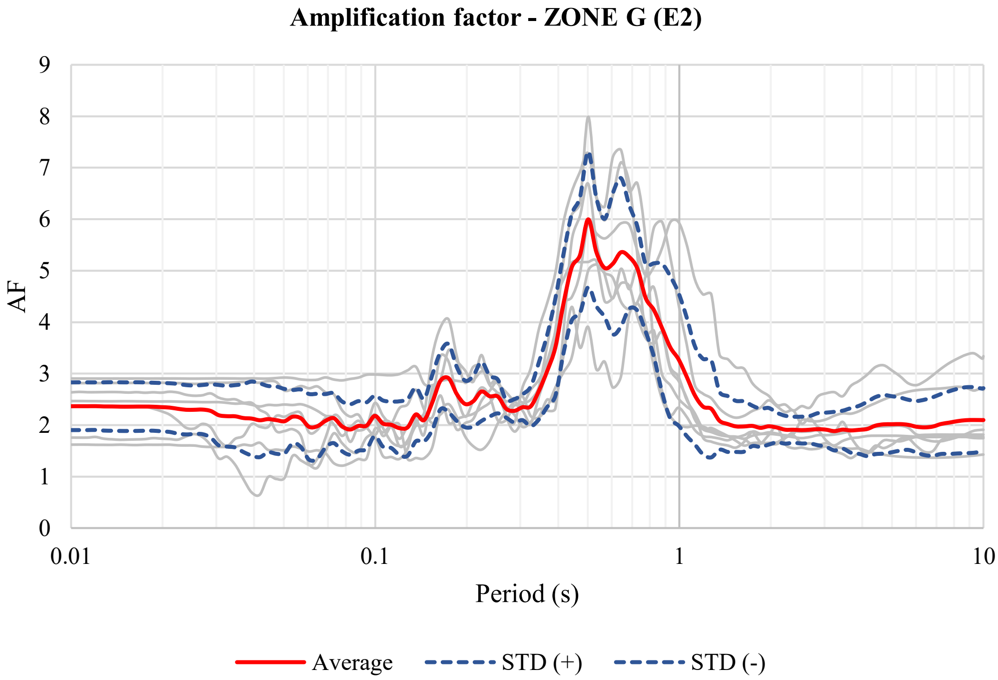

Figure 444. Amplification factor average curves for remolded samples of Zone G (Period)

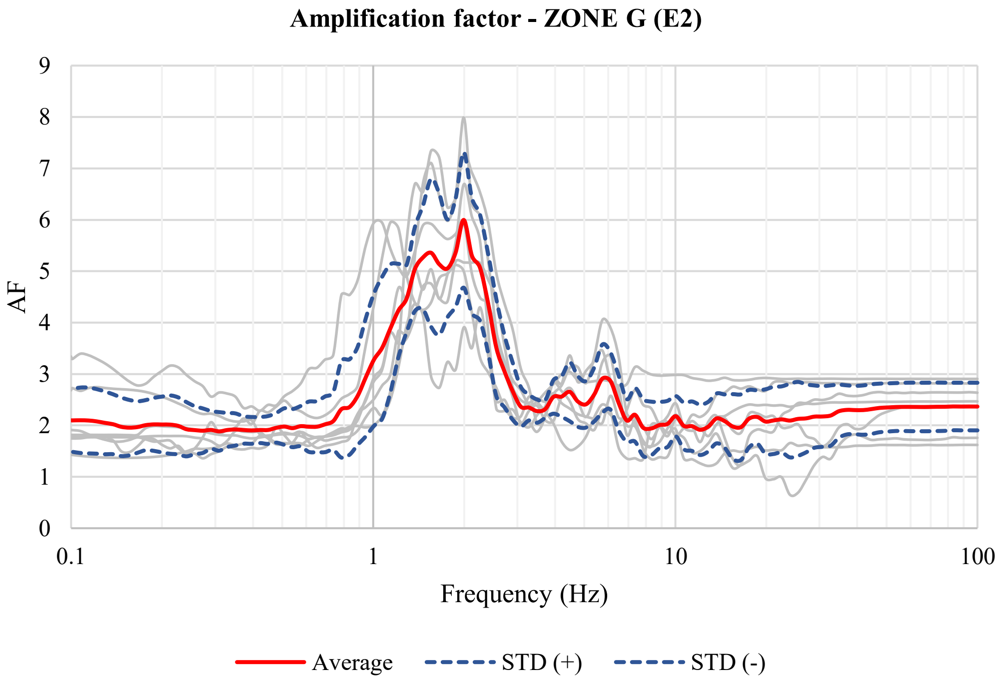

Figure 445. Amplification factor average curves for remolded samples of Zone G (Frequency)

Table 79. Maximun values of Amplification factor for remolded samples of Zone G

Zone G (E2)			
	Amplification factor	**T (s)**	**F (Hz)**
1	6.00	0.50	1.99
2	5.36	0.53	1.87
3	5.36	0.64	1.55

- Zone H

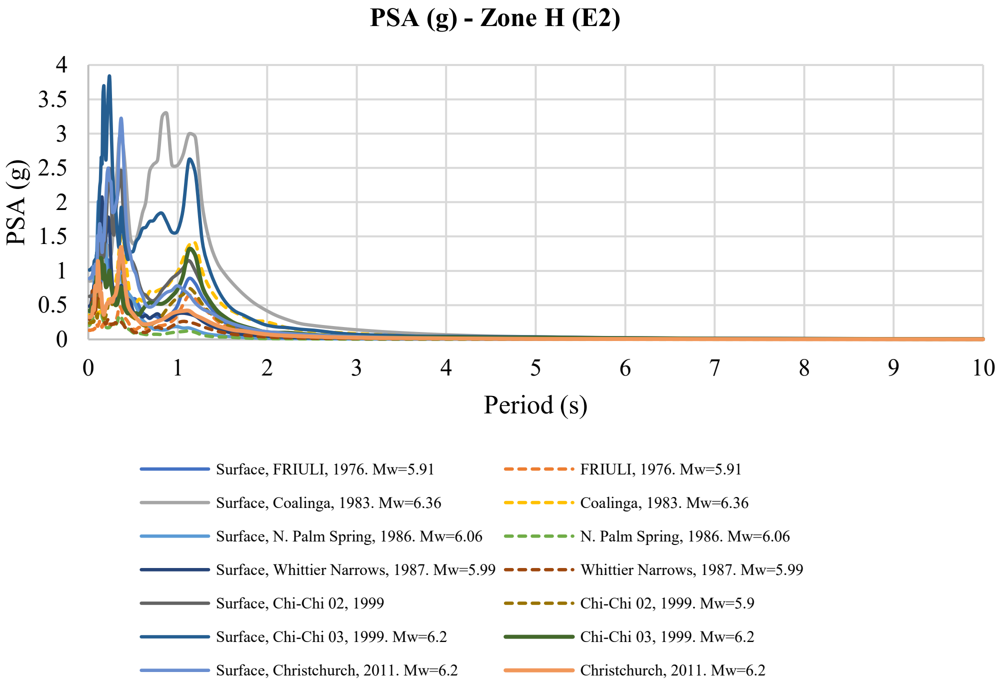

Figure 446. PSA (g) curves for remolded samples of Zone H

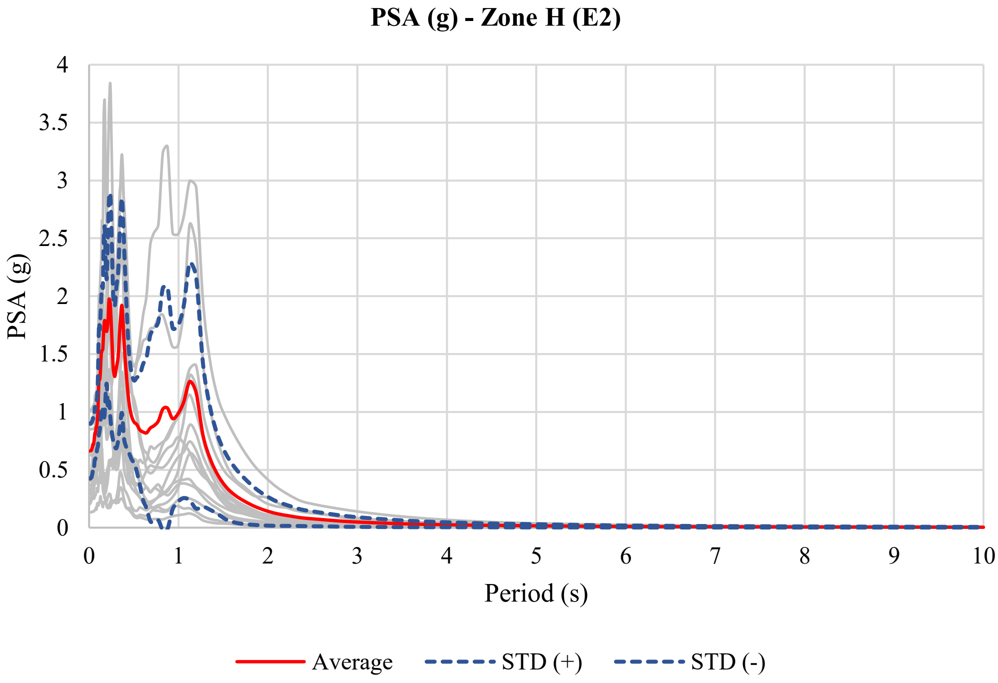

Figure 447. PSA (g) average curves for remolded samples of Zone H

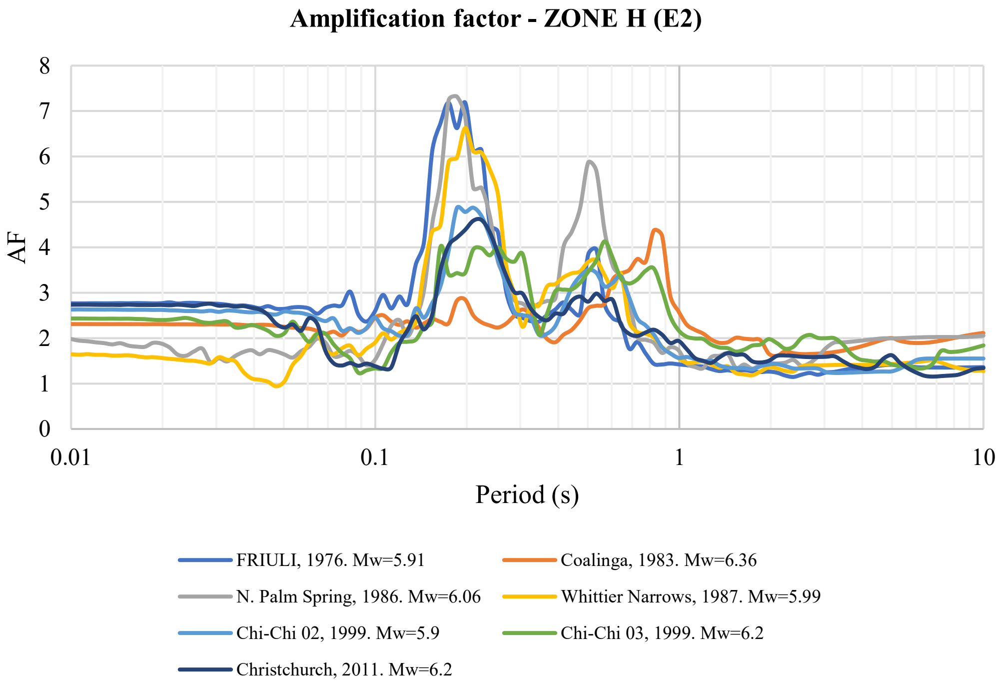

Figure 448. Amplification factor curves for remolded samples of Zone H

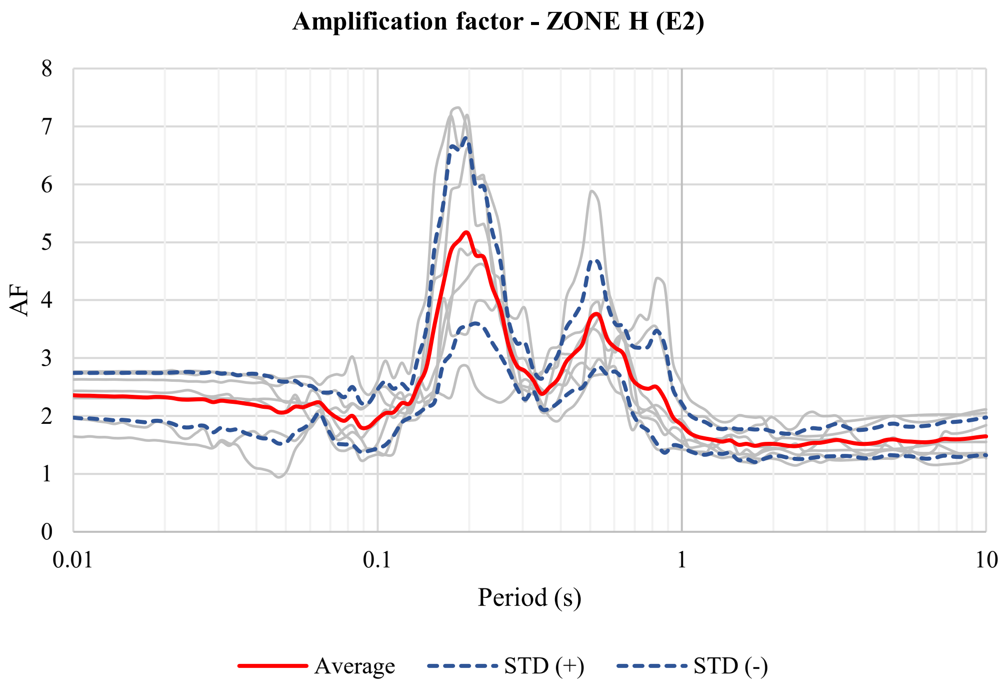

Figure 449. Amplification factor average curves for remolded samples of Zone H (Period)

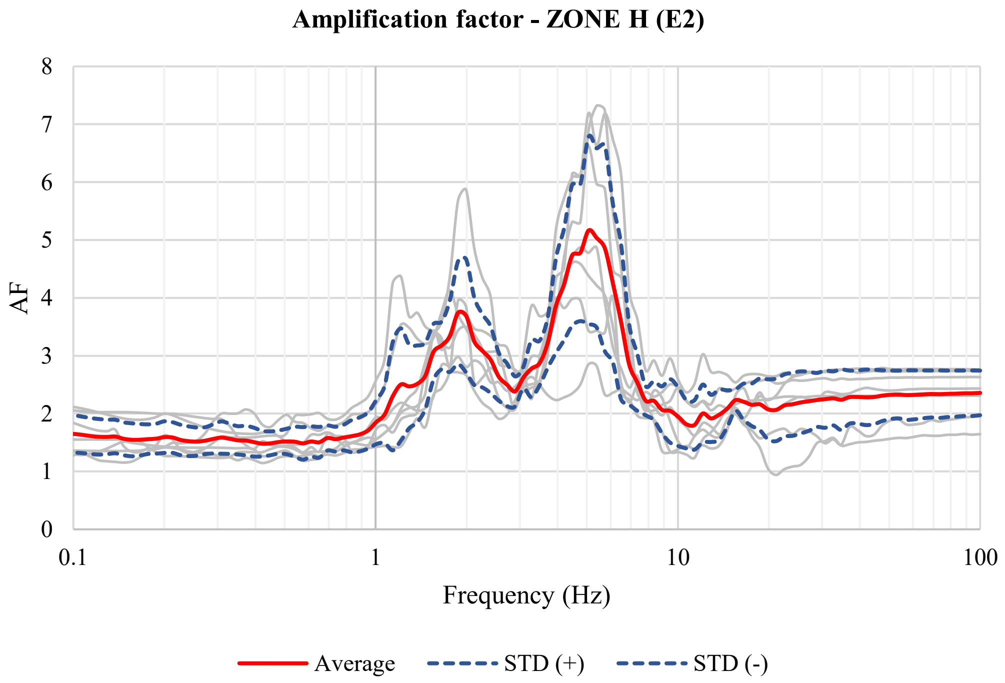

Figure 450. Amplification factor average curves for remolded samples of Zone H (Frequency)

Table 80. Maximun values of Amplification factor for remolded samples of Zone H

	Zone H (E2)		
	Amplification factor	T (s)	F (Hz)
1	5.16	0.20	5.06
2	5.04	0.19	5.39
3	4.86	0.17	5.73

- Zone I

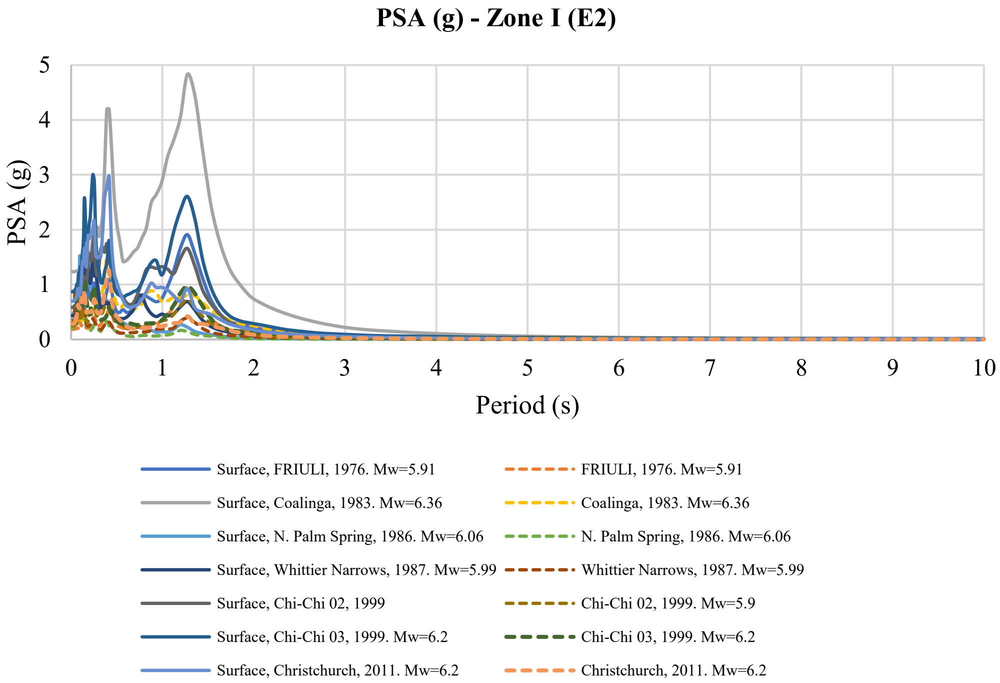

Figure 451. PSA (g) curves for remolded samples of Zone I

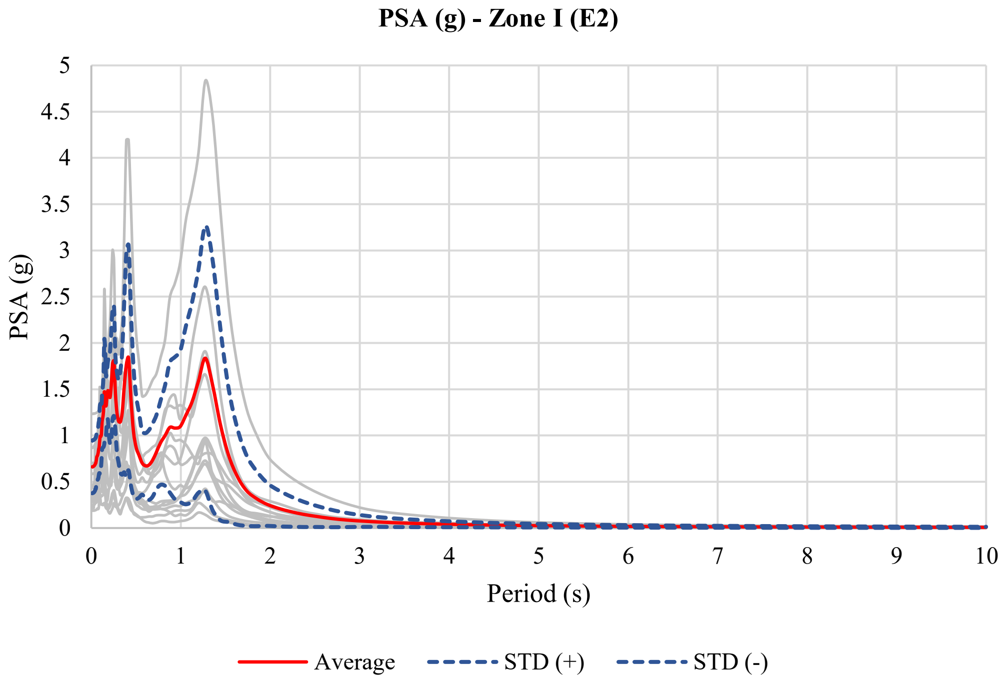

Figure 452. PSA (g) average curves for remolded samples of Zone I

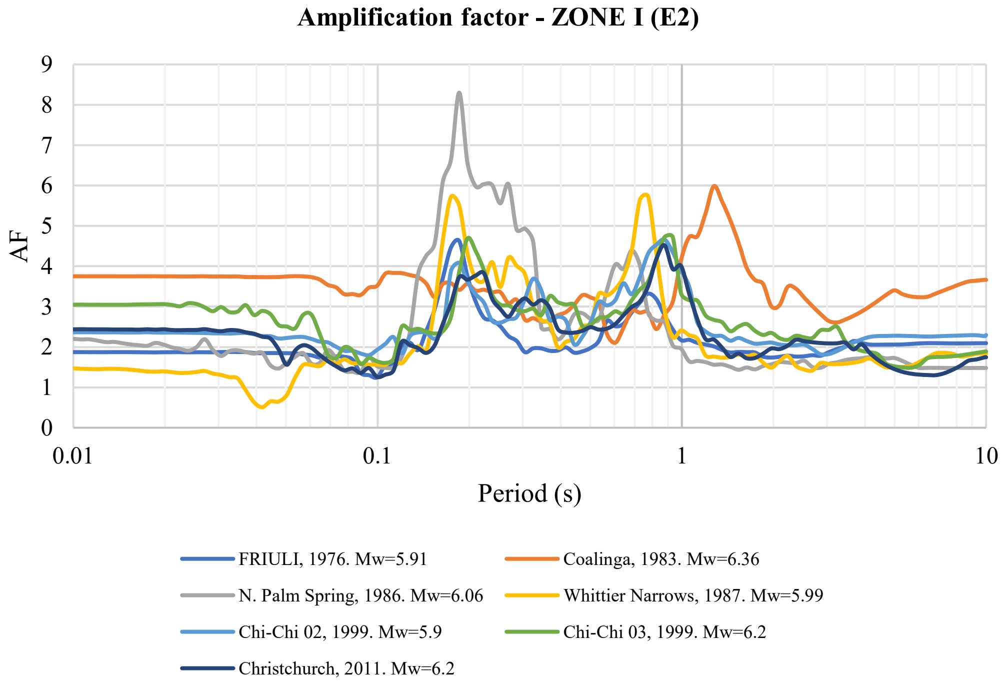

Figure 453. Amplification factor curves for remolded samples of Zone I

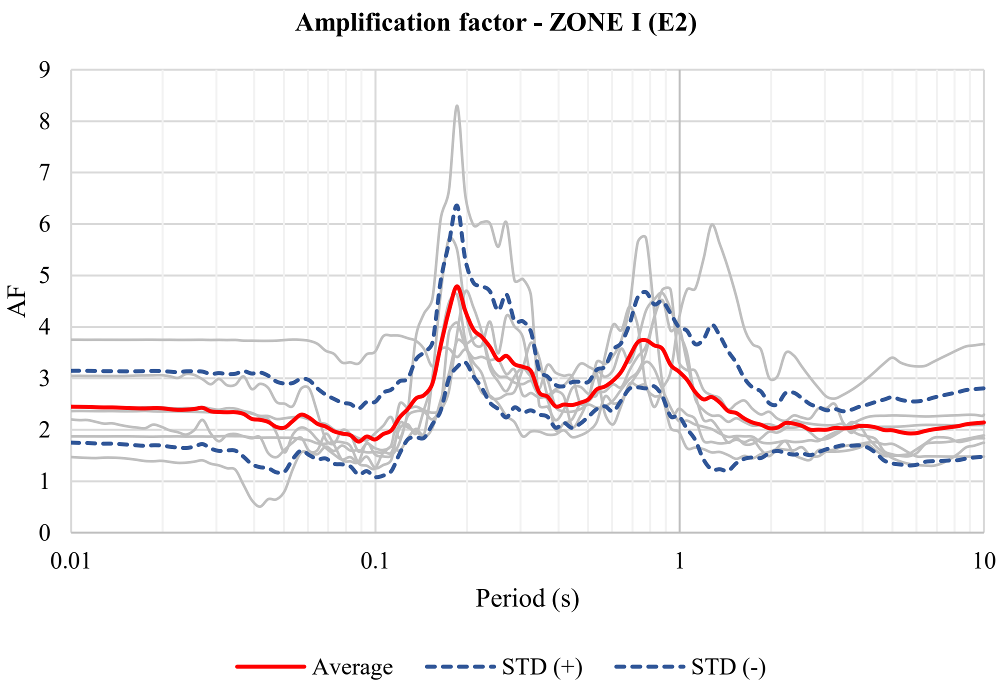

Figure 454. Amplification factor average curves for remolded samples of Zone I (Period)

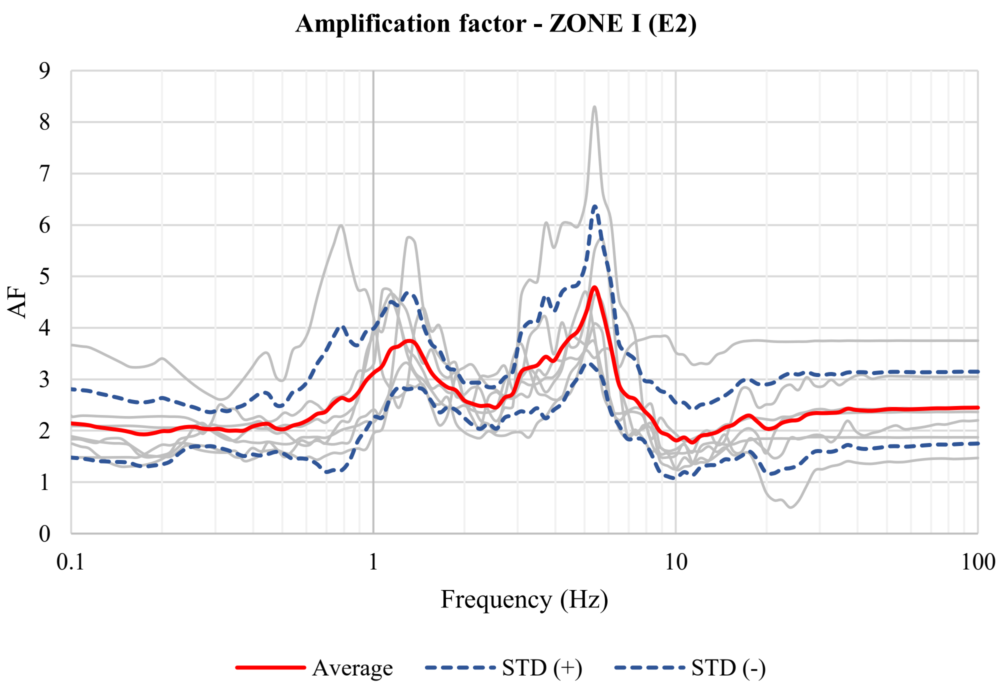

Figure 455. Amplification factor average curves for remolded samples of Zone I (Frequency)

Table 81. Maximun values of Amplification factor for remolded samples of Zone I

Zone I (E2)			
	Amplification factor	**T (s)**	**F (Hz)**
1	4.79	0.19	5.39
2	4.31	0.20	5.06
3	4.31	0.17	5.73

APPENDIX D – Generated Maps

D.1. Zoning Map of Southern Quito

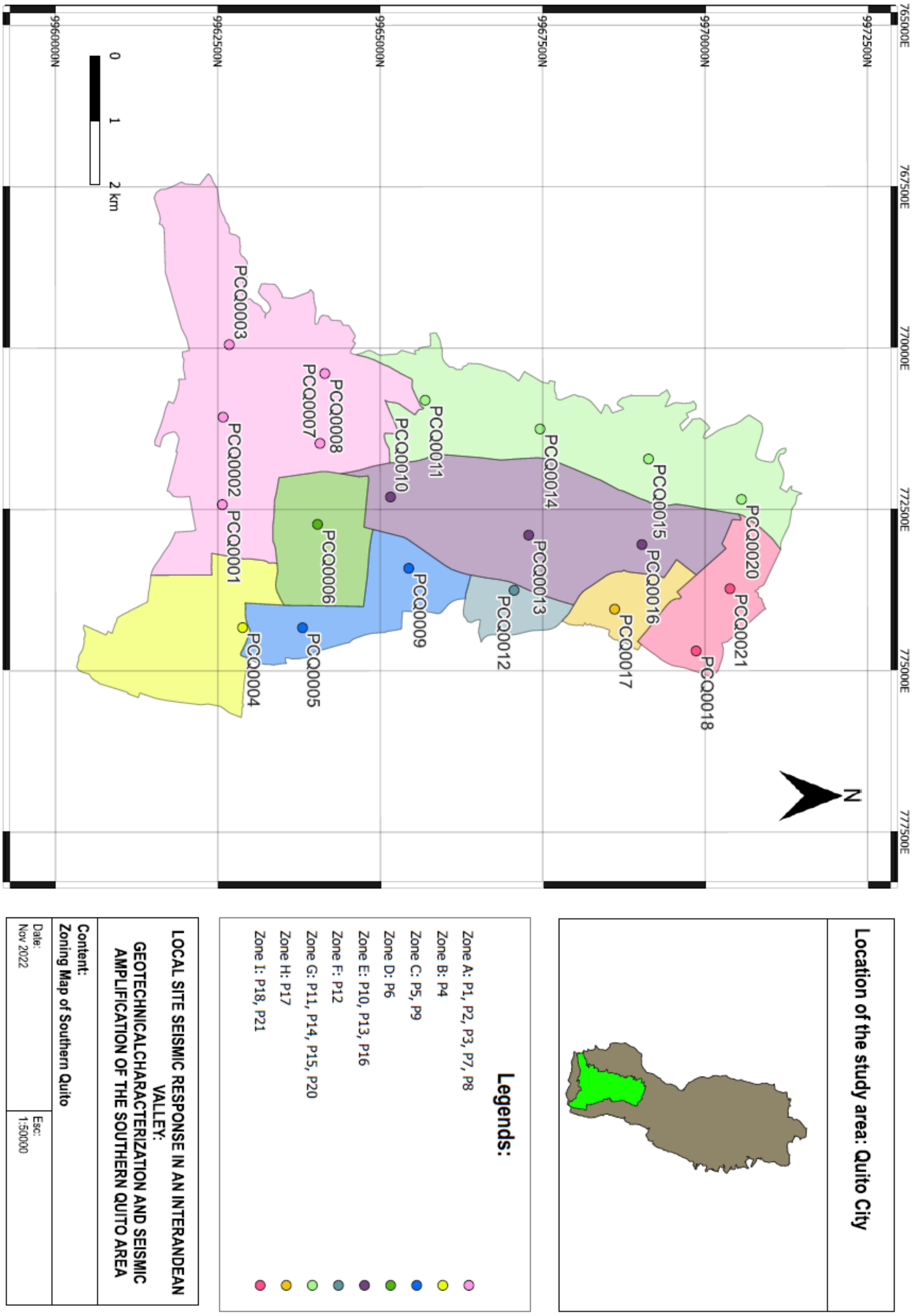

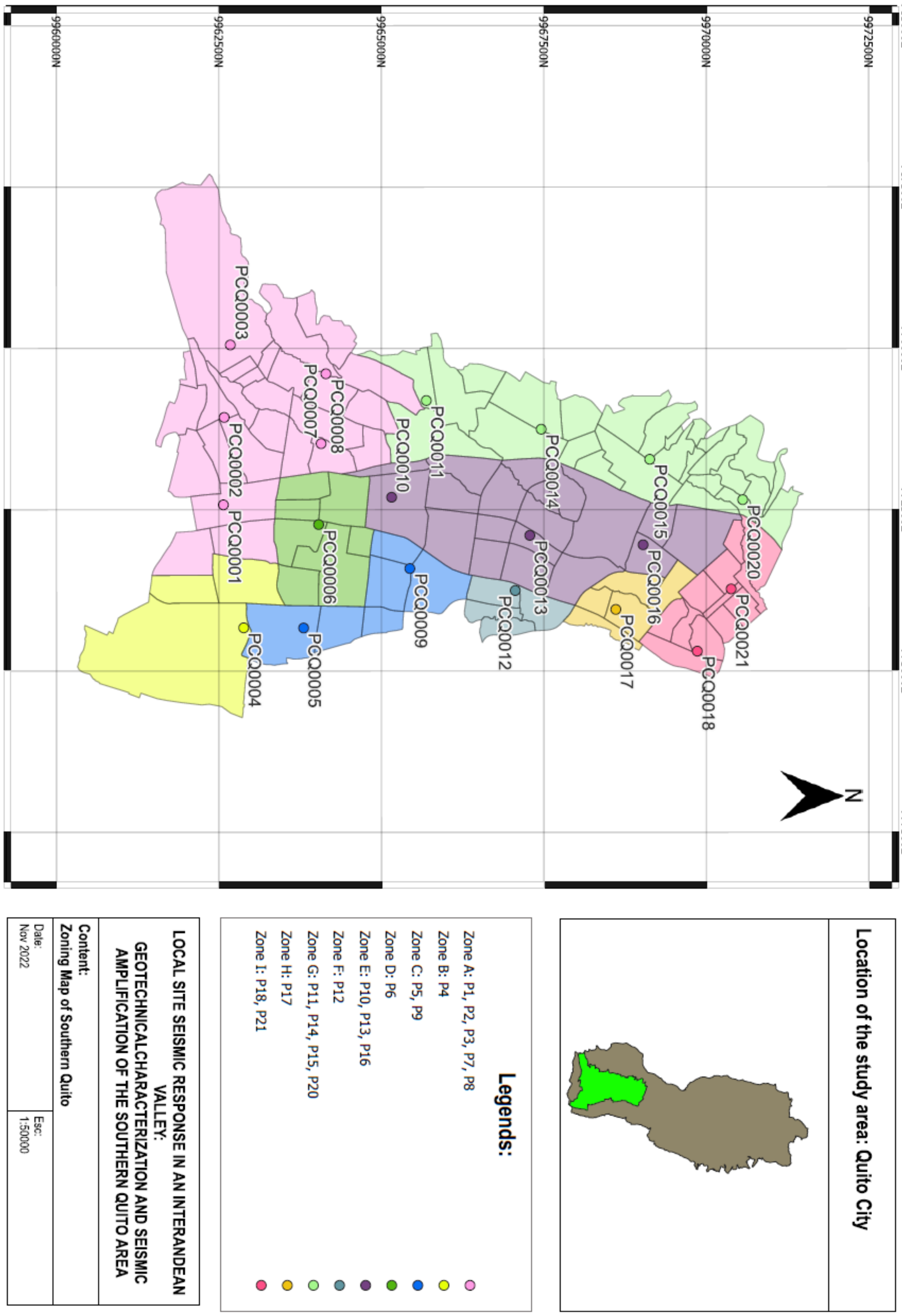
765000E
767500E
770000E
772500E
775000E
777500E
9960000N
9962500N
9965000N
9967500N
9970000N
9972500N
N
PCQ0001
PCQ0002
PCQ0003
PCQ0004
PCQ0005
PCQ0006
PCQ0007
PCQ0008
PCQ0009
PCQ0010
PCQ0011
PCQ0012
PCQ0013
PCQ0014
PCQ0015
PCQ0016
PCQ0017
PCQ0018
PCQ0020
PCQ0021
Location of the study area: Quito City
Legends:
Zone A: P1, P2, P3, P7, P8
Zone B: P4
Zone C: P5, P9
Zone D: P6
Zone E: P10, P13, P16
Zone F: P12
Zone G: P11, P14, P15, P20
Zone H: P17
Zone I: P18, P21
LOCAL SITE SEISMIC RESPONSE IN AN INTERANDEAN VALLEY:
GEOTECHNICALCHARACTERIZATION AND SEISMIC AMPLIFICATION OF THE SOUTHERN QUITO AREA
Content:
Zoning Map of Southern Quito
Date:
Nov 2022
Esc:
1:50000

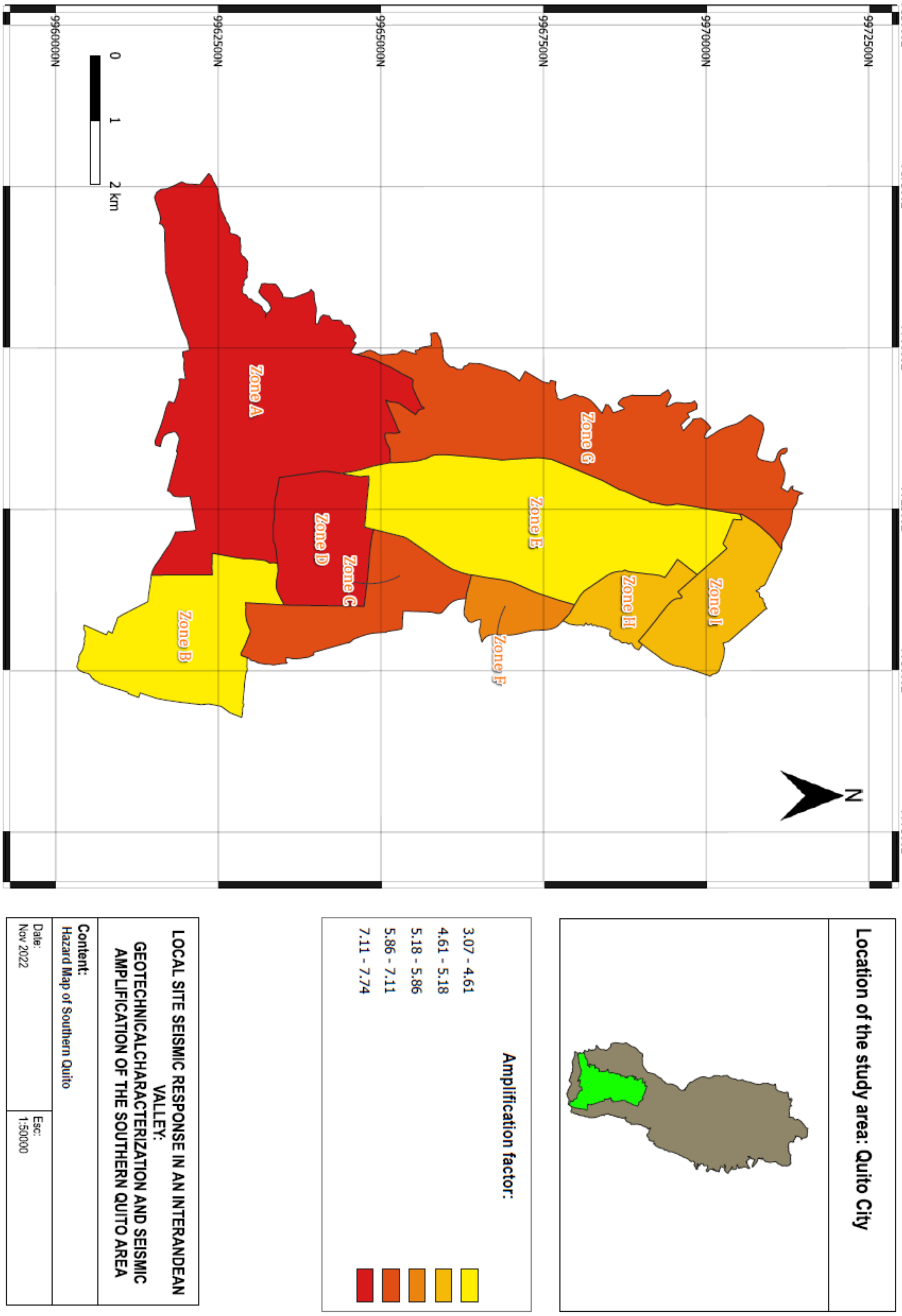
Zone A
Zone B
Zone C
Zone D
Zone E
Zone F
Zone G
Zone H
Zone I
0 1 2 km
N
765000E
767500E
770000E
772500E
775000E
777500E
9960000N
9962500N
9965000N
9967500N
9970000N
9972500N
Location of the study area: Quito City
Amplification factor:
3.07 - 4.61
4.61 - 5.18
5.18 - 5.86
5.86 - 7.11
7.11 - 7.74
LOCAL SITE SEISMIC RESPONSE IN AN INTERANDEAN VALLEY:
GEOTECHNICALCHARACTERIZATION AND SEISMIC AMPLIFICATION OF THE SOUTHERN QUITO AREA
Content:
Hazard Map of Southern Quito
Date:
Nov 2022
Esc:
1:50000

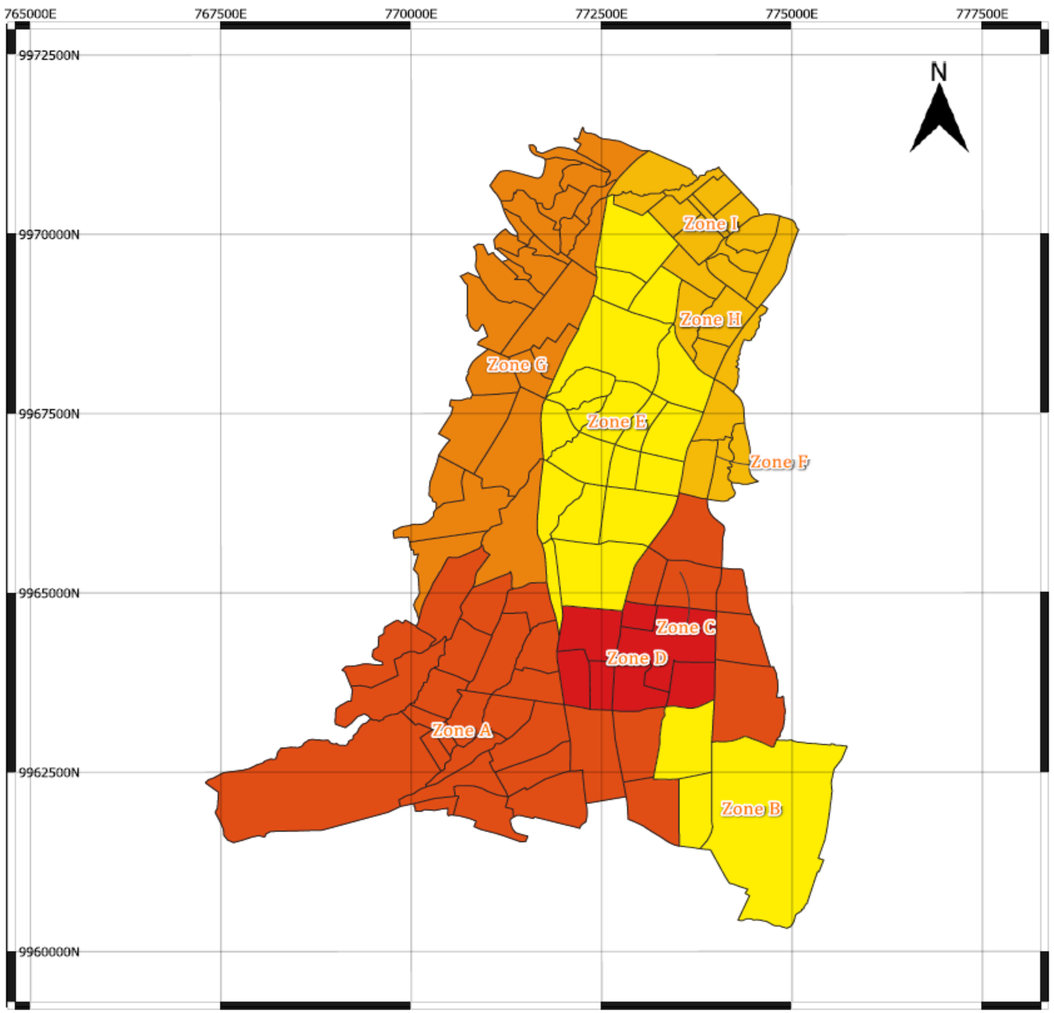

Location of the study area: Quito City

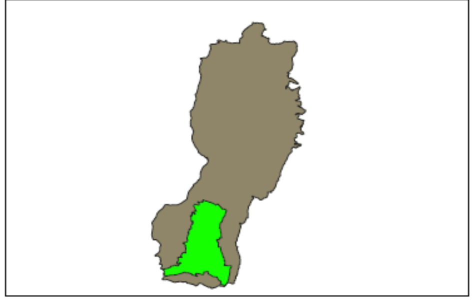

Amplification factor:

3.07 - 4.61	
4.61 - 5.18	
5.18 - 5.86	
5.86 - 7.11	
7.11 - 7.74	

LOCAL SITE SEISMIC RESPONSE IN AN INTERANDEAN VALLEY: GEOTECHNICALCHARACTERIZATION AND SEISMIC AMPLIFICATION OF THE SOUTHERN QUITO AREA

Content:
Hazard Map of Southern Quito

Date:	Esc:
Nov 2022	1:50000

APPENDIX E – List of equations